ΕΘΝΙΚΟ ΜΕΤΣΟΒΙΟ ΠΟΛΥΤΕΧΝΕΙΟ
ΣΧΟΛΗ ΠΟΛΙΤΙΚΩΝ ΜΗΧΑΝΙΚΩΝ
ΤΟΜΕΑΣ ΓΕΩΤΕΧΝΙΚΗΣ

NATIONAL TECHNICAL UNIVERSITY OF ATHENS
SCHOOL OF CIVIL ENGINEERING
GEOTECHNICAL DEPARTMENT

Διδακτορική Διατριβή

PhD Thesis

ΑΛΛΗΛΕΠΙΔΡΑΣΗ ΕΔΑΦΟΥΣ-ΚΑΤΑΣΚΕΥΗΣ ΥΠΟ ΚΑΘΕΣΤΩΣ ΡΕΥΣΤΟΠΟΙΗΣΗΣ: ΕΠΙΔΡΑΣΗ ΣΤΗΝ ΚΑΘΙΖΗΣΗ ΕΠΙΦΑΝΕΙΑΚΩΝ ΘΕΜΕΛΙΩΣΕΩΝ

SOIL-STRUCTURE INTERACTION IN LIQUEFIABLE SOILS: EFFECT ON SETTLEMENTS OF SHALLOW FOUNDATIONS

Κωνσταντίνος Μπαζαίος
Πολιτικός Μηχανικός

Konstantinos Bazaios
Civil Engineer

Επιβλέπων:
Γεώργιος Μπουκοβάλας
Καθηγητής ΕΜΠ

Supervisor:
George Bouckovalas
NTUA Professor

Αθήνα, Μάρτιος 2022 / Athens, March 2022

ΕΘΝΙΚΟ ΜΕΤΣΟΒΙΟ ΠΟΛΥΤΕΧΝΕΙΟ

ΣΧΟΛΗ ΠΟΛΙΤΙΚΩΝ ΜΗΧΑΝΙΚΩΝ - ΤΟΜΕΑΣ ΓΕΩΤΕΧΝΙΚΗΣ

ΑΛΛΗΛΕΠΙΔΡΑΣΗ ΕΔΑΦΟΥΣ-ΚΑΤΑΣΚΕΥΗΣ ΥΠΟ ΚΑΘΕΣΤΩΣ ΡΕΥΣΤΟΠΟΙΗΣΗΣ: ΕΠΙΔΡΑΣΗ ΣΤΗΝ ΚΑΘΙΖΗΣΗ ΕΠΙΦΑΝΕΙΑΚΩΝ ΘΕΜΕΛΙΩΣΕΩΝ

ΔΙΔΑΚΤΟΡΙΚΗ ΔΙΑΤΡΙΒΗ

Κωνσταντίνου Ν. Μπαζαίου

Διπλωματούχος Πολιτικός Μηχανικός Πανεπιστημίου Πατρών,

M.Sc. TU Delft

ΤΡΙΜΕΛΗΣ ΣΥΜΒΟΥΛΕΥΤΙΚΗ ΕΠΙΤΡΟΠΗ

Γ. ΜΠΟΥΚΟΒΑΛΑΣ, Καθηγητής Ε.Μ.Π. (Επιβλέπων)

Α.ΠΑΠΑΔΗΜΗΤΡΙΟΥ, Αν. Καθηγητής Ε.Μ.Π.

Ν.ΓΕΡΟΛΥΜΟΣ, Αν. Καθηγητής Ε.Μ.Π.

ΕΠΤΑΜΕΛΗΣ ΕΞΕΤΑΣΤΙΚΗ ΕΠΙΤΡΟΠΗ

Γ. ΜΠΟΥΚΟΒΑΛΑΣ, Καθηγητής Ε.Μ.Π. (Επιβλέπων)

Α.ΠΑΠΑΔΗΜΗΤΡΙΟΥ, Αν. Καθηγητής Ε.Μ.Π.

Ν.ΓΕΡΟΛΥΜΟΣ, Αν. Καθηγητής Ε.Μ.Π.

Χ.ΓΑΝΤΕΣ, Καθηγητής Ε.Μ.Π.

Π.ΝΤΑΚΟΥΛΑΣ, Καθηγητής Παν. Θεσσαλίας

Χ.ΜΟΥΖΑΚΗΣ, Αν. Καθηγητής Ε.Μ.Π.

Δ.ΛΟΥΚΙΔΗΣ, Αν. Καθηγητής Παν. Κύπρου

Αθήνα, Μάρτιος 2022

NATIONAL TECHNICAL UNIVERSITY OF ATHENS
SCHOOL OF CIVIL ENGINEERING - GEOTECHNICAL DEPARTMENT

SOIL-STRUCTURE INTERACTION IN LIQUEFIABLE SOILS: EFFECT ON SETTLEMENTS OF SHALLOW FOUNDATIONS

DOCTORAL THESIS

Konstantinos N. Bazaios

Civil Engineer, University of Patras

M.Sc. TU Delft

ADVISORY COMMITTEE:

G.BOUCKOVALAS, Professor N.T.U.A. (Supervisor)

A.PAPADIMITRIOU, Assoc. Professor N.T.U.A.

N.GEROLYMOS, Assoc. Professor N.T.U.A.

EXAMINATION COMMITTEE:

G.BOUCKOVALAS, Professor N.T.U.A. (Supervisor)

A.PAPADIMITRIOU, Assoc. Professor N.T.U.A.

N.GEROLYMOS, Assoc. Professor N.T.U.A.

CH.GANTES, Professor N.T.U.A.

P.DAKOULAS, Professor Univ. of Thessaly

H.MOUZAKIS, Assoc. Professor N.T.U.A.

D.LOUKIDIS, Assoc. Professor Univ. of Cyprus

Athens, March 2022

ΕΚΤΕΝΗΣ ΠΕΡΙΛΗΨΗ

Ι. ΠΕΡΙΓΡΑΦΗ ΤΟΥ ΠΡΟΒΛΗΜΑΤΟΣ & ΣΚΟΠΟΣ ΤΗΣ ΔΙΑΤΡΙΒΗΣ

Ο αντισεισμικός σχεδιασμός κατασκευών σε ρευστοποιήσιμα εδάφη αποτελεί ένα αντικείμενο με σημαντικές προκλήσεις για τη σύγχρονη Μηχανική. Παρατηρήσεις πεδίου κατά τη διάρκεια ισχυρών σεισμών (Niigata, 1964; Luzon, 1990; Kocaeli, 1999; Christchurch, 2011; Durres, 2019) επιδεικνύουν μια σειρά καταστροφικών φαινομένων σχετιζόμενων με τη ρευστοποίηση. Τα φαινόμενα αυτά μπορούν να προκαλέσουν είτε επιφανειακές εκδηλώσεις (π.χ. πλευρική εξάπλωση, ανάδυση αμμώδους υλικού) είτε σημαντικές καταστροφές στις υποδομές λόγω απώλειας φέρουσας ικανότητας των εδραζόμενων κατασκευών. Για την αποφυγή παρόμοιων φαινομένων οι υφιστάμενοι Αντισεισμικοί Κανονισμοί (Eurocode 8, ΕΑΚ2003, FEMA) απαγορεύουν την κατασκευή κτιριακών υποδομών σε ρευστοποιήσιμα εδάφη χωρίς την προγενέστερη λήψη ειδικών μέτρων, όπως: (α) την εξυγίανση του υποκείμενου εδάφους (π.χ. μέσω συμπύκνωσης ή/και τοποθέτησης στραγγιστηρίων) καθώς και (β) την κατασκευή πασσάλων για την μεταφορά των επιβαλλόμενων φορτίων σε βαθύτερα, μη-ρευστοποιήσιμα στρώματα.

Νεότερες παρατηρήσεις πεδίου έχουν δείξει ότι η ύπαρξη μιας μη-ρευστοποιήσιμης εδαφικής κρούστας κάτω από τη θεμελίωση είναι σε θέση να περιορίσει δραστικά τη συσσώρευση σεισμικών καθιζήσεων ακόμα και σε περιπτώσεις επιφανειακών θεμελίων. Βάσει των παρατηρήσεων αυτών, κατά τη διάρκεια της τελευταίας δεκαετίας αναπτύχθηκε μια καινοτόμος μεθοδολογία σχεδιασμού των κατασκευών σε ρευστοποιήσιμα εδάφη, η οποία αντικαθιστά την παραδοσιακή αντιμετώπιση που περιλάμβανε την τοποθέτηση πασσάλων σε συνδυασμό με μια βαθιά εδαφική εξυγίανση. Η νέα μεθοδολογία εξετάζει την κατασκευή επιφανειακών θεμελίων με την εξυγίανση μιας ρηχής σχετικά εδαφικής κρούστας. Οι θεωρητικές και πειραματικές μελέτες που έχουν πραγματοποιηθεί (Liu και Dobry 1997; Naesgaard et al. 1998; Adalier et al. 2003; Dashti et al. 2010; Sitar and Hausler 2012; Dimitriadi et al. 2017) καταδεικνύουν ότι οι σεισμικές καθιζήσεις των θεμελιώσεων οφείλονται κατά κύριο λόγο στις διατμητικές παραμορφώσεις του υποκείμενου εδάφους, ενώ δευτερεύουσα σημασία αποδίδεται σε φαινόμενα όπως η στερεοποίηση και η ιζηματοποίηση μετά το πέρας της ρευστοποίησης καθώς και στις ογκομετρικές εδαφικές παραμορφώσεις λόγω της υδατικής ροής. Βάσει των ανωτέρω, η προτεινόμενη μεθοδολογία σχεδιασμού περιλαμβάνει την ενίσχυση μιας εδαφικής κρούστας κάτω και περιμετρικά του θεμελίου [1.0-1.5Β σε βάθος και 2-3Β σε πλάτος, όπου Β το πλάτος του θεμελίου (Dimitriadi et al. 2018)] μέσω δυναμικής συμπύκνωσης και τοποθέτησης κατακόρυφων στραγγιστηρίων με σκοπό την αύξηση

της αντοχής, της αντίστασης σε ρευστοποίηση και της διαπερατότητας του εδάφους θεμελίωσης. Ο συγκεκριμένος σχεδιασμός εξασφαλίζει τα εξής πλεονεκτήματα έναντι της συμβατικής μεθόδου:

- Η αύξηση της αντοχής και της αντίστασης σε ρευστοποίηση της βελτιωμένης εδαφικής κρούστας εξασφαλίζει την ασφαλή μεταφορά των κατασκευαστικών φορτίων στο υποκείμενο έδαφος. Η ανάπτυξη ενός πρισματοειδούς-τύπου μηχανισμού αστοχίας Coulomb αποτρέπεται λόγω της εξασφάλισης της διατμητικής αντοχής του ενισχυμένου εδάφους τόσο κάτω από το θεμέλιο όσο και περιμετρικά αυτού, όπου και αναδύεται το πρίσμα αστοχίας.
- Η διατήρηση των ρευστοποιημένων εδαφών κάτω από την –ρηχή– βελτιωμένη κρούστα λειτουργεί ευεργετικά καθώς η ύπαρξή τους κατά τη διάρκεια του σεισμού αποτελεί ένας είδος «φυσικής σεισμικής μόνωσης». Η μερική ρευστοποίηση του εδάφους αποσβένει την μετάδοση των διατμητικών κυμάτων προς την επιφάνεια με αποτέλεσμα τη μείωση των σεισμικών απαιτήσεων κατά το σχεδιασμό.
- Λόγω των ανωτέρω ευεργετικών δράσεων, το συνολικό κατασκευαστικό κόστος καθώς και η διάρκεια των οικοδομικών εργασιών μπορούν να μειωθούν σημαντικά.

Το **Σχήμα 1** παρουσιάζει σχηματικά τον συμβατικό και τον νέο σχεδιασμό κατασκευών σε ρευστοποιήσιμα εδάφη.

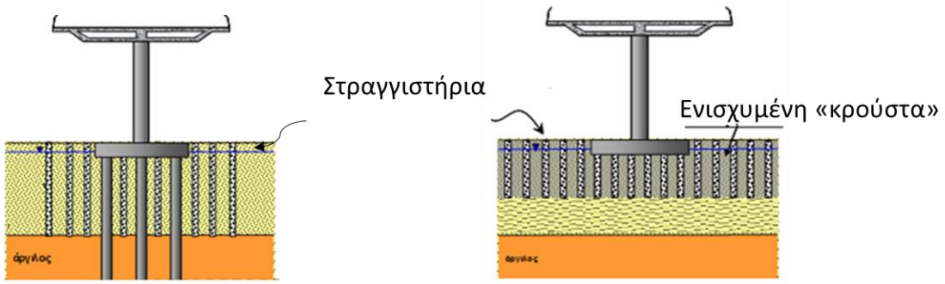

Σχήμα 1: (α) Συμβατικός και (β) νέος σχεδιασμός θεμελιώσεων σε ρευστοποιήσιμα εδάφη.

Σκοπό της παρούσας Διατριβής αποτελεί η διερεύνηση της συμπεριφοράς των συστημάτων ανωδομής-θεμελίου-εδάφους σε καθεστώς ρευστοποίησης και πιο συγκεκριμένα η ανάπτυξη μίας ολοκληρωμένης μεθοδολογίας για τον αντισεισμικό σχεδιασμό των θεμελιώσεων βάσει κριτηρίων επιτελεστικότητας και λαμβάνοντας παράλληλα υπόψη την αλληλεπίδραση εδάφους-θεμελίου-ανωδομής. Τα κυριότερα στοιχεία της Διατριβής συνοψίζονται στα εξής:

- Μια σειρά από τρισδιάστατες αριθμητικές αναλύσεις πραγματοποιήθηκε προκειμένου να διερευνηθούν οι κυριότερες παράμετροι που επιδρούν στη δυναμική απόκριση των συστημάτων

ανωδομής-θεμελίου-εδάφους σε καθεστώς ρευστοποίησης. Προγενέστερες ερευνητικές μελέτες έχουν διερευνήσει διεξοδικά τη δυναμική απόκριση συστημάτων θεμελίου-εδάφους. Για το λόγο αυτό η παρούσα Διατριβή επικεντρώνεται στην επίδραση της αδράνειας της ανωδομής στην συνολική απόκριση του συστήματος. Οι βασικές παράμετροι που διέπουν το πρόβλημα εξετάζονται στο πλαίσιο των αδιαστατοποιημένων παραμέτρων της αλληλεπίδρασης εδάφους-κατασκευής, βάσει των υφιστάμενων διαδικασιών των σύγχρονων Κανονισμών.

- Η αριθμητική μεθοδολογία που αναπτύχθηκε στην παρούσα Διατριβή χρησιμοποιεί το προηγμένο καταστατικό προσομοίωμα NTUA-Sand για την προσομοίωση της μονοτονικής και της ανακυκλικής συμπεριφοράς αμμωδών εδαφών για διάφορες συνθήκες κορεσμού και στράγγισης. Το συγκεκριμένο προσομοίωμα βασίζεται στη θεωρεία Κρίσιμης Κατάστασης και η ακρίβειά του έχει επαληθευτεί εκτενώς μέσω δοκιμών στοιχείου και προβλημάτων οριακής κατάστασης έναντι των πειραμάτων του προγράμματος VELACS.
- Για τη διερεύνηση της επίδρασης των χαρακτηριστικών της ανωδομής, διενεργήθηκαν και συγκρίθηκαν αριθμητικές αναλύσεις για: (α) ολοκληρωμένα συστήματα ανωδομής-θεμελίου-εδάφους (ΑΘΕ), όπου η ανωδομή συνίσταται σε έναν απλοποιημένο μονοβάθμιο ταλαντωτή (Single-Degree-of-Freedom system), και (β) για απλούστερα – ισοδύναμα – συστήματα θεμελίου-εδάφους (ΘΕ). Τα ισοδύναμα συστήματα ΘΕ έχουν τις ίδιες ιδιότητες εδάφους με τα συστήματα ΑΘΕ, στα οποία οι επιβαλλόμενες πιέσεις επαφής στη στάθμη θεμελίωσης αντιστοιχούν στις πιέσεις λόγω του συνολικού βάρους του αντίστοιχου συστήματος ΑΘΕ.
- Βάσει των αποτελεσμάτων των παραμετρικών αναλύσεων, αναπτύχθηκε τελικώς μια απλοποιημένη μεθοδολογία για τον πρωτοβάθμιο υπολογισμό των σεισμικών καθιζήσεων συστημάτων ανωδομής-θεμελίου-εδάφους με επιφανειακές θεμελιώσεις σε καθεστώς ρευστοποίησης. Η διαδικασία αυτή, πέραν της συμβολής της παρούσας διατριβής που αφορά στις συνέπειες της αδρανειακής ταλάντωσης της ανωδομής, βασίστηκε σε υφιστάμενες διαδικασίες για την πρόβλεψη άλλων βασικών παραμέτρων του σχεδιασμού οι οποίοι έχουν αποτελέσει αντικείμενο προγενέστερης έρευνας, όπως οι καθιζήσεις απλών συστημάτων (θεμελίου-εδάφους), ο χρόνος εκδήλωσης της ρευστοποίησης, η εκτίμηση των θεμελιωδών ιδιοπεριόδων του συστήματος εδάφους-θεμελίους-ανωδομής, κτλ.
- Πιο συγκεκριμένα, η προτεινόμενη διαδικασία βασίστηκε στις ακόλουθες παραδοχές:
  i) Η επίδραση επί των καθιζήσεων των αδρανειακών δυνάμεων της ανωδομής θεωρείται ασύζευκτη με αυτή των εδαφικών χαρακτηριστικών, η οποία έχει διεξοδικά διερευνηθεί σε προγενέστερες ερευνητικές προσπάθειες. Ως εκ τούτου, η επίδραση των παραμέτρων της

ανωδομής εισάγεται ως διορθωτικός συντελεστής σε προϋπάρχουσες μεθοδολογίες υπολογισμού των σεισμικών καθιζήσεων.

ii) Κρίσιμη παράμετρος για τον υπολογισμό των σεισμικών καθιζήσεων υπό ρευστοποιήσιμες συνθήκες αποτελεί ο χρόνος εκδήλωσης της ρευστοποίησης, μετά την έναρξη της σεισμικής δόνησης, δεδομένου ότι η δυναμική απόκριση του ελεύθερου πεδίου και της κατασκευής διαφέρουν ποιοτικά και ποσοτικά πριν και μετά την εκδήλωση της ρευστοποίηση. Για τον λόγο αυτό, η προτεινόμενη μεθοδολογία στην παρούσα Διατριβή διαφοροποιείται για το τμήμα της σεισμικής δόνησης πριν και μετά την εκδήλωση της ρευστοποίησης.

ΙΙ. ΕΜΠΕΙΡΙΑ ΑΠΟ ΠΡΟΗΓΟΥΜΕΝΕΣ ΕΡΕΥΝΕΣ

Η συστηματική καταγραφή των καταστροφών λόγω ρευστοποίησης στα έργα υποδομής ξεκίνησε τη δεκαετία του 1960 για τους μεγάλους σεισμούς της Niigata στην Ιαπωνία (1964) και του Prince William Sound στην Αλάσκα (1964). Και οι δυο αυτοί σεισμοί προκάλεσαν σημαντικές καθιζήσεις κατασκευών από οπλισμένο σκυρόδεμα και θεμελίων γεφυρών λόγω εκτεταμένης ρευστοποίησης του υποκείμενου εδάφους (Ross et al. 1969, Yoshimi and Tokimatsu 1977). Οι καταστροφικοί σεισμοί στη Luzon των Φιλιππινών (1990), στο Kocaeli της Τουρκίας (1999), στο Tohoku της Ιαπωνίας (2011), στο Sulawezi της Ινδονησίας (2018) και στο Δυρράχιο της Αλβανίας (2019) είναι τα πιο πρόσφατα παραδείγματα σημαντικών καταστροφών στα έργα υποδομής λόγω ρευστοποίησης. Η σεισμική απόκριση των κτιρίων σε ρευστοποιήσιμο έδαφος ερευνήθηκε αρχικά με πειραματικές δοκιμές δυναμικής φόρτισης (Yoshimi and Tokimatsu 1977; Liu και Dobry 1997; Kawasaki et al. 1998; Acacio et al. 2001; Adalier et al. 2003; Coelho et al. 2004; Deng and Kutter 2012; Hughes and Madabhushi 2019) και αριθμητικές αναλύσεις (Liu and Dobry 1997; Naesgaard et al. 1998; Adalier et al. 2003; Dashti et al. 2010; Sitar and Hausler 2012; Dimitriadi et al. 2017) θεμελίων και άκαμπτων κατασκευών υποκείμενων σε δυναμικές φορτίσεις. Μέσω αυτών των ερευνητικών προσπαθειών προσδιορίστηκε με μεγαλύτερη ακρίβεια ο ρόλος των βασικών παραμέτρων που διέπουν το φαινόμενο, όπως η πίεση επαφής και το πλάτος του θεμελίου, η πυκνότητα του εδάφους, κτλ. Η αποκτηθείσα τεχνογνωσία συνετέλεσε στο να επεκταθούν οι προϋπάρχουσες μεθοδολογίες που υπολόγιζαν τις καθιζήσεις στο ελεύθερο πεδίο, αποκλειστικά λόγω ογκομετρικών παραμορφώσεων (Tokimatsu and Seed 1987, Ishihara and Yoshimine 1992), σε πιο εξελιγμένες αναλυτικές σχέσεις που προβλέπουν τις σεισμικές καθιζήσεις των κατασκευών λόγω διατμητικών παραμορφώσεων κάτω από το θεμέλιο (Bray and Macedo 2017; Dimitriadi et al. 2017; Bullock et al. 2019). Οι προτεινόμενες σχέσεις βασίζονται σε αναλύσεις παλινδρόμησης (regression analysis) των αριθμητικών αποτελεσμάτων υπολογισμού των καθιζήσεων για μια σειρά διαφορετικών γεωτεχνικών,

σεισμικών και κατασκευαστικών παραμέτρων. Σε πιο πρόσφατες μελέτες διερευνήθηκε η δυναμική απόκριση πλήρων συστημάτων ανωδομής-θεμελίωσης-εδάφους μέσω πειραμάτων φυγοκεντριστή (Adamidis and Madabhushi 2017; Dashti et al. 2010a; Tokimatsu et al. 2019) και αριθμητικών αναλύσεων (Chaloulos et al. 2020 ; Hughes and Madabhushi 2019; Karimi and Dashti 2016b; Macedo and Bray 2018). Παρ' όλα αυτά, η πλειονότητα των αντίστοιχων ερευνητικών προσπαθειών δεν λαμβάνει υπόψη την συσχέτιση μεταξύ του χρόνου εκδήλωσης της ρευστοποίησης και των χρονικά μεταβαλλόμενων δυναμικών χαρακτηριστικών του συστήματος ανωδομής-θεμελίωσης-εδάφους.

Πειραματικές διερευνήσεις. Μια από τις πρώτες ερευνητικές προσπάθειες που έθεσαν τις βάσεις για την κατανόηση της σεισμικής απόκρισης των θεμελίων σε καθεστώς ρευστοποίησης αποτέλεσε η πειραματική διερεύνηση των Yoshimi και Tokimatsu (1977), οι οποίοι πραγματοποίησαν μια σειρά από δοκιμές σεισμικής τράπεζας άκαμπτων θεμελίων που εδράζονται επί κορεσμένου αμμώδους εδαφικού στρώματος. Το πειραματικό προσομοίωμα υποβλήθηκε σε οριζόντια σεισμική διέγερση κατά τη διάρκεια της οποίας μετρήθηκαν οι καθιζήσεις του θεμελίου και οι πιέσεις πόρων του νερού σε διάφορα βάθη. Από τα πειραματικά αποτελέσματα προέκυψαν τα ακόλουθα ευρήματα:

- Ο λόγος της υπερπίεσης του νερού των πόρων $r_u=\Delta u/\sigma'_{v0}$ ακριβώς κάτω από το θεμέλιο είναι σημαντικά μικρότερος από 1.0 λόγω των αυξημένων διατμητικών τάσεων που προκύπτουν από την επιφόρτιση της κατασκευής. Για αυξανόμενες τιμές της εφαρμοζόμενης πίεσης, ο λόγος r_u τείνει να απομειώνεται.
- Οι σεισμικές καθιζήσεις – κανονικοποιημένες με το πάχος της αμμώδους στρώσης – συσχετίζονται με το ποσοστό της περιοχής κάτω από το θεμέλιο που διατηρεί λόγους της υπερπίεσης πόρων μικρότερους από 0.60 (**Σχήμα 2α**). Η τιμή 0.60 είναι η κρίσιμη τιμή του λόγου r_u που προκαλεί την εκδήλωση της ρευστοποίησης στις δεδομένες εδαφικές συνθήκες του πειράματος.
- Παρατηρήθηκε ότι η συσσώρευση σεισμικών καθιζήσεων είναι αντιστρόφως ανάλογη της σχετικής πυκνότητας (**Σχήμα 2γ**) και του πλάτους της βάσης του θεμελίου (**Σχήμα 2δ**).

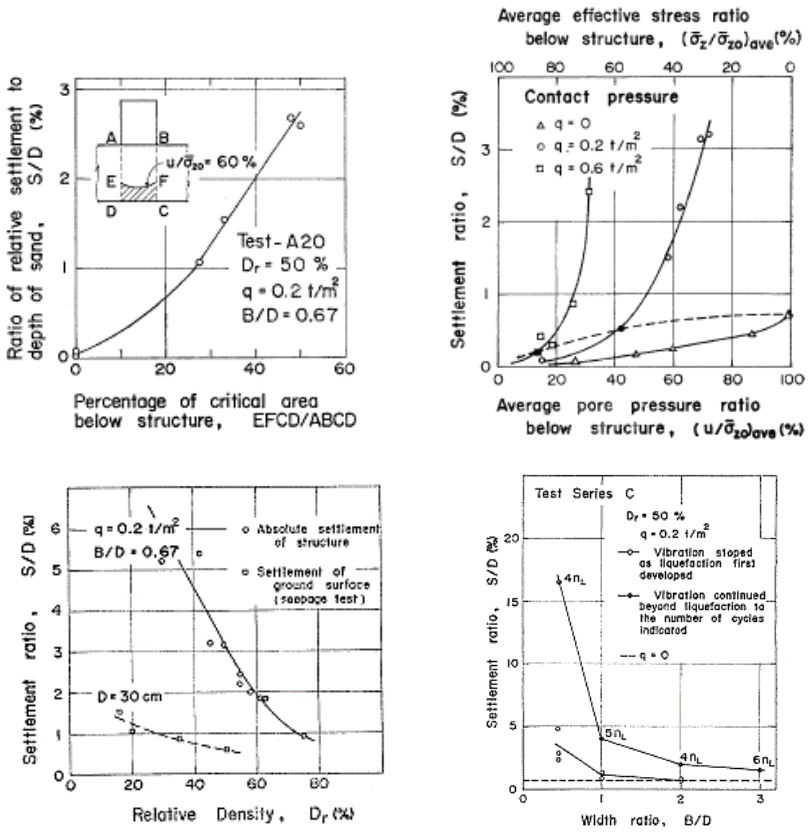

Σχήμα 2: Πειραματική διερεύνηση των σεισμικών καθιζήσεων θεμελίων συναρτήσει (α) της ανάπτυξης υπερπιέσεων του νερού των πόρων κάτω από τη θεμελίωση, (β) της επιβαλλόμενης πίεσης επαφής του θεμελίου, (γ) της πυκνότητας του εδάφους και (δ) του κανονικοποιημένου πλάτους του θεμελίου (Yoshimi and Tokimatsu 1977).

Στην πιο πρόσφατη πειραματική διερεύνηση των Liu και Dobry (1997) μελετήθηκε η επίδραση της πυκνότητας του εδάφους στις σεισμικές καθιζήσεις κυκλικών θεμελίων μέσω οκτώ πειραμάτων φυγοκεντριστή, για ένα εδαφικό προφίλ που αποτελείται από μεσαίας πυκνότητας ρευστοποιήσιμη άμμο. Στην πρώτη ομάδα δοκιμών, το έδαφος κάτω από το θεμέλιο συμπυκνώθηκε με δονητική συμπύκνωση εντός ακτίνας r και βάθους D_c, όπως παρουσιάζεται στο **Σχήμα 3**, ενώ στη δεύτερη ομάδα ορίστηκαν διαφορετικά επίπεδα διαπερατότητας με ρύθμιση του ιξώδους του υγρού των πόρων. Τα ακόλουθα συμπεράσματα εξήχθησαν από τους συγγραφείς:

- Οι υπερπιέσεις του νερού των πόρων που μετρήθηκαν στο ελεύθερο πεδίο έδειξαν ότι η ολική ρευστοποίηση (δηλαδή, r_u=1.0) εκδηλώθηκε αρχικά σε ρηχά βάθη και στη συνέχεια επεκτάθηκε σε βαθύτερα στρώματα. Επιπρόσθετα, παρατηρήθηκε ότι η ροή του νερού κατευθυνόταν από τις βαθιές στρώσεις προς την επιφάνεια του ελεύθερου πεδίου και προς την περιοχή κάτω από το θεμέλιο, όπου οι υπερπιέσεις πόρων ήταν σημαντικά μικρότερες.

- Οι σεισμικές δονήσεις στην επιφάνεια του εδάφους μειώνονται σημαντικά μετά την επέκταση της ρευστοποίησης στα υποκείμενα εδαφικά στρώματα.
- Οι καθιζήσεις του θεμελίου συσσωρεύονται, ως επί το πλείστον, κατά τη διάρκεια των ισχυρών σεισμικών δονήσεων του εδαφικού σχηματισμού, ενώ μόνο ένα μικρό μέρος τους αποδίδεται στις ογκομετρικές παραμορφώσεις που προκαλούνται από τις υδατικές ροές κατά την εκτόνωση των υπερπιέσεων του νερού των πόρων που προκάλεσε η σεισμική δόνηση. Αυτό υποδηλώνει ότι, υπό αυτές τις συνθήκες, οι θεμελιώσεις καθιζάνουν κυρίως λόγω υπέρβασης της απομειωμένης φέρουσας ικανότητας του εδάφους θεμελίωσης.
- Η εδαφική συμπύκνωση μείωσε τις σεισμικές καθιζήσεις έως και 65%, δηλαδή, από 58cm σε 20cm, περίπου. Διαπιστώθηκε ότι η επίδραση της συμπύκνωσης στις καθιζήσεις είναι σημαντική για τιμές βάθους συμπύκνωσης έως 1.5 φορά το πλάτος του θεμελίου, ενώ για μεγαλύτερα βάθη συμπύκνωσης τα οφέλη είναι περιορισμένα (**Figure 2.16**).

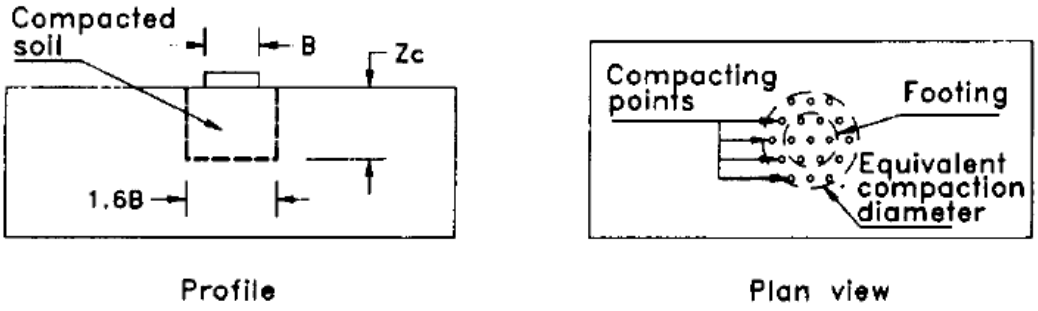

Σχήμα 3: Σχηματική αναπαράσταση του συμπυκνωμένου εδάφους στα πειράματα φυγοκεντριστή των Liu and Dobry (1997).

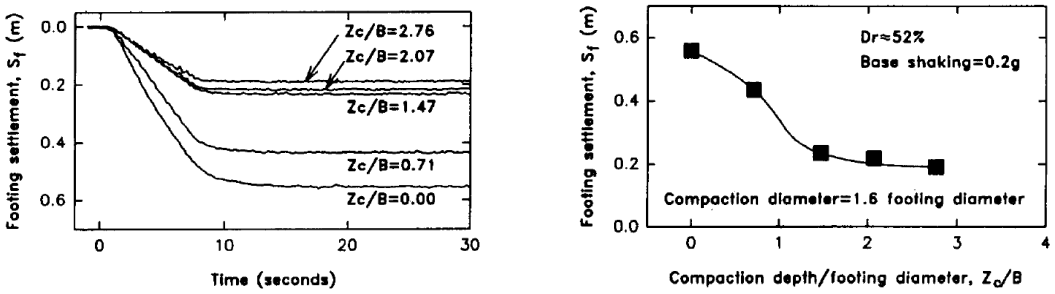

Σχήμα 4: (α) Χρονοϊστορίες σεισμικών καθιζήσεων θεμελίων για διαφορετικά βάθη συμπύκνωσης z_c και (β) διακύμανση της τελικής σεισμικής καθίζησης με το βάθος συμπύκνωσης βάσει των πειραματικών αποτελεσμάτων των Liu και Dobry (1997).

Αριθμητικές διερευνήσεις. Τις τελευταίες δεκαετίες, αναπτύχθηκε μια σειρά από καταστατικά μοντέλα που προσομοιώνουν με ικανοποιητική ακρίβεια την ανακυκλική συμπεριφορά της άμμου σε καθεστώς

ρευστοποίησης χρησιμοποιώντας τη θεωρία της Κρίσιμης Κατάστασης (Cubrinovski and Ishihara 1998; Yang Z. 2003; Byrne et al. 2004; Andrianopoulos et al. 2010; Boulanger and Ziotopoulou 2013; Tasiopoulou and Gerolymos 2016; Yang M. et al. 2020; Cheng and Detournay 2021). Η σύγκριση των μοντέλων αυτών με πειραματικά δεδομένα και παρατηρήσεις πεδίου έδειξε ότι μπορούν να προβλεφθούν ικανοποιητικά οι σεισμικές καθιζήσεις των κατασκευών που προκαλούνται από διατμητικές και ογκομετρικές παραμορφώσεις λόγω ρευστοποίησης. Η εκτεταμένη ερευνητική χρήση αυτών των καταστατικών προσομοιωμάτων βελτίωσε σημαντικά την κατανόηση της μη-γραμμικής δυναμικής απόκρισης συστημάτων θεμελίου-εδάφους τις τελευταίες δεκαετίες.

Μια από τις πρώτες συστηματικές αριθμητικές διερευνήσεις του φαινομένου διενεργήθηκε από τους Karamitros et al. (2013), οι οποίοι πραγματοποίησαν μια σειρά από μη-γραμμικές δυναμικές αναλύσεις θεμελιώσεων με άκαμπτη ανωδομή εδραζόμενων σε εδαφικά προφίλ ρευστοποιήσιμης άμμου Νεβάδα. Η συγκεκριμένη μελέτη αφενός αναδεικνύει τους κύριους μηχανισμούς που διέπουν το φαινόμενο (π.χ. υπερβολική συσσώρευση πίεσης πόρων κάτω από το θεμέλιο, συσσώρευση καθίζησης , υποβάθμιση της φέρουσας ικανότητας, αλληλεπίδραση θεμελίου-εδάφους), και αφετέρου διερευνά το ρόλο μιας φυσικής μη-ρευστοποιήσιμης αργιλικής εδαφικής κρούστας ως μέθοδο περιορισμού των σεισμικών καθιζήσεων της κατασκευής χωρίς περαιτέρω μέτρα εξυγίανσης (π.χ. βελτίωση εδάφους ή κατασκευή πασσάλων). Τα κύρια συμπεράσματα που προέκυψαν είναι τα ακόλουθα:

- Οι λόγοι υπερπιέσων του νερού των πόρων κάτω από το θεμέλιο παραμένουν μικρότεροι από r_u=1.0 λόγω της παρουσίας σημαντικών κατακόρυφων τάσεων. Επιπλέον, μετά την μεγιστοποίησή τους ($r_u \approx 0.8$) – στα αρχικά στάδια της δόνησης – μειώνονται λόγω της διαστολικής συμπεριφοράς του υποκείμενου εδάφους (**Σχήμα 5α**). Το συγκεκριμένο φαινόμενο επιδεικνύεται με τη διαδρομή των ενεργών τάσεων στο χώρο q-p κατά τη διάρκεια της δόνησης (**Σχήμα 5γ-δ**). Παρατηρείται ότι η κατακόρυφη παραμόρφωση ε_v και η οριζόντια παραμόρφωση ε_h είναι περίπου ίσες με 1%, επομένως, η αποκλίνουσα παραμόρφωση είναι ίση με $\varepsilon_q = \varepsilon_v - \varepsilon_h$ = 2%. Η τιμή αυτή της αποκλίνουσας παραμόρφωσης είναι επαρκής για να προκαλέσει αρχική συστολικότητα (θετικές υπερπιέσεις πόρων) και επακόλουθη διαστολικότητα (αρνητικές υπερπιέσεις πόρων). Οι επιπρόσθετες διατμητικές παραμορφώσεις κάτω από τα άκρα του θεμελίου, που οφείλονται στην καθίζησή του, προκαλούν απομείωση των υπερπιέσεων των πόρων, με αποτέλεσμα να δημιουργείται ένας μηχανισμός αντιστάθμισης της συσσώρευσης καθιζήσεων.

- Σύμφωνα με τους Karamitros et al. (2013) η συσσώρευση καθιζήσεων αποδίδεται στον σχηματισμό και την ολίσθηση ενός πρίσματος αστοχίας υπό το θεμέλιο, η οποία συμβαίνει δύο φορές ανά κύκλο ταλάντωσης, δηλαδή την πρώτη φορά όταν η δόνηση κατευθύνεται προς τα αριστερά και τη δεύτερη όταν κατευθύνεται προς τα δεξιά (**Σχήμα 6β**). Η εν λόγω θεώρηση είναι συμβατή προς τους Richards et al. (1993) οι οποίοι ήταν από τους πρώτους που συσχέτισαν τις σεισμικές καθιζήσεις με τη δημιουργία ενός μηχανισμού πρίσματος τύπου Coulomb, ο οποίος προκαλείται λόγω της υπέρβασης της φέρουσας ικανότητας της θεμελίωσης. Η προγενέστερη θεώρηση συσχέτιζε κατά κύριο λόγο τις καθιζήσεις του ελεύθερου πεδίου με τις ογκομετρικές παραμορφώσεις καθώς και τη συμπύκνωση του εδάφους θεμελίωσης. Σύμφωνα με τους Richards et al., η υπέρβαση της φέρουσας ικανότητας και η επακόλουθη ολίσθηση του πρίσματος του εδάφους προκαλούνται τόσο από την απομείωση της αντοχής του εδάφους λόγω της σεισμικής φόρτισης όσο και από τη μετάδοση των αδρανειακών δυνάμεων της κατασκευής στο υπέδαφος. Ειδικά στην περίπτωση της ρευστοποίησης, η ραγδαία απομείωση της αντοχής του εδάφους λόγω της συσσώρευσης υπερπιέσεων του νερού των πόρων επιδεινώνει το σχηματισμό και την ολίσθηση του εδαφικού πρίσματος.
- Σε συνέχεια των παρατηρήσεων πεδίου, η παραμετρική διερεύνηση κατέδειξε ότι η παρουσία της μη-ρευστοποιήσιμης επιφανειακής κρούστας είναι ευεργετική για την απόκριση της θεμελίωσης, καθώς οι σεισμικές καθιζήσεις μειώνονται με την αύξηση του πάχους της κρούστας (**Σχήμα 6β**). Επιπλέον, η θεώρηση μιας άκαμπτης κατασκευής επί του θεμελίου έχει αμελητέα επίδραση στην ανάπτυξη υπερπιέσεων του νερού των πόρων και στη συσσώρευση καθιζήσεων (**Σχήμα 7**).

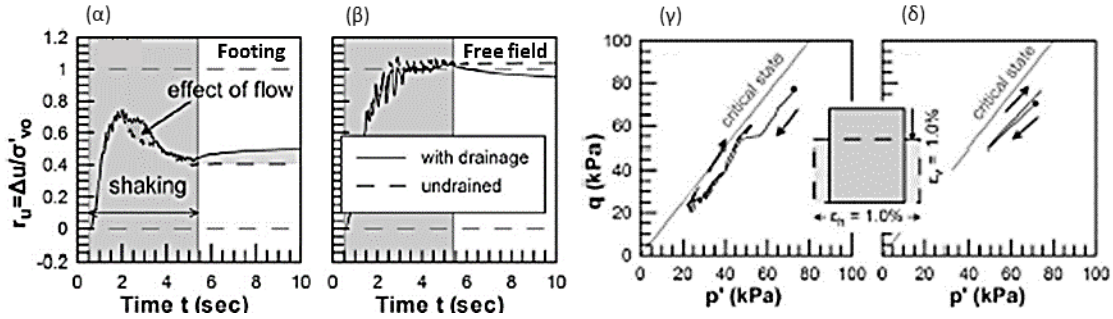

Σχήμα 5: Χρονοϊστορίες του λόγου υπερπιέσεων πόρων (α) κάτω από το θεμέλιο και (β) στην επιφάνεια του εδάφους, διαδρομές τάσεων εδαφικού στοιχείου κάτω από το θεμέλιο στο πεδίο q-p' για (γ) σεισμική διέγερση και (δ) μονοτονική φόρτιση.

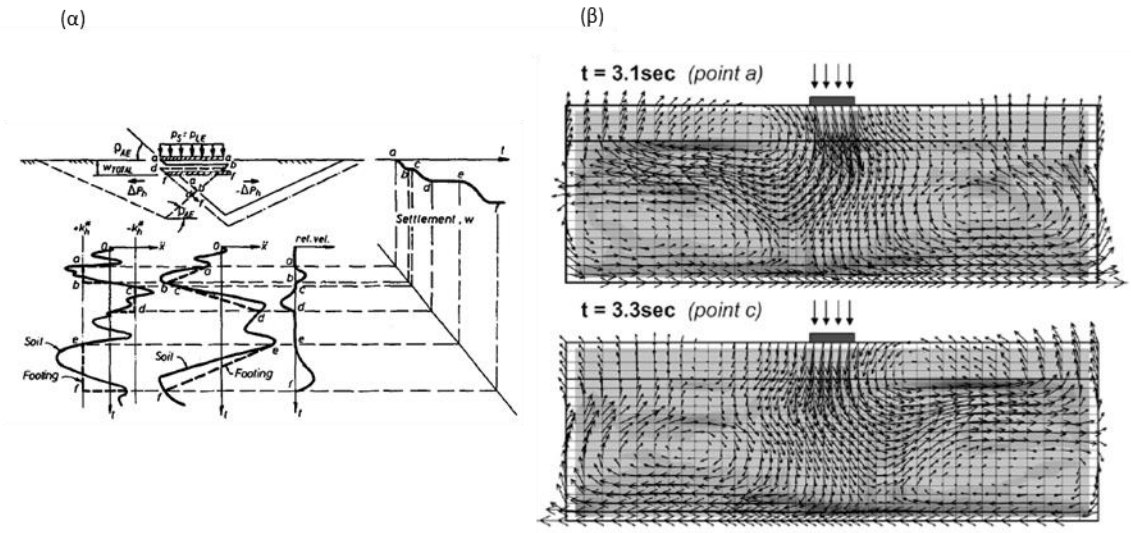

Σχήμα 6: (α) Σχηματική αναπαράσταση του μηχανισμού αστοχίας τύπου Coulomb και συσσώρευση καθιζήσεων λόγω ολίσθησης της εδαφικής «σφήνας» (Richards et al. 1993), (β) διανύσματα ταχυτήτων που δείχνουν το σχηματισμό και την ολίσθηση της εδαφικής «σφήνας» σε συνθήκες ρευστοποίησης (Karamitros et al. 2013c).

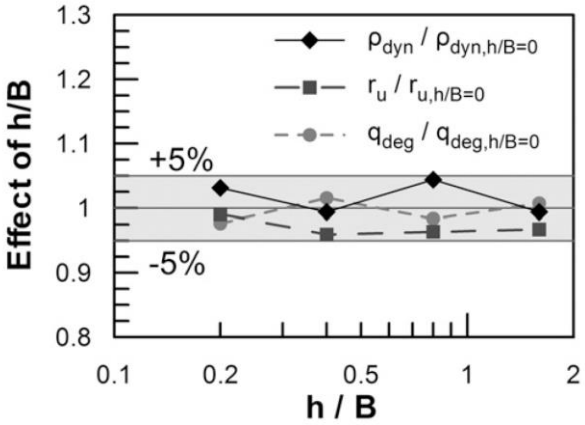

Σχήμα 7: Διακύμανση του λόγου καθιζήσεων με το ύψος της δύσκαμπτης κατασκευής (Karamitros et al. 2013c).

ΙΙΙ. ΜΕΘΟΔΟΛΟΓΙΑ ΑΡΙΘΜΗΤΙΚΩΝ ΑΝΑΛΥΣΕΩΝ

Αριθμητικό μοντέλο. Η αριθμητική διερεύνηση της παρούσας Διατριβής περιλαμβάνει μια σειρά από τρισδιάστατες αριθμητικές αναλύσεις που πραγματοποιήθηκαν με τον Κώδικα Πεπερασμένων Διαφορών *FLAC3D* (Itasca 2012). Το τρισδιάστατο αριθμητικό προσομοίωμα του συστήματος ανωδομής-θεμελίου-εδάφους απεικονίζεται στο **Σχήμα 8**. Το αριθμητικό προσομοίωμα συνίσταται σε ένα εδαφικό στρώμα από ρευστοποιήσιμη άμμο Nevada ύψους 20m και σχετικής πυκνότητας D_r = 45%. Μια επιφανειακή εδαφική κρούστα πάχους 2m βελτιώνεται με εδαφική συμπύκνωση (D_r = 60%) και

εγκατάσταση κατακόρυφων στραγγιστηρίων προκειμένου να εξασφαλιστεί η επαρκής αντίσταση σε ρευστοποίηση του εδάφους θεμελίωσης. Οι διαστάσεις του καννάβου επιλέχθηκαν αρκετά μεγάλες ώστε να αποφευχθούν προβλήματα συνοριακών συνθηκών κατά τη στατική και δυναμική φόρτιση. Πιο συγκεκριμένα, το πλάτος του τετραγωνικού θεμελίου ήταν 4.0m, ενώ το πλάτος του καννάβου είναι ίσο με L_x = 50m, το βάθος είναι L_y = 25m και το ύψος είναι H = 20m. Η διακριτοποίηση του καννάβου περιλαμβάνει ένα λεπτό πλέγμα, με ζώνες 1m x 1m x 1m κάτω από το θεμέλιο με σταδιακά αυξανόμενο μέγεθος εδαφικών στοιχείων προς τα πλευρικά σύνορα του καννάβου με λόγο αύξησης ίσο με 1.15. Το χρονικό βήμα των δυναμικών αναλύσεων είναι της τάξης των 10^{-6} sec δευτερολέπτων, όπως καθορίζεται από το πιο δύσκαμπτο στοιχείο του αριθμητικού προσομοιώματος – στην περίπτωση αυτή από τα γραμμικά στοιχεία δοκού που χρησιμοποιούνται για την προσομοίωση της ανωδομής.

Οι δυναμικές αναλύσεις πραγματοποιούνται με εφαρμογή της χρονοϊστορίας της επιτάχυνσης στη βάση του καννάβου. Για την προσομοίωση των πλευρικών ορίων του ελεύθερου πεδίου χρησιμοποιείται η μέθοδος «tied nodes», η οποία επιβάλλει ίσες οριζόντιες και κάθετες μετατοπίσεις στους αντίθετους και ισοϋψείς κόμβους που βρίσκονται επί των πλευρικών συνόρων. Η συγκεκριμένη μέθοδος υιοθετείται, ως επί το πλείστον, σε περιπτώσεις δυναμικών προβλημάτων που σχετίζονται με υψηλά επίπεδα μη-γραμμικότητας. Η μονοτονική και ανακυκλική συμπεριφορά της άμμου και η συνεπακόλουθη ανάπτυξη υπερπιέσεων του νερού των πόρων μοντελοποιείται με το καταστατικό προσομοίωμα Κρίσιμης Κατάστασης NTUA Sand.

Το προσομοίωμα της ανωδομής συνίσταται σε έναν απλοποιημένο μονοβάθμιο ταλαντωτή (SDOF) που αντιπροσωπεύει μικρού και μεσαίου μεγέθους βάθρα γεφυρών, με τη μάζα του καταστρώματος να θεωρείται συγκεντρωμένη στην κορυφή του βάθρου. Η επιλογή του συγκεκριμένου τύπου κατασκευής πηγάζει από το γεγονός ότι αφενός πρόκειται για αρκετά συνηθισμένη κατασκευή σε ρευστοποιήσιμα εδάφη (π.χ. αλλουβιακές αποθέσεις σε κοίτες ποταμών και λιμνών) και αφετέρου κατασκευάζεται με μεμονωμένες – και ασύνδετες με την υπόλοιπη κατασκευή – θεμελιώσεις, οι οποίες επηρεάζονται περισσότερο από φαινόμενα λικνισμού του βάθρου. Παρ 'όλα αυτά, το αναλυτικό πλαίσιο που χρησιμοποιείται επιτρέπει μια πιο γενικευμένη εφαρμογή της διαδικασίας σε πολυβάθμια συστήματα με την προϋπόθεση της ρεαλιστικής εκτίμησης των δομικών παραμέτρων (π.χ. ισοδύναμο ύψος κατασκευής, θεμελιώδης ιδιοπερίοδος του συστήματος κ.λπ.). Πιο συγκεκριμένα, η ανωδομή έχει μεταβαλλόμενο ύψος h = 3.0 – 5.1m και συγκεντρωμένη μάζα m = 108.8 – 228.8tn. Επιπλέον, η ανωδομή και τα στοιχεία θεμελίωσης προσομοιώνονται με ελαστικά στοιχεία δοκού και κελύφους, αντίστοιχα. Η καμπτική δυσκαμψία του βάθρου είναι EI = 5.0-12.7·10^5 (kNm^2) και αντιστοιχεί στη δυσκαμψία του

ρηγματωμένου στοιχείου, η οποία λαμβάνεται ως το μισό της αντίστοιχης ελαστικής δυσκαμψίας του μη ρηγματωμένου στοιχείου, σύμφωνα με τον EC8-1 4.3.1 (7). Σημειώνεται ότι αυτό το επίπεδο απομείωσης της δυσκαμψίας αναφέρεται στην έναρξη της διαρροής του οπλισμού, επομένως, υποτιμά την πραγματική απομείωση της δυσκαμψίας κατά τη διάρκεια ισχυρών σεισμών.

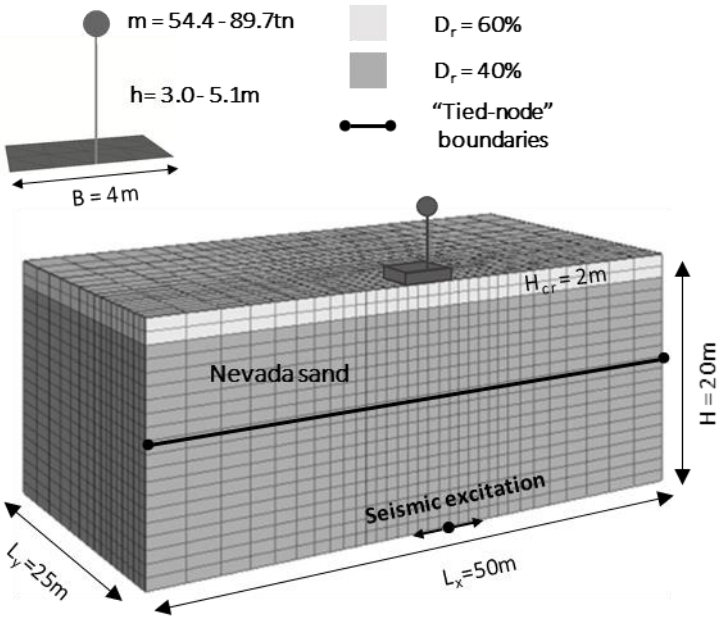

Σχήμα 8: Αριθμητικό προσομοίωμα των αναλύσεων που πραγματοποιήθηκαν στο *FLAC*^{3D}.

Παραμετρική διερεύνηση. Οι βασικές κατασκευαστικές, γεωτεχνικές και σεισμικές παράμετροι που εξετάζονται στην παρούσα Διατριβή εκφράζονται με τη μορφή των αδιαστατοποιημένων παραμέτρων που χρησιμοποιούνται στο πλαίσιο της αλληλεπίδρασης εδάφους-κατσκευής (*soil-structure interaction - SSI*). Πιο συγκεκριμένα, εξετάζονται οι ακόλουθες παράμετροι (**Πίνακας 1**) των Αντισεισμικών Κανονισμών (π.χ. NEHRP): (i) Ο λόγος περιόδων κατασκευής - διέγερσης T_{sys}/T_{exc}, (ii) ο λόγος λυγηρότητας h/r, όπου h είναι το ισοδύναμο ύψος της ανωδομής και r είναι η ακτίνα θεμελίωσης, (iii) ο σχετικός λόγος μάζας $\gamma = m/(\pi \cdot \rho_s \cdot h \cdot r^2)$, όπου ρ_s είναι η πυκνότητα του εδάφους (iv) ο λόγος δυσκαμψίας κατασκευής - εδάφους $s = h/(V_s \cdot T_{str.f})$, όπου V_s είναι η ταχύτητα του διατμητικού κύματος και $T_{str.f}$ είναι η ιδιοπερίοδος της πακτωμένης κατασκευής, καθώς και (v) η μέγιστη εδαφική επιτάχυνση (*PGA*).

Το εύρος των παραπάνω παραμέτρων στον Πίνακα 1 επιλέχθηκε έτσι ώστε να αποτυπώνει τους μηχανισμούς που διέπουν τις σεισμικές καθιζήσεις, ανταποκρινόμενο, ταυτόχρονα, στα συνήθη κατασκευαστικά δεδομένα. Οι γεωτεχνικές παράμετροι παραμένουν, ως επί το πλείστον, αμετάβλητες στην παραμετρική έρευνα της παρούσας Διατριβής. Αυτό οφείλεται σε δύο κύριους λόγους. Αφενός, η

επίδραση των γεωτεχνικών παραμέτρων στην απόκριση του συστήματος έχει εξεταστεί διεξοδικά σε προηγούμενες μελέτες (Dimitriadi et al. 2017, 2018) και, αφετέρου, η παραμετρική διερεύνηση εστιάζει στους λόγους καθιζήσεων μεταξύ συστημάτων ανωδομής-θεμελίου-εδάφους και συστημάτων θεμελίου-εδάφους, προκειμένου η επίδραση των εδαφικών χαρακτηριστικών να καταστεί δευτερεύουσα, αν όχι αμελητέα.

Πίνακας 1: Εύρος των εξεταζόμενων παραμέτρων στο πλαίσιο της αλληλεπίδρασης εδάφους-κατασκευής.

Parameters		Range
Λόγος περιόδων	T_{sys}/T_{exc}	0.40-2.20
Σχετικός λόγος μάζας	$\gamma = m/(\pi \cdot \rho_s \cdot h \cdot r^2)$	2.40-5.10
Λόγος λυγηρότητας	h/r	1.06-1.88
Λόγος δυσκαμψίας κατασκευής-εδάφους s	$s = h/(V_s \cdot T_{str.f})$	0.05-0.35
Μέγιστη εδαφική επιτάχυνση	*PGA* (g)	0.15-0.40

Προσομοίωση ρευστοποιήσιμων συνθηκών. Η προτεινόμενη μεθοδολογία για τον υπολογισμό σεισμικών καθιζήσεων σε ρευστοποιήσιμο έδαφος βασίζεται σε προηγούμενες μελέτες που επιτρέπουν τον διαχωρισμό της σεισμική διέγερσης σε δύο φάσεις: πριν ($t \leq t_{L,gr}$) και μετά ($t > t_{L,gr}$) την εκδήλωση ρευστοποίησης, όπου $t_{L,gr}$ είναι ο χρόνος από την έναρξη της σεισμικής δόνησης μέχρι την εκδήλωση των συμπτωμάτων της ρευστοποίησης την ελεύθερη επιφάνεια του εδάφους (Youd and Carter 2005; Kramer et al. 2016; Bouckovalas et al. 2017; Özener et al. 2020). Κατά την πρώτη φάση, η συμπεριφορά του εδάφους προσεγγίζεται αρκετά ικανοποιητικά με την παραδοχή στραγγιζόμενων συνθηκών φόρτισης, σε αντίθεση με την δεύτερη φάση όπου επικρατούν αστράγγιστες συνθήκες φόρτισης.

Κρίσιμο παράγοντα για αυτόν το διαχωρισμό αποτελεί το γεγονός ότι η εκδήλωση της ρευστοποίησης συνοδεύεται από σημαντική απομείωση του Μέτρου Διάτμησης και της διατμητικής αντοχής του εδάφους, η οποία είναι αρκετά σημαντική ώστε να προκαλέσει μια ξεχωριστή φάση δόνησης. Πιο συγκεκριμένα, η φάση ρευστοποίησης χαρακτηρίζεται από σημαντικά τροποποιημένες εδαφικές ιδιότητες (V_s, T_{soil}) σε σύγκριση με τις αρχικές ιδιότητες, προ ρευστοποίησης. Επιπλέον, η μετάβαση από τις αρχικές στις ρευστοποιημένες ιδιότητες είναι αρκετά απότομη. Πιο συγκεκριμένα, η θεμελιώδης ιδιοπερίοδος της εδαφικής στήλης T_{soil} έχει παρατηρηθεί ότι αυξάνεται ελάχιστα για λόγους υπερπίεσης πόρων r_u μικρότερους από περίπου 0.80, ενώ αυξάνεται ραγδαία για λόγους r_u που πλησιάζουν την τιμή 1.0 (Kramer et al. 2016).

Διάφορες μελέτες εκτιμούν το χρόνο έναρξης της ρευστοποίησης $t_{L,gr}$ μέσω αριθμητικών αναλύσεων της σεισμικής απόκρισης της εδαφικής στήλης (Kramer et al. 2016; Bouckovalas et al. 2017). Στο πλαίσιο της παρούσας διατριβής, ο χρόνος εκδήλωσης της ρευστοποίησης για ένα ομοιόμορφο στρώμα εδάφους που υποβάλλεται σε αρμονική διέγερση με περίοδο T_{exc} υπολογίζεται έμμεσα, από τον αριθμό των κύκλων φόρτωσης N_L που απαιτούνται μέχρι την εκδήλωση της ρευστοποίησης (έως r_u = 0.80-1.0) επί την περίοδο της ισοδύναμης αρμονικής διέγερσης T_{exc}:

$$t_L = N_L \cdot T_{exc} \tag{1}$$

Επιπλέον, υιοθετείται η απλουστευμένη συσχέτιση του αριθμού κύκλων φόρτισης N_L με ευρέως διαθέσιμα γεωτεχνικά και σεισμικά δεδομένα (π.χ. τον διορθωμένο αριθμό κτύπων πρότυπης διείσδυσης $N_{1,60}$ και την μέγιστη εδαφική επιτάχυνση PGA) (Bouckovalas et al. 2017).

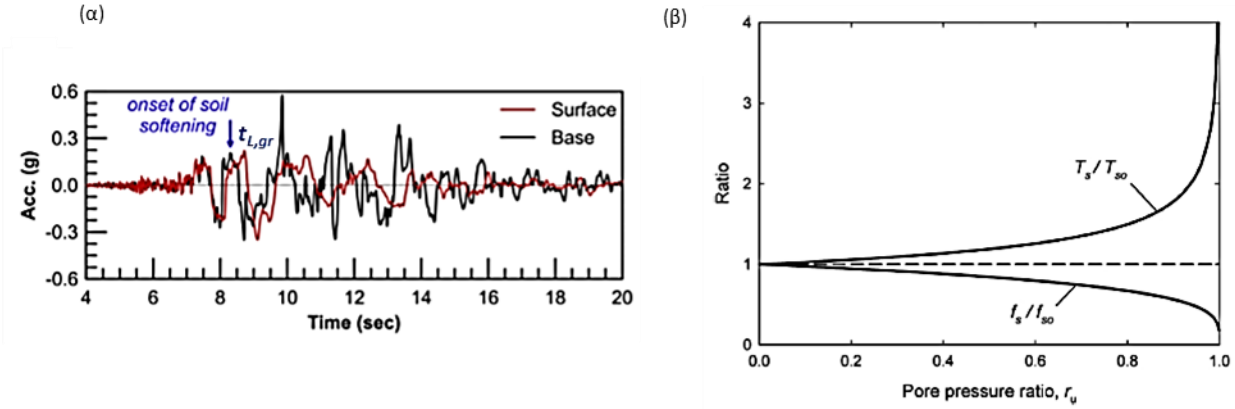

Σχήμα 9: (α) Χρονοϊστορίες επιταχύνσεων στην επιφάνεια του εδάφους και στη βάση του ρευστοποιήσιμου εδαφικού προφίλ για το σεισμό του Kobe 1995 (Port Island) (Bouckovalas et al. 2016) and (β) διακύμανση του λόγου της θεμελιώδους ιδιοπεριόδου της εδαφικής στήλης πριν και μετά τη ρευστοποίηση $T_s/T_{s,o}$ συναρτήσει του λόγου υπερπιέσεων πόρων r_u (Kramer et al. 2016).

IV. ΕΚΤΙΜΗΣΗ ΤΗΣ ΙΔΙΟΠΕΡΙΟΔΟΥ ΣΥΣΤΗΜΑΤΩΝ ΑΝΩΔΟΜΗΣ-ΘΕΜΕΛΙΟΥ-ΕΔΑΦΟΥΣ

Η συνήθης μεθοδολογία για την εκτίμηση της ιδιοπεριόδου των συστημάτων ανωδομής-θεμελίου-εδάφους χρησιμοποιεί τις αναλυτικές διαδικασίες των Αντισεισμικών Κανονισμών (π.χ. NEHRP). Οι διαδικασίες αυτές παρέχουν μια ακριβή εκτίμηση της ελαστικής περιόδου του συστήματος $T_{sys.el}$, εκφραζόμενη συνηθέστερα ως ο λόγος επιμήκυνσης της ιδιοπεριόδου $T_{sys.el}/T_{str.f}$, όπου $T_{str.f}$ είναι η ιδιοπερίοδος της πακτωμένη κατασκευής. Παρ ’όλα αυτά, οι διαδικασίες αυτές είναι ανεπαρκείς για να περιγράψουν τη χρονική μεταβολή των ιδιοτήτων του εδάφους, η οποία, με τη σειρά της, οδηγεί σε μια

μη γραμμική επιμήκυνση της ιδιοπεριόδου. Στην υποβαθμισμένη του κατάσταση, το σύστημα μπορεί να χαρακτηριστεί από μια ισοδύναμη *ενεργό ιδιοπερίοδο* $T_{sys.eff}$ που ενσωματώνει την χαλάρωση του ρευστοποιημένου εδάφους κατά τη διάρκεια της δεύτερης φάσης της δόνησης.

Με βάση τα παραπάνω, για να υπολογιστεί μια ρεαλιστική ιδιοπερίοδος του συστήματος κατά τη διάρκεια της δόνησης είναι χρήσιμο να γίνει διάκριση της επιμήκυνσης της περιόδου μεταξύ του ελαστικού της τμήματος $T_{sys.el}/T_{str.f}$ και του ανελαστικού $T_{sys.eff}/T_{sys.el}$. Ο υπολογισμός της επιμήκυνσης της ελαστικής περιόδου $T_{sys.el}/T_{str.f}$ ακολουθεί την αναλυτική διαδικασία των Κανονισμών (π.χ. NEHRP) χρησιμοποιώντας τις αρχικές συνθήκες του ελαστικού εδάφους, δηλαδή αυτές που προηγούνται της σεισμικής διέγερσης. Αναφορικά με το ανελαστικό τμήμα της επιμήκυνσης $T_{sys.eff}/T_{sys.el}$, η χρονικά μεταβαλλόμενη απομείωση της εδαφικού Μέτρου Διάτμησης G – ιδίως κάτω από το θεμέλιο – καθιστά τον άμεσο υπολογισμό της ενεργού ιδιοπεριόδου $T_{sys.eff}$ εξαρτώμενο από την κατάλληλη επιλογή ενός ισοδύναμου Μέτρου Διάτμησης για το υπέδαφος θεμελίωσης. Στην παρούσα Διατριβή, προκειμένου να ξεπεραστεί η δυσκολία εκτίμησης μιας μοναδικής αντιπροσωπευτικής τιμής του Μέτρου Διάτμησης, η ενεργός ιδιοπερίοδος του συστήματος $T_{sys.eff}$ προσδιορίζεται έμμεσα, μέσω της Συνάρτησης Μεταφοράς (Transfer Function) μεταξύ των φασμάτων επιτάχυνσης εισόδου (ελεύθερου πεδίου) και εξόδου (ανωδομής) στο πεδίο των συχνοτήτων. Στο πλαίσιο αυτό, οι παράγοντες της ανελαστικότητας του συστήματος μπορούν να συσχετιστούν μακροσκοπικά με μια ρεαλιστική – ενεργό – ιδιοπερίοδο του συστήματος.

Μη-ρευστοποιήσιμες συνθήκες. Το ανελαστικό τμήμα της επιμήκυνσης της ιδιοπεριόδου $T_{sys.eff}/T_{sys.el}$ εκτιμάται στην παρούσα Διατριβή με μια σειρά αριθμητικών αναλύσεων. Πιο αναλυτικά, το σύστημα ανωδομής-θεμελίου-εδάφους διεγείρεται στη βάση του καννάβου με μια χρονοϊστορία οριζόντιας σεισμικής επιτάχυνσης, η οποία προσομοιώνει ένα κατακόρυφα διαδιδόμενο διατμητικό κύμα. Το εδαφικό προφίλ περιγράφεται αναλυτικά στην προηγούμενη Ενότητα (Σχήμα 8), ενώ οι συνθήκες πλήρους στράγγισης προσομοιώνονται με το υπό άνωση ειδικό βάρος του εδάφους. Η εφαρμοζόμενη εδαφική διέγερση συνίσταται σε ένα σήμα λευκού θορύβου (white noise), το οποίο περιέχει συχνότητες ίσης έντασης εντός ενός μεγάλου εύρους στο πεδίο των συχνοτήτων με αποτέλεσμα μια οιονεί σταθερή φασματική πυκνότητα. Οι οριζόντιες επιταχύνσεις καταγράφονται στο ελεύθερο πεδίο (σε απόσταση $x > 2B$ από το άκρο του θεμελίου, όπου B είναι το πλάτος του θεμελίου, και στο ύψος της συγκεντρωμένης μάζας της ανωδομής.

Το **Σχήμα 10α** συγκρίνει τα φάσματα ελαστικής απόκρισης με 5% ιξώδη απόσβεση που αντιστοιχούν στις προαναφερθείσες σεισμικές δονήσεις της ανωδομής και του ελεύθερου πεδίου. Οι φασματικές

επιταχύνσεις της κίνησης του ελεύθερου πεδίου ενισχύονται κυρίως στο εύρος των χαμηλών περιόδων, δηλαδή μεταξύ T = 0.10-0.35sec. Αντίθετα, η δόνηση της ανωδομής παρουσιάζει ενίσχυση της φασματικής επιτάχυνσης στο εύρος περιόδων T = 0.40-1.00sec. Η σχετική ενίσχυση μεταξύ των δύο κινήσεων εκτιμάται καλύτερα με την εξέταση της Συνάρτησης Μεταφοράς (TF) των επιταχύνσεων της ανωδομής ως προς το ελεύθερο πεδίο (**Σχήμα 10β**). Λόγω της έντονης μη γραμμικότητας της ανακυκλικής απόκρισης του εδάφους και της διακύμανσης των εδαφικών ιδιοτήτων με το χρόνο, οι ιδιοτιμές του συστήματος δεν αντιστοιχούν απαραίτητα σε μοναδικές κορυφές των TF, αλλά κατανέμονται σε ένα διευρυμένο φάσμα περιόδων. Συγκεκριμένα, παρατηρείται ότι η επικρατέστερη κορυφή TF βρίσκεται εγγύς της «ελαστικής» ιδιοπεριόδου του συστήματος $T_{sys.el}$ = 0.46sec. Παρ 'όλα αυτά, σημαντικές κορυφές φασματικής ενίσχυσης παρατηρούνται επίσης στο εύρος περιόδων T ≈ 0.46 – 1.00sec, γεγονός που υποδεικνύει σημαντική επιμήκυνση της περιόδου που σχετίζεται με την απομείωση της δυσκαμψίας του εδάφους λόγω των διατμητικών παραμορφώσεων που προκαλούνται από (i) τη διάδοση του διατμητικού κύματος και (ii) από τον λικνισμό της κατασκευής. Το εν λόγω διευρυμένο εύρος ιδιοπεριόδων αναφέρεται ακολούθως ως το «ενεργό εύρος ιδιοπεριόδων» του συστήματος κατά τη σεισμική διέγερση.

Το **Σχήμα 11α** παρουσιάζει τις Συναρτήσεις Σχήματος των φασμάτων ελαστικής απόκρισης της σεισμικής επιτάχυνσης της ανωδομής ως προς το ελεύθερο πεδίο. Τα ελαστικά φάσματα προκύπτουν από αριθμητικές αναλύσεις για διαφορετικά επίπεδα σεισμικής έντασης, με μέγιστες εδαφικές επιταχύνσεις ελεύθερου πεδίου (PGA) μεταξύ 0.01g και 0.92g. Παρατηρείται ότι η κορυφή της Συνάρτησης Σχήματος – που αντιστοιχεί στη θεμελιώδη ιδιοπερίοδο του συστήματος – είναι πιο έντονη για χαμηλότερα επίπεδα σεισμικής έντασης, ενώ η συμβολή των φασματικών ενισχύσεων για περιόδους μεγαλύτερες από την θεμελιώδη περίοδο ενισχύεται με την αύξηση του PGA και την, συνεπαγόμενη, εντονότερη πλαστικοποίηση του εδάφους. Είναι χαρακτηριστικό πως για επίπεδα PGA > 0.72g, η θεμελιώδης ιδιοπερίοδος του συστήματος δεν μπορεί να προσδιοριστεί με σαφήνεια. Η διαφορά μεταξύ της απόκρισης του συστήματος για υψηλό (PGA = 0.72g) και μέσο (PGA = 0.30g) επίπεδο σεισμικής έντασης παρουσιάζεται στα Σχήματα **Σχήμα 11β**-**γ**. Όπως φαίνεται στο **Σχήμα 11β**, οι μέγιστες επιταχύνσεις της ανωδομής για PGA = 0.72g είναι περίπου διπλάσιες από αυτές για PGA = 0.30g, γεγονός που οδηγεί σε σημαντικά μεγαλύτερους μη-γραμμικούς υστερητικούς βρόχους στο διάγραμμα ροπής-γωνίας στροφής στο **Σχήμα 11γ**.

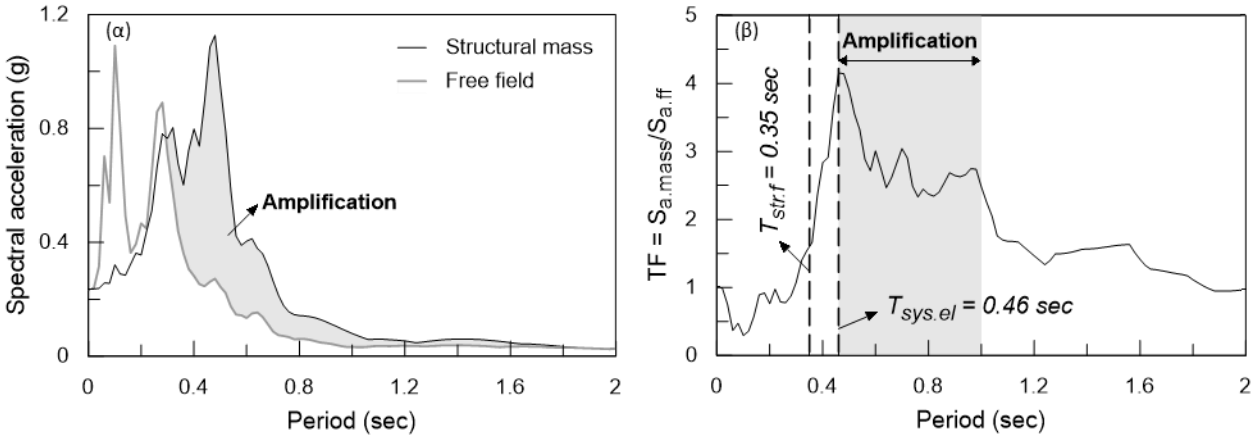

Σχήμα 10: (α) Σύγκριση των ελαστικών φασμάτων απόκρισης της ανωδομής και της επιφάνειας του εδάφους (β) Συναρτήσεις Σχήματος (Transfer Functions) μεταξύ του ελαστικού φάσματος απόκρισης της ανωδομής ($S_{a.mass}$) και της επιφάνειας του εδάφους ($S_{a.ff}$).

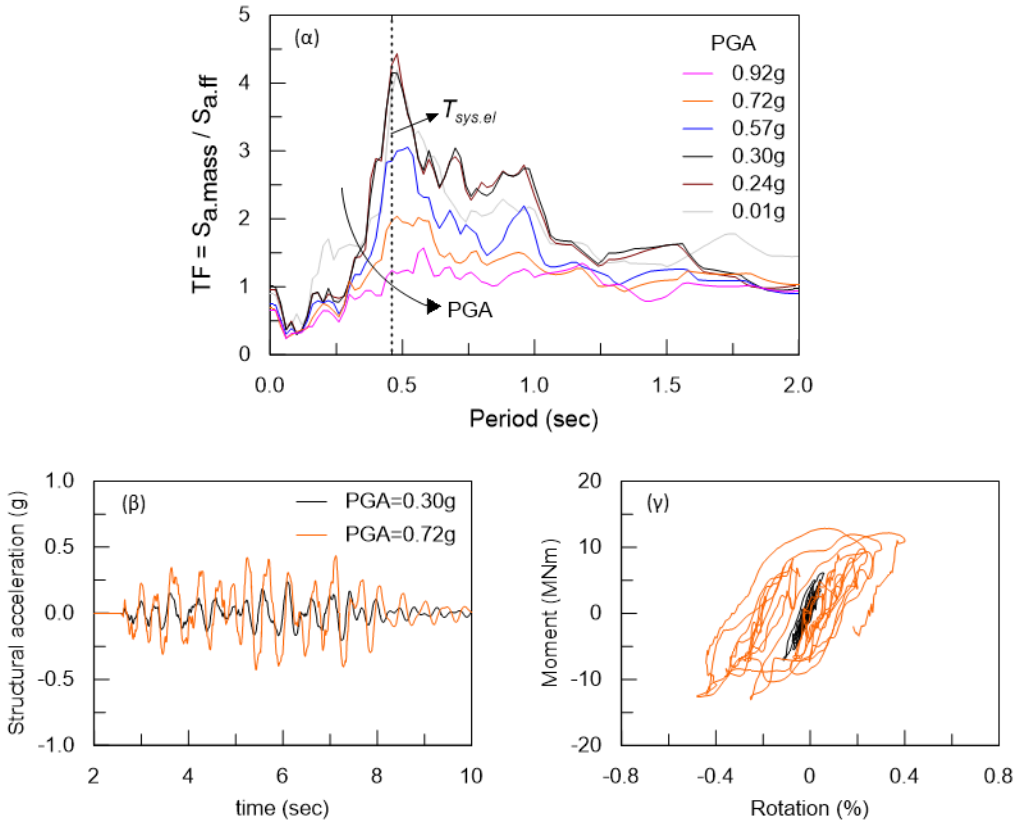

Σχήμα 11: (α) Συναρτήσεις Σχήματος μεταξύ των φασματικών επιταχύνσεων της ανωδομής και της επιφάνειας του εδάφους για διαφορετικά τιμές της μέγιστης εδαφικής επιτάχυνσης (PGA), (β) χρονοϊστορία επιταχύνσεων της ανωδομής για υψηλή (PGA=0.72g) και μέση (PGA=0.30g) σεισμική ένταση και (γ) χρονοϊστορία ροπής-στροφής θεμελίου.

Η επίδραση των σεισμικών, εδαφικών και κατασκευαστικών παραμέτρων στη μη γραμμική επιμήκυνση της περιόδου $T_{sys.eff}/T_{sys.el}$ διερευνάται παραμετρικά μέσω των προαναφερθέντων αριθμητικών αναλύσεων. Η μέγιστη εδαφική επιτάχυνση (PGA) και η θεμελιώδης ιδιοπερίοδος του εδαφικού προφίλ T_{soil} προσδιορίζονται ως οι βασικές παράμετροι. Για την εκτίμηση του συχνοτικού περιεχομένου των Συναρτήσεων Σχήματος χρησιμοποιούνται μεθοδολογίες που προτείνονται στη βιβλιογραφία (Rathje et. al, 1998) με σκοπό τον χαρακτηρισμό του εύρους των ενεργών ιδιοπεριόδων με μία μόνο παράμετρο. Εν προκειμένω, εξετάζονται οι εξής παράμετροι:

- Η θεμελιώδης περίοδος $T_{sys.p}$, η οποία είναι η περίοδος που αντιστοιχεί στη μέγιστη τιμή των φασματικών επιταχύνσεων.
- Η εξομαλυμένη φασματική περίοδος $T_{sys.o}$, η οποία ενσωματώνει τις σημαντικές φασματικές ενισχύσεις, ως εξής:

$$T_{sys.o} = \frac{\sum_i T_i \cdot \ln\left[TF(T_i)\right] \cdot H[TF(T_i) - \max\left[TF(T_i)\right]/2]}{\sum_i \ln\left[TF(T_i)\right] \cdot H[TF(T_i) - \max\left[TF(T_i)\right]/2]} \quad (2)$$

όπου T_i είναι η διακριτή περίοδος i του φάσματος απόκρισης, TF (T_i) είναι η τιμή της Συνάρτησης Σχήματος για περίοδο T_i και H[x] είναι η συνάρτηση «heaviside function» που ισούται με 1 για x > 0 και 0 για x < 0.

Το **Σχήμα 12** παρουσιάζει το λόγο περιόδων του ενεργού προς το ελαστικό σύστημα $T_{sys.eff}/T_{sys.el}$ ως συνάρτηση του PGA και για τις δύο προαναφερθείσες μεθοδολογίες. Οι λόγοι $T_{sys.o}/T_{sys.el}$ παρουσιάζουν αυξημένες τιμές έως 30-40% σε σύγκριση με τους αντίστοιχους λόγους $T_{sys.p}/T_{sys.el}$. Επιπλέον, παρατηρείται περιορισμένη επιμήκυνση του λόγου $T_{sys.p}/T_{sys.el}$ για τιμές PGA μικρότερες από 0.35g, ενώ η επιμήκυνση αυξάνεται με σχετικά γραμμικό τρόπο για μεγαλύτερες τιμές του PGA. Αντίθετα, ο λόγος $T_{sys.o}/T_{sys.el}$ αυξάνεται ραγδαία μέχρι την τιμή PGA = 0.20g, ενώ ο ρυθμός αύξησής του μειώνεται σημαντικά για μεγαλύτερες τιμές PGA. Σημειώνεται ότι η αριθμητική εκτίμηση της ιδιοπεριόδου του συστήματος για πολύ χαμηλές τιμές του PGA εμφανίζει σημαντικές δυσκολίες ως προς την επεξεργασία των σεισμικών σημάτων λόγω της ταυτόχρονης παρεμβολής του αριθμητικού θορύβου στο υπό εξέταση σήμα.

Το **Σχήμα 12β** παρουσιάζει αριθμητικά αποτελέσματα του λόγου περιόδων $T_{sys.eff}/T_{sys.el}$ ως συνάρτηση της θεμελιώδους περιόδου της εδαφικής στήλης T_{soil}, κανονικοποιημένη ως προς την ελαστική περίοδο του συστήματος $T_{sys.el}$. Η θεμελιώδης περίοδος της εδαφικής στήλης εκτιμάται χρησιμοποιώντας τη μέση ελαστική ταχύτητα των διατμητικών κυμάτων καθ' ύψος του εδαφικού προφίλ, χρησιμοποιώντας την έκφραση $T_{soil} = 4H/V_{s,o}$. Σημειώνεται ότι η επίδραση της μη-γραμμικής απόκρισης του εδάφους στην

περίοδο επιμήκυνσης του εδαφικού προφίλ είναι ανάλογη της σεισμικής έντασης και μπορεί να ληφθεί υπόψιν χρησιμοποιώντας αναλυτικές διαδικασίες που είναι διαθέσιμες στη βιβλιογραφία (Bouckovalas and Papadimitriou 2003).

Τα αποτελέσματα δείχνουν ότι ο συντονισμός μεταξύ της διέγερσης της ελεύθερης επιφάνειας του εδάφους και της ελαστικής ιδιοπεριόδου $T_{sys.el}$ επιμηκύνει σημαντικά την ενεργό ιδιοπερίοδο του συστήματος $T_{sys.eff}$, έως και 70% σε σύγκριση με την – αρχική – ελαστική τιμή της περιόδου. Είναι ενδιαφέρον ότι τα όρια του γραφήματος προσομοιάζουν στα τυπικά φάσματα απόκρισης: στην περίπτωση δύσκαμπτων εδαφικών προφίλ (π.χ. μικρές τιμές του ύψους της ανωδομής H), η επιφανειακή κίνηση ενισχύεται λόγω των υψίσυχνων κυμάτων και κατά συνέπεια οι λόγοι $T_{sys.eff}/T_{sys.el}$ τείνουν στο 1.0, ενώ στην περίπτωση των εύκαμπτων εδαφικών προφίλ (π.χ. μεγάλες τιμές H) τα κύματα χαμηλής συχνότητας ενισχύονται και κατά συνέπεια οι λόγοι $T_{sys.eff}/T_{sys.el}$ μειώνονται σταδιακά σε σχέση με τη μέγιστη τιμή κατά το συντονισμό. Σημειώνεται ότι οι τιμές $T_{sys.eff}$ γίνονται μέγιστες για λόγο $T_{soil}/T_{sys.el}$ κοντά στο 1.25, δηλαδή, μακριά από την τιμή 1.0 που είναι η συμβατική τιμή του «ελαστικού» συντονισμού. Αυτή η διαφορά ουσιαστικά έγκειται στη χρήση της ελαστικής τιμής της ιδιοπεριόδου $T_{sys.el}$ στον παρονομαστή αντί της – μεγαλύτερης – ενεργού ιδιοπεριόδου $T_{sys.eff}$. Στην πραγματικότητα, μια εκ των υστέρων κανονικοποίηση των τιμών του T_{soil} με τις υπολογισμένες τιμές $T_{sys.eff}$ θα "μεταφέρει" σωστά την κορυφή ακριβώς στον συντονισμό, δηλαδή, στο $T_{soil}/T_{sys.eff} \approx 1$. Ωστόσο, η επιλογή αυτή δεν είναι πρακτικά εφαρμόσιμη, δεδομένου ότι η τιμή της $T_{sys.eff}$ δεν είναι εκ των προτέρων γνωστή, και επομένως δεν μελετάται περαιτέρω.

Με βάση την ανάλυση παλινδρόμησης των αριθμητικών αποτελεσμάτων που παρουσιάζονται στα **Σχήμα 12α** και **β**, έχουν προκύψει οι ακόλουθες αναλυτικές εκφράσεις για τους λόγους $T_{sys.eff}/T_{sys.el}$, η πρώτη (Εξίσωση 3) με χρήση της παραμέτρου $T_{sys.o}$ για τον υπολογισμό του $T_{sys.eff}$ και η δεύτερη (Εξίσωση 4) με χρήση της παραμέτρου $T_{sys.p}$:

$$\frac{T_{sys.eff}}{T_{sys.el}} = (0.91 + 0.55 \cdot PGA^{0.21}) \frac{1.53 + 0.94\left(T_{soil}/T_{sys.el}\right)^2}{\sqrt{\left[2.05 - \left(T_{soil}/T_{sys.el}\right)^2\right]^2 + 3.65\left(T_{soil}/T_{sys.el}\right)^2}} \quad (3)$$

$$\frac{T_{sys.eff}}{T_{sys.el}} = \max\left\{1.00; (0.57 + 0.54 \cdot PGA^{0.44}) \frac{1.35 + 0.87\left(T_{soil}/T_{sys.el}\right)^2}{\sqrt{\left[1.69 - \left(T_{soil}/T_{sys.el}\right)^2\right]^2 + 3.24\left(T_{soil}/T_{sys.el}\right)^2}}\right\} \quad (4)$$

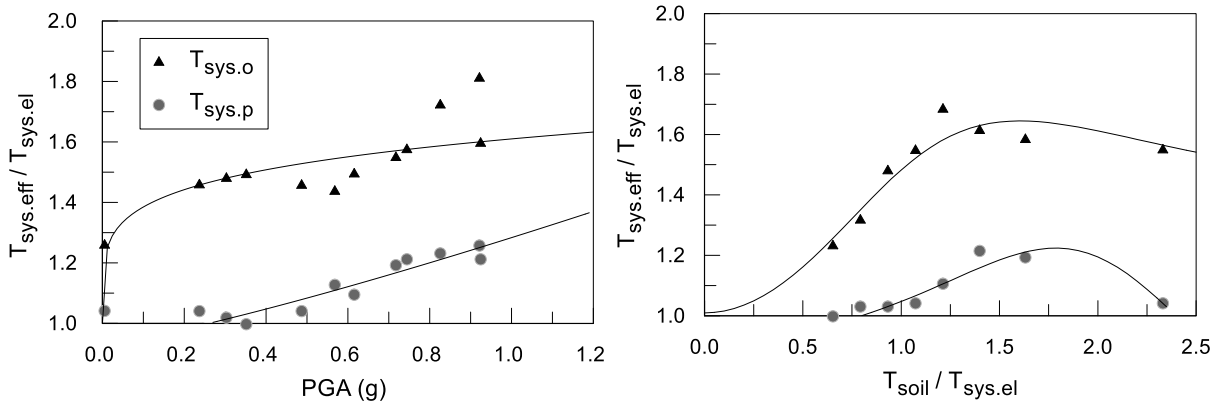

Σχήμα 12: Λόγοι περιόδων του ενεργού προς το ελαστικό σύστημα $T_{sys.eff}/T_{sys.el}$ ως συνάρτηση: (α) της μέγιστης εδαφικής επιτάχυνσης και (β) της θεμελιώδους ιδιοπεριόδου του εδαφικού T_{soil} κανονικοποιημένης ως προς την ελαστική περίοδο $T_{sys.el}$.

Συνθήκες ρευστοποίησης. Η επίδραση των ρευστοποιημένων στρωμάτων στην απόκριση της κατασκευής είναι διπλή: (i) τα ρευστοποιημένα στρώματα λειτουργούν ως φυσική «σεισμική μόνωση» με αποτέλεσμα τη δραστική απομείωση των επιταχύνσεων εδάφους και κατασκευής, και (ii) η δραστικά απομειωμένη αντοχή του εδάφους επιδεινώνει τη συμπεριφορά της θεμελίωσης. Όσον αφορά την πρώτη επίδραση, αναφέρεται βιβλιογραφικά πως "*ένα ρευστοποιημένο στρώμα εδάφους μπορεί να εξασθενίσει αποτελεσματικά ορισμένες συχνότητες της διέγερσης, δηλαδή να παρέχει φυσική μόνωση της σεισμικής κίνησης του εδάφους, μόνο όταν το πάχος του υπερβαίνει ένα μέρος των αντίστοιχων μηκών κύματος* λ_L" (Bouckovalas et al. 2016). Οι συγγραφείς συσχετίζουν το κρίσιμο πάχος $H_{L,ampl}$, πέραν του οποίου απομειώνεται το διαδιδόμενο κύμα, με το λόγο του πάχους του ρευστοποιήσιμου στρώματος άμμου προς το πάχος της επιφανειακής μη-ρευστοποιήσιμης κρούστας H_L/H_c ως εξής:

$$\left(\frac{H_L}{\lambda_L}\right)_{ampl} = 0.275\left(\frac{H_L}{H_c}\right)^{0.35} \quad (5)$$

Συνέπεια αυτής της σχέσης αποτελεί το φιλτράρισμα των σεισμικών κυμάτων μέσω ενός ρευστοποιημένου στρώματος με δεδομένο πάχος H_L. Συγκεκριμένα, η παραπάνω εξίσωση μπορεί να οδηγήσει στον υπολογισμό της περιόδου διέγερσης T_{exc} που αντιστοιχεί στην κρίσιμη περίοδο $T_{L,ampl} = \lambda_L/V_{S,L}$ μικρότερες τιμές από την οποία οδηγούν σε δραστική απομείωση του εύρους της επιβαλλόμενης ταλάντωσης:

$$T_{L,ampl} = 3.64\left(\frac{H_L}{H_c}\right)^{-0.35}\frac{H_L}{V_{S,L}} \quad (6)$$

Στην παρούσα Διατριβή, το εδαφικό προφίλ που εξετάζεται μέσω των αριθμητικών αναλύσεων περιλαμβάνει μια βελτιωμένη κρούστα εδάφους 2m επί ενός ρευστοποιήσιμου στρώματος άμμου πάχους 18m, δηλαδή διαθέτει λόγο H_L/H_c = 9. Η αρχική τιμή της μέσης ταχύτητας διατμητικού κύματος είναι $V_{s.o}$ ≈ 125 m/s, ενώ η εκτιμώμενη τιμή για το ρευστοποιημένο στρώμα είναι $V_{s.L}$ ≈ 27 m/s. Με βάση την Εξίσωση 8, εκτιμάται ότι οι φασματικές επιταχύνσεις στην επιφάνεια του εδάφους θα απομειωθούν για περιόδους $T_{exc} < T_{L,ampl}$ ≈ 1.10sec, δηλαδή, σε ολόκληρο το εύρος περιόδων που συνήθως απαντάται στα σεισμικά γεγονότα.

Βάσει των ανωτέρω, η επίδραση της σεισμικής έντασης στις επιταχύνσεις του ελεύθερου πεδίου και κατ' επέκταση και στην ενεργό ιδιοπερίοδο του συστήματος $T_{sys.eff}$ διαφέρει ουσιωδώς μετά την εκδήλωση της ρευστοποίησης. Το γεγονός αυτό είναι ιδιαίτερα εμφανές σε περιπτώσεις μέτριων έως χαμηλών Συντελεστών Ασφαλείας έναντι της ρευστοποίησης (FS_L < 0.4), όπου ο χρόνος εκδήλωσης της ρευστοποίησης είναι μικρός και το σύνολο της δόνησης κυριαρχείται – σε μεγάλο βαθμό – από «καθαρά» ρευστοποιημένες συνθήκες.

Προκειμένου να ποσοτικοποιηθεί η επίδραση των σεισμικών, γεωτεχνικών και κατασκευαστικών παραμέτρων στην ενεργό ιδιοπερίοδο του συστήματος $T_{sys.eff}$ πραγματοποιείται μια σειρά αριθμητικών αναλύσεων συστημάτων ανωδομής-θεμελίου-εδάφους υπό συνθήκες ρευστοποίησης. Πιο συγκεκριμένα, το σύστημα αναφοράς ΑΘΕ, όπως περιγράφηκε προηγουμένως, διεγείρεται στη βάση του με ένα οριζόντιο κύμα επιτάχυνσης, με το προαναφερθέν συχνοτικό περιεχόμενο τύπου white noise. Για το εξεταζόμενο εύρος της σεισμικής επιτάχυνσης ($\alpha^{bedrock}_{max}$ = 0.05g-0.60g), οι αντίστοιχες μέσες τιμές των Συντελεστών Ασφαλείας έναντι της ρευστοποίησης των εδαφικών στρωμάτων είναι μικρότερες από FS_L = 0.4-0.5, υποδεικνύοντας ότι επικρατούν «καθαρά» ρευστοποιήσιμες συνθήκες κατά τη δόνηση. Οι οριζόντιες επιταχύνσεις καταγράφονται στην επιφάνεια του ελεύθερου πεδίου (x> 2B) καθώς και στο επίπεδο της συγκεντρωμένης μάζας ανωδομής.

Το **Σχήμα 13α** παρουσιάζει τις Συναρτήσεις Μεταφοράς που προκύπτουν από τα φάσματα ελαστικής απόκρισης (με απόσβεση ζ = 5%) της χρονοϊστορίας των επιταχύνσεων μεταξύ των κινήσεων στην συγκεντρωμένη μάζα της ανωδομής και στην ελεύθερη επιφάνεια του εδάφους, για μεταβαλλόμενες τιμές της μέγιστης εδαφικής επιτάχυνσης PGA. Πρώτον, παρατηρείται ότι στις Συναρτήσεις Μεταφοράς εμφανίζεται, στην περίπτωση αυτή, μια διακριτή κορυφή και όχι μια κατανομή των ενισχύσεων εντός

ενός εύρους περιόδων όπως παρατηρήθηκε προηγουμένως για μη ρευστοποίήσιμες συνθήκες. Το εύρημα αυτό υποδηλώνει ότι η απόκριση του συστήματος διέπεται κατά κύριο λόγο από μια δεσπόζουσα ιδιοπερίοδο, κυριαρχείται, δηλαδή, από τις ιδιότητες του ρευστοποιημένου υπεδάφους, σε αντίθεση με την προαναφερθείσα περίπτωση των μη-ρευστοποιήσιμων συνθηκών όπου οι αντίστοιχες Συναρτήσεις Σχήματος έχουν δείξει μια διευρυμένη κατανομή των φασματικών ενισχύσεων για αυξανόμενες τιμές του PGA. Η παρατήρηση ότι η παρουσία ενός ρευστοποιημένου υποστρώματος δεν επηρεάζει σημαντικά την ιδιοπερίοδο του συστήματος μπορεί να ερμηνευτεί βάσει των εξής: i) η επιφόρτιση που επιβάλλεται λόγω του βάρους της κατασκευής οδηγεί σε σημαντική αύξηση των ενεργών ορθών κι διατμητικών τάσεων κάτω από το θεμέλιο και, συνεπώς, σε αντίστοιχη απομείωση των υπερπιέσεων του νερού των πόρων, και ii) το βάθος επιρροής της θεμελίωσης στη στροφική κίνηση (που καθορίζει την ιδιοπερίοδο της κατασκευής) είναι μια τάξη μεγέθους μικρότερη από τα τυπικά βάθη επιρροής, δηλαδή, ≈ 0.2B (Gazetas 1991) και, ως εκ τούτου, οποιαδήποτε παραμόρφωση του εδάφους που προκαλείται από το λικνισμό βρίσκεται εντός της προαναφερθείσας «ισχυρής» ζώνης των μειωμένων πιέσεων του νερού των πόρων.

Αναφορικά με τη σεισμική ένταση, επισημαίνεται ότι το πλάτος της σεισμικής διέγερσης στη βάση του καννάβου κυμαίνεται από 0.05g έως 0.60g, ενώ στην επιφάνεια του ελεύθερου πεδίου η μέγιστη εδαφική επιτάχυνση PGA κυμαίνεται από 0.08g έως 0.19g, υποδηλώνοντας δραστική εξασθένηση της σεισμικής κίνησης για έντονες σεισμικές διεγέρσεις. Τα παραπάνω καταδεικνύονται εξετάζοντας την απόκριση του συστήματος για υψηλή ($\alpha^{bedrock}_{max}$ = 0.60g) και μέση ($\alpha^{bedrock}_{max}$ = 0.15g) σεισμική ένταση (**Σχήμα 13β** και **γ**, αντίστοιχα). Και στις δύο περιπτώσεις η κίνηση στο ελεύθερο πεδίο είναι σημαντικά απομειωμένη λόγω της ρευστοποίησης του υπεδάφους με τις επιταχύνσεις στην επιφάνειά του να εμφανίζουν τιμές PGA ίσες με 0.17g και 0.11g για την υψηλή και μέση σεισμική ένταση, αντίστοιχα. Οι χρονοϊστορίες της επιτάχυνσης της ανωδομής (**Σχήμα 13**) και της σχέσης ροπής-στροφής του θεμελίου (**Σχήμα 13γ**) συνηγορούν στο συμπέρασμα ότι οι σεισμικές εντάσεις στην ανωδομή είναι παρόμοιες ανεξάρτητα από το πλάτος του σεισμικού κύματος στο βραχώδες υπόβαθρο. Σημειώνεται ότι η διέγερση υψηλής έντασης συνοδεύεται από κάποιες παραμένουσες στροφές του θεμελίου στο τέλος της δόνησης.

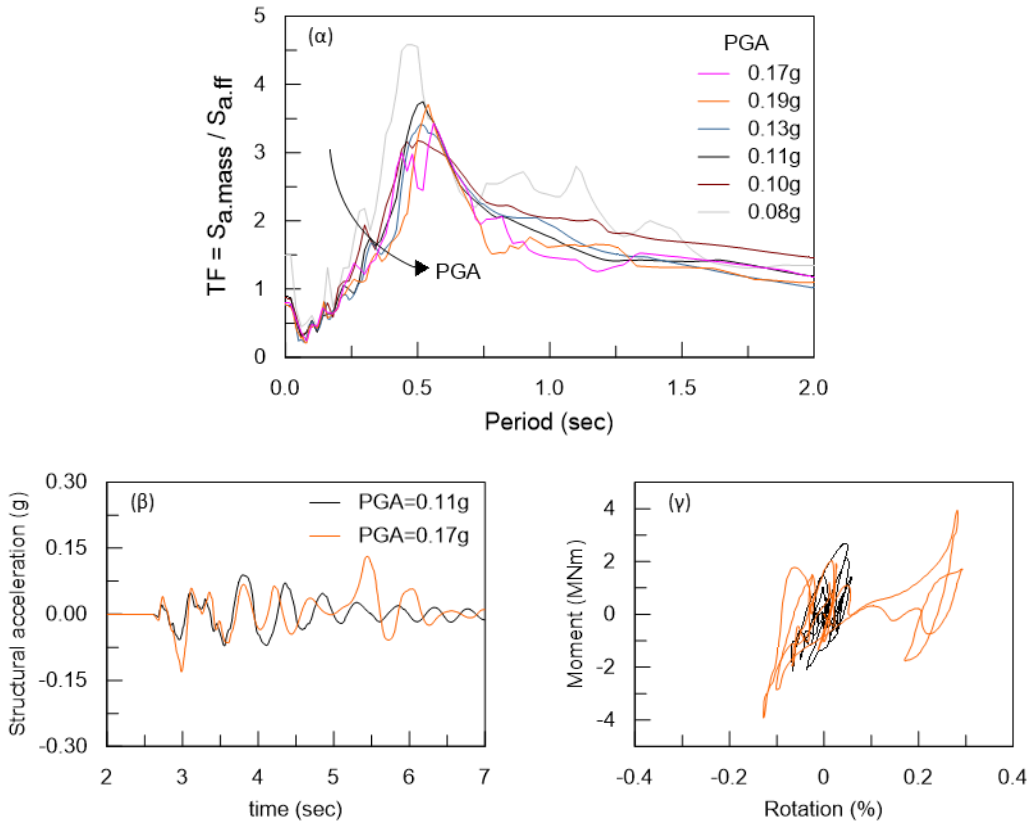

Σχήμα 13: (α) Συναρτήσεις Σχήματος μεταξύ των φασματικών επιταχύνσεων της ανωδομής και της επιφάνειας του εδάφους για διαφορετικές τιμές της μέγιστης εδαφικής επιτάχυνσης (PGA), (β) χρονοϊστορία επιταχύνσεων της ανωδομής για υψηλή ($a^{max}_{bedrock}$ = 0.60g – *PGA* = 0.17g) και μέση ($a^{max}_{bedrock}$ = 0.15g – *PGA* = 0.11g) σεισμική ένταση και (γ) χρονοϊστορία ροπής-στροφής θεμελίου.

Όπως και στην προγενέστερη περίπτωση των μη-ρευστοποιήσιμων συνθηκών, για το χαρακτηρισμό του εύρους των ιδιοπεριόδων του συστήματος με μία παράμετρο, χρησιμοποιούνται ως παράμετροι εκτίμησης η θεμελιώδης περίοδος $T_{sys.p}$ και η εξομαλυμένη φασματική περίοδος $T_{sys.o}$ (Εξίσωση 2).

Το **Σχήμα 14** παρουσιάζει τους λόγους περιόδων (ενεργού προς ελαστικής) $T_{sys.eff}/T_{sys.el}$ ως συνάρτηση της μέγιστης εδαφικής επιτάχυνσης PGA και για τις δύο προαναφερθείσες παραμέτρους $T_{sys.p}$ και $T_{sys.o}$. Αρχικά παρατηρείται ότι η διακύμανση του $T_{sys.o}$ με το PGA δείχνει σημαντική διασπορά, χωρίς να παρουσιάζει κάποια συγκεκριμένη συσχέτιση. Αντίθετα, το $T_{sys.p}$ δείχνει ισχυρότερη συσχέτιση με το PGA, με τους λόγους $T_{sys.eff}/T_{sys.el}$ να παρουσιάζουν αύξηση έως και 20% με αύξηση του PGA. Το γεγονός αυτό έρχεται σε συμφωνία με τα διαγράμματα των Συναρτήσεων Σχήματος, τα οποία χαρακτηρίζονται από μια δεσπόζουσα κορυφή. Αυτό οφείλεται στο γεγονός ότι, όπως έχει ήδη περιγραφεί, η απόκριση της κατασκευής κυριαρχείται από τις εδαφικές συνθήκες στην ρευστοποιημένη τους κατάσταση και, ως εκ τούτου, χαρακτηρίζεται ακριβέστερα από τη θεμελιώδη περίοδο $T_{sys.p.}$ Έτσι, για αυτή την περίπτωση,

προτείνονται οι ακόλουθες αναλυτικές εκφράσεις για τον υπολογισμό του λόγου $T_{sys.eff}/T_{sys.el}$ συναρτήσει της μέγιστης εδαφικής επιτάχυνσης PGA:

$$\frac{T_{sys.eff}}{T_{sys.el}} = 1.00 \qquad for\ PGA \leq 0.075g$$

$$\frac{T_{sys.eff}}{T_{sys.el}} = \alpha \cdot PGA^{b} \qquad for\ PGA > 0.075g \tag{7}$$

όπου α=1.69 και b=0.20 (R^2=0.85).

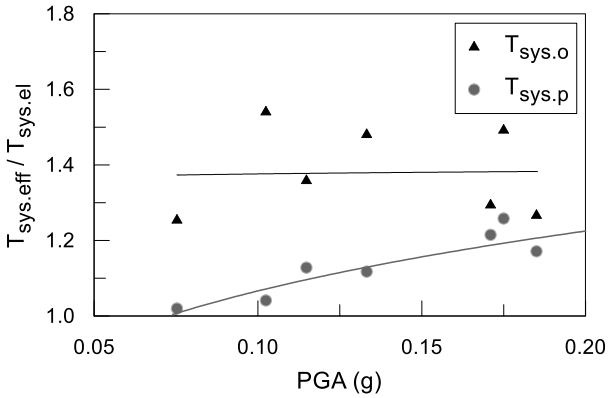

Σχήμα 14: Λόγοι περιόδων ενεργού προς ελαστικού συστήματος $T_{sys.eff}/T_{sys.el}$ ως συνάρτηση της μέγιστης εδαφικής επιτάχυνσης.

V. ΕΠΙΡΡΟΗ ΤΗΣ ΑΛΛΗΛΕΠΙΔΡΑΣΗΣ ΕΔΑΦΟΥΣ-ΚΑΤΑΣΚΕΥΗΣ ΣΤΙΣ ΣΕΙΣΜΙΚΕΣ ΚΑΘΙΖΗΣΕΙΣ: ΡΕΥΣΤΟΠΟΙΗΣΙΜΕΣ ΣΥΝΘΗΚΕΣ

Οι σεισμικές καθιζήσεις των κατασκευών σε ρευστοποιημένο έδαφος οφείλονται κατά κύριο λόγο στη δημιουργία μηχανισμού ολίσθησης τύπου πρίσματος Coulomb, ο οποίος δημιουργείται εξαιτίας της σοβαρής υποβάθμισης της φέρουσας ικανότητας του εδάφους θεμελίωσης (Karamitros et al. 2013). Δευτερεύοντας ρόλος αποδίδεται στη δυναμική συνίζηση και τη στερεοποίηση που ακολουθούν τη ρευστοποίηση, καθώς και στις ογκομετρικές παραμορφώσεις λόγω της εκροής του ρευστοποιημένου εδάφους προς την επιφάνεια (Dashti et al. 2010a). Οι κρίσιμες παράμετροι που καθορίζουν τις καθιζήσεις των θεμελίων έχουν διερευνηθεί διεξοδικά στη βιβλιογραφία, με έμφαση στις γεωτεχνικές πτυχές του προβλήματος, όπως το πάχος και η σχετική πυκνότητα του ρευστοποιημένου στρώματος, το πλάτος του θεμελίου, η εφαρμοζόμενη πίεση κλπ. Την τελευταία δεκαετία, αναπτύχθηκαν αναλυτικές εκφράσεις για

την πρόβλεψη των σεισμικών καθιζήσεων που προκαλούνται από διατμητικού τύπου παραμορφώσεις κατά τη διάρκεια της δόνησης (Bray and Macedo 2017; Dimitriadi et al. 2017; Bullock et al. 2019), οι οποίες συσχετίζουν τη συσσώρευση των σεισμικών καθιζήσεων με τις προαναφερθείσες γεωτεχνικές παραμέτρους. Η παρούσα Διατριβή στοχεύει στην επέκταση των μεθοδολογιών αυτών με τη εισαγωγή στον υπολογισμό των σεισμικών καθιζήσεων της επιρροής της αλληλεπίδρασης εδάφους-κατασκευής. Για πρακτικούς λοιπόν λόγους, κρίθηκε σκόπιμο να εκφραστούν τα αποτελέσματα της αλληλεπίδρασης μέσω του λόγου $\rho_{A\Theta E}/\rho_{\Theta E}$, δηλαδή του λόγου των σεισμικών καθιζήσεων μεταξύ του συστήματος ανωδομής-θεμελίου-εδάφους (ΑΘΕ) και του συστήματος θεμελίου-εδάφους (ΘΕ). Με τον τρόπο αυτό, η πρόσθετη συμβολή της αλληλεπίδρασης μπορεί να εκφραστεί ως ο διορθωτικός παράγοντας $\rho_{A\Theta E}/\rho_{\Theta E}$ επί των καθιερωμένων σχέσεων για τις καθιζήσεις των συστημάτων θεμελίου-εδάφους.

Η επίδραση της ανωδομής υπεισέρχεται ως αδρανειακή δύναμη που δρα είτε εντός είτε εκτός φάσης σε σχέση με την κίνηση του ολισθαίνοντος πρίσματος του εδάφους θεμελίωσης, ενισχύοντας ή απομειώνοντας, αντίστοιχα, τη συσσώρευση των καθιζήσεων. Ως εκ τούτου, τα δυναμικά χαρακτηριστικά του συστήματος ΑΘΕ διέπουν σε μεγάλο βαθμό τη συσσώρευση των καθιζήσεων. Η παραμετρική διερεύνηση που ακολουθεί επικεντρώθηκε στις πιο κρίσιμες παραμέτρους που ποσοτικοποιούν την αλληλεπίδραση εδάφους-θεμελίου ανωδομής [λόγος περιόδων T_{sys}/T_{exc}, λόγος λυγηρότητας h/r, σχετικός λόγος μάζας γ, σχετική δυσκαμψία της ανωδομής προς την εδαφική δυσκαμψία $s=h/(V_s T_{str.f})$] καθώς και η μέγιστη εδαφική επιτάχυνση PGA. Συνολικά πραγματοποιήθηκαν 191 αριθμητικές αναλύσεις για το εύρος πρακτικού ενδιαφέροντος των ανωτέρω παραγόντων.

Μηχανισμός συσσώρευσης σεισμικών καθιζήσεων. Ο μηχανισμός συσσώρευσης σεισμικών καθιζήσεων θεμελίων, χωρίς αδρανειακή αλληλεπίδραση με την ανωδομή, είχε αρχικά αναλυθεί από τους Richards et al. (1993) σε συνθήκες ξηρού εδάφους. Δεδομένου ότι επιτόπιες και εργαστηριακές παρατηρήσεις δείχνουν ότι η διατμητική αστοχία του εδάφους θεμελίωσης έχει ως αποτέλεσμα τη συσσώρευση καθιζήσεων ακόμη και σε μέτριες εντάσεις σεισμού (Richards et al. 1990), οι συγγραφείς συσχέτισαν τις σεισμικές καθιζήσεις επιφανειακών θεμελίων με την υποβάθμιση της φέρουσας ικανότητας, λόγω επαλληλίας των δυνάμεων βαρύτητας με τις αδρανειακές λόγω σεισμού. Θεώρησαν δηλαδή ότι αποτελεί έναν ξεχωριστό μηχανισμό από τις καθιζήσεις που αποδίδονται στη συμπύκνωση του εδάφους. Επιπρόσθετες μελέτες για ρευστοποιήσιμα εδάφη, προσδιορίζουν την υποβάθμιση της αντοχής του εδάφους λόγω ρευστοποίησης και τον επακόλουθο σχηματισμό ενός εδαφικού πρίσματος τύπου Coulomb ως τον κύριο μηχανισμό για τη συσσώρευση σεισμικών καθιζήσεων συστημάτων θεμελίου-εδάφους (Dimitriadi et al. 2017; Karamitros et al. 2013).

Η παρούσα Διατριβή στοχεύει στην επέκταση του εν λόγω μηχανισμού καθιζήσεων και στην περίπτωση του πλήρους συστήματος ανωδομής-θεμελίου-εδάφους (ΑΘΕ). Η απόκριση των συστημάτων ΑΘΕ και ΘΕ σε ρευστοποιήσιμες συνθήκες αναλύεται ενδεικτικά μέσω των αποτελεσμάτων των αριθμητικών αναλύσεων που παρουσιάζονται στα επόμενα σχήματα. Τα χαρακτηριστικά και οι παράμετροι των εξεταζόμενων συστημάτων αντιστοιχούν σε μια κατασκευή κοντά στο συντονισμό, δηλαδή με λόγο περιόδων T_{sys}/T_{exc} = 0.90, με χαμηλό προς μέσο λόγο λυγηρότητας h/r = 1.04 και μέσο λόγο μάζας γ = 4.00. Σημειώνεται ότι η περίοδος του συστήματος T_{sys} αναφέρεται στην ενεργό ιδιοπερίοδο $T_{sys.eff}$.

Το **Σχήμα 15** συγκρίνει τις χρονοϊστορίες των σεισμικών καθιζήσεων μεταξύ του συστήματος ανωδομής-θεμελίου-εδάφους και του αντίστοιχου συστήματος θεμελίου-εδάφους. Είναι αξιοσημείωτο ότι οι τελικές καθιζήσεις του συστήματος ΑΘΕ είναι περίπου 30% μικρότερες από αυτές του συστήματος ΘΕ, ενώ, αντίστοιχα, και οι διατμητικές παραμορφώσεις εμφανίζονται μειωμένες (**Σχήμα 15γ**). Σημειώνεται ότι μετά την πλήρη ρευστοποίηση στο ελεύθερο πεδίο τη χρονική στιγμή t = 2.5sec (**Σχήμα 15β**), τα ρευστοποιημένα στρώματα λειτουργούν ως φυσική σεισμική μόνωση προκαλώντας την απομείωση της σεισμικής διέγερσης του θεμελίου (**Σχήμα 15β**). Σημαντικές στροφές του θεμελίου εκδηλώνονται μόνο στην περίπτωση του συστήματος ΑΘΕ λόγω της ταλάντωσης της ανωδομής, ενώ, αντίθετα, το σύστημα ΘΕ παρουσιάζει μια μόνιμη – παραμένουσα – στροφή χωρίς ταλαντώσεις.

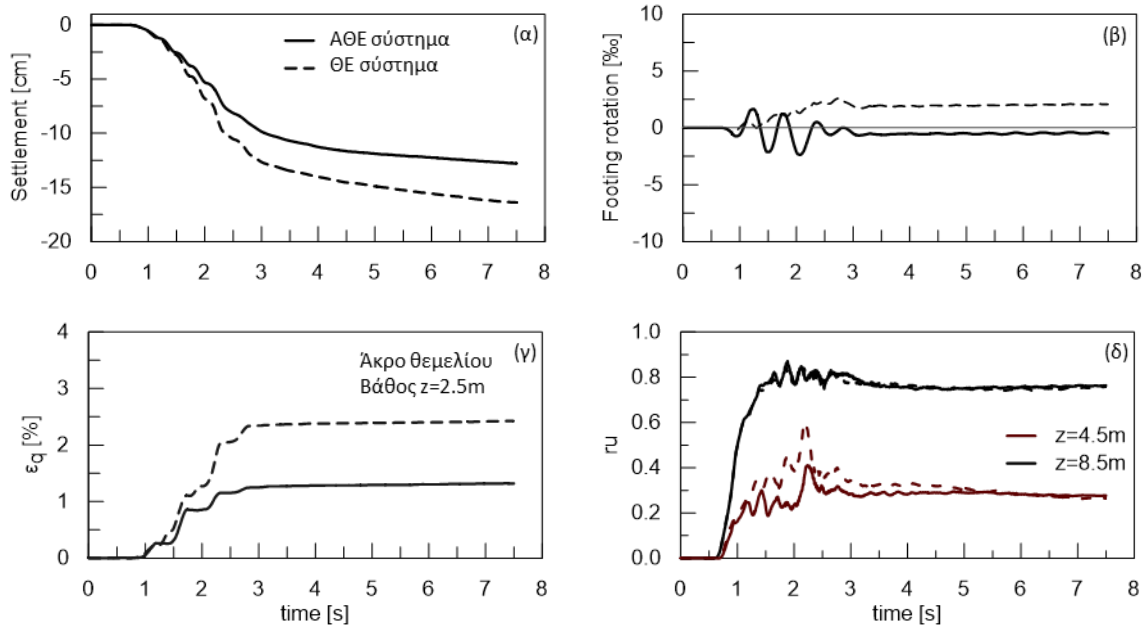

Σχήμα 15: Χρονοϊστορίες απόκρισης των συστημάτων ΑΘΕ και ΘΕ: (α) σεισμική καθίζηση, (β) οριζόντιες μετακινήσεις του θεμελίου, (γ) διατμητικές παραμορφώσεις κάτω από τα άκρα του θεμελίου, (δ) λόγοι υπερπιέσεων πόρων κάτω από το θεμέλιο (σε βάθος z=4.5m και 8.5m).

Βάσει των ανωτέρω παρατηρήσεων, δύο βασικά ερωτήματα προκύπτουν σχετικά με την απόκριση των συστημάτων ΑΘΕ και ΘΕ:

- Γιατί το σύστημα ΑΘΕ καθιζάνει λιγότερο από το σύστημα ΘΕ, ενώ – την ίδια στιγμή – είναι αυτό που παρουσιάζει τις μεγαλύτερες ταλαντώσεις;
- Είναι ο ρόλος της αλληλεπίδρασης εδάφους-κατασκευής, γενικά, ωφέλιμος ή επιζήμιος στην απόκριση των κατασκευών σε ρευστοποιήσιμο έδαφος;

Προς απάντηση των ερωτημάτων αυτών, το **Σχήμα 16** παρουσιάζει την απόκριση του συστήματος ΑΘΕ σε όλο το χρονικό εύρος της δόνησης (t = 0-8 sec), εστιάζοντας, παράλληλα, στις βασικές παραμέτρους απόκρισης κατά τη διάρκεια ενός κύκλου ταλάντωσης (για t = 1-2 sec). Πιο αναλυτικά, η χρονοϊστορία της κατακόρυφης ταχύτητας στο κέντρο του θεμελίου, δηλαδή ο ρυθμός καθίζησης, παρουσιάζεται στη δεύτερη σειρά του σχήματος (c, d), ενώ οι οριζόντιες μετακινήσεις και ταχύτητες της ανωδομής και του θεμελίου παρουσιάζονται στην τρίτη και τέταρτη σειρά αντίστοιχα (e, f και g, h). Ένας πλήρης κύκλος κίνησης της συγκεντρωμένης μάζας του μονοβάθμιου ταλαντωτή και της θεμελίωσης προσδιορίζεται στα ακόλουθα σχήματα με τα σημεία a'-e 'και a-e, αντίστοιχα. Επιλέγεται εδώ η εστίαση στο πρώτο τέταρτο του κύκλου ταλάντωσης, δηλαδή από το σημείο a στο σημείο b. Το τμήμα της κίνησης αυτής συμβαίνει εντός του χρονικού παραθύρου t = 1-2 sec όπου και παρατηρείται το μεγαλύτερο μέρος της καθίζησης (**Σχήμα 16α**).

Αρχικά, παρατηρείται ότι το πρώτο τέταρτο του κύκλου από το σημείο a στο b αντιστοιχεί στην κίνηση του εδάφους (και του θεμελίου) από την ουδέτερη θέση του (u = 0) στη μέγιστη μετατόπιση του προς τα αριστερά ($u = u_{min}$), όπως παρατηρείται στο **Σχήμα 16η**. Ταυτόχρονα, η ανωδομή, ως μονοβάθμιος ταλαντωτής, υπόκειται σε μια εξαναγκασμένη ταλάντωση με δυναμική φόρτιση στη βάση της. Δεδομένου ότι ο λόγος περιόδων T_{sys}/T_{exc} είναι κοντά στον συντονισμό (ίσος με 0.90), αναμένεται υστέρηση φάσης μεταξύ της κίνησης του ταλαντωτή (της ανωδομής) και της πηγής της διέγερσης (κίνηση θεμελίωσης) κοντά στο ένα τέταρτο του κύκλου ταλάντωσης, γεγονός που επιβεβαιώνεται με την εξέταση των χρονοϊστοριών οριζόντιας μετατόπισης και ταχύτητας του σχήματος **Σχήμα 16η** και **στ**. Πιο συγκεκριμένα, όταν το θεμέλιο βρίσκεται στην ουδέτερη θέση (σημείο a) η ανωδομή υστερεί ένα τέταρτο του κύκλου, επομένως, βρίσκεται στη μέγιστη μετατόπιση της προς τα δεξιά ($u_{str} = u_{max}$). Στο σημείο a της μέγιστης μετατόπισης, η ανωδομή έχει μηδενική ταχύτητα (**Σχήμα 16δ**) ($\dot{u}$ = 0) και τη μέγιστη – με αρνητικό πρόσημο – επιτάχυνση ($\ddot{u} = \ddot{u}_{min}$). Το **Σχήμα 16α** απεικονίζει τη θέση της ανωδομής και την εδαφική μετατόπιση που αντιστοιχούν στο σημείο (α). Στο σημείο αυτό ασκείται στην ανωδομή η μέγιστη αδρανειακή δύναμη η οποία, σύμφωνα με το δεύτερο νόμο του Νεύτωνα, είναι ίση με $F_{inertia}$ = -

$m \cdot a$ και έχει αντίθετο πρόσημο με αυτό της επιτάχυνσης. Στη συνέχεια, καθώς το θεμέλιο κινείται προς τα αριστερά, δηλαδή προς την ελάχιστη μετατόπιση του (a -> b), η ανωδομή επιστρέφει στην ουδέτερη θέση της (**Σχήμα 16β**). Ο μισός κύκλος ταλάντωσης ολοκληρώνεται καθώς το θεμέλιο επιστρέφει στην ουδέτερη θέση του (b->c) και ο ρυθμός καθίζησης (δ) μηδενίζεται καθώς έχει ολοκληρωθεί η ολίσθηση του εδαφικού πρίσματος. Ο μισός κύκλος από το σημείο c στο σημείο e αντιπροσωπεύει τη συμμετρική κίνηση της θεμελίωσης προς τα δεξιά. Το μοτίβο της συσσώρευσης καθιζήσεων επαναλαμβάνεται ανά μισό κύκλο ταλάντωσης.

Ως αποτέλεσμα των παραπάνω, η αδρανειακή δύναμη της ανωδομής κατευθύνεται προς τα δεξιά τη στιγμή που το θεμέλιο κινείται προς τα αριστερά και καθιζάνει. Είναι, επομένως, η καθυστέρηση φάσης μεταξύ των ταλαντώσεων της ανωδομής και του θεμελίου – στην περίπτωση του συντονισμού – που αντισταθμίζει εν μέρει τις αδρανειακές δυνάμεις του εδάφους και την ολίσθηση του εδαφικού πρίσματος, εξηγώντας τη μικρότερη συσσώρευση καθιζήσεων του συστήματος ΑΘΕ. Στην παραμετρική διερεύνηση που ακολουθεί, επιχειρείται η σε βάθος διερεύνηση και ποσοτικοποιήση της επίδρασης του εν λόγω μηχανισμού στη συσσώρευση σεισμικών καθιζήσεων για δομικά συστήματα με ποικίλα δυναμικά χαρακτηριστικά.

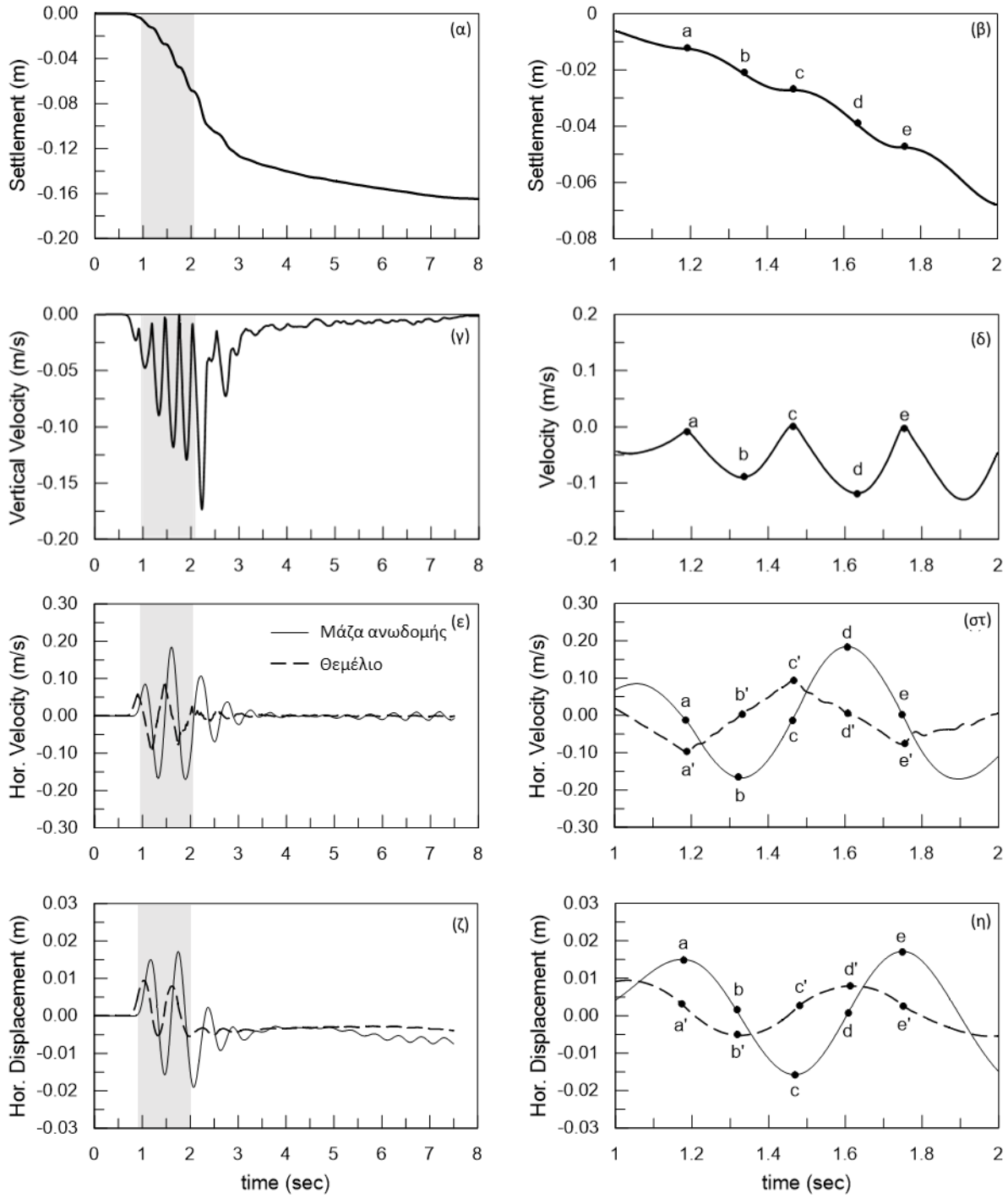

Σχήμα 16: Χρονοϊστορίες απόκρισης του συστήματος ΑΘΕ και της επιφάνειας του εδάφους: (α, β) σεισμικές καθιζήσεις, (γ, δ) κατακόρυφη ταχύτητα θεμελίου (ρυθμός καθίζησης), (ε, στ) οριζόντιες ταχύτητες (μάζας ανωδομής και επιφάνειας εδάφους), (ζ, η) οριζόντιες μετακινήσεις ταχύτητες (μάζας ανωδομής και επιφάνειας εδάφους) (α), (γ), (ε), (ζ) για την πλήρη διάρκεια της δόνησης t = 0-8 sec, (β), (δ), (στ), (η) για τη χρονική περίοδο t = 1-2 sec.

Επίδραση του λόγου περιόδων T_{sys}/T_{exc}. Ο λόγος περιόδων T_{sys}/T_{exc} αποτελεί τη βασική παράμετρο που καθορίζει τη συσσώρευση καθιζήσεων των συστημάτων ΑΘΕ. Στο πλαίσιο αυτής της μελέτης, η περίοδος T_{sys} αποτελεί τη θεμελιώδη ιδιοπερίοδο του συστήματος ΑΘΕ, αντιστοιχώντας επί της ουσίας στην ενεργό περίοδο $T_{sys.eff}$, και η περίοδος T_{exc} αποτελεί τη θεμελιώδη περίοδο διέγερσης στην επιφάνεια του εδάφους. Τα **Σχήμα 17α-γ** παρουσιάζουν τη διακύμανση του λόγου καθιζήσεων $\rho_{AΘE}/\rho_{ΘE}$ με το λόγο περιόδων T_{sys}/T_{exc}. Παράλληλα, παρουσιάζονται οι επιδράσεις των λοιπών παραμέτρων της αλληλεπίδρασης, και συγκεκριμένα του λόγου λυγηρότητας *h/r* (Σχήμα 17α), του λόγου μάζας γ (Σχήμα 17β) και της σεισμικής επιτάχυνσης a^b_{max} (17γ).Συνοπτικά, παρατηρείται ότι:

- Τα «άκαμπτα» συστήματα ΑΘΕ ($T_{sys}/T_{exc} \rightarrow 0.0$) καθιζάνουν στον ίδιο βαθμό με τα συστήματα ΘΕ (δηλαδή, $\rho_{AΘE}/\rho_{ΘE} \approx 1.0$). Σημειώνεται ότι και τα δύο συστήματα κινούνται ως άκαμπτες κατασκευές και οι αναπτυσσόμενες αδρανειακές δυνάμεις της ανωδομής είναι, αφενός μεν ίσες μεταξύ τους και αφετέρου δρουν εντός φάσης με τις αδρανειακές δυνάμεις του εδάφους. Η διαφορά των δύο συστημάτων έγκειται στο γεγονός ότι το πρώτο έχει υψηλότερο σημείο εφαρμογής της αδρανειακής του δύναμης, δηλαδή εφαρμόζεται σε ύψος h = 3.0m και, επομένως, είναι επιρρεπές στο λικνισμό.
- «Εύκαμπτα» συστήματα ΑΘΕ ($T_{sys}/T_{exc} > 1.40$) καθιζάνουν περίπου 10-20% λιγότερο από τα συστήματα ΘΕ ($\rho_{AΘE}/\rho_{ΘE} \approx 0.8$-$0.9$). Το γεγονός αυτό αποδίδεται στις αδρανειακές δυνάμεις της ανωδομής οι οποίες, αν και παραμένουν μικρές, δρουν εκτός φάσης με αυτές του εδάφους θεμελίωσης, αντισταθμίζοντας έτσι εν μέρει την ολίσθηση της εδαφικής σφήνας.
- Στην περίπτωση του συντονισμού ($T_{sys}/T_{exc} \approx 1.00$-$1.25$), η μείωση των καθιζήσεων του συστήματος ΑΘΕ παίρνει τη μέγιστη τιμή της, έως και 35% ($\rho_{AΘE}/\rho_{ΘE} \approx 0.65$). Αυτό οφείλεται στο γεγονός ότι οι αδρανειακές δυνάμεις της ανωδομής παρουσιάζουν φασματική ενίσχυση, ενώ, ταυτόχρονα, η διαφορά φάσης μεταξύ της κίνησης της κατασκευής και του εδάφους παραμένει σημαντική (ένα τέταρτο του κύκλου ταλάντωσης). Ως εκ τούτου, η αδρανειακή δύναμη της ανωδομής αναστέλλει στο μέγιστο βαθμό την ολίσθηση του εδαφικού πρίσματος.

Επίδραση του σχετικού λόγου μάζας *γ* και του λόγου λυγηρότητας *h/r*. Ο σχετικός λόγος μάζας *γ* και ο λόγος *λυγηρότητας h/r* επηρεάζουν την απόκριση του συστήματος ΑΘΕ, αν και σε μικρότερο βαθμό σε σύγκριση με τον λόγο περιόδων T_{sys}/T_{exc}. Αύξηση του σχετικού λόγου μάζας *γ* οδηγεί σε αύξηση των αδρανειακών δυνάμεων της κατασκευής, ενώ αύξηση του λόγου λυγηρότητας *h/r* σε αύξηση των ροπών ανατροπής, λόγω της αύξησης του μοχλοβραχίονα άσκησης των αντίστοιχων δυνάμεων. Και οι δύο αυτές επιδράσεις οδηγούν σε επιδείνωση του λικνισμού της κατασκευής. Η μέγιστη αύξηση του λόγου καθιζήσεων είναι περίπου 40% για τιμές του λόγου λυγηρότητας *h*/r =1.88 και παρατηρείται στην

περιοχή του συντονισμού. Επίσης, αξίζει να σημειωθεί ότι στην περίπτωση ημι-άκαμπτων κατασκευών (T_{sys}/T_{exc} = 0.55-0.80) με υψηλούς λόγους λυγηρότητας (h/r > 1.36), οι καθιζήσεις των συστημάτων ΑΘΕ αυξάνονται έως και 20% σε σχέση με αυτές των αντίστοιχων ΘΕ, γεγονός που αποδίδεται στο συνδυασμό αυξημένων ροπών ανατροπής με εντός φάσης κίνηση κατασκευής και εδάφους.

Επίδραση λιγότερο σημαντικών παραμέτρων.

Η εξέταση της σεισμικής έντασης στην περίπτωση της ρευστοποίησης σχετίζεται, ουσιαστικά, με το χρόνο εκδήλωσής της. Μετά την εμφάνισή της, η διάδοση των σεισμικών κυμάτων, όπως και η αντίστοιχη διέγερση της κατασκευής, εξασθενούν σημαντικά. Αυτό υποδεικνύεται στο **Σχήμα 15α** όπου παρατηρείται ότι η διαφορά στη συσσώρευση καθιζήσεων μεταξύ των συστημάτων ΑΘΕ και ΘΕ αμβλύνεται αφού γενικευθεί η ρευστοποίηση καθ' ύψος του εδαφικού προφίλ. Ως εκ τούτου, οι αυξανόμενες τιμές της μέγιστης επιτάχυνσης του σεισμικού υποβάθρου a^b_{max} έχουν περιορισμένη επίδραση στους λόγους $\rho_{A\Theta E}/\rho_{\Theta E}$. Στο εξεταζόμενο πρόβλημα, ο μειωμένος Συντελεστής Ασφάλειας έναντι της ρευστοποίησης (FS_L < 0.3-0.4) έχει ως αποτέλεσμα την πλήρη ρευστοποίηση των στρωμάτων του υπεδάφους, δηλαδή προκύπτουν τιμές του λόγου υπερπιέσεων του νερού των πόρων r_u κοντά στο 1.0, ακόμη και για μικρά επίπεδα επιτάχυνσης.

Η διερεύνηση της επίδρασης του λόγου δυσκαμψίας κατασκευής-εδάφους $s=h/(V_s \cdot T_{str.f})$ βασίζεται στην εξέταση συστημάτων με μεταβαλλόμενη δυσκαμψία k_{str} και σταθερή μάζα M_{str} ανωδομής και, επομένως, με μεταβαλλόμενη ιδιοπεριόδο (της πακτωμένης ανωδομής) $T_{str.f}$. Οι εξεταζόμενες τιμές του λόγου s έχουν επιλεγεί αποσκοπώντας να καλύψουν ένα πρακτικά χρήσιμο εύρος τιμών σύμφωνα με τον Κανονισμό NEHRP (2012), δηλαδή s = 0.05 – 0.33. Τα αποτελέσματα των σχετικών αριθμητικών αναλύσεων παρουσιάζονται στο **Σχήμα 17δ**, το οποίο δείχνει τη διακύμανση του λόγου καθίζησης $\rho_{A\Theta E}/\rho_{\Theta E}$ με το λόγο δυσκαμψίας s, για διαφορετικές τιμές του λόγου περιόδων T_{sys}/T_{exc}. Τα αποτελέσματα δείχνουν ότι οι λόγοι καθίζησης δεν επηρεάζονται σημαντικά από το λόγο s, ενώ οι τιμές τους είναι εν γένει συνεπείς με τα προηγούμενα ευρήματα. Συγκεκριμένα, για κατασκευές κοντά στο συντονισμό, καθώς και εύκαμπτες κατασκευές με λόγους περιόδων T_{sys}/T_{exc} ίσους με 1.0 και 1.3, αντίστοιχα, τα συστήματα ΑΘΕ καθιζάνουν συστηματικά κατά 10-20% λιγότερο από τα συστήματα ΘΕ, δηλαδή $\rho_{A\Theta E}/\rho_{\Theta E}$ ≈ 0.8 - 0.9. Αντίθετα, οι δύσκαμπτες κατασκευές με λόγο περιόδων T_{sys}/T_{exc} =0.5 εμφανίζουν μια πιο σημαντική διακύμανση στις τιμές του λόγου καθιζήσεων ($\rho_{A\Theta E}/\rho_{\Theta E}$ ≈ 0.75 – 1.00).

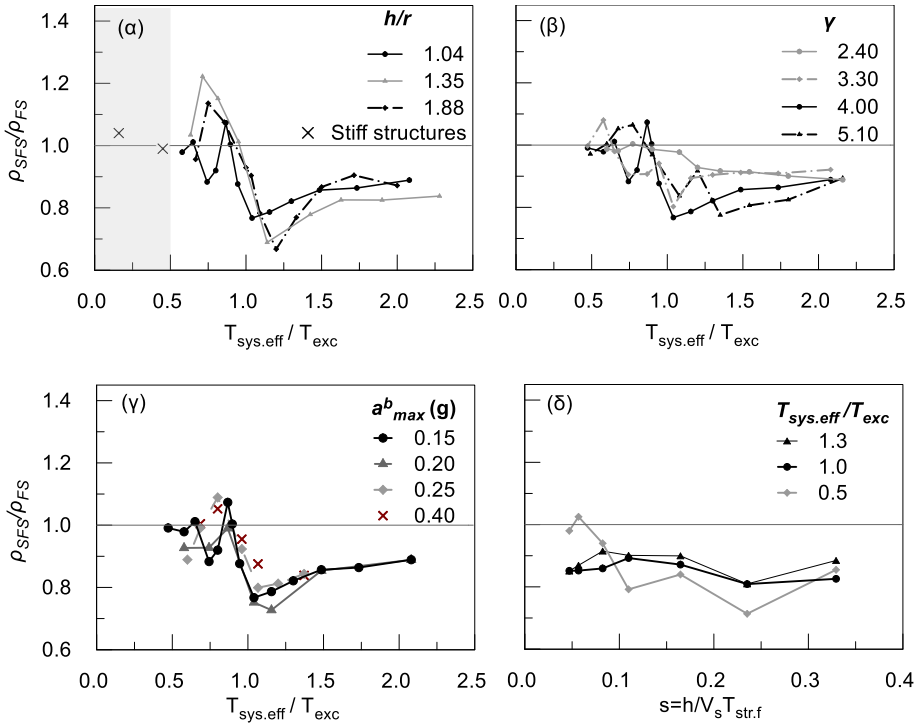

Σχήμα 17: (α)-(γ) Διακύμανση του λόγου καθιζήσεων $\rho_{A\Theta E}/\rho_{\Theta E}$ με το λόγο περιόδων T_{sys}/T_{exc} για ομάδες διαφορετικών (α) λόγων λυγηρότητας h/r, (β) λόγου σχετικής μάζας γ και (γ) μέγιστης επιτάχυνσης βραχώδους υποβάθρου a^b_{max}; (δ) Διακύμανση του λόγου καθιζήσεων $\rho_{A\Theta E}/\rho_{\Theta E}$ με το λόγο δυσκαμψίας s για ομάδες διαφορετικού λόγου περιόδων T_{sys}/T_{exc}.

Αναλυτικές σχέσεις για την επιρροή της αλληλεπίδρασης εδάφους-κατασκευής στο λόγο καθιζήσεων $\rho_{A\Theta E}/\rho_{\Theta E}$.

Στην ενότητα αυτή παρουσιάζονται οι αναλυτικές εκφράσεις που αναπτύχθηκαν για το λόγο καθιζήσεων $\rho_{A\Theta E}/\rho_{\Theta E}$ μεταξύ συστημάτων ΑΘΕ και ΘΕ μετά από ανάλυση παλινδρόμησης πολλαπλών μεταβλητών των αποτελεσμάτων των αριθμητικών αναλύσεων. Με βάση την παραμετρική διερεύνηση που προηγήθηκε, εξετάστηκαν οι ακόλουθες κύριες παράμετροι αλληλεπίδρασης εδάφους-κατασκευής και σεισμικής διέγερσης: ο λόγος περιόδων T_{sys}/T_{exc}, ο λόγος λυγηρότητας h/r και ο σχετικός λόγος μαζών γ.

Η ανάπτυξη των σχέσεων αυτών διακρίνει δύο φασματικές περιοχές: i) την άκαμπτη και ημι-άκαμπτη περιοχή ($T_{sys}/T_{exc} < 0.80$), όπου οι αδρανειακές δυνάμεις και, επομένως, οι καθιζήσεις είναι, αρχικά, παρόμοιες για τα συστήματα ΑΘΕ και ΘΕ – ειδικά για το $T_{sys}/T_{exc} < 0.45$ – και, στη συνέχεια, τείνουν να γίνονται μεγαλύτερες για τα συστήματα ΑΘΕ, και ii) η περιοχή με εύρος που περιλαμβάνει τον συντονισμό και επεκτείνεται μέχρι τα εύκαμπτα συστήματα ($T_{sys}/T_{exc} > 0.80$), όπου οι καθιζήσεις τείνουν να είναι μεγαλύτερες για τα συστήματα ΘΕ. Εν προκειμένω, ο λόγος καθιζήσεων $\rho_{A\Theta E}/\rho_{\Theta E}$ εκφράζεται ως εξής:

$$\frac{\rho_{SFS}}{\rho_{FS}} = \begin{cases} 1 + C_a \cdot \left(T_{sys}/T_{exc}\right)^2 & T_{sys}/T_{exc} \leq 0.80 \\ \left[\dfrac{C_{1.b} + \left(T_{sys}/T_{exc}\right)^2}{\sqrt{\left[C_{2.b} - \left(T_{sys}/T_{exc}\right)^2\right]^2 + C_{3.b}\left(T_{sys}/T_{exc}\right)^2}}\right]^{-1} & T_{sys}/T_{exc} \geq 0.80 \end{cases} \quad (8)$$

Με βάση τα δεδομένα από τα **Σχήμα 17α**-**β**, οι συντελεστές C_{α}, $C_{1.b}$, $C_{2.b}$ και $C_{3.b}$ εκφράζονται συναρτήσει των λόγων *h*/*r* και *γ* ως εξής:

$$C_a = \begin{cases} 0.00 & h/r \leq 1.06 \\ 0.77 \cdot (h/r) - 0.81 & 1.06 \leq h/r \leq 1.36 \\ 0.23 & h/r \geq 1.36 \end{cases} \quad (9)$$

$$C_{1,b} = \begin{cases} 0.16 & h/r \leq 1.06 \\ -0.70 \cdot (h/r) + 0.90 & 1.06 \leq h/r \leq 1.36 \\ -0.05 & h/r \geq 1.36 \end{cases} \quad (10)$$

$$C_{2.b} = [0.82 + 0.24 \cdot tanh(\gamma - 2.95)] \cdot [0.33 \cdot (h/r) + 0.47] \quad (11)$$

$$C_{3.b} = (0.85 + 0.31 \cdot e^{-0.30 \cdot \gamma}) \cdot g(h/r) \quad (12)$$

$$g(h/r) = \begin{cases} 1.00 & h/r \leq 1.06 \\ -1.07 \cdot (h/r) + 2.13 & 1.06 \leq h/r \leq 1.36 \\ 0.62 & h/r \geq 1.36 \end{cases} \quad (13)$$

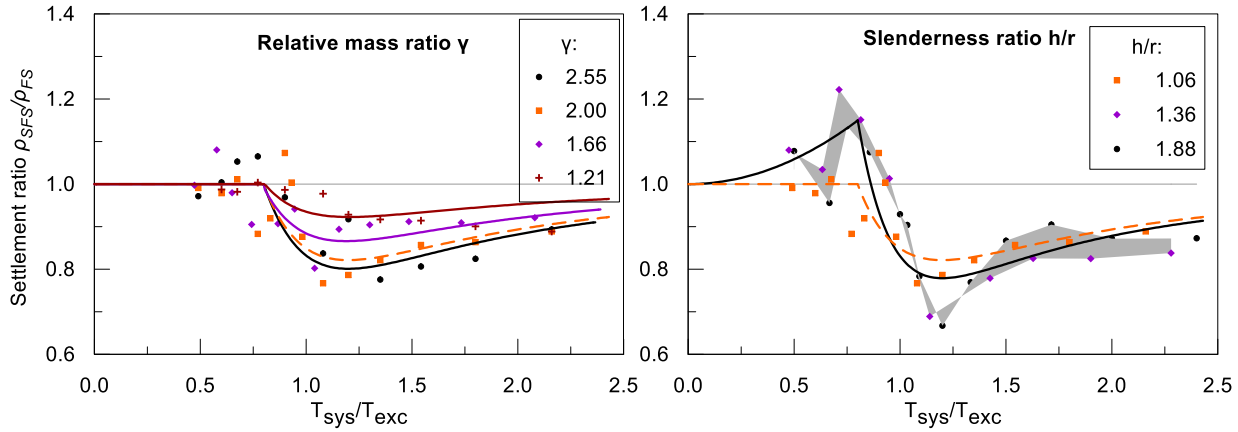

Σχήμα 18: Επίδραση του λόγου περιόδων T_{sys}/T_{exc} στο λόγο καθιζήσεων $\rho_{A\Theta E}/\rho_{\theta E}$: Σύγκριση των αριθμητικών αποτελεσμάτων με τις αναλυτικές προβλέψεις για διαφορετικές ομάδες (α) του λόγου σχετικής μάζας *γ* και (β) του λόγου λυγηρότητας *h/r*.

Οι ανωτέρω αναλυτικές σχέσεις συγκρίνονται με τα αριθμητικά αποτελέσματα στο Σχήμα 18. Επιπλέον, προκειμένου να εξακριβωθεί η αξιοπιστία των προτεινόμενων σχέσεων, γίνεται σύγκριση one-to-one μεταξύ των προβλέψεων (prediction) και των αντίστοιχων τιμών από τις αριθμητικές αναλύσεις (numerical). Η ακρίβεια της μεθοδολογίας ποσοτικοποιείται μέσω του σχετικού σφάλματος R στην πρόβλεψη του λόγου καθιζήσεων, οριζόμενο ως:

$$R = \frac{SR_{pred} - SR_{num}}{SR_{num}} \tag{14}$$

Τα αντίστοιχα στατιστικά στοιχεία (μέση τιμή και τυπική απόκλιση του σχετικού σφάλματος R) παρουσιάζονται στα **Σχήμα 19α-β**. Η μέση τιμή και η τυπική απόκλιση του σφάλματος που προκύπτει για το συνολικό αριθμό των δεδομένων είναι -0.001 και 0.07 αντίστοιχα. Τα αποτελέσματα δείχνουν ότι η κατανομή των σχετικών σφαλμάτων είναι αρκετά ομοιόμορφη για τα διαφορετικά σύνολα παραμέτρων που εξετάστηκαν.

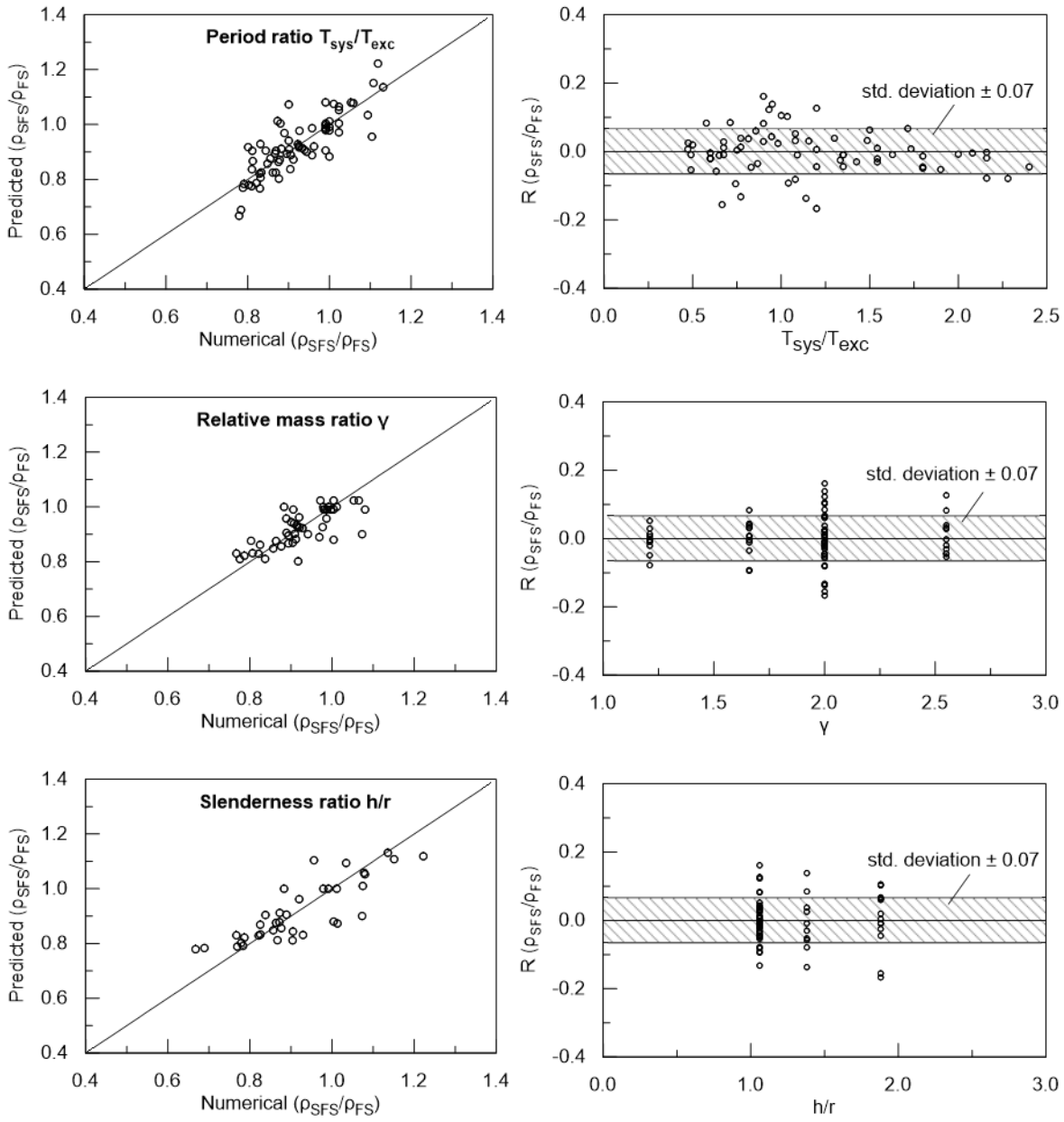

Σχήμα 19: Αξιολόγηση του σχετικού σφάλματος στον αναλυτικό υπολογισμό του λόγου $\rho_{A\Theta E}/\rho_{\Theta E}$ έναντι των αριθμητικών προβλέψεων: (α) σύγκριση one-to-one και (β) διακύμανση του σχετικού σφάλματος με τις κύριες παραμέτρους του προβλήματος: (i) T_{sys}/T_{exc}, (ii) *h/r και* (iii) *γ*.

VI. ΕΠΙΡΡΟΗ ΤΗΣ ΑΛΛΗΛΕΠΙΔΡΑΣΗΣ ΕΔΑΦΟΥΣ-ΚΑΤΑΣΚΕΥΗΣ ΣΤΙΣ ΣΕΙΣΜΙΚΕΣ ΚΑΘΙΖΗΣΕΙΣ: ΜΗ-ΡΕΥΣΤΟΠΟΙΗΣΙΜΕΣ ΣΥΝΘΗΚΕΣ

Αποτελεί συνηθισμένο φαινόμενο κατά τη διάρκεια των σεισμικών διεγέρσεων, εδαφικά προφίλ με Συντελεστή Ασφάλειας έναντι της ρευστοποίησης FS_L μικρότερο από τη μονάδα να εμφανίζουν μια αρχική περίοδο δόνησης κατά την οποία οι υπερπιέσεις πόρων παραμένουν μικρές και η επίδραση τους στην σεισμική απόκριση του εδάφους και της θεμελιώσεις είναι πρακτικά αμελητέα. Το μέρος αυτό της δόνησης ενδέχεται να είναι σημαντικό σε διάρκεια και από τη στιγμή που κυριαρχείται από συνθήκες μη ρευστοποιημένου εδάφους, παρουσιάζει ενισχυμένες εδαφικές επιταχύνσεις, σε σύγκριση με τις ρευστοποιημένες συνθήκες. Στόχος του κεφαλαίου αυτού είναι να απομονωθεί η απόκριση τέτοιων συστημάτων κατά το πρώτο μέρος της δόνησης και, ως επόμενο βήμα, να διερευνηθεί ο ρόλος της αλληλεπίδρασης εδάφους-κατασκευής στις καθιζήσεις. Για το σκοπό αυτό, τα χαρακτηριστικά σχεδιασμού των συστημάτων ΑΘΕ ανταποκρίνονται σε αυτά των ρευστοποιήσιμων συνθηκών, τα οποία εξετάστηκαν προηγουμένως. Συγκεκριμένα, οι κατασκευαστικές παράμετροι διατηρούνται σταθερές, ενώ οι μη ρευστοποιήσιμες συνθήκες του εδάφους διαμορφώνονται εν προκειμένω χρησιμοποιώντας το υπό άνωση ειδικό βάρος της άμμου. Η επίδραση της αδράνειας της ανωδομής στις σεισμικές καθιζήσεις διερευνάται εκ νέου εξετάζοντας τις κρίσιμες παραμέτρους αλληλεπίδρασης εδάφους-κατασκευής, δηλαδή το λόγο περιόδων T_{sys}/T_{exc}, το λόγο λυγηρότητας h/r και το λόγο σχετικής μάζας γ, καθώς και τις σημαντικότερες σεισμικές παράμετρους. Όπως και προηγουμένως, οι καθιζήσεις των συστημάτων ΑΘΕ συγκρίνονται με τις καθιζήσεις των αντίστοιχων συστημάτων ΘΕ. Τέλος, αναπτύσσονται απλοποιημένες εκφράσεις για τον αναλυτικό υπολογισμό του λόγου καθιζήσεων, με βάση την πολυπαραμετρική στατιστική ανάλυση των αριθμητικών αποτελεσμάτων. Δεδομένου ότι η εκτίμηση των σεισμικών καθιζήσεων για συστήματα ΘΕ είναι πιο άμεσα υπολογίσιμη, τόσο αριθμητικά όσο και αναλυτικά, μέσω της τροποποιημένης μεθοδολογίας των Richards et al. (1993), οι προτεινόμενες σχέσεις στοχεύουν να χρησιμοποιηθούν ως διορθωτικοί συντελεστές αναφορικά με το ρόλο της αλληλεπίδρασης εδάφους-κατασκευής στις σεισμικές καθιζήσεις κατασκευών.

Μηχανισμός συσσώρευσης σεισμικών καθιζήσεων.

Στα σχήματα που ακολουθούν παρουσιάζεται συγκριτικά η απόκριση ενός συστήματος ΑΘΕ και του αντίστοιχου ΘΕ εστιάζοντας στο μηχανισμό συσσώρευσης καθιζήσεων. Συγκεκριμένα, το **Σχήμα 20** συγκρίνει τα αριθμητικά αποτελέσματα του συστήματος αναφοράς ΑΘΕ, για παραμέτρους αλληλεπίδρασης εδάφους-κατασκευής s = 0.07, γ = 4.00 και h/r = 1.06 και του αντίστοιχου ΘΕ. Και στις

δύο αριθμητικές αναλύσεις η διέγερση της βάσης του καννάβου συνίσταται σε ένα αρμονικό σήμα επιτάχυνσης με μέγιστη επιτάχυνση a^b_{max} = 0.15g, περίοδο διέγερσης T_{exc} = 0.50sec και αριθμό κύκλων N = 12. Η ενεργός ιδιοπερίοδος $T_{sys.eff}$ είναι ίση με 0.68sec, γεγονός που οδηγεί σε λόγους περιόδων $T_{sys.eff}/T_{exc}$ = 1.36. Στα **Σχήμα 20α-β** συγκρίνονται οι χρονοϊστορίες των καθιζήσεων και των στροφών θεμελίου, ενώ στα **Σχήμα 20γ-δ** συγκρίνονται οι χρονοϊστορίες διατμητικών τάσεων και παραμορφώσεων σε βάθος 0.5m κάτω από το άκρο του θεμελίου. Όπως φαίνεται, το σύστημα ΑΘΕ καθιζάνει περισσότερο κατά τη διάρκεια της δόνησης σε σύγκριση με το ισοδύναμο σύστημα ΘΕ, με τη συνολική καθίζηση του πρώτου να είναι περίπου 2-3 φορές μεγαλύτερη (δηλαδή, 11cm έναντι 5cm). Το γεγονός αυτό αποδίδεται στις ταλαντώσεις της κατασκευής οι οποίες οδηγούν σε σημαντικές στροφές της θεμελίωσης (**Σχήμα 20β**), εν αντιθέσει με τις κατά μία τάξη μεγέθους μικρότερες στροφές στην περίπτωση του συστήματος ΘΕ. Ως εκ τούτου, το έδαφος κάτω από τα άκρα του θεμελίου του συστήματος ΑΘΕ υπόκειται σε σημαντικές διακυμάνσεις των διατμητικών τάσεων γύρω από τη σταθερή μέση τιμή q ≈ 25 kPa, όπως παρατηρείται στα **Σχήμα 20γ** και **δ**. Αξίζει να σημειωθεί ότι, για το σύστημα ΑΘΕ, η βύθιση του θεμελίου οδηγεί σε μια σταδιακά αυξανόμενη συσσώρευση παραμορφώσεων, η οποία εμφανίζει χαρακτηριστικές "αιχμές" που συμπίπτουν με τις μέγιστες στροφές του θεμελίου ("χρόνος t_A" στα **Σχήμα 20**b, c & d).

Βάσει των ανωτέρω, καταδεικνύεται ότι η σημαντική διαφορά στη συσσώρευση διατμητικών παραμορφώσεων κάτω από τα άκρα του θεμελίου μεταξύ των συστημάτων ΑΘΕ και ΘΕ οδηγεί και στη διαφορά του τελικού μεγέθους της σεισμικής καθίζησης.

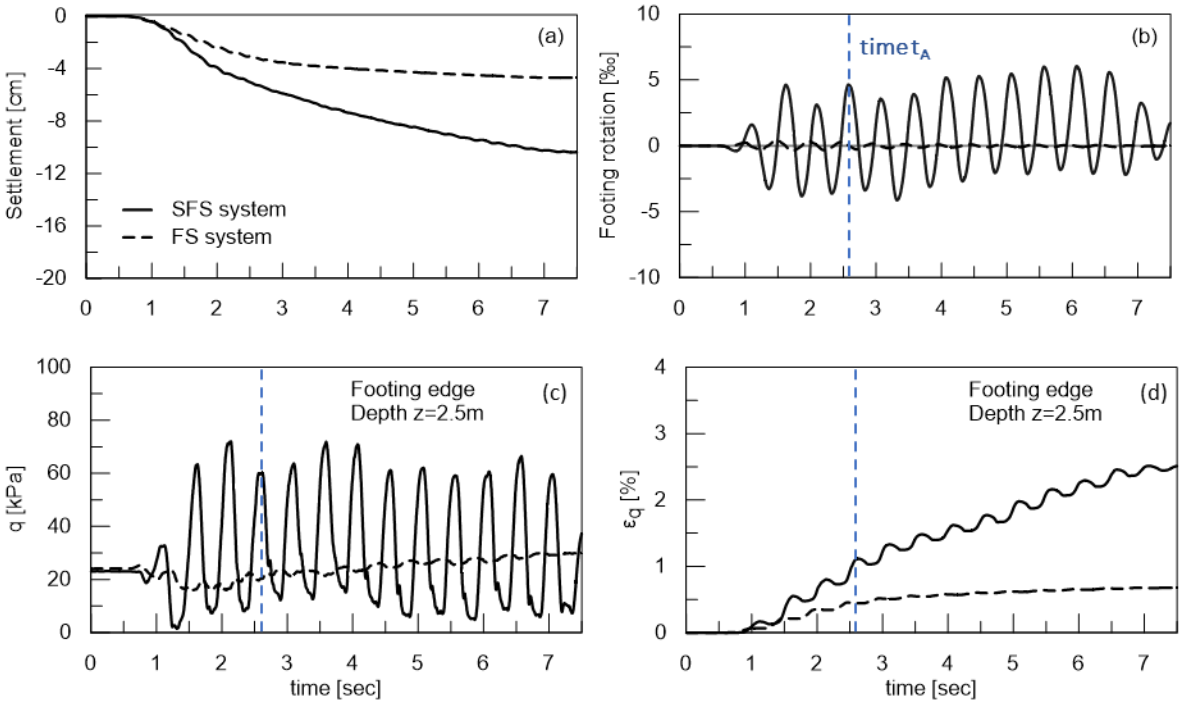

Σχήμα 20: Χρονοϊστορίες απόκρισης των συστημάτων ΑΘΕ και ΘΕ: (α) σεισμική καθίζηση, (β) στροφές θεμελίου, διατμητικές (γ) τάσεις και (δ) παραμορφώσεις κάτω από τα άκρα του θεμελίου.

Σε συνέχεια των ανωτέρω, στο **Σχήμα 21**c φαίνεται ότι στην περίπτωση του συστήματος ΘΕ τη στιγμή της μέγιστης στροφής θεμελίου (χρόνος t_A) η κατανομή των διατμητικών τάσεων κάτω από το θεμέλιο είναι αρκετά ομοιόμορφη, γεγονός που υποδηλώνει ότι οι πρόσθετες τάσεις που προκαλούνται από το λικνισμό είναι αμελητέες σε αυτή την περίπτωση. Επιπρόσθετα, στο **Σχήμα 21d** διακρίνεται ο σχηματισμός του εδαφικού πρίσματος κάτω και αριστερά του θεμελίου, υποδεικνύοντας την υπέρβαση της φέρουσας ικανότητας της θεμελίωσης. Αντίθετα, η κατανομή των διατμητικών τάσεων στην περίπτωση του συστήματος ΑΘΕ είναι ανομοιόμορφη (**Σχήμα 21α**), δεδομένου ότι παρατηρείται τοπική συγκέντρωση τάσεων κάτω από το άκρο του θεμελίου τη στιγμή της μέγιστης μετακίνησης της ανωδομής και, κατά συνέπεια, της στροφής του θεμελίου. Επιπλέον, οι επιπρόσθετες διατμητικές παραμορφώσεις αναπτύσσονται σε μια πολύ πιο ρηχή ζώνη, σε σύγκριση με το σύστημα ΘΕ, υποδεικνύοντας έτσι τη σημαντική συμβολή των διατμητικών παραμορφώσεων που προκαλούνται από το λικνισμό στη συσσώρευση καθιζήσεων. Συνεπώς, ο σχηματισμός του μηχανισμού εδαφικού πρίσματος δεν μπορεί να φανεί καθαρά (**Σχήμα 21β**), όπως συνέβαινε για το σύστημα ΘΕ.

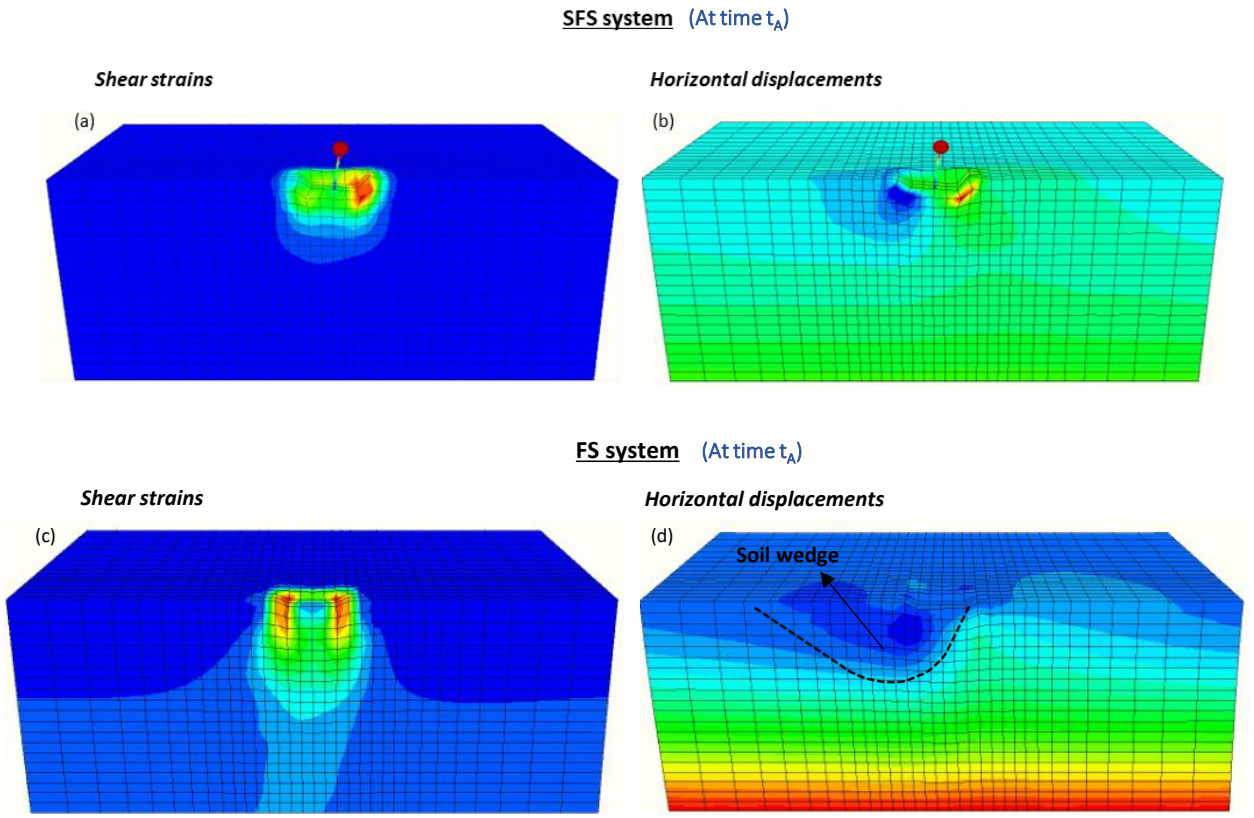

Σχήμα 21: Σύγκριση των αποκρίσεων μεταξύ του συστήματος ΑΘΕ και ΘΕ τη στιγμή της μέγιστης στροφής θεμελίου t_A: κατανομή διατμητικών παραμορφώσεων (α, γ) and οριζόντιων μετακινήσεων (β, δ).

Επίδραση του λόγου περιόδων T_{sys}/T_{exc}. Ο λόγος περιόδων T_{sys}/T_{exc} αποτελεί βασική παράμετρο για τη συσσώρευση καθιζήσεων των συστημάτων ΑΘΕ. Στο **Σχήμα 22** παρουσιάζονται τα αριθμητικά αποτελέσματα (με σύμβολα διαφορετικού σχήματος και χρώματος) της διακύμανσης του λόγου καθιζήσεων $\rho_{A\Theta E}/\rho_{\Theta E}$ με το λόγο περιόδων T_{sys}/T_{exc}, παράλληλα με την παραμετρική επίδραση του λόγου σχετικής μάζας γ (Σχήμα 22a), του λόγου λυγηρότητας h/r (Σχήμα 22b), της μέγιστης σεισμικής επιτάχυνσης PGA (Σχήμα 22c) και του αριθμού κύκλων φόρτισης N_o (Σχήμα 22d). Όπως έχει αναφερθεί προηγουμένως, η περίοδος T_{sys} λαμβάνεται ως η ενεργός ιδιοπερίοδος του συστήματος $T_{sys.eff}$, ενώ ως T_{exc} λαμβάνεται η περίοδος διέγερσης στο επίπεδο της επιφάνειας του εδάφους. Τα αποτελέσματα προσιδιάζουν σε τυπικά φάσματα ενίσχυσης της δυναμικής απόκρισης μονοβάθμιου ταλαντωτή. Δηλαδή, στην περίπτωση του συντονισμού (T_{sys}/T_{exc} ≈ 0.50-1.50), τα συστήματα ΑΘΕ υπόκεινται σε αυξημένες φασματικές επιταχύνσεις και λικνισμό, και επομένως καθιζάνουν σημαντικά περισσότερο από τα συστήματα ΘΕ ($\rho_{A\Theta E}/\rho_{\Theta E}$ ≈ 4.0-7.0). Αντίθετα, στην περίπτωση των άκαμπτων συστημάτων (T_{sys}/T_{exc} < 0.50) τείνουν να καθιζάνουν εξίσου με τα ισοδύναμα συστήματα ΘΕ, καθώς η φασματική επιτάχυνση των δύο συστημάτων είναι παρόμοια. Τέλος, τα εύκαμπτα συστήματα ΑΘΕ (T_{sys}/T_{exc} > 1.50) τείνουν να

καθιζάνουν εξίσου ή λιγότερο από τα συστήματα ΘΕ, από τη στιγμή που οι φασματικές επιταχύνσεις τους τείνουν να απομειώνονται σε σχέση με την απόκριση των άκαμπτων συστημάτων ΘΕ.

Επίδραση του σχετικού λόγου μάζας *γ*. Ο λόγος μάζας *γ* σχετίζεται κυρίως με τις αδρανειακές δυνάμεις της ανωδομής που μεταφέρονται στη θεμελίωση κατά τη διάρκεια του σεισμού. Υψηλότερες τιμές του *γ* αντιστοιχούν σε αυξημένες ταλαντώσεις της κατασκευής, οι οποίες με τη σειρά τους οδηγούν σε αύξηση της συσσώρευσης διατμητικών παραμορφώσεων στο έδαφος της θεμελίωσης. Παρατηρείται ότι, στην περιοχή συντονισμού για εύρος περιόδων 0.75-1.35sec, ο λόγος καθιζήσεων αυξάνεται συστηματικά από 3.0 σε 5.2 (δηλαδή έως 70%) όταν το *γ* αυξάνεται από 2.4 σε 5.1.

Επίδραση του λόγου λυγηρότητας *h/r*. Σύμφωνα με το κανονιστικό πλαίσιο της αλληλεπίδρασης εδάφους-κατασκευής, τα ψηλά κτίρια είναι γενικά πιο εύκαμπτα και επομένως λιγότερο επιρρεπή σε επιμήκυνση της ιδιοπεριόδου τους λόγω της ενδοσιμότητας του εδάφους θεμελίωσης (NEHRP 1997). Παρ 'όλα αυτά, στην περίπτωση της ανελαστικής συμπεριφοράς του εδάφους, πρέπει να συνεκτιμηθεί το γεγονός ότι οι αυξημένες ροπές ανατροπής επιδεινώνουν την απόκριση του συστήματος δεδομένου ότι ο λικνισμός της ανωδομής αυξάνει τη συσσώρευση διατμητικών παραμορφώσεων στο έδαφος της θεμελίωσης. Το **Σχήμα 22β** παρουσιάζει τη διακύμανση του λόγου $\rho_{A\Theta E}/\rho_{\Theta E}$ με το λόγο περιόδων T_{sys}/T_{exc}, για διαφορετικά επίπεδα λόγων λυγηρότητας (h/r = 1.06, 1.38 και 1.88). Παρατηρείται ότι η αύξηση του λόγου καθιζήσεων με το λόγο λυγηρότητας είναι εντονότερη σε συνθήκες συντονισμού, με τη μέγιστη αύξηση να είναι 21% καθώς το h/r αυξάνεται από 1.06 σε 1.88. Αντίθετα, για ημι-άκαμπτα προς άκαμπτα συστήματα με $T_{sys}/T_{exc} \leq 0.5$, οι λόγοι καθιζήσεων δεν επηρεάζονται από το λόγο λυγηρότητας, ενώ για τα εύκαμπτα συστήματα με $T_{sys}/T_{exc} \geq 1.5$, παρατηρείται μια μικρή, μόνο, αύξηση του $\rho_{A\Theta E}/\rho_{\Theta E}$.

Επίδραση των χαρακτηριστικών της διέγερσης. Τα χαρακτηριστικά της σεισμικής διέγερσης επηρεάζουν την απόκριση του συστήματος κυρίως μέσω της μέγιστης εδαφικής επιτάχυνσης PGA και – σε μικρότερο βαθμό – μέσω του αριθμού των κύκλων φόρτισης N_o. Στο **Σχήμα 22γ** και **δ** παρουσιάζεται η διακύμανση του λόγου $\rho_{A\Theta E}/\rho_{\Theta E}$ με τις τιμές του PGA και του N_o, αντίστοιχα. Παρατηρείται ότι ο λόγος καθιζήσεων αυξάνεται συστηματικά με το PGA σε ολόκληρο το φάσμα περιόδων T_{sys}/T_{exc}. Η μέγιστη αύξηση παρατηρείται υπό συνθήκες συντονισμού (T_{sys}/T_{exc} = 0.80 - 1.20 sec) και ανέρχεται περίπου σε 110% όταν η PGA αυξάνεται από 0.23g σε 0.36g. Ο αριθμός των κύκλων διέγερσης N_o αυξάνει το λόγο καθιζήσεων στο στενότερο εύρος περί τον συντονισμό με παρατηρούμενη αύξηση έως και 30% όταν το N_o αυξάνεται από 4 σε 12 κύκλους. Η σχετικά μικρή επίδραση του αριθμού των κύκλων N_o στο λόγο καθιζήσεων υποδηλώνει ότι το μεγαλύτερο μέρος της συσσώρευσης καθιζήσεων των συστημάτων ΑΘΕ λαμβάνει χώρα στα αρχικά στάδια της δόνησης.

Αναλυτικές σχέσεις για την επιρροή της αλληλεπίδρασης εδάφους-κατασκευής στο λόγο καθιζήσεων $\rho_{A\Theta E}/\rho_{\Theta E}$.

Στην ενότητα αυτή παρουσιάζονται οι αναλυτικές σχέσεις που αναπτύχθηκαν για το λόγο καθιζήσεων $\rho_{A\Theta E}/\rho_{\Theta E}$, μετά από ανάλυση παλινδρόμησης πολλαπλών μεταβλητών των σχετικών αριθμητικών δεδομένων. Οι προτεινόμενες σχέσεις απεικονίζονται στο **Σχήμα 22** με συνεχείς γραμμές. Με βάση την παραμετρική διερεύνηση και τους μηχανισμούς που συζητήθηκαν σε προηγούμενες ενότητες, εξετάστηκαν οι ακόλουθες κύριες παράμετροι αλληλεπίδρασης εδάφους-κατασκευής και σεισμικής διέγερσης: ο λόγος περιόδων T_{sys}/T_{exc}, ο λόγος λυγηρότητας h/r, ο σχετικός λόγος μαζών γ, η μέγιστη επιτάχυνση του εδάφους PGA και ο αριθμός κύκλων διέγερσης N_o.

Σημειώνεται ότι η στατιστική ανάλυση που πραγματοποιήθηκε δεν είναι «τυφλή», αλλά αποσκοπεί να είναι συνεπής προς τους φυσικούς μηχανισμούς που διέπουν το πρόβλημα. Εν προκειμένω, ελήφθη υπόψη ότι οι λόγοι καθιζήσεων εμφανίζουν διακύμανση τύπου καμπάνας με το λόγο περιόδων T_{sys}/T_{exc}. Για το λόγο αυτό, οι προτεινόμενες εκφράσεις που καταγράφουν τη διακύμανση του $\rho_{A\Theta E}/\rho_{\Theta E}$ με το T_{sys}/T_{exc} βασίζονται στις σχέσεις που τυπικά χρησιμοποιούνται για να περιγράψουν το φάσμα ενίσχυσης ενός μονοβάθμιου ταλαντωτή. Εν προκειμένω, ο λόγος καθιζήσεων $\rho_{A\Theta E}/\rho_{\Theta E}$ εκφράζεται ως εξής:

$$\frac{\rho_{SFS}}{\rho_{FS}} = \frac{1+C_1\left(T_{sys}/T_{exc}\right)^2}{\sqrt{\left[1-\left(T_{sys}/T_{exc}\right)^2\right]^2+C_2\left(T_{sys}/T_{exc}\right)^2}} \tag{15}$$

όπου

$$C_1 = f_1(\gamma)\cdot f_2(h/r) \tag{16}$$

$$f_1(\gamma) = max\{a_1 + b_1\cdot e^{c_1\cdot\gamma}, 0\} \tag{17}$$

$$f_2(h/r) = d_1 + e_1\cdot(h/r) \tag{18}$$

$$C_2 = g_1(\gamma)\cdot g_2(h/r)\cdot g_3(PGA)\cdot g_4(N_o) \tag{19}$$

$$g_1(\gamma) = a_2 + b_2\cdot\gamma \tag{20}$$

$$g_2(h/r) = c_2 + d_2\cdot(h/r) \tag{21}$$

$$g_3(PGA) = e_2 + f_2\cdot PGA \tag{22}$$

$$g_4(N_o) = \min\{g_2 + h_2 \cdot e^{i_2 \cdot N_o}, 0.3\} \quad (23)$$

Οι σταθερές στις παραπάνω εξισώσεις λαμβάνονται από την ανάλυση παλινδρόμησης των διαθέσιμων δεδομένων και ορίζονται ως εξής: a_1=0.68, b_1=-3.39, c_1=-0.73, d_1=0.82, e_1=0.24, a_2=1.78, b_2=-0.19, c_2=1.52, d_2=-0.53, e_2=3.85, f_2=-9.45, g_2=0.11, h_2=0.31, i_2=-0.4.

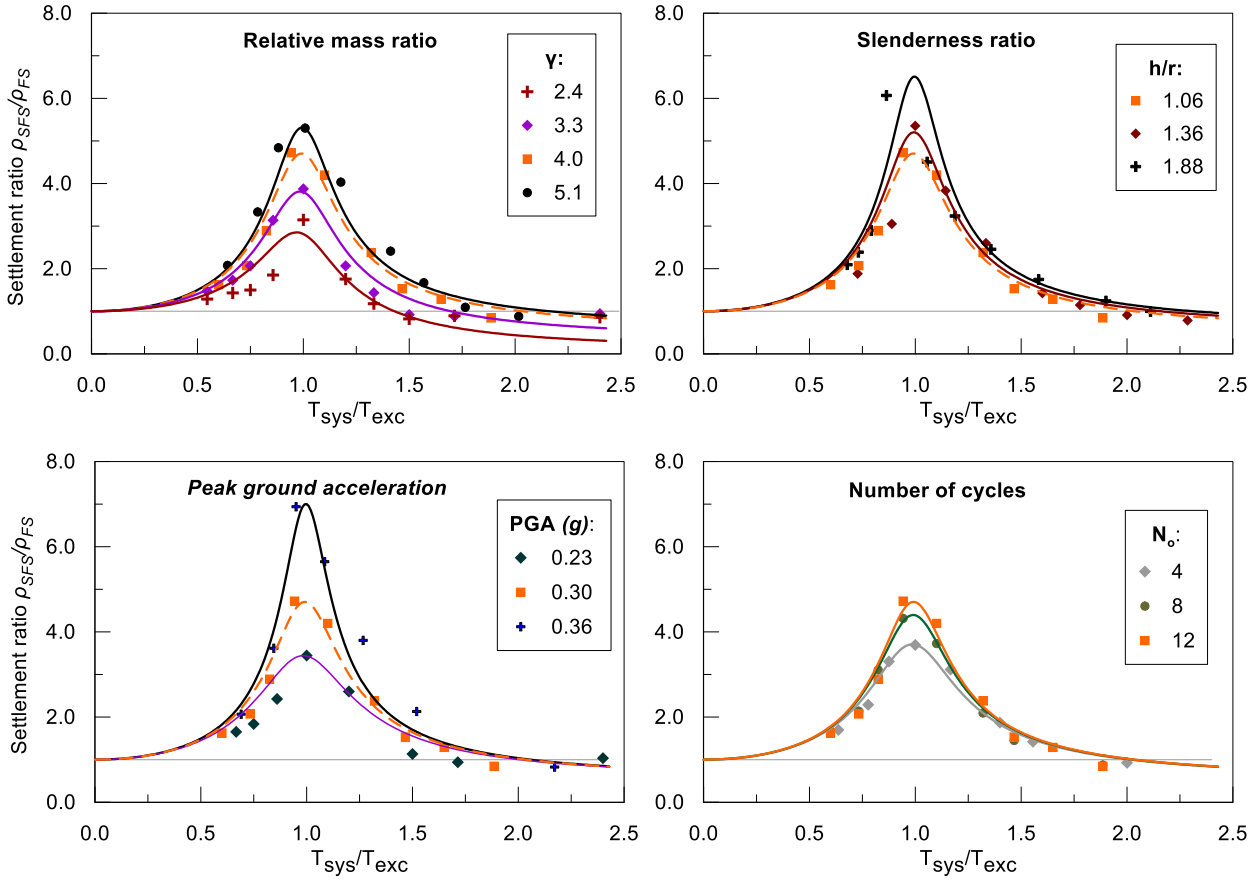

Σχήμα 22: Επίδραση του λόγου περιόδων T_{sys}/T_{exc} στο λόγο καθιζήσεων $\rho_{A\Theta E}/\rho_{\Theta E}$: Σύγκριση των αριθμητικών αποτελεσμάτων με τις αναλυτικές προβλέψεις για διαφορετικές ομάδες (α) του λόγου σχετικής μάζας *γ* και (β) του λόγου λυγηρότητας *h/r*, (γ) της μέγιστης εδαφικής επιτάχυνσης PGA και (δ) του αριθμού των κύκλων φόρτισης N_o.

Η προτεινόμενη αναλυτική μεθοδολογία αξιολογείται στη συνέχεια συγκρίνοντας τις αναλυτικές προβλέψεις με τα αντίστοιχα αποτελέσματα των αριθμητικών αναλύσεων. Το σχετικό σφάλμα μεταξύ των αναλυτικών προβλέψεων και των αριθμητικών αναλύσεων χρησιμοποιείται για να ποσοτικοποιήσει την ακρίβεια των πρώτων. Η στατιστική αξιολόγηση των σχετικών σφαλμάτων στην πρόβλεψη του λόγου καθιζήσεων $\rho_{A\Theta E}/\rho_{\Theta E}$ παρουσιάζεται στο **Σχήμα 23**. Συνολικά, η σύγκριση δείχνει ένα σχετικά μικρό και ομοιόμορφα κατανεμημένο σφάλμα για όλες τις μεταβλητές που εξετάστηκαν. Η μέση τιμή και η τυπική απόκλιση του σχετικού σφάλματος είναι -0.04 και 0.18, αντίστοιχα.

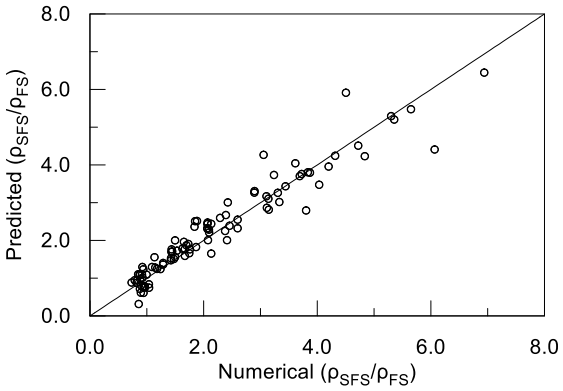
Predicted (ρ_{SFS}/ρ_{FS})
Numerical (ρ_{SFS}/ρ_{FS})
0.0
2.0
4.0
6.0
8.0

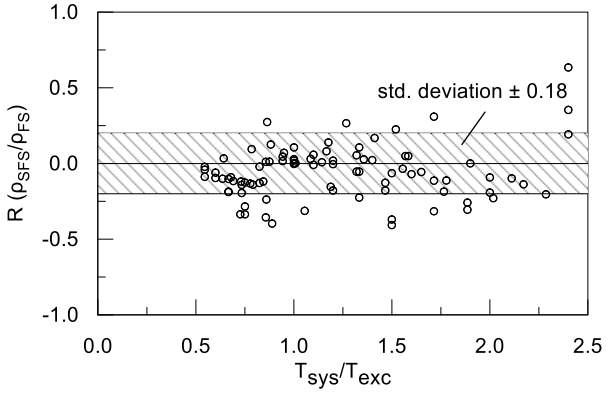
R (ρ_{SFS}/ρ_{FS})
T_{sys}/T_{exc}
std. deviation ± 0.18
1.0
0.5
0.0
-0.5
-1.0
0.0
0.5
1.0
1.5
2.0
2.5

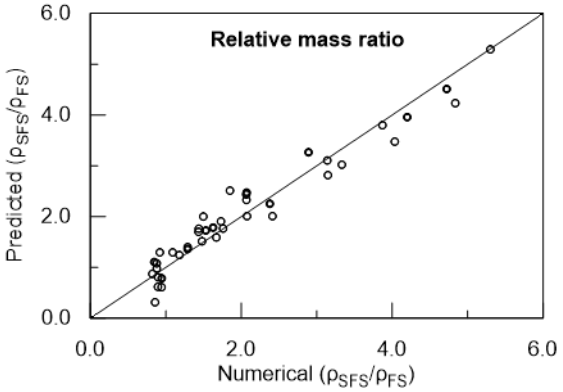
Relative mass ratio
Predicted (ρ_{SFS}/ρ_{FS})
Numerical (ρ_{SFS}/ρ_{FS})
0.0
2.0
4.0
6.0

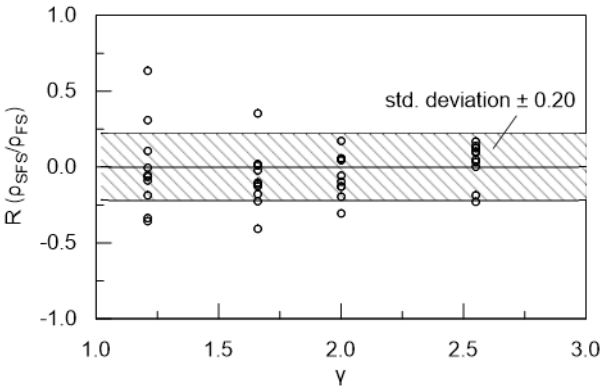
R (ρ_{SFS}/ρ_{FS})
γ
std. deviation ± 0.20
1.0
0.5
0.0
-0.5
-1.0
1.0
1.5
2.0
2.5
3.0

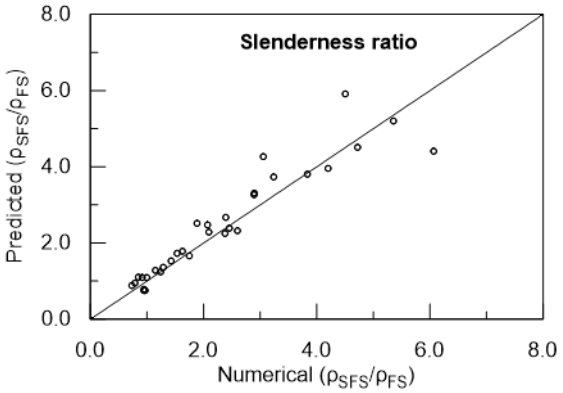
Slenderness ratio
Predicted (ρ_{SFS}/ρ_{FS})
Numerical (ρ_{SFS}/ρ_{FS})
0.0
2.0
4.0
6.0
8.0

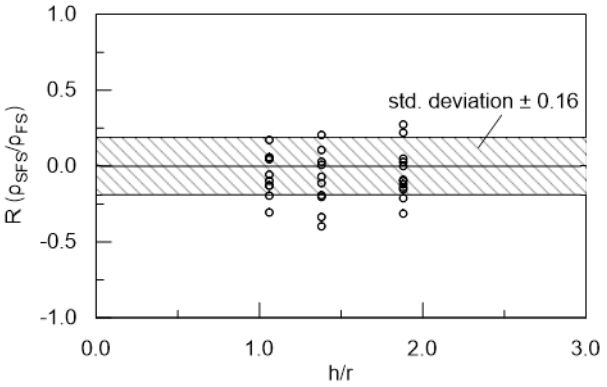
R (ρ_{SFS}/ρ_{FS})
h/r
std. deviation ± 0.16
1.0
0.5
0.0
-0.5
-1.0
0.0
1.0
2.0
3.0

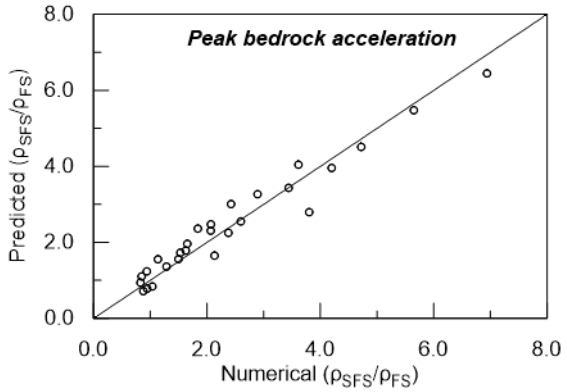
Peak bedrock acceleration
Predicted (ρ_{SFS}/ρ_{FS})
Numerical (ρ_{SFS}/ρ_{FS})
0.0
2.0
4.0
6.0
8.0

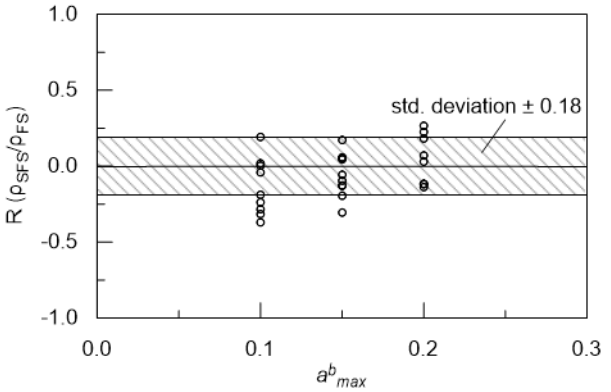
R (ρ_{SFS}/ρ_{FS})
a^b_{max}
std. deviation ± 0.18
1.0
0.5
0.0
-0.5
-1.0
0.0
0.1
0.2
0.3

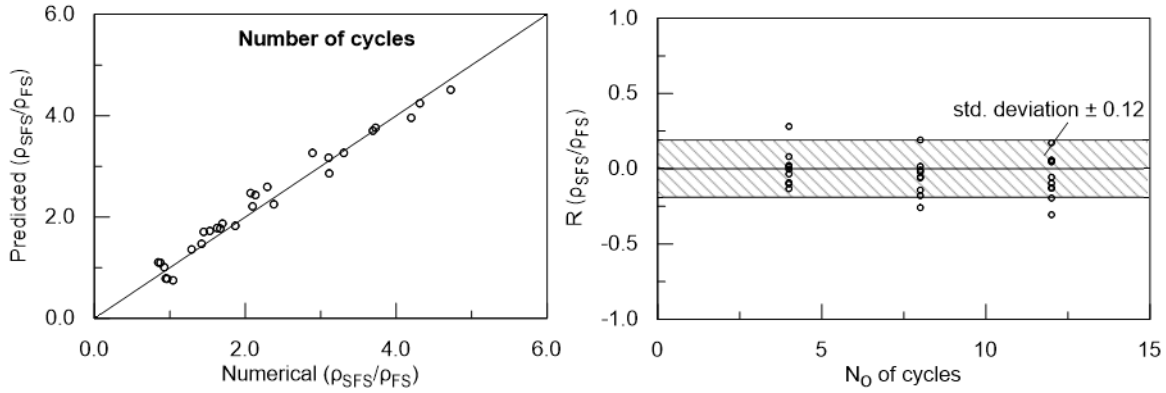

Σχήμα 23: Αξιολόγηση του σχετικού σφάλματος στον αναλυτικό υπολογισμό του λόγου $\rho_{A\Theta E}/\rho_{\Theta E}$ έναντι των αριθμητικών προβλέψεων: (a) σύγκριση one-to-one και (b) διακύμανση του σχετικού σφάλματος με την κύρια παράμετρο του προβλήματος (i) T_{sys}/T_{exc}, (ii) h/r, (iii) γ, (iv) a^b_{max}, (v) No.

VII. ΜΕΘΟΔΟΛΟΓΙΑΣ ΣΧΕΔΙΑΣΜΟΥ

Περίληψη της μεθοδολογίας υπολογισμού σεισμικών καθιζήσεων

Εκτός από την κατανόηση των μηχανισμών αλληλεπίδρασης εδάφους-θεμελίου-ανωδομής και της σπουδαιότητας τους στην πράξη, σκοπός αυτής της μελέτης είναι να παράσχει επίσης μια πλήρη αναλυτική μεθοδολογία για την προκαταρκτική εκτίμηση των σεισμικών καθιζήσεων των κατασκευών σε ρευστοποιήσιμο έδαφος. Τα βασικά βήματα της μεθοδολογίας συνοψίζονται ως ακολούθως:

- **Υπολογισμός του χρόνου εκδήλωσης ρευστοποίησης $t_{L.gr}$**. Με βάση τα αποτελέσματα των επιτόπιων δοκιμών και των ιδιοτήτων της εδαφικής κίνησης (σε όρους FS_L) το $t_{L.gr}$ μπορεί να εκτιμηθεί χρησιμοποιώντας τη διαδικασία που περιγράφεται στο Κεφάλαιο 7.3 του παρόντος κειμένου. Βάσει του $t_{L.gr}$, η δόνηση χωρίζεται σε δυο μέρη: πριν και μετά τη ρευστοποίηση.

- **Υπολογισμός των σεισμικών καθιζήσεων θεμελίων $\rho_{\Theta E.NL}$ για μη ρευστοποιημένες συνθήκες**. Η τροποποιημένη διαδικασία των Richards et al. (1993), η οποία παρουσιάζεται στο Κεφάλαιο 7.4.2, μπορεί να χρησιμοποιηθεί για την αναλυτική εκτίμηση των σεισμικών καθιζήσεων $\rho_{\Theta E.NL}$ συστημάτων ΘΕ σε μη ρευστοποιήσιμες συνθήκες, αγνοώντας δηλαδή την επίδραση της ανωδομής. Αυτή η διαδικασία απαιτεί γνώση των βασικών παραμέτρων σχεδιασμού, όπως τα χαρακτηριστικά της σεισμικής διέγερσης (PGA, T_{exc}), των εδαφικών ιδιοτήτων (ϕ, γ) και της θεμελίωσης (B, q, FS).

- **Υπολογισμός των σεισμικών καθιζήσεων θεμελίων $\rho_{\Theta E.L}$ για ρευστοποιημένες συνθήκες**. Διάφορες μεθοδολογίες μπορούν να χρησιμοποιηθούν για το σκοπό αυτό (Bray and Macedo 2017; Bullock et al. 2019; Dimitriadi et al. 2017). Στο παράδειγμα εφαρμογής που ακολουθεί επιλέγεται η αναλυτική

διαδικασία των Dimitriadi et al. (2017), δεδομένου ότι παρέχει μια βήμα-προς-βήμα μεθοδολογία σχεδιασμού για επιφανειακά θεμέλια σε ρευστοποιήσιμο έδαφος. Επιπρόσθετα, το εύρος των παραμέτρων σχεδιασμού που εξετάστηκαν (βελτιωμένη κρούστα, υποκείμενο φυσικό έδαφος άμμου Νεβάδα κ.λπ.) καθώς και τα χαρακτηριστικά της αριθμητικής προσομοίωσης (καταστατικό μοντέλο, απόσβεση εδάφους, οριακές συνθήκες κ.λπ.) είναι συμβατά με τα αντίστοιχα χαρακτηριστικά της παρούσας μελέτης.

- **Υπολογισμός της ενεργού ιδιοπεριόδου συστήματος $T_{sys.eff}$.**

  i. Αρχικά, υιοθετούνται οι αναλυτικές διαδικασίες των Κανονισμών Σχεδιασμού (π.χ. NEHRP) για τον υπολογισμό του ελαστικού τμήματος της επιμήκυνσης περιόδου $T_{sys.el}/T_{str.f}$. Στο στάδιο αυτό, οι ιδιότητες του εδάφους – συνήθως ως προς το συντελεστή διάτμησης G – εισάγονται με τις αρχικές, μετρήσιμες στο πεδίο, τιμές.

  ii. Στη συνέχεια, το μη γραμμικό τμήμα της επιμήκυνσης της περιόδου $T_{sys.eff}/T_{sys.el}$ μπορεί να υπολογιστεί για το μη ρευστοποιημένο μέρος της δόνησης χρησιμοποιώντας την εξίσωση 3 και για το ρευστοποιημένο μέρος χρησιμοποιώντας την εξίσωση 7.

- **Εκτίμηση των χαρακτηριστικών διέγερσης:**

  i. **Συχνοτικό περιεχόμενο**. Ποικίλες εκτιμήσεις προτείνονται στη βιβλιογραφία και μπορούν να χρησιμοποιηθούν για τον προσδιορισμό του συχνοτικού περιεχομένου της εδαφικής διέγερσης. Στην παρούσα μελέτη, επιλέγεται η θεμελιώδης περίοδος T_p και η εξομαλυμένη θεμελιώδης περίοδος T_o.

  ii. **Σεισμική διάρκεια**. Για να αναπαρασταθεί η ακανόνιστη χρονοϊστορία επιταχύνσεων της εδαφικής κίνησης προτείνεται ένας ισοδύναμος αριθμός σημαντικών κύκλων διέγερσης N_{eq} (Bouckovalas et al. 2017):

$$N_{eq} = \frac{\pi^2 \int_0^{Td} |v(t)| dt}{a_{eff} \cdot {T_{exc}}^2} \tag{24}$$

όπου a_{eff} είναι η μέγιστη ενεργός εδαφική επιτάχυνση (συνήθως λαμβάνεται ως τα 2/3 της μέγιστης εδαφικής επιτάχυνσης), T_{exc} είναι η προαναφερθείσα περίοδος της εδαφικής διέγερσης και v(t) η ταχύτητά της.

- **Υπολογισμός του λόγου καθιζήσεων $(\rho_{A\Theta E}/\rho_{\Theta E})_{NL}$ για το μη ρευστοποιημένο τμήμα της διέγερσης.** Η επίδραση της ανωδομής στις σεισμικές καθιζήσεις εισάγεται ως ο συντελεστής διόρθωσης $(\rho_{A\Theta E}/\rho_{\Theta E})_{NL}$ στην εμπειρικά ή αριθμητικά υπολογισμένη καθίζηση $\rho_{\Theta E.NL}$. Η προτεινόμενη μεθοδολογία περιγράφεται στις εξισώσεις 15-23.
- **Υπολογισμός του λόγου καθιζήσεων $(\rho_{A\Theta E}/\rho_{\Theta E})_{L}$ για το ρευστοποιημένο τμήμα της διέγερσης.** Όπως και προηγουμένως, η επίδραση της ανωδομής στις σεισμικές καθιζήσεις εισάγεται ως ο συντελεστής διόρθωσης $(\rho_{A\Theta E}/\rho_{\Theta E})_{L}$ στην εμπειρικά ή αριθμητικά υπολογισμένη καθίζηση $\rho_{\Theta E.L}$. Η προτεινόμενη μεθοδολογία περιγράφεται στις εξισώσεις **8**-**13**.

Παράδειγμα εφαρμογής της μεθοδολογίας σχεδιασμού

Η προτεινόμενη μεθοδολογία για τον υπολογισμό των σεισμικών καθιζήσεων επιδεικνύεται μέσω της σεισμικής απόκρισης δυο συστημάτων (ΑΘΕ και του αντίστοιχου ΘΕ) προσομοιώντας πραγματικές συνθήκες σεισμικής διέγερσης και εδαφικού προφίλ. Πραγματοποιούνται αριθμητικές αναλύσεις για το σύστημα αναφοράς, δηλαδή, με ιδιότητες αλληλεπίδρασης εδάφους-κατασκευής h/r = 1.06, γ = 4.00 και s = 0.07. Το εδαφικό προφίλ βασίζεται στις ιδιότητες του πραγματικού προφίλ εδάφους που βρίσκεται στην κοίτη του ποταμού Στρυμόνα στη Βόρεια Ελλάδα και αποτελείται από ένα ρευστοποιήσιμο στρώμα άμμου βάθους 23 μέτρων. Η σεισμική διέγερση που χρησιμοποιείται ως κίνηση του βραχώδους υποβάθρου είναι η καταγραφή του φράγματος Matahima (083) του σεισμού της Νέας Ζηλανδίας (1987). Παράλληλα με τα αριθμητικά αποτελέσματα, εφαρμόζεται και αξιολογείται η διαδικασία σχεδιασμού που αναπτύχθηκε σε αυτή τη μελέτη ως μια βήμα-προς-βήμα εφαρμογή.

Προκειμένου να συσχετιστεί το δυναμικό ρευστοποίησης με τη συσσώρευση σεισμικών καθιζήσεων, εξετάζονται τρία σενάρια σεισμικής έντασης, καθώς η μεταβολή της οδηγεί σε διαφορετικές τιμές του Συντελεστή Ασφαλείας έναντι ρευστοποίησης FS_L, η οποία με τη σειρά της οδηγεί σε διαφορετικό χρόνο εκδήλωσης της ρευστοποίησης t_L. Έχοντας ορίσει το t_L, είναι δυνατό να διακρίνουμε, ως επόμενο βήμα, τη συσσώρευση καθιζήσεων στο τμήμα πριν από την έναρξη της ρευστοποίησης ($t < t_L$) και μετά τη ρευστοποίηση ($t > t_L$). Ο χρόνος εκδήλωσης της ρευστοποίησης συνδέεται με την τιμή του FS_L, με τις ειδικές περιπτώσεις καθαρά μη ρευστοποιήσιμων ή καθαρά ρευστοποιήσιμων συνθηκών να αντιστοιχούν περίπου σε $FS_L > 1.0$ και $FS_L < 0.30$, αντίστοιχα. Το επιλεγμένο εύρος FS_L επιτρέπει την εξέταση των αποκρίσεων του συστήματος με διαφορετικό χρόνο εκδήλωσης της ρευστοποίησης t_L. επομένως, ποικίλει και η διάρκεια των τμημάτων πριν και μετά τη ρευστοποίηση.

Διαχωρισμός της σεισμικής διέγερσης: πριν και μετά την εκδήλωση της ρευστοποίησης

Ο προσδιορισμός του χρόνου εκδήλωσης της ρευστοποίησης στην επιφάνεια του εδάφους $t_{L.gr}$ και η διάκριση της διέγερσης στο τμήμα πριν και μετά τη ρευστοποίηση παρουσιάζεται στο **Σχήμα 24**. Τα τρία διαφορετικά σενάρια σεισμικής έντασης, με μέγιστη επιτάχυνση στο βραχώδες υπόβαθρο a^b_{max} = 0.04g, 0.10g και 0.40g, εξετάζονται με βάση τις χρονοϊστορίες: i) του λόγου υπερπιέσεων του νερού των πόρων r_u στο μέσο – και πλέον κρίσιμο – βάθος z = 8.5m και ii) των επιταχύνσεων επιφάνειας και βάσης του εδαφικού προφίλ.

Βιβλιογραφικά ευρήματα έχουν δείξει ότι τα φαινόμενα ρευστοποίησης στην επιφάνεια του εδάφους εμφανίζονται μόλις το ασθενέστερο στρώμα ικανού πάχους του υπεδάφους προσεγγίσει τη ρευστοποίηση (Bouckovalas et al. 2017). Οι συγγραφείς καταδεικνύουν ότι ανάπτυξη υπερπιέσεων πόρων r_u ίση με 0.6-0.8 καθ' ύψος του εδαφικού προφίλ αρκεί για την έναρξη των φαινομένων ρευστοποίησης στην επιφάνεια. Για το λόγο αυτό, ο χρόνος εκδήλωσης της ρευστοποίησης στην επιφάνεια $t_{L.gr}$ (δηλαδή, όταν αρχίζει η απομείωση της επιφανειακής κίνησης) λαμβάνει χώρα νωρίτερα από τον χρόνο έναρξης της ρευστοποίησης $t_{L.min}$ του ασθενέστερου στρώματος υπεδάφους (δηλαδή, όταν $r_u \approx 1.0$ στο συγκεκριμένο στρώμα).

Η εμφάνιση της ρευστοποίησης στην επιφάνειας ορίζεται στις χρονοϊστορίες επιτάχυνσης του **Σχήμα 24** (2η στήλη) ως το χρονικό σημείο $t_{L.gr}$ μετά το οποίο η επιφανειακή κίνηση αρχίζει να απομειώνεται. Όπως είναι αναμενόμενο, το $t_{L.gr}$ μειώνεται με την αύξηση του a^b_{max} ή - εναλλακτικά - με την μείωση του FS_L. Στην περίπτωση του FS_L = 1.05, οι υπερπιέσεις πόρων φτάνουν μέχρι την τιμή $r_u \approx 0.80$ μόνο στο τέλος της δόνησης, επομένως, φαινόμενα ρευστοποίησης δεν εμφανίζονται στην επιφάνεια. Για τις περιπτώσεις πλήρους ρευστοποίησης, παρατηρείται ότι το $t_{L.gr}$ (εκτιμώμενο ως η στιγμή που η εδαφική κίνηση αμβλύνεται δραστικά) συμπίπτει με τη χρονική στιγμή κατά την οποία οι υπερπιέσεις πόρων του ασθενέστερου εδαφικού στρώματος προσεγγίζουν την τιμή $r_u \approx 0.80$, επιβεβαιώνοντας έτσι ότι $t_{L.gr} < t_{L.min}$. Οι τιμές του $t_{L.gr}$ για διαφορετικά σενάρια FS_L συνοψίζονται στον **Πίνακα 2**.

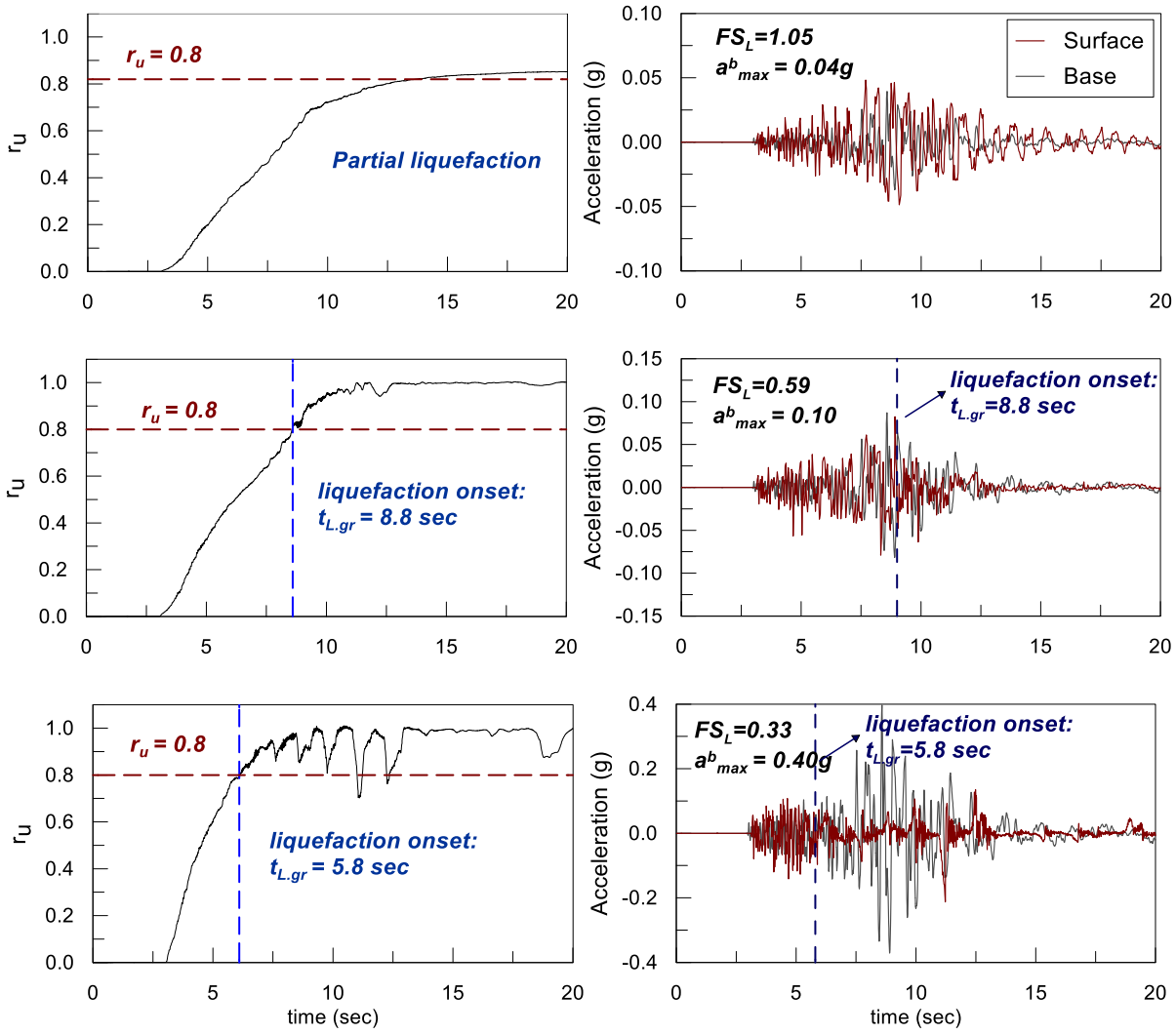

Σχήμα 24: (1η στήλη) Χρονοϊστορίες του λόγου υπερπιέσεων r_u του ασθενέστερου εδαφικού στρώματος (σε βάθος z=8.5m) και (2η στήλη) χρονοϊστορίες των επιταχύνσεων στην επιφάνεια του εδάφους για τις τρεις διαφορετικές τιμές του Συντελεστή Ασφαλείας έναντι ρευστοποίησης FS_L.

Υπολογισμός της ενεργού ιδιοπεριόδου συστήματος $T_{sys.eff}$

Το σύστημα αναφοράς ΑΘΕ που χρησιμοποιείται στις αριθμητικές αναλύσεις έχει ιδιοπερίοδο πακτωμένης ανωδομής ίση με $T_{str.f}$ = 0.35 sec. Προκειμένου να υπολογιστεί η ελαστική περίοδος του συστήματος $T_{sys.el}$, εφαρμόζεται η αναλυτική διαδικασία, που συνήθως χρησιμοποιείται στις διατάξεις του Κανονισμού (NEHRP - FEMA 1997). Σύμφωνα με αυτό, η επιμήκυνση ελαστικής περιόδου $T_{sys.el}/T_{str.f}$ υπολογίζεται με την ακόλουθη έκφραση:

$$\frac{T_{sys.el}}{T_{str.fix}} = \sqrt{1 + \frac{k_{str}}{k_x} + \frac{k_{str} \cdot h^2}{k_{ry}}} \tag{25}$$

Σε αντίθεση με τον υπολογισμό της ελαστικής περιόδου του συστήματος $T_{sys.el}$ βάσει των αρχικών ιδιοτήτων του εδάφους, η ενεργός ιδιοπερίοδος $T_{sys.eff}$ εξαρτάται από τις χρονικά μεταβαλλόμενες ιδιότητες του εδάφους κατά τη διάρκεια της σεισμικής διέγερσης. Εν προκειμένω, υπολογίζεται ο λόγος περιόδων $(T_{sys.eff}/T_{sys.el})_{NL}$ για το μη ρευστοποιημένο τμήμα της διέγερσης συναρτήσει της μέγιστης εδαφικής επιτάχυνσης PGA και του λόγου περιόδων $T_{soil}/T_{sys.el}$ επαναλαμβάνοντας την εξίσωση 3:

$$\left(\frac{T_{sys.eff}}{T_{sys.el}}\right)_{NL} = (0.91 + 0.55 \cdot PGA^{0.21}) \frac{1.53 + 0.94\left(T_{soil}/T_{sys.el}\right)^2}{\sqrt{\left[2.04 - \left(T_{soil}/T_{sys.el}\right)^2\right]^2 + 3.65 \cdot \left(T_{soil}/T_{sys.el}\right)^2}} \tag{26}$$

Στην περίπτωση του ρευστοποιημένου τμήματος της υπολογίζεται ο λόγος περιόδων $(T_{sys.eff}/T_{sys.el})_L$ συναρτήσει της μέγιστης εδαφικής επιτάχυνσης PGA, επαναλαμβάνοντας την εξίσωση 7:

$$\left(\frac{T_{sys.eff}}{T_{sys.el}}\right)_L = 1.00 \qquad for\ PGA \leq 0.075g$$

$$\left(\frac{T_{sys.eff}}{T_{sys.el}}\right)_L = 1.69 \cdot PGA^{0.014} \qquad for\ PGA > 0.075g \tag{27}$$

Τα αποτελέσματα των υπολογισμών συνοψίζονται στον **Πίνακας 2**.

Εκτίμηση της δυναμικής απόκρισης του συστήματος

Για την εκτίμηση της δυναμικής απόκρισης του συστήματος είναι απαραίτητο να προσδιοριστεί το συχνοτικό περιεχόμενο της σεισμικής διέγερσης. Το **Σχήμα 25** συγκρίνει τα φάσματα ελαστικής απόκρισης της κίνησης της επιφάνειας και της βάσης του εδαφικού προφίλ με την ενεργό ιδιοπερίοδο του συστήματος ($T^{NL}_{sys.eff}$ για το μη ρευστοποιημένο και $T^{L}_{sys.eff}$ για το ρευστοποιημένο έδαφος) για διαφορετικά σενάρια της μέγιστης επιτάχυνσης του βραχώδους υποβάθρου. Προκειμένου να ποσοτικοποιηθεί η συσχέτιση μεταξύ του $T_{sys.eff}$ και της περιόδου διέγερσης (στην επιφάνεια του εδάφους) T_{exc}, απαιτείται ο χαρακτηρισμός της τελευταίας μέσω μιας παραμέτρου. Οι ακόλουθες

εκτιμήσεις περιεχομένου συχνότητας που χρησιμοποιούνται στη βιβλιογραφία προτείνονται εδώ (Rathje et al. 1998):

- Η θεμελιώδης περίοδος T_p, η οποία είναι η περίοδος που αντιστοιχεί στη μέγιστη τιμή των φασματικών επιταχύνσεων
- Η εξομαλυμένη φασματική περίοδος οριζόμενη ως:

$$T_o = \frac{\sum_i T_i \cdot \ln\left[S_a(T_i)\right]]}{\sum_i \ln\left[S_a(T_i)\right]} \tag{28}$$

Στα αποτελέσματα του **Πίνακας 2** ορίζεται η θεμελιώδης περίοδος διέγερσης ως $T_{exc.p}$ και η εξομαλυμένη φασματική ως $T_{exc.o}$. Οι λόγοι του $T_{sys.eff}$ ως προς τις περιόδους $T_{exc.p}$ και $T_{exc.o}$ παρουσιάζονται συγκριτικά στις δύο τελευταίες στήλες του Πίνακα, προκειμένου να ποσοτικοποιηθούν τυχόν φαινόμενα ενίσχυσης ή απομείωσης μεταξύ του συστήματος και της διέγερσης. Τα αποτελέσματα παρουσιάζονται για το τμήμα πριν και μετά τη ρευστοποίηση και για κάθε σενάριο a^b_{max}. Σημειώνεται ότι η κατάλληλη επιλογή της μέγιστης φασματικής περιόδου – στην περίπτωση του $T_{exc.p}$ – ή του φασματικού εύρους – στην περίπτωση του $T_{exc.o}$ – διαφέρει, συχνά, ανά περίπτωση. Στη συγκεκριμένη διερεύνηση, η μέγιστη φασματική περίοδος που βρίσκεται πλησιέστερα στην ενεργό περίοδο διέγερσης (δηλαδή $T_{exc.p}$ ≈ 0.50-0.60sec) επιλέγεται ως η θεμελιώδης περίοδος $T_{exc.p}$, αντί για τη συνολικά μεγίστη (δηλαδή, $T_{exc.p}$ ≈ 0.12sec), αφού η τελευταία απέχει σημαντικά από τις ενεργές περιόδους του συστήματος. Επιπλέον, για τον υπολογισμό του $T_{exc.o}$, το φασματικό εύρος των ενεργών συχνοτήτων περιορίζεται σε T ≈ 1.0-1.5sec.

Τα αποτελέσματα καταδεικνύουν ότι η θεμελιώδης περίοδος $T_{exc.p}$ έχει σταθερή τιμή ίση με 0.60sec για το εύρος τιμών a^b_{max} = 0.04g – 0.26g και μειώνεται σε $T_{exc.p}$ = 0.55sec για a^b_{max} = 0.40g. Τα ευρήματα αυτά υποδηλώνουν ότι η παράμετρος T_p δεν καταγράφει επαρκώς το συχνοτικό περιεχόμενο των φασμάτων απόκρισης. Το φαινόμενο αυτό, μάλιστα, αναμένεται να ενταθεί με την αύξηση της σεισμικής έντασης, λόγω της μειούμενης σημασίας της – μοναδικής – θεμελιώδους περιόδου. Αντίθετα, η εξομαλυμένη φασματική περίοδος $T_{exc.o}$ δείχνει καλύτερη συσχέτιση μεταξύ της επιμήκυνσης της περιόδου και της σεισμικής έντασης, καθώς κινείται εντός του εύρους $T_{exc.o}$ = 0.52-0.90sec.

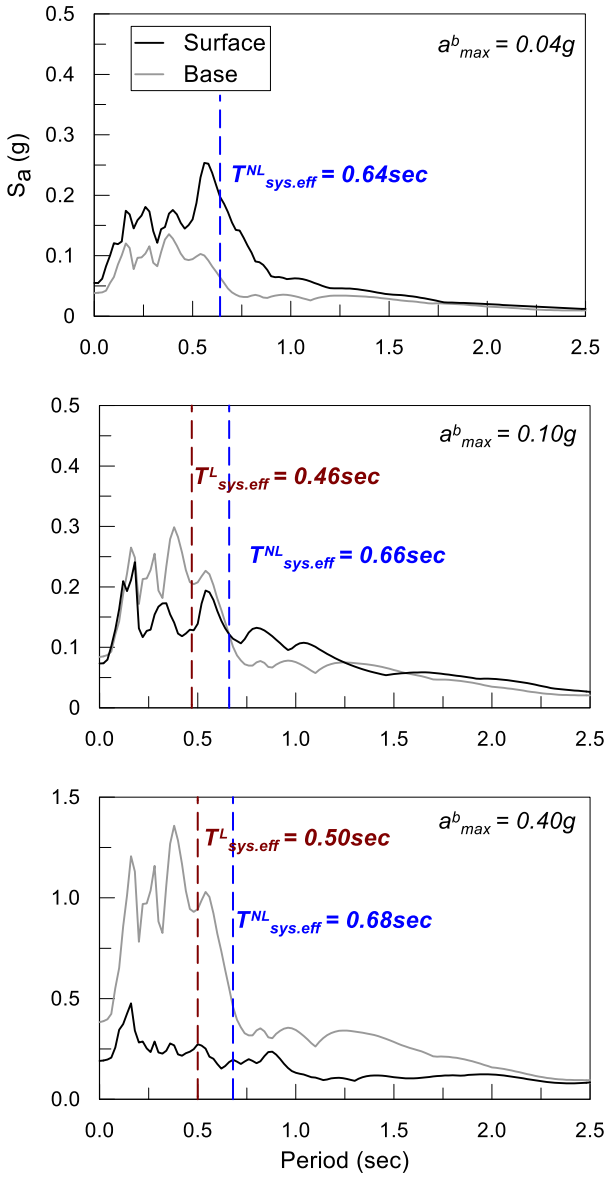

Σχήμα 25: Ελαστικά φάσματα απόκρισης της επιτάχυσνης του εδάφους και του βραχώδους υποβάθρου για την καταγραφή Matahima Dam (083) του σεισμού της Νέας Ζηλανδίας (1986). Τρία επίπεδα a^b_{max} εξετάζονται: 0.04g, 0.10g και 0.40g. Η ενεργός ιδιοπερίοδος του συστήματος σχεδιάζεται διακριτά για μη-ρευστοποιήσιμες $T^{NL}_{sys.eff}$ (*μπλε γραμμή*) και ρευστοποιήσιμες συνθήκες $T^{L}_{sys.eff}$ (*κόκκινη γραμμή*).

Πίνακας 2: Τιμές του χρόνου εκδήλωσης της ρευστοποίησης $t_{L.gr}$, της ενεργού ιδιοπεριόδου του συστήματος και της σεισμικής κίνησης του εδάφους για διαφορετικές τιμές του FS_L.

Scenario No	*FS_L*	*$t_{L,gr}$ (sec)*	*Part of motion*	*Tsys.eff (sec)*	*Texc.p (sec)*	*Texc.o (sec)*	*Tsys.eff / Texc.p*	*Tsys.eff/ Texc.o*
1	*1.05*	-	*NL*	0.64	0.60	0.52	*1.06*	*1.23*
			$L^{(1)}$	-			-	-
2	*0.59*	*8.8*	*NL*	0.66	0.60	0.55	*1.10*	*1.39*
			L	0.46			*0.76*	*0.83*
3	*0.33*	*5.8*	*NL*	0.68	0.55	0.59	*1.23*	*1.49*
			L	0.50			*0.91*	*0.85*

- **Εκτίμηση σεισμικών καθιζήσεων**

Έχοντας ήδη καθορίσει τα δυναμικά χαρακτηριστικά του συστήματος, σε όρους αλληλεπίδρασης εδάφους-κατασκευής καθώς και του λόγου περιόδων $T_{sys.eff}/T_{exc}$, είναι, πλέον, δυνατός ο προσδιορισμός της συσσώρευσης καθιζήσεων κατά τη διάρκεια της σεισμικής διέγερσης. Το **Σχήμα 26** συγκρίνει τις χρονοϊστορίες συσσώρευσης καθιζήσεων μεταξύ συστημάτων ΑΘΕ και ΘΕ που προέκυψαν μέσω αριθμητικών αναλύσεων για τα εξεταζόμενα σενάρια μεταβαλλόμενου FS_L ή –εναλλακτικά- a^b_{max} (με συνεχείς γραμμές). Παράλληλα, παρουσιάζεται η αναλυτική λύση της καθίζησης του συστήματος ΑΘΕ (με διάστικτη γραμμή) η οποία έχει προκύψει πολλαπλασιάζοντας την αριθμητική λύση του συστήματος ΘΕ με τις προτεινόμενες σχέσεις της Διατριβής για το προ-ρευστοποίησης (Εξισώσεις 15-23) και μετά τη ρευστοποίηση (Εξισώσεις 8-13) τμήμα της δόνησης. Η συσσώρευση -καθιζήσεων διακρίνεται σε δύο φάσεις, πριν και μετά τη ρευστοποίηση, για τις αριθμητικές αναλύσεις με FS_L <1.0. Στην περίπτωση της πρώτης αριθμητικής ανάλυσης του σχήματος **Σχήμα 26α** επικρατούν μη ρευστοποιημένες συνθήκες, δεδομένου ότι οι λόγοι υπερπίεσης πόρων στο υπέδαφος είναι ίσοι ή μικρότεροι από 0.8 (βλέπε **Σχήμα 24**).

Τα αποτελέσματα στο **Σχήμα 26** δείχνουν την ειδοποιό διαφορά στη συσσώρευση καθίζησης πριν και μετά τη ρευστοποίηση. Συγκεκριμένα, κατά τη διάρκεια του μη ρευστοποιημένου μέρους της κίνησης, η επίδραση της ανωδομής είναι κρίσιμη με το ρόλο της να είναι επιβλαβής για την απόδοση του συστήματος, καθώς το σύστημα ΑΘΕ καθιζάνει σημαντικά περισσότερο από το ΘΕ. Η διάρκεια αυτού του μέρους της δόνησης είναι ο πιο σημαντικός παράγοντας για τις τελικές τιμές των λόγων $\rho_{ΑΘΕ}/\rho_{ΘΕ}$, εντός της εξεταζόμενης περιοχής (δηλαδή για διάρκειες σεισμικών διεγέρσεων έως 15-20 δευτερόλεπτα). Αυτές οι παρατηρήσεις έρχονται σε συμφωνία με τα αποτελέσματα της προηγούμενης φασματικής ανάλυσης, όπου η δυναμική απόκριση του συστήματος κατά τη διάρκεια του μη ρευστοποιημένου

τμήματος της δόνησης χαρακτηρίζεται από σημαντικές φασματικές ενισχύσεις και αντίστοιχη αύξηση του λόγου $\rho_{A\Theta E}/\rho_{\Theta E}$ για λόγους περιόδων $T_{sys.eff}/T_{exc}$ εντός της περιοχής 1.06-1.49 (**Πίνακας 2**).

Αντίθετα, κατά τη διάρκεια του ρευστοποιημένου τμήματος της δόνησης, η επίδραση της ανωδομής είναι μικρότερη με το ρόλο της να αποδεικνύεται ευεργετικός για τη συσσώρευση καθιζήσεων. Τα αποτελέσματα από τις προηγούμενες φασματικές αναλύσεις έδειξαν ότι η δυναμική απόκριση του συστήματος εντός της ημι-άκαμπτης φασματικής περιοχής, δηλαδή για $T_{sys.eff}/T_{exc} \approx 0.76\text{-}0.81$ (**Πίνακας 2**), επιδεικνύουν μείωση της συσσώρευσης καθιζήσεων για το σύστημα ΑΘΕ σε σύγκριση με το ισοδύναμο σύστημα ΘΕ.

Συμπερασματικά, καταδεικνύεται ότι οι τελικές τιμές (στο τέλος της δόνησης) του λόγου $\rho_{A\Theta E}/\rho_{\Theta E}$ μειώνονται με την αντίστοιχη μείωση του Συντελεστή Ασφαλείας έναντι ρευστοποίησης FS_L. Το εύρημα αυτό αποδίδεται στη συσχέτιση του FS_L με το χρόνο εκδήλωσης της ρευστοποίησης $t_{L.gr}$ ή, διαφορετικά, με τη διάρκεια του τμήματος δόνησης πριν και μετά τη ρευστοποίηση. Παρ 'όλα αυτά, η συνολική καθίζηση του συστήματος ΑΘΕ αυξάνεται με τη μείωση του FS_L.

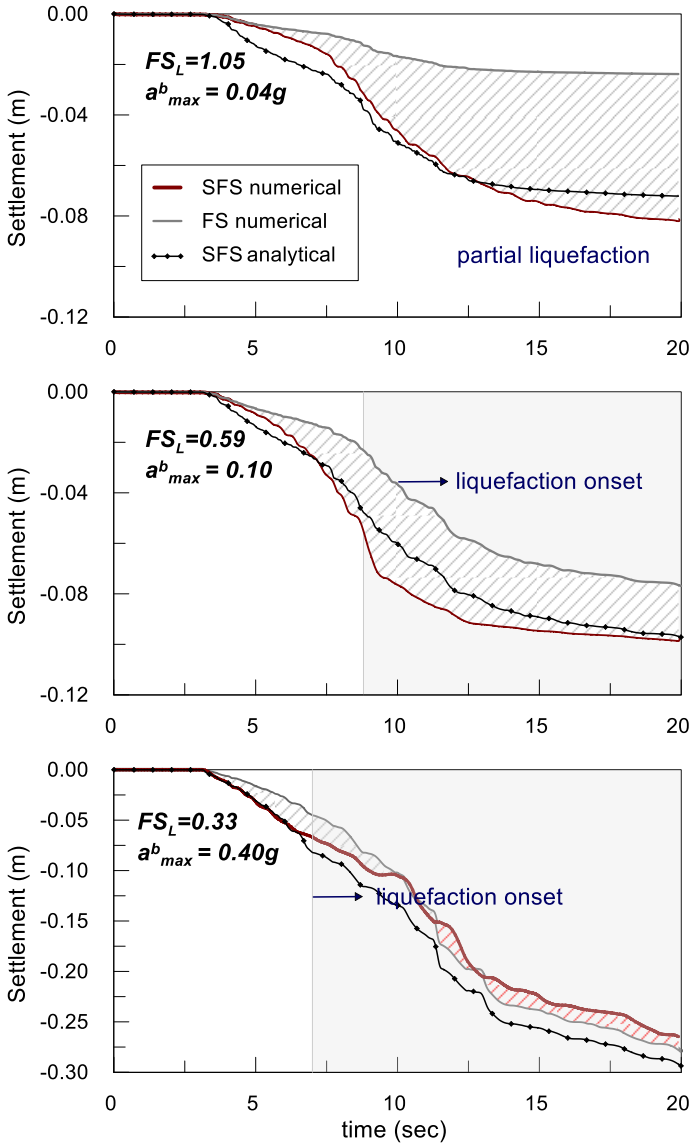

Σχήμα 26: Σύγκριση των χρονοϊστοριών σεισμικών καθιζήσεων μεταξύ συστημάτων ΑΘΕ και ΘΕ υποβαλλόμενα στη σεισμική διέγερση Matahima Dam (083) του σεισμού της Νέας Ζηλανδίας (1986), για τρεις διαφορετικές τιμές του Συντελεστή Ασφάλειας έναντι ρευστοποίησης FS_L.

VII. ΣΥΜΠΕΡΑΣΜΑΤΑ

Σκοπό της παρούσας Διατριβής αποτελεί η επέκταση και ολοκλήρωση της νέας μεθοδολογίας σχεδιασμού επιφανειακών θεμελιώσεων σε καθεστώς ρευστοποίησης, λαμβάνοντας υπόψη την αδρανειακή αλληλεπίδραση εδάφους-θεμελίου-ανωδομής. Ως πρώτο βήμα, η Διατριβή στοχεύει στη διερεύνηση των μηχανισμών που διέπουν τη σεισμική συμπεριφορά κατασκευών με επιφανειακές θεμελιώσεις, με έμφαση στη συσσώρευση σεισμικών καθιζήσεων. Τελικός στόχος της Διατριβής είναι η

ανάπτυξη μιας ολοκληρωμένης αναλυτικής μεθοδολογίας για την εκτίμηση των σεισμικών καθιζήσεων η οποία να μπορεί να χρησιμοποιηθεί σε πρακτικές εφαρμογές.

Μετά την ολοκλήρωση των εργασιών της παρούσας Διατριβής, προέκυψαν τα ακόλουθα κύρια ευρήματα και συμπεράσματα:

i) Αναπτύχθηκε μια αριθμητική μεθοδολογία για το σχεδιασμό με κριτήρια επιτελεστικότητας του συστήματος θεμελίωσης σε ρευστοποιήσιμες συνθήκες. Ο Κώδικας Πεπερασμένων Διαφορών *FLAC3D* (Itasca 2012) χρησιμοποιήθηκε για τις αριθμητικές αναλύσεις, ενώ η ανακυκλική συμπεριφορά της άμμου προσομοιώθηκε με το καταστατικό προσομοίωμα κρίσιμης κατάστασης NTUA-Sand (Andrianopoulos et al. 2010; Karamitros 2010). Πραγματοποιήθηκε μια σειρά δυναμικών αναλύσεων συστημάτων ανωδομής-θεμελίωσης-εδάφους προκειμένου να κατανοηθούν οι μηχανισμοί που διέπουν τη δυναμική απόκριση των κατασκευών σε ρευστοποιήσιμες συνθήκες. Δόθηκε ιδιαίτερη έμφαση στα κρίσιμα χαρακτηριστικά της απόκρισης του συστήματος, όπως είναι η μεταβολή της θεμελιώδους ιδιοπεριόδου του συστήματος ΑΘΕ και η συσσώρευση σεισμικών καθιζήσεων κατά τη διάρκεια της διέγερσης. Η απότομη μεταβολή των εδαφικών ιδιοτήτων μετά την εκδήλωση της ρευστοποίησης λαμβάνεται υπόψη με τη διάκριση της δόνησης σε δύο φάσεις, δηλαδή πριν και μετά τη ρευστοποίηση. Με βάση τα αποτελέσματα της παραμετρικής διερεύνησης αναπτύσσονται σχέσεις πολλαπλών μεταβλητών για την πρόβλεψη της θεμελιώδους ιδιοπεριόδου των συστημάτων καθώς και για την επίδραση της αλληλεπίδρασης εδάφους-κατασκευής στις καθιζήσεις. Η εφαρμογή της προτεινόμενης μεθοδολογίας επιδεικνύεται μέσω ενός παραδείγματος σχεδιασμού.

ii) Η δυναμική απόκριση των συστημάτων ΑΘΕ κατά τη διάρκεια ενός συγκεκριμένου σεισμικού γεγονότος συσχετίζεται σε μεγάλο βαθμό με τον χρόνο εκδήλωσης της ρευστοποίησης του υπεδάφους. Προηγούμενες μελέτες έχουν δείξει ότι η απομείωση της αντοχής και της δυσκαμψίας του εδάφους λόγω της ρευστοποίησης είναι αρκετά μεγάλη ώστε να προκαλέσει μια ξεχωριστή φάση δόνησης η οποία χαρακτηρίζεται από σημαντικά μεταβληθείσες εδαφικές ιδιότητες (V_s, T_{soil}) σε σύγκριση με τις αρχικές ιδιότητες προ ρευστοποίησης. Η μετάβαση στην ρευστοποιημένη κατάσταση του εδάφους είναι αρκετά απότομη και συνήθως συμβαίνει για λόγους υπερπίεσης πόρων περίπου 0.6-0.8.

iii) Ο χρόνος εκδήλωσης των αποτελεσμάτων της ρευστοποίησης στην επιφάνεια του εδάφους φαίνεται να είναι ελαφρώς μικρότερος (περίπου 15%) από τον χρόνο που απαιτείται για την πλήρη ρευστοποίησης (δηλ., r_u = 1.0) της ασθενέστερης στρώσης. Με βάση τα ευρήματα αυτά, η δυναμική

απόκριση των κατασκευών διακρίνεται σε δύο φάσεις, πριν και μετά τη ρευστοποίηση. Η διάρκεια της κάθε φάσης ελέγχεται έμμεσα από την τιμή του Συντελεστή Ασφάλειας έναντι της ρευστοποίησης FS_L, με τις ειδικές περιπτώσεις καθαρά μη ρευστοποιήσιμων ή καθαρά ρευστοποιημένων συνθηκών να αντιστοιχούν, περίπου, σε $FS_L > 1.0$ και $FS_L < 0.30$ αντίστοιχα.

iv) Στο συμβατικό πλαίσιο της αλληλεπίδρασης εδάφους-κατασκευής, η ιδιοπερίοδος του εύκαμπτου συστήματος ανωδομής-θεμελίου-εδάφους ενσωματώνει, έμμεσα, την ανελαστικότητα του εδάφους, μέσω της μείωσης του Μέτρου Διάτμησης και της αύξησης του λόγου απόσβεσης, παραγνωρίζοντας, κατ΄ αυτόν τον τρόπο, σημαντικές παραμέτρους της ανακυκλικής συμπεριφοράς του εδάφους, όπως η συμπύκνωσή του, η απώλεια αντοχής λόγω συσσώρευσης υπερπιέσεων κλπ. Η συγκεκριμένη υπεραπλούστευση ενδέχεται αν αποβεί είτε υπέρ είτε κατά της ασφάλειας, δεδομένου ότι η επιμήκυνση της ιδιοπεριόδου – που σχετίζεται με την απομείωσης της δυσκαμψίας του εδάφους – μπορεί να οδηγήσει είτε σε αύξηση είτε σε μείωση των φασματικών επιταχύνσεων. Κατά τη διάρκεια ισχυρών σεισμικών δονήσεων ή –ειδικότερα – σε περιπτώσεις ρευστοποίησης, η χρονικά μεταβαλλόμενη απομείωση της δυσκαμψίας του εδάφους καθιστά τον άμεσο υπολογισμό της ιδιοπεριόδου άμεσα εξαρτώμενο από την κατάλληλη επιλογή ενός ισοδύναμου Μέτρου Διάτμησης για το έδαφος θεμελίωσης.

v) Για να ξεπεραστεί η δυσκολία αυτή, η ανελαστική περίοδος του συστήματος προσδιορίζεται έμμεσα, μέσω της Συνάρτησης Μεταφοράς μεταξύ των σημάτων επιτάχυνσης εισόδου (ελεύθερου πεδίου) και εξόδου (ανωδομής) στο πεδίο των συχνοτήτων. Σε αυτό το πλαίσιο, οι παράγοντες της ανελαστικότητας του συστήματος μπορεί να σχετίζονται με μια πραγματική – ή ενεργό – ιδιοπερίοδο του συστήματος ΑΘΕ. Στην παρούσα Διατριβή, η ενεργός ιδιοπερίοδος υπολογίζεται για συστήματα που υποβάλλονται σε διέγερση στη βάση του εδαφικού προφίλ με σήμα λευκού θορύβου (white noise), για ρευστοποιήσιμες και μη συνθήκες εδάφους.

vi) Η συμβολή της μη γραμμικότητας του εδάφους στην επιμήκυνση της περιόδου είναι σημαντική στην περίπτωση **μη ρευστοποιήσιμων** συνθηκών και αυτό υποδεικνύεται από τις Συναρτήσεις Σχήματος μεταξύ των φασματικών επιταχύνσεων της ανωδομής και της επιφάνειας του εδάφους, οι οποίες εμφανίζουν ενισχύσεις σε μεγάλο εύρος περιόδων. Οι εκτιμώμενες ενεργές περίοδοι επηρεάζονται κυρίως από την ένταση του σεισμού και τα φαινόμενα συντονισμού ανωδομής-εδάφους. Μεγαλύτερες τιμές PGA οδηγούν σε επιμήκυνση της ενεργού ιδιοπεριόδου του συστήματος έως και 80% σε σύγκριση με την "ελαστική" περίοδο. Είναι αξιοσημείωτο ότι, ακόμη και για μέτριες έως χαμηλές εντάσεις σεισμών (π.χ. PGA ≈ 0.20g), ο σχεδιασμός με βάση την περίοδο του “ελαστικού” συστήματος θα είχε ως αποτέλεσμα την υποτίμηση της ενεργού περιόδου έως και 40%. Λόγω της σταδιακής υποβάθμισης της δυσκαμψίας του εδάφους, οι ενεργές περίοδοι του συστήματος

εκτιμώνται καλύτερα από εξομαλυμένες φασματικές περιόδους συστήματος $T_{sys.o}$ που αποτυπώνουν τη χρονικά μεταβαλλόμενη φύση των υλικών.

vii) Στην περίπτωση **ρευστοποιήσιμων** συνθηκών, η απόκριση του συστήματος διέπεται από τις ιδιότητες του εδάφους στη ρευστοποιημένη κατάσταση. Αυτό εκδηλώνεται με τις Συναρτήσεις Σχήματος μεταξύ των φασματικών επιταχύνσεων της ανωδομής και της επιφάνειας του εδάφους, οι οποίες εμφανίζουν μια μοναδική κορυφή που αντιστοιχεί στην περίοδο του συστήματος σε ρευστοποιημένη κατάσταση. Ως εκ τούτου, οι ενεργές περίοδοι του συστήματος εκτιμώνται καλύτερα με χρήση της θεμελιώδους περίοδου του συστήματος $T_{sys.p}$. Η επίδραση της έντασης του σεισμού έχει ένα ανώτατο όριο περίπου 20% στην επιμήκυνση της ανελαστικής περιόδου σε σύγκριση με τις "ελαστικές" τιμές, λόγω του γεγονότος ότι τα ρευστοποιημένα υποστρώματα λειτουργούν ως "φυσική σεισμική μόνωση" και αμβλύνουν τη διάδοση των σεισμικών κυμάτων στην επιφάνεια. Το βάθος της βελτιωμένης ζώνης H_{imp} φαίνεται να έχει μικρή επίδραση στην επιμήκυνση της περιόδου σε σύγκριση με το ρόλο του στη συνολική συμπεριφορά της θεμελίωσης.

viii) Οι σεισμικές καθιζήσεις των συστημάτων ΑΘΕ συγκρίνονται με τις αντίστοιχες των ισοδύναμων συστημάτων ΘΕ προκειμένου να απομονωθούν οι επιδράσεις της αδράνειας της ανωδομής στη δυναμική απόκριση των κατασκευών. Σχέσεις πολλαπλών μεταβλητών αναπτύσσονται για την πρόβλεψη του λόγου καθιζήσεων μεταξύ των προαναφερθέντων συστημάτων ΑΘΕ-ΘΕ, δεδομένου ότι προϋπάρχουσες βιβλιογραφικές μελέτες εκτιμούν τη συσσώρευση σεισμικών καθιζήσεων συστημάτων ΘΕ με επιφανειακά θεμέλια. Οι αναπτυσσόμενες σχέσεις εκφράζονται με όρους διορθωτικών συντελεστών που προστίθενται στις καθιερωμένες διαδικασίες υπολογισμού καθιζήσεων. Η επίδραση της αδράνειας της κατασκευής στη συσσώρευση καθιζήσεων διερευνάται μέσω εξέτασης των κρίσιμων παραμέτρων στο πλαίσιο της αλληλεπίδρασης εδάφους-κατασκευής.

ix) Οι σεισμικές καθιζήσεις των κατασκευών σε **ρευστοποιημένο έδαφος** κυριαρχούνται από τη δημιουργία ενός ολισθαίνοντος πρίσματος τύπου Coulomb, το οποίο λαμβάνει χώρα λόγω της δραστικής υποβάθμισης της φέρουσας ικανότητας του εδάφους θεμελίωσης. Η επίδραση της ανωδομής υπεισέρχεται ως μια αδρανειακή δύναμη που δρα σε φάση ή εκτός φάσης με την ολίσθηση του πρίσματος, ενισχύοντας ή απομειώνοντας τη συνολική σεισμική καθίζηση. Η πιο κρίσιμη παράμετρος στην απόκριση του συστήματος ΑΘΕ είναι ο λόγος περιόδων μεταξύ της θεμελιώδους περιόδου του συστήματος και αυτής της σεισμικής διέγερσης T_{sys}/T_{exc}. Στην περίπτωση του συντονισμού, η υστέρηση της δόνησης της ανωδομής κατά ένα τέταρτο του κύκλου ταλάντωσης σε σχέση με τη θεμελίωση έχει ως αποτέλεσμα τη μέγιστη μείωση της ολίσθησης του πρίσματος και, ως εκ τούτου, τη μέγιστη μείωση της συσσώρευσης καθιζήσεων, η οποία μπορεί να φτάσει έως και το 40%. Τα δύσκαμπτα συστήματα τείνουν να καθιζάνουν εξίσου με τα ισοδύναμα συστήματα ΘΕ, ενώ τα εύκαμπτα κινούνται εκτός φάσης με αποτέλεσμα τη μείωση των καθιζήσεων, η οποία, όμως, είναι

μικρότερου μεγέθους σε σχέση με αυτήν στο συντονισμό. Ο σχετικός λόγος μάζας *γ* και ο λόγος λυγηρότητας *h/r* επηρεάζουν την απόκριση του συστήματος, αν και σε μικρότερο βαθμό σε σύγκριση με τον λόγο περιόδων T_{sys}/T_{exc}. Είναι αξιοσημείωτο ότι στην περίπτωση ημι-άκαμπτων κατασκευών (T_{sys}/T_{exc} = 0.55-0.80) με μεγάλους λόγους λυγηρότητας (*h/r* > 1.36), οι καθιζήσεις αυξάνονται έως και 20% σε σχέση με τα συστήματα ΘΕ λόγω της επιπρόσθετης φόρτισης του εδάφους που προκαλείται από το λικνισμό της κατασκευής.

x) Αντίθετα, οι σεισμικές καθιζήσεις των κατασκευών σε **μη ρευστοποιήσιμες συνθήκες** αυξάνονται σημαντικά λόγω της επιπρόσθετης φόρτισης του εδάφους θεμελίωσης που προκαλείται από τις κατασκευαστικές ταλαντώσεις. Ως εκ τούτου, η κατανομή των διατμητικών τάσεων κάτω από τη θεμελίωση φαίνεται να είναι τοπικά συγκεντρωμένη σε σύγκριση με το βαθύτερο σχηματισμό εδαφικών πρισμάτων των ρευστοποιήσιμων συνθηκών και, επιπρόσθετα, οι μέγιστες τιμές τους συγκεντρώνονται συμμετρικά κάτω από τις άκρες του θεμελίου. Λόγω της συσχέτισης της συσσώρευσης καθιζήσεων με τις ταλαντώσεις της κατασκευής η πιο κρίσιμη παράμετρος για την επιδείνωση των καθιζήσεων είναι ο λόγος περιόδων T_{sys}/T_{exc} μεταξύ του συστήματος και της διέγερσης. Οι συνθήκες συντονισμού μπορεί να οδηγήσουν σε ενίσχυση των φασματικών επιταχύνσεων και, συνεπακόλουθα, των λόγων $\rho_{A\Theta E}/\rho_{\Theta E}$ έως και 2 με 6 φορές, αντίστοιχα. Ο σχετικός λόγος μάζας *γ* και ο λόγος λυγηρότητας *h/r* επηρεάζουν, επίσης, σημαντικά τη συσσώρευση καθιζήσεων. Οι επιδράσεις τους σχετίζονται με την επιδεινούμενη ταλάντωση της ανωδομής με την αύξηση των λόγων αυτών. Τέλος, τα χαρακτηριστικά της σεισμικής διέγερσης επηρεάζουν την απόκριση του συστήματος κυρίως μέσω της μέγιστης σεισμικής επιτάχυνσης PGA και – σε μικρότερο βαθμό – μέσω του αριθμού των κύκλων διέγερσης N_o.

Table of Contents

Chapter 1

Introduction

1.1 Problem outline

The design of structures founded on soils susceptible to liquefaction poses a challenge for contemporary engineering. Field observations during major earthquakes (Niigata, 1964; Luzon, 1990; Kocaeli, 1999; Christchurch, 2011; Durres, 2019) have shown a variety of liquefaction-related phenomena which are manifested either at the free field (e.g., sand boils and permanent ground displacements) or – more importantly – through infrastructure damage due to settlement accumulation caused by bearing capacity failure, as shown in **Figure 1.1** (Cubrinovski et al. 2011; Ishihara et al. 1993; Tokimatsu et al. 1994; Yoshimi and Tokimatsu 1977).

(a)

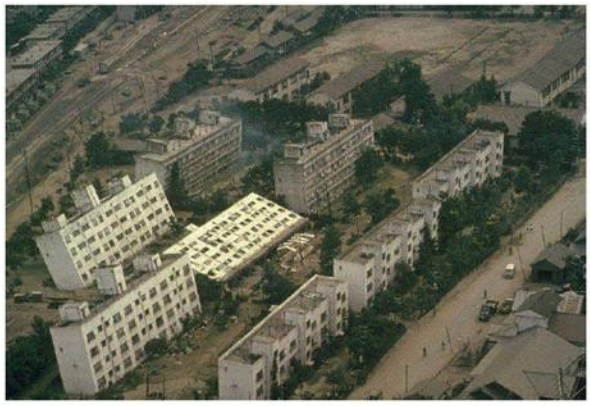

(b)

Figure 1.1: Liquefaction-related phenomena during major earthquakes. (a) Bearing capacity failure of shallow foundations, (b) floating of light structures, (c) ground failure due to lateral spreading, (d) soil ejecta of the liquefied soil to the ground surface and (e) sinking of heavy objects.

Design codes typically prohibit the construction of structures on such conditions without eliminating the risk of liquefaction. Thus, the conventional design involves the construction of piles, in order to transfer loads into deeper non-liquefiable layers, in combination with shallow or extended ground improvement. However, recent field observations (Acacio et al. 2001; Bray et al. 2014; Ishihara and Yoshimine 1992) showed that the presence of a non-liquefiable surface crust prevented the accumulation of excessive settlements and, thus, ensured a feasible alternative to the conventional – and more expensive – design. Based on this conclusion, a novel approach of designing structures with only shallow foundations – instead of piles – has been investigated, in the last two decades, with a number of experimental and theoretical studies (Liu and Dobry 1997; Naesgaard et al. 1998; Adalier et al. 2003; Dashti et al. 2010; Sitar and Hausler 2012; Dimitriadi et al. 2017). These studies have shown that seismic settlements of footings are primarily attributed to the *shear-induced* deformation of the foundation soil, while secondary effects are attributed to post-liquefaction sedimentation and consolidation, as well as volumetric strains due to drainage and the outflow of soil-ejecta to the surface. This design concept involves a surficial ground improvement (i.e., up to approximately 4m) with vibrocompaction and installation of drains in order to increase soil's strength and permeability, respectively (**Figure 1.2**).

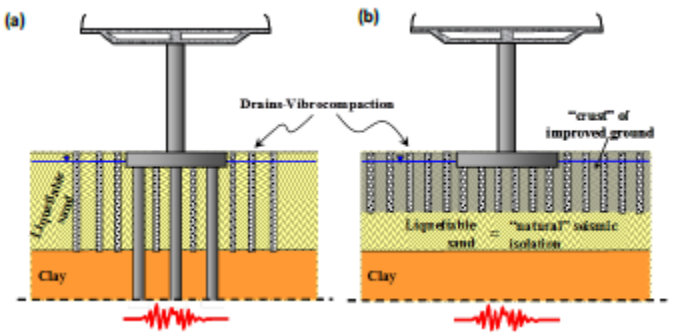

Figure 1.2: (a) Typical foundation design in liquefiable conditions involving deep soil improvement and pile construction, (b) novel foundation design involving shallow foundations with improvement of a surficial crust.

Seismic settlement accumulation was initially examined for foundation-soil (FS) systems – i.e., without superstructure effects – in dry conditions and it was attributed to the exceedance of the foundation bearing capacity and the subsequent sliding of the Coulomb-type soil wedge (Richards et al. 1993). In the case of liquefied conditions, the severe degradation of soil's strength further aggravates the wedge sliding. Following the above, an improved soil crust with adequate strength, dimensions and drainage – in order to prohibit pore pressure build-up – can limit settlement accumulation within the acceptable limits. It is noteworthy that a sufficient ground improvement can be quite shallow since its principal operation is to prohibit the formation of the passive – and reaching to the surface – soil wedge on the sideways of the footing. Following the above, Dimitriadi et al. (2018) observed that a ground improvement with width and depth 2 to 3 and 1 to 1.5 times the footing width, respectively, is sufficient to reduce settlements up to 90% compared to an improvement of infinite depth and width. Most recently, analytical relationships have also been proposed to predict the shear-induced building settlements during shaking (Bray and Macedo 2017; Dimitriadi et al. 2017; Bullock et al. 2019). These relationships correlate the accumulated seismic settlements ρ with the key geotechnical parameters.

As a continuation of the foregoing studies, the dynamic performance of complete structure-foundation-soil systems (SFS) in liquefiable conditions has been investigated lately with a number of centrifuge (Adamidis and Madabhushi 2017; Dashti et al. 2010; Tokimatsu et al. 2019) and numerical (Chaloulos et al. 2020; Hughes and Madabhushi 2019; Karimi and Dashti 2016; Macedo and Bray 2018) studies. The effect of the superstructure is mainly introduced through the rocking-induced development of – additional – shear straining. Compared to the formation of the – deep – soil-wedge failure mechanism, shear strains due to rocking are localized under the footing edges. It is observed that seismic settlements are mostly increased for heavier structures while the increase of the structural height leads to only

marginal seismic settlement increase. Overall, the conducted research has shown the dependency of seismic settlements on a wide variety of structural, soil and excitation parameters. Nevertheless, the dynamic response of the structure depends on the time-varying properties of the SFS system, the soil profile and the ground motion. Thus, it is important to employ the soil-structure interaction (SSI) framework in order to estimate the vibrational characteristics of the system, usually expressed in terms of the flexible-base system period T_{sys}. Especially in the case of liquefiable conditions, and depending on the soil susceptibility to liquefaction for the given ground motion, it is common to observe that the onset of liquefaction distinguishes soil properties to prior- and post-liquefaction, neither of which can be ignored (Bouckovalas et al. 2017; Kramer et al. 2016; Özener et al. 2020; Youd and Carter 2005).

1.2 Scope of work

The scope of the present Thesis is to develop a design methodology for the construction of structures founded upon liquefiable soil layers. The examined design concept assumes the presence of a surficial non-liquefiable layer and the construction of shallow foundations – instead of piles. The surficial layer is improved by means of densification and permeability increase following the vibrocompaction and installation of drains, respectively, of the foundation soil. This concept is developed following abundant field, experimental and numerical findings suggesting that the presence of a deeper non-liquefiable soil layer acts as “natural isolation” for the upward propagation of seismic waves while the presence of the non-liquefiable crust is able to ensure the integrity of the foundation system during the earthquake.

Following the above, the present Thesis aims to investigate the performance of structure-foundation-soil (SFS) systems in liquefiable conditions and to propose a complete methodology for the performance-based design of the foundation. The key elements of this study can be summarized in the following:

- A series of 3-dimensional numerical analyses are performed in order to parametrically investigate the primary parameters that affect the dynamic performance of SFS systems in liquefiable conditions. Due to the fact that an ample number of previous studies has investigated the dynamic performance of foundation-soil (FS) systems in such conditions, the present study focuses on the effect of structural inertia on the response of the system. The key structural parameters are examined in the dimensionless framework of soil-structure interaction (SSI) which is typically prescribed in the Codes.
- The numerical methodology employs the advanced constitutive model NTUA-Sand which is based on Critical State soil plasticity theory and may capture soil nonlinearity in both monotonic and cyclic

loading. The accuracy of this constitutive model has been extensively verified with element tests and boundary value problems against the centrifuge experiments of the VELACS project.

- Based on the results of the parametric analysis a simplified methodology is proposed for the prediction of seismic settlements of SFS systems. Its development is based on the following assumptions:
  i) Inertial effects of the superstructure are considered uncoupled with the effects of soil characteristics which are thoroughly investigated in previous studies. As a result, structural effects are introduced as a correction factor to the well-established procedures of estimating seismic settlements for FS systems.
  ii) A key element in the calculation of seismic settlements in liquefiable conditions is the accurate estimation of the liquefaction onset time, since the dynamic performance of structures is fundamentally different before and after liquefaction of the subsoil. In this study, the dynamic response of SFS systems is separately examined for soil conditions with and without liquefaction. Therefore, the proposed relationships for the structural effects on seismic settlements are also distinguished to those prior to and after liquefaction.

1.3 Methodology outline

The Thesis includes seven chapters with the following content:

In **Chapter 2** an extended literature review is conducted regarding the dynamic response of buildings in liquefiable conditions. This survey follows the progressive accumulation of related knowledge within the engineering community. Namely, the initial acquaintance of engineers with liquefaction-induced damages to infrastructure occurred during seismic events in the last half of the 20th century. A concise review of such events in presented along with the findings that emerged after the renaissance surveys. As a continuation of these findings, the results of a number of experimental and numerical studies on the seismic response of FS and SFS systems are presented.

Chapter 3 focuses on modeling aspects of the numerical analysis of SFS systems. Various aspects of the numerical methodology are discussed here, such as characteristics of the mesh, boundary conditions, verification of the constitutive model and the foundation-soil interface, numerical stability of the calculation scheme, modeling of the foundation and the structure, numerical modeling of the improved zone.

The dynamic characteristics of the SFS system play a key role in the seismic response of the overall system, in general, and the foundation more specifically. **Chapter 4** parametrically investigates the effect of the significant soil, excitation and structural parameters on the natural period evolution of SFS systems during shaking. Based on the foregoing findings multi-variable relations are proposed for the analytical prediction of the system natural period. The developed relations treat separately soil conditions prior to and after liquefaction.

Chapter 5 investigates the effect of structure inertia on the response of shallow foundations constructed on liquefied ground with an improved non-liquefiable crust. The conducted parametric investigation emphasizes on the effects of the significant structural and excitation parameters on the ratio of the accumulated settlements between SFS and FS systems. Based on these results, multi-variable relations are developed for the analytical prediction of the aforementioned settlement ratio. **Chapter 6** repeats this procedure for non-liquefiable soil conditions.

Finally, **Chapter 7** describes a step-by-step procedure for the calculation of seismic settlements of structures. As a first step, this chapter presents published analytical methodologies for seismic settlement computation, under *non-liquefiable* and *liquefied* soil conditions, without any SSI effects. In the sequence, literature studies that transform the earthquake motion into an equivalent harmonic signal are discussed. Additionally, the most up-to-date methodologies that estimate the liquefaction onset time are presented. Lastly, a design example of four SFS systems subjected to earthquake motions are presented in order to demonstrate the proposed methodology.

Chapter 2

Literature survey on seismic settlements of structures in liquefiable conditions

2.1 General

Liquefaction-related phenomena that have been observed during major earthquakes in the last century are manifested either at the free field (e.g., sand boils, permanent ground displacements) or – more importantly – through infrastructure damage (e.g., settlement or tilting of structures, floating of buried pipelines or tanks). A more systematic documentation of infrastructure damage started during the decade of 1960 for the major earthquakes of Niigita in Japan (1964) and Prince William Sound in Alaska (1964), where liquefaction-induced settlements of concrete buildings and bridge foundations were recorded, respectively (Ross et al. 1969; Yoshimi and Tokimatsu 1977). The devastating earthquakes of Luzon in Philippines (1990), Koaceli in Turkey (1999), Tohoku in Japan (2011), Sulawesi in Indonesia (2018) and Durres in Albania (2019) are the most recent records of the hazard that liquefaction poses for the infrastructure. The seismic response of buildings on liquefiable soil was initially investigated by experimental shaking tests (Acacio et al. 2001; Adalier et al. 2003a; Coelho et al. 2004; Deng and Kutter 2012; Hughes and Madabhushi 2019a; Kawasaki et al. 1998; Liu and Dobry 1997a; Yoshimi and Tokimatsu 1977) and numerical analyses (Adalier et al. 2003b; Dashti and Bray 2013a; Dimitriadi et al. 2017a; Liu and Dobry 1997b; Naesgaard et al. 1998a; Sitar and Hausler 2012a) of footings and rigid structures subjected to seismic excitations. The role of the key parameters – such as contact pressure, footing width, soil density – was identified. The acquired knowledge helped to expand the volumetric-based

methodologies for the estimation of free field settlements (Ishihara and Yoshimine 1992; Tokimatsu and Seed 1987) and develop analytical relationships that predict the shear-induced building settlements during shaking (Bray and Macedo 2017; Dimitriadi et al. 2017; Bullock et al. 2019). The proposed relationships are based on regression analysis of the numerical predictions of settlements for a number of different geotechnical, earthquake and building characteristics. In more recent studies, the dynamic performance of complete structure-foundation-soil systems has been investigated with a number of centrifuge studies (Adamidis and Madabhushi 2017; Dashti et al. 2010b; Tokimatsu et al. 2019) and numerical (Chaloulos et al. 2020; Hughes and Madabhushi 2019b; Karimi and Dashti 2016b; Macedo and Bray 2018).

2.2 Field observations

2.2.1 Niigata, Japan 1964

The earthquake of 1964 in the city of Niigata in Japan was the first major event where liquefaction-induced structural damage was systematically recorded (Kishida 1966; Oshaki 1966; Seed and Idrisss 1967; Yoshimi and Tokimatsu 1977). Oshaki (1966) reports that reinforced concrete houses were damaged by the earthquake in a rate of 22%, i.e., 340 cases out of 1530 total number of houses. Out of these cases of damage, the 2/3 were attributed to foundation failure in the form of settlement, tilt or overturning of the building without any structural damage. Yoshimi and Tokimatsu (1977) correlated the basic characteristics of 35 of these concrete buildings with the accumulated settlement due to liquefaction. The depth of the liquefied soil D was estimated by the standard penetration resistance to range from 4m to 20m in the affected region. The width B of the structure was found to play a significant role, since for width ratios $B/D < 1.5$ (where D is the depth of the liquefied sand) building settlements were drastically increased up to 2m (**Figure 2.1**). Other structural characteristics, such as the number of stories, the presence of basement or the pile depth did not appear to affect building settlements significantly.

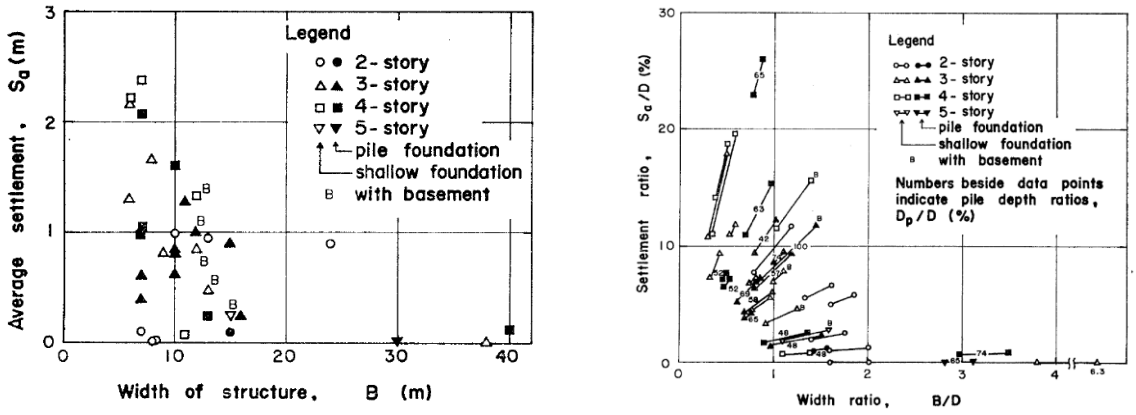

Figure 2.1: Settlements of reinforced concrete buildings during the Niigata earthquake of 1964: (a) average settlements vs building width B and (b) settlement ratio Sa/D vs width ratio B/D (Yoshimi and Tokimatsu 1977)

2.2.2 Dagupan, Philippines 1990

The earthquake of Dagupan City in the Philippines (1990) occurred in the north-central part of Luzon Island and it caused extensive soil liquefaction along the southern coast of the Lingayen Gulf. This resulted in numerous damages to infrastructure due to liquefaction, such as building settlements and inclinations, ground lateral spreading, collapse of bridge decks etc. (Acacio et al. 2001; Adachi et al. 1992; Ishihara et al. 1993; Tokimatsu et al. 1994). Adachi et al. (1992) documented 30 cases of reinforced concrete buildings that experienced significant liquefaction-induced settlement and tilt. The authors estimated the depth of the liquefied layers by SPT tests along Perez Boulevard where the most infrastructure damages were concentrated. **Figure 2.2** summarizes the main findings of the investigation. Namely, accumulated settlements in the majority of the affected buildings range between 25cm and 150cm, while the recorded inclination was found to range between 0° and 7.5° (**Figure 2.2a**-**b**). Additionally, values of inclination seem to increase for increasing settlements (**Figure 2.2c**). The number of stories does not appear to affect the magnitude of settlements and tilt (**Figure 2.2d**-**e**). As in the case of Niigata earthquake, the area of foundation is inversely correlated to the accumulated settlement (**Figure 2.2f**).

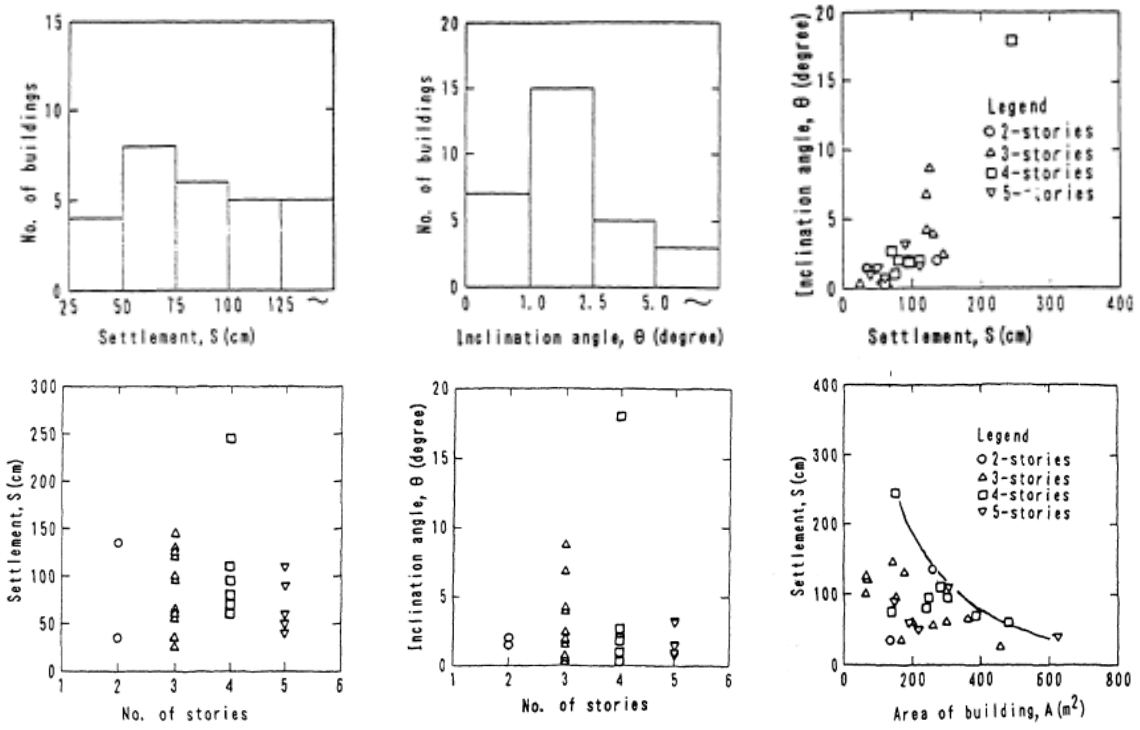

Figure 2.2: Settlement and inclination angle of reinforced concrete buildings during the Dagupan City earthquake of 1990 (Adachi et al. 1992)

2.2.3 Kocaeli, Turkey 1999

The Kocaeli earthquake of 1999 is one of the most devasting seismic events that took place in the last decades. It had a magnitude of M_w=7.8 and caused excessive damages in the Izmit bay area and mostly in the cities of Izmit and Adapazari. The city of Adapazari is located within a plain of fluvial deposits that is formed by the estuaries of Sakarya and Cark rivers. The earthquake caused severe damage or collapse to a total number of 5078 buildings in the city of Adapazari and a large number of buildings suffered from excessive settlements or tilting due to liquefaction. Yoshida et al. (2001) identified the location of the liquefied sites to be at the riverbed of Sakarya river circling the city center, i.e., the "ring" of **Figure 2.3**, whereas the non-liquefied sites are located at the center of urban area. The site investigation of the liquefied areas revealed a 1m deep surface fill which overlays a 1m silty clay layer and a 2.5m liquefiable non plastic silt with N_{spt} = 8. Below that, there is a dense gravely sand with N_{spt} = 20-40. The water table lies, in general, 1m to 3m under the ground surface. The authors identified that buildings located in the non-liquefied area mainly suffered from structural damages, whereas buildings in liquefied areas experienced foundation failure without exhibiting severe structural damages.

Sancio et al. (2002) conducted a detailed survey of soil conditions in the urban area of Adapazari by performing 59 CPTs and 15 exploratory borings. They distinguished the four characteristic types of soil profiles presented in **Figure 2.4**. The most susceptible to liquefaction profile is soil type 1, which is formed by a 4m loose non-plastic silt underlain by a layer of low plasticity clay and dense silt of about 5m in thickness. Below that, there is a layer of interbedded clays, silt and sands. To evaluate the liquefaction potential of these soil profiles the authors used the soil behavior index type I_c in combination with the Chinese criteria (Seed 1982). **Figure 2.5** presents the variation of the soil index I_c with depth for different soil profiles. Values of I_c greater than 2.6 are indicative of liquefaction susceptibility. It is seen that soil profile 1 exhibits values of I_c greater or around the value of 2.6 to the greatest extend along its depth. Overall, ground failure, in terms of building settlements and tilting, was principally observed in ground types 1 and 2. **Figure 2.6** summarizes the recorded settlements of buildings for the aforementioned ground types as a function of the building width and the number of stories. The accumulation of settlements seems to be independent of the building width. On the other hand, it increases for increasing number of stories, probably, as a result of the additional contact pressure of taller buildings.

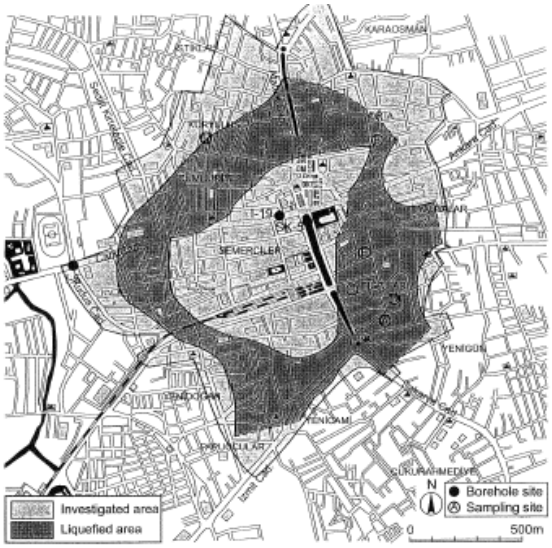

Figure 2.3: Map of the urban area of Adapazari (Yoshida et al. 2001).

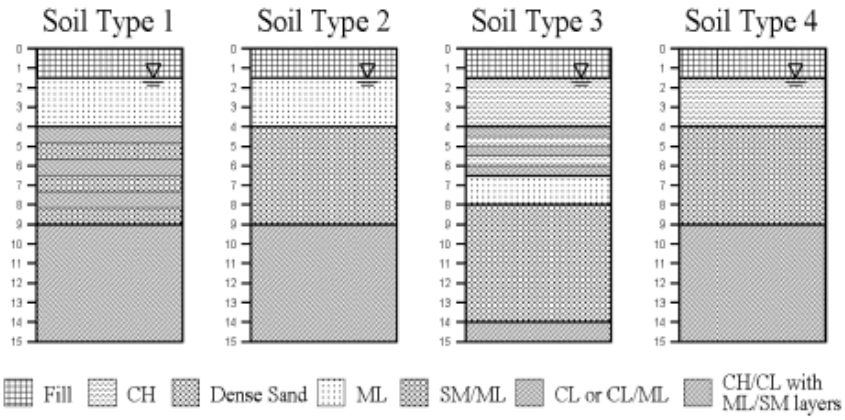

Figure 2.4: Most common soil profile types in the urban area of Adapazari (Sancio et al. 2002).

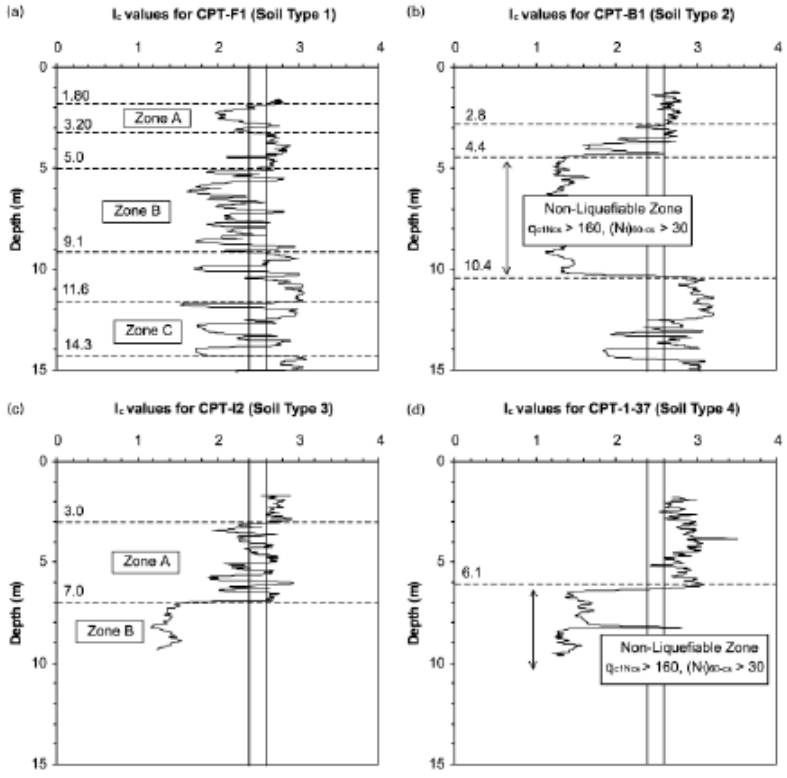

Figure 2.5: Soil behavior index I_c of the four types of soil profiles (Sancio et al. 2002).

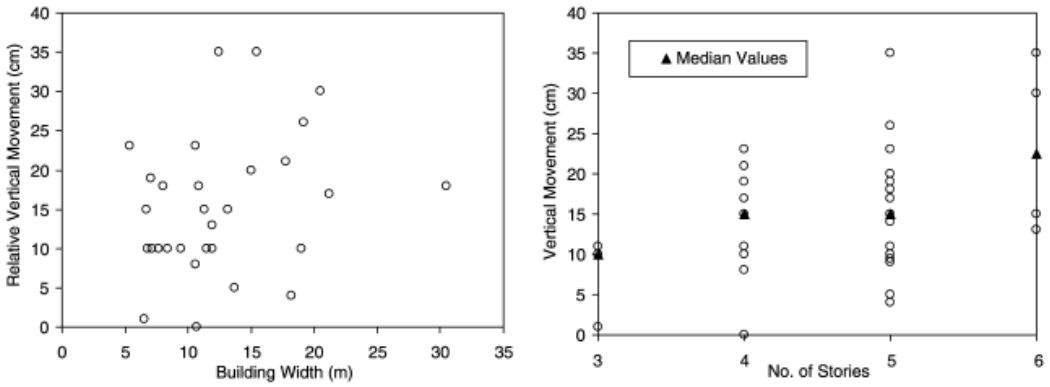

Figure 2.6: Recorded settlements of buildings after the earthquake of Adapazari (1999) as a function of building width and the number of stories (Sancio et al. 2002).

2.2.4 Christchurch, New Zealand 2011

The Canterbury earthquake sequence that occurred in 2010-2011 in New Zealand consisted of several seismic events, including seven events with magnitude M_w greater than 5.5 and values of PGA ranging from 0.09g to 0.44g. The most devastating event was the earthquake of the 22nd of February 2011 in Christchurch with a source-to-site distance R around 3 to 6 km. The most affected area was the Central Business District were over 1.500 buildings out of the total number of 4.000 were severely damaged. Several reconnaissance teams documented extensive liquefaction in the Central Business District and in the eastern suburbs (Bray et al. 2014; Cubrinovski et al. 2011b; a; Quigley et al. 2013). **Figure 2.7** shows the spatial distribution of liquefaction phenomena in the urban area of Christchurch, i.e., moderate-to-severe liquefaction is depicted with pink color and low-to-moderate with yellow color. The primary zone of liquefaction lies from west to east along the Avon River and the network of its tributaries. The shallow alluvial soils consist of sands of various densities, sandy gravels, silts etc. A representative soil profile within the liquefied area of the Central Business District is presented in **Figure 2.8**. Surficial layers consist of either sandy gravels (i.e., in the southwest part) or loose silts and silty sands (i.e., in the southeast part). Deeper layers up to 25m are dominated by clean sands of increasing density with depth.

Damage to infrastructure due to liquefaction was extensive and took many forms. Severe ground settlements were observed due to post-liquefaction volumetric strains which resulted in infrastructure damage to roads, pavements etc. Lateral spreading took place towards the banks of the Avon River which resulted in ground cracking, lateral movement of buildings and extensive damage to the underground network of pipelines. The location of faults in the pipeline system is

marked with red dots in **Figure 2.7**. Several buildings in the Central Business District suffered from excessive settlements, including differential settlements and tilts, due to shear-induced deformation of the foundation soil. Various foundation types are constructed in the urban area of Christchurch reflecting the complexity of soil conditions. Overall, buildings with shallow foundations suffered the most severe settlements while buildings founded on piles were left, in general, intact. Notable examples of foundation performance during the Christchurch earthquake are the following:

- The buildings of **Figure 2.9** are multistory structures constructed with three different foundation types. They are located in neighboring regions with similar soil conditions that resulted in generalized liquefaction in all cases. The response of these buildings as well as the soil conditions were investigated by Bray et al. (2014). Namely, the first (PILE-6) is a 6-story building with a mat foundation in combination with piles and ground improvement. The second structure (FTG-7) is a 7-story steel frame supported on a system of interconnected strip footings with total dimensions in plan 29m x 32m. The third structure (FTG-4) consists of a 4-story reinforced concrete frame founded on a similar with the FTG-7 foundation system of strip footings but with smaller dimensions, i.e., 15m x 23m. As expected, seismic settlements of the building PILE-6 were minimal, while the adjacent ground surface experienced settlements due to post-liquefaction volumetric strains. On the other hand, both buildings on strip footings experienced substantial settlements and tilting which resulted also in structural damages. The taller FTG-7 building settled less than the FTG-4, which might seem counterintuitive at first, but it is in accordance with previous field observations indicating that buildings with wider foundations settle less (Yoshimi and Tokimatsu 1977).
- The CTUC building was a 6-story reinforced concrete building supported on shallow foundations which were connected with tie beams. The particularity of this case is that soil conditions at the site vary significantly under the building. Six CPT tests were performed at the CTUC building site by Bray et al. (2014) along with a simplified liquefaction evaluation. The subsurface conditions along the east side of the building are depicted in **Figure 2.10**. The liquefaction potential is estimated with the soil behavior type index I_c (i.e., values of $I_c < 2.6$ indicating susceptibility to liquefaction). The survey revealed that under the southeast corner of the building liquefiable SM/ML layers at shallow depths were observed, which was not the case near the center and under the northeast corner of the building. As a result, the

southeast side settled 20cm to 25cm more compared to the northeast side, i.e., an angular distortion of 1/50. Structural damage at the beam-column connections was observed due to the differential settlement of the foundation.

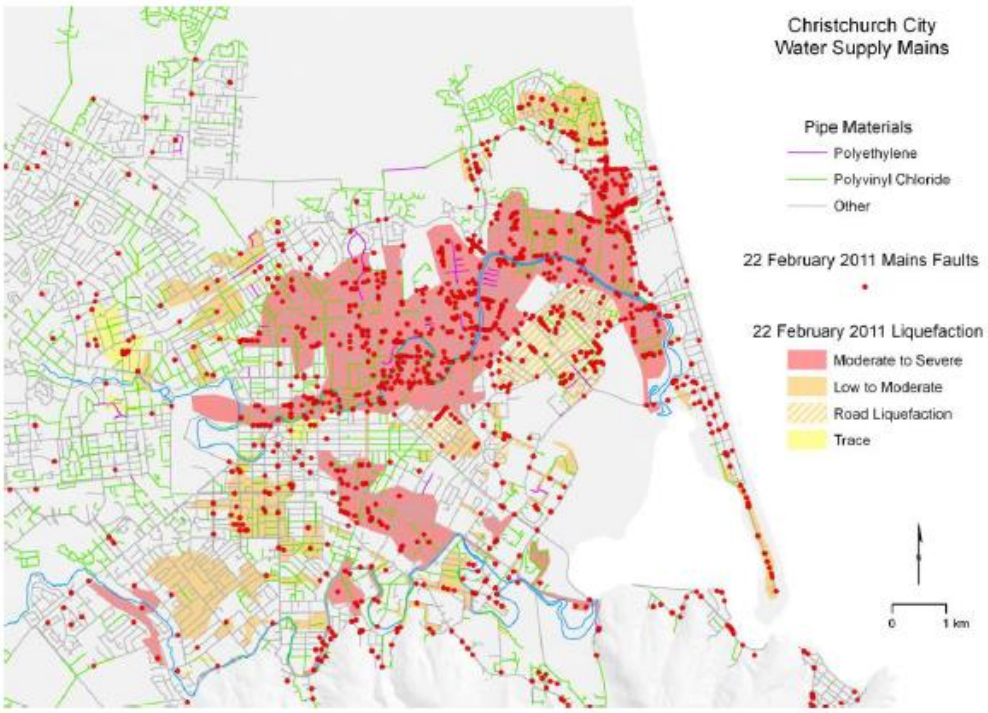

Figure 2.7: Map of the urban area of Christchurch. Different colors depict the severity of liquefaction and red dots indicate the locations of pipeline failures due to liquefaction (Cubrinovski et al. 2011b).

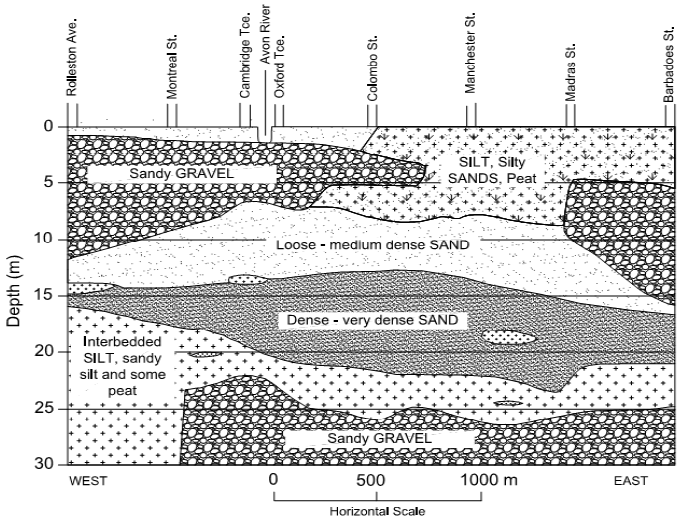

Figure 2.8: Representative soil prolife layering in the Central Business District of Christchurch (Cubrinovski et al. 2011a)**.**

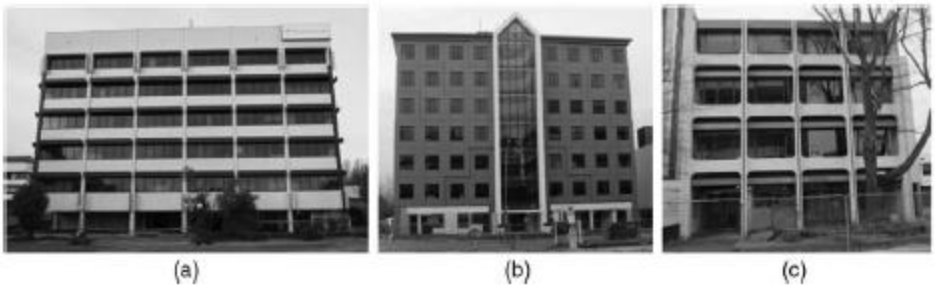

Figure 2.9: Multistory buildings in the affected by liquefaction Central Business District of Christchurch with different foundation systems (Bray et al. 2014).

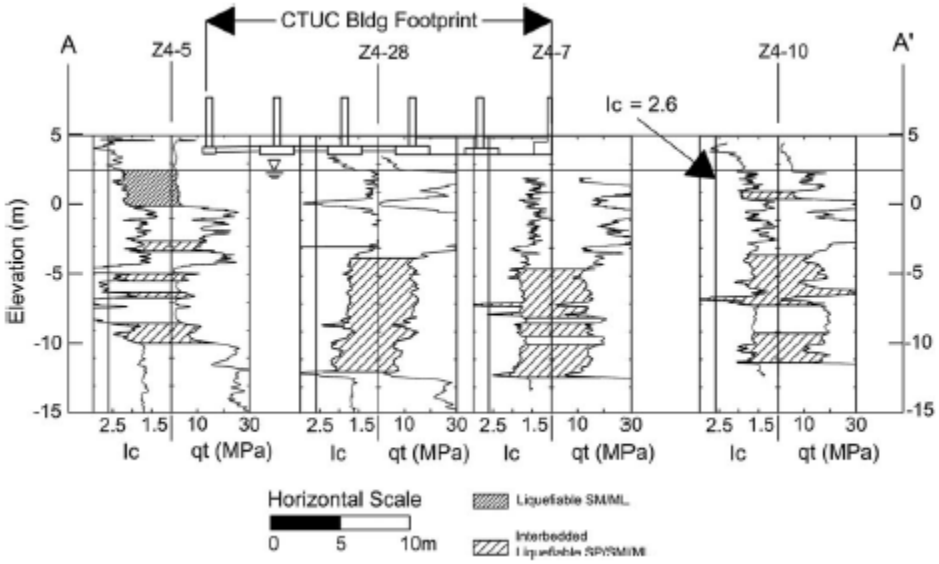

Figure 2.10: Liquefaction potential of soil layers under the east side of the CTUC building in Christchurch (Bray et al. 2014).

2.2.5 Durres, Albania 2019

The Albania earthquake of 2019 had a moderate magnitude $M_w = 6.4$ and its epicenter was located approximately 30km west of the city of Tirana with an estimated 10km to 20km source depth. The coastal city of Durres and the surrounding area experienced the heaviest damages, where severe damages were documented in 29% and 14% of buildings constructed before and after 1993, respectively (Hellenic Society of Earthquake Eng. 2020). Several liquefaction phenomena were documented in the coastal region of Durres, including building settlement and tilting, ground displacement, soil ejecta etc. (Blagov et al. 2020; Duni and Theodoulidis 2020; Hellenic Society of Earthquake Eng. 2020). Site surveys prior to the earthquake of 2019 had already identified that liquefiable soils extend in coastal area of the Adriatic Sea from Vlore to Ulqini (Daja et al. 2016;

Kociu 2004). **Figure 2.11** shows the assessment of liquefaction potential for the Durres city conducted by Kociu (2004) based on empirical correlations of in-situ measurements. The city of Durres is located within the highly susceptible to liquefaction area 1. Daja et al. (2016) performed a series of CPT tests in order to evaluate the liquefaction potential of a representative region of the Adriatic coast, near the city of Fier. The areas of the Adriatic coast with liquefaction potential extend to the north and south of Durres city, marked with pink color in **Figure 2.12**, consisting of sands, silty sands or clay sands. CPT tests confirmed the liquefaction hazard of soil close to coast.

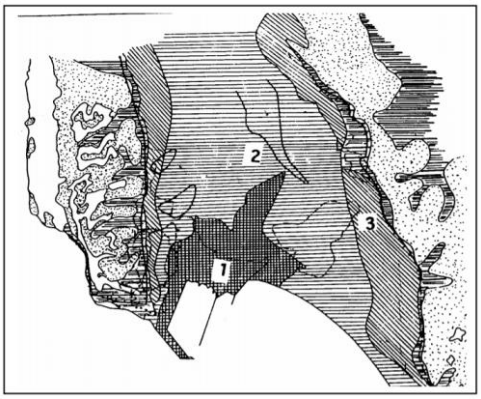

Figure 2.11: Liquefaction susceptibility assessment of Durres city and the surrounding area: (1) highly, (2) moderately and (3) less susceptible to liquefaction (Kociu 2004).

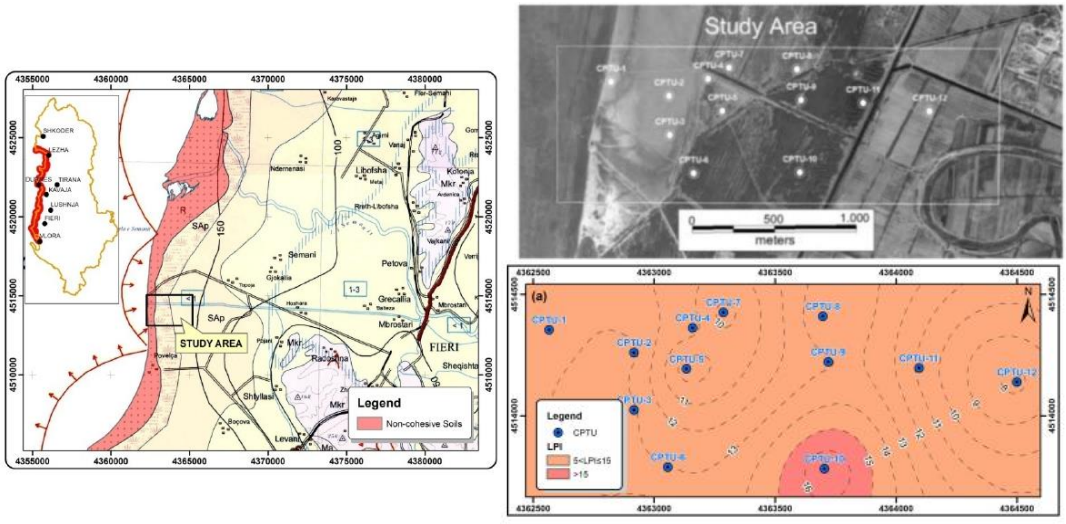

Figure 2.12: (a) Liquefaction potential of the coastal area in Albanian part of Adriatic Sea and (b), (c) study area and borehole locations of the CPT tests.

2.3 Experimental results

Yoshimi and Tokimatsu (1977) laid the ground for the investigation of the seismic response of footings on liquefied conditions with the conducted experiments of 1977. The authors performed a series of shaking table tests of rigid structures resting on top of a saturated sand deposit placed within a wooden box. The model was subjected to horizontal vibrations during which the settlements of the structure and the pore water pressures at various depths were measured. The model configuration of the ground and structural details is presented in **Figure 2.13**. The experimental results led to the following findings:

- Excess pore pressure ratios directly under the foundation are significantly smaller than 1.0 due to the presence of the footing's overburden stresses. For increasing values of the applied pressure these excess pore pressure ratios tend to decrease (**Figure 2.14b**).
- Footing settlements – normalized by the depth of the sand layer – are correlated with the percentage of the area under the footing that maintains excess pore pressure ratios below 0.6 (**Figure 2.1a**). The value of 0.6 is the critical value of excess pore pressure ratio that triggers liquefaction failure within the prescribed conditions of the experiment. This is obtained by torsion tests that related the level of excess pore pressure ratios with the dynamic shear ratio $\tau_d/\sigma'_v = 0.18$ which corresponds to the horizontal acceleration during the shaking table tests.
- Additional structural settlements were observed to decrease for increasing values of relative density (**Figure 2.14c**) and footing width (**Figure 2.14d**).

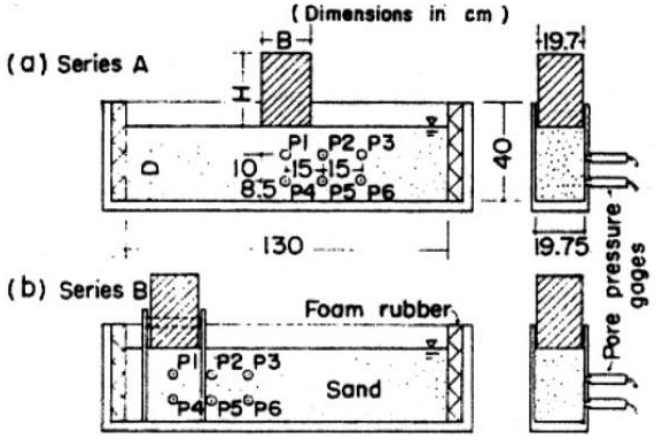

Figure 2.13: Model configuration of the shaking table tests performed by Yoshimi and Tokimatsu (1977).

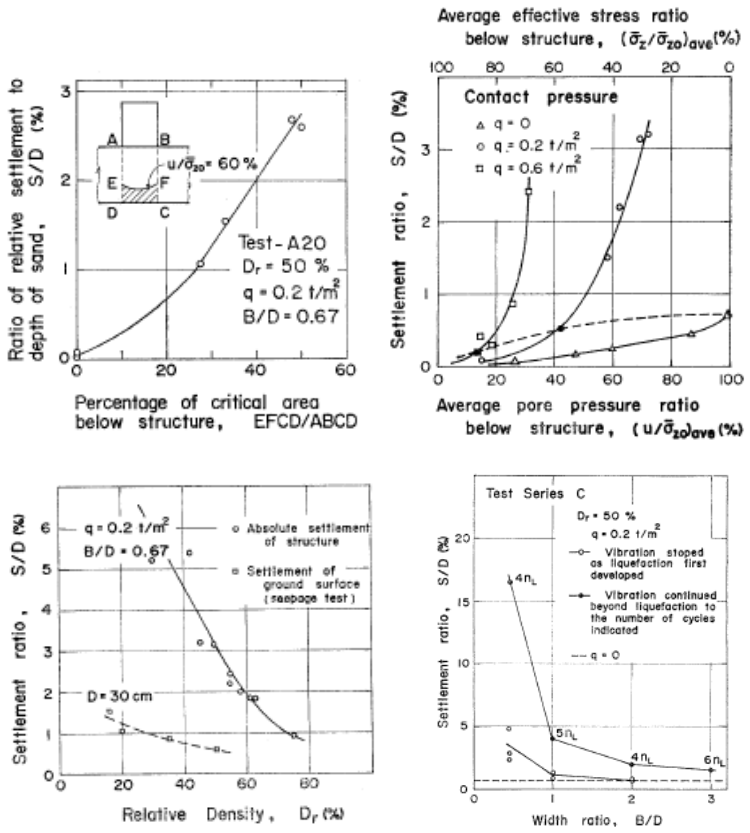

Figure 2.14: Effect of (a) pore pressure build-up below the foundation, (b) applied pressure, (c) soil density and (d) width ratio on structural settlements (Yoshimi and Tokimatsu 1977).

Liu and Dobry (1997) investigated the effect of foundation soil densification on the seismic settlements of footing in liquefied conditions. They conducted eight centrifuge model experiments of circular surface footings resting on a medium-to-dense liquefiable sand deposit. In the first set of tests, the soil underneath the footing was densified by vibrocompaction within a radius *r* and depth D_c, as presented in **Figure 2.15**, while in the second set different levels of soil permeability were designated by adjusting the viscosity of the pore fluid used in the model setup. The following conclusions were drawn by the authors:

- Excess pore pressures measured in the free field indicated complete liquefaction which was first observed in shallow depths and then propagated to deeper layers. Additionally, it was observed that water flow was directed from the bottom layers to the surface and towards the area under the footing, where excess pore pressure ratios were substantially smaller.
- Ground shaking in the free field is significantly reduced after the onset of liquefaction due to stiffness degradation of the underlying layers.

- Footing settlements essentially accumulated during shaking, while only a small part was attributed to the post-shake volumetric strains due to the dissipation of excess pore pressures. This suggests that footings in such conditions principally settle due to a bearing capacity type failure of the foundation soil.
- Soil compaction reduced footing settlements up to 65%, i.e., from 58cm to 20cm, approximately. The effect of compaction on settlements is significant for values of compaction depth up to 1.5 times the footing width and thereafter it is limited (**Figure 2.16**).

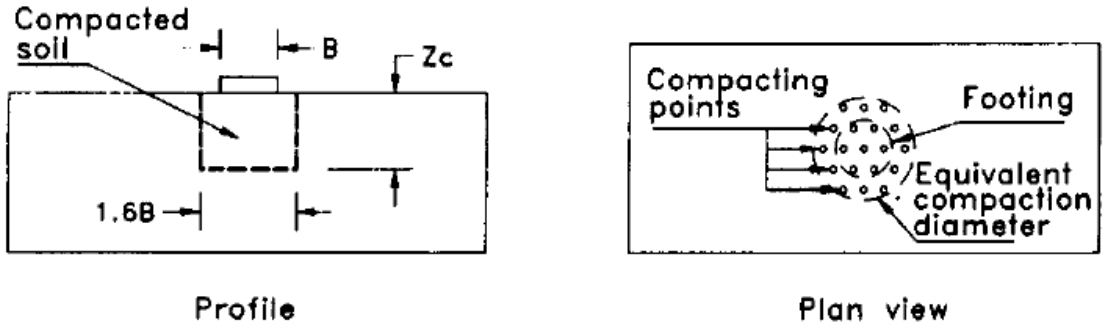

Figure 2.15: Schematic representation of the soil compaction area in the centrifuge experiments of Liu and Dobry (1997).

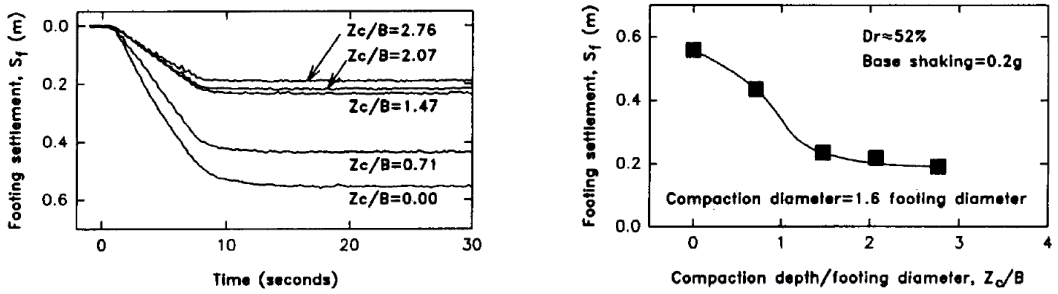

Figure 2.16: (a) Recorded timehistories of footing settlements for different levels of compaction depth z_c/B (normalized by the footing width B) and (b) variation of footing settlement with the compaction depth ratio z_c/B.

Early experiments of foundation-soil systems were followed in the last decades by more elaborate experimental setups that included the superstructure into the model. One of the first studies of such structure-foundation-soil systems in liquefied conditions was conducted by Coelho et al. (2004) with the centrifuge test of 2004 at Cambridge University's Schofield Centre (**Figure 2.17**). The examined model consisted of a bridge pier under a deck which was also supported at the container sides with rollers (i.e. allowing horizontal displacements and rotations). The structure was founded on a strip footing resting on a silica sand deposit with an average relative density of

57%. The model was dynamically excited at its base. Experimental results confirmed that the presence of significant vertical effective stresses under the structure resulted in reduced excess pore pressure ratios. Structural vibrations, on the other hand, led to additional shear straining under the footing edges, which in turn increases excess pore pressures, at first, and eventually decreases them due to the soil's tendency to dilate.

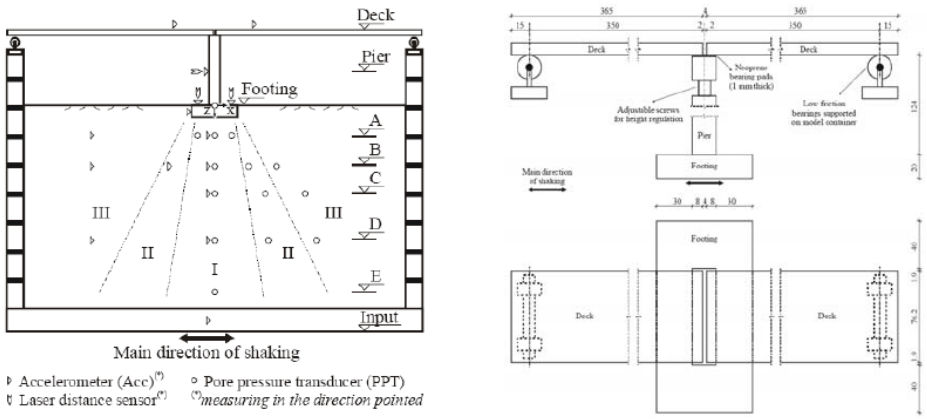

Figure 2.17: Experimental model setup (Coelho et al. 2004).

Dashti et al. (2010b) conducted four centrifuge experiments of simplified structures on rigid mat foundations resting on relatively thin deposits of liquefiable sand. The effects of two liquefaction mitigation measures, i.e., the case of a perimetrical structural wall installed around the foundation and the case of an impermeable vertical barrier that prohibits water flow towards the foundation soil, were investigated and compared with the case of no remediation (**Figure 2.18**). The following were observed by the authors:

- The effect of sand density on settlement accumulation is twofold. On one hand, denser sand increases the foundation soil's strength which in turn reduces settlements. On the other hand, denser sand has greater resistance to liquefaction, thus, liquefaction is either delayed or partially reached. This allows greater ground vibrations and, as a result, greater rocking-induced shear straining of the foundation soil.
- The in-ground structural wall reduced the deviatoric deformations adjacent to the structure. As a result, the installation of the wall reduced seismic settlements of the buildings in all tests.
- Overall, the installation of water barriers had a limited effect on footing settlements. Timehistories of settlement accumulation in **Figure 2.20** show that in the case of the

Moderate Port Island earthquake the system with water barriers (Structure WB) settles approximately 25% less than the system without any remediation (Structure BL), whereas in the case of the TCU078 earthquake both systems settle practically the same. That is because the water barrier prohibits the water flow under the foundation and as a result the volumetric component of strains due to drainage is reduced.

- The rate of the ground shaking intensity is related to the initiation, rate and amount of settlement accumulation. **Figure 2.19** shows that the rate of structural settlement during the strong part of shaking increases for increasing shaking intensity rate and decreasing relative density of the liquefiable layer.

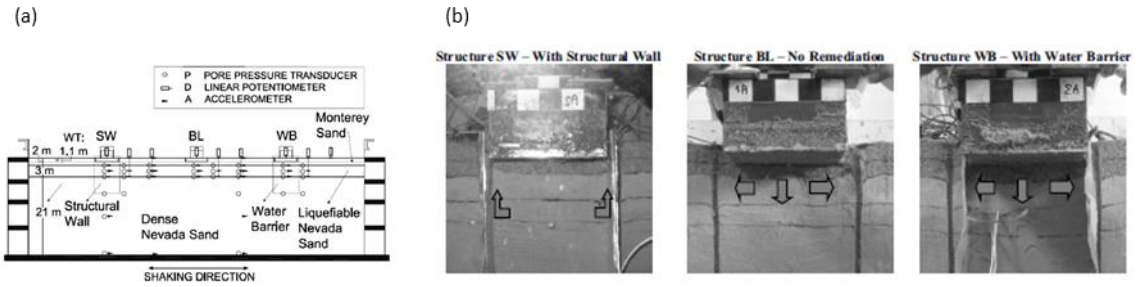

Figure 2.18: (a) Model configuration and (b) photographs of the examined systems: with a perimetrical structural wall around the foundation, without any remediation and with a flexible water barrier around the foundation (Dashti et al. 2010c).

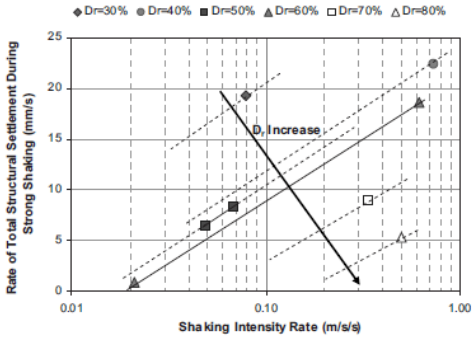

Figure 2.19: Variation of the structural settlement during the strong part of shaking with the shaking intensity rate for varying values of relative density of the liquefiable layer (Dashti et al. 2010c).

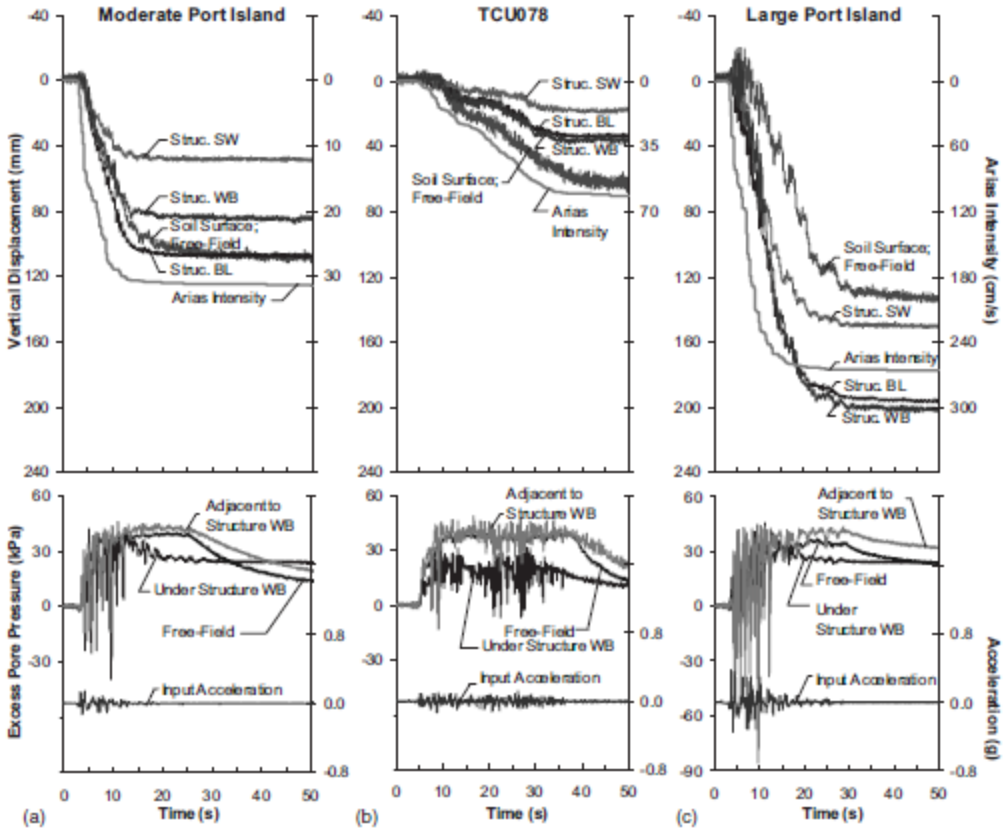

Figure 2.20: Timehistories of settlements and excess pore pressures for structures with water barrier (WB), structural wall (SW) and without remediation (BL) for three earthquakes (Moderate Port Island, TCU078 and Large Port Island) (Dashti et al. 2010c).

Olarte et al. (2018) performed a series of centrifuge experiments in order to evaluate the effect of soil densification in the seismic performance of structure-foundation-soil systems in liquefiable conditions. In total, four centrifuge tests were conducted for a 3- (Structure A) and a 9-story (Structure B) inelastic structure. The soil deposit consists of Ottawa sand overlaid by a shallow layer of denser Monterey sand. The densification area, as shown in **Figure 2.21** with grey colour, extends 6m under the footing and its width is one and a half times the improved depth. Two levels of relative density are selected, i.e., D_r = 40 and 90%. The looser sand layer exhibited greater excess pore pressures leading to strength loss and increased structural settlements. Both structures experienced significant reduction of settlement accumulation when ground densification was performed. In general, Structure B with and without densification exhibits large deformations and nonlinear response due to increased role of P-δ effects.

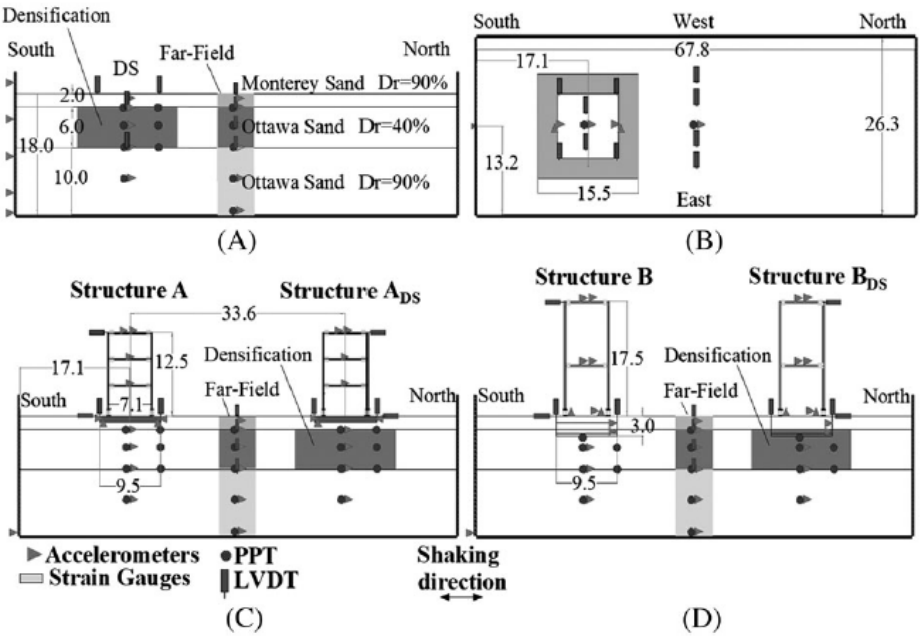

Figure 2.21: Configuration setup of centrifuge experiments, dimensions are in prototype scale (m) (Olarte et al. 2018).

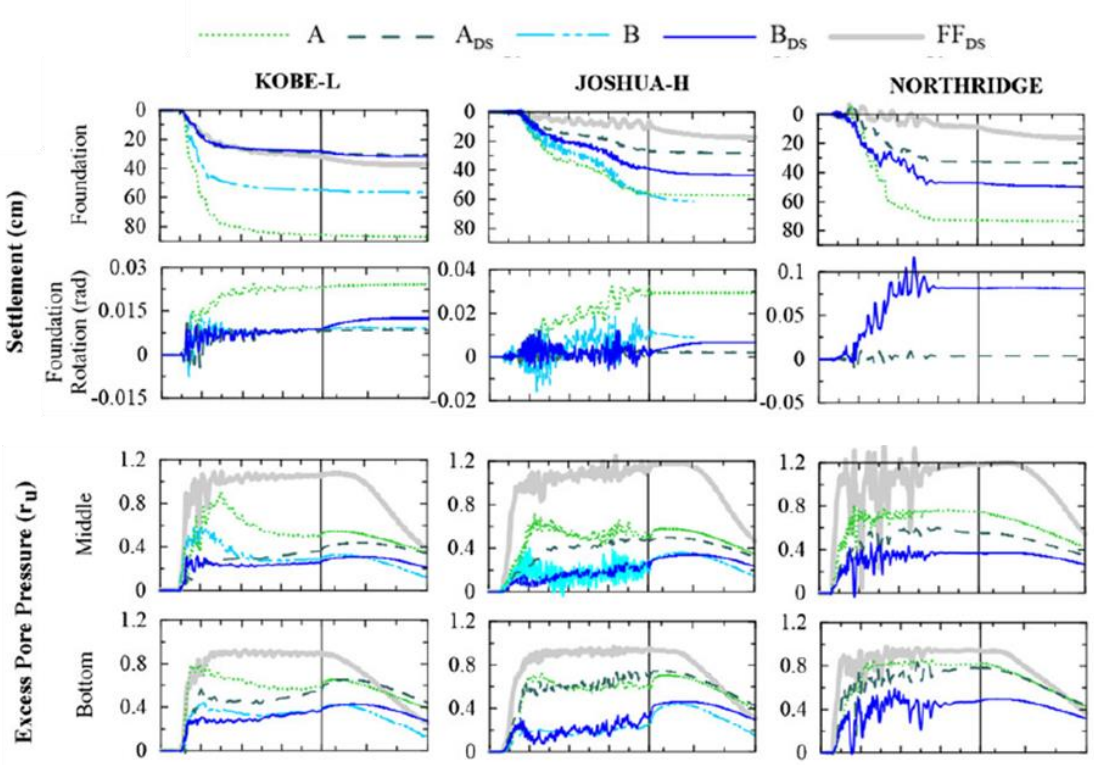

Figure 2.22: Timehistories of settlements, rotations and excess pore pressures for three earthquakes (Kobe-L, Joshua-H and Northbridge). A: Structure A, A_{DS}: Structure A with soil densification, B: Structure B, B_{DS}: Structure B with soil densification, FF_{DS}: Free field with densification (Olarte et al. 2018).

Hughes and Madabhushi (2019) examined the results of three centrifuge experiments conducted at the Schofield Centre of Cambridge University (Schofield 1980, 1981) aiming to investigate the response of structures with wide basements in liquefied conditions. The model setup consists of a simplified structure with a wide basement resting upon a homogenous layer of loose liquefiable sand. Three structural systems are examined with varying applied pressure and point of application of the structural weight (**Figure 2.23**). The following are observed:

- In the event of complete liquefaction, the presence of the wide basement creates an uplift force which counteracts the structural weight and, thus, reduces overall settlements. This effect is diminished for decreasing ratios of uplift force to total weight.
- In the case of symmetrical loading the accumulated rotations of the structures (Test A and B) were negligible. However, P-δ effects due to the eccentrically applied weight resulted in substantial rotations of the system (Test C). This is manifested with the contours of displacement vectors in **Figure 2.24**.

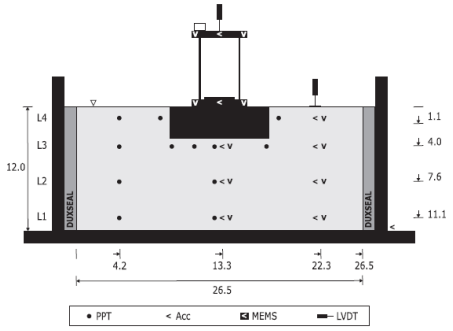

Properties of structures (prototype scale).

Property	Symbol	Test A	Test B	Test C
Total bearing pressure (kPa)	q	68.1	55.0	55.0
Buoyancy force (static) (kN)	$F_{U,H}$	2860	2860	2860
Effective bearing pressure (static) (kPa)	q'	40.1	29.0	29.2
Ratio of uplift to total weight during liquefaction	U/W	0.75	0.93	0.92
Symmetric superstructure		Y	Y	N
CoG height above top of basement (m)	y_{CoM}	− 0.044	0.526	1.37
CoG horizontal distance from centreline (m)	x_{CoM}	0	0	− 0.184
Fixed base natural frequency (Hz)	f_n	1	1	0.83

Figure 2.23: Model configuration and structural properties of the conducted centrifuge experiments (Hughes and Madabhushi 2019a).

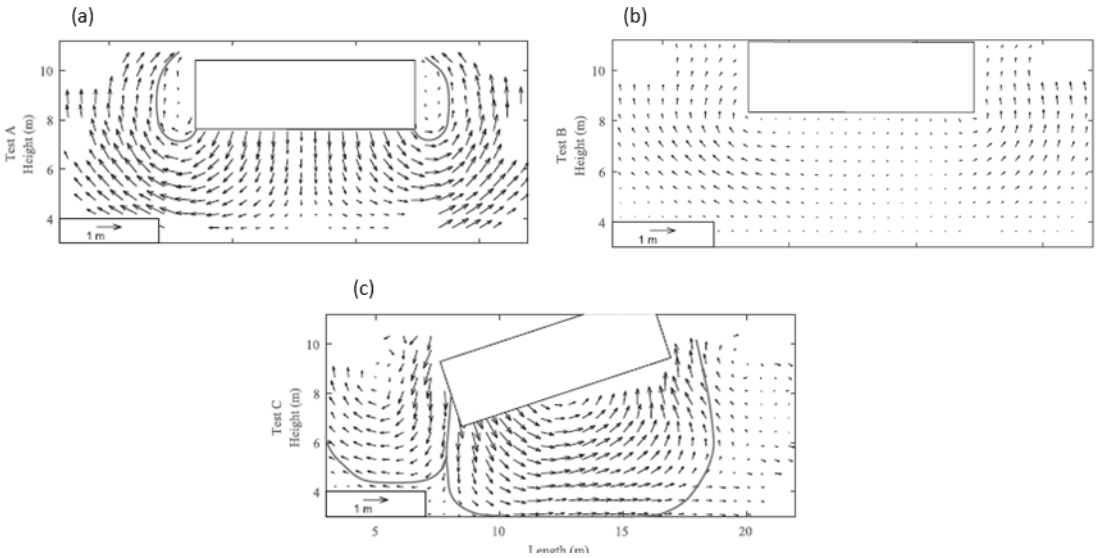

Figure 2.24: Displacement vectors for Test A, B and C at the end of shake (failure mechanism depicted with grey lines) (Hughes and Madabhushi 2019a).

2.4 Results from numerical analyses

In the last decades, a number of constitutive models have been developed that capture the cyclic behavior of sands using the effective stress and critical state concepts (Andrianopoulos et al. 2010; Boulanger and Ziotopoulou 2013; Byrne et al. 2004; Cheng and Detournay 2021; Tasiopoulou and Gerolymos 2016; Yang et al. 2020, 2003). Comparison of these models with experimental data and field observations has shown that shear- and volumetric-induced settlements of buildings due to liquefaction can be adequately predicted. As a result, the nonlinear dynamic response of structure-foundation-soil systems has been widely assessed in recent decades by means of numerical analyses.

Namely, Karamitros et al. (2013a) performed a number of nonlinear dynamic analyses of footings and rigid structures resting on a liquefiable Nevada sand deposit aiming, on one hand, to shed more light into the emerging mechanisms (e.g., excess pore-pressure buildup under the foundation, settlement accumulation, bearing capacity degradation, interaction of foundation-soil inertia) and, on the other hand, to investigate the role of a natural or artificial non-liquefiable soil crust as a method of reducing seismic settlements of the structure without additional measures (i.e. ground improvement or construction of piles). The authors observed the following:

- Excess pore pressure ratios under the footing remain lower than 1.0 due to the presence of substantial effective stresses. Additionally, after reaching their peak value – at the early

stages of shaking – they decrease due to the tendency of the soil to dilate (**Figure 2.25a**). This is manifested by the effective stress path in q-p' of the foundation soil during shaking (**Figure 2.25b).** Shaking causes compressive strains ε_v in the vertical direction and tensile strains ε_h in the horizontal direction equal to 1%, thus, the deviatoric strains are equal to $\varepsilon_q = \varepsilon_v - \varepsilon_h = 2\%$. This level of deviatoric strains is adequate to cause initial contraction (i.e., positive excess pore pressures) and subsequent dilation (i.e., negative excess pore pressures). This is evidence that the additional shear straining due to the seismic settlements of the footing causes excess pore pressures to decrease which serves as a counteracting mechanism to settlement accumulation.

- Richards et al. (1993) were among the first to recognize that seismic settlements of footings are primarily attributed to the formation of a Coulomb-type wedge mechanism, which is also responsible for the bearing capacity failure in static conditions, rather than to the soil densification. The bearing capacity exceedance and the subsequent sliding of the soil wedge are caused by both the degradation of soil's strength during shaking and the transmission of structural inertial forces to the foundation soil (**Figure 2.26a**). Especially in the case of liquefaction, the severe degradation of soil's strength due to the excess pore pressure buildup aggravates the formation and sliding of the soil wedge. Karamitros et. al observed that the formation and sliding of the soil wedge occurs twice per cycle of oscillation, i.e., the first time to the left and the second to the right (**Figure 2.26b**).
- Through parametric investigation it was shown that the presence of the non-liquefiable surface crust is beneficial for the performance of the foundation, as seismic settlements decreased for increasing thickness of the crust (**Figure 2.27**). On the other hand, the inclusion of a rigid structure has only a minimal effect on excess pore pressures and settlement accumulation (**Figure 2.28**).

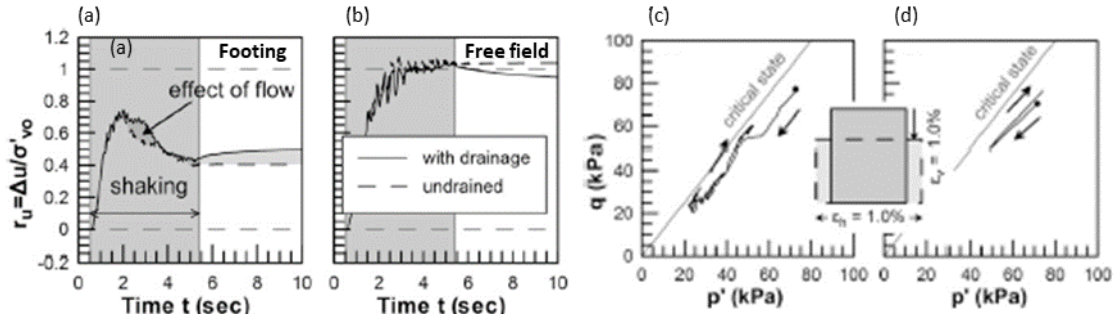

Figure 2.25: Time-histories of excess pore pressure ratios (a) under the footing and (b) at the free field, stress path of a soil element under the footing in the q-p' space (c) during shaking and (d) for monotonic loading.

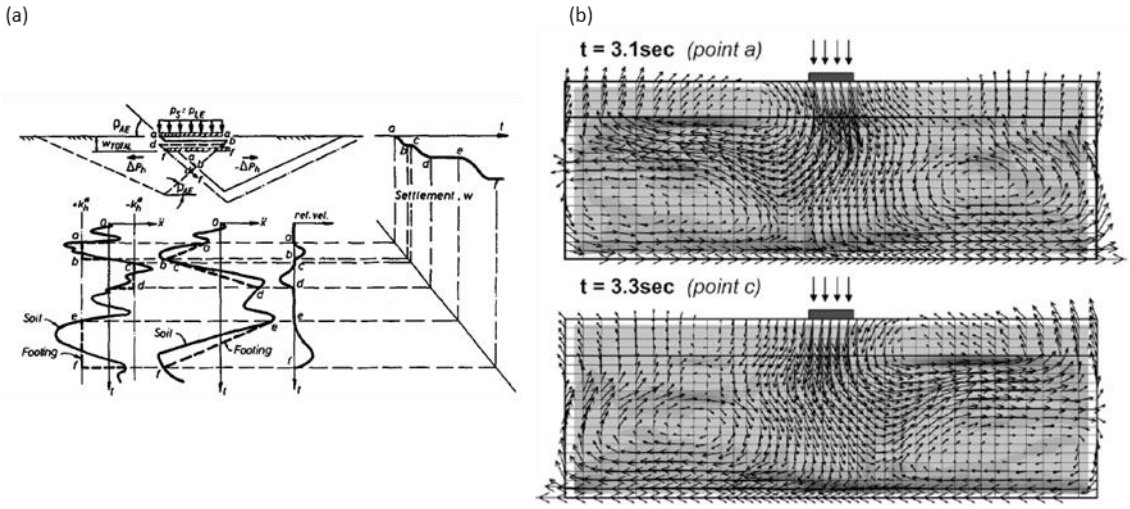

Figure 2.26: (a) Schematic representation of the Coulomb-type soil wedge mechanism and of the incremental footing settlement accumulation (Richards et al. 1993a) and (b) velocity vectors depicting the formation of the soil wedge in liquefied conditions (Karamitros et al. 2013e).

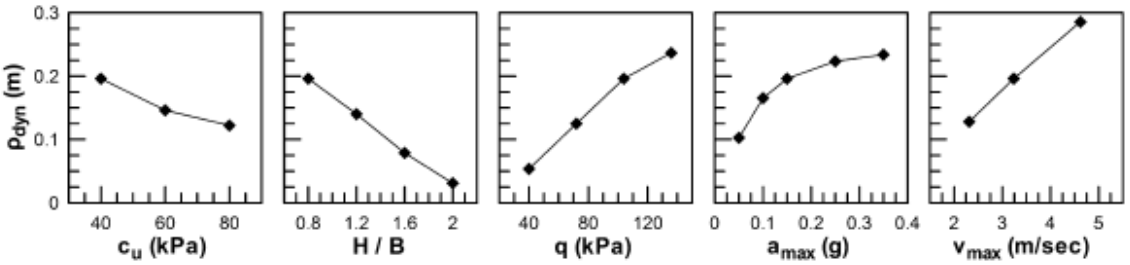

Figure 2.27: Variation of seismic settlements on soil crust characteristics c_u and *H/B*, foundation applied pressure *q* and seismic excitation parameters a_{max} and v_{max} (Karamitros et al. 2013c)**.**

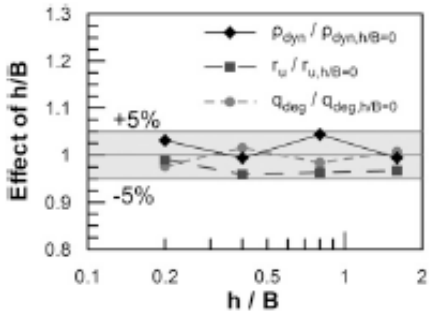

Figure 2.28: Effect of structural height h/b on settlements, excess pore pressure ratios and degraded bearing capacity of the foundation (Karamitros et al. 2013c).

The beneficial role of an improved soil crust in mitigating seismic settlements of footings is further investigated by Dimitriadi et al. (2017). The authors considered a shallow crust (natural or artificial) which is non-liquefiable. As a result, the soil layer under and around the footing does not develop substantial excess pore pressures and, therefore, a significant portion of the developing soil wedge under failure lies within the strengthened soil. The particular effect on the development of excess pore pressures is presented in **Figure 2.29**. It is observed that maximum excess pore pressure ratios during shaking are significantly reduced inside the non-liquefiable crust (with thickness designated in the Figure as H_{imp}), since the corresponding values are approximately equal to 0.4 and 0.2 at the free field and under the footing, respectively. The underlying sand layer experiences complete liquefaction with the exception of a narrow transition zone between the liquefied layer and the improved crust where excess pore pressure ratios have intermediate values around 0.5.

Based on the concept of bearing capacity failure due to the Coulomb-type wedge sliding, Richards et al. (1993) correlated the seismic settlements of footings with the ground motion characteristics (i.e., the peak velocity v_{max} and acceleration a_{max}), the critical acceleration a_{cr} required to trigger the wedge sliding and the static Factor of Safety *FS*. Following this rationale, Dimitriadi et al. developed the multi-variable relationship of Equation 2.1 for the assessment of the forgoing settlements. The accumulated seismic settlements of the footing ρ_{dyn} are correlated with the ground motion parameters (a_{max}, T_{exc}, N_o) and the degraded Factor of Safety FS_{deg}, as follows:

$$\rho_{dyn} = c_1 a_{max} (T_{exc} + aT_{soil})^2 (N_o + 2) \left(\frac{1}{FS_{deg}^{inf}}\right)^{c_2} \left[1 + c_3 \left(\frac{1}{FS_{deg}^{inf}}\right)^{c_4}\right] \quad 2.1$$

This approach assumes that all the remaining soil and foundation parameters are introduced through the degraded Factor of Safety FS_{deg}. **Figure 2.30** presents the inverse relation between seismic settlements of the footing ρ_{dyn} and FS_{deg}.

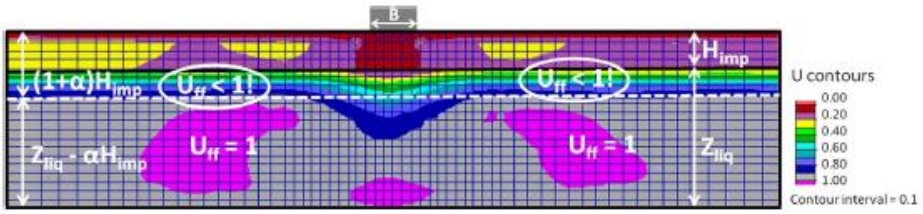

Figure 2.29: Contour of excess pore pressure ratios at the end of shake.

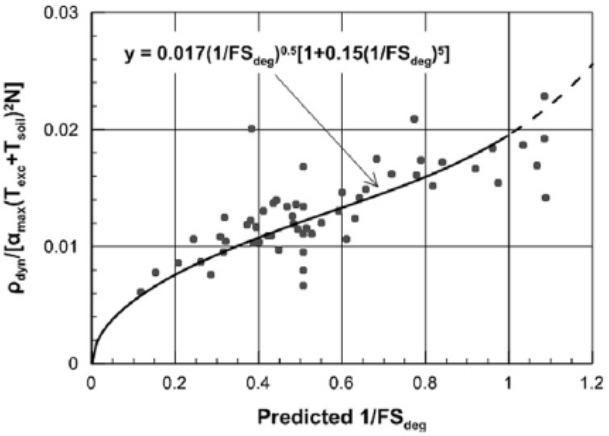

Figure 2.30: Variation of the seismic settlements ρ_{dyn} normalized by the excitation and soil period characteristics with the degraded Factor of Safety FS_{deg}.

As a continuation of the previous study, Dimitriadi et al. (2018) investigated the effect of the dimensions of ground improvement on the seismic settlements and the degraded bearing capacity of strip footings during shaking with a series of numerical analyses. The superficial sand layer is improved by means of vibrocompaction and installation of vertical drains, thus, both its strength and permeability are increased. Based on experimental data, it is observed that excess pore pressure ratios lower than 0.5 are adequate to ensure the integrity of the foundation soil. Numerical and experimental results show that a ground improvement with depth 1 to 1.5 times the footing width (z_c = 1-1.5B) is sufficient to reduce settlements up to 90% compared to an improvement of infinite depth, i.e., $\rho_{dyn}/\rho^{inf}_{dyn} \approx 0.90$. The beneficial role of ground improvement essentially vanishes for improvement depths greater than approximately z_c = 1.5B (**Figure 2.31**).

Additionally, seismic settlement ratios $\rho_{dyn}/\rho^{inf}_{dyn}$ are reduced for increasing values of the ground improvement width ratio B_{imp}/B (**Figure 2.32**). The remaining parameters examined in **Figure 2.32** seem to have only a minor effect on footing settlements.

Based on the results of the parametric investigation the authors related the seismic settlement ratio $\rho_{dyn}/\rho^{inf}_{dyn}$ with the key parameters, i.e., the width ratio B_{imp}/B and the depth ratio H_{imp}/B of the ground improvement, as follows:

$$\frac{\rho_{dyn}}{\rho^{inf}_{dyn}} = \frac{1}{1 - \exp\left[-\left(\frac{H_{imp}}{B}\right)^{-1}\left(\frac{B_{imp}}{B}\right)^{0.30}\right]} \qquad 2.2$$

In order to facilitate the cost-effective design of ground improvement, the authors constructed the design chart of **Figure 2.33**. Namely, seismic settlement ratios $\rho_{dyn}/\rho^{inf}_{dyn}$ are derived for the normalized volume of ground improvement V_{imp}/B^2, where $V_{imp} = B_{imp} \cdot H_{imp}$ per running unit length of the strip foundation, for different values of H_{imp}/B.

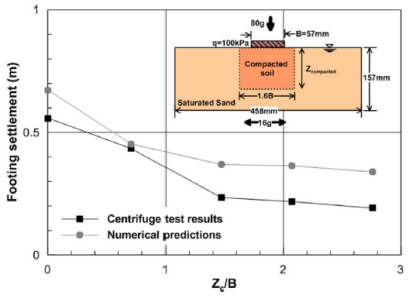

Figure 2.31: Variation of seismic settlements ρ_{dyn} with the densification depth ratio z_c/B for numerical and experimental results (Dimitriadi et al. 2018).

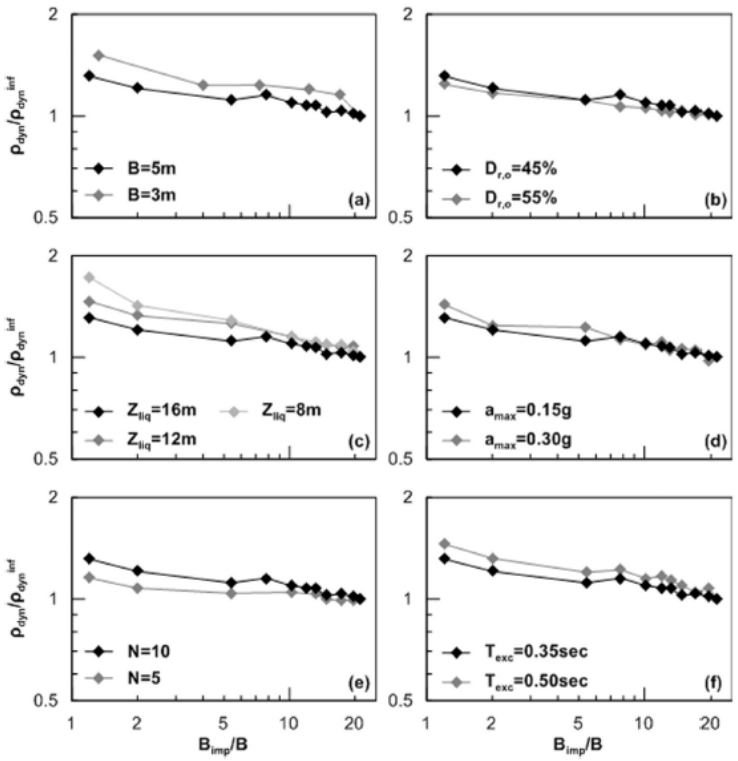

Figure 2.32: Variation of seismic settlement ratios $\rho_{dyn}/\rho^{inf}_{dyn}$ with the width ratio B_{imp}/B of the ground improvement. Effect of: (a) footing width B, (b) initial density $D_{r,o}$, (c) thickness of the underlying liquefiable layer z_{liq}, (d) peak outcropping bedrock acceleration a_{max}, (e) number of excitation cycles N and (f) excitation period T_{exc} (Dimitriadi et al. 2018).

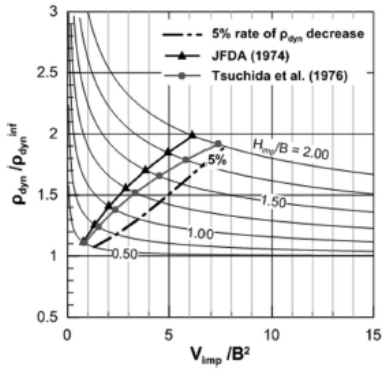

Figure 2.33: Design chart for the calculation of seismic settlement ratios $\rho_{dyn}/\rho^{inf}_{dyn}$ as a function of the volume of ground improvement ratio V_{imp}/B (Dimitriadi et al. 2018).

Bray and Macedo (2017) developed a simplified procedure for the estimation of seismic settlements of structures on liquefied conditions based on a regression analysis of the numerical results. The authors identified the principal earthquake, site, and building characteristics that govern the shear-induced settlements during shaking and, thus, developed the following relation:

$$ln(D_s) = a_1 + a_2 \ln(Q) + a_3 \ln(Q)^2 + a_4 D_r + a_5 \ln\left(tanh\left(\frac{HL}{a_6}\right)\right) + a_7 B + a_8 HC + a_9 \ln(IM1) + a_{10} \ln(IM2) \quad 2.3$$

where D_s designates the building settlements during shaking (in *mm*), *Q* is the applied pressure due to the building's weight, D_r is the relative density of the foundation soil, *B* is the foundation width, *HL* and *HC* are the respective depths of the liquefiable layer and the non-liquefied crust and the parameters $IM1$ and $IM2$ represent intensity ground motion measures. In order to obtain the intensity ground parameters that ensure the most accurate prediction of seismic settlements, the researchers compared results of the regression analysis for the parameters shown in **Figure 2.34**, using free-field (**Figure 2.34a**) and outcrop bedrock (**Figure 2.34b**) motions. The IM parameters with the greatest coefficient of determination R^2 were found to be the standardized cumulative absolute velocity (CAV), the Arias Intensity (I_a), and the spectral acceleration at a period equal to 1s (i.e., S_a[T = 1 s]).

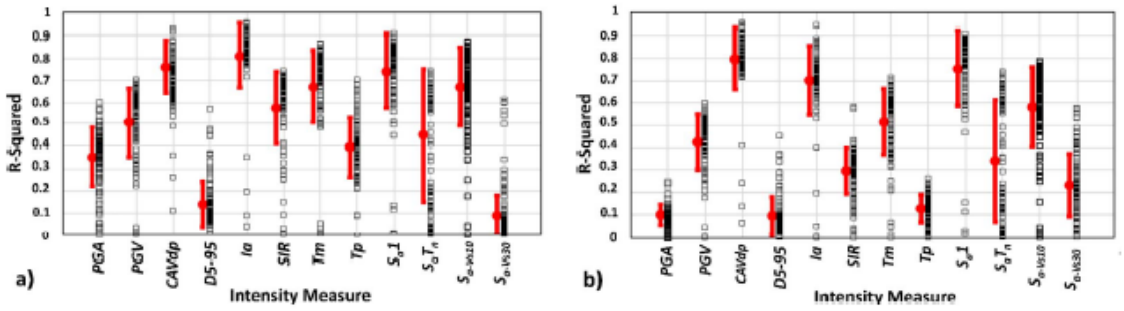

Figure 2.34: Values of R^2 for the examined intensity measures of the ground motion. Motion recorded (a) at the free field and (b) at the outcropping bedrock.

Bullock et al. (2019) conducted a series of numerical analyses of soil-structure systems with shallow foundations using a constitutive model that captures cyclic loading of sands in drained as well as undrained conditions, i.e., PDMY02 (Elgamal et al. 2002). Numerical results are validated with previously conducted centrifuge experiments (Karimi and Dashti 2015, 2016a; c). Based on a regression analysis of the numerical data, the researchers developed a predictive model for building settlements in liquefiable conditions during earthquakes. Namely, the structure's permanent settlements are expressed as:

$$ln(S) = f_{so} + f_{fnd} + f_{st} + s_0 ln(CAV) \quad 2.4$$

where f_{so}, f_{fnd} and f_{st} are functions that capture the effects of the soil profile, foundation and structural properties on seismic settlements. More specifically,

$$f_{so} = \left(\sum_i H\left(H_{s,i} - 1 + \varepsilon\right) f_{s,i} f_{H,i} + \left(c_0 + c_1 ln(CAV)\right) \right) F_{LPC} \quad 2.5$$

$$f_{s,i(SPT)} = \begin{cases} a_0, N_{1,60,i} < 12.6 \\ a_0 + a_{1,SPT}\left(N_{1,60,i} - 12.6\right), 12.6 \le N_{1,60,i} < 17.2 \\ a_0 + 4.6 a_{1,SPT}, 17.2 \le N_{1,60,i} \end{cases} \quad 2.6$$

$$f_{s,i(CPT)} = \begin{cases} a_0, q_{c1N,i} < 112.4 \\ a_0 + a_{1,CPT}\left(q_{c1N,i} - 112.4\right), 112.4 \le q_{c1N,i} < 140.2 \\ a_0 + 27.8 a_{1,CPT}, 140.2 \le q_{c1N,i} \end{cases} \quad 2.7$$

$$f_{H,i} = b_0 H_{S,i} exp\left[b_1 \left(max\left(D_{s,i}\right)^2 - 4 \right) \right] \quad 2.8$$

where H_{si} is the thickness of the layer i, $N_{1,60,i}$ is the corrected SPT blow count of the i-th layer, $q_{c1N,i}$ is the corrected normalized CPT resistance of the i-th layer and D_{si} is the depth from the foundation level to the i-th layer. H() is the Heaviside step function which takes the value of 1 for values of H_{si} greater or equal to 1 and the value of zero for any other value. F_{LPC} is a flag that is equal to 1 if a layer of low permeability is overlaid ontop of the uppermost layer susceptible to liquefaction. The function f_{si} is equal to the function f_{si}(SPT) or f_{si}(CPT) in the case of SPT or CPT results, respectively.

The function f_{fnd} representing the influence of the foundation is expressed as:

$$f_{fnd} = f_q + f_{B,L} \quad 2.9$$

with

$$f_q = \left[d_0 + d_1 ln\left(min(CAV, 1000)\right) \right] ln(q) exp\left[d_2 min\left(0, B - max\left(D_{S,1}, 2\right)\right) \right] \quad 2.10$$

$$f_{B,L} = \left[e_0 + e_1 ln\left(max(CAV, 1500)\right) \right] ln(B)^2 + e_2 (L/B) + e_3 D_f \quad 2.11$$

where q is the applied pressure due to the weight of the building, B and L are the dimensions of the foundation, CAV is the cumulative absolute velocity and D_f is the embedment depth of the foundation.

Lastly, the influence of the superstructure on seismic settlements is expressed with the function f_{st}, as:

$$f_{st} = [f_0 + f_1 ln(\min(CAV, 1000))]h_{eff}^2 + f_2 min[M_{st}/10^6, 1] \quad 2.12$$

where h_{eff} is the effective height of the structure and M_{st} is the inertial mass of the structure.

Figure 2.35 presents the seismic settlements obtained through the numerical analyses as well as the predictions of the foregoing equations. Overall, the following trends are observed:

- The presence of a superficial, non-liquefiable crust is crucial for the limitation of seismic settlements, since the top layer maintains its strength to a great extend during shaking. On the other hand, seismic settlements were found to increase for increasing thickness $H_{s,1}$ of the underlying liquefiable layer. Accumulated settlements reach a plateau for values of $H_{s,1}$ up to 8m. The researchers note that this plateau is attributed to numerical restrictions to accurately capture volumetric strains and, thus, its replicability in reality is questioned.
- Seismic settlements are reduced for increasing foundation width B, as it is already observed in past earthquakes. This is attributed to the increased strength of the foundation soil due to the greater stress bulb under the footing, which in turn results in greater confining pressures for a larger volume of soil. An exception to these findings constitutes the case of increased seismic intensity (i.e., CAV = 35m/s), where the increased shear stresses under a larger area result in greater deformations.
- The length-to-width L/B ratio of the footing's dimensions affects the performance of the foundation in a similar manner with the total area of the footing. Namely, greater L/B ratios result in greater volume of soil in the transversal direction with greater confining pressures and, as a result, seismic settlements are reduced.
- Structural height h_{eff} and structural mass M_{st} lead to increasing seismic settlements due to the increased values of the applied moments and shear forces to the foundation soil.

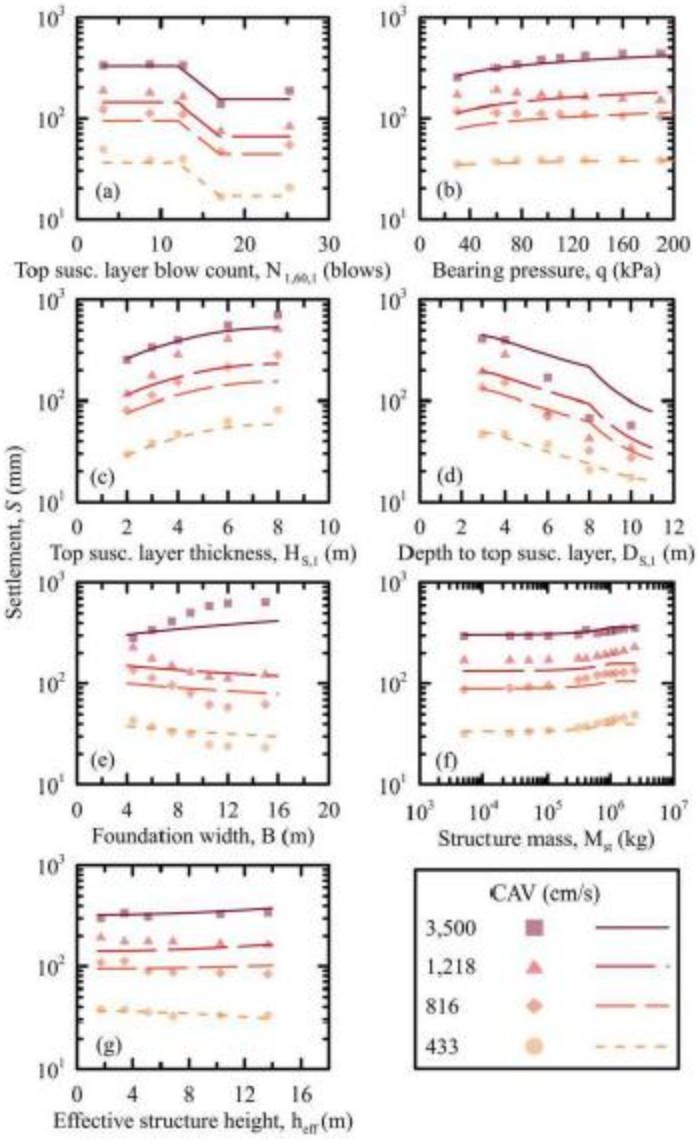

Figure 2.35: Seismic settlement predictions of the numerical analyses and the developed methodology of Bullock et al. (2019) for a different soil, foundation, structure and excitation parameters.

Chapter 3

Numerical Modeling of Soil-Foundation-Structure Interaction

3.1 General

The present chapter focuses on modeling characteristics of soil-foundation-structure interaction which is numerically simulated in this study with the Finite Difference Code *FLAC*^{3D}. Firstly, the numerical modeling of the dynamic free field response is examined with reference to its main aspects, such as: the required dimensions and discretization size of the mesh, the boundary conditions employed to represent half-space conditions, the appropriate modeling of soil hysteretic damping etc. Additionally, the numerical stability of the explicit calculation scheme used in *FLAC*^{3D} is discussed, as well as the effect of the element properties (soil zones and structural elements) on the minimum value of the critical dynamic timestep. The modeling of the foundation and the superstructure is described, next, with respect to the characteristics of the structural elements used and the behavior of the soil-foundation interface. Lastly, the numerical modeling of the improved ground is analyzed.

3.2 Numerical methodology

The seismic performance of SFS systems with shallow foundations is investigated with 3-dimensional numerical analyses performed with the Finite Difference Code *FLAC*^{3D}. The numerical model configuration of the reference system as well as the input parameters are illustrated in **Figure 3.1**. It consists of an idealized Single-Degree-of-Freedom (SDOF) superstructure and a square foundation, resting upon a uniform layer of liquefiable Nevada sand with relative density D_r = 45%. A thin crust of improved sand has been created at the top of the liquefied sand layer. Namely, vertical drains are installed for the dissipation of excess pore pressures towards the surface and the relative density is increased to D_r = 60%. A sinusoidal seismic excitation of N=14 cycles with amplitude a^b_{max} = 0.15g is applied at the base of the model.

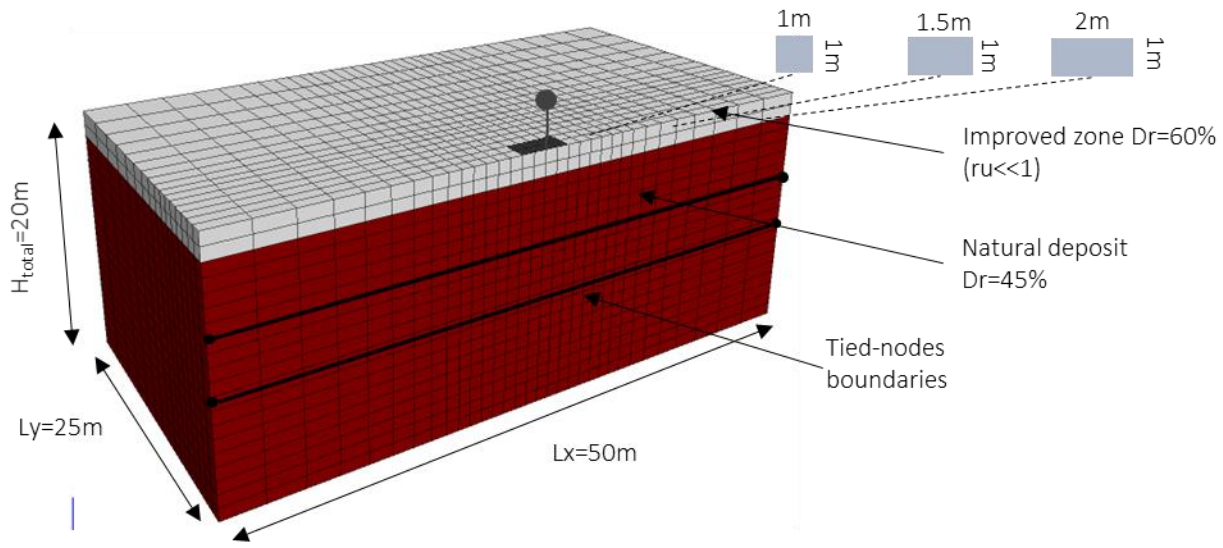

Figure 3.1: Numerical model and input parameters used for the parametric analyses performed with *FLAC*^{3D}.

Mesh. _ Mesh dimensions were selected sufficiently large in order to avoid any boundary effects during static and dynamic loading. More specifically, mesh width is equal to L_x = 50m, mesh depth is L_y = 25m and mesh height is H = 20m. The selection of width dimensions needs to ensure that the failure mechanism of the footing lies within the mesh lateral boundaries. Typical methodologies of bearing capacity estimation correlate the width of the failure soil wedge with the footing width and the soil angle of friction φ. For instance, according to DIN 4017 (**Figure 3.2**), in the most extreme scenario of friction angles (≈ 40°) the failure wedge extends laterally 8.5 times the footing width. In the problem considered here, soil strength and the corresponding friction angle is significantly degraded due to liquefaction and as a result the requirements for lateral mesh width are also reduced. For the selected dimensions of mesh and footing width, the ratio L_x/B is equal to 6.25, which corresponds to a friction angle ≈ 35° according to DIN 4017, hence, boundary effects are not expected.

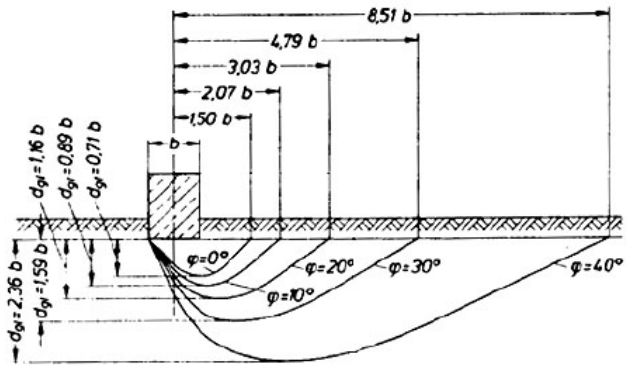

Figure 3.2: Failure wedge width of shallow footings on cohesionless soil as a function of friction angle, according to DIN 4017.

Mesh discretization involves a total of 32 x 32 x 20 = 20480 3-dimensional zone elements and 20472 gridpoints. A fine mesh, i.e. 1m x 1m x 1m, was used under the footing in order to capture more accurately stress and strain distribution in the area of interest. The zone size was gradually increased horizontally towards the mesh boundaries with a ratio of increase equal to 1.15 (i.e., horizontal length is increased 15% for each zone moving from center to the edge of the mesh). Mesh discretization in the vertical direction keeps a constant zone element size of 1m to ensure accurate modelling of vertically propagating waves. More specifically, accurate modeling of wave transmission through the discretized mesh requires element size Δl sufficiently smaller than the wave length λ. According to Itasca (2012) an adequately small element size would be:

$$\Delta l \leq \frac{\lambda}{8 \div 10} \qquad 3.1$$

A consequence of the above is that modeling of seismic waves with small wave length λ necessitates a proportional reduction in element size resulting in, often, prohibitively time-consuming numerical analyses. This limitation applies, thus, principally to high frequency waves in combination with a soil medium characterized by small shear wave velocity, since wave length is defined as $\lambda = V_s \cdot T_{exc}$, where T_{exc} is the excitation period of the propagating waves. In the examined problem, for the given element size of 1m and soil profile average shear wave velocity $V_{s.o}$ = 125 m/s, the cut off period excitation of the propagating waves would be approximately $T_{exc,o} = 8 \cdot \lambda / V_s = 0.06$ *sec.*

Boundary conditions. _ Different boundary conditions are applied for static and dynamic loading in order to adequately represent half-space conditions at the bottom of the mesh and free field conditions at the sides of the mesh. For static loading, horizontal displacements are restrained in all vertical boundaries (represented with horizontal rollers in **Figure 3.3a**) and vertical displacements are restrained in the bottom surface (represented with vertical rollers). For dynamic loading, tied-node conditions are used as boundaries for the mesh sides, which are commonly used in cases of dynamic problems associated with high levels of nonlinearity, such as liquefaction (Ghosh and Madabhushi 2003; Elgamal et al. 2005; Karamitros et al. 2013; Dimitriadi et al. 2017). This method imposes identical movement of nodes at the same elevation on both sides of the mesh in order to simulate the "free-field" movement at the boundaries. In more detail, horizontal (v_x) and vertical (v_z) velocities of gridpoints with equal elevation are

summed and the average velocity is commonly applied to the corresponding gridpoints. The applied velocity for x and z direction is calculated as follows:

$$v_x = \frac{\sum_{i=1}^{N}\left(v_{x,i}^{left} + v_{x,i}^{right}\right)}{N}$$
$$v_z = \frac{\sum_{i=1}^{N}\left(v_{z,i}^{left} + v_{z,i}^{right}\right)}{N} \quad 3.2$$

The response of the examined mesh is shown in **Figure 3.3b.** Namely, horizontal accelerations are applied at the soil base whereas the boundaries at the left and right side are subjected to tied-node conditions. The presented contour shows the horizontal displacements obtained from the numerical analysis of the soil profile in the absence of structural elements. It is seen that horizontal displacements u_x are evenly distributed at gridpoints of equal elevation representing, thus, free-field conditions.

Other methods to simulate free-field boundary conditions include the use of *absorbing boundaries*, such as dashpots, or *free-field boundaries.* Concerning the former, the particular method involves the attachment of normal and shear viscous dashpots to the gridpoints of the mesh sides. The application of absorbing boundaries is more appropriate when the dynamic source lies within the bounding surfaces of the mesh, since the application of the dynamic loading at a boundary surface would result in energy seepage at the absorbing boundary (Itasca 2012). Free-field boundaries, on the other hand, consist of 1-dimensional soil columns which are numerically solved in parallel with the numerical analysis of the mesh. They are connected to the lateral boundaries with dashpots and they exert their inertial forces as reaction forces to the connected gridpoints. The 1D column adopts the soil properties of the mesh enabling, thus, a nonlinear numerical analysis. In the case, though, of user defined constitutive models, such as NTUA-Sand, *FLAC 3D* reads an estimation of the actual tangential shear modulus of the UDM, the latter being always lower due to the elasto-plastic model behavior. As a result, the free-field boundaries become stiffer resulting in reflection of the incoming waves. Additionally, free-field boundaries cannot provide the lateral support required in cases of lateral spreading due to liquefaction (Karamitros 2010).

Based on the above, the application of tied-nodes at lateral boundaries is deemed preferable in this study. It should be noted that tied-nodes are mostly suitable for problems with significant material damping and an adequately large mesh, as the one examined herein, in order to ensure negligible wave reflections.

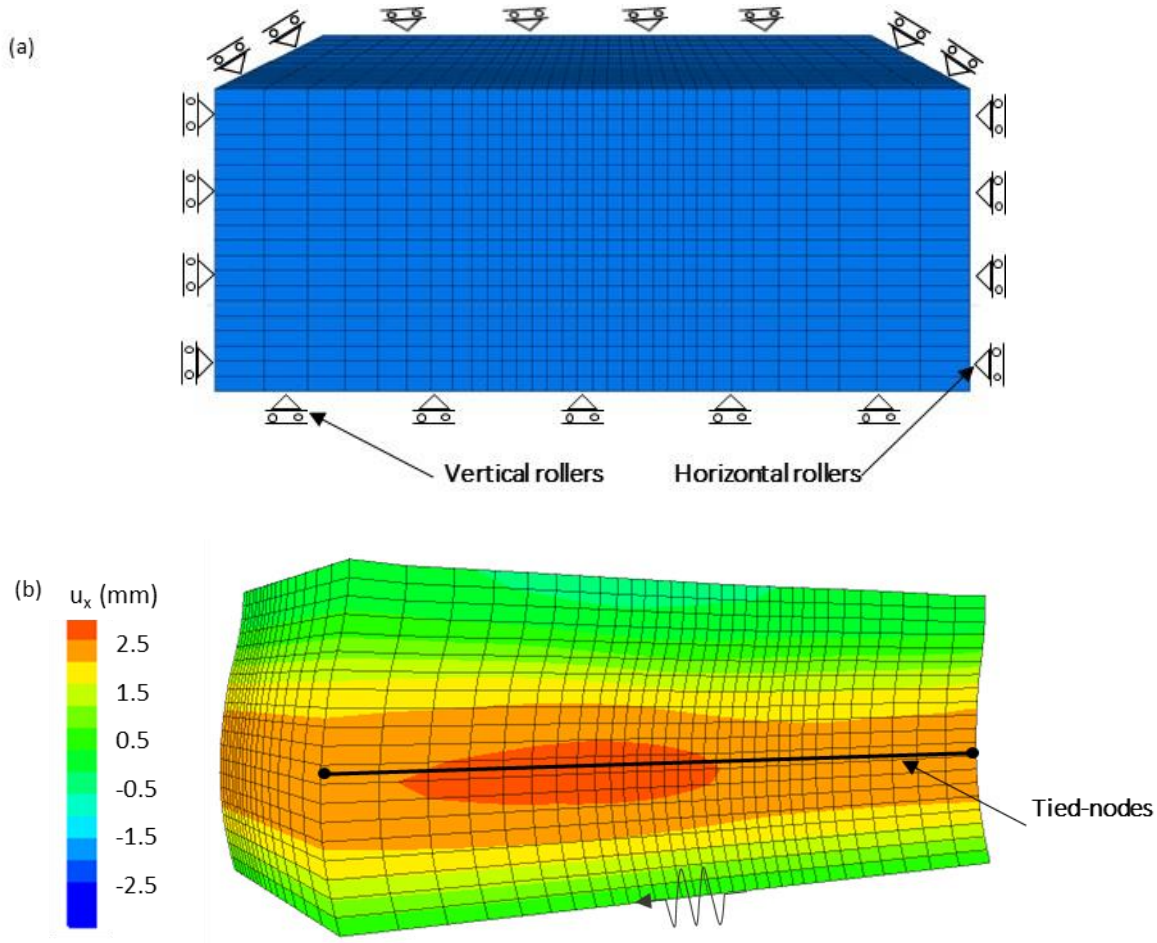

Figure 3.3: Boundary conditions: (a) rollers during *static loading* and (b) tied-node boundaries during *dynamic loading* at the sides and applied acceleration at the bottom (contour of horizontal displacements).

The NTUA-Sand constitutive model. _ The monotonic and cyclic response of non-cohesive soils is captured in the presented numerical methodology with the constitutive model NTUA-Sand, which is introduced as a User-Defined model in the Finite Difference Code FLAC3D (Itasca 2012). This model is principally developed to simulate the cyclic response of sands and the associated pore water pressure build-up under seismic excitation. The formulation of the model incorporates the critical state theory of soil mechanics and it relies on the bounding surface plasticity. The current version of the model is based on the formulation of Andrianopoulos et al. (2010) and is constituted by a three-surface model platform (i.e., dilatancy, critical and bounding surface). The initial version of the model was developed by Papadimitriou et al. (2001), which in turn employed the state parameter ψ concept introduced by Manzari and Dafalias (1997). The initial model by Papadimitriou et al. included an additional yield surface in *p-q* space, which is removed in the current version, thus, a zero elastic range is adopted. This modification was performed in order to reduce numerical computation time rather than to increase the accuracy of

the model. The hysteretic response of non-cohesive soils is simulated for all levels of cyclic strains with the same set of values of the model constants. In particular, shear modulus degradation and hysteretic damping increase for small-to-medium level of shear strains is governed by a Ramberg-Osgood type of non-linear hysteretic formulation, whereas medium-to-great level of shear strains are captured with a scalar multiplier K_p of the plastic modulus. The calibration of the model is based on the properties of Nevada sand, which is a uniformly graded, fine sand. The particular soil material is selected since it is widely used in many testing programs (Arulmoli et al. 1992; Kammerer et al. 2001; Kutter et al. 1994; Trombetta et al. 2013; Yamamuro and Lade 1998). The accuracy of the model is evaluated by comparing results of the numerical analyses with the ones from the laboratory testing program of VELACS (Arulmoli et al. 1992). Initially, comparisons of simulations to data were performed for a large number of element tests on Nevada sand by Papadimitriou et al. (2001) and Papadimitriou and Bouckovalas (2002), including resonant column tests, cyclic triaxial and cyclic direct simple shear tests. In extension to the these model comparisons, Andrianopoulos et al. (2010) investigated the accuracy of the model by additionally conducting two boundary value problem comparisons between the simulations and the results from the VELACS tests of Models 1 and 12 (Arulmoli et al. 1992). These problems include the earthquake-induced liquefaction of a free-field model consisting of liquefiable Nevada sand as well as the seismic response of a rigid foundation on the same sand profile.

In more detail, the particular model has three open conical surfaces that intersect at the origin of the stress space, as depicted in **Figure 3.4**:

i) The **Dilatancy Surface** which designates the transition from contractive to dilative behavior.
ii) The **Critical State Surface** at which the void ratio corresponds to the constant density at large strains, (i.e., the critical void ratio) and deviatoric deformations are accumulated for constant stresses.
iii) The **Bounding Surface** which is the locus of points with the peak deviatoric stress ratios.

The shape of these model surfaces is determined by the deviatoric stress ratios for triaxial compression (i.e., M_c^c, M_c^b, M_c^d) and triaxial extension (i.e., M_e^c, M_e^b, M_e^d), which are interrelated via the state parameter ψ, as defined in Equations 3.7-3.9 of **Table 3.1**. The critical state surface slopes $M_{c,e}^c$ are constant model parameters. On the contrary, $M_{c,e}^{b,d}$ are functions of the varying value of the state parameter ψ, thus, they do not remain constant during loading. Following the dependency of the surfaces slope on ψ, they can be outside or inside the Critical State Surface for contractive or dilative soil response, respectively. The multiaxial generalization of these surfaces is presented in the π-plane (i.e., perpendicular

to the hydrostatic p axis) in **Figure 3.4**. The model surfaces $M_{c,e}^{b,c,d}$ are a function of the Lode angle θ, which is defined in the p-plane as the angle between the deviatoric stress-ratio space **r=s**/p (where s is the deviatoric stress tensor) and the principal axis r_1, according to the relevant equations in **Table 3.1**.

The "elastic" strain rate $\dot{\boldsymbol{\varepsilon}}^e$ of the model is governed by the nonlinear hysteretic "elastic" response defined in Equation 3.12 which constitutes a modification of the nonlinear hysteretic model of Ramberg and Osgood (1943). Thus, in the absence of a yield surface, the term "elastic" refers to the part of stress and strain accumulation that are governed by the modified Ramberg-Osgood formulation. The tangential "elastic" shear modulus G_t is given based on the generalized Ramberg-Osgood formula of **Table 3.1**, where the degradation of G_t is described by the scalar variable T. The load increment contributes to the tangential shear modulus degradation by the difference of the deviatoric stress-ratios **r** - $\mathbf{r_{ref}}$, where $\mathbf{r_{ref}}$ refers to the last load reversal stress state. This formulation entails that radial loading in the π-space (i.e., r is constant) results in zero reduction of G_t.

The calculation of the plastic component of stresses and strains is based on the correlation of the current state with the distance from the model surfaces. As observed in **Figure 3.4**, the distance from the corresponding surface is defined as:

$$d^{c,b,d} = \left(\boldsymbol{r}_i^{c,b,d} - \boldsymbol{r}\right) : \boldsymbol{n} \tag{3.3}$$

Where r is the current stress state and $\boldsymbol{r}_i^{c,b,d}$ are the conjugate (image) points on the critical state, bounding and dilatancy surface, respectively, which are determined by the projection of the **n** vector on the corresponding surface:

$$\boldsymbol{r}_i^{c,b,d} = \sqrt{\frac{3}{2}} M_\theta^{c,b,d} \boldsymbol{n} \tag{3.4}$$

The vector $\boldsymbol{n}$ in this version of the model is calculated with a radial mapping rule and the surface inclination $M_\vartheta^{c,b,d}$ for the particular Lode ϑ according to Equation 3.11.

The calculation of the plastic strain and stress increments follows Equations 3.15-3.16. The model employs the non-associated flow rule of Equation 3.18. The plastic modulus K_p, as defined in Equation 3.21, is a function of the dimensionless positive function h_b and h_f, while the previously defined distance d^b from the bounding surface controls the sign of K_p. The parameter h_b is defined by the interpolation rule:

$$h_b = h_0 \frac{\left|d^b\right|^3}{< d^b_{max} - |d^b| >} \quad 3.5$$

The parameter h_f is a scalar function that macroscopically expresses the effect of fabric evolution during shearing on the plastic modulus K_p. It takes into account experimental data suggesting that loading reversals for contractive soil response (i.e., within the dilatancy surface) result in a stiffer response due to the rearrangement of the sand particles, while they result in softer response for dilative soil response (i.e., outside the dilatancy surface). It is expressed with the following formula:

$$h_f = \frac{1 + < \boldsymbol{F}: \boldsymbol{I} >^2}{1 + < \boldsymbol{F}: \boldsymbol{I} >} = \frac{1 + < f_p >^2}{1 + < \boldsymbol{f}: \boldsymbol{n} >} \quad 3.6$$

where the numerator represents the summation of the plastic volumetric strain rate (i.e., the stiffening response) and the denominator the history of loading reversals in dilation (i.e., the softening response). The particular formulation entails that h_f increase results in greater values of the plastic modulus K_p and, thus, the contribution of plastic strains is reduced.

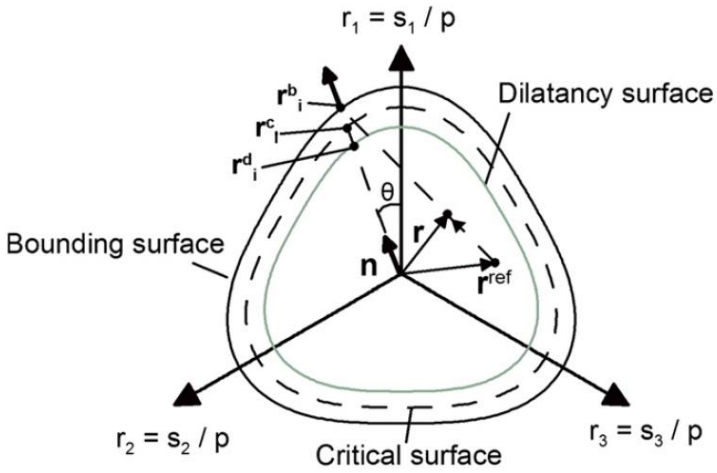

Figure 3.4: Model surfaces (Dilatancy, Critical State, Bounding) and adopted mapping rule for the determination of the vector **n** in the π-plane of the deviatoric stress ratios space.

Table 3.1: Summary of the adopted equations of the constitutive model NTUA-Sand.

Description	Equation	Constant
Deviatoric stress ratio on bounding surface in triaxial compression	$M_c^b = M_c^c + k_c^b < \psi >$ (3.7)	M_c^b, k_c^b
Deviatoric stress ratio on	$M_c^d = M_c^c + k_c^d \psi$ (3.8)	k_c^d

dilatancy surface in triaxial compression			
Critical State Line in [*e*,*p*]	$\psi = e - e_{cs} = e - \Gamma_{cs} + \lambda \cdot \ln(p)$	(3.9)	Γ_{cs}, λ
Multiaxial generalization of model surfaces on the basis of the Lode angle ϑ and *c*	$M_\theta^{c,b,d} = g(\theta, c) M_\theta^{c,b,d}$	(3.10)	$c = M_e^c / M_c^c$
Shape of model surfaces on the π- plane of the deviatoric stress ratio space	$g(\theta, c) = \frac{4c}{(1+c) - (1-c)\cos(3\theta)} - \left[\frac{(1+c) + (1-c)\cos(3\theta)}{2}\right]$		
Lode angle ϑ on the basis of the deviatoric stress ratio tensor r_i^b on the bounding surface	$\cos(3\theta) = \frac{\sqrt{3}}{2} \frac{(r_i^b : r_i^b : r_i^b)}{(0.5(r_i^b : r_i^b))^{3/2}}$	(3.11)	
"Elastic" strain rate estimation, on the basis of the effective stress increment $\dot{\boldsymbol{\sigma}} = \dot{\boldsymbol{s}} + \dot{p}\boldsymbol{I}$	$\dot{\boldsymbol{\varepsilon}}^e = \dot{\boldsymbol{e}}^e + \left(\dot{\boldsymbol{e}}_p^e / 3\right)\boldsymbol{I} = \frac{\dot{\boldsymbol{s}}}{2G_t} + \left(\dot{\boldsymbol{p}} / K_t\right)\boldsymbol{I}$	(3.12)	
Tangential "elastic" shear modulus	$G_t = \frac{G_{max}}{T} = \left(\frac{Bp_a}{0.3+0.7e^2}\sqrt{p / p_a}\right)\frac{1}{T}$	(3.13)	
Scalar variable introducing tangential shear modulus degradation	$T = 1 + \left(\frac{1}{a_1} - 1\right)\left(\frac{\sqrt{1/2(\boldsymbol{r}-\boldsymbol{r}^{ref}):(\boldsymbol{r}-\boldsymbol{r}^{ref})}}{a_1\left(\frac{G_{max}^{ref}}{p^{ref}}\right)\gamma_1}\right)$	(3.14)	
Plastic strain increment	$\dot{\boldsymbol{\varepsilon}}^p = \dot{\boldsymbol{e}}^p + \left(\dot{\boldsymbol{e}}_p^p / 3\right)\boldsymbol{I} = < \Lambda > \boldsymbol{R}$	(3.15)	
Loading index	$\Lambda = \frac{\boldsymbol{L}:\dot{\boldsymbol{\sigma}}}{K_p}$	(3.16)	
Loading direction	$\mathbf{L} = \mathbf{n} - \frac{\boldsymbol{n}:\boldsymbol{r}}{3}\boldsymbol{I}$	(3.17)	
Plastic strain rate direction (non-associated flow rule)	$\boldsymbol{R} = \boldsymbol{n} + (D/3)\,\boldsymbol{I}$	(3.18)	
Effective stress $\dot{\boldsymbol{\sigma}}$ increment	$\dot{\boldsymbol{\sigma}} = 2G_t\dot{\boldsymbol{e}} + K_t\dot{\varepsilon}_p\boldsymbol{I} - < \Lambda > (2G_t\boldsymbol{n} + K_t D\boldsymbol{I})$	(3.19)	
Loading index, in terms of the applied strain increment	$\Lambda = \frac{2G_t\boldsymbol{n}:\dot{\boldsymbol{e}} - (\boldsymbol{n}:\boldsymbol{r})K_t\dot{\varepsilon}_p}{K_p + 2G_t - (\boldsymbol{n}:\boldsymbol{r})K_t D}$	(3.20)	
Plastic modulus	$K_p = p h_b h_f d^b$	(3.21)	

The model requires the calibration of 11 dimensionless parameters for monotonic loading and 13 parameters for cyclic loading. **Table 3.2** summarizes the values of the model parameters used as well as the typical range of these parameters for Nevada sand. The particular set of values is used for the evaluation of the model performance according to Andrianopoulos et al. (2010), who conducted

comparisons of the model simulations against the laboratory testing program of VELACS (Arulmoli et al. 1992). **Figure 3.5 - Figure 3.8** present results of these comparisons for a number of element response tests. Namely, results from monotonic drained (**Figure 3.5a**) and undrained (**Figure 3.5b**) triaxial tests on Nevada sand are presented for density values of 40% and 60%, in the case of the drained test, and for initial effective stress p_o = 80 and 160 kPa, in the case of the undrained test. The model's predictions of the cyclic response at the element level are evaluated with a series of resonant column tests, presented in **Figure 3.6**. The pertinent comparisons examine the maximum shear modulus G_{max} (**Figure 3.6a**), the degradation of the secant shear modulus G/G_{max} (**Figure 3.6b**) and the hysteretic damping increase ξ (**Figure 3.6c**) with the amplitude of the cyclic shear strain. The response of a soil element subjected to large cyclic shear strains is examined in **Figure 3.7** with a cyclic undrained simple shear test on Nevada sand with relative density D_r = 40%. Finally, **Figure 3.8** compares the resistance to liquefaction from cyclic simple shear tests for D_r = 40 and 60%.

Table 3.2: *NTUA-SAND* model constants: physical meaning and values for Nevada sand.

#	Physical meaning	Typical Range	Value
M_c^c	Deviatoric stress ratio at critical state in triaxial compression (TC)	1.20-1.37	1.25
c	Ratio of deviatoric stress ratios at critical state in triaxial extension over triaxial compression	0.68-0.80	0.72
Γ_{cs}	Void ratio at critical state for p=1kPa	0.77-1.03	0.910
λ	Slope of critical state line in the [e-lnp] space	0.01-0.03	0.022
B	Elastic shear modulus constant	550-950	600*
ν	Elastic Poisson's ratio	0.10-0.40	0.33
k_c^b	Effect of ψ on peak deviatoric stress ratio in TC	0.5-4.0	1.45
k_c^d	Effect of ψ on dilatancy deviatoric stress ratio in TC	0.1-3.0	0.30
γ_1	Reference cyclic shear strain for nonlinearity of "elastic" shear modulus	0.0065%-0.025%	0.025%
α_1	Nonlinearity of "elastic" shear modulus	0.45-0.85	0.6*
A_o	Dilatancy constant	0.5-1.5	0.8
h_o	Plastic modulus constant	3.000-100.000	15,000
N_o	Fabric evolution constant	30.000-80.000	40,000

* for monotonic loading of Nevada sand: B = 180, a_1 = 1.0.

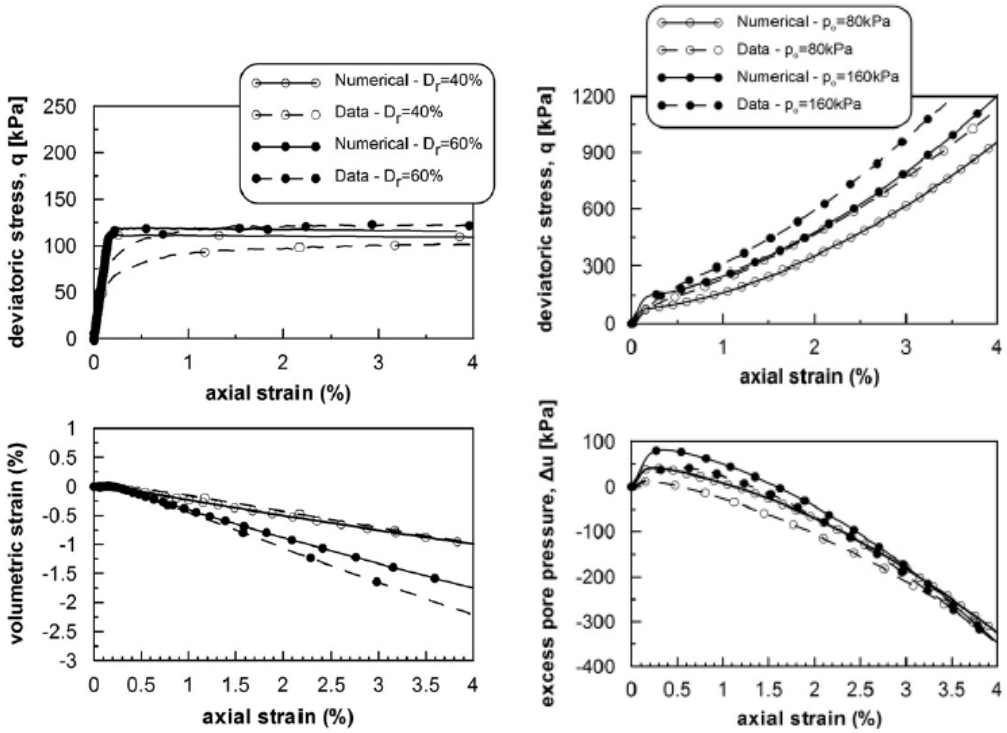

Figure 3.5: Comparison of the model predictions with data from the testing program VELACS (Arulmoli et al. 1992) for: (a) drained and (b) undrained triaxial tests on Nevada sand.

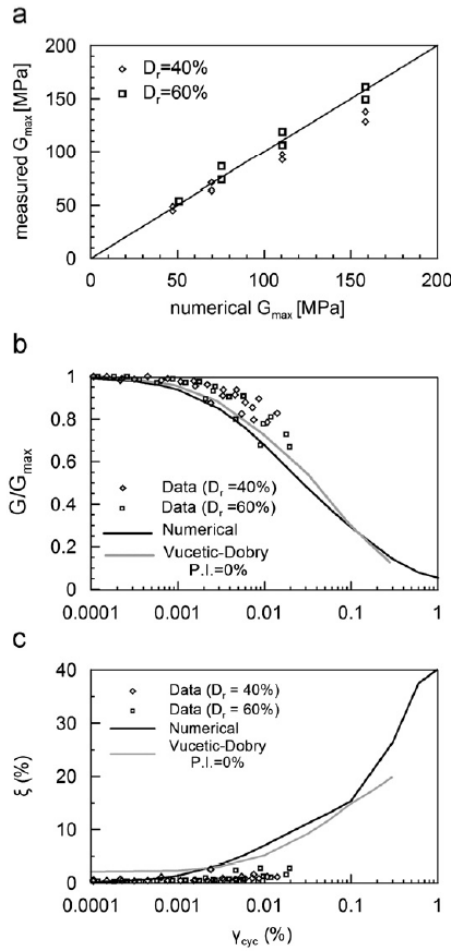

Figure 3.6: Comparison of the model predictions with data from the testing program VELACS in terms of (a) the maximum shear modulus G_{max}, the degradation of the secant shear modulus G/G_{max}, and the hysteretic damping increase ξ with the amplitude of the cyclic shear strain.

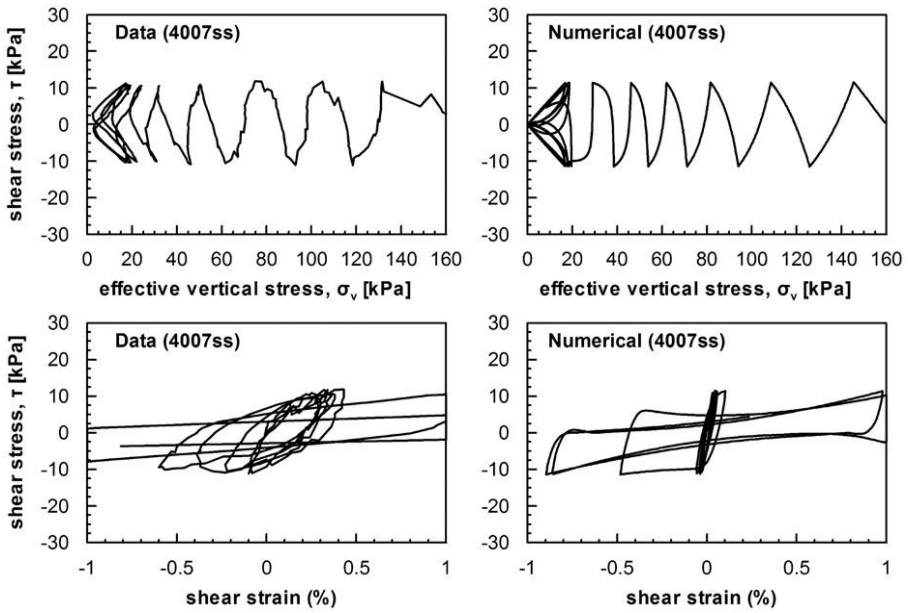

Figure 3.7: Comparison of the model predictions with data from the testing program VELACS for a cyclic undrained simple shear test on Nevada sand with D_r = 40%.

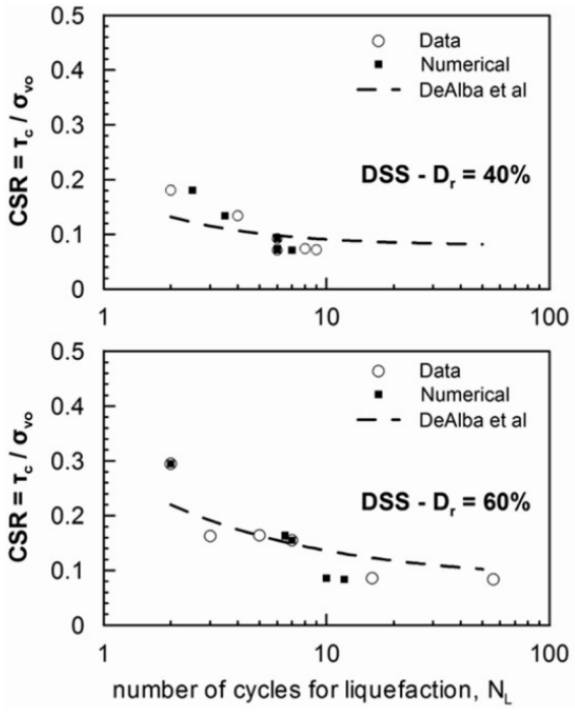

Figure 3.8: Summary of comparisons of the model predictions with data from the testing program VELACS for the cyclic undrained simple shear tests on Nevada sand.

Damping. _ Soil damping during dynamic loading originates from the hysteretic response of the constitutive formulation of the User-Defined-Model NTUA-Sand. The principal source of hysteretic damping is the nonlinear soil response of sand during cyclic loading. The constitutive model incorporates, also, the Ramberg-Osgood formulation which captures the non-linear hysteretic response of sands for low-to-medium levels of shear strains. In general, the level of damping invoked by the model is proportional to the shear strain amplitude γ_{cyc}, following the experimental data from the VELACS research program (Arulmoli et al. 1992). In addition to the inherent damping of the constitutive model, local damping of 2% is employed in dynamic analyses. The formulation of local damping in *FLAC*^{3D} is similar to that for hysteretic damping. Namely the damping force that opposes motion at each gridpoint is related to the inertial force of the gridpoint lumped mass, in the form:

$$F_{d.i} = -a \cdot F_{inertial.i} \cdot sign(v_i) \qquad 3.22$$

where:

$F_{d.i}$, $F_{inertial.i}$ are the damping and inertial forces, respectively, at the gridpoint *i*

v_i is the velovity of the gridpoint *i*

α is the local damping coefficient

and the function *sign(x)* provides the sign (positive, negative or zero) of the variable x.

In essence, the function of local damping is to subtract kinetic energy ΔW from the gridpoint during every cycle of oscillation following the sign of velocity. The amount of the subtracted energy is $\Delta W = 1/2\,\Delta M_i v_i^2$, where ΔM_i is the equivalent mass that corresponds to the inertial force $F_{inertial.i}$. Consequently, the normalized subtracted energy ΔW/W is independent of the rate and frequency of loading, a fact that makes the selection of local damping advantageous compared to Rayleigh damping. The particular method exhibits limitations in modelling waveforms with a wide frequency content as well as motions where the velocity sign remains constant, such as the steady-state phase of pulse excitations.

Based on the above, the modelled sand response during cyclic loading and the associated damping can be summarized as follows, with respect to the cyclic shear strain γ_{cyc} level:

- For **small strains** ($\boldsymbol{\gamma_{cyc} \leq \gamma_{tl}}$, with γ_{tl} being the linear cyclic threshold shear strain ≈ $5 \cdot 10^{-5}$ for sands) soil response is practically *linear visco-elastic* since i) the secant shear modulus *G* is virtually equal to the initial value G_{max} and ii) experimental data indicate the presence of a minimum value of damping ξ_{min} =0.5-5% (Vucetic and Dobry 1991), related to viscous damping. Due to the fact that

the constitutive model predicts values of hysteretic damping that tend to zero for decreasing values of γ_{cyc}, local damping serves as the primary source of damping at this γ_{cyc} range.

- For **medium strains** ($\gamma_{tl} \leq \gamma_{cyc} \leq \gamma_{tv}$, with γ_{tv} being the volumetric cyclic threshold shear strain ≈ 10^{-4}-10^{-3} for sands) soil response is *non-linear purely-hysteretic,* since shear modulus degradation and damping are increased, yet strain accumulation is not significant especially for a small number of loading cycles *N*. At this range of γ_{cyc} the hysteretic damping of the Ramberg-Osgood formulation has the most significant contribution.
- For **large strains** ($\gamma_{cyc} \geq \gamma_{tv}$) soil response is principally elasto-plastic, since strain accumulation becomes significant, while shear modulus *G* and damping deviate considerably from their initial values. Thus, at this stage, damping is principally associated with energy dissipation in the larger stress-strain loops predicted by the soil plasticity formulation.

Critical timestep. _ As previously mentioned, the explicit calculation scheme used in *FLAC 3D* for solving the finite difference equations is conditionally stable as it requires "the speed of the calculation front (to) be greater than the maximum speed at which information propagates" (Itasca 2012). Thus, in order to ensure numerical stability, the timestep must be smaller than the time needed for the propagating wavefront (with maximum speed *C*) to travel through the solid medium that is discretized in elements of size Δx. The critical timestep Δt_{crit} for stability is given by the Courant-Friedrichs-Lewy condition:

$$\Delta t_{crit} < \frac{\Delta x}{C} \tag{3.23}$$

For discretization of the soil continuum in zones of volume *V* and with maximum face area A^f_{max}, the calculation of the critical timestep results in the following equation:

$$\Delta t_{crit} = min\left\{\frac{V}{C_p \cdot A^f_{max}}\right\} \tag{3.24}$$

where C_p is the speed of the p-wave which is the maximum speed that information can propagate and it is given as a function of the bulk modulus *K,* the shear modulus *G* and the soil density ρ:

$$C_p = \sqrt{\frac{K+4G/3}{\rho}} \tag{3.25}$$

where K and G are the soil bulk and shear moduli, respectively, whereas ρ represents the soil density.

By transformation of equation 3.24), the system of interconnected masses and springs can be associated with the smallest natural period of the system T_{min} in the following manner (Bathe and Wilson 1976):

$$\Delta t_{crit} < \frac{T_{min}}{\pi} \tag{3.26}$$

In the case of *static analyses*, a pseudo-timestep Δt = 1 is selected by default in the program. Given this selection and in order to provide a numerically stable scheme, the lumped mass of each gridpoint is adjusted to be greater or equal to the spring stiffness. In more detail, the local stiffness matrix $\boldsymbol{k}$ of gridpoint *n* includes the stiffness contribution $k_{i,j}$ in the degree-of-freedom *i* due to unit force in the direction *j,* where the directions *i* refer to the 3 translational degrees-of-freedom in space. The diagonal term (*i,i*) of the stiffness matrix is expressed in *FLAC*^{3D} as:

$$k_{ii} = \frac{K + 4G/3}{9V} [n_i S]^2 \tag{3.27}$$

where n_i is the unit normal to the surface of the zone and *S* is the area of the surface. The upper-bound value of the nodal stiffness is, thus:

$$k_n = \max (k_{11}, k_{22}, k_{33}) \tag{3.28}$$

The adjusted lumped mass at gridpoint *n* is, thus, for Δt = 1 according to equation 3.28):

$$m_n = \frac{K + 4G/3}{9V} \max ([n_i S]^2, i = 1,3) \tag{3.29}$$

In the case of *dynamic analyses*, the critical timestep is a modification of equation 3.26) based on Belytschko (1983):

$$\Delta t_{stab} = \frac{T_{min}}{\pi} (\sqrt{1 + \lambda^2} - \lambda) \tag{3.30}$$

where the value of λ depends on the damping scheme; in the examined case λ is the local damping coefficient.

It is evident that, in essence, it is the minimum eigenperiod of the system that determines the dynamic timestep of the analysis. Since, the explicit finite difference method used in *FLAC*^{3D} solves the equations

of motion without the formation of the mass and stiffness matrices, the eigenvalue solution is also not performed. As a result, the minimum eigenperiod of the system is estimated using equation 3.26) as T_{min} =0.5$\pi \cdot \Delta t_{cr}$, where 0.5 serves as a safety factor. Additionally, when structural elements are used, the maximum eigenfrequency is estimated by applying the Gerschgorin Theorem (Isaacson and Keller 1963), which is formulated as:

$$\omega_{max}^2 \leq \max\left(G_i/M_i\right) \tag{3.31}$$

where G_i is the stiffness sum for ith row of the stiffness matrix and M_i is the lumped node mass.

Thus, in a numerical model containing soil and structural elements the stiffest (i.e. greater k)- or lightest (i.e. smaller m) elements of the model will be decisive for the determination of the critical timestep. To illustrate this, we assume a typical model consisting of soil with the following elastic -or initial- properties: maximum shear modulus G = 98MPa, maximum bulk modulus K = 255MPa and density ρ = 2.0 Mgr/m^3. The soil mesh is discretized in cubic -*brick*- elements of volume V = 1m^3 and face area A^f = 1m^2. Additionally, structural beam elements have length l = 0.3m, modulus of elasticity E = 26GPa, moment of inertia I = 0.01m^4 and density ρ = 2.5 Mgr/m^3. Finally, the foundation is modelled with triangular shell elements with plan dimensions 1m x 1m x 1.4m, thickness 0.6m, density ρ = 2.5 Mgr/m^3 and modulus of elasticity E = 30GPa. The critical timesteps for the soil brick zones, shell elements and beam elements are deduced by performing dynamic analysis of the free-soil profile, soil-foundation system and structure-foundation-soil system, respectively. The results summarized in **Table 3.3** indicate that the inclusion of shell and structural elements reduces the critical timestep one and two orders of magnitude, respectively.

Table 3.3: Critical timestep for the dynamic analysis of the i) soil mesh, ii) soil-foundation mesh and iii) soil-foundation-structure mesh.

Type of element:	**Soil mesh (brick zones)**	**FS mesh (with shell elements)**	**SFS mesh (with beam elements)**
Δt_{crit} **(sec)**	$5.4 \cdot 10^{-4}$	$6.7 \cdot 10^{-5}$	$7.8 \cdot 10^{-6}$

Structural elements. _ The surface foundation is numerically modelled with shell-type finite elements rigidly connected to the underlying soil gridpoints. The shell elements of *FLAC^{3D}* are 3-noded triangular elements that resist both bending and membrane loading. Each node contains 6 degrees-of-freedom, i.e. 3 translational and 3 rotational, as seen in **Figure 3.9a**. The reference footing examined in this study is

square with dimensions 4m x 4m x 0.6m, modelled, though, as a 4m x 2m x0.6m footing since the mesh is symmetrical with respect to the direction of horizontal shaking. Rotation and out-of-plane translation are fixed at the footing edge on the axis of symmetry in order to appropriately simulate the physical model of the square footing. Discretization of the foundation with shell elements adopts the underlying soil mesh dimensions in order to ensure the connection of structural and soil nodes without the use of a redundant interface. Shell material properties follow typical elastic properties of concrete footing, i.e. Young's modulus E = 30MPa, Poisson's ratio v = 0.2 and density ρ = 2.5 Mgr/m^3.

The superstructure is modelled with the linear beam element shown in **Figure 3.9b.** *FLAC 3D* beam elements employ Euler-Bernoulli beam theory which assumes that the rotation of the cross section is always perpendicular to the bending line. Shear deformations are neglected and as a result the modelled beam is relatively stiffer compared to the physical model. Euler-Bernoulli beams are, thus, better suited for flexible elements with high length-to-thickness ratio. The modelled structure is a single degree-of-freedom system with the mass concentrated on the top of the column, as in the case of a bridge deck connected to the pier. Since the nodal masses of structural elements in *FLAC^{3D}* are derived from the adjacent element densities, the concentrated top mass originates from the distributed density of the top beam element. It is evident that the single degree-of-freedom approximation requires small element length in order for the mass to be considered concentrated, yet by reducing the element length the critical timestep is significantly decreased since it is reciprocal to the element stiffness, i.e. $k = EI/h^3$, as described previously. In order to balance the above, the structure is discretized in elements of 0.3m in length. Additionally, the column cross section has an area A = 0.245m^2 and moment of inertia around the strong axis I = 0.01m^4. Young's modulus is E = 26MPa while the density of beam elements under the top element is artificially increased to ρ = 5.4 Mgr/m^3 in order to reduce the dynamic timestep of the numerical integration scheme.

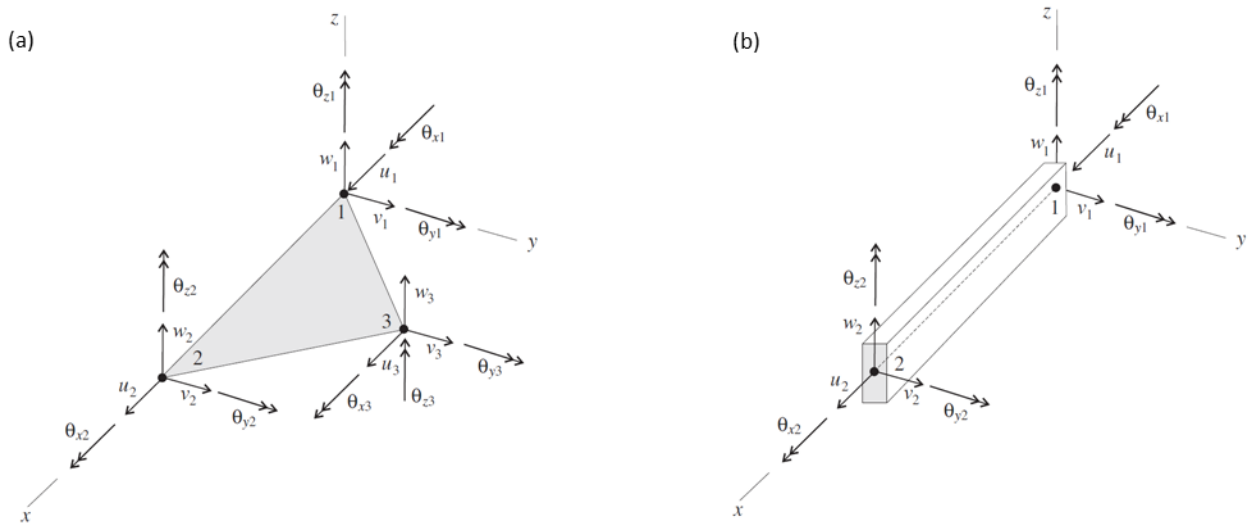

Figure 3.9: Configuration of (a) shell and (b) beam elements used for numerical analyses in *FLAC*^{3}.

3.3 Numerical simulation of gravel performance

Crust improvement. _ In the present study the surface crust is assumed to be improved by i) densification of the natural soil with vibrocompaction and ii) gravel drains used to accelerate excess pore pressure dissipation. This improvement alters the mechanical characteristics of the top soil crust in the following ways:

- Gravel drains increase the overall system permeability. As a result, excess pore pressures are dissipated through vertical and horizontal flow of the water under and around the installed drains, respectively.
- Vibrocompaction results in an increased soil relative density D_r of the soil around the axis of the vibrocone. This effect is reduced with the radial distance from the vibrocone, but leads to an overall increase of the shear strength of the improved surface crust.

The detailed numerical modelling of such mechanisms is possible by utilizing the capabilities of *FLAC*^{3D} for simulating the coupled fluid-solid interaction, as well as, in the complex stress-strain-pore pressure response of liquefiable sand. Nevertheless, the computational time required for such detailed analyses prohibits their use in the present study. Instead, the concept of the *equivalent uniform improved ground* was employed herein. According to this approach, the improved crust is modelled as a uniform layer with uniform soil properties (permeability, relative density etc.), which refer to an estimation of average values between the gravel drains and the surrounding soil. The applicability of the particular procedure has been thoroughly investigated by (Dimitriadi et al. 2017).

In more detail, the improved ground is characterized by a single value of the replacement ratio α_s, which is defined as the ratio of the total gravel drain area (in plan view) over the area of the surrounding ground around the drain. Typically, values of α_s vary between 0.05-0.20. In the examined problem the intermediate value of $\alpha_s = 0.08$ is selected. The corrected N_{SPT} value of the improved ground is computed, next, as the weighted average of the SPT values between the gravel drain N_{pile} and the surrounding ground after improvement N_{ground}, as follows:

$$N_{imp} = a_s N_{pile} + (1 - a_s) N_{ground} \tag{3.32}$$

where

N_{pile} is the corrected N_{SPT} blow count of the gravel drain,

N_{ground} is the corrected N_{SPT} blow count of the surrounding ground at the mid-distance between consecutive gravel drains.

The values of N_{pile} and N_{ground} are given as a function of the corrected N_{SPT} value for the natural soil (N_o) and the replacement ratio a_s according to the Japanese Geotechnical Society (JGS, 1998) guidelines (**Figure 3.10**). Next, relative density D_r can be related to the blow count number of the improved zone $(N_1)_{60}$ - corrected with depth, applied pressure and fines- by the empirical formula of Tokimatsu and Seed (1987):

$$(N_1)_{60} = 44 {D_r}^2 \tag{3.33}$$

Regarding the permeability of the improved zone, the weighted average approximation between the respective permeability coefficients of the gravel drains and the surrounding ground is employed, as follows:

$$k_{eq} = a_s k_{drain} + (1 - a_s) k_{sand} \tag{3.34}$$

The variation of permeability with relative density D_r for Nevada sand is plotted in **Figure 3.11,** according to Arulmoli et al. (1992). It is observed that initial values of D_r around 40% are related to permeability coefficients equal to $k \approx 6.5 \cdot 10^{-5}$ m/s. Permeability values are vastly decreased for D_r levels greater than 60%, with final values of permeability reaching $k \approx 1.2 \cdot 10^{-5}$ m/s.

Table 3.4 summarizes the selected values No of the natural soil, the replacement ratio as, as well as the final values of relative density and permeability coefficient of the equivalent uniform improved zone.

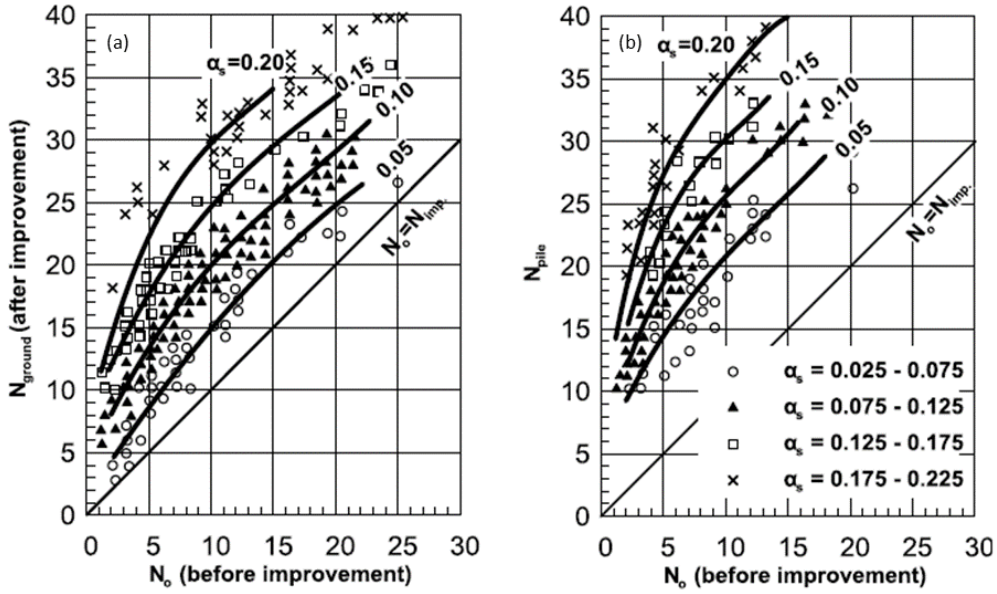

Figure 3.10: Design charts of N_{SPT} values of (a) the improved ground after vibrocompaction N_{ground} and (b) the gravel drain N_{pile} as a function of the natural soil SPT value N_o and the replacement ratio α_s.

Table 3.4: Summarized values of soil properties before and after improvement.

D_r (%)	N_o	a_s	N_{ground}	N_{pile}	$N_{imp.zone}$	$D_{imp.zone}$	k_{drain} (*m/s*)	k_{nat} (*m/s*)	$K_{impr.zone}$ (*m/s*)
45	8.9	0.08	17	22.2	16.5	60	$1.2\cdot10^{-5}$	$6.5\cdot10^{-5}$	$2.0\cdot10^{-3}$

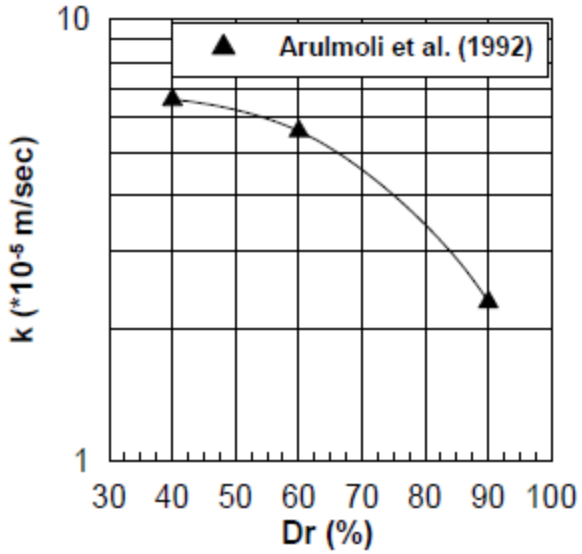

Figure 3.11: Permeability coefficient *k* of Nevada sand as a function of the relative density D_r (Arulmoli et al. 1992).

3.4 Numerical verification

3.4.1 Seismic response of shallow foundations on liquefiable soil

The ability of the constitutive model NTUA-Sand to model the seismic response of shallow foundations on liquefiable soil is validated through a number of comparisons between the model predictions and the experimental results of the VELACS testing program (Arulmoli et al. 1992) by Andrianopoulos et al. (2010). The experimental setup of the pertinent Model test No 12 is depicted in **Figure 3.12**. In prototype scale, the soil profile consists of a 7m deep liquefiable Nevada sand with 60% relative density and permeability coefficient equal to $2.1 \cdot 10^{-5}$m/s which is overlaid by a 1m surficial crust of Bonnie silt with low permeability ($5 \cdot 10^{-9}$m/s). The water table lies 1m above the surface. The structure consists of a rigid block of 4m in total height, 3m in width and 0.5m in embedment depth which corresponds to a total bearing pressure of 150kPa. The soil profile lays within a rigid box with planar dimensions 28m x 8m and subjected to a centrifuge acceleration equal to 100g. The response of the soil profile and the structure are recorded with three accelerometers (AccB, AccC and AccD), four pore pressure transducers (PPT1, PPT2, PPT3 and PPT4) and the structural settlement recorder LVDT. The location of the foregoing recorders is depicted in **Figure 3.12**.

The finite element mesh used in the numerical analyses is shown in the same Figure and consists of soil zones with sizes varying from 0.75m x 0.5m in the vicinity of the foundation to 1.5m x 1.0m far from the foundation. The surficial crust of Bonnie silt was modeled with the hysteretic Ramberg-Osgood model in

order to capture the shear modulus degradation and the hysteretic damping for the observed range of cyclic shear strains. The structure is modeled with linear-elastic soil elements of increased stiffness in order to represent a rigid structure. The input motion is applied as a horizontal acceleration at the base and the sides of the rigid box.

The described experimental setup of the Model No 12 was employed in three different testing programs that were conducted at Princeton University (PRNU, Krstelj and Prevost 1994), at Rensselaer Polytechnic Institute (PRI, Carnevalle and Elgamal 1994) and at the University of California at Davis (UCD, Farrel and Kutter 1994). The aforementioned model was subjected to a harmonic base input motion with constant amplitude and ten, more or less, cycles of excitation. The maximum and average values of the input accelerations, i.e., a_{max} and a_{aver}, as well as the duration of ground motion t_d varied in the performed tests, as presented in **Table 3.5**.

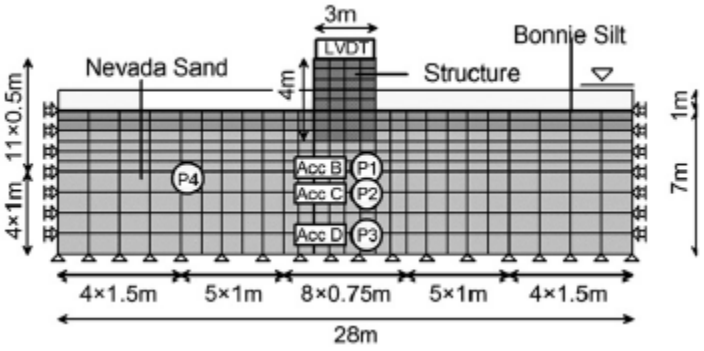

Figure 3.12: Schematic illustration of experimental setup of VELACS centrifuge Model No. 12. The location of the accelerometers (AccB, AccC, AccD), pore pressure transducers (PPT1, PPT2, PPT3, PPT4) and structural settlement recorder (LVDT) are indicated in the figure.

Table 3.5: Characteristics of the base input motion and corresponding structural settlement measured during the centrifuge tests and the numerical simulation.

Source	*# test*	a_{max} (g)	a_{aver} (g)	t_d (sec)	settlement (cm)
Princeton University (PRNU)	1	0.30	0.26	6.65	27
	3	0.40	0.34	6.70	47
	5	0.21	0.18	5.40	22
	6	0.24	0.21	5.50	21
University of California at Davis (UCD)	2	0.37	0.31	7.50	18
	3	0.25	0.21	6.40	9
Rensselaer Polytechnic Institute (RPI)	1	0.26	0.21	5.70	13
Numerical	1	0.24	0.21	5.75	10.8
	2	0.32	0.30	7.25	15.2

Comparisons between numerical simulations and the respective recordings from the testing programs are presented in **Figure 3.13**, **Figure 3.14** and **Figure 3.15**. Namely, **Figure 3.13** compares numerical predictions and experimental results from the centrifuge test at Rensselaer Polytechnic Institute (RPI) of the horizontal accelerations time-histories at the base of the soil profile (**Figure 3.13a**) and at the locations B (**Figure 3.13b**) and C (**Figure 3.13c**). Numerical predictions are sufficiently close to experimental results during the strong part of shaking, while afterwards, there is a deviation between them which is attributed to residual oscillations of the experimental setup. **Figure 3.14** presents the time-histories of the excess pore pressure ratios $\Delta u/\sigma_{vo}$ from the three conducted testing programs (PRNU, RPI and UCD) and the respective numerical results. The transducers PPT1, PPT2 and PPT3, which are located in the vicinity of the foundation, show that $\Delta u/\sigma_{vo}$ ratios never exceed the value of 0.5-0.6, indicating partial liquefaction, whereas the transducer PPT4, which is located at the free-field, shows complete liquefaction. Overall, comparisons between experimental data and numerical predictions show satisfactory agreement. It is noted that the recorded excess pore pressure ratios are smoothed in these Figures (Prevost et al. 1994). Lastly, **Figure 3.15** compares structural settlements between numerical predictions and the three testing

programs, namely, PRNU tests #5 and #6, UCD test #3 and RPI test. Both numerical and experimental results show that structural settlements are accumulated during the strong part of shaking. Numerical simulation predicts a total value of structural settlement equal to 10.8cm, which is close to the lower limit of the experimentally obtained values, i.e., 9cm to 22cm. The variation of structural settlements in the performed tests is significant (i.e., 9 to 47cm), with greater values of settlement being observed for greater values of base input acceleration. **Figure 3.16** presents the variation of structural settlements with the foregoing acceleration a_{max}. Numerical results compare well with experimental data from the testing programs of Rensselaer Polytechnic Institute and University of California at Davis, whereas data from the Princeton University exhibit consistently increased values of settlements (upper solid line).

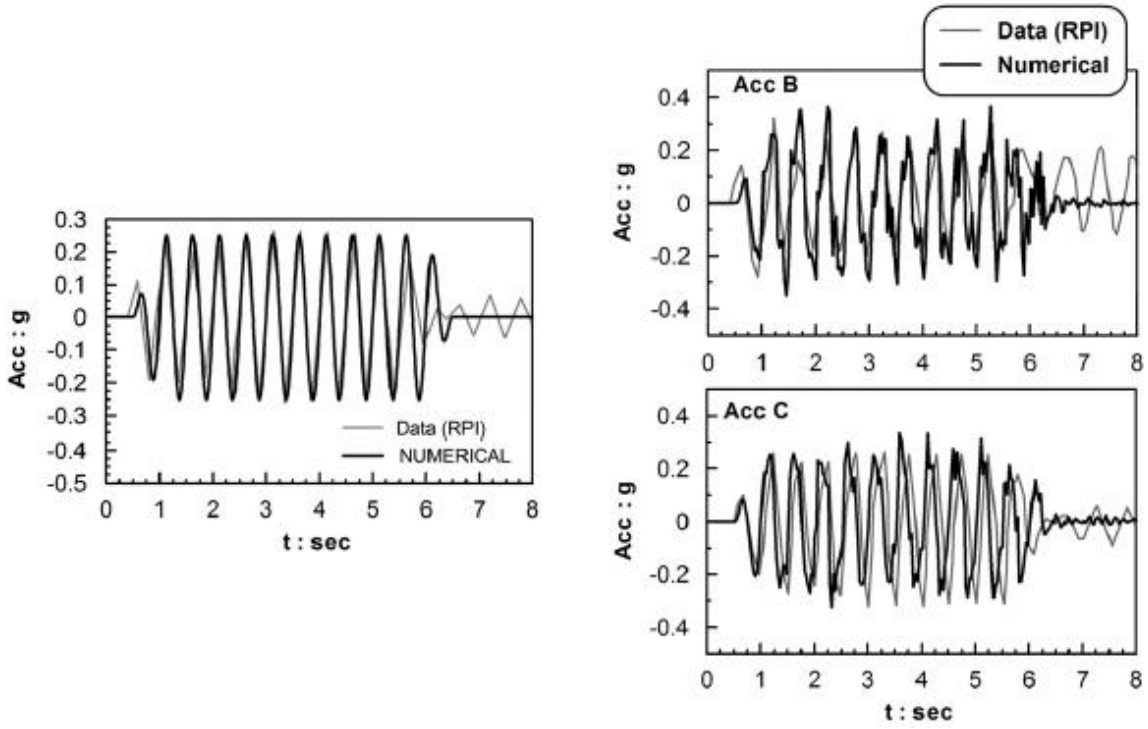

Figure 3.13: Comparison between time-histories of numerical predictions and recorded data from the RPI test of the horizontal accelerations at (a) the base, (b) location b and (c) location C of the soil profile.

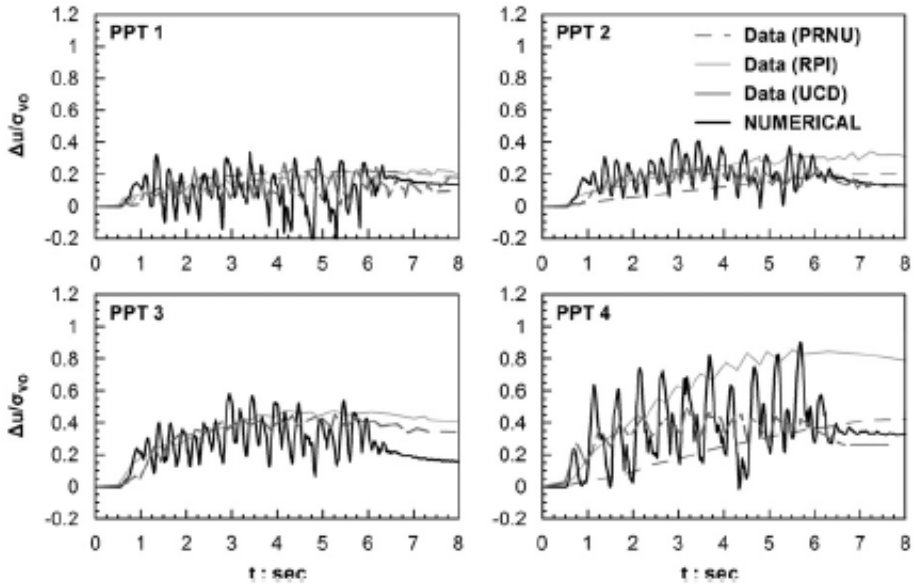

Figure 3.14: Comparison between time-histories of numerical predictions and recorded data from the three testing programs (PRNU, RPI, UCD) of the excess pore pressure ratios at various locations (PPT1, PPT2, PPT3, PPT4).

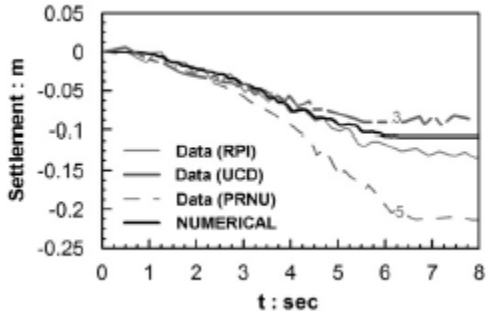

Figure 3.15: Comparison between time-histories of structural settlements obtained from numerical predictions and recorded data from the three testing programs (PRNU, RPI, UCD).

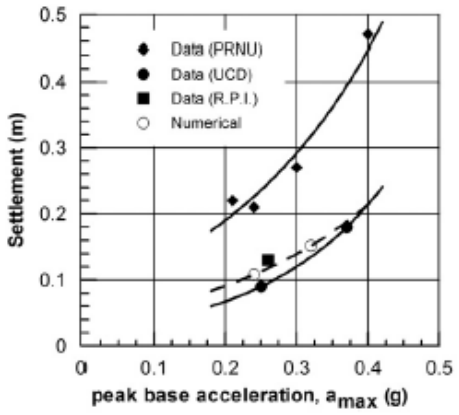

Figure 3.16: Variation of structural settlements with the maximum base acceleration a_{max} of the VELACS Model No. 12 based on numerical predictions and experimental data from the testing programs PRNU, RPI and UCD.

3.4.2 Nonlinear response of soil-foundation interaction in lateral loading

The nonlinear soil-foundation interaction is simulated in *FLAC 3D* with the use of an interface, which permits uplift of the foundation, i.e., it has zero tension cut-off. Sliding of the foundation is not allowed in the model, taking into account that, in practical applications, even a small embedment of the foundation is enough to activate passive earth resistance and prevent sliding, assuming a well-compacted backfill. The particular modeling configuration is able to capture the principal aspects of the rocking behavior of the structure, namely:

- *Soil nonlinearity* due to the strength and stiffness degradation of soil during cyclic loading. More pronounced soil nonlinearity is mainly concentrated at the footing edges where SSI-induced strains are accumulated as well as in cases of pore water pressure build up.
- *Geometric nonlinearity* due to gapping between the foundation and the soil. Foundation uplift and separation between the foundation sidewalls and the soil embedment are such cases of geometric nonlinearity.

In order to evaluate the nonlinear soil-foundation interaction of the numerical model developed in *FLAC 3D*, the present section examines the performance of the particular model in lateral loading and compares the results with limit-state analytical predictions. Rocking of a shallow footing subjected to combined loading of vertical force and moment (*N*-*M*) is depicted in the following figures. The moment-rotation (*M*-ϑ) relationship of such a footing is presented in **Figure 3.17**. The figure distinguishes the following scenarios of soil-foundation response:

- *Elastic soil* conditions are designated with the path 1-2-3-5a. In this case, foundation uplift initiates at point 2 and, as a result, a reducing part of the footing area is in contact with the soil as the loading increases (i.e., 3-5a branch). The limiting value of the applied moment is $N{\cdot}B/2$, upon further – displacement controlled – loading it reduces due to P-δ effects.
- *Soil* y*ielding after foundation uplift* is depicted with the path 1-2-3-4-5b. In this case, also, foundation uplift initiates at point 2, whereas soil yielding occurs at point 4.
- *Soil* y*ielding before foundation uplift* is depicted with the path 1-2-3c-5c-6c. In this case, soil yielding initiates at point 2c, whereas foundation uplift occurs at point 4c.

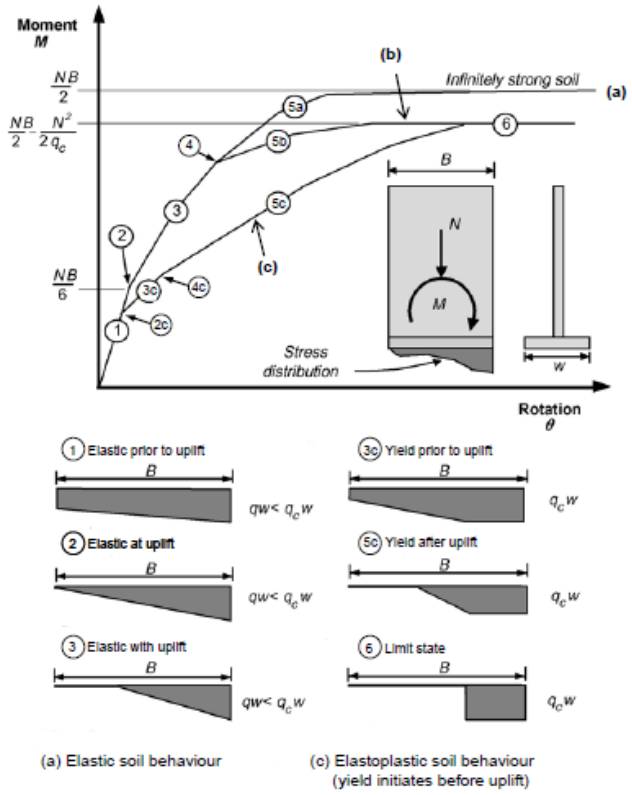

Figure 3.17: Possible scenarios of soil-foundation response examined through the moment-rotation (M-ϑ) relationship of a shallow footing subjected to lateral loading.

A closed-form relation for a simplified analytical modeling of the soil-foundation interaction at limit state can be provided by examining the limit equilibrium of the rigid footing (**Figure 3.18**). In this case, a rigid strip footing of width 2*b* is considered resting on top of an inelastic soil medium. Soil response assumes elastic-perfectly plastic behavior and zero tensile strength, thus, allowing footing uplift. The applied loads include the structural weight *W* and a lateral force *F*, both of which have a position of application at height

h above the soil surface. The examined force equilibrium considers P-δ effects and, as a result, the induced moment at the footing is derived by both the structural weight *W* and the lateral force *F.* Namely, the pertinent force equilibrium of the rigid footing at the limit state (i.e., assuming full soil yielding and footing uplift) is expressed as follows:

- *Moment equilibrium about point O':*

$$\Sigma M_{o'} = 0 \Rightarrow F[h \cdot cos\theta + (b-\beta) \cdot sin\theta] - W_1[(b-\beta) - (b-\beta) \cdot (1-cos\theta) - h \cdot sin\theta] - W_2(b-\beta) \cdot cos\theta = 0 \Rightarrow$$

$$F[h \cdot cos\theta + (b-\beta) \cdot sin\theta] - W_1[(b-\beta) \cdot cos\theta - h \cdot sin\theta] - W_2(b-\beta) \cdot cos\theta = 0 \quad (3.35)$$

- *Force equilibrium in the vertical direction:*

$$\Sigma F_y = 0 \Rightarrow W = q_{ult} \cdot 2 \cdot b \cdot \beta \cdot cos\theta \quad (3.36)$$

where W_1 and W_2 decompose the total structural weight to foundation and top structural weight (i.e., $W = W_1 + W_2$), respectively, 2β is the footing length in contact with the soil, q_{ult} is the limit-state bearing capacity of the footing and ϑ is the footing inclination angle. By combining Equations 3.35 and 3.36, the following expression for the applied moment is derived as a function of the inclination angle ϑ:

$$M(\theta) = W \cdot \left(b - \frac{W}{2 \cdot q_{ult} \cdot b \cdot cos\theta}\right) \cdot cos\theta - W_1 \cdot h \cdot sin\theta$$

$$\Rightarrow \quad (3.37)$$

$$M(\theta) = W \cdot b \cdot \left(1 - \frac{W}{N_{ult} \cdot cos\theta}\right) \cdot cos\theta - W_1 \cdot h \cdot sin\theta$$

The ultimate moment capacity of the foundation M_u, in this case, serves as an upper-limit which includes the compliance of the soil (in terms of N/N_u, where N_u refers to the total bearing capacity of the foundation $q_{ult} \cdot A$) and the P-δ effects. Namely, the maximum moment of Equation 3.37 is derived by setting:

$$\theta = 0 \quad \Rightarrow \quad M_{ult} = F \cdot h = W_{o\lambda} \cdot \left(b - \frac{W_{o\lambda}}{2q^*_{ult}b}\right) = N \cdot b \cdot \left(1 - \frac{N}{N_u}\right) \quad (3.38)$$

The ultimate angle of rotation ϑ_u at which the moment capacity of the foundation becomes zero is obtained as:

$$M = 0 \quad => \quad tan\theta_{ult} = \frac{N \cdot b \cdot \left(1 - {}^{N}/_{N_u}\right)}{N_1 \cdot h} \tag{3.39}$$

Comparatively, the ultimate angle of rotation in the case of elastic soil, i.e., assuming $N_u \rightarrow \infty$, refers to the critical value of the rotation angle ϑ_c. The exceedance of ϑ_c signifies the toppling of the structure and is typically used in correlation with ϑ_u, which is a fraction of ϑ_c, since it additionally depends on soil yielding. The critical angle of rotation ϑ_c is derived as:

$$M = 0 \;\; \kappa\alpha\iota \;\; {}^{N}/_{N_u} \rightarrow 0 \quad => \quad tan\theta_c = \frac{N \cdot b}{N_1 \cdot h} \tag{3.40}$$

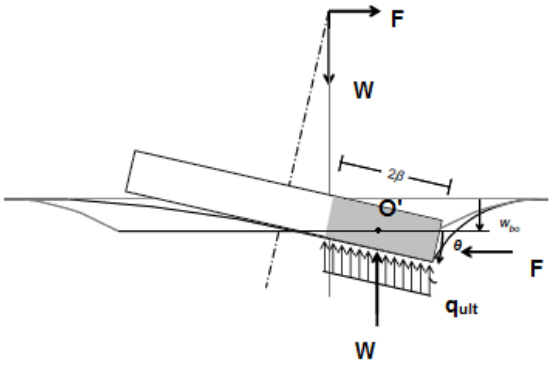

Figure 3.18: Schematic illustration of the force equilibrium of a shallow footing at limit-state.

Based on the foregoing limit-state analysis of the foundation-soil interaction, it is, thus, possible to evaluate the soundness of the proposed numerical model which is developed in *FLAC 3D*. To that end, a number of numerical analyses of structure-foundation-soil systems subjected to lateral loading is performed. The numerical model configuration of section 3.2 is employed here. Namely, the examined SFS system, as illustrated in **Figure 3.1**, has mesh width equal to L_x = 50m, depth L_y = 25m and height *H* = 20m. The superstructure is modeled as a SDOF of height h=3.0m and fixed-base fundamental period $T_{str.f}$ = 0.35sec. A square shallow foundation is selected with dimensions 4m x 4m. In contrast to the soil deposit of Nevada sand, which is generally used in the present Thesis, a non-cohesionless soil profile is employed in this section. The Mohr-Coulomb constitutive model is used to simulate the response of soil in monotonic loading, since the elastic-perfectly plastic formulation of the particular model is in accordance with the foregoing limit-state analytical formulation. The numerical analyses are performed for undrained soil conditions with the undrained shear strength of clay being c_u = 50 kPa. The application of the horizontal force is schematically depicted in **Figure 3.18**.

Figure 3.19a–f presents the resulting moment-rotation curves of the described SFS system. The particular Figure examines six different systems with varying structural mass, i.e., M_{str} = 44tn – 280tn, and, thus, with varying Static Factors of Safety (FS_s = 1.25 - 5.50). Results are presented in terms of the normalized moment M/c_uB^3, where B is the footing width, and the normalized footing rotation ϑ/ϑ_c, where ϑ_c is the previously discussed critical angle of rotation. Results show that the limit-state predictions of the ultimate angle of rotation ϑ_u are in agreement with the numerical results. On the other hand, the limit-state predictions of the ultimate moment capacity M_u serve as an upper-bound solution of the numerically obtained one. It is observed that the reduction of the numerically predicted M_u compared to the analytical value increases for decreasing values of FS_v. This reduction is attributed to the increased role of P-δ effects (Apostolou 2011). This is further elaborated in **Figure 3.20**, which presents the variation of the normalized ultimate moment capacity M/c_uB^3 with FS_v. Results show that the aforementioned reduction of the moment capacity is observed for values of FS_v greater than 0.5. Apostolou (2011) further notes that the tendency for "bulging" of the numerical values as FS_v tends to 1.0 is attributed to the passive forces that develop under the footing corner point.

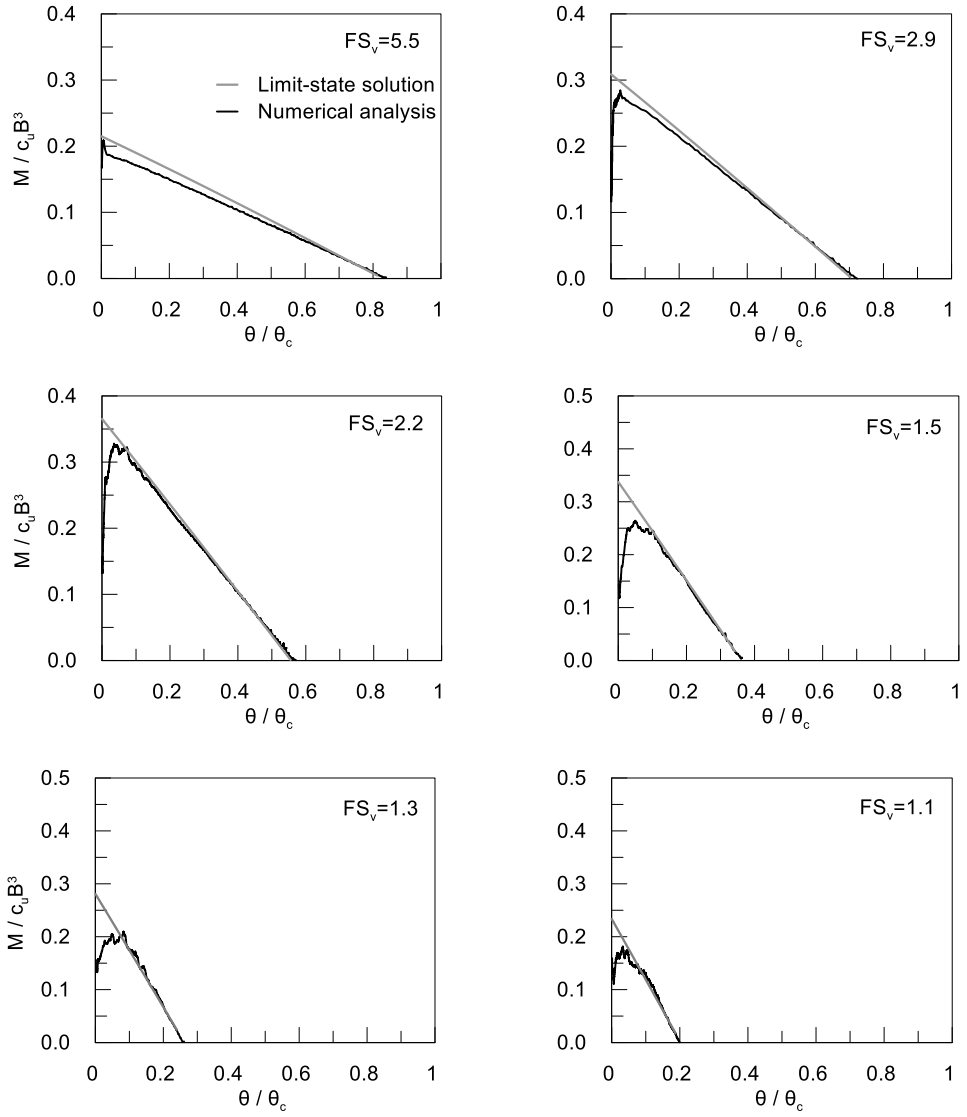

Figure 3.19: Moment-rotation curves of a rigid footing for varying values of FS subjected to monotonic lateral loading.

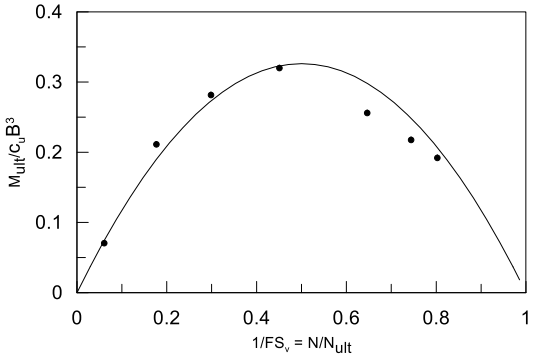

Figure 3.20: Comparison between the monotonic failure envelope in the M-N space calculated by analytical limit-state relations and predictions of the numerical analyses in *FLAC 3D*.

Chapter 4

Natural Period Estimation of Structure-Foundation-Soil Systems

4.1 General

The natural period is a key-role parameter for the dynamic response of a structure. In its most common use, it is employed in design procedures to estimate seismic demands for a given seismic hazard and geotechnical profile through a pseudo-acceleration design spectrum. Simplified approaches often consider a *fixed-base* structural system which implies infinite stiffness of the supporting soil. More accurate design procedures (NEHRP, FEMA 440), though, model *flexible-base* systems that take also into account soil compliance and propagating seismic waves. As such, typical soil-structure interaction (*SSI*) procedures regard equivalent linear soil-structure systems that replace soil continuum with (vertical, lateral and rocking) springs connected to the foundation. Dynamic impedance functions of soil springs have been rigorously developed and are able to capture a wide range of related design factors, such as foundation embedment, depth to the rigid bedrock, horizontal-rocking motion coupling, etc. (Gazetas 1991b; Mylonakis et al. 2006; Pais and Kausel 1988a). The equivalent system is characterized by a single *natural period* and *damping ratio* both of which are calculated through analytical procedures (Veletsos, A. S., & Meek 1974). In general, higher soil compliance results to greater increase of the *flexible system* natural period and damping compared to the *fixed-base* system.

In this framework, soil nonlinearity is introduced indirectly, in terms of shear modulus reduction and damping ratio increase, neglecting dominant patterns of cyclic behaviour of soil such as densification, loss of strength due to pore water pressure build up, load induced anisotropy etc. Shear modulus and damping ratio curves are derived by stress-strain behavior at free field conditions and as a result the development of shear strains and the subsequent soil softening, i.e., *G* reduction, due to structural vibration is

essentially overlooked. It is noteworthy that this over-simplification can either be on the safe or on the unsafe side depending on whether period elongation – related to soil softening – may lead to an increase or decrease of seismic spectral demands, depending on the initial reference period (without soil softening). During strong seismic events or in the presence of liquefaction, soil and structural nonlinearity becomes significant, rendering a nonlinear *SSI* approach mandatory. Related research has addressed the response of structure-foundation-soil systems on realistic conditions by field or real scale studies (de Barros and Luco 1995; Stewart et al. 1999b; Tileylioglu et al. 2011; Todorovska 2002; Trifunac et al. 2001a), centrifuge experiments (Chen et al. 2013b; Dashti et al. 2010; Gajan and Kutter 2008; Ghosh and Madabhushi 2007; Trombetta et al. 2013) and numerical analyses (Dashti and Bray 2013b). These studies correlate system ductility with period elongation and identify seismic intensity as the primary source of nonlinearity. Nevertheless, an explicit correlation between soil nonlinearity and period elongation is not established since both structural and soil yielding are simultaneously examined and also the parametric investigation is mostly focused on the seismic intensity.

The first step in the present study is to use the analytical procedure for *flexible-base* systems employed in design codes (NIST 2012) for the calculation of the elongated natural period of structure-foundation-soil systems assuming *elastic* soil conditions, i.e., prior to the seismic event. Next, a characteristic natural period of the system during shaking is assessed. During the earthquake motion, the time-varying degradation of soil stiffness renders the direct calculation of the system natural period dependent on the appropriate selection of an equivalent shear modulus for the supporting soil. To overcome this difficulty, the nonlinear system period is identified indirectly, through the Transfer Function between the input (*free field*) and output (*structural*) acceleration signals in the frequency domain. Within this framework the factors of system nonlinearity can be related to an actual – or *effective* – natural period of the system. Finally, analytical expressions are developed that correlate the aforementioned numerical predictions of *effective system periods* with the readily obtained – in practice – *elastic system periods* prescribed in design codes.

4.2 Overview of natural period estimation

4.2.1 Analytical relations of linear elastic SSI theory

Analytical *SSI* procedures simulate a *flexible-base* system as an equivalent single-degree-of-freedom oscillator with structural stiffness k_{str} supported by a set of springs representing soil compliance against a rigid foundation (i.e., the horizontal spring stiffness k_x in the direction of motion and the associated

rotational spring stiffness k_{ry}). The elongated period of the flexible system T_{sys} is thus related to the period of the *fixed-base* structure $T_{str.fix}$ with the widely used expression of (Veletsos, A. S., & Meek 1974):

$$\frac{T_{sys}}{T_{str.fix}} = \sqrt{1 + \frac{k_{str}}{k_x} + \frac{k_{str} \cdot h^2}{k_{ry}}} \quad 4.1$$

The influence of soil and structural parameters on period elongation is usually expressed in terms of specific *SSI* dimensionless parameters. The governing parameter is identified as the *structure-to-soil stiffness ratio* $s=h/(V_s T_{str.fix})$, where h is the structural height and V_s is the shear wave velocity of the soil profile, with the period elongation increasing with s (**Figure 1.1**). Typically, stiff structures (e.g. shear walls, braced frames) have large values of $h/(T_{str.fix})$ resulting in greater period elongations (**Figure 4.1**). Soil stiffness is introduced through the shear wave velocity V_s and has the opposite effect, i.e., structures on soft soil experience the greatest period elongation. According to Stewart et al. (1999b), buildings on soil and weathered rock sites exhibit $s < 0.1$ in the case of moment frame structures and $s = 0.1$ to 0.5 in the case of shear walls and braced frame structures.

The effect of *structural height* on period lengthening is twofold (**Figure 4.1a)**. According to (Federal Emergency Management Agency (FEMA) 1997) "*all other factors being equal, period lengthening increases with the slenderness ratio h/r, (r is the radius of the foundation) due to increased overturning moments and foundation rotation ϑ. This implies that inertial SSI effects would be more significant in tall buildings. However, this is not the case, as tall buildings typically have low* structure-to-soil stiffness ratios $s=h/(V_s T_{str.fix})$*, which is more important for controlling inertial SSI effects. Hence, the overall period lengthening in tall buildings is near unity (i.e., little or no period lengthening)*."

According to equation 4.1, *structural mass* does not directly affect period lengthening. Nevertheless, it is indirectly introduced through the mass ratio $\gamma=m/(\rho_s \cdot r)^3$ so that "*period lengthening could be related to easily recognizable characteristics such as structural first mode period, T, and soil shear wave velocity,* V_s*, rather than structural stiffness, k, and soil shear modulus, G*" ((Federal Emergency Management Agency (FEMA) 1997). The effect of mass ratio on period lengthening has been found in literature varying from modest ((Federal Emergency Management Agency (FEMA) 1997)]) to significant (Maravas et al. 2014; P.Wolf 1985) (**Figure 4.1b**). It is worth to be mentioned that Mylonakis and Karatzia (2019) have proposed an alternative formalism of nondimensional SSI parameters to avoid the redundancy of mass ratio.

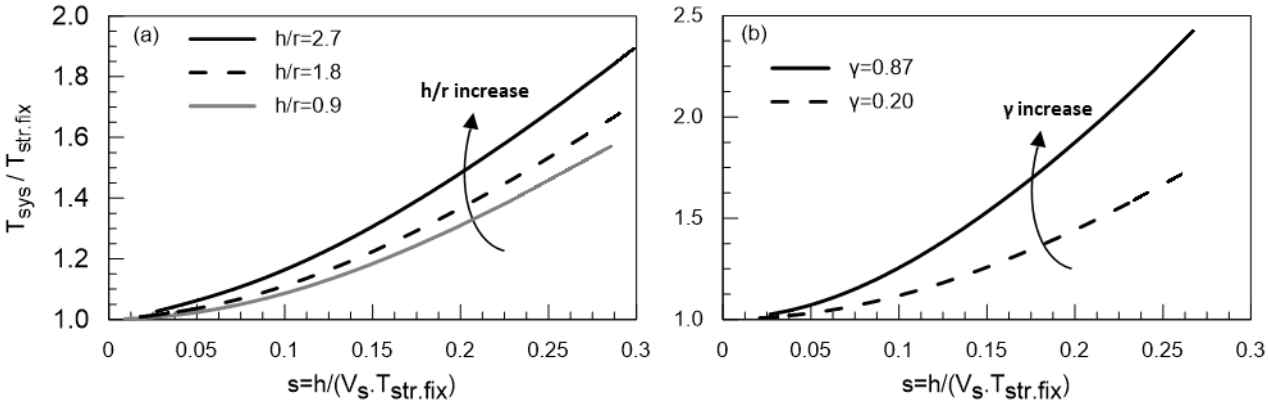

Figure 4.1: Plot of period elongation $T_{sys}/T_{str.fix}$ versus structure-to-soil stiffness ratio $s=h/(V_sT_{str.fix})$ for varying values of (a) slenderness ratios h/r and (b) relative mass ratio γ (system properties: ν≈0.45, ζ=5%)

In typical formulations, dynamic stiffness and damping characteristics of the soil-foundation interface are expressed through complex-valued impedance functions, in the form:

$$\bar{k}_i = k_i + i\omega c_i \qquad 4.2$$

where k_i and c_i denote the frequency-dependent stiffness (spring) and damping (dashpot) coefficients, respectively, for the mode of oscillation i and ω is the circular frequency of vibration. There are abundant analytical solutions in literature for the impedance of rigid footings on an elastic half-space, dependent on various design factors such as footing shape, embedment depth, bedrock depth and soil heterogeneity, among others (Dobry and Gazetas 1986; Gazetas 1991a; Mylonakis et al. 2006; Pais and Kausel 1988b; Wong and Luco 1985).

In this study, the spring stiffnesses for horizontal translation and rocking, which are necessary for the calculation of period elongation, are derived from the code specifications of (Federal Emergency Management Agency (FEMA) 1997), summarized in **Table 6**. It is important to note that during strong seismic events, and especially in the case of liquefied soil, the shear wave velocity V_S of the foundation ground varies with time. Due to the dependency of the described analytical procedures on the selection of a single (equivalent) value of shear modulus G, these procedures are merely employed for the evaluation of the initial – *elastic* – properties of the system when the value of G is known. Note that the frequency dependency of spring stiffness mostly affects the rotational impedance in the high frequency range (Gazetas 1991a). In the examined case, the range of frequencies is such that its effect is marginal. For example, the dynamic stiffness modification required for the examined soil profile of V_s = 125m/s, a

rectangular footing with width *B*=4m and for an average excitation with T_{exc} = 0.25sec has approximately a factor of 0.97 and 1.00 for the rocking and translational mode, respectively (NEHRP). Therefore, only the static part of the spring stiffness is considered in this study. Moreover, it is noted that the numerical model that is used in this study (see Chapter 3) considers only one half of the physical model due to geometrical symmetry with respect to the (horizontal) direction of the applied seismic motion. As a result, for a square *B*x*B* footing, stiffness values k_i are computed for a rectangular Bx(B/2) footing whereas the respective footing shape factors assume the square footing of the *physical model*.

Table 6: Elastic solutions for the static stiffness of rigid footings at the ground surface [(Federal Emergency Management Agency (FEMA) 1997)]

Degree of freedom	Pais and Kausel (1988)	Gazetas (1991); Mylonakis et al.(2006)
Translation along y-axis	$K_y = \frac{GB}{2-v}\left[6.8\left(\frac{L}{B}\right)^{0.65} + 0.8\left(\frac{L}{B}\right) + 1.6\right]$	$K_y = \frac{2GB}{2-v}\left[2 + 2.5\left(\frac{L}{B}\right)^{0.85}\right]$
Translation along x-axis	$K_x = \frac{GB}{2-v}\left[6.8\left(\frac{L}{B}\right)^{0.65} + 2.4\right]$	$K_x = K_y - \frac{0.2}{0.75-v}GL\left[1 - \frac{B}{L}\right]$
Rocking about y-axis	$K_{ry} = \frac{GB^3}{1-v}\left[3.73\left(\frac{L}{B}\right)^{2.4} + 0.27\right]$	$K_{ry} = \frac{G}{1-v}(I_y)^{0.75}\left[3\left(\frac{B}{L}\right)^{0.15}\right]$
Rocking about x-axis	$K_{rx} = \frac{GB^3}{1-v}\left[3.73\left(\frac{L}{B}\right)^{2.4} + 0.27\right]$	$K_{rx} = \frac{G}{1-v}(I_x)^{0.75}\left(\frac{B}{L}\right)^{0.25}\left[2.4 + 0.5\left(\frac{B}{L}\right)\right]$

Notes: i) Axes should be oriented such that $L \geq B$, with B along the x-axis.

ii) I_i = area moment of inertia of soil-foundation contact, i denotes the axis of foundation rotation

4.2.2 Period estimation in nonlinear SSI

As mentioned before, the response of structure-foundation-soil systems during strong seismic events naturally exhibits nonlinear behavior and therefore the aforementioned analytical solutions for linear elastic systems are often deemed inadequate. Inherent inelasticity may be attributed to the cyclic soil response (e.g. residual settlement, rocking or sliding), as well as to the structural yielding and P-δ effects. At its degraded state, the system can be characterized by an effective period $T_{sys.eff}$ which incorporates soil and structural ductility and is related to the elastic system period $T_{sys.el}$ by the system ductility parameter μ_{sys} ("FEMA 440 Improvement of Nonlinear Static Seismic Analysis Procedures" 2005):

$$\frac{T_{sys.eff}}{T_{sys.el}} = f(\mu_{sys}) \quad 4.3$$

The most widely used procedure for estimating the effective period of systems employs Transfer Functions (TF) that relate the acceleration of the structural mass (*output motion*) to the foundation or free-field ground acceleration (*input motion*). More specifically, the frequency content of each acceleration signal is analyzed using *Fourier Transformation* or *Elastic Response Spectra* and, thus, the peaks of the related Transfer Function can be used to identify the respective eigen-frequencies. The ratio of output-to-input motion may take into account the various modes of vibration in a particular SSI system, provided that the excitation signal has an adequately wide frequency content. These vibration modes include the (relative) structural deformation *u,* as well as the translation and rocking deformations of the footing, u_f and ϑ respectively. In a dynamic analysis, the characteristic frequencies of the various modes of vibration are identified by a proper selection of the input and output signals used to compute the TF, as shown in **Table 7:**

Table 7: System flexibilities based on input/output signal selection

Type of System	Input	Output
Flexible-Base	u_{ff}	$u_{ff} + u_f + h\cdot\theta + u$
Pseudo Flexible-Base	$u_{ff} + u_f$	$u_{ff} + u_f + h\cdot\theta + u$
Fixed-Base	$u_{ff} + u_f + h\theta$	$u_{ff} + u_f + h\cdot\theta + u$

Symbols refer to the following motions: *free field* u_{ff}, *foundation* u_f, *rocking* ϑ *and structural distortion u.*

An application example of the particular procedure for the estimation of flexible systems' period can be found in the centrifuge tests of (Karimi and Dashti 2016a)), presented in **Figure 4.2**. These tests examine the response of the single-degree-of-freedom (SDOF) structure A with a fixed-base natural frequency ≈ 2.5Hz founded on two sets of layered soil profiles. The soil deposits, designated as T3-30 and T3-50, consist of a liquefiable intermediate layer of Nevada sand with (prototype scale) thickness of H_L = 3m and relative density D_r ≈ 30 and 50%, respectively, both of which are laid in between denser sand layers non-susceptible to liquefaction. The base of the soil profile is excited with a number of earthquake motions with values of PGA ranging from 0.04g to 0.58g. Experimental and numerical findings of the particular study indicated that the liquefied sublayer greatly affects the structural response, in terms of residual settlements and system characteristics. Namely, **Figure 4.2a, b** and **c** present the TFs of the mass-over-

foundation motions which correspond to the eigenfrequency of the *pseudo-flexible* system f_{sys} (**Table 6**), previously designated as the *effective system period*, (continuous lines) as well as the eigenfrequency of the fixed-base structure $f_{str.fix}$ (dotted lines) for two earthquake motions: i) the weak *Port Island 1995 Kobe* (SM PI) record with PGA=0.04g (**Figure 4.2b**) and the ii) strong *Port Island 1995 Kobe (LG PI)* record with PGA=0.38g (**Figure 4.2c**). It is noteworthy that, in the case of the large PGA event the observed period elongation has a factor of ≈ 2.0, as f_{sys} ≈ 1.25Hz and $f_{str.fix}$ ≈ 2.5Hz, whereas during the small PGA event period elongation is minimal and around 1.10, i.e., f_{sys} ≈ 2.2Hz and $f_{str.fix}$ ≈ 2.5Hz.

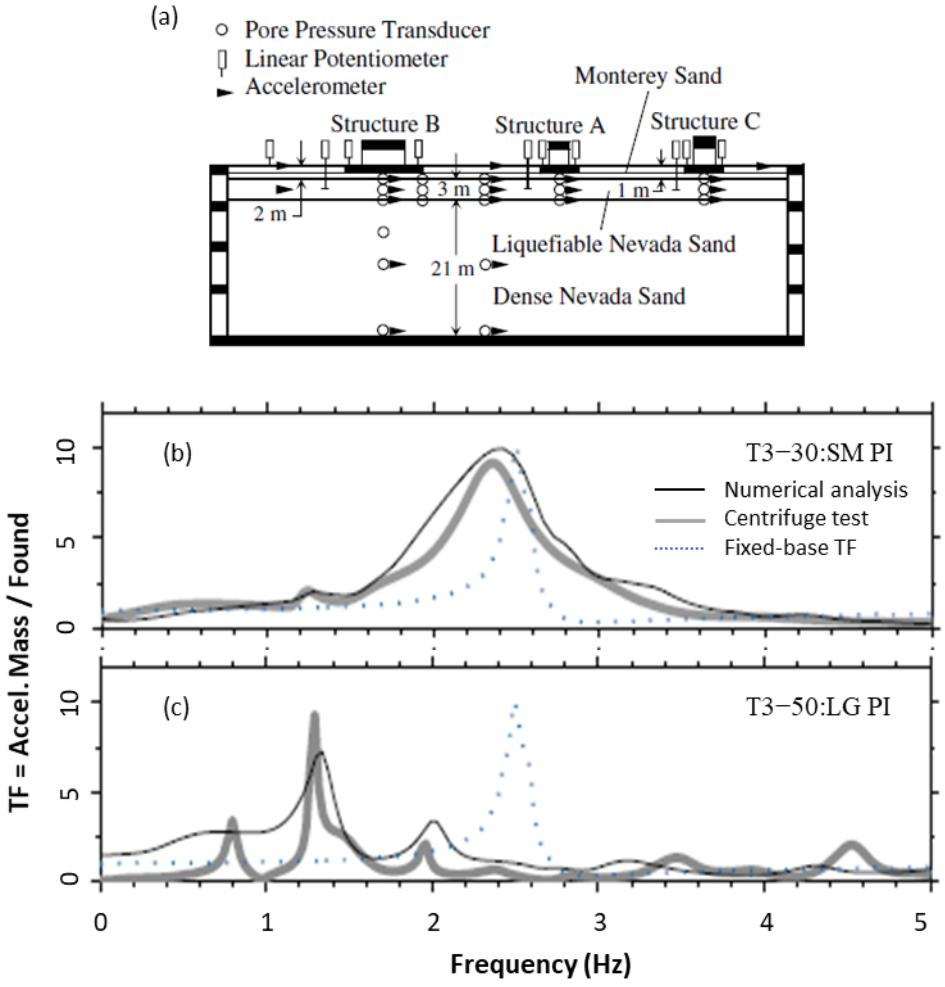

Figure 4.2: (a) Centrifuge test setup of SSI experiments by (Karimi and Dashti 2016b)) and transfer functions (TFs) of accelerations (structure-to-foundation) obtained from numerical analysis (*black line*) and experimental results (*grey line*) for (b) *small intensity* (SM PI) and (c) *large intensity* (LG PI) earthquake motions. The *dotted line* represents fixed-base TF.

System identification of existing buildings during earthquake motions has been an area of research in the last decades due to the advance of structural monitoring technology and system identification techniques.

Most notably, Stewart et al. (1999c) have evaluated SSI effects for 77 strong motion recordings at 57 sites and estimated period lengthening and damping values by analyzing the recordings of structural motion with the analytical system identification procedures described in Stewart et al. (1999a). Period lengthening has been thus estimated for a variety of seismic intensities as well as structural, foundation and geotechnical characteristics. **Figure 4.3** presents the effect of structure-to-soil stiffness factor $s = h/V_sT_{str.f}$ on period lengthening for different cases of earthquake events, sites and buildings. These results confirm the importance of structure-to-soil stiffness on period elongation. In general, in this or similar field and real-scale studies (Todorovska 2002b; Trifunac et al. 2001b) structural and soil nonlinearity are indirectly identified as factors contributing in period elongation.

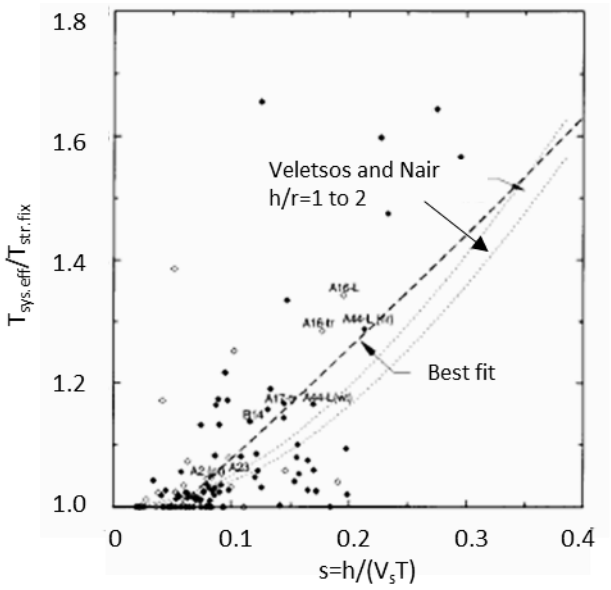

Figure 4.3: Period lengthening $T_{sys.eff}/T_{sys.f}$ ratio for sites (Stewart et al. 1999c) and analytical estimation from Veletsos and Nair (1975)

A more firm correlation of period elongation with earthquake intensity is found in the study of Chen et al. (2013a), which is based on centrifuge experiments on two structure-foundation-soil models subjected to a number of seismic motions. The centrifuge experiments were performed with two configurations; in the first experiment, the two structures were sufficiently apart (Test 1), whereas in the second the two structures were next to each other in order to simulate structure-soil-structure interaction (Test 2). The time-varying system characteristics were extracted by time-domain identification procedures based on the work of Stewart and Fenves (1998).

Period elongation, *aPLR,* is defined in this study as the ratio of the period of the nonlinear *flexible-base* system T_{sys} over the period of the fixed-base structure $T_{str.fix}$. **Figure 4.4a** presents the time-variation of

aPLR during the high intensity earthquake motion SCS-H for Test 1. It is observed that elastic *aPLR* values, which correspond to the initial (i.e. prior to shaking) system properties are below 1.1. During strong shaking peak values of *aPLR* reach 1.35 and by the end of shaking *aPLR* values tend to return to their initial – elastic – state. These results indicate that period elongation due to soil softening during a high intensity earthquake may become greater than the analytically estimated for the *flexible* system within the linear elastic SSI framework which is equal to $\alpha PLR=1.09$ (ordinate value for t=0 sec in Figure 4a). Dynamic compaction and densification of the underlying soil during shaking contributes to the return to the initial soil properties after the end of the shake. This is not the case when nonlinear period elongation is caused by, e.g., concrete nonlinear behavior, since concrete softening due to cracking is irreversible. **Figure 4.4b** quantifies the effect of peak ground acceleration (*PGA*) on peak period lengthening in the centrifuge experiments (white symbols) and the corresponding lumped system analytical computations (black symbols). A direct correlation of *PGA* with period elongation is thus established, while maximum *aPLR* values seem to reach a plateau for *PGA* > 0.50g.

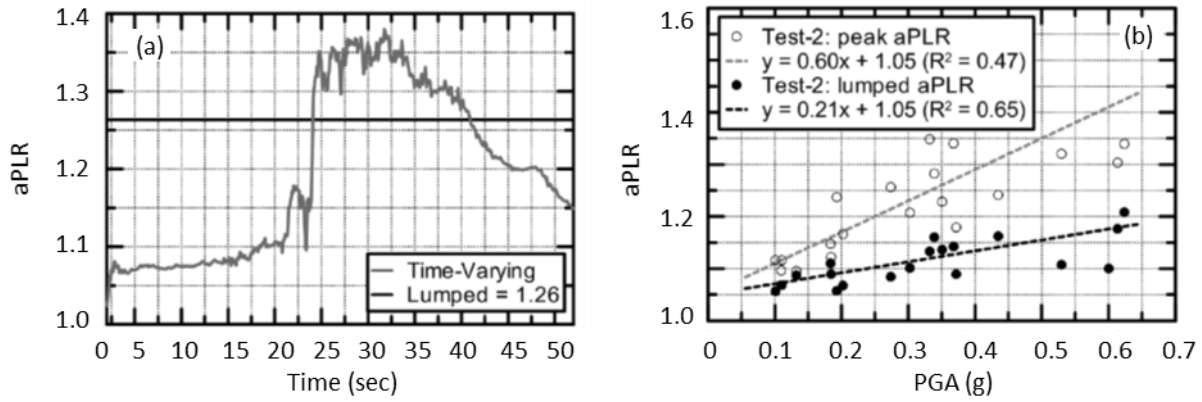

Figure 4.4: (a) Time-varying period elongation (aPLR) during the strong shake event (SCS-H Test 1) and (b) correlation of peak aPLR values (white cirles) with peak ground acceleration (PGA).

Concluding this selective review of published studies, it is seen that the estimation of the effective period for shallow foundation-structure systems resting either on dry or on liquefiable soil is at the center of research interest. Principally, period elongation is correlated to the seismic intensity and to the structure-to-soil stiffness factor $s=h/V_sT$. Nevertheless, it should be acknowledged that the scarcity of data for intense shaking, combined with the complexity of the SSI mechanisms, prohibits a systematic quantitative identification of all important SSI parameters and their effect on the system response.

4.3 Numerical estimation of characteristic system periods of vibration

4.3.1 Estimation of the "elastic" (pre-shaking) system period, $T_{sys.el}$

Estimation of shear wave velocity in the foundation soil. _ The analytical procedure described in paragraph 4.2.1 is employed for the estimation of the natural period of system at their elastic state, i.e., prior to any seismic shaking and damage accumulation, designated as $T_{sys.el}$. Following the analytical procedure of (Federal Emergency Management Agency (FEMA) 1997), soil properties are introduced in the rotational and horizontal stiffness springs of **Table 6** in terms of the shear modulus *G* of the foundation soil, which depends on the stress state and relative density. In this case, the soil properties that need to be determined concern the soil layers under the footing area influenced by the building weight. From a practical point of view, a direct calculation of the soil modulus using geotechnical data under such conditions is essentially impossible without experimentally obtaining the associated stress-strain relations. As far as the numerical analyses are concerned, the formulations of the constitutive model NTUA-Sand, which is employed in the present study, also prohibit the direct estimation of shear modulus. More specifically, this model follows the classical constitutive formulation of elasto-plasticity, in which strains are decomposed into an "elastic" and a "plastic" part. As mentioned in Chapter 3, the "elastic" stress-strain relation is that of a non-linear hysteretic "elastic" form and the corresponding maximum shear modulus G_{max} is given from the well-established Hardin (1978) formula:

$$G_{max} = \frac{B p_\alpha}{0.3 + 0.7e} \sqrt{\frac{p}{p_a}} \qquad 4.4$$

where:

- B model parameter
- e void ratio
- p isotropic stress
- p_a atmospheric pressure (=98.1kPa)

The maximum shear modulus serves, thus, as an upper limit value of the actual stiffness obtained through stress-strain loading cycles. Since it is a function of the average effective normal stress, its variation with depth under the footing compared to the one at the free-field is a useful tool to estimate the foundation influence depth. As observed in **Figure 4.5,** the overburden pressure of the 4m × 4m footing considered

in this study, and a total super-structure weight of 179.4kN, leads to increased values of G_{max} for a depth of approximately 8-10m, i.e., about twice the foundation width.

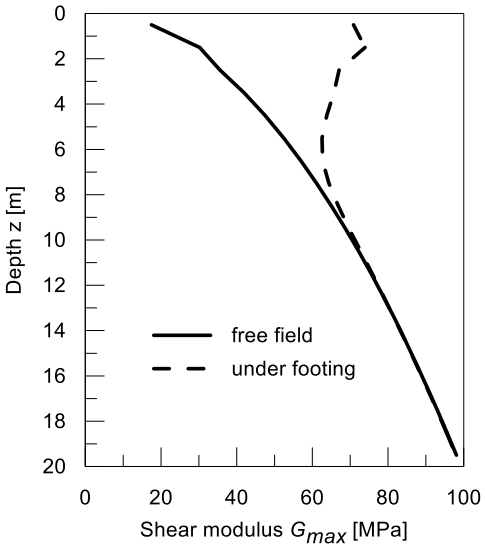

Figure 4.5: Maximum shear modulus G_{max} variation with depth under the footing and at the free field (numerical analysis results).

Given the difficulties in the direct estimation of the foundation soil shear modulus, the "pulse method" is used in this study, as it is schematically described in **Figure 4.6**. Specifically, a sinusoidal pulse is applied at the soil base and the time difference Δt between the first arrival times of the pulse at the footing level and at depth of influence H under the footing is estimated. Thus, the average shear wave velocity is estimated as:

$$V_s = \frac{H}{\Delta t} \tag{4.5}$$

The examined soil stratum is selected in the proximity of the footing and has a thickness of H = 10m which is the estimated influence depth from Figure 4.5. It is noted that engineering practice would typically involve: i) measurement of V_s profiles near the building of interest using crosshole and downhole testing, or ii) correlation of free-field soil properties with V_s values according to Code provisions and literature investigations. The latter is widely used in practice and would either derive values of V_s based on the ground type, e.g., as specified in CEN (European Committee for Standardization) 2004) (2004), or correlate them with corrected N_{SPT} values (corrected for soil profile non-uniformity, structure weight etc.) measured at the free field (NIST 2012a). Nevertheless, in the present study shear wave velocities are

measured near the building as in the former scenario, since it provides more accurate soil properties with reasonable ease of application.

The "elastic" shear wave velocity $V_{s,o}$ of the foundation soil is obtained by applying a pulse at the base of the model prior to the earthquake excitation. The maximum acceleration and the excitation period of the pulse is set at a_{max} = 0.15g and $T_{ex\,c}$= 0.25 sec, respectively. First arrival times are determined as the time when propagating wave amplitudes – at the footing and at the z=10m level – first exceeded 0.05g in their respective acceleration time-histories. The same procedure is also used for the estimation of post-shake values of shear wave velocities $V_{s.fin}$ for the soil stratum under the footing, as explained above. For that purpose, two cases are considered; one where liquefaction occurs and another where soil conditions are non-susceptible to liquefaction. A "quiet" period of 2-3sec follows the end of shaking so that soil and structural vibrations cease. In the case of liquefaction, excess pore water pressure drainage is not permitted during the "quiet" period in order to ensure liquefied soil conditions. A single pulse is applied at the soil base with acceleration amplitude (a_{max} = 0.30g) chosen as such in order to ensure incoming waves at the surface with sufficient – and measurable – amplitude.

Table 8 summarizes average values of shear wave velocities $V_{s,o}$ under footings with different levels of overburden pressure. It is seen that shear wave velocity for the reference soil and foundation parameters (D_r = 45/60%, H_c = 2m, *BxB* = 4m×4m) has an average value of approximately 125m/s, while the effect of overburden pressure within the examined range is minimal. The post- to pre-shaking shear wave velocity ratios $V_{s,fin}/V_{s,o}$ calculated under the footing are presented in **Figure 4.7a** and **b** for liquefied and non-liquefiable soil conditions respectively. In the first case, ratios average ≈ 0.30 indicating a severe – overall – stiffness degradation of the foundation soil, despite the fact that r_u ratios at the improved crust are approximately zero. For comparison, $V_{s,fin}/V_{s,o}$ ratios at free field conditions after complete liquefaction were calculated equal to 0.2 (dotted red line in **Figure 4.7a**), while literature suggests values in the range 0.10 – 0.23 (yellow shaded area in **Figure 4.7a)** (Tsiapas 2017a). In the non-liquefiable case $V_{s,fin}/V_{s,o}$ ratios average more than unity (≈1.2), a fact that is attributed to soil densification due to seismic settlements.

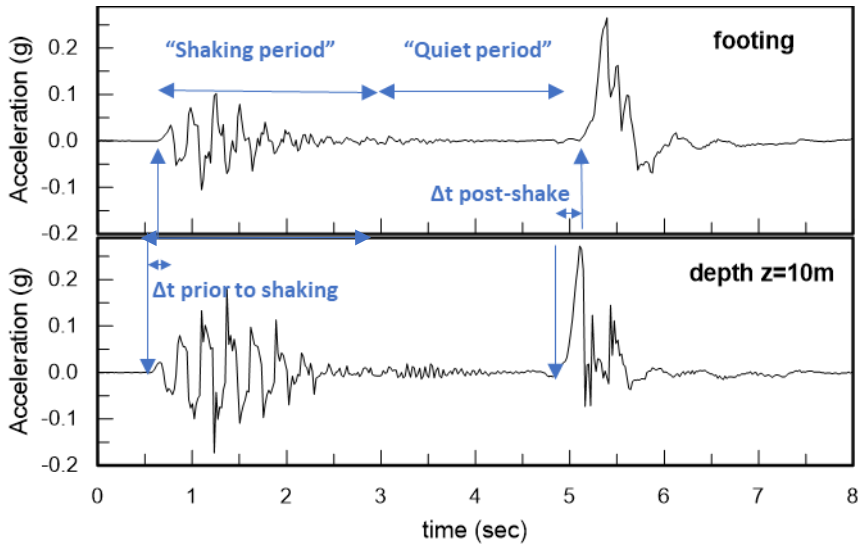

Figure 4.6: Example of the "pulse method" for the shear wave evaluation of "elastic", i.e. *prior to shake*, and *post-shaking* foundation soil.

Table 8: Initial "elastic" (pre-shake) values of average shear wave velocities $V_{s,o}$ under footings with different overburden pressure.

	Overburden pressure (kPa)			
	52	**68**	**80**	**100**
***Vs,o* (m/s²)**	123.2	121.1	123.2	127.3

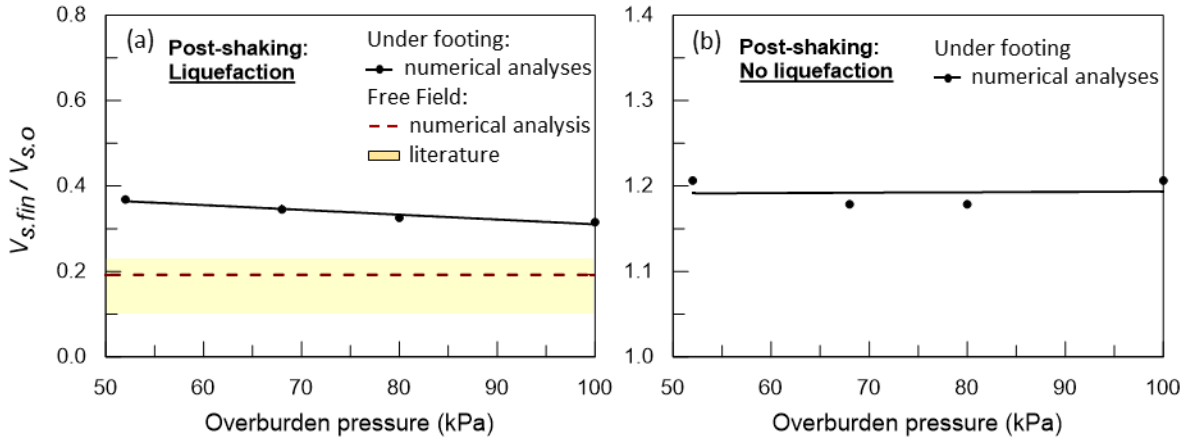

Figure 4.7: Average post- to pre-shake shear wave velocity ratios $V_{s,fin}/V_{s,o}$ foundation soil (up to ≈2B) for (a) liquefied and (b) non-liquefiable conditions.

Analytical calculation of $T_{sys.el}$ values ._ The incentive of this chapter is to estimate "elastic" values of system periods $T_{sys.el}$ from an engineering practice perspective, thus, utilizing the prescribed soil-structure interaction framework of code provisions (Equation 4.1) and employing realistically computed (with the foregoing procedure) values of shear wave velocity V_s for the initial (pre-shaking) foundation soil conditions.

The analytical approach of soil-structure interaction is illustrated by examining the reference structure of **Figure 4.8** which simulates a typical design of a single bridge pier modeled as a simplified single-degree-of-freedom system on a flexible base, with translational spring stiffness k_x and rotational spring stiffness k_{ry}. The structure is h = 3.0m in height, has an uncracked cross-section area of 0.49m^2 and concentrated deck mass of 179.4tn. It is supported upon a shallow square footing with width B = 4m and thickness d = 0.6m. The soil profile consists of a 20m deep sand deposit with the water table 1m over ground surface. Under the structure, an improved shallow crust with depth H_{imp} = 2m and relative density D_r = 60% lays on top of a natural sand deposit of D_r = 45% with an average pre-shake shear wave velocity $V_{s,o}$ = 125m/s under the footing, as described previously. The resulting values of structural stiffness k_{str} and static spring stiffnesses k_x and k_{ry} are summarized in **Table 9** along with values of the corresponding soil-structure interaction parameters. Namely: (a) structure-to-soil stiffness ratio is s = 0.07, thus, indicating a relatively flexible structure compared to soil compliance, (b) slenderness ratio h/r = 1.06, indicating an average-to-short structure, and (c) mass ratio γ = 4.00 indicating a medium-to-light mass structure. The corresponding period elongation of the structure-foundation-soil system is $T_{sys.el}/T_{str.f}$ = 1.32. All computations are summarized in **Table 9**.

It is noteworthy that Code provisions characterize structural systems with structure-to-soil stiffness ratio s < 0.1 as "typical building structures on soil and weathered rock sites" and suggest small values of period elongation, i.e., smaller than 1.10 ((Federal Emergency Management Agency (FEMA) 1997)). The particular discrepancy in period elongation between the examined structure and code guidelines is attributed to differences in the structural characteristics between the bridge pier and typical structures considered in codes. More specifically, bridge piers are essentially cantilever structures and as a result they are considerably more flexible for their given height than framed buildings. Typical frame structures, on the other hand, with equivalent structural stiffness $h/T_{str.f}$ and, thus, s = $h/V_sT_{str.f}$ ratio would most probably be designed with greater mat foundation dimensions B. As a result, it is expected that horizontal and rocking spring values K_x and K_{ry} will be increased and period elongation $T_{sys.el}/T_{str.f}$ of frame structures

will be decreased compared to the examined bridge piers. The above considerations are better illustrated in **Figure 4.8**.

Table 9: System properties and soil-structure interaction parameters of the reference SDOF system.

System Properties		SSI Parameters	
$k_{str} = \frac{3EI}{h^3}$	57.560 kN/m	$s = \frac{h}{V_s T_{str}}$	0.07
$k_x = \frac{GB}{2-v}\left[6.8\left(\frac{L}{B}\right)^{0.65} + 2.4\right]$	445.160 kN/m	h/r	1.06
$k_{ry} = \frac{GB^3}{1-v}\left[3.73\left(\frac{L}{B}\right)^{2.4} + 0.27\right]$	852.280 kNm	$\gamma = \frac{m}{\rho r^3}$	4.00
$T_{str.f} = 0.35\ sec$		$T_{sys.el}/T_{str.f} = \sqrt{1 + \frac{k_{str}}{k_x} + \frac{k_{str} \cdot h^2}{k_{ry}}} = 1.32$	

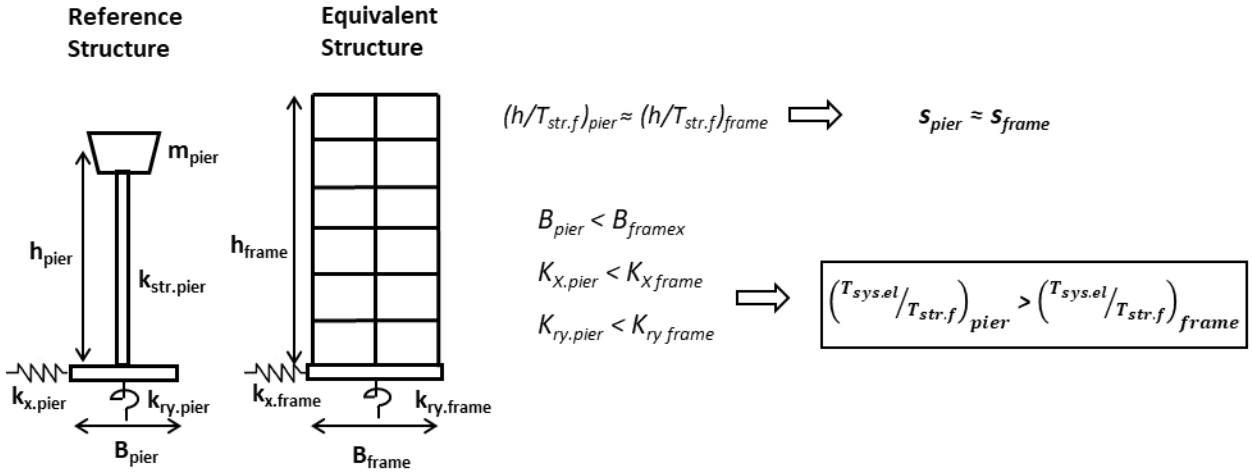

Figure 4.8: Bridge-pier (reference structure) and typical frame structure of equivalent flexibility.

The effects of soil-structure interaction on period elongation are examined, next, by parametrically varying the structural characteristics of the reference single-degree-of-freedom structure so that the aforementioned dimensionless SSI parameters (i.e., structure-to-soil-stiffness *s*, slenderness ratio *h/r* and mass ratio *γ*) remain within the typical working range. An important consideration of the particular effort is to modify system characteristics while ensuring soil-structure interaction soundness and realistic

properties of the physical models at the same time. To this end, parametric investigation primarily focuses on modifying structural instead of geotechnical parameters, since the highly-nonlinear soil response may introduce secondary effects on the dynamic response of systems which are not easy to assess a-priori. More specifically:

a) The effect of *structure-to-soil-stiffness ratio s* is examined for dynamic systems with different structural stiffness k_{str} and constant structural mass, thus, with varying fixed-base structural period $T_{str.f}$. The rest of the soil-structure interaction parameters, i.e., h/r and γ, are kept constant.
b) Regarding the effect of *relative mass ratio γ,* dynamic systems with different structural mass *m* were examined. In order to ensure equivalent fixed-base structural period $T_{str.f}$ and, thus, structure-to-soil-stiffness ratio s = $h/V_sT_{str.f}$, structural stiffness k_{str} varied along with the variation of structural mass.
c) Lastly, concerning systems with varying *slenderness ratio h/r* two scenarios are considered:

   Scenario A ($h/T_{str.f}$ constant): The structural height *h* is increased while structural flexibility, in terms of $h/T_{str.f}$, remains constant. In this manner the remaining soil-structure interaction parameters (*s*, *γ*) are kept moderately constant. Nevertheless, the significant increase of $T_{str.fix}$ – and of the associated $T_{sys.el}$ – for greater heights *h*, requires similarly significant increase of the excitation period T_{exc} in order to capture the working spectrum of period ratios $T_{sys.el}/T_{exc}$. Consequently, although this scenario is the most methodologically sound, its application in soil dynamic problems is a difficult task. Hence, it is examined in this chapter only for completeness reasons.

   Scenario B ($T_{sys.el}$ constant): The structural height *h* is increased along with the cross-section area, i.e. with *EI,* aiming at maintaining the "elastic" system period $T_{sys.el}$ constant. As a result, for the given design specifications, the variation of structure-to-soil-stiffness ratio *s* is minimal. This scenario proves to be the most suitable one for the problem at hand in order to focus on the effects of slenderness ratio and at the same time to isolate the effects of the remaining factors.

Cumulative results from the parametric study are presented in **Figure 4.9.** It is noted that:

(a) The effect of structure-to-soil stiffness ratio *s* on period elongation (**Figure 4.9a**) is examined for the range of *s* = 0.0-0.25, which extends from stiff structures with fixed-base period $T_{str.f} \approx 0.01$sec to very flexible structures with $T_{str.f} \approx 1.80$sec. All structures examined are founded on loose-to-medium cohesionless soil, i.e. $V_s \approx 125$m/s. Period elongation increases for increasing *s* ratios or, alternatively, for decreasing structural periods $T_{str.f,}$ from $T_{sys.el}/T_{str.f} = 1.0$ for stiff structures to $T_{sys.el}/T_{str.f} \approx 2.8$ very flexible structures.
(b) The mass ratio *γ* has only moderate effect on period elongation, as shown in **Figure 4.9b**. The examined range of mass ratios, i.e. $\gamma \approx 0.1$-3.5, varies from light systems with structural mass equal

to 5tn to heavy systems with mass equal to 155tn. In this case, period elongation increases almost linearly from $T_{sys.el}/T_{str.f} \approx 1.0$ for light systems to $T_{sys.el}/T_{str.f} \approx 1.4$ for heavy systems. As mentioned earlier, structural mass is not introduced in Equation 4.1 and therefore it does not directly affect period elongation. In fact, period elongation in this case is the outcome of structural stiffness k_{str} increase, which follows the increase in structural mass m, as explained earlier in this chapter. Essentially, heavier structures experience increased period elongation since they constitute systems with greater structural stiffness.

(c) Slenderness ratio h/r effects are examined for scenario A (i.e. for constant structural stiffness expressed in terms of $h/T_{str.f}$) in **Figure 4.9c** and for scenario B (constant $T_{sys.el}$) in **Figure 4.9d**. The two scenarios examine fundamentally different dynamic systems and their characteristics are inverse. In scenario A, structures with increased slenderness ratio are more flexible, i.e. $T_{str.f}$ is larger, and consequently they experience less period elongation. On the contrary, in scenario B structures with increased slenderness ratio are stiffer, i.e. $T_{str.f}$ is larger, in order to maintain $T_{sys.el}$ constant and consequently they experience smaller period elongation. It is noted that the former findings are compatible with the findings of P.Wolf (1985) while the latter agree with the results presented in (NIST 2012; Veletsos, A. S., & Meek 1974).

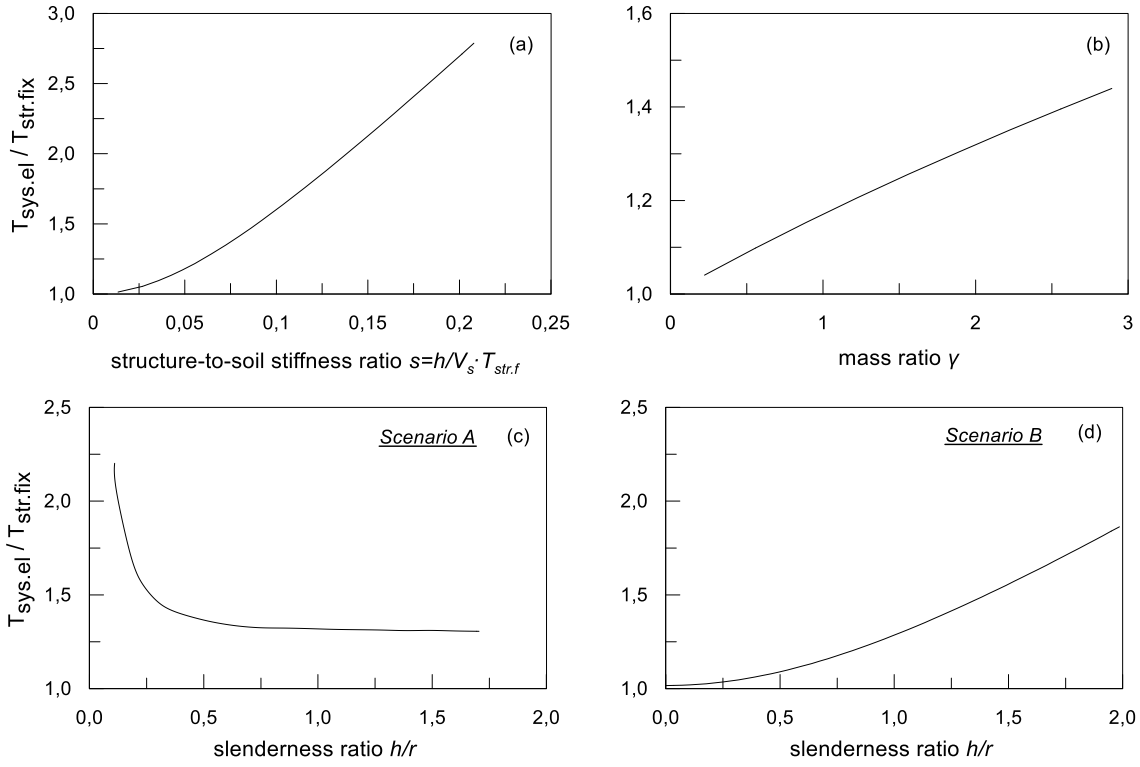

Figure 4.9: Period elongation of the "elastic" system according to analytical calculations (NIST 2012) as a function of (a) structure-to-soil stiffness, (b) mass ratio γ and slenderness ratio h/r for (c) constant $h/T_{str.f}$ ratio (scenario A) and (d) constant system period T_{sys} (scenario B).

4.3.2 Estimation of effective (non-linear) system period during shaking, $T_{sys.eff}$

The use of Transfer Functions._ As previously mentioned, nonlinear soil-structure response during strong earthquakes cannot be based on linear elastic theory for capturing the dynamic system properties. Increased levels of soil nonlinearity, more pronounced in the case of liquefaction, result in time varying soil properties and, consequently, system periods. The proposed procedure to estimate system periods employs Transfer Functions (TF) that relate horizontal accelerations of the structural mass and at the free field in the frequency domain, as shown in the schematic **Figure 4.10.** In more detail, the soil model is dynamically excited at its base with a horizontal acceleration wave, which physically simulates a vertically propagating shear wave in the underlying bedrock. The input motion applied is a white-noise signal, i.e., a random signal containing frequencies of equal intensity resulting in – theoretically – constant spectral density (**Figure 4.11e**). Horizontal accelerations are recorded at the free-field (x>2B) and at the structural mass level as shown in **Figure 4.11a** and **c** for non-liquefiable and in **Figure 4.11b** and **11d** for liquefied soil conditions. It is observed that the onset of liquefaction takes place at approximately $t \approx$ 3.5-4.0sec, at which point free-field and structural accelerations start to attenuate.

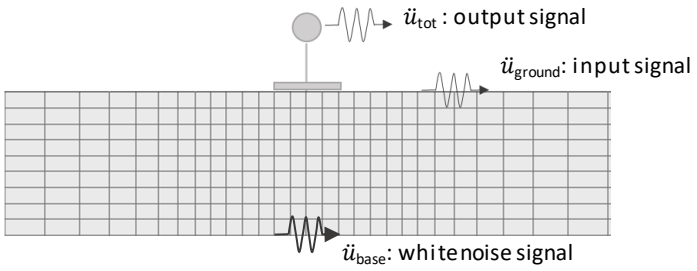

Figure 4.10: Schematic representation of signal monitoring in the structure-foundation-soil numerical model.

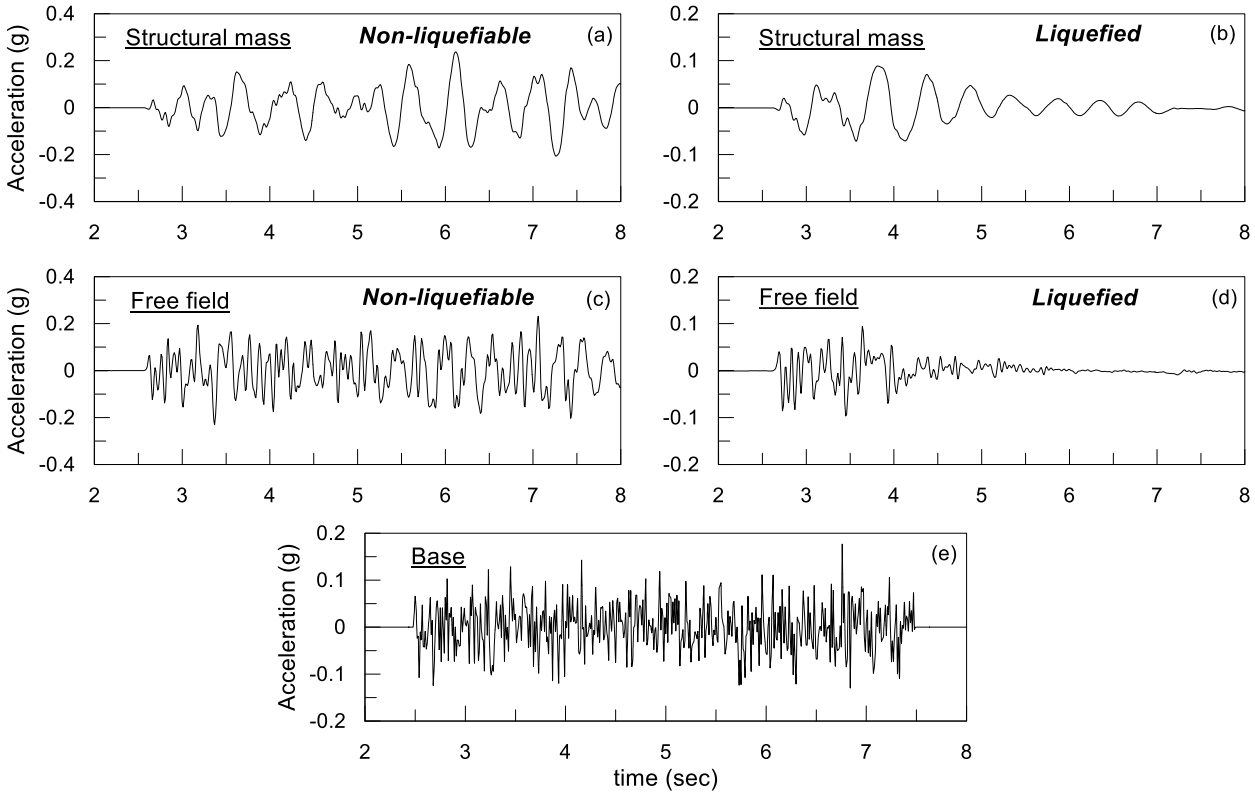

Figure 4.11: Horizontal acceleration time-histories for non-liquefiable (*first column*) and liquefied conditions (*second column*), at structural mass level (*first* row) and at ground level (second row). White-noise signal used as base excitation for both conditions with PGA = 0.15g (figure e).

Figure 4.12a and **b** compare the elastic response spectra with 5% viscous damping corresponding to structural and free-field recordings for both non-liquefiable and liquefied conditions. The structure-foundation-soil system for both cases is described in detail in chapter 3. Recorded motions are subjected to lowpass filtering of frequencies higher than 10 Hz in order to address numerical noise issues which are common for highly-nonlinear problems, such as liquefaction (Tsiapas and Bouckovalas 2018). It is observed that spectral amplifications of the structural motion occur around period values greater than approximately 0.35sec, which corresponds to the fixed-base structural period $T_{str.f}$. Regarding the free-field motion, spectral accelerations are mostly amplified in the low period range 0.10-0.35sec for non-liquefiable conditions and in the higher period range 0.40-0.80sec in the presence of liquefaction.

The frequency response characteristics of the structural system are estimated by examining the Transfer Function of structure-to-free-field accelerations in the frequency domain for non-liquefiable (**Figure 4.12c**) and liquefied conditions (**Figure 4.12d**). Due to the intense nonlinearity of the cyclic soil response, system eigenvalues do not necessarily correspond to singular peaks of the TFs. On the contrary, time-varying soil properties result in distribution of TF peaks in a wider range of periods, more pronounced in

the case of non-liquefiable soil conditions. Thus, focusing first on **Figure 4.12c** for non-liquefiable soil, it is observed that the predominant TF peak occurs is in the proximity of the previously discussed "elastic" system period $T_{sys.el}$ = 0.46 sec. Nevertheless, significant spectral amplifications are also observed in the period range $T \approx 0.46$ - 1.00sec, indicating significant period elongation related to soil softening due to the horizontal translation and rocking-induced shear straining under the footing. This extended range of periods is thus defined as the *effective* range period of the system $T_{sys.eff}$ during shaking.

In the case of liquefied conditions (**Figure 4.12d**) the TF graph exhibits a more or less singular peak instead of the previously observed wide range distribution of peaks. The period of this singular peak is $T \approx 0.52$sec, i.e., about 12% higher than the "elastic" system period $T_{sys.el} \approx 0.46$ sec, indicating significant soil softening. The above findings are indicative of the structure-foundation-soil system dynamic response under the prescribed conditions. More specifically, low values of the Factor of Safety against liquefaction (FS_L) result in swift pore-pressure built up and therefore ground motions are drastically attenuated. Moreover, the presence of the improved shallow crust and the increased shear stress offset under the structure result in decreased pore-pressure ratios compared to the free-field. Consequently, the dominant properties of the foundation soil are essentially constant in time and the associated liquefaction-induced softening is significant but less than in the free field. The above explain the presence of a single peak in the computed TF, as well as the moderate (by 12%) elongation of the system period. The range of effective system periods T ≈0.40-0.65sec, shown with the shaded area in **Figure 4.12d**, is much narrower in the presence of liquefaction and it is practically centered on the singular peak of the TF graph.

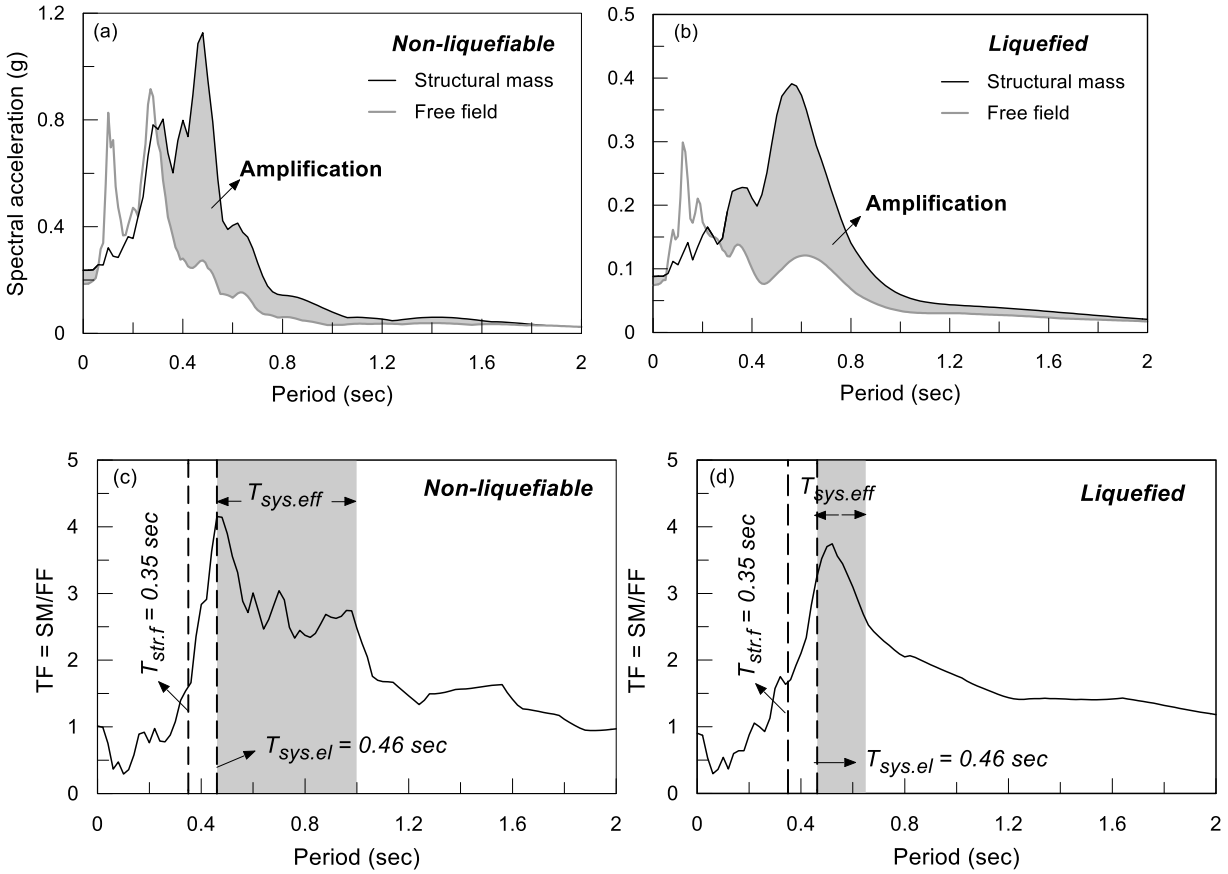

Figure 4.12: (a)-(b) Comparison between structural and free-field spectral accelerations, (c)-(d) Transfer Functions (TF) of structural (SM) and free-field (FF) motion in the frequency domain, for non-liquefiable (a, c) and liquefied (b, d) conditions (Results for reference system: $T_{str.f}$ = 0.35 sec, h/r = 1.06, s = 0.07, γ =4.00)

Simplified frequency content estimates of Transfer Functions. _ The frequency content characterization of spectra with a single parameter is not straightforward, especially when the spectral response is characterized by nonlinearity. The most relevant field that has received wide attention so far is that for the frequency content characterization of seismic ground motions. For instance, various simplified estimates have been proposed for the single-parameter characterization of ground motion response spectra, such as (Rathje et al. 1998a):

- The predominant period $T_{p,}$ which is the period corresponding to the maximum value of spectral accelerations
- The mean period T_m defined as

$$T_m = \frac{\sum_i C_i^2 T_i}{\sum_i C_i^2} \qquad 4.6$$

where C_i is the Fourier amplitude corresponding to a discrete period T_i

- The smoothed spectral predominant period T_o defined as

$$T_o = \frac{\sum_i T_i \cdot \ln\left[S_a(T_i)\right] \cdot H[S_a(T_i) - 1.2MHA]}{\sum_i \ln\left[S_a(T_i)\right] \cdot H[S_a(T_i) - 1.2MHA]} \quad 4.7$$

where T_i is the discrete period of the response spectrum, $S_a(T_i)$ is the spectral acceleration at period T_i, *MHA* is the maximum ground acceleration and *H[x]* is the "heavy-side" function that equals 1 for $x > 0$ and 0 for $x < 0$.

The above simplified estimates (descriptors) of ground motion frequency content can be used for the determination of a single-valued system period that best characterizes the frequency content of Transfer Function (TF) spectra. Essentially, the particular estimate represents an "effective" system period $T_{sys.eff}$ which is an approximation of the varying period of the structure-foundation-soil system during a seismic event. The framework employed herein for the calculation of $T_{sys.eff}$ focuses on the aforementioned estimates found in literature. Specifically:

- The predominant system period $T_{sys.p}$ is utilized in Transfer Functions derived from Fourier amplitude spectra (**Figure 4.13a-b**) as well as from elastic response spectra with 5% viscous damping (**Figure 4.13c-d**). $T_{sys.p}$ is the most straightforward estimate since it directly calculates the period at which the peak spectral amplification is observed.
- The mean system period $T_{sys.m}$ is used in the case of Fourier spectra and weights the contribution of TF amplifications by the square of C_i at each period following the definition of Equation 4.6. In this case, C_i (T_i) is defined as the TF amplitude at period T_i . Necessary adjustments in $T_{sys.m}$ determination constitutes the inclusion of C_i contributions greater than unity, i.e., representing structural motion amplification, and filtering high frequency amplifications by considering TF amplifications for $T_i > T_{str.f}$.
- Lastly, the smoothed spectral predominant system period $T_{sys.o}$ modifies Equation 4.7 in order to incorporate TF amplifications of significant spectral contributions, as follows:

$$T_{sys.o} = \frac{\sum_i T_i \cdot \ln\left[TF(T_i)\right] \cdot H[TF(T_i) - \max\left[TF(T_i)\right]/2]}{\sum_i \ln\left[TF(T_i)\right] \cdot H[TF(T_i) - \max\left[TF(T_i)\right]/2]} \quad 4.8$$

Figure 4.13 presents $T_{sys.eff}$ estimation by considering the reference system examined before, i.e. $T_{str.f}$ = 0.35 sec, h/r = 1.06, s = 0.07, γ =4.00. Predominant system period $T_{sys.p}$ is the most commonly used estimate of spectra frequency content due to its simplicity. Nevertheless, its applicability is limited in cases with spectral contributions concentrated around a single frequency. In that way, two spectra peaking at the same frequency but with drastically different frequency content will exhibit identical $T_{sys.p}$. Additionally, in cases where multiple spectral peaks are present, arbitrary selection of the maximum value does not

necessarily characterize the frequency content. $T_{sys.p}$ estimates evaluated in **Figure 4.13** exemplify the above considerations. In the case of non-liquefiable conditions and for TF derived from Fourier amplitude spectra (**Figure 4.13a**), $T_{sys.p}$ appears to overestimate system period, i.e. $T_{sys.p}$ = 0.57 sec, due to the presence of consecutive spectral peaks. On the contrary, in the case of TF derived from response spectra (**Figure 4.13c**) $T_{sys.p}$ is equal to 0.48sec, for non-liquefiable conditions, a value that underestimates system period since it does not account for spectral amplifications other than the predominant. The use of $T_{sys.p}$ seems most suited for the case of liquefaction where TF spectra are dominated by a single peak that corresponds to the liquefied subsoil properties (**Figure 4.13b** and **d**). In this case $T_{sys.p}$ values are equal to 0.49sec and 0.52sec for Fourier and response spectra, respectively.

Next, the application of the mean system period $T_{sys.m}$ is evaluated as an estimate of Fourier spectra TFs (**Figure 4.13a,b**). In the case of liquefied conditions $T_{sys.m}$ equals 0.52sec, i.e. slightly greater than $T_{sys.p}$ since period elongation due to soil softening through time is accounted for. However, in the case of non-liquefiable conditions $T_{sys.m}$ equals to 0.51sec which is lower than the respective value of $T_{sys.p.}$ This is primarily attributed to the aforementioned potential overestimation of system period by $T_{sys.p}$ in the presence of multiple peaks. Overall, the use of mean system period may prove equivalent, as in **Figure 4.13b**, or advantageous, as in **Figure 4.13a**, compared to that of predominant system period.

Lastly, smoothed spectral predominant system period $T_{sys.o}$ is used for TFs derived from elastic response spectra with 5% damping (**Figure 4.13c** and **d).** As expected, $T_{sys.o}$ estimates predict greater values of system periods compared to $T_{sys.p}$ ones, since spectral contributions for the whole spectrum of periods are accounted for. This is more pronounced in the non-liquefiable case, in which $T_{sys.o}$ = 0.68sec, compared to the liquefied one, in which $T_{sys.o}$ = 0.63sec. Concludingly, the use of $T_{sys.o}$ estimates provides a better characterization of the TF frequency content, a fact that is more pronounced in the case of systems with significant spectral amplification at a wide period range.

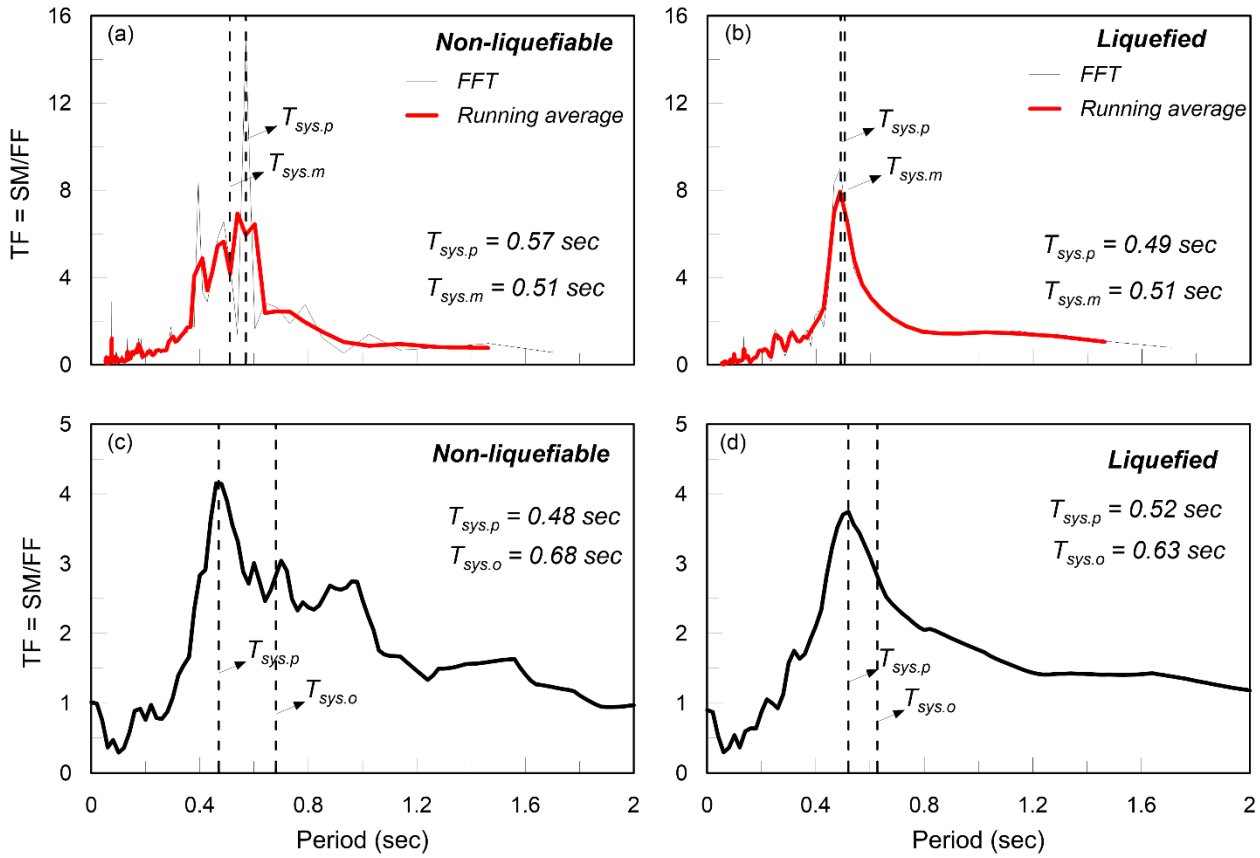

Figure 4.13: Comparison of system period estimates $T_{sys.p}$, $T_{sys.m}$ for TF derived from Fourier Spectra (a, b) and $T_{sys.p}$, $T_{sys.o}$ for TF derived from elastic response spectra with ζ = 5% (c, d).

4.3.3 Results of parametric investigation

The procedure followed herein aims, at first, to shed more light into the mechanisms of nonlinear period elongation during seismic events and, additionally, to explicitly express the effect of certain parameters on the effective system period $T_{sys.eff}$. Based on the methodology mentioned above, the effective system period $T_{sys.eff}$ is assessed as a function of different excitation, structural and soil parameters. Specifically, the varying excitation characteristics of the incoming seismic waves, in terms of amplitude and frequency content, are controlled by the underlying soil profile characteristics (i.e. profile height on top of stiff "bedrock", soil dynamic properties, soil strata spatial distribution) in combination with seismological characteristics (i.e. distance from the epicenter, orientation and type of the fault). In this study, the *peak ground acceleration* (*PGA*) and the *soil profile natural period* (T_{soil}) are examined by controlling the input motion amplitude and the profile height, respectively. Regarding structural parameters, the governing soil-structure interaction (*SSI*) parameters, examined before, are investigated herein, i.e. slenderness ratio

h/r and relative mass ratio *γ*. Additionally, geotechnical parameters affecting foundation bearing capacity, i.e. factor of safety (*FS*) and depth of improved zone (H_{imp}), need also to be considered.

The smoothed spectral predominant system period $T_{sys.o}$ and the predominant system period $T_{sys.p}$ are employed comparingly in order to assess their applicability as measures of the effective system period. Transfer functions (TF) are derived from elastic response spectra with ζ = 5% since the latter provide smoother distribution of amplifications compared to Fourier Spectra, as it is seen in the foregoing section. The obtained effective system period $T_{sys.eff}$ is correlated to the elastic system period $T_{sys.el}$, calculated in paragraph 4.3.1, since analytical relations of "elastic" period elongation are widely used in practice according to code provisions (NIST 2012a). Moreover, the particular formulation enables the direct identification of nonlinearity sources in the response of structure-foundation-soil systems.

4.3.3.1 Non-Liquefiable soil conditions

Overview. In this section, effective system periods $T_{sys.eff}$ of structure-foundation-soil systems are assessed parametrically for *non-liquefiable soil conditions*. The following parameters controlling the structural response and, in extent $T_{sys.eff}$, are examined: the peak ground acceleration *PGA,* the period ratio $T_{soil}/T_{sys.el}$, the Factor of Safety *FS*, the relative mass ratio *γ* and the slenderness ratio *h/r.* The effect of soil-to-structure stiffness ratio *s* is not considered herein, since this parameter is directly related to $T_{soil}/T_{sys.el}$ ratio and the associated soil-to-structure resonance phenomena.

It is noted that, for customary soil and seismic conditions, the seismic motion characteristics at the ground surface (*PGA* and T_{soil}) are typically computed through numerical 1-D seismic ground response analyses, although analytical solutions may be also used for preliminary estimates. For instance, assuming a uniform visco-elastic soil layer resting on rigid bedrock, i.e. $T_b/T_{soil} \rightarrow 0$, soil amplification of a harmonic motion amplitude may be expressed in terms of the ground surface-to-outcropping bedrock amplitude ratio A_s, as:

$$|A_s| = \frac{1}{\left|\cos\left(\frac{\pi}{2}\frac{T^*_{soil}}{T_{exc}}\right) + ia^* sin\left(\frac{\pi}{2}\frac{T^*_{soil}}{T_{exc}}\right)\right|} \quad 4.9$$

where T_{exc} denotes the excitation period, T_b is the fundamental vibration period of a layer of outcropping bedrock with the same thickness *H*, $T^*_{soil} = T_{soil}(1 - i\xi_s)$ and $a^* = a(1 + i\xi_s)/(1 - i\xi_s)$, $\alpha = \rho_s/\rho_b$.

In the above equation soil nonlinearity is implicitly introduced through the elongated period of the soil column T_{soil} and the associated critical damping ratio ξ_s. In a more direct analytical approach, the earthquake magnitude, in terms of the peak bedrock acceleration a_{max}^b and the number of significant cycles *n,* is explicitly introduced into relations of soil amplification formulated via statistical analysis of a large number of numerical seismic ground response analyses (Bouckovalas and Papadimitriou 2003). Namely, the relative amplification ratio for the peak ground acceleration A_a is expressed as a function of the normalized soil period T_{soil}/T_{exc}, the peak bedrock acceleration a_{max}^b and the number of significant cycles *n,* as:

$$|A_a| = \frac{1 + C_{1,a}(T_{soil}/T_{exc})^2}{\sqrt{[1-(T_{soil}/T_{exc})^2]^2 + C_{2,a}(T_{soil}/T_{exc})^2}} \quad 4.10$$

with $$C_{1,a} = d_{1,a}\left(\frac{a_{max}^b}{g}\right)^{d_{2,a}} g(n)$$

$$g(n) = \frac{n^{d_{3,a}}}{1 + n^{d_{3,a}}}$$

$$C_{2,a} = d_{4,a} + d_{5,a}\frac{T_b}{T_{soil}}$$

with $d_{1,a}$ = 1.20, $d_{2,a}$ =-0.17, $d_{3,a}$ = 0.50, $d_{4,a}$ = 1.05 and $d_{5,a}$ = 0.57.

Similarly, the soil period T_{soil} is affected by the nonlinear soil response during shaking. Thus, the elongation of the nonlinear soil period T_{soil} is correlated to the average elastic shear wave velocity of the soil profile $V_{s,o}$ and the peal acceleration at the outcropping bedrock a_{max}^b as:

$$\frac{T_{soil}}{T_{soil,o}} = 1 + d_{1,T}\left(\bar{V}_{s,o}\right)^{d_{2,T}}\left(\frac{a_{max}^b}{g}\right)^{d_{3,T}} \quad 4.11$$

with $d_{1,T}$ = 5330, $d_{2,T}$ = -1.30 and $d_{3,T}$=1.04.

The above expressions enable the decoupling of the earthquake intensity and the soil parameters that govern soil amplification from the structural response identification process, reducing, thus, ground response parameters, merely, to *PGA* and $T_{soil}/T_{sys.el}$. The practical application of Bouckovalas and Papadimitriou (2003) methodology, is illustrated here for the reference soil profile with depth *H* = 20 m, shear wave velocity $V_{s.o} \approx$ 125 m/s and a rigid underlying bedrock, i.e. $T_b/T_{soil} \rightarrow 0$. Equation 4.11 is then solved for the excitation period T_{exc} considering two levels of peak bedrock acceleration a_{max}^b, i.e. 0.15g

and 0.60g and n=2 number of significant cycles. Regarding the small seismic intensity, Equation 4.11 results to $A_a \geq 1.0$, i.e. soil amplification, for excitation periods $T_{exc} \geq 0.05$ sec, which practically implies that the vast majority of the signal harmonics will result to soil amplification. In the case of greater seismic intensity, soil amplification takes place for a narrower spectrum of harmonics, i.e. for excitation periods $T_{exc} \geq 0.25$ sec. **Figure 4.14** shows the discussed effect of seismic intensity on soil amplification.

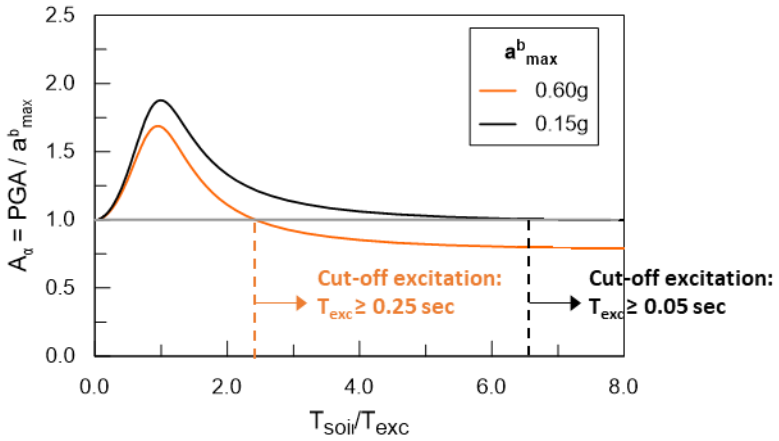

Figure 4.14: Variation of soil amplification A_a with the period ratio T_{soil}/T_{exc} for two levels of peak bedrock acceleration a^b_{max}.

Next, the above reference soil profile was subjected to base excitation using white-noise acceleration signals with amplitude a^b_{max} = 0.15g (seen in **Figure 4.11e**). **Figure 4.15a** presents the elastic response spectra TFs from these numerical analyses, for different levels of earthquake intensity, with free-field peak ground acceleration *PGA* ranging from 0.01 g to 0.92 g. It is observed that the peak of the TFs – corresponding to the predominant system period $T_{sys.p}$ – is more pronounced for the lower levels of seismic intensity, while the contribution of spectral amplifications for periods greater than the predominant period is enhanced with increasing intensity and more intense soil softening. For levels of *PGA* > 0.72g, the predominant system period is not clearly identifiable. The difference between the structural response for high (*PGA*= 0.72g) and medium (*PGA*=0.30g) intensity levels is presented in **Figure 4.15b-c.** As shown in **Figure 4.15b** maximum structural accelerations for the high intensity level (about 0.50g) are approximately double than those for moderate intensity level (approximately 0.25g). As a result, softening of the foundation soil is more significant during the high intensity shaking, as it is also indicated by the associated highly nonlinear moment-rotation loops shown in **Figure 4.15c**.

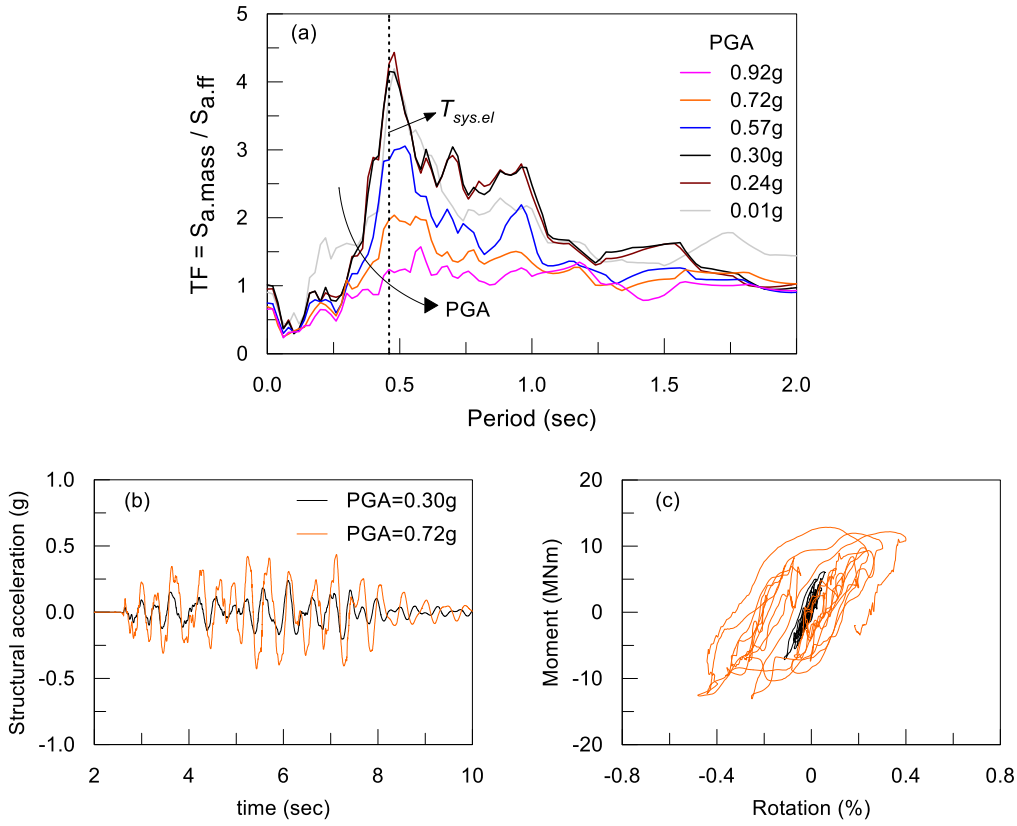

Figure 4.15: (a) Transfer functions of structural-to-free field acceleration response spectra for different levels of peak ground accelerations (*PGA*), (b) structural accelerations for high (*PGA*=0.72g) and medium (*PGA*=0.30g) intensity earthquakes and (c) corresponding moment-rotation response of the foundation.

Parametric Investigation._ The following parametric investigation focusses on the elongation of the effective system period $T_{sys.eff}$, utilizing two frequency estimates, i.e. the *smoothed spectral predominant system period* $T_{sys.o}$ and the *predominant system period* $T_{sys.p}$, as defined in previous paragraphs. **Figure 4.16** presents ratios of effective-to-elastic system periods $T_{sys.eff}/T_{sys.el}$ as functions of PGA for both the aforementioned effective period measures. $T_{sys.o}$ estimates appear up to 30-40% greater than $T_{sys.p}$ estimates. Moreover, there is only minimal elongation of the predominant system periods $T_{sys.p}$ for *PGA* values up to 0.35g, while the elongation increases more or less linearly for greater *PGA* values. On the other hand, using the $T_{sys.o}$ estimate, period ratios increase rapidly to $T_{sys.eff}/T_{sys.el} \approx 1.45$ for *PGA* = 0.20g while the rate of increase is considerably reduced for larger *PGA* values. It is noted that the numerical estimation of system period for *PGA* → 0 stumbles upon the difficulty of processing signals with amplitudes small enough to be close to numerical noise.

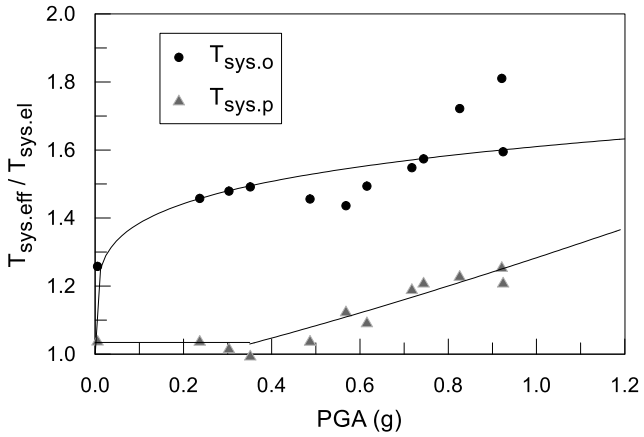

Figure 4.16: Ratios of effective-to-elastic system periods as a function of *PGA* obtained using the smoothed spectral predominant system period $T_{sys.o}$ (*black dots*) and the predominant system period $T_{sys.p}$ (*grey dots*) estimates.

In addition to the amplitude of ground motion, soil profile characteristics affect the frequency content of the incident waves propagating from the underlying bedrock to the ground surface. As a result, wave periods that are compatible with the natural period of the soil deposit are amplified, whereas other wave periods are de-amplified. It is, thus, expected that structures with system periods close to soil natural periods will exhibit the greatest motion amplification, as it is systematically observed in earthquake recordings (Garini et al. 2019; Vlachakis et al. 2020).

In this study, the effect of soil profile characteristics on the frequency properties of surface motion is examined by varying the height *H* of the soil deposit overlying the rigid bedrock. The reference soil profile examined, also, before, assumes a soil profile of Nevada sand with height *H* = 20m, relative density of the natural soil D_r = 45% and an improved zone with 2m depth and relative density D_r = 60%, whereas the parametric investigation includes values of *H* in the working range 14m-50m. The elastic soil period is estimated using the average elastic shear wave velocity of the soil profile $\bar{V}_{s,o}$ with the expression $T_{soil} = 4H/V_{s,o}$. To account for nonlinear soil response during shake, the fundamental nonlinear soil period is calculated by employing equation 4.11 for the given $\bar{V}_{s,o}$ and peak bedrock acceleration a_{max}^{b}, in this case $a_{max}^{b} = 0.15\text{g}$.

Figure 4.17 presents numerical predictions of $T_{sys.eff}/T_{sys.el}$ ratios as a function of the ratio $T_{soil}/T_{sys.el}$, i.e., the fundamental nonlinear soil period T_{soil} normalized with the elastic system period $T_{sys.el}$. $T_{sys.eff}$ predictions are obtained using the *smoothed spectral predominant system period* $T_{sys.o}$, as well as the *predominant system period* $T_{sys.p}$, as previously discussed. The fundamental nonlinear soil period T_{soil} is computed for every soil profile (with varying height *H*) using Equation 4.11. Results indicate that soil-to-excitation resonance significantly elongates the system period $T_{sys.eff}$, i.e., up to 70% compared to the –

initial – elastic value of system period. Interestingly, the extremes of the graph are reminiscent of typical response spectra: in the case of rigid soil profiles (small values of *H*) surface motion is governed by high frequency waves and $T_{sys.eff}/T_{sys.el}$ ratios tend to 1.0, whereas in the case of flexible soil profiles (great values of *H*) low frequencies waves prevail and the $T_{sys.eff}/T_{sys.el}$ ratios are gradually reduced. It is noted that $T_{sys.eff}$ values peak *for* $T_{soil}/T_{sys.el}$ ratio around 1.25, i.e. beyond 1.0 which is the "elastic" resonance condition. This difference is, essentially, attributed to the introduction of the smaller – elastic – value of system period in the denominator instead of the actual – effective – value $T_{sys.eff}$. Additionally, a possible inaccuracy in the computation of T_{soil} is also factoring in the deviation of the $T_{soil}/T_{sys.el}$ ratio from unity. It should be underlined that an a posteriori normalization of the computed T_{soil} values with the obtained $T_{sys.eff}$ values would "correctly" shift the peak exactly at resonance, i.e. $T_{soil}/T_{sys.el} \approx 1$. Nevertheless, since this option would not be practical for design applications, it is not presented here.

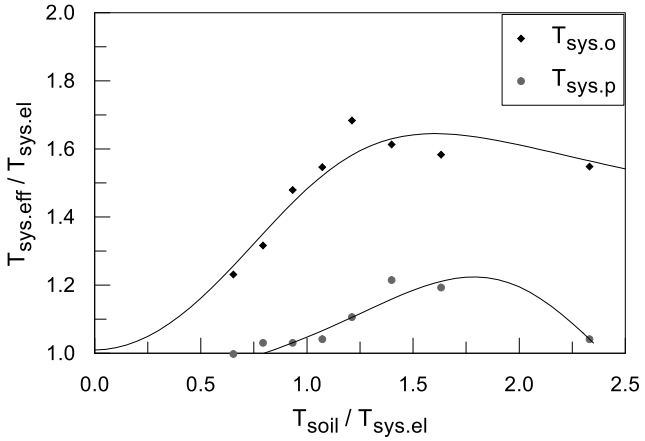

Figure 4.17: Ratios of effective-to-elastic system periods $T_{sys.eff}/T_{sys.el}$ as a function of the natural period of the soil deposit T_{soil} normalized with $T_{sys.el}$.

For the sake of practical applications, the data presented in **Figure 4.16** and **Figure 4.17** have been fitted with regression analyses to give the following analytical expressions for the elongation of the smoothed spectral predominant system period $T_{sys.o}$ and the predominant system period $T_{sys.p}$:

i) Smoothed spectral predominant system periods $T_{sys.o}$ (with $R^2=0.71$)

$$\frac{T_{sys.eff}}{T_{sys.el}} = (0.91 + 0.55 \cdot PGA^{0.21}) \frac{1.53 + 0.94\left(T_{soil}/T_{sys.el}\right)^2}{\sqrt{\left[1.43^2 - \left(T_{soil}/T_{sys.el}\right)^2\right]^2 + 1.91^2\left(T_{soil}/T_{sys.el}\right)^2}} \quad 4.12$$

ii) Spectral predominant system periods $T_{sys.p}$ (with R^2=0.92)

For PGA < 0.35g:

$$\frac{T_{sys.eff}}{T_{sys.el}} = 1.03 \frac{1.35 + 0.87\left(T_{soil}/T_{sys.el}\right)^2}{\sqrt{\left[1.30^2 - \left(T_{soil}/T_{sys.el}\right)^2\right]^2 + 1.80^2\left(T_{soil}/T_{sys.el}\right)^2}} \quad (4.13)$$

For PGA ≥ 0.35g:

$$\frac{T_{sys.eff}}{T_{sys.el}} = (0.57 + 0.54 \cdot PGA^{0.44}) \frac{1.35 + 0.87\left(T_{soil}/T_{sys.el}\right)^2}{\sqrt{\left[1.30^2 - \left(T_{soil}/T_{sys.el}\right)^2\right]^2 + 1.80^2\left(T_{soil}/T_{sys.el}\right)^2}} \quad (4.14)$$

Overall, results show that due to the gradual degradation of soil stiffness during shaking, effective system periods are better estimated by *smoothed spectral predominant system periods* $T_{sys.o}$ that better capture the time-varying nature of periods rather than by using the *spectral predominant system periods* $T_{sys.p}$ that only depict the fundamental period of the spectrum. Thus, for simplicity, the effect of the remaining – less influential – variables (*FS*, *γ*, *h/r*) on system period is examined using the $T_{sys.o}$ estimate.

The *Factor of Safety* (FS) against static bearing capacity failure of the foundation affects the structural response by controlling the level of the initial plastification in the foundation soil invoked and, in extent, the additional plastification due to shaking-induced rocking of the structure. Thus, **Figure 4.18a** correlates the $T_{sys.eff}/T_{sys.el}$ ratios – obtained for $T_{sys.o}$ estimates – to the *FS* of the corresponding system. Note that *FS* was varied by applying an additional overburden pressure to the footing, so that the structural mass is not affected. As expected, systems with greater *FS* values exhibit less plastification of the foundation soil and consequently less elongation of the effective system period. In the *FS* range examined herein, the effect on effective period elongation is moderate to low, as the $T_{sys.eff}/T_{sys.el}$ ratio decreases from about 1.40 for *FS* = 1.00 to 1.25 for *FS* ≈ 6.0.

The effect of the SSI parameters *γ* and *h/r* on effective system period is examined in **Figure 4.18b** and **c**, respectively. The variation of relative mass ratio *γ* (**Figure 4.18b**) involves systems with varying structural mass, therefore being – in principle – reciprocal to the variation of the Factor of Safety discussed above. Nevertheless, this case also includes the effect of rocking-induced soil softening due to the additional structural mass and the resulting overturning moments applied to the foundation. Taking this into account, the examined relative mass ratios *γ* correspond to the range of Factors of Safety *FS* > 3.0 where

the effect of FS on $T_{sys.eff}/T_{sys.el}$ is minimal. Thus, **Figure 4.18b** essentially shows the effect of varying the foundation shear force and overturning moment on the effective period elongation. In any case, the effect of γ on period elongation is not significant as the $T_{sys.eff}/T_{sys.el}$ ranges from 1.40 to 1.50 when γ increases from 1 to 2.5. To compare with previous findings, it is noted that in the transition from a "light" system ($\gamma \approx 1.0$) to a "heavy" one ($\gamma \approx 2.5$) structural mass corresponds to an increase of the inertial force equal to the ratio of the respective masses, i.e. 2.5/1.0. This is similar as to keep the structural mass constant and increase of *PGA* from 0.20g to 0.50g. In doing so, the effect on period elongation obtained from Figure 4.16 is practically the same as varying γ from 1 το 2.5.

Lastly, the effect of slenderness ratio *h/r* is examined by increasing the height *h* of the structure and keeping the "elastic" system period $T_{sys.el}$ constant (*scenario B in section 4.3.1*). **Figure 4.18c** plots computed $T_{sys.eff}/T_{sys.el}$ ratios against slenderness ratios within the range *h/r* = 0.88-1.70. It is thus observed, that this parameter has a minimal effect of the system period elongation which can be readily overlooked.

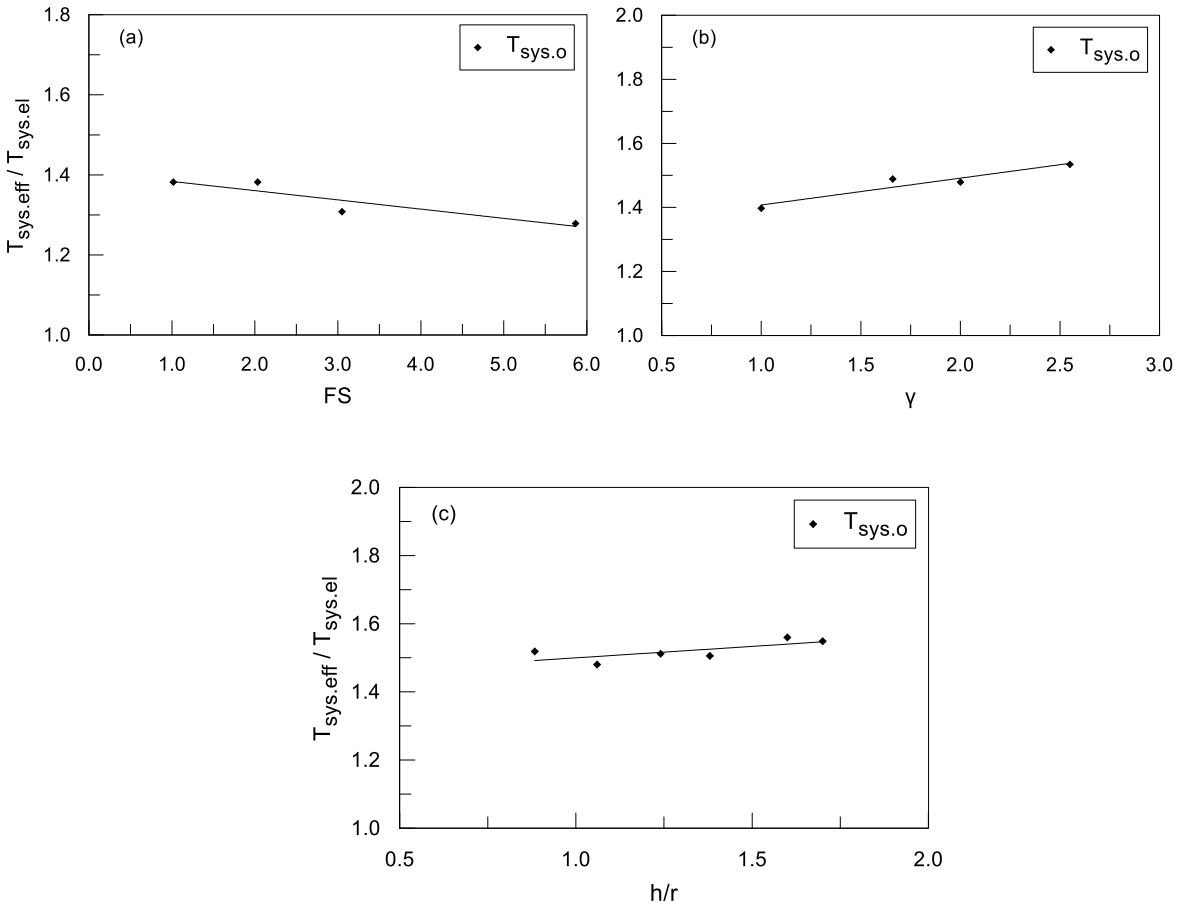

Figure 4.18: Ratios of effective-to-elastic system periods $T_{sys.eff}/T_{sys.el}$ as a function of (a) the *Factor of Safety* (FS), (b) relative mass ratio γ and (c) slenderness ratio *h/r*.

The accuracy of the proposed analytical relationships is evaluated by comparing the predicted values of $T_{sys.eff}/T_{sys.el}$ ratios with the corresponding predictions of the numerical analyses. The relative error between the numerical (observed) and the analytical (predicted) values is used herein to quantify the accuracy of the proposed methodology. It is defined as:

$$Relative\ error = \frac{Observed - Predicted}{Observed} \tag{4.15}$$

Figure 4.19 presents the statistical evaluation of relative errors for the independent variables $T_{soil}/T_{sys.el}$ and *PGA*. Overall, results show that relative errors remain small for both the estimates used herein, i.e. $T_{sys.o}$ and $T_{sys.o,}$ with the aggregate standard deviation and the average value of relative errors being 0.03 and -0.006, respectively. Additionally, the distribution of relative errors is, on the whole, quite uniform for all the examined variables.

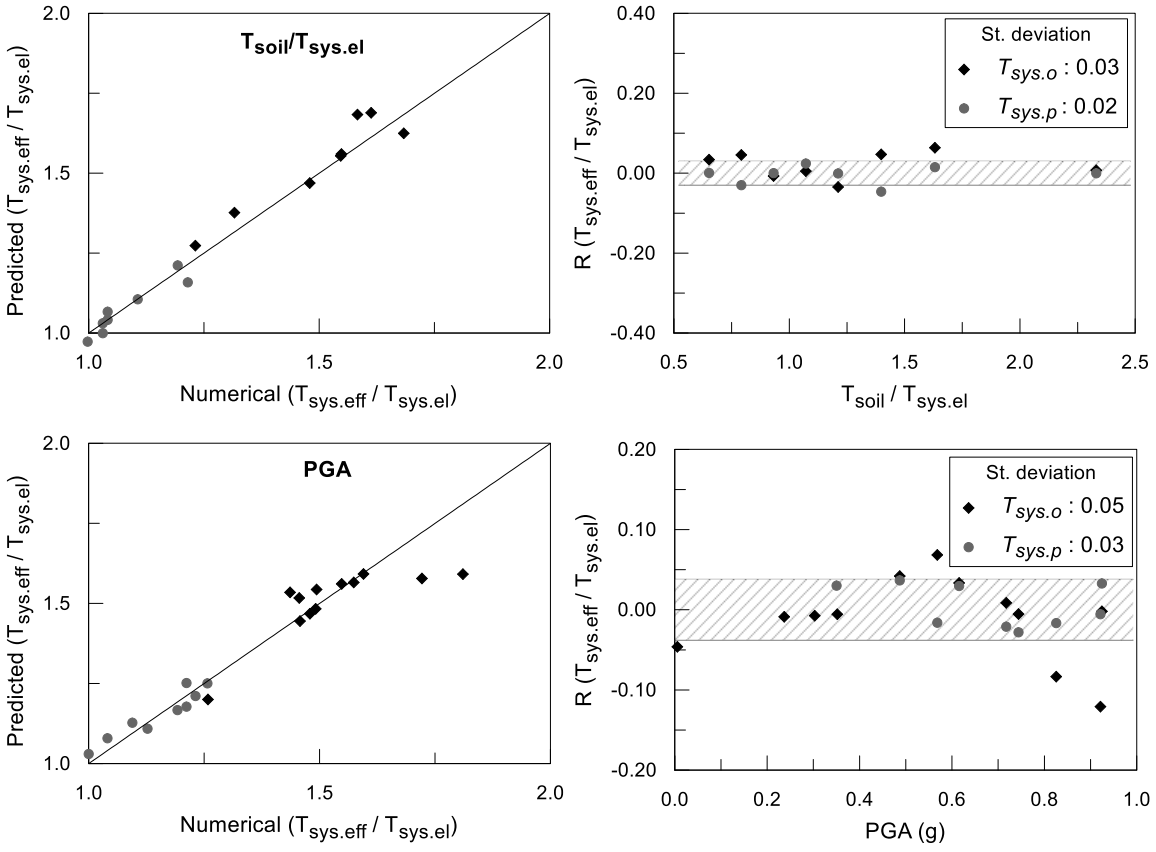

Figure 4.19: Relative error evaluation in the analytical calculation of $T_{sys.eff}/T_{sys.el}$ against numerical predictions by separate examination of the variables: (a) period ratio $T_{soil}/T_{sys.el}$, (b) peak ground acceleration (PGA).

4.3.3.2 Liquefied soil conditions

Overview._ In this section, effective system periods $T_{sys.eff}$ of structure-foundation-soil systems are assessed for liquefaction conditions. The effect of liquefied sublayers on structural response is twofold: i) the liquefied layer acts as a natural "seismic isolation" and therefore ground and structural accelerations are drastically attenuated and ii) the drastically reduced shear strength of the subsoil deteriorates the foundation performance. Regarding the former, it is shown in literature that "*a liquefied soil layer may effectively attenuate certain harmonic excitation components, i.e., provide natural isolation of the seismic ground motion, only when its thickness exceeds a portion of the corresponding wave lengths* λ_L" (Bouckovalas et al. 2016a). The authors correlate numerical predictions of limiting thickness $H_{L,ampl}$ with the liquefied wave length λ_L and the ratio of liquefied sand over the non-liquefied crust H_L/H_c as follows:

$$\left(\frac{H_L}{\lambda_L}\right)_{ampl} = 0.275\left(\frac{H_L}{H_c}\right)^{0.35} \quad 4.16$$

A practical consequence of this relation regards the filtering of propagating seismic waves through a liquefied layer with a given thickness H_L. Specifically, the above equation can, be solved for the excitation period T_{exc} which corresponds to the limiting period $T_{L,ampl} = \lambda_L/V_{S,L}$ below which the harmonic excitation components are drastically de-amplified:

$$T_{L,ampl} = 3.64\left(\frac{H_L}{H_c}\right)^{-0.35}\frac{H_L}{V_{S,L}} \quad 4.17$$

The reference soil formation in this study, includes an improved soil crust of 2m on top of an 18m thick liquefiable sand layer, i.e. H_L / H_c = 9. The initial value of the average shear wave velocity is $V_{s.o}$ ≈ 125m/s, while the estimated value for the liquefied soil is $V_{s.L}$ ≈ 27m/s (for $V_{s.L}/V_{s.o}$ = 27/125 = 0.21). Thus, based on Equation 4.17 it is estimated that spectral accelerations at ground surface will be de-amplified for periods $T_{exc} < T_{L,ampl}$ ≈ 1.10 sec, i.e. for the entire range of significant periods in common seismic excitations.

Following the above, the effect of earthquake intensity on system effective period $T_{sys.eff}$ is intrinsically different in the presence of liquefied sublayers, since *PGA* will be drastically reduced, compared to acceleration amplitudes at the bedrock, especially for moderate to low Factors of Safety against liquefaction when the onset of liquefaction precedes the peak time of the seismic excitation. **Figure 4.20a** presents Transfer Functions of structure-to-free-field elastic response spectra (with ζ=5%) for varying *PGA*

values, obtained with the procedure described in section 4.3.2. Firstly, it is observed that, in contrast to TFs obtained for non-liquefiable conditions, in the particular case TFs exhibit a distinct peak rather than a distribution of amplifications within a period range. This finding suggests that structural response is governed by a single set of properties, i.e., the properties of the liquefied subsoil. Regarding the earthquake intensity, it is remarked that the input motion amplitudes at bedrock range from 0.05g to 0.60g, while the ground surface *PGA* ranges from 0.08g to 0.19g, suggesting drastic attenuation of the seismic motion. The former is exemplified by examining the structural responses for earthquakes with high (a^b_{max} = 0.60g) and medium (a^b_{max}= 0.15g) intensities (**Figure 4.20b** and **c**); during both seismic events natural subsoil is liquefied. In both cases motion is de-amplified and the resulting surface accelerations exhibit *PGA* values equal to 0.17g and 0.11g for the high and low intensities, respectively. Time-histories of structural acceleration (**Figure 4.20b**) and moment-rotation (**Figure 4.20c**) agree to the conclusion that structural responses are relatively similar irrespectively of seismic intensity, while peak structural accelerations are substantially smaller compared to the non-liquefiable case examined in Figure 4.15b. It is noted that high intensity shaking is accompanied by some residual rotations at the end of shaking.

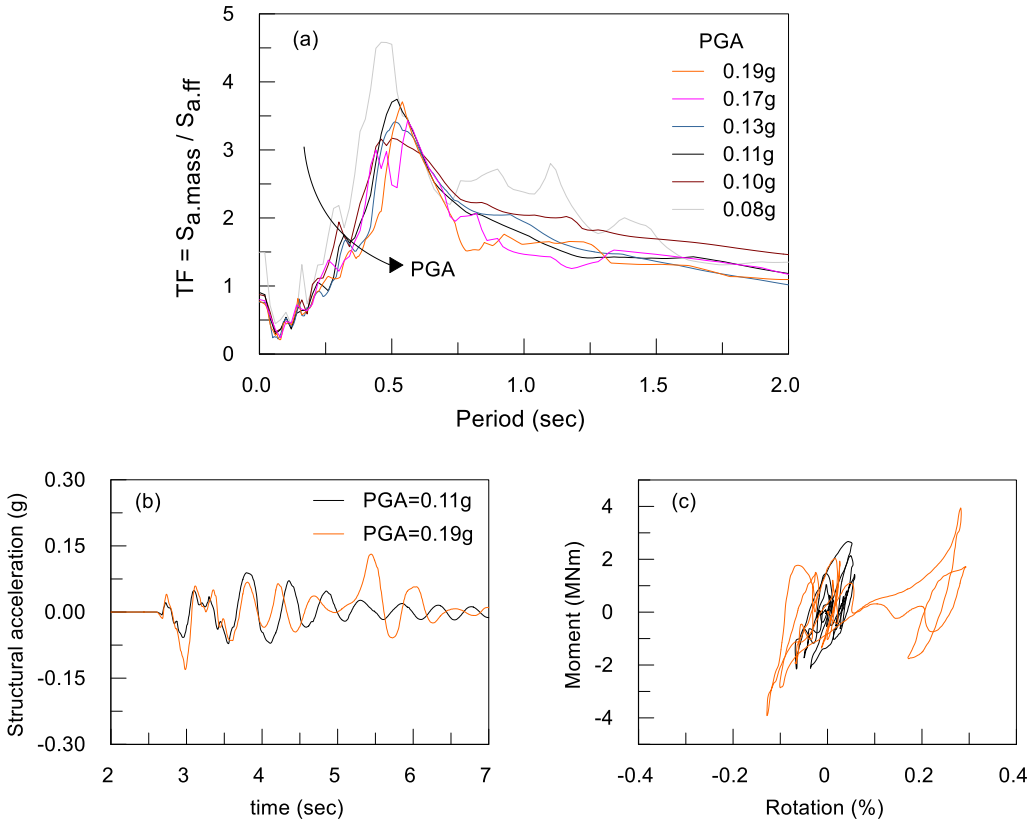

Figure 4.20: (a) Transfer functions of structural-to-free field acceleration response spectra for different level of peak ground accelerations (*PGA*), (b) structural accelerations for high (a^b_{max}= 0.60g – *PGA* = 0.17g) and medium (a^b_{max} = 0.15g – *PGA* = 0.11g) intensity earthquakes and (c) corresponding moment-rotation response of the foundation.

Parametric Investigation._ As for the non-liquefiable soil conditions, the smoothed spectral predominant system period $T_{sys.o}$ and the predominant system period $T_{sys.p}$ are used comparatively as measures of the effective system periods $T_{sys.eff}$ in order to effectively characterize the frequency content of the numerically obtained TFs. **Figure 4.21** presents ratios of effective-to-elastic system periods $T_{sys.eff}/T_{sys.el}$ as a function of *PGA* for both the aforementioned frequency estimates. It is noted that $T_{sys.el}$ refers to the initial – prior to liquefaction – conditions. It is initially observed that the variation of $T_{sys.o}$ with *PGA* shows significant scatter and no particular trend seems to emerge. On the other hand, $T_{sys.p}$ shows a better correlation with *PGA*, which is consistent with the TFs of **Figure 4.20**, namely, peak values of the TFs appear to moderately increase with PGA. This is because, as previously explained, the structural response is governed by soil at its liquefied state and, as a result, it is best characterized by a single system period estimate, i.e. $T_{sys.p}$, rather than one that is derived within a period range, i.e. $T_{sys.o}$.

For completeness, analytical relationships are derived for both the aforementioned frequency estimates. Values of $T_{sys.p}/T_{sys.el}$ ratio show an increase with *PGA* up to 20%, while they are equal to unity for *PGA* < 0.075g. As a result, the following relations are proposed:

i) <u>Smoothed spectral predominant system periods $T_{sys.o}$</u>

$$\frac{T_{sys.eff}}{T_{sys.el}} = 1.00 \qquad for\ PGA \leq 0.075g$$

$$\frac{T_{sys.eff}}{T_{sys.el}} = \alpha \cdot PGA^{b} \qquad for\ PGA > 0.075g \tag{4.18}$$

with α=1.69 and b=0.20 (R^2=0.85).

ii) <u>Spectral predominant system periods $T_{sys.o}$</u>

$$\frac{T_{sys.eff}}{T_{sys.el}} = \alpha \cdot PGA^{b} \tag{4.19}$$

with α=1.40 and b=0.014 (R^2=0.51).

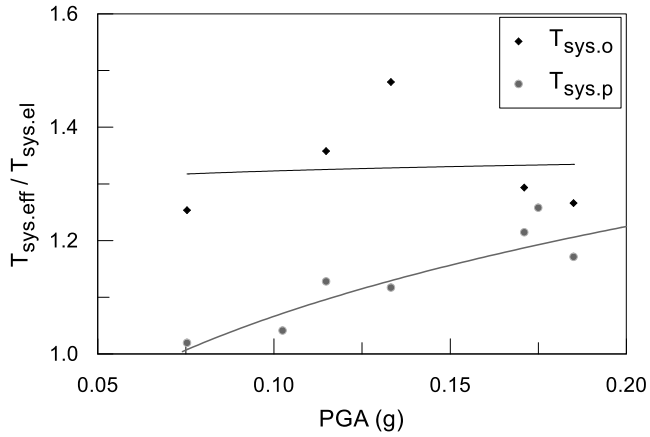

Figure 4.21: Ratios of effective-to-elastic system periods as a function of *PGA* obtained using the smoothed spectral predominant system period $T_{sys.o}$ (*black dots*) and the predominant system period $T_{sys.p}$ (*grey dots*) estimates.

The depth of the improved zone H_{imp} is a crucial parameter in the design of structures on liquefiable conditions, since an increased H_{imp} reduces foundation settlements and increases the degraded Factor of Safety FS_{deg} (Dimitriadi et al. 2017c; Karamitros et al. 2013d). As such, the impact of the improved zone on system period is examined herein for the range of practical interest H_{imp} = 0-3m. **Figure 4.22** shows that H_{imp} effect on $T_{sys.p}/T_{sys.el}$ ratios is minimal, starting from a ratio of $T_{sys.p}/T_{sys.el}$ ≈ 1.15 for zero improvement and decreasing to slightly below 1.10 for H_{imp}=3.0m. The observation that the presence of an improved zone does not significantly affect system period may draw upon two facts: i) the structural overburden pressure results in increased effective stresses under the footing and, thus, reduced excess pore pressure ratios, and ii) the influence depth of footings in the rocking mode of vibration is an order of magnitude smaller than typical influence depths, i.e. ≈0.2B, (Gazetas 1991b) and, therefore, any rocking-induced soil straining lies well within the aforementioned "strong" zone of reduced pore pressures. Consequently, the increase of H_{imp} does not significantly affect $T_{sys.eff}$ conversely to its role regarding foundation settlements and FS_{deg} (Dimitriadi et al. 2017; Karamitros et al. 2013a).

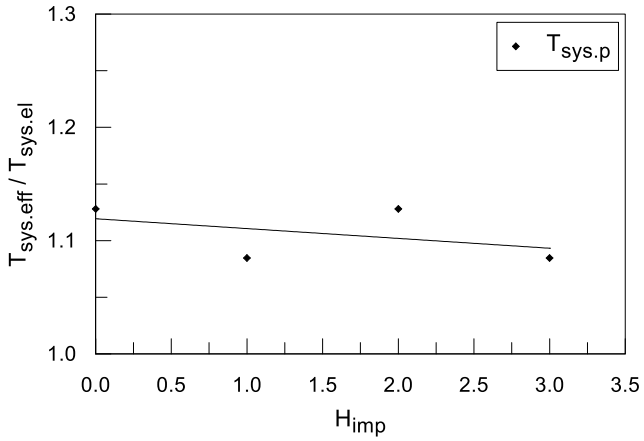

Figure 4.22: Ratios of effective-to-elastic system periods $T_{sys.eff}/T_{sys.el}$ as a function of the depth of the improved zone *Himp*.

Similarly to the findings of the parametric investigation for non-liquefiable conditions, the effect of relative mass ratio *γ* and slenderness ratio *h/r* on system period is minimal within the examined range and, thus, not presented here. Regarding the factor of safety *FS,* it is noted that the proposed design concept of structures on liquefiable conditions requires for *FS* to remain on the safe side, i.e., significantly greater than unity. What is more, the numerical problem that needs to be addressed for a fully coupled nonlinear dynamic analysis using an effective stress constitutive model requires numerical convergence that cannot be met in the case of reduced bearing capacities. As a result, the effect of *FS* on system period is not addressed in liquefied conditions. Lastly, the effect of soil period T_{soil} is not examined here, since the fundamental period of the soil profile increases significantly during liquefaction, i.e. $T_{soil} = 4H/V_s \approx$ 5-10 $T_{soil.o}$, due to the severe stiffness degradation of the ground and as a result values of $T_{soil}/T_{sys.el}$ tend to the flexible end of **Figure 4.17**.

The accuracy of the proposed analytical relationships is evaluated by comparing the predicted values of $T_{sys.eff}/T_{sys.el}$ ratios with the corresponding predictions of the numerical analyses. The statistical evaluation of relative errors is presented in **Figure 4.23** for the independent variable *PGA*. Overall, results show that relative errors remain small for both the estimates used herein, i.e., $T_{sys.o}$ and $T_{sys.o,}$, with the aggregate standard deviation and average value of relative errors being 0.06 and -0.005, respectively.

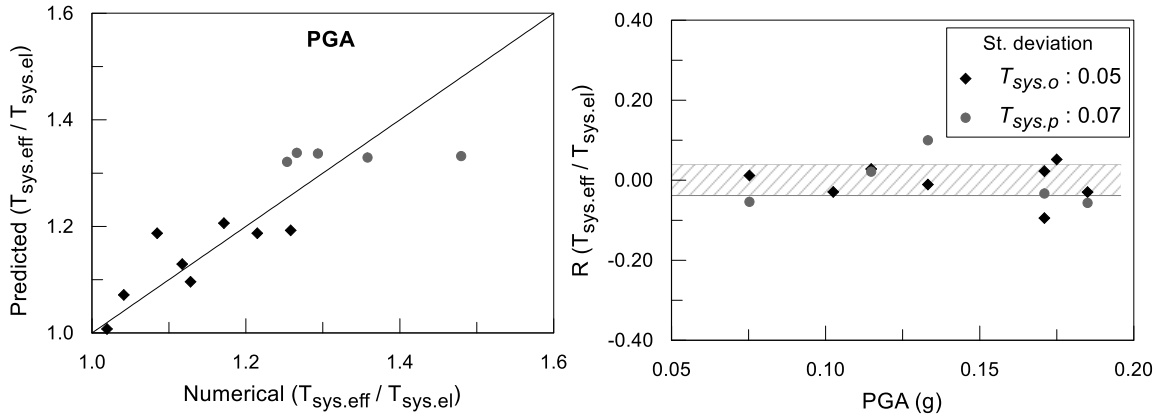

Figure 4.23: Relative error evaluation in the analytical calculation of $T_{sys.eff}/T_{sys.el}$ against numerical predictions.

4.4 Summary and conclusions

The importance of period elongation due to soil-structure interaction is widely discussed and systematically addressed in studies and Code provisions utilizing a linear elastic framework. Soil nonlinearity is indirectly introduced in this methodology by appropriately modifying soil properties based on dynamic analysis of the soil profile, but neglecting any soil-structure interaction effects. Field and real-scale studies as well as numerical analyses have shown the significance of nonlinearity for the elongation of the structure-foundation-soil system period. Nevertheless, a systematic parameter identification is overlooked in the bulk of literature.

In the present study, the linear elastic framework is employed, at first, in order to estimate the "*elastic*" – initial – *periods* of the examined systems. Next, the *effective period* is estimated for systems excited at the soil base with white-noise signals, for both liquefied and non-liquefiable soil conditions, employing the widely used frequency content estimates of predominant period and smoothed spectral predominant period. Subsequent parametric identification aimed to correlate the numerically predicted effective system periods with the readily obtained – in practice – "elastic" system periods and to develop simplified expressions for design purposes.

A. Non-liquefiable conditions

- The contribution of soil nonlinearity in period elongation is significant in the case of *non-liquefiable* conditions and this is manifested by TFs of structure-to-surface motion that exhibit amplifications in a wide range of periods. The estimated effective periods are mostly influenced by *earthquake intensity* and *soil-structure resonance* phenomena.
- Greater values of *PGA* lead to an increase of the effective system period up to 80% compared to the "elastic" system period. It is noteworthy that, even for moderate to low earthquakes

intensities (e.g. *PGA* ≈ 0.20g), consideration of the "elastic" system period would result in underestimation of the effective period to the magnitude of 40%.

- Resonance of soil-to-system natural period leads to a corresponding 60% increase of period.
- Due to the gradual degradation of soil stiffness, effective system periods are better estimated by smoothed spectral predominant system periods $T_{sys.o}$ that capture the time-varying nature of periods.

B. Liquefied conditions

- Structural response in the presence of *liquefaction* is governed by soil properties at the liquefied state. This is manifested by TFs of structure-to-surface motion that exhibit a singular peak corresponding to the system period at the liquefied state.
- The effect of *earthquake intensity* has an upper limit of about 20% in nonlinear period elongation compared to "elastic" values, due to the fact that liquefied sublayers act as "natural seismic isolation" and attenuate surface motion.
- The depth of the improved zone H_{imp} has a minor effect on period elongation compared to its role in the overall foundation performance (e.g., settlement accumulation and bearing capacity degradation).
- Due to the single-phase nature of structural response after the onset of liquefaction, effective system periods are better estimated by the predominant system period $T_{sys.p}$.

Chapter 5

Soil-Structure Interaction Effects on Seismic Settlements: Liquefied Soil Conditions

5.1 General

The primary objective of the present chapter is to investigate the effect of structure inertia on the response of shallow foundations constructed on liquefied ground with an improved non-liquefiable crust. The simulation of *purely liquefied* conditions in this chapter assumes Factors of Safety against liquefaction $FS_L < 0.3$, in order to minimize the non-liquefied part of shaking, i.e., *prior* to liquefaction triggering. Firstly, the numerical response of SFS systems is investigated and the mechanisms of excess water pore pressure generation and settlement accumulation are identified for the foundation-soil (FS) system, as well as the structure-foundation-soil (SFS) system. The effect of structural inertia on seismic settlements is investigated through parametric consideration of the critical soil-structure interaction (SSI) parameters, i.e. system-to-excitation period ratio T_{sys}/T_{exc}, slenderness ratio h/r, relative mass ratio γ and structure-to-soil stiffness ratio s. Settlements of SFS systems are then compared with the respective settlements of equivalent foundation-soil systems (FS) in order to isolate the effects of structural inertia on the dynamic response of systems. Lastly, simplified expressions are developed in order to analytically predict settlement ratios between SFS and FS systems, based on a multi-variable statistical analysis of the available numerical predictions. These expressions may be used to form a correction factor for seismic settlements, that are estimated on the basis of existing methodologies in literature (e.g., Dimitriadi et al. 2017) for the simpler case of vertically loaded foundations without any SSI effects.

5.2 Dynamic response of SFS and FS systems

5.2.1 Mechanism of excess pore water pressure generation

The profound differences of soil response between the near field of structures and the free field has been frequently observed in earthquake recordings (Niigata 1964, Luzon 1990, Kocaeli 1999) and later confirmed by extensive shake table and centrifuge experiments (Coelho et al. 2004; Kawasaki et al. 1998; Liu and Dobry 1997). Most notably, the following observations have been made:

- The soil under and near the structure develops reduced excess pore pressure during the seismic event in comparison to the free field soil, i.e. $r_{u.foot} < r_{u.ff}$. In more detail, the excess pore pressure ratio at the free field is expressed as:

$$r_{u.ff} = \frac{\Delta u_{ff}}{\sigma'_{v,o,ff}} \tag{5.1}$$

where Δu_{ff} expresses the excess pore pressure during shaking and $\sigma'_{v,o,ff}$ expresses the vertical effective stress, both at the free field. Under the footing, the excess pore pressure ratio can be expressed as:

$$r_{u.found} = \frac{\Delta u_{found}}{\sigma'_{v,o,found}} = \frac{\Delta u_{found}}{\sigma'_{v,o,ff} + \Delta\sigma'_{v,o,found}} \tag{5.2}$$

where Δu_{found} expresses the excess pore pressure under the footing and $\Delta\sigma'_{v,o,found}$ expresses the surcharge of the vertical effective stress at the same location due to the footing. The interconnection of the above equations has been thoroughly investigated by Karamitros et al. (2013) and it will be briefly discussed here. An important characteristic of the liquefied soil, derived from soil mechanics principles, is that – due to the constrain of lateral strains at the free field – the horizontal total stresses $\sigma_{h,ff}$ will increase and become equal to the vertical total stresses $\sigma_{v,ff}$, at the onset of complete liquefaction, since:

$$\sigma'_{h,ff} = \sigma'_{v,ff} = 0 \qquad => \qquad \sigma_{h,ff} = \sigma_{v,ff} = u_{ff} = \gamma \cdot z \tag{5.3}$$

The above imply that the total geostatic vertical stress serves as the upper limit of the pore pressure at the free field, but also of the horizontal total stress (in the most common case that the coefficient of earth pressures at rest $K_o < 1$ at geostatic conditions). Additionally, if loss of soil

shear strength during shaking appears in both the free field and under the footing, this eventually equalizes horizontal total stresses in the two regimes, i.e.:

$$\sigma_{h,found} \approx \sigma_{h,ff} = u_{ff} \quad 5.4$$

Consequently, under the footing the pore pressures u_{found} will also have as an upper limit the free field pore pressures (i.e., $u_{found} \leq u_{ff}$), while the overburden pressure of the building adds to the vertical stresses, as follows:

$$\sigma_{v,found} \approx \sigma_{v,ff} + \Delta\sigma_{v,found} \quad 5.5$$

$$\sigma'_{v,found} \approx \left(\sigma_{v,ff} + \Delta\sigma_{v,found}\right) - u_{found} > \sigma'_{v,ff} = \sigma_{v,ff} - u_{ff}$$

As a result

$$r_{u.found} = \frac{\Delta u_{found}}{\sigma'_{v,o,found}} = \frac{\Delta u_{ff}}{\left(\sigma_{v,ff} + \Delta\sigma_{v,found}\right) - u_{found}} \leq \frac{\Delta u_{ff}}{\sigma'_{v,found,min}} \quad 5.6$$

In essence, the additional vertical effective stresses $\Delta\sigma'_{v.found}$ due to the structural weight in combination with the upper limit of pore pressures u_{found} result in considerably reduced excess pore pressure ratios under the building:

$$r_{u.found} \ll r_{u.ff}$$

- Furthermore, excess pore pressure reduction is frequently attributed to soil dilation. Shear straining due to the propagation of shear waves is, naturally, common for free field and near field conditions and, therefore responsible for the dilation spikes observed in the time-histories of excess pore pressure ratios (Liu and Dobry 1997). Moreover, building settlement (Elgamal et al. 2005) and rocking (Karamitros et al. 2013a; Karimi and Dashti 2016b) cause additional shear-induced dilation of the foundation soil, which results to larger dilation spikes in the foregoing time-histories and – depending on the stress state – a gradual decrease of the overall r_u.
- Water flow is observed from areas with high r_u to areas with lower r_u values during and after shaking. This, mostly, results to upward flow towards the zero pressure surface zone, whereas a secondary flow towards the area under the footing is also observed (Adalier et al. 2003a).

The above literature findings are also observed in the present examination. Emphasis is put at Locations A and B that lie under the footing, whereas location C lies at the free field, as shown in **Figure 5.1**. More specifically, excess pore water pressure ratios r_u are examined in **Figure 5.2** for the numerical analysis of

the previously described (Chapter 2) structure-foundation-soil system with the following main characteristics: a liquefiable natural deposit of thickness H_L = 18m overlaid by an improved zone of H_C = 2m, square footing of width B = 4m and overburden pressure q = 80kPa, structure with fundamental period $T_{str.f}$ = 0.35sec and SSI parameters s = 0.07, h/r = 1.06 and γ = 4.00. The described system is excited with a harmonic acceleration signal at its base with peak bedrock acceleration a^b_{max} = 0.15g and period of excitation T_{exc} = 0.35sec. The liquefiable layers have a Factor of Safety against liquefaction FS_L < 0.3 for the examined range of seismic intensity. Concerning the free field, it is shown that r_u values gradually increase and suggest complete liquefaction (r_u ≈ 1.0) after approximately 3 seconds of shaking. Shear-induced dilation due to the wave propagation is suggested due to the spikes of the r_u time-histories that initiate after the first 1.5 seconds. Conversely to the free field, r_u values underneath the footing are lower than 1.0 in both locations (A and B). Additionally, larger additional effective stresses $\Delta\sigma'_{v.foot}$ due to the building weight at location A (at depth equal to one footing width B underneath the footing) result in more intense reduction of excess pore pressures (maximum r_u ≈ 0.28), in comparison with the r_u time-history at the deeper location B (maximum r_u ≈ 0.90). Similarly to the free field, dilation spikes are observed in both locations underneath the footing during shaking. Interestingly, a permanent drop of the excess pore pressure ratio takes place at location B after 2.0 seconds of shaking. This behavior can be attributed, on one hand, to the dilative response of soil at the particular depth, where additional vertical effective stresses due the structure weight are small whereas deviatoric straining due to building settlement is significant. Additionally, water flow to the surface is also responsible for the reduction of r_u values, although to a lesser extent (Karamitros 2010).

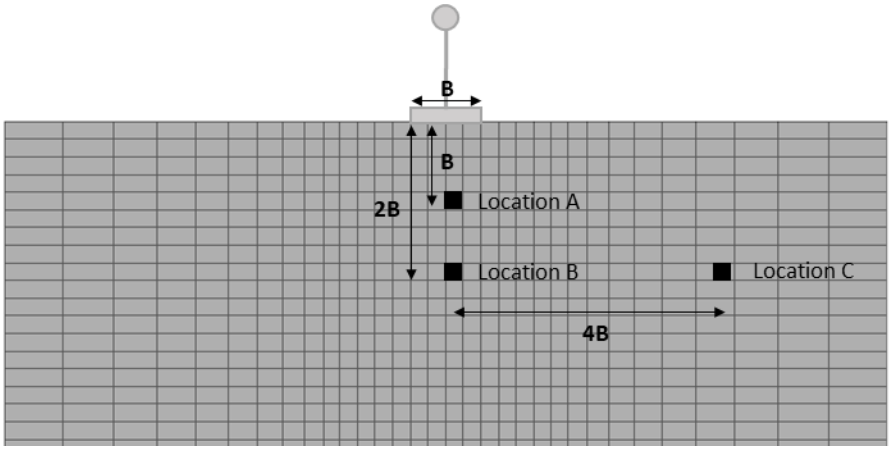

Figure 5.1: Schematic illustration of analyzed problem and locations A, B and C of interest in the numerical model.

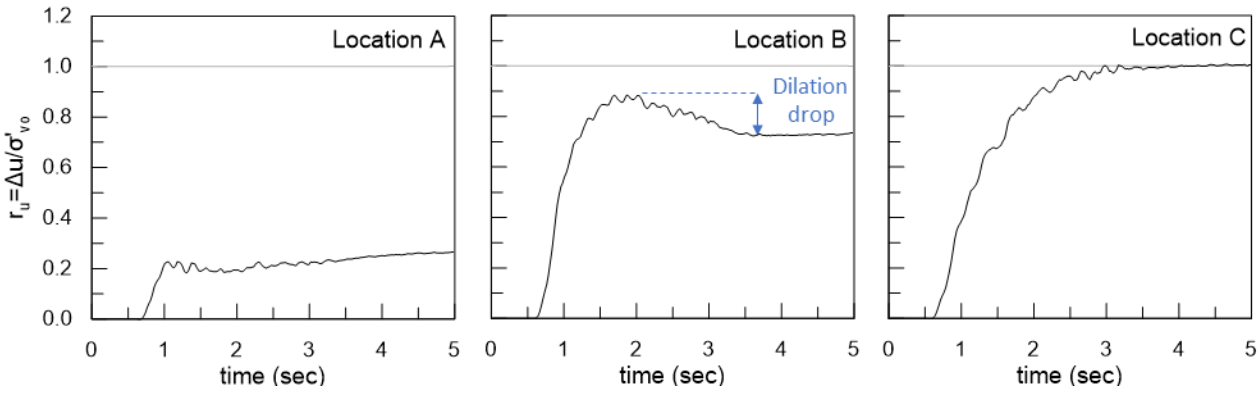

Figure 5.2: Time-histories of excess pore pressure ratios at locations A, B and C.

Contours of pore pressures *u* and the corresponding r_u ratios are presented in **Figure 5.3** at two stages: i) at the onset of liquefaction in the free field (set at *t=1.8sec, i.e.* when $r_u \approx 0.8$) and ii) when shaking is complete (*t=5.4sec*). Results from the presented Figures are in qualitative agreement with the general trends described previously. Namely, pore pressures at the free field are always larger or equal to the corresponding values at the same depth under the footing. Specifically, at the onset of liquefaction (*t=1.8sec*) free field pore pressures are clearly larger ($u_{found} < u_{ff}$), whereas when liquefaction is complete (*t=5.4sec*) pore pressures tend to equalize ($u_{found} \approx u_{ff}$). On the contrary, pore pressure ratios exhibit fundamentally different evolution at the free field and underneath the structure, where they never exceed the value of 0.2 for depths smaller than one footing width. Moreover, the presence of the improved shallow crust (of 2m thickness) results in reduced r_u values for the whole area of improvement. Nevertheless, it is observed that the effect of overburden pressure on r_u extends deeper than the depth of the improved zone. **Figure 5.4** presents the water flow vectors at the same two instances with respect to liquefaction occurrence. In both of them it is observed that the water flows from areas with increased pore pressure towards areas with smaller pore pressures. As such water flows mainly towards the free-draining surface, while secondarily there is also flow towards the area of lower r_u under the structure.

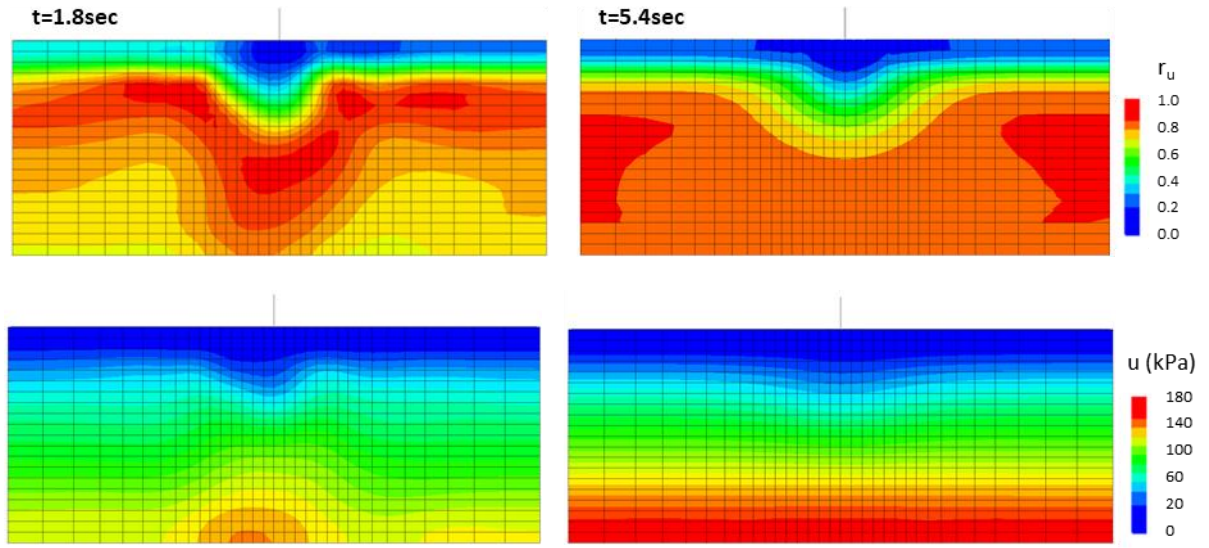

Figure 5.3: Contours of excess pore pressure ratios r_u (*top row*) and pore pressures *u* (*bottom row*) at the onset of liquefaction (*first row*) and at the end of shaking (*left row*).

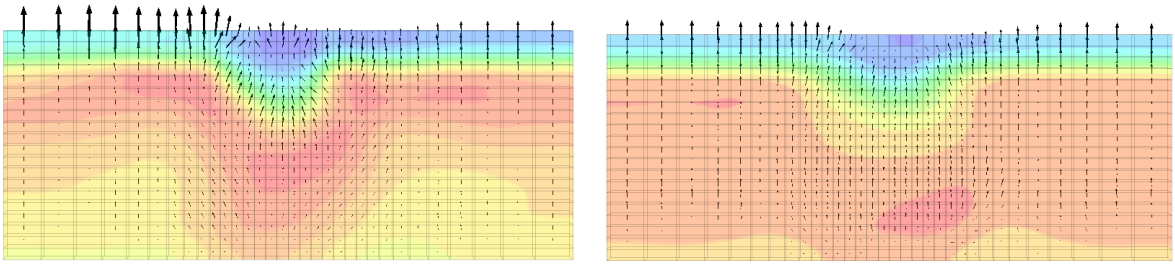

Figure 5.4: Qualitative illustration of water flow vectors at the onset of liquefaction (*left*) and at the end shaking (*right*).

5.2.2 Settlement mechanism of Foundation-Soil Systems

The problem of excessive footing settlements in the case of liquefaction is widely assessed in literature. Experimental (Adalier et al. 2003, Liu and Dobry 1997, Dashti et al. 2010b), as well as, numerical (Elgamal et al. 2005; Karamitros et al. 2013b; Karimi and Dashti 2016a; Dimitriadi et al. 2017) studies have shown that building settlements accumulate mainly during the shaking period and they are attributed to deviatoric strains caused by the foundation contact pressure and the developing soil and structure inertial forces. Post-liquefaction volumetric strains, due to excess water pore pressure dissipation, account only for a small portion of the accumulated seismic settlements. The aforementioned deviatoric-type mechanism of settlement accumulation is affected by the presence of liquefied soil layers in two counteracting ways. Firstly, liquefied soil layers prohibit shear wave propagation to the ground surface, creating a natural seismic isolation effect (Karamitros et al. 2013b; Bouckovalas et al. 2016). Thus, seismic

ground accelerations and spectral accelerations are significantly reduced after the onset of liquefaction. Consequently, shear-induced settlements are de-amplified. The second implication of liquefaction is that the severe shear strength degradation caused by the excess pore-pressure generation, amplifies the settlements associated with bearing capacity degradation in the subsoil.

To demonstrate the above, **Figure 5.5** and **Figure 5.6** present numerical results of the reference foundation-soil (FS) system, i.e., the equivalent FS system of the previously examined SFS system. Thus, the examined system has an overburden pressure q = 80kPa, Factor of Safety against liquefaction FS_L < 0.3 and it is subjected to a harmonic base excitation with T_{exc} = 0.50 sec and a^b_{max} = 0.15g. The other characteristics of the FS system are: a liquefiable natural deposit of thickness H_L = 18m overlaid by an improved zone of H_C = 2m, square footing of width B = 4m. In more detail, **Figure 5.5** shows time-histories of (a) the footing settlement, (b) the respective settlement rate and (c) the deviatoric strain $\varepsilon_q = 2/3\ (\varepsilon_1 - \varepsilon_3)$ under the footing edge. The horizontal motion time-histories of the foundation and the soil base, in terms of acceleration, velocity and displacement, are presented in **Figure 5.6**. It is seen that while the total duration of the input motion is 7.5 seconds (**Figure 5.5**) the strong part of the ground motion lasts up to 3 seconds, until liquefaction is complete, as depicted indirectly by the essential nullification of the accelerations. During the particular period, the largest part of settlement accumulation takes place, as observed in **Figure 5.5a**. At the same time, the vertical settlement rate of the footing (**Figure 5.5b**) exhibits strong oscillations, indicative of the footing downward motion. As a result, deviatoric strains under the footing edge accumulate mostly during the same period (**Figure 5.5c**).

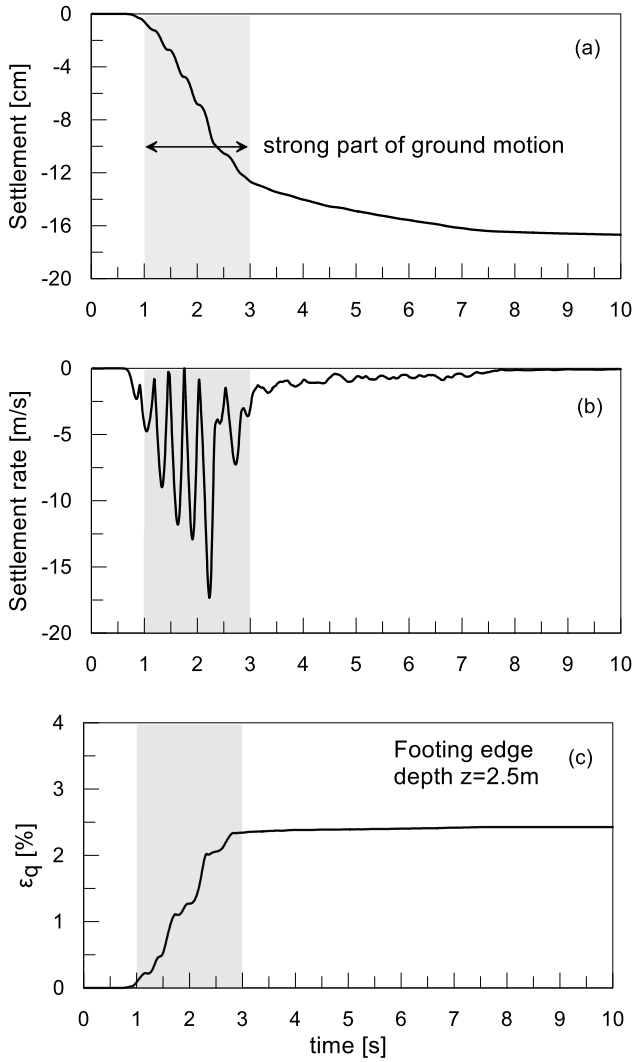

Figure 5.5: Typical time-histories of the FS system response; (a) footing settlement, (b) settlement rate and (c) deviatoric strain under the footing edge.

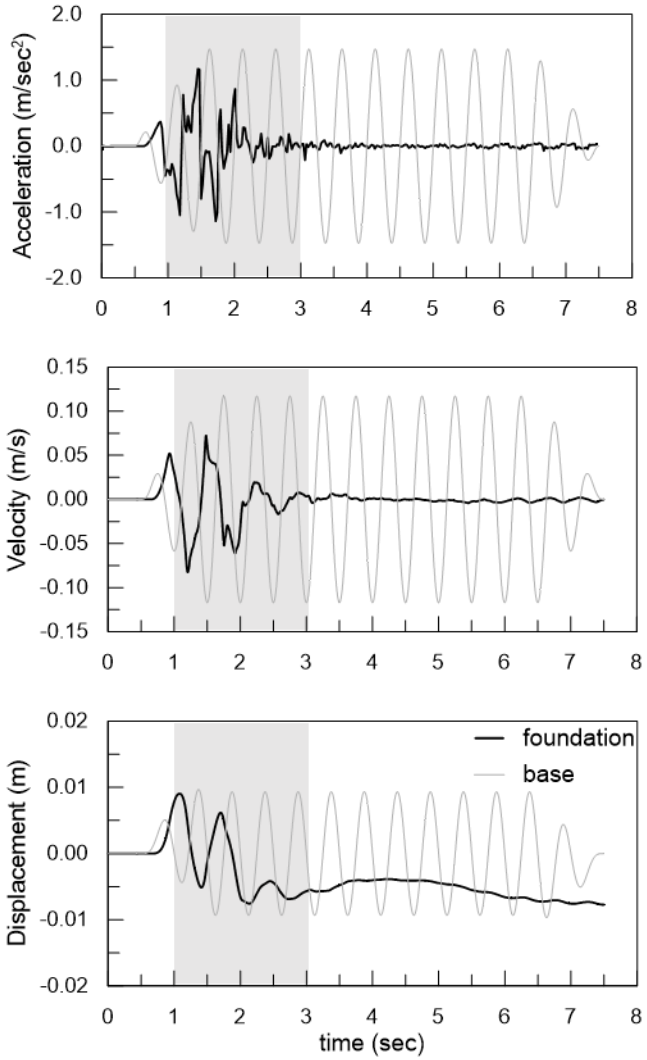

Figure 5.6: Horizontal (a) acceleration, (b) velocity and (c) displacement time-histories at the soil base and at the foundation level of the FS system.

The pattern of footing settlement accumulation during an earthquake was initially identified by Richards et al. (1993) for dry soil conditions. The authors related seismic settlements of shallow foundations to the bearing capacity degradation as a separate mechanism from settlements attributed to soil densification. Field and laboratory observations show that shear failure of the foundation soil and the subsequent seismic fluidization result in settlement accumulation even in moderate earthquake intensities (Richards et al. 1990). On this basis, a Coulomb-type mechanism was used for the limit state analysis of the degraded bearing capacity. In addition to the static components of foundation and soil forces, the suggested analysis included inertial forces in the soil, thus, resulting to a reduced bearing capacity. Footing settlements were calculated by the authors with a sliding block procedure, that is similar to the procedure for the calculation

of lateral seismic displacements of retaining walls. Namely, the sliding of the Coulomb wedge is calculated as the distance it travels on the failure surface when the critical acceleration is exceeded.

The effect of the particular mechanism on the accumulation of dynamic settlements is, naturally, more pronounced in the case of liquefied subsoil, due to the associated severe shear strength degradation of the sand. An example of this mechanism is presented in the following by examining the dynamic response of the aforementioned FS system. The principal function of the Coulomb sliding block theory relies on the oscillation of the involved masses, i.e., of the foundation soil and the footing itself, presented in **Figure 5.6.** In order to shed more light into the movement characteristics, **Figure 5.7** zooms into the vertical (*left* column) and horizontal (*right* column) motion of the foundation and soil base during the strong part of shaking, namely for *t* = 1-3 sec. The transition from point a to point b corresponds to foundation horizontal movement from the center of oscillation (x=0) to the minimum displacement $x=x_{min}$ (or maximum – in absolute terms – to the left), as seen in **Figure 5.7b** and **5.7d**. At the same period, settlement rate increases from its minimum value (point a) to its maximum (point b), as observed in **Figure 5.7a** and **5.7c**. To rephrase the above, settlement accumulates as the footing moves from its neutral position to the right and it is associated with the formation and sliding of the soil wedge. Next, as the foundation returns to its neutral position (x=0), i.e., transition from point b to c, settlement rate is reduced to its minimum level since wedge sliding is reversed. The same half-cycle of oscillation and settlement accumulation is repeated as the foundation moves to the right and back to its neutral position, i.e., transition to points c-d-e. The suggested formation and sliding of a Coulomb wedge are validated by the displacement contours and the velocity vectors of **Figure 5.8.** At point b, the displacement contour shows the clear formation of the Coulomb wedge while the velocity vectors direction to side and upward suggest the sliding of the wedge.

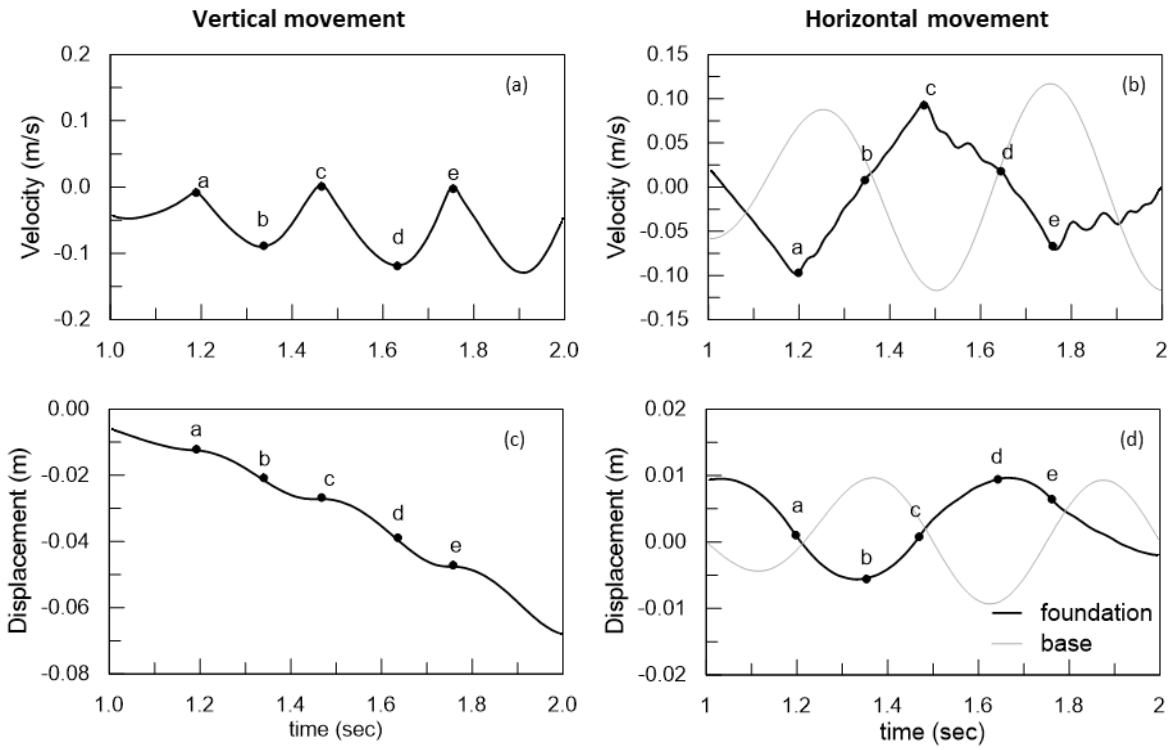

Figure 5.7: Detail of vertical and horizontal velocity and displacement time-histories at the foundation and soil base level of the FS system.

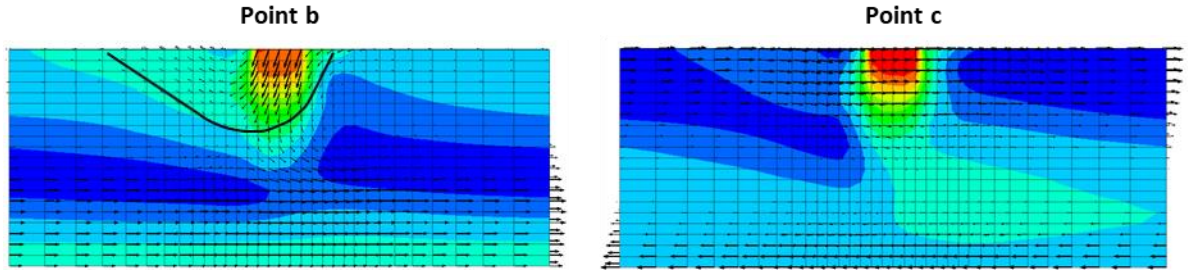

Figure 5.8: Displacement contours and velocity vectors at the momement of the maximum (point b) and minimum (point c) settlement rate of the FS system.

5.2.3 Settlement mechanism of Structure-Foundation-Soil Systems

Section 5.2.2 identified soil strength degradation due to liquefaction and the subsequent formation of a Coulomb-type wedge as the principal mechanism for the accumulation of seismic settlements of single footings, i.e., FS systems. In this section, the described framework is extended in order to investigate the seismic response of structures founded with a single footing, i.e., modeled as SFS systems. The importance of soil-structure interaction (SSI) in structural settlements is widely discussed in literature (Dashti et al. 2010a; Kourkoulis et al. 2012), since rocking of the foundation during strong vibrations creates significant

shear straining and, thus, soil softening under the foundation edges. Through this mechanism, building settlements are accumulated every half-cycle, when rocking occurs.

In this section the response of SFS and FS systems in liquefied conditions is comparatively examined. The selected model configuration characteristics and the system parameters correspond to the reference case, described previously Chapter 3. To outline the model details, an improved zone is constructed with thickness H = 2m, relative density D_r = 60% and permeability k = $2.0 \cdot 10^{-3}$ m/s on top of the natural soil of D_r =45% and thickness z_{liq}=18 m. A square 4m x 4m footing is selected that applies an average pressure of 80kPa. The structural characteristics, expressed in terms of SSI parameters, correspond to a system close to resonance, namely T_{sys}/T_{exc} = 0.90, with average relative mass ratio γ = 4.00, and low to average slenderness ratio h/r=1.04. It is noted that the system period T_{sys} refers to the effective system period $T_{sys.eff}$, i.e., during shaking (in the context of Chapter 4).

Figure 5.9 compares settlement accumulation time-histories for the foregoing SFS and the equivalent FS system. It is noteworthy that the final settlements of the SFS system are about 30% smaller than those of the FS system. Following the greater settlement of the FS system footing into the liquefied soil, the corresponding deviatoric strains are also greater (**Figure 5.9f**). Note that, following complete liquefaction at the free field at about t=1.8 sec (**Figure 5.2**), the liquefied soil deposit acts as a natural seismic isolator and therefore horizontal vibrations of the foundation are de-amplified (**Figure 5.9b**). For this reason, settlement accumulation in SFS and FS models will be compared separately for the following two time-windows: i) before the onset of complete liquefaction (i.e., for t < 1.8sec) and ii) after it (i.e., for t > 1.8sec). Observe that, during the first time-window, the FS system accumulates settlements faster than the SFS system, while during the second time window settlements accumulate with the same rate, which is significantly lower than the initial for both systems (**Figure 5.9d**). Significant rocking-induced footing rotation is only present in the SFS system (**Figure 5.9c**) and for the time period before the onset of liquefaction. On the contrary, the FS system experiences only a permanent foundation tilt, i.e., without oscillations. The de-amplification of structural vibrations results in reduced deviatoric stresses under the footing edges for the SFS system, which now become comparable to the deviatoric stresses of the FS system (**Figure 5.9e**).

Two main questions need to be answered concerning the response of SFS and FS systems:

- Why does the SFS system settle less than the FS one, while – at the same time – it is the former that experiences greater oscillations?

- Is the role of SSI, in general, beneficial or detrimental for the performance of structures on liquefiable ground?

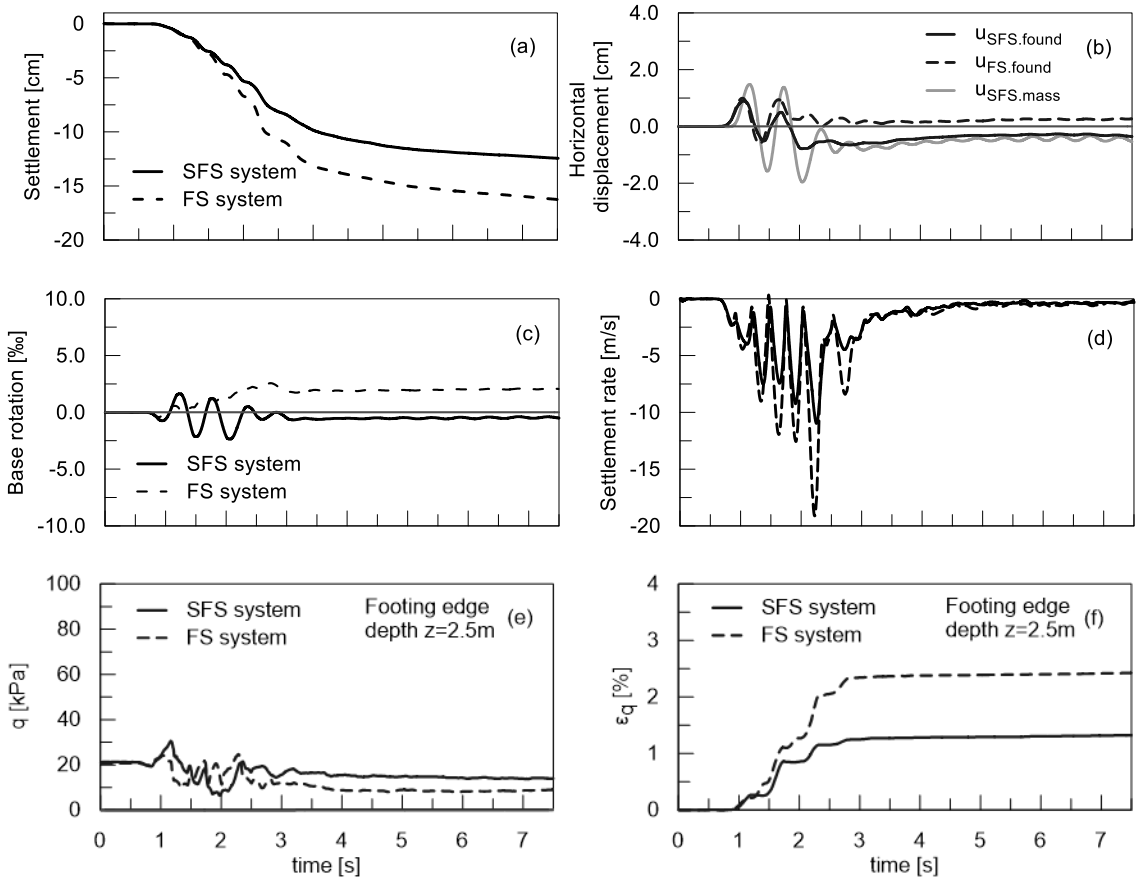

Figure 5.9: Structural response time-histories of the SFS and the FS system in terms of the footing's : a) settlement, b) horizontal displacements, c) rotation, d) settlement rate and deviatoric e) stresses and f) strains under the footing edge.

To answer the above questions, **Figure 5.10** presents the response of the SFS system during the whole period of shaking (t = 0-8 sec), but also focusing on the basic response parameters during a single cycle of oscillation (for t = 1-2 sec, specifically). In more detail, the vertical velocity time-history of the footing, i.e., the settlement rate, is presented in the first row of the Figure (subplots a, b), while horizontal displacement and velocity time-histories of the structural mass and at the free field level are presented in the second and third row, respectively (subplots c, d and e, f). A full cycle of motion is identified in the following figures with the markings a'-e' and a-e regarding the structural mass and footing oscillations, respectively. It is selected here to focus mostly on the quarter cycle from point a to point b of the full cycle of interest, which occurs within the time window t = 1-2 sec when settlements accumulate at the highest pace (**Figure 5.10a**).

At first, it is observed that this quarter of cycle from point a to b corresponds to movement of the ground (and of the foundation) from its neutral position ($u = 0$) to its maximum displacement to the left ($u = u_{min}$), as observed in **Figure 5.10f**. At the same time, the structure, being a single degree-of-freedom oscillator, is subjected to a forced vibration with dynamic loading at its base. Since the ratio T_{sys}/T_{exc} is close to resonance (equal to 0.90), theory of vibrations predicts phase lag between the motion of the oscillator (the structure) and the excitation source (the foundation motion) equal to 90 degrees, or, in other words, a quarter cycle phase lag of the structural movement. The above theoretical observations are confirmed by examining the horizontal displacement and horizontal velocity time-histories of **Figure 5.10h** and **5.10f**. More specifically, when the foundation is at the neutral position (point a) the structure lags a quarter cycle, therefore, it is located at its maximum displacement to the right ($u_{str} = u_{max}$). At this point (a') of maximum displacement, the structure experiences zero velocity (**Figure 5.10d**) ($\dot{u} = 0$) and minimum acceleration ($\ddot{u} = \ddot{u}_{min}$). The snapshot of the structural position and horizontal displacement pattern of the foundation soil is depicted in **Figure 5.11a**. Observe that at this point the maximum inertial force is exerted upon the structure, according to Newton's second law, equal to $F_{inertia} = -m \cdot a$ and having opposite sign to that of the acceleration. Next, as the foundation moves to the left, towards its minimum displacement (a -> b), the structure returns to its neutral location (**Figure 5.10h**), while the snapshot of the structure location and horizontal displacement pattern of the foundation soil is depicted in **Figure 5.11b**. The half-cycle of oscillation is concluded as the foundation returns to its neutral position (b -> c) and the settlement rate (d) is reduced to zero due to the nullification of the Coulomb-wedge sliding. The half-cycle from point c to point e represents the symmetrical motion of the foundation to the right. The pattern of settlement accumulation is identical for every half-cycle.

As a result of the above, the structural inertial force is directed to the right at the time when the foundation moves to the left and settles, and vice versa. It is, therefore, the phase lag between the structural and the foundation vibrations – in the case of structural resonance – that counteracts soil inertia forces and sliding of the failure wedge (to the left), explaining, thus, the reduced – overall – settlement accumulation of the SFS system.

Thus, the examination of the resonant system underlines the correlation between phase lag and settlement accumulation. In the parametric investigation that follows it possible to investigate in depth and quantify settlement accumulation of systems with varying vibrational characteristics, in terms of phase lag and spectral acceleration.

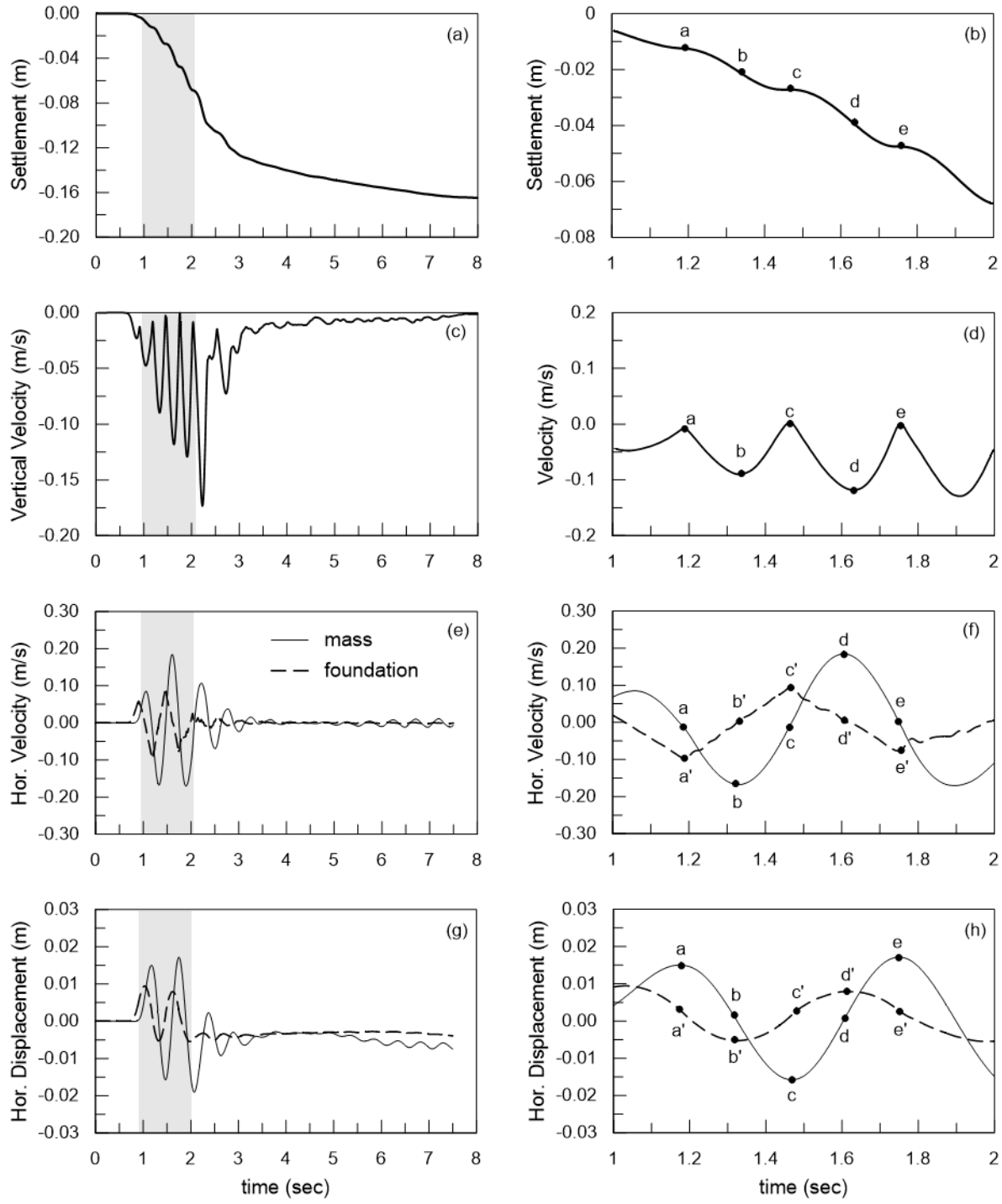

Figure 5.10: Time-histories of SFS system and free field vibration: (a, b) footing settlement, (c, d) footing vertical velocity, (e, f) horizontal velocities (structural mass and free field), (g, h) horizontal displacements (structural mass and free field); (a), (c), (e), (g) for the whole time range t = 0-8 sec, (b), (d), (f), (h) for specific time range t = 1-2 sec.

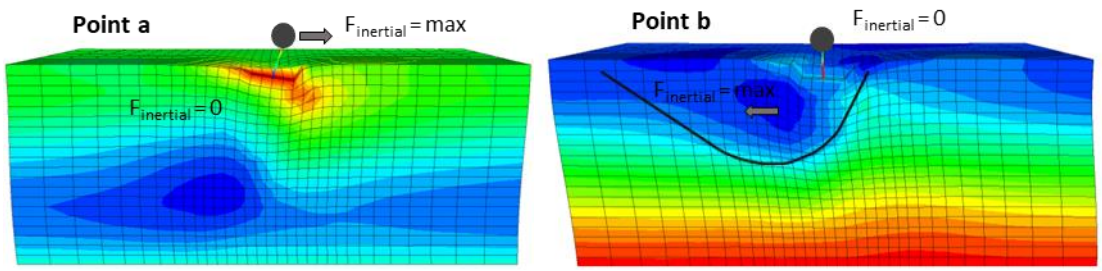

Figure 5.11: Schematic representations of horizontal displacements of the foundation soil and the structure at points a and b of a vibration cycle of an SFS system.

5.3 Parametric investigation

5.3.1 Input data and assumptions

The response of structure-foundation-soil (SFS) and foundation-soil (FS) systems is parametrically investigated in this chapter. The main focus of this investigation is to examine the effect of critical structural and excitation parameters, which are explicitly described in the following and also summarized in **Table 5.10**. Input structural parameters are correlated with the corresponding SSI dimensionless parameters within the soil-structure interaction (SSI) framework. The geotechnical model parameters are also described in the following, although they do not constitute the main aim of the parametric study. This is due to two main reasons. The first is that the effects of geotechnical parameters on system response have been thoroughly examined in previous studies (Dimitriadi et al. 2017, 2018). The second reason is that the parametric investigation is performed for the SFS-to-FS response ratio for which soil effects become of secondary importance, if not insignificant.

- In particular, structural mass is concentrated at the top of the structure for SFS systems and at the foundation level for FS systems. The selected values are M_{str} = 54.4, 74.4, 89.7, 114.4Mgr which correspond to average applied contact pressure at the foundation equal to q = 52, 68, 80, 100kPa, since the width of the square foundation is 4.0m. The corresponding relative mass ratios are $\gamma = M_{str}/(\gamma \cdot r^3)$ = 2.40, 3.30, 4.00, 5.10, where γ is the soil unit weight and r is the equivalent radius of the footing, i.e., r = 2.82m herein.
- The structural height is h = 3.0, 3.9, 5.1 m, corresponding to slenderness ratios h/r = 1.06, 1.38, 1.88.
- The examined values of fixed-base natural period of the structure are $T_{str.f}$ = 0.05, 0.07, 0.10, 0.15, 0.20, 0.29, 0.35sec, which correspond inversely to structure-to-soil stiffness ratios s = 0.05, 0.06, 0.08, 0.11, 0.16, 0.24, 0.33. It is reminded here that the structure-to-soil stiffness ratio s is defined as $s = h/(V_s \cdot T_{str.f})$.

- The excitation periods of the acceleration input motion are T_{exc} = 0.25, 0.35, 0.45, 0.50, 0.60, 0.70, 0.80, 0.90, 1.10sec, with number of cycles N=12.
- Peak ground acceleration values (at the base of the mesh, i.e., at depth of 20m) are a^b_{max} = 0.15, 0.20, 0.25 and 0.40g.
- The basic geotechnical parameters of the model include relative density D_r = 45% and 60% of the natural and the improved soil, respectively, improved zone thickness H_c = 2m and thickness of the liquefiable sand layer z_{liq} = 18m. These were not varied in the hereby performed analyses.
- The Factor of Safety against liquefaction of the soil layers is FS_L < 0.3 for the examined range of seismic intensity, therefore, soil conditions may be assumed as *purely liquefied.* The liquefaction onset time t_L, thus, is adequately small to ensure that the non-liquefied part of shaking – and the associated seismic settlements – are negligibly small compared to the liquefied part of shaking.

The differentiation of the aforementioned input parameters is summarized in the **Table 5.1** below, where these parameters are categorized as structural, excitation and SSI parameters. A total of 191 analyses was performed, namely 83 for FS systems and 108 for SFS systems.

Table 5.10: Input data of 3-dimensional parametric analyses (colored cells indicate the examined parameter).

No	-System	Structural Parameters			Excitation Parameters		SSI Parameters			
		M_{str} (tn)	$T_{str.f}$ (sec)	h (m)	T_{exc} (sec)	a^b_{max} (g)	h/r	γ	s	$T_{sys.el}$ / $T_{str.f}$
1	SFS	54.4	0.35	3	0.25	0.15	1.06	2.40	0.05	1.20
2	SFS	54.4	0.35	3	0.30	0.15	1.06	2.40	0.05	1.20
3	SFS	54.4	0.35	3	0.35	0.15	1.06	2.40	0.05	1.20
4	SFS	54.4	0.35	3	0.40	0.15	1.06	2.40	0.05	1.20
5	SFS	54.4	0.35	3	0.45	0.15	1.06	2.40	0.05	1.20
6	SFS	54.4	0.35	3	0.50	0.15	1.06	2.40	0.05	1.20
7	SFS	54.4	0.35	3	0.60	0.15	1.06	2.40	0.05	1.20
8	SFS	54.4	0.35	3	0.70	0.15	1.06	2.40	0.05	1.20
9	SFS	54.4	0.35	3	0.80	0.15	1.06	2.40	0.05	1.20
10	SFS	54.4	0.35	3	0.90	0.15	1.06	2.40	0.05	1.20
11	FS	54.4	0.35	3	0.25	0.15	-	-	-	-
12	FS	54.4	0.35	3	0.30	0.15	-	-	-	-
13	FS	54.4	0.35	3	0.35	0.15	-	-	-	-
14	FS	54.4	0.35	3	0.40	0.15	-	-	-	-
15	FS	54.4	0.35	3	0.45	0.15	-	-	-	-
16	FS	54.4	0.35	3	0.50	0.15	-	-	-	-
17	FS	54.4	0.35	3	0.60	0.15	-	-	-	-
18	FS	54.4	0.35	3	0.70	0.15	-	-	-	-
19	FS	54.4	0.35	3	0.80	0.15	-	-	-	-

No	-System	Structural Parameters			Excitation Parameters		SSI Parameters			
		M_{str} (tn)	$T_{str.f}$ (sec)	h (m)	T_{exc} (sec)	a^b_{max} (g)	h/r	γ	s	$T_{sys.el}$ / $T_{str.f}$
20	FS	54.4	0.35	3	0.90	0.15	-	-	-	-
21	SFS	74.4	0.35	3	0.25	0.15	1.06	3.30	0.05	1.27
22	SFS	74.4	0.35	3	0.30	0.15	1.06	3.30	0.05	1.27
23	SFS	74.4	0.35	3	0.35	0.15	1.06	3.30	0.05	1.27
24	SFS	74.4	0.35	3	0.40	0.15	1.06	3.30	0.05	1.27
25	SFS	74.4	0.35	3	0.45	0.15	1.06	3.30	0.05	1.27
26	SFS	74.4	0.35	3	0.50	0.15	1.06	3.30	0.05	1.27
27	SFS	74.4	0.35	3	0.60	0.15	1.06	3.30	0.05	1.27
28	SFS	74.4	0.35	3	0.70	0.15	1.06	3.30	0.05	1.27
29	SFS	74.4	0.35	3	0.80	0.15	1.06	3.30	0.05	1.27
30	SFS	74.4	0.35	3	0.90	0.15	1.06	3.30	0.05	1.27
31	SFS	74.4	0.35	3	1.10	0.15	1.06	3.30	0.05	1.27
32	FS	74.4	0.35	3	0.25	-	-	-	-	-
33	FS	74.4	0.35	3	0.30	-	-	-	-	-
34	FS	74.4	0.35	3	0.35	-	-	-	-	-
35	FS	74.4	0.35	3	0.40	-	-	-	-	-
36	FS	74.4	0.35	3	0.45	-	-	-	-	-
37	FS	74.4	0.35	3	0.50	-	-	-	-	-
38	FS	74.4	0.35	3	0.60	-	-	-	-	-
39	FS	74.4	0.35	3	0.70	-	-	-	-	-
40	FS	74.4	0.35	3	0.80	-	-	-	-	-
41	FS	74.4	0.35	3	0.90	-	-	-	-	-
42	FS	74.4	0.35	3	1.10	-	-	-	-	-
43	SFS	89.7	0.35	3	0.25	0.15	1.06	4.00	0.05	1.32
44	SFS	89.7	0.35	3	0.30	0.15	1.06	4.00	0.05	1.32
45	SFS	89.7	0.35	3	0.35	0.15	1.06	4.00	0.05	1.32
46	SFS	89.7	0.35	3	0.40	0.15	1.06	4.00	0.05	1.32
47	SFS	89.7	0.35	3	0.45	0.15	1.06	4.00	0.05	1.32
48	SFS	89.7	0.35	3	0.50	0.15	1.06	4.00	0.05	1.32
49	SFS	89.7	0.35	3	0.60	0.15	1.06	4.00	0.05	1.32
50	SFS	89.7	0.35	3	0.70	0.15	1.06	4.00	0.05	1.32
51	SFS	89.7	0.35	3	0.80	0.15	1.06	4.00	0.05	1.32
52	SFS	89.7	0.35	3	0.90	0.15	1.06	4.00	0.05	1.32
53	SFS	89.7	0.35	3	1.10	0.15	1.06	4.00	0.05	1.32
54	SFS	89.7	0.35	3	1.20	0.15	1.06	4.00	0.05	1.32
55	FS	89.7	0.35	3	0.25	-	-	-	-	-
56	FS	89.7	0.35	3	0.30	-	-	-	-	-
57	FS	89.7	0.35	3	0.35	-	-	-	-	-
58	FS	89.7	0.35	3	0.40	-	-	-	-	-
59	FS	89.7	0.35	3	0.45	-	-	-	-	-
60	FS	89.7	0.35	3	0.50	-	-	-	-	-
61	FS	89.7	0.35	3	0.60	-	-	-	-	-
62	FS	89.7	0.35	3	0.70	-	-	-	-	-

No	-System	Structural Parameters			Excitation Parameters		SSI Parameters			
		M_{str} (tn)	$T_{str.f}$ (sec)	h (m)	T_{exc} (sec)	a^b_{max} (g)	h/r	γ	s	$T_{sys.el}$ / $T_{str.f}$
63	FS	89.7	0.35	3	0.80	-	-	-	-	-
64	FS	89.7	0.35	3	0.90	-	-	-	-	-
65	FS	89.7	0.35	3	1.10	-	-	-	-	-
66	FS	89.7	0.35	3	1.20	-	-	-	-	-
67	SFS	114.4	0.35	3	0.25	0.15	1.06	5.10	0.05	1.39
68	SFS	114.4	0.35	3	0.30	0.15	1.06	5.10	0.05	1.39
69	SFS	114.4	0.35	3	0.35	0.15	1.06	5.10	0.05	1.39
70	SFS	114.4	0.35	3	0.40	0.15	1.06	5.10	0.05	1.39
71	SFS	114.4	0.35	3	0.45	0.15	1.06	5.10	0.05	1.39
72	SFS	114.4	0.35	3	0.50	0.15	1.06	5.10	0.05	1.39
73	SFS	114.4	0.35	3	0.60	0.15	1.06	5.10	0.05	1.39
74	SFS	114.4	0.35	3	0.70	0.15	1.06	5.10	0.05	1.39
75	SFS	114.4	0.35	3	0.80	0.15	1.06	5.10	0.05	1.39
76	SFS	114.4	0.35	3	0.90	0.15	1.06	5.10	0.05	1.39
77	SFS	114.4	0.35	3	1.10	0.15	1.06	5.10	0.05	1.39
78	FS	114.4	0.35	3	0.25	0.15	-	-	-	-
79	FS	114.4	0.35	3	0.30	0.15	-	-	-	-
80	FS	114.4	0.35	3	0.35	0.15	-	-	-	-
81	FS	114.4	0.35	3	0.40	0.15	-	-	-	-
82	FS	114.4	0.35	3	0.45	0.15	-	-	-	-
83	FS	114.4	0.35	3	0.50	0.15	-	-	-	-
84	FS	114.4	0.35	3	0.60	0.15	-	-	-	-
85	FS	114.4	0.35	3	0.70	0.15	-	-	-	-
86	FS	114.4	0.35	3	0.80	0.15	-	-	-	-
87	FS	114.4	0.35	3	0.90	0.15	-	-	-	-
88	FS	114.4	0.35	3	1.10	0.15	-	-	-	-
89	SFS	89.7	0.35	3.9	0.25	0.15	1.38	4.00	0.06	1.49
90	SFS	89.7	0.35	3.9	0.30	0.15	1.38	4.00	0.06	1.49
91	SFS	89.7	0.35	3.9	0.35	0.15	1.38	4.00	0.06	1.49
92	SFS	89.7	0.35	3.9	0.40	0.15	1.38	4.00	0.06	1.49
93	SFS	89.7	0.35	3.9	0.45	0.15	1.38	4.00	0.06	1.49
94	SFS	89.7	0.35	3.9	0.50	0.15	1.38	4.00	0.06	1.49
95	SFS	89.7	0.35	3.9	0.60	0.15	1.38	4.00	0.06	1.49
96	SFS	89.7	0.35	3.9	0.70	0.15	1.38	4.00	0.06	1.49
97	SFS	89.7	0.35	3.9	0.80	0.15	1.38	4.00	0.06	1.49
98	SFS	89.7	0.35	3.9	0.90	0.15	1.38	4.00	0.06	1.49
99	SFS	89.7	0.35	3.9	1.20	0.15	1.38	4.00	0.06	1.49
100	SFS	89.7	0.35	5.1	0.25	0.15	1.88	4.00	0.08	1.74
101	SFS	89.7	0.35	5.1	0.30	0.15	1.88	4.00	0.08	1.74
102	SFS	89.7	0.35	5.1	0.35	0.15	1.88	4.00	0.08	1.74
103	SFS	89.7	0.35	5.1	0.40	0.15	1.88	4.00	0.08	1.74
104	SFS	89.7	0.35	5.1	0.45	0.15	1.88	4.00	0.08	1.74
105	SFS	89.7	0.35	5.1	0.50	0.15	1.88	4.00	0.08	1.74

No	-System	Structural Parameters			Excitation Parameters		SSI Parameters			
		M_{str} (tn)	$T_{str.f}$ (sec)	h (m)	T_{exc} (sec)	a^b_{max} (g)	h/r	γ	s	$T_{sys.el}$ / $T_{str.f}$
106	SFS	89.7	0.35	5.1	0.60	0.15	1.88	4.00	0.08	1.74
107	SFS	89.7	0.35	5.1	0.70	0.15	1.88	4.00	0.08	1.74
108	SFS	89.7	0.35	5.1	0.80	0.15	1.88	4.00	0.08	1.74
109	SFS	89.7	0.35	5.1	0.90	0.15	1.88	4.00	0.08	1.74
110	SFS	89.7	0.35	5.1	1.20	0.15	1.88	4.00	0.08	1.74
111	SFS	89.7	0.35	3	0.25	0.20	1.06	4.00	0.05	1.32
112	SFS	89.7	0.35	3	0.35	0.20	1.06	4.00	0.05	1.32
113	SFS	89.7	0.35	3	0.45	0.20	1.06	4.00	0.05	1.32
114	SFS	89.7	0.35	3	0.50	0.20	1.06	4.00	0.05	1.32
115	SFS	89.7	0.35	3	0.60	0.20	1.06	4.00	0.05	1.32
116	SFS	89.7	0.35	3	0.70	0.20	1.06	4.00	0.05	1.32
117	SFS	89.7	0.35	3	0.90	0.20	1.06	4.00	0.05	1.32
118	FS	89.7	0.35	3	0.25	0.20	-	-	-	-
119	FS	89.7	0.35	3	0.35	0.20	-	-	-	-
120	FS	89.7	0.35	3	0.45	0.20	-	-	-	-
121	FS	89.7	0.35	3	0.50	0.20	-	-	-	-
122	FS	89.7	0.35	3	0.60	0.20	-	-	-	-
123	FS	89.7	0.35	3	0.70	0.20	-	-	-	-
124	FS	89.7	0.35	3	0.90	0.20	-	-	-	-
125	SFS	89.7	0.35	3	0.25	0.25	1.06	4.00	0.05	1.32
126	SFS	89.7	0.35	3	0.35	0.25	1.06	4.00	0.05	1.32
127	SFS	89.7	0.35	3	0.45	0.25	1.06	4.00	0.05	1.32
128	SFS	89.7	0.35	3	0.50	0.25	1.06	4.00	0.05	1.32
129	SFS	89.7	0.35	3	0.60	0.25	1.06	4.00	0.05	1.32
130	SFS	89.7	0.35	3	0.70	0.25	1.06	4.00	0.05	1.32
131	SFS	89.7	0.35	3	0.90	0.25	1.06	4.00	0.05	1.32
132	FS	89.7	0.35	3	0.25	0.25	-	-	-	-
133	FS	89.7	0.35	3	0.35	0.25	-	-	-	-
134	FS	89.7	0.35	3	0.45	0.25	-	-	-	-
135	FS	89.7	0.35	3	0.50	0.25	-	-	-	-
136	FS	89.7	0.35	3	0.60	0.25	-	-	-	-
137	FS	89.7	0.35	3	0.70	0.25	-	-	-	-
138	FS	89.7	0.35	3	0.90	0.25	-	-	-	-
139	SFS	89.7	0.35	3	0.35	0.40	1.06	4.00	0.05	1.32
140	SFS	89.7	0.35	3	0.45	0.40	1.06	4.00	0.05	1.32
141	SFS	89.7	0.35	3	0.50	0.40	1.06	4.00	0.05	1.32
142	SFS	89.7	0.35	3	0.60	0.40	1.06	4.00	0.05	1.32
143	SFS	89.7	0.35	3	0.70	0.40	1.06	4.00	0.05	1.32
144	FS	89.7	0.35	3	0.25	0.40	-	-	-	-
145	FS	89.7	0.35	3	0.35	0.40	-	-	-	-
146	FS	89.7	0.35	3	0.45	0.40	-	-	-	-
147	FS	89.7	0.35	3	0.50	0.40	-	-	-	-
148	FS	89.7	0.35	3	0.60	0.40	-	-	-	-

No	-System	Structural Parameters			Excitation Parameters		SSI Parameters			
		M_{str} (tn)	$T_{str.f}$ (sec)	h (m)	T_{exc} (sec)	a^b_{max} (g)	h/r	γ	s	$T_{sys.el}$ / $T_{str.f}$
149	FS	89.7	0.35	3	0.70	0.40	-	-	-	-
150	SFS	89.7	0.05	3	0.19	0.15	1.06	4.00	0.33	3.60
151	SFS	89.7	0.07	3	0.19	0.15	1.06	4.00	0.24	3.30
152	SFS	89.7	0.10	3	0.19	0.15	1.06	4.00	0.16	3.16
153	SFS	89.7	0.15	3	0.19	0.15	1.06	4.00	0.11	2.26
154	SFS	89.7	0.20	3	0.23	0.15	1.06	4.00	0.08	1.80
155	SFS	89.7	0.29	3	0.27	0.15	1.06	4.00	0.06	1.43
156	SFS	89.7	0.35	3	0.31	0.15	1.06	4.00	0.05	1.32
157	FS	89.7	0.05	3	0.19	0.15	-	-	-	-
158	FS	89.7	0.07	3	0.19	0.15	-	-	-	-
159	FS	89.7	0.10	3	0.19	0.15	-	-	-	-
160	FS	89.7	0.15	3	0.19	0.15	-	-	-	-
161	FS	89.7	0.20	3	0.23	0.15	-	-	-	-
162	FS	89.7	0.29	3	0.27	0.15	-	-	-	-
163	FS	89.7	0.35	3	0.31	0.15	-	-	-	-
164	SFS	89.7	0.05	3	0.50	0.15	1.06	4.00	0.33	3.60
165	SFS	89.7	0.07	3	0.50	0.15	1.06	4.00	0.24	3.30
166	SFS	89.7	0.10	3	0.50	0.15	1.06	4.00	0.16	3.16
167	SFS	89.7	0.15	3	0.50	0.15	1.06	4.00	0.11	2.26
168	SFS	89.7	0.20	3	0.60	0.15	1.06	4.00	0.08	1.80
169	SFS	89.7	0.29	3	0.70	0.15	1.06	4.00	0.06	1.43
170	SFS	89.7	0.35	3	0.80	0.15	1.06	4.00	0.05	1.32
171	FS	89.7	0.05	3	0.50	-	-	-	-	-
172	FS	89.7	0.07	3	0.50	-	-	-	-	-
173	FS	89.7	0.10	3	0.50	-	-	-	-	-
174	FS	89.7	0.15	3	0.50	-	-	-	-	-
175	FS	89.7	0.20	3	0.60	-	-	-	-	-
176	FS	89.7	0.29	3	0.70	-	-	-	-	-
177	FS	89.7	0.35	3	0.80	-	-	-	-	-
178	SFS	89.7	0.05	3	0.25	0.15	1.06	4.00	0.33	3.60
179	SFS	89.7	0.07	3	0.25	0.15	1.06	4.00	0.24	3.30
180	SFS	89.7	0.10	3	0.25	0.15	1.06	4.00	0.16	3.16
181	SFS	89.7	0.15	3	0.25	0.15	1.06	4.00	0.11	2.26
182	SFS	89.7	0.20	3	0.30	0.15	1.06	4.00	0.08	1.80
183	SFS	89.7	0.29	3	0.35	0.15	1.06	4.00	0.06	1.43
184	SFS	89.7	0.35	3	0.40	0.15	1.06	4.00	0.05	1.32
185	FS	89.7	0.05	3	0.25	0.15	-	-	-	-
186	FS	89.7	0.07	3	0.25	0.15	-	-	-	-
187	FS	89.7	0.10	3	0.25	0.15	-	-	-	-
188	FS	89.7	0.15	3	0.25	0.15	-	-	-	-
189	FS	89.7	0.20	3	0.30	0.15	-	-	-	-
190	FS	89.7	0.29	3	0.35	0.15	-	-	-	-
191	FS	89.7	0.35	3	0.40	0.15	-	-	-	-

5.3.2 Effect of T_{sys}/T_{exc}

The influence of SSI on seismic settlements is investigated with the aid of **Figure 5.12a**, **b** and **c**. The aim of these figures is to examine the role of the vibrational characteristics of the structure on settlement accumulation and also to correlate the associated effects with the spectral amplification acceleration and phase lag of the structure. In more detail, **Figure 5.12a** correlates the settlement ratio between the SFS and the FS system, i.e. ρ_{SFS}/ρ_{FS} , to the period ratio T_{sys}/T_{exc}, whereas **Figure 5.12b** and **5.12c** present similar correlations for two key vibrational parameters of the SFS system, namely:

i. The normalized absolute acceleration of the structural mass S_a/PGA, which determines directly the magnitude of inertial forces.
ii. The phase angle ϕ between the vibration of structural mass and the vibration of the foundation, defined as:

$$\varphi = 2\pi \frac{\Delta t}{T_{exc}} = 2\pi \frac{[t_{max}^{mass} - t_{max}^{found}]}{T_{exc}} \quad 5.7$$

The phase angle determines, essentially, the synchronization between the structural inertial force and the movement of the soil surface. For small values of phase angles, the inertial force acting on the structural mass is in-phase ($\varphi < \pi/2$) with soil movement and therefore it aggravates phenomena of soil wedge sliding, since it is concurrent with soil inertial force. For large values of phase angles ($\varphi > \pi/2$), the inertial force on the structural mass is out-of-phase with the inertial force on the soil and therefore it counteracts soil wedge sliding.

At this point it should be noted that the magnitude of the system period T_{sys} is calculated using the effective system properties, namely $T_{sys.eff}$ as defined in Chapter 4. In this case, the reference system has SSI parameters s = 0.07, h/r = 1.06, γ = 4.00 and corresponding elastic period $T_{sys.el}$ = 0.46sec. The peak ground acceleration *PGA* (at the surface level) for the reference soil profile and excitation is measured equal to 0.14g (**Figure 5.6a**). Thus, for PGA = 0.14g, the effective system period is calculated, from Equation 4.18 as:

$$T_{sys.eff} = \alpha \cdot PGA^b \cdot T_{sys.el} = 1.69 \cdot 0.14^{0.20} \cdot 0.46\, sec = 0.52\, sec \quad 5.8$$

Based on **Figure 5.12**, which includes results from analyses No 43-66 of **Table 5.1**, the correlation of settlement ratio ρ_{SFS}/ρ_{FS} to the vibrational characteristics of the structural response can be summarized as follows:

- *Stiff* SFS systems ($T_{sys}/T_{exc} \rightarrow 0.0$) settle equally with FS systems (i.e., $\rho_{SFS}/\rho_{FS} \approx 1.0$). It is noted that both systems move as rigid blocks and the developed inertial forces of the structural mass are equal for both systems and act in-phase with soil inertial forces (**Figure 5.13c**). There is a difference, though, in that the former has a higher point-of-application of its structural inertial force, i.e., applied at h=3.0m, and is prone to rocking. Thus, in essence, the above observation indicates that rocking-induced deviatoric strains under the footing do not contribute significantly to any additional settlement accumulation.
- *Flexible* SFS systems ($T_{sys}/T_{exc} > 1.40$) settle approximately 10% less than FS systems (i.e., $\rho_{SFS}/\rho_{FS} \approx 0.9$). This is because structural inertial forces, even though they are small (**Figure 5.13b**), act out-of-phase with soil inertial forces (**Figure 5.13c**), thus counteracting the failure wedge formation and sliding below the foundation.
- *At resonance* ($T_{sys}/T_{exc} \approx 1.00$), the reduction of settlements for SFS systems becomes maximum ($\rho_{SFS}/\rho_{FS} \approx 0.75$). This is because structural inertial forces are amplified (**Figure 5.13b**), while they still experience considerable phase lag ($\phi \approx 90$ deg, i.e., quarter cycle) relative to the soil inertial forces (**Figure 5.13c**). As a result, the increased structural inertial force inhibits wedge sliding to the greatest extent.

The described rationale suggests that the primary mechanism of settlement accumulation in liquefied conditions is the Coulomb-type wedge sliding. On the other hand, rocking-induced shear straining under the structure has, merely, a secondary contribution.

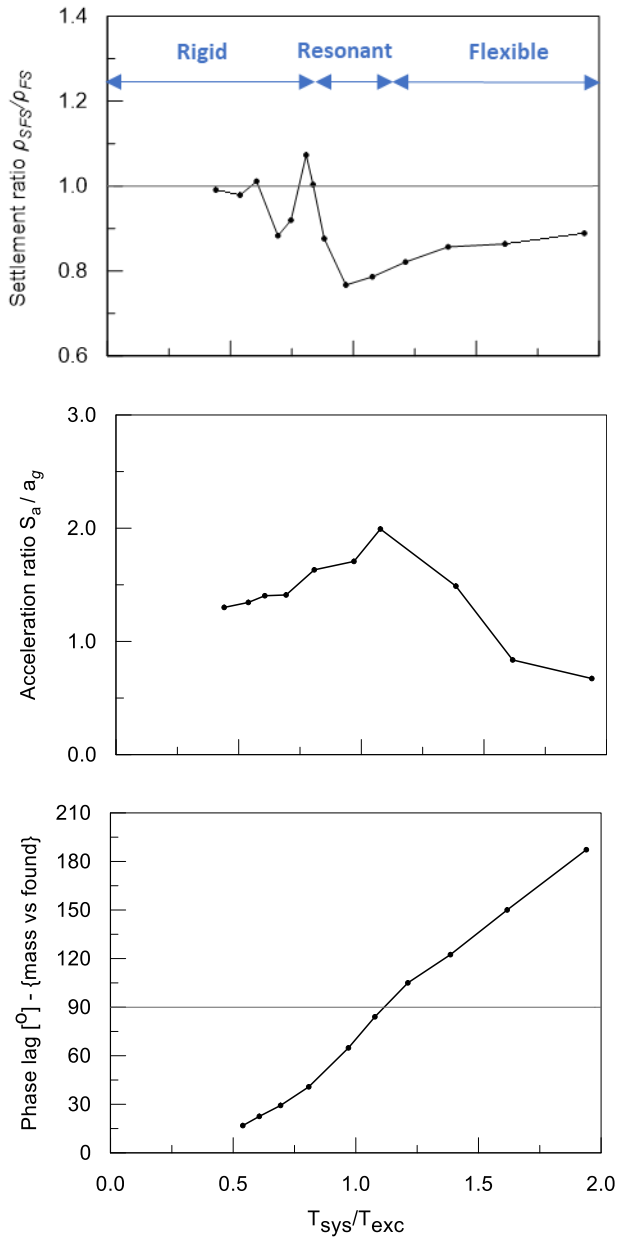

Figure 5.12: Effect of T_{sys}/T_{exc} of SFS systems on: (a) Seismic settlement ratio of SFS-to-FS systems, (b) response spectra of the normalized absolute acceleration of the structural mass S_a/PGA, (c) phase angle φ between the vibration of structural mass and the vibration of the foundation.

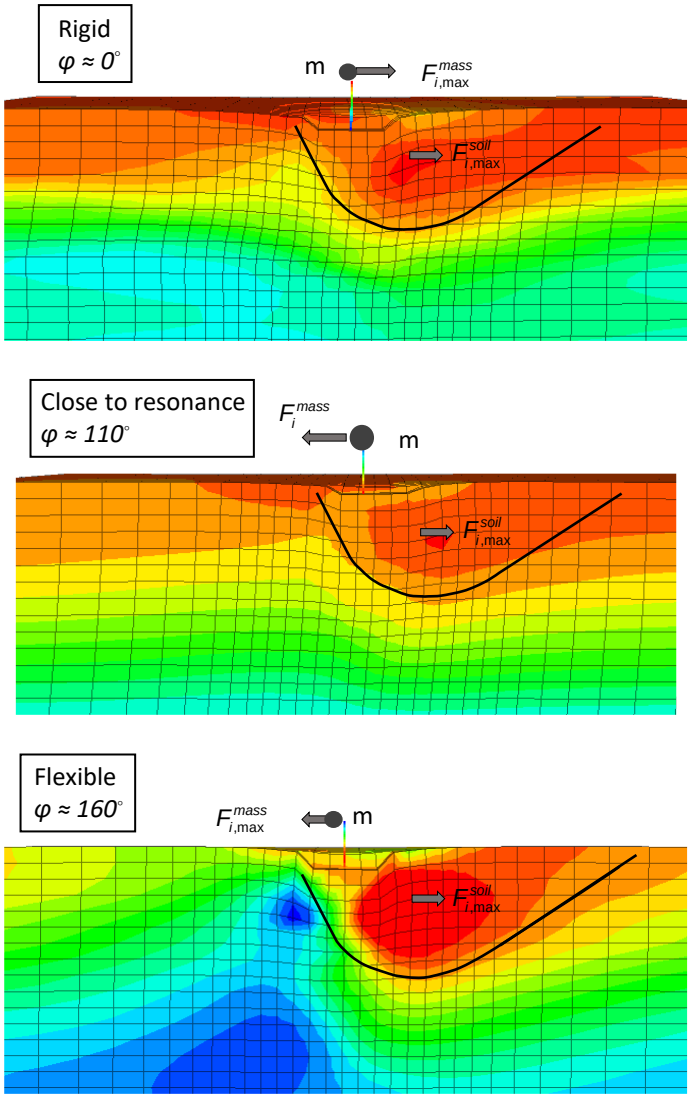

Figure 5.13: Schematic representation of wedge formation in the soil and phase difference between structural and soil inertial forces for three characteristic cases, i.e., a) *rigid* structure: concurrent inertial forces, b) structure *close to resonance:* ≈ quarter cycle difference between inertial forces, c) *flexible* structure: opposite inertial forces.

5.3.3 Effect of slenderness ratio

The effect of slenderness ratio *h*/*r* on the dynamic response of SFS and FS systems is parametrically examined in this section. **Table 5.2** summarizes the numerical analyses performed for that purpose as well as the corresponding structural and SSI properties examined (Analyses No. 43-66, 89-110). The variation of slenderness ratio was materialized by examining structures with varying height *h* in the context described in **Chapter 4**. More specifically, structural height *h* is increased while the structural period $T_{str.f}$ is kept constant in order to maintain variations of the other SSI parameters (s, γ) fairly constant. Elongated structural periods are calculated and introduced herein using the methodology in the previous section.

Namely, the elastic part of period elongation, $T_{sys.el}/T_{str.f}$, is analytically calculated by the procedure described in Design Codes with the measured shear wave velocity V_s used as an input value (Section 4.3.1). The inelastic part of period elongation, i.e. $T_{sys.eff}/T_{sys.el}$, is calculated with the use of Transfer Functions, as described in Section 4.3.2. In the particular case of liquefied soil, the frequency content measure used is the predominant period $T_{sys.p}$ (for more details see Section 4.3.2.2). Results suggest that the elastic part of period elongation $T_{sys.el}/T_{str.f}$ is greatly affected by slenderness ratio ranging from 1.32 to 1.74 (**Table 5.11**). Nevertheless, the inelastic part of period elongation, i.e. $T_{sys.eff}/T_{sys.el}$, is only minimally affected by the slenderness ratio, as previously discussed. **Table 5.11** summarizes values of the aforementioned components of period elongation, as well as the final values of effective system periods $T_{sys.eff}$. These values are used as the numerator input value of the ratio T_{sys}/T_{exc} in the parametric investigation that follows.

Table 5.11: System period elongation data from the numerical analyses for varying slenderness ratio h/r

h (m)	h/r	$T_{sys.el}/T_{str.f}$	$T_{sys.eff}/T_{sys.el}$	$T_{sys.eff}$ (sec)
3.0	*1.06*	*1.32*	*1.13*	*0.50*
3.9	1.38	1.49	1.09	0.57
5.1	1.88	1.74	1.05	0.63

Figure 5.14 presents the main vibration responses of the SFS and FS systems, in the same context as in the previous section, but for different slenderness ratios *h/r*. The following observations can be noted:

- The principal mechanism of settlement accumulation, as described in the previous paragraph, appears for all slenderness ratios. Namely, a resonant area is identified where the ratio ρ_{SFS}/ρ_{FS} experiences its minimum value. For rigid systems, i.e., when $T_{sys}/T_{exc} \rightarrow 0$, ρ_{SFS}/ρ_{FS} ratio tends to 1.0, while for flexible systems, i.e., $T_{sys}/T_{exc} \rightarrow 2.0$, it tends to a constant value approximately equal to 0.8.
- Increasing slenderness ratio reduces minimum values of ρ_{SFS}/ρ_{FS} ratio up to 15%, namely from 0.76 to 0.66 in the range of period ratios $T_{sys}/T_{exc} = 1.0 \div 1.2$.
- Interestingly, increased values of slenderness ratio may lead to ρ_{SFS}/ρ_{FS} ratios significantly greater than unity for relatively "stiff" systems. Maximum values reach up to $\rho_{SFS}/\rho_{FS} \approx 1.2$ in the semi-rigid spectral region $T_{sys}/T_{exc} = 0.60\text{-}0.80$. The particular increase in SFS system settlements is attributed to

soil softening due to rocking, which is observed in "slender" structures with greater overturning moments. Soil softening is mainly localized under the footing edges, where shear strain accumulation (e.g., see **Figure 5.5c**) leads to decreasing values of the associated shear modulus *G*.

- The aforementioned soil softening, introduced due to increased values of structural height, is also responsible for the increased phase lag, which is observed in **Figure 5.14c** as an upward shift of phase lag curves for increasing *h*/*r* ratios.
- Minimum values of ρ_{SFS}/ρ_{FS} ratios occur for T_{sys}/T_{exc} = 1.0 in the case of *h/r* = 1.04 and shift to higher period ratios for increasing levels of slenderness ratio. As previously mentioned, the maxima and minima of settlement ratios are sensitive to the vibrational characteristics of every system, i.e., to the combination of spectral acceleration and phase lag.

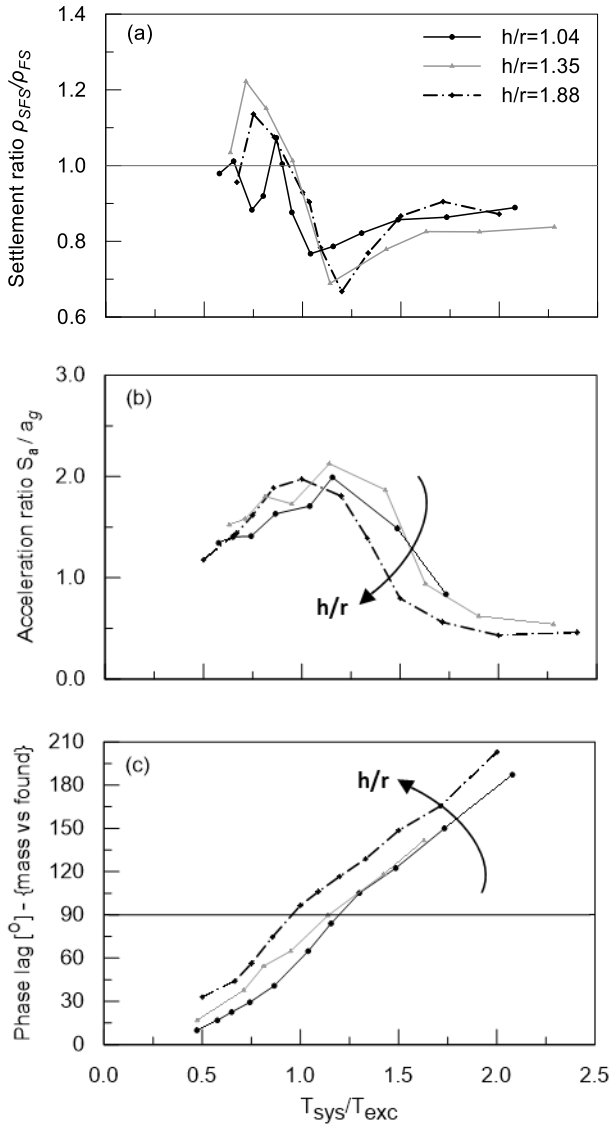

Figure 5.14: Effect of T_{sys}/T_{exc} of SFS systems with different slenderness ratios h/r on: (a) Seismic settlement ratio of SFS-to-FS systems, (b) response spectra of the normalized absolute acceleration of the structural mass S_a/PGA, (c) phase angle φ between the vibration of structural mass and the vibration of the foundation.

5.3.4 Effect of relative mass ratio

The effect of the relative mass ratio γ on the dynamic response of SFS and FS systems is parametrically examined in this section. Structural and SSI properties of the examined systems are summarized in **Table 5.10** (numerical analyses No 1-88). As discussed in the Section 4.3.1, varying relative mass ratios are obtained by considering systems with different structural mass. To ensure equivalent fixed-base structural period $T_{str.f}$ and, thus, structure-to-soil-stiffness ratio s ($=h/V_sT_{str.f}$), structural stiffness k_{str} was varied along with the variation of structural mass.

The influence of relative mass ratio γ on both the elastic and inelastic parts of period elongation, i.e. $T_{sys.el}/T_{str.f}$ and $T_{sys.eff}/T_{sys.el}$ respectively, is moderate with the corresponding ratios ranging from 1.20 to 1.39 for the former and 1.11 to 1.28 for the latter (**Table 5.12**). The above entail that the elastic period $T_{sys.el}$ is moderately increasing with γ, whereas the effective period $T_{sys.eff}$, essentially, remains constant around the value 0.52-0.54 sec. The latter is attributed to the frequency content estimate for $T_{sys.eff}$ which is the predominant system period $T_{sys.p}$, as previously described. The particular estimate designates the highest spectral amplification as the system period, underestimating, thus, any secondary amplifications.

Overall, an underestimation of the effective system period $T_{sys.eff}$ is observed with the use of the predominant system period $T_{sys.p}$, that also results in reducing values of $T_{sys.eff}/T_{sys.el}$ ratio (3rd row, **Table 5.12**).

Table 5.12: Systme period elongation data from the numerical analyses for varying relative mass ratio γ.

M_{str} (tn)	γ	$T_{sys.el}/T_{str.f}$	$T_{sys.eff}/T_{sys.el}$	$T_{sys.eff}$ (sec)
54.4	2.40	1.20	1.28	0.54
74.4	3.30	1.27	1.17	0.52
89.7	*4.00*	*1.32*	*1.13*	*0.52*
114.4	5.10	1.39	1.11	0.54

The main vibrational characteristics of the examined SFS and FS system response are presented in **Figure 5.15.** The following remarks can be made:

- In contrast with the previously examined effects of slenderness ratio h/r, where ρ_{SFS}/ρ_{FS} ratios significantly greater than 1.0 were observed, varying the relative mass ratio γ does not significantly affect the performance of SFS systems.
- Specifically, for low relative mass ratios (e.g., γ = 2.40, 3.30), the effects of superstructure on settlements are small and the observed ρ_{SFS}/ρ_{FS} ratios range between 0.9 and 1.0 mostly (**Figure 5.15a**).
- As in all examined cases, maximum settlement reduction is observed for resonant SFS systems (**Figure 5.15a**). In this particular spectral region, there is a *lower limit* for the settlement ratio, which appears for SFS systems with γ equal to or greater than 4.00 (e.g., γ =4.00, 5.10). This lower limit of ρ_{SFS}/ρ_{FS} ratio is approximately equal to 0.75.

- Spectral accelerations S_a/PGA decrease for increasing relative mass ratios (**Figure 5.15b**), thus suggesting increase of system damping. This is associated with greater levels of soil hysteretic damping due to increased structural inertial forces exerted upon the foundation system for greater γ values.
- Based on all the above, it may be inferred that the lower limit in settlement ratios is introduced due to the additional soil hysteretic damping and the associated reduction in structural inertial forces developed during shaking.
- Lastly, the effect of relative mass ratio γ on the phase lag between the structural and foundation motion is minimal, i.e., slightly increasing with γ (**Figure 5.15c**).

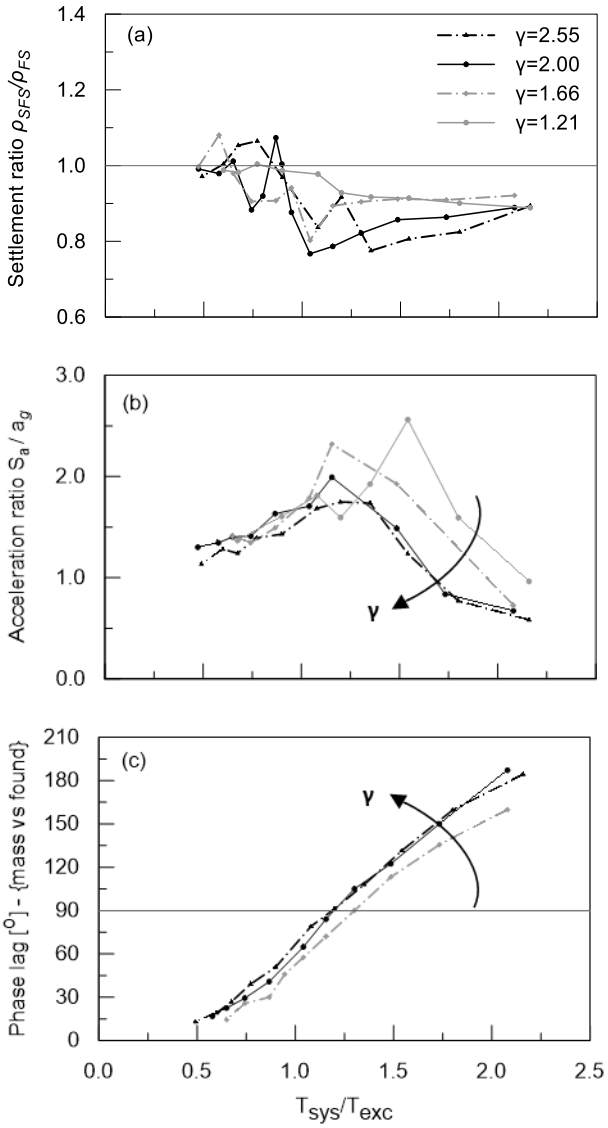

Figure 5.15: Effect of T_{sys}/T_{exc} of SFS systems with different relative mass ratios γ on: (a) Seismic settlement ratio of SFS-to-FS systems, (b) response spectra of the normalized absolute acceleration of the structural mass S_a/PGA, (c) phase angle ϕ between the vibration of structural mass and the vibration of the foundation.

5.3.5 Effect of structure-to-soil stiffness ratio

The effect of structure-to-soil stiffness ratio *s* on the system response is parametrically investigated in the present section with the structural and SSI system properties summarized in **Table 5.10** (numerical analyses No 125-166). The investigation of *s* ratio effects is performed, as described in Section 4.3.1, by considering systems with varying structural stiffness k_{str} and constant structural mass M_{str}, thus, with varying fixed-base natural period $T_{str.f}$. The examined range of *s* ratio values covers the engineering practice according to NEHRP (2012), namely *s* = 0.05 - 0.33. Due to the necessity of capturing the particular

wide range of *s* values, numerical predictions of settlement ratios are correlated directly to the *s* ratio here. Additionally, the effect of period ratio T_{sys}/T_{exc}, which is the governing settlement mechanism, is introduced by examining 3 sets of *s* ratios for 3 different levels of period ratios, i.e., T_{sys}/T_{exc} = 0.5, 1.0 and 1.3. The aforementioned values were selected as such in order to capture the response of rigid, resonant and flexible systems, as described in paragraph 5.3.2.

Results of the pertinent numerical analyses are presented in **Figure 5.16**, which shows the variation of settlement ratio ρ_{SFS}/ρ_{FS} with the structure-to-soil stiffness ratio *s*. Results indicate that settlement ratios are essentially not affected by *s*, while their values are consistent with previous findings, as discussed in paragraph 5.3.2. Namely, for resonant and flexible systems with period ratios T_{sys}/T_{exc} equal to 1.0 and 1.3, respectively, SFS systems settle 10-20% less than FS systems, i.e., the ρ_{SFS}/ρ_{FS} ratio ranges between 0.8 and 0.9. On the contrary, rigid systems with period ratios T_{sys}/T_{exc} equal to 0.5 exhibit a more significant variation in settlement ratios values, i.e., $\rho_{SFS}/\rho_{FS} \approx$ 0.75 - 1.0. The particular behavior in the rigid spectral region was also discussed in paragraphs 5.3.2 and 5.3.3.

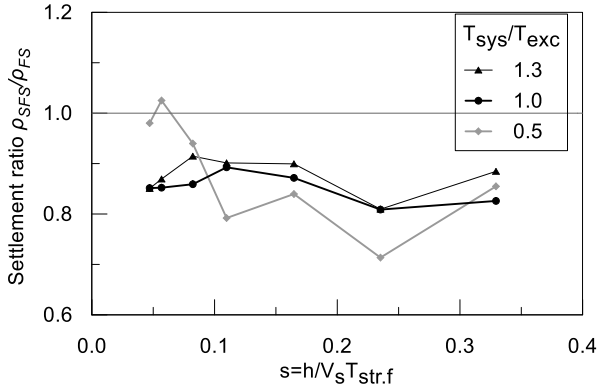

Figure 5.16: Variation of settlement ratio ρ_{SFS}/ρ_{FS} with the stiffness-to-soil ratio *s* for different levels of the period ratio T_{sys}/T_{exc} of SFS systems

5.3.6 Effect of earthquake intensity

The effect of earthquake intensity is investigated for the reference system with SSI parameters *s* = 0.07, *h/r* = 1.06 and *γ* = 4.00. Four cases of earthquake intensity are considered for the harmonic base input motion, i.e., peak bedrock acceleration a^b_{max} = 0.15g, 0.20g, 0.25g and 0.40g. The first three levels of earthquake intensity were systematically examined by numerical analyses in the whole period spectrum, whereas the level of 0.40g was indicatively examined in order to ensure compliance of the developed methodology to extreme values of earthquake intensity. Concerning the range of intensities selected herein, the following are remarked:

i. The base input motion corresponds to the bedrock acceleration, which is reduced compared to the amplified ground acceleration.

ii. The harmonic input motion has a constant peak amplitude a^b_{max} which is realistically equivalent to the effective peak acceleration of the recorded seismic motion, usually calculated as the 2/3 of the actual recorded peak value.

In order for the selected earthquake intensities of input accelerations to correspond to the actual peak ground accelerations of engineering interest, the aforementioned remarks need to be considered. Thus, the four selected intensities of the *effective* input motion correspond to *actual* peak values, equal to 0.23g, 0.3g, 0.38g and 0.60g (after multiplication by 3/2). Additionally, soil amplification effects for the reference soil profile were estimated by performing ground response analyses using as a base input motion the previously discussed white-noise signal (see Chapter 4). Numerical analyses were performed for non-liquefiable ground conditions, at first, in order to avoid any seismic isolation of the motion due to liquefaction. Results showed that peak bedrock accelerations in the range a^b_{max} = 0.23g – 0.60g were amplified at the surface of the soil profile in the range 0.30g – 0.72g. On the other hand, in the case of liquefied soil conditions peak ground accelerations did not exceed the value of 0.20g due to the swift initiation of liquefaction, regardless of the a^b_{max} value.

Figure 5.17 plots the effect of period ratio T_{sys}/T_{exc} of SFS systems on the settlement ratio ρ_{SFS}/ρ_{FS} for different levels of peak bedrock acceleration. The following points can be remarked:

- The examination of the acceleration intensity in the case of liquefaction is essentially correlated with the time of liquefaction onset. After its occurrence, seismic wave propagation is substantially attenuated and the response of the system is practically unaffected. As a result, increasing values of a^b_{max} have a marginal effect on ρ_{SFS}/ρ_{FS} ratios.
- For the same reason, the value of a^b_{max} is essentially correlated to the extent of liquefaction that takes place. In the present problem definition, the reduced Factor of Safety against liquefaction (FS_L) results in complete liquefaction of the subsoil layers, i.e., r_u values close to 1.0, even for small levels of acceleration.
- An additional reason for the negligible acceleration level effects is related to relative mass ratio effects (also discussed in paragraph 5.3.4). Namely, inertial forces $F_i=mS_a$ of the structure result to an increase of hysteretic soil damping and, thus, the particular mechanism imposes a lower limit on settlement reduction of SFS systems.

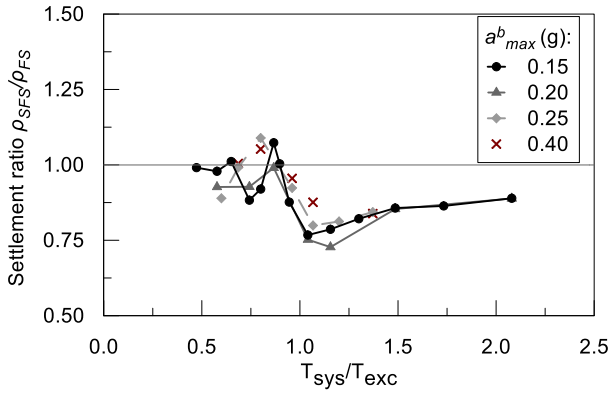

Figure 5.17: Variation of settlement ratio ρ_{SFS}/ρ_{FS} with the period ratio T_{sys}/T_{exc} for different levels of input acceleration intensity a^b_{max}.

5.4 Multi-variable relations for SSI effects

In the present section, multi-variable relations are developed in order to express the numerical predictions for the settlement ratio ρ_{SFS}/ρ_{FS} as a function of the problem parameters, on the basis of the parametric investigation of the previous sections. The main parameters affecting the settlement ratio are introduced in the multi-variable relations that follow, namely the period ratio T_{sys}/T_{exc}, the slenderness ratio h/r and the relative mass ratio γ. Concurrently, for reasons of simplicity, the structure-to-soil stiffness ratio s and the earthquake intensity (via a^b_{max}) are not included due to their minimal effect. The development of these approximate relations is based on a statistical analysis of the numerical predictions; however, the rationale and the general form of these relations is grounded on physical representation of the emerging phenomena.

Following the discussion in previous sections, the formation of these relations distinguishes two spectral regions: i) the *rigid* and *semi-rigid region* ($T_{sys}/T_{exc} < 0.80$), where inertial forces and, hence, settlements are, initially, identical for SFS and FS systems – especially for $T_{sys}/T_{exc} < 0.45$ – and, subsequently, they tend to become greater for SFS systems, and ii) the *resonant-to-flexible region* ($T_{sys}/T_{exc} > 0.80$), where settlement ratio variations are milder and they tend to be greater for FS systems. Namely, the following piecewise function is formulated:

$$\frac{\rho_{SFS}}{\rho_{FS}} = \begin{cases} 1 + C_a \cdot \left(T_{sys}/T_{exc}\right)^2 & T_{sys}/T_{exc} \leq 0.80 \\ \left[\dfrac{C_{1.b}+C_{2.b}\left(T_{sys}/T_{exc}\right)^2}{\sqrt{\left[C_{3.b}-\left(T_{sys}/T_{exc}\right)^2\right]^2+C_{4.b}\left(T_{sys}/T_{exc}\right)^2}}\right]^{-1} & T_{sys}/T_{exc} \geq 0.80 \end{cases} \quad (5.9)$$

The first part of relation 5.9 predicts settlement ratios that start from unity for perfectly-rigid systems and they gradually increase to a peak value for semi-rigid systems. The numerical data suggest that the coefficient C_α is primarily affected by the independent variable *h*/*r,* while T_{sys}/T_{exc} and *γ* do not play an important role (see also **Figure 5.20a** and **Figure 5.20a**). Appropriate values of the coefficient C_a for each value of *h*/*r* and *γ* are summarized in **Table 5.13**:

Table 5.13: Values of coefficient Cα, (applied for the *rigid* and *semi-rigid spectral region* T_{sys}/T_{exc} < 0.80).

h/r	γ	(ρ_{SFS}/ρ_{FS}), average	C_α
1.06	4.00	0.96	0.00
1.36	4.00	1.12	0.23
1.88	4.00	1.06	0.23
1.06	2.40	0.99	
1.06	3.30	0.99	0.00
1.06	5.10	1.02	

The proposed expression concerning coefficient C_α as a function of *h/r* ratio, on the basis of the data from **Table 5.4**, reads:

$$C_a = \begin{cases} 0.00 & h/r \le 1.06 \\ 0.77 \cdot (h/r) - 0.81 & 1.06 \le h/r \le 1.36 \\ 0.23 & h/r \ge 1.36 \end{cases} \quad (5.10)$$

The second part of Equation 5.9 draws upon amplification relations used in vibration theory of structures. It introduces four coefficients ($C_{1.b}$, $C_{2.b}$, $C_{3.b}$, $C_{4.b}$) in order to capture the four boundary conditions of interest: the left and right end-of-spectra values, the minimum value (point of zero curvature) and the point where the minimum value takes place (abscissa). Namely, the characteristic values are the following:

$$\frac{\rho_{SFS}}{\rho_{FS}} = \begin{cases} C_a & T_{sys}/T_{exc} = 0.80 \\ \dfrac{\sqrt{C_{3.b} \cdot C_{4.b}}}{C_{3.b} \cdot C_{2.b} + C_{1.b}} & T_{sys}/T_{exc} = C_{3.b} \\ C_{2.b} & T_{sys}/T_{exc} \to \infty \end{cases} \quad (5.11)$$

$$\frac{d(\rho_{SFS}/\rho_{FS})}{d(T_{sys}/T_{exc})} = 0 \qquad T_{sys}/T_{exc} = C_{3.b}$$

The described coefficients are, in general, functions of the remaining variables *h/r* and *γ*. Based on the available data and, at the same time, grounded on physical rationale, it is expected that settlement ratios tend to 1.0 for period ratios T_{sys}/T_{exc} that tend to infinity, i.e., for structures with very large flexibility. Following the 3rd boundary condition, this, also, implies $C_{2.b} \rightarrow 1.0$. The resulting system of 3 boundary conditions (1st, 2nd and 4th) and 3 coefficients ($C_{1.b}$, $C_{3.b}$, $C_{4.b}$) is further simplified by the fact that the 1st boundary condition equates ρ_{SFS}/ρ_{FS} to C_{α}, which is a single-variable function, i.e., of *h/r.* On the other hand, in the 2nd and 4th boundary conditions both variables remaining variables (*h/r* , *γ)* are introduced, since the data indicate that minimum settlement ratios are affected by these variables (**Figure 5.19a** and **Figure 5.20a**). As a result of the above, the variable *γ* is considered in the relations of two of the remaining coefficients ($C_{3.b}$, $C_{4.b}$), while the *h/r* is considered in all three of them ($C_{1.b}$, $C_{3.b}$, $C_{4.b}$).

The analytical expressions of the aforementioned coefficients are presented in Equations 5.12 – 5.14. The extreme values of the formulations correspond to the physical restrains of the described phenomena. More specifically, for relative mass ratio *γ* reducing to zero, the settlement ratio ρ_{SFS}/ρ_{FS} tends, naturally, to 1.0. The particular response is modelled by calibrating coefficient $C_{3.b} = 0.45$ for $\gamma = 0$ (**Figure 5.18c**). For increasing levels of relative mass ratio *γ*, related effects are gradually attenuated and the proposed coefficients are calibrated to the residual values $C_{3.b} \approx 0.95$ and $C_{4.b} \approx 0.85$. Regarding slenderness ratio *h/r*, as described in section 5.3.3, its influence is minimal for an increase of *h/r* from 1.36 to 1.88 (**Figure 5.20a-d**). Thus, for simplicity constant values of the respective coefficients $C_{1.b}$, $C_{3.b}$ and $C_{4.b}$ are designated for values of *h/r* greater than 1.36, as seen in equations 5.12, 5.13 and 5.14. On the other hand, the parametric investigation followed herein entails that fixed-base natural periods are kept constant even for *h/r* tending to zero. Thus, in theory, settlement ratios ρ_{SFS}/ρ_{FS} do not necessarily tend to unity, as it was stipulated in the case of relative mass ratio γ. Nevertheless, in practice, structures with reduced height are rigid enough to be assumed that ρ_{SFS}/ρ_{FS} tends to 1.0. Consequently, coefficient $C_{3.b}$ is also calibrated to 0.45 for $h/r = 0$.

Based on the above the following expressions are formulated:

$$C_{1.b} = \begin{cases} 0.16 & \text{h/r} \leq 1.06 \\ -0.70 \cdot (h/r) + 0.90 & 1.06 \leq \text{h/r} \leq 1.36 \\ -0.05 & \text{h/r} > 1.36 \end{cases} \qquad 5.12$$

$$C_{3.b} = [0.82 + 0.24 \cdot \tanh(\gamma - 2.95)] \cdot [0.33 \cdot (h/r) + 0.47] \quad 5.13$$

$$C_{4.b} = (0.87 + 0.31 \cdot e^{-0.30 \cdot \gamma}) \cdot g(h/r) \quad 5.14$$

with

$$g(h/r) = \begin{cases} 1.00 & \text{h/r} \le 1.06 \\ -1.07 \cdot (h/r) + 2.13 & 1.06 \le \text{h/r} \le 1.36 \\ 0.62 & \text{h/r} > 1.36 \end{cases} \quad 5.15$$

The relevant plots of the aforementioned coefficients are presented in the subplots of **Figure 5.18**.

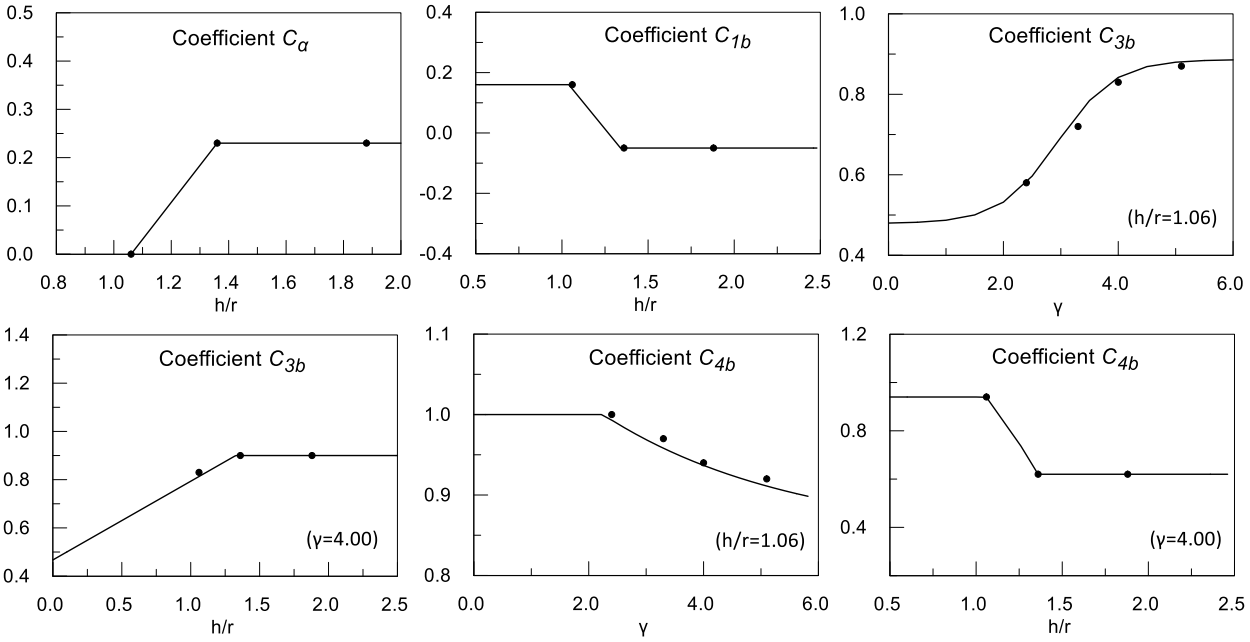

Figure 5.18: Plots of coefficients C_{α}, C_{1b} , C_{3b}, C_{4b} utilized in the proposed multi-variable relations, as function of the slenderness ratio *h/r* and the relative mass ratio *γ*.

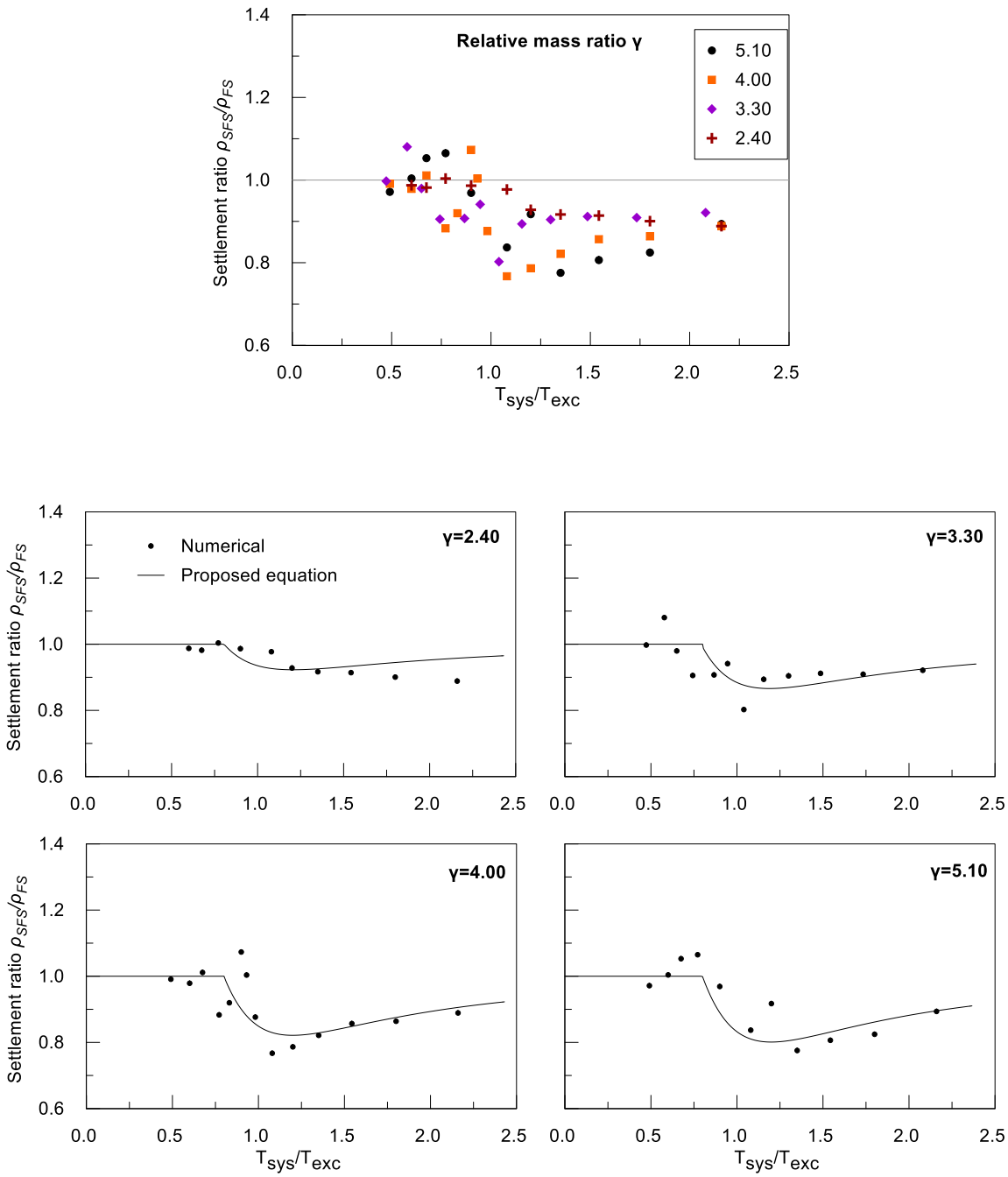

Figure 5.19: Effect of T_{sys}/T_{exc} on settlement ratio ρ_{SFS}/ρ_{FS}: (a) Summary of numerical data for different values of relative mass ratio γ; Comparison of numerical data to predictions for: (b) γ = 2.40, (c) γ = 3.30, (d) γ = 4.00, (e) γ = 5.10.

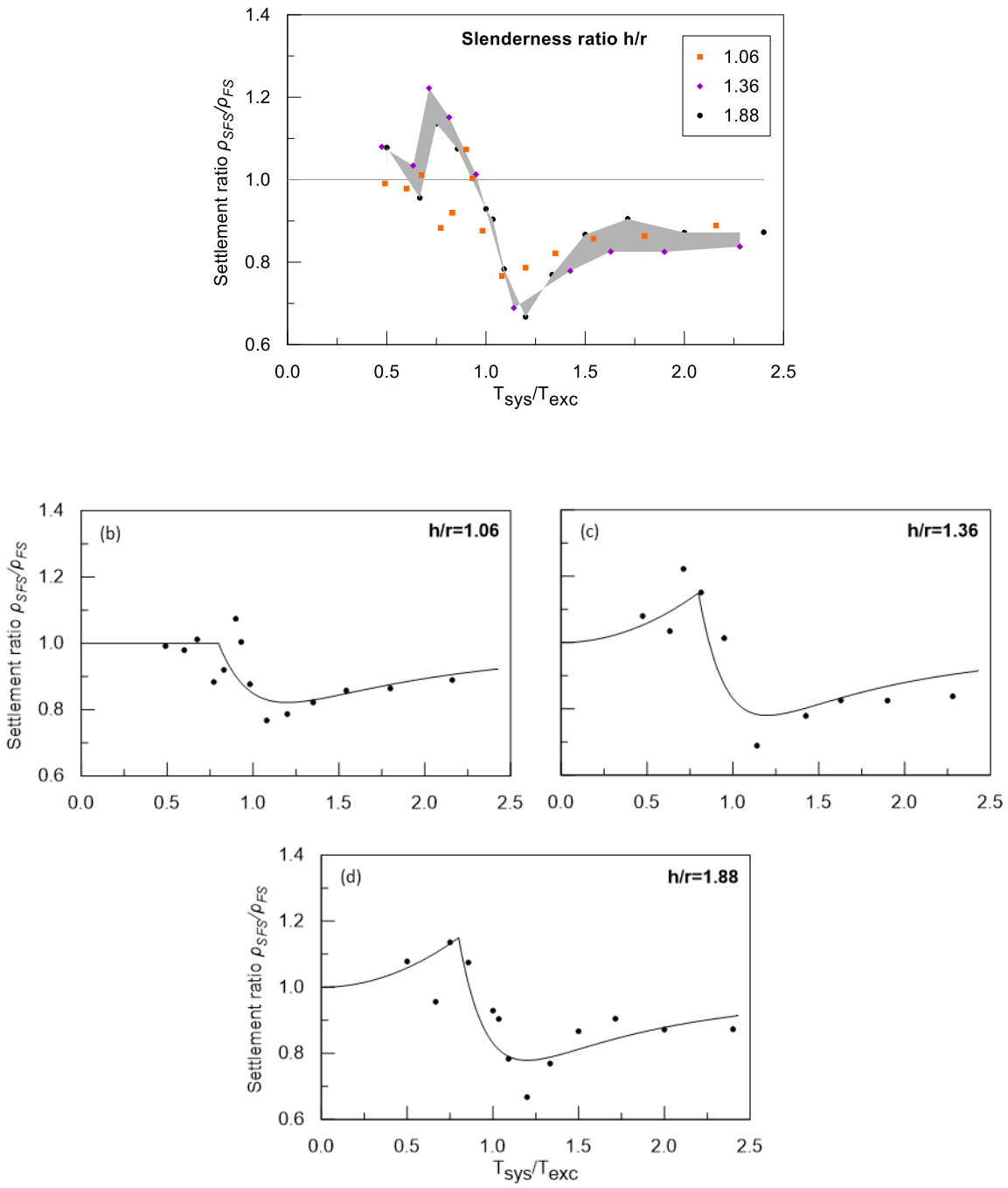

Figure 5.20: Effect of T_{sys}/T_{exc} on settlement ratio ρ_{SFS}/ρ_{FS}: (a) Summary of numerical data for different values of slenderness ratio h/r; Comparison of numerical data to predictions for: (b) h/r = 1.06, (c) h/r = 1.36, (d) h/r = 1.88.

In order to ascertain the reliability of the proposed multi-variable relations (Equations 5.9 – 5.14) for estimating the settlement ratio SR = ρ_{SFS}/ρ_{FS}, a one-to-one comparison is made between their predictions (SR_{pred}) and their respective values from the 191 numerical analyses (SR_{num}). The achieved accuracy is quantified via the relative error *R* in the prediction of the settlement ratio, that is defined as:

$$R = \frac{SR_{pred} - SR_{num}}{SR_{num}} \quad 5.16$$

The corresponding statistics (average and standard deviation of the relative error *R*) are presented in a one-to-one comparison is made between predictions (SR_{pred}) and their respective values from numerical analyses (SR_{num}) and b) the variation of the relative error with the main problem parameter T_{sys}/T_{exc}. Three values of *L/B* ratios are examined here *L/B* =1.0, 1.5 and 2.0. Results show that relative errors do not appear to have any systematic correlation with *L/B* ratio.

Table 5.14 and **Figure 5.21a-c** for the – separately examined – independent variables, i.e., the period ratio T_{sys}/T_{exc}, the slenderness ratio *h/r* and the relative mass ratio *γ*. The standard deviation derived for the total number of predictions is 0.07. Results indicate that the distribution of relative errors is quite uniform for different sets of the examined parameters.

The accuracy of the proposed methodology is, additionally, evaluated by conducting a sensitivity analysis for the role of the footing's length-to-width ratio *L/B*, which is a key-role parameter for the accumulation of settlements. **Figure 5.22** presents the results of the sensitivity analysis in the same format as the foregoing Figures, i.e., in terms of: a) a one-to-one comparison is made between predictions (SR_{pred}) and their respective values from numerical analyses (SR_{num}) and b) the variation of the relative error with the main problem parameter T_{sys}/T_{exc}. Three values of *L/B* ratios are examined here *L/B* =1.0, 1.5 and 2.0. Results show that relative errors do not appear to have any systematic correlation with *L/B* ratio.

Table 5.14: Relative error of the proposed methodology against numerical predictions for separate sets of variable examination.

h/r	γ	R_{RS} average (%)	R_{RS} st.deviation (%)
1.06	4.00	-0.3	7.4
1.36	4.00	-0.8	8.1
1.88	4.00	0.1	8.6
1.06	2.40	-0.7	3.7
1.06	3.30	0.1	5.3
1.06	5.10	1.0	5.7
Cumulative:		-0.1	7.0

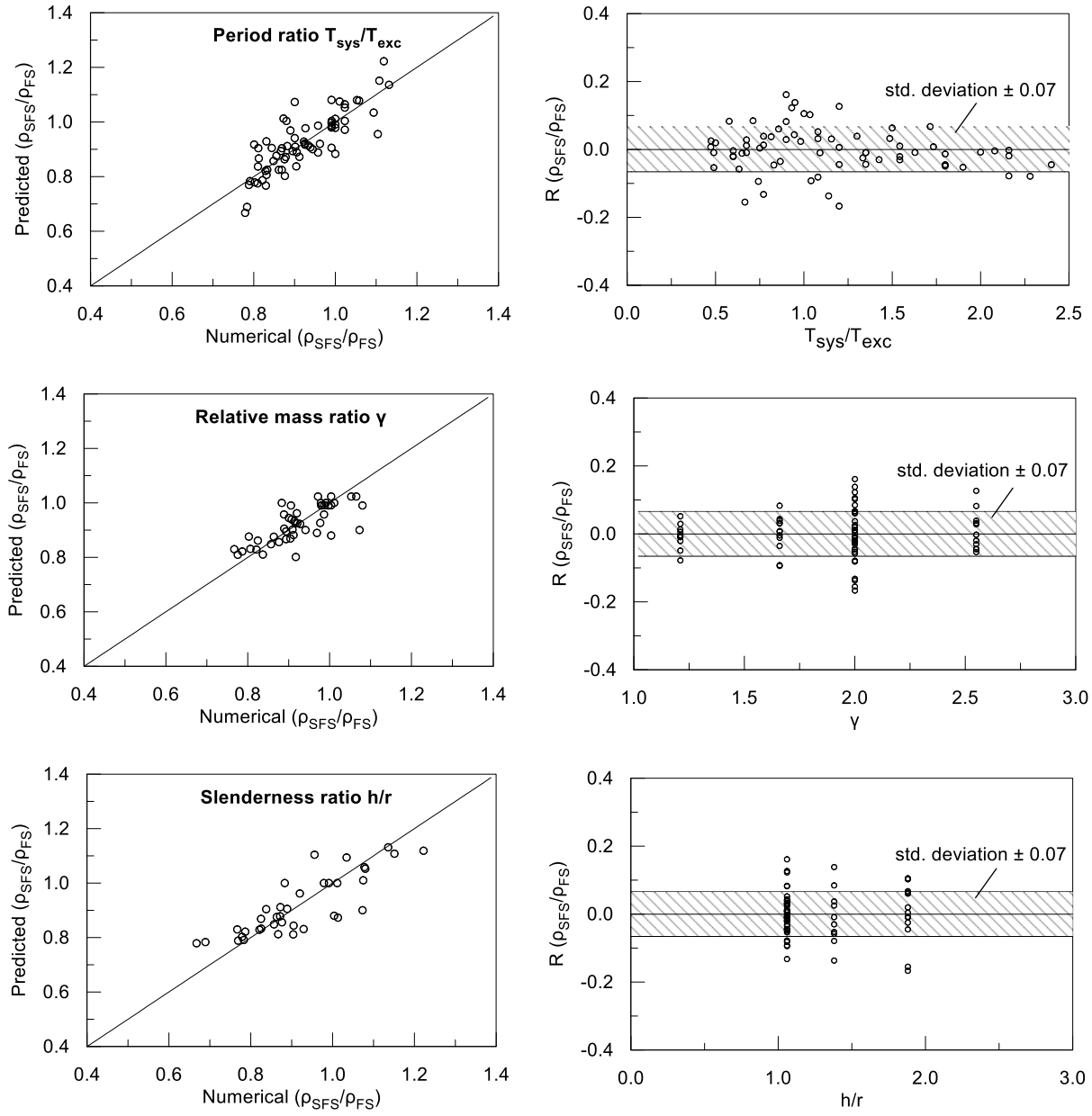

Figure 5.21: Evaluation of relative error and bias in the analytical estimation of ρ_{SFS}/ρ_{FS} against results from numerical analyses, as a function of the main problem parameters: (a) T_{sys}/T_{exc}, (b) h/r and *(c)* γ.

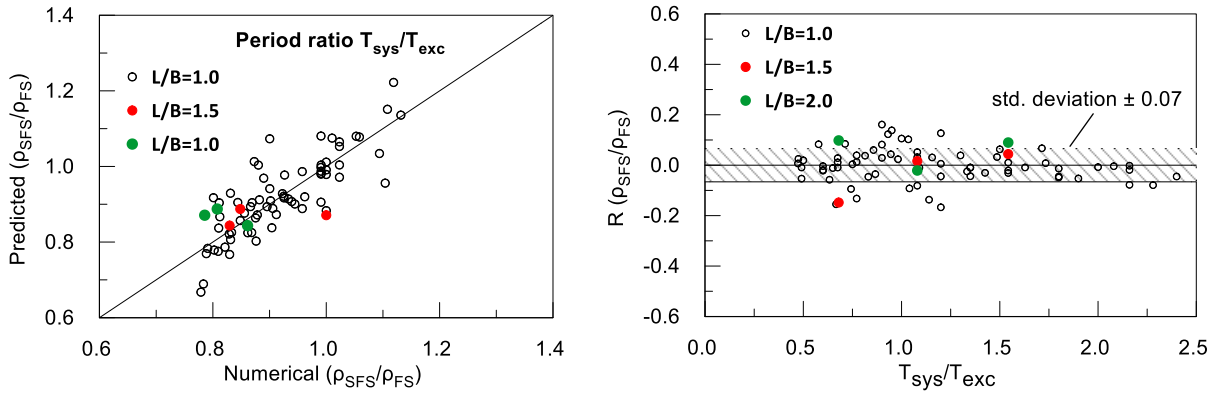

Figure 5.22: Sensitivity analysis for the evaluation of the effect of footing's length-to-width ratio *L/B*.

5.5 Summary and conclusions

The present chapter studies SSI effects on the proposed methodology of designing structures on liquefiable conditions with the construction of shallow foundations and the improvement of a superficial soil crust. The effects of the superstructure on the dynamic response of structure-foundation-soil (SFS) systems are examined for varying structural characteristics, which are expressed in terms of the dimensionless parameters of the soil-structure interaction framework. Results are expressed in terms of settlement ratios between the SFS system and the equivalent FS system, isolating, in this way, the influence of structural inertial on system response. In particular, the end goal of this effort is to develop multi-variable relations for the prediction of the settlement ratio, in order to take advantage of existing literature studies for estimating seismic settlement accumulation of FS systems with shallow foundations (e.g., Karamitros et al. 2013; Dimitriadi et al. 2017). These relations are expressed in terms of correction factors that add up to the established procedures of settlement calculation for FS systems. Based on the analyses of this Chapter, the following can be remarked:

- Seismic settlements of SFS systems on liquefied ground are controlled by a Coulomb-type wedge sliding, which takes place due to the severe degradation of the bearing capacity of the foundation soil. The effect of the superstructure is mainly introduced as an inertial force that acts in-phase or out-of-phase with the wedge sliding, thus amplifying or de-amplifying the overall seismic settlement.
- The most crucial parameter in the SFS system response is the period ratio T_{sys}/T_{exc}, where T_{sys} and T_{exc} are the fundamental period of the system and the predominant period of the excitation. In the case of resonance, the – quarter cycle – lag of the structural vibration with respect to the foundation results in the greatest reduction of the wedge sliding and, hence, the greatest

reduction of settlement accumulation. Rigid systems tend to settle equally with the equivalent FS systems, whereas flexible systems experience out-of-phase motion which, also, results in settlement reduction, but less intense than that at resonance.

- Relative mass ratio γ and slenderness ratio h/r affect the SFS system response, although to a lesser degree compared to the period ratio T_{sys}/T_{exc}. In the case of relative mass ratio γ the effects are principally due to increased structural inertial forces, while in the case of slenderness ratio h/r the effects are due to overturning moments. Both of these effects lead to increased system damping and structural rocking. In general, increased inertial forces further inhibit the wedge sliding and, thus, they tend to reduce settlements for resonant SFS systems, with the maximum reduction being approximately 40% with respect to the FS systems. It is noteworthy here that in the case of semi-rigid structures (T_{sys}/T_{exc} = 0.55-0.80) with high slenderness ratios (h/r > 1.36), the settlements are increased by up to 20% with respect to the FS systems due to the additional rocking-induced soil softening.
- Multi-variable relations were developed for the ratio of seismic settlement of the SFS system over that of the equivalent foundation-soil (FS) system on the basis of 191 numerical analyses. The proposed relations consider the critical SSI parameters (i.e., the period ratio T_{sys}/T_{exc}, the slenderness ratio h/r and the relative mass ratio γ) as independent variables. The physical restrains of the examined phenomena (e.g. extreme values, upper and lower limits) are introduced in the formulations by incorporating appropriate boundary conditions. Overall, predictions of the proposed relations agree well with the numerical predictions. A statistical analysis showed that the standard deviation of the relative errors has an aggregate standard deviation equal to 0.07 and a quite uniform distribution for the different variables. SSI parameters in the numerical analyses were considered within a range of variation, namely: T_{sys}/T_{exc} = 0.4 – 2.5, h/r = 1.04 – 1.88, γ = 2.40 – 5.10. This range of variation may also be considered the range of application of the foregoing conclusions and the proposed relations.

Finally, it is important to mention that the examined soil conditions refer to *purely liquefied* ground, i.e., after the onset of liquefaction, and not a soil that is merely liquefiable. In practice, this applies to cases of severe liquefaction, which appears for factors of safety against liquefaction significantly smaller than 1.0 (FS_L < 0.40 - 0.50). This entails that the liquefaction onset time t_L is adequately small to ensure that the non-liquefied part of shaking – and the associated seismic settlements – are negligibly small compared to the liquefied part of shaking.

Chapter 6

Soil-Structure Interaction Effects on Seismic Settlements: Non-Liquefiable Soil Conditions

6.1 General

The present chapter examines the response of the previously examined structure-foundation-soil systems, but on non-liquefiable soil conditions. In practice, it is common that sites with factor of Safety against liquefaction FS_L moderately less than unity experience an initial shaking period, i.e. *prior to liquefaction*, during which excess pore pressures remain negligible. As a result, this part of shaking will be governed by non-liquefied soil conditions, which are characterized by amplified ground accelerations, as well as, sufficient foundation bearing capacity, compared to the subsequent liquefied conditions. Thus, the objective of this chapter is to isolate the response of such systems during the first part of shaking and, as a next step, to investigate the role of soil-structure interaction on the system settlements. To that end, the design characteristics of the examined SFS systems adhere to the previously examined concept of designing structures in liquefiable conditions, which involves the use of a shallow foundation and the improvement of a superficial soil zone. Namely, structural and the corresponding soil-structure interaction parameters are kept constant, while the non-liquefiable soil conditions are modelled herein by using the buoyant unit weight of sand. The effect of structural inertia on seismic settlements is, once more, investigated through parametric investigation of the critical SSI parameters, i.e. the system-to-excitation period T_{sys}/T_{exc}, the slenderness ratio h/r and the relative mass ratio γ. As previously, settlements of SFS systems are compared with the respective settlements of equivalent foundation-soil systems (FS). Finally, simplified relations are developed for the analytical calculation of settlement ratios, based on a multi-variable statistical analysis of the available numerical predictions. Since the estimation of seismic settlements for FS systems is readily accessible both numerically and analytically (Richards et

al. 1993), the obtained relations aim to serve as correction factors for the role of SSI on foundation settlements.

6.2 Dynamic response of SFS and FS systems

6.2.1 Numerical methodology

The dynamic response of SFS systems with shallow foundation is investigated in the present chapter with 3-dimensional numerical analyses performed with the Finite Difference Code *FLAC 3D.* The numerical model configuration followed in the previous chapter for liquefied conditions is also adopted with the following differences:

- The non-liquefiable ground conditions were simulated by performing numerical analysis without water flow simulation. The unit weight was set equal to the buoyant unit weight of the saturated sand so that the effective consolidation stresses remain the same with those of the saturated soil profile, used in the previous chapter.
- An interface is introduced in order to model the foundation-to-soil connection. In the case of liquefaction conditions, the rigid connection between the nodes of the shell elements and the nodes of the underlying soil zones is reasonable due to the attenuation of any significant structural rocking on the onset of liquefaction. On the other hand, uplift of the foundation is possible during shaking in non-liquefiable conditions due to the increased levels of rocking and as a result a rigid connection between footing and soil does not model the response accurately. Thus, the introduced interface permits uplift of the foundation, i.e., has zero tension cut-off. More details on the subjected are described in Chapter 3.

6.2.2 Settlement mechanism of SFS systems

6.2.2.1 General

The seismic response of SFS systems considering inelastic soil behavior has received wide attention in literature recently, both experimentally (Gajan et al. 2005; Knappett et al. 2006; Paolucci et al. 2008; Kokkali et al. 2015) and numerically (Drosos et al. 2012; Kourkoulis et al. 2012; Zamani and El Shamy 2012; Paolucci et al. 2013; Pecker et al. 2014). Studies have addressed soil inelasticity through soil plastification and foundation uplift by analyzing systems with various design parameters, such as footing width, structural height, soil density, static Factor of Safety, excitation properties etc. Reported results refer to footing settlement and rotation, overturning moment capacity, as well as to the degraded rotational

stiffness and damping of the inelastic soil-footing system (Pecker et al. 2014). These studies have indicated the aggravating – through structural rocking – role of SSI on settlement accumulation. Most interestingly, Gajan et al. (2005) directly related the magnitude of the footing cycling rotation to the accumulated settlements suggesting great dependance of the former to the latter.

Nevertheless, the aforementioned studies do not provide analytical relationships that can be used for the estimation of seismic settlements for systems with varying characteristics. In fact, the only analytical method than can be used for this purpose is that of Richards et al. (1993) that estimate seismic settlements of shallow foundations by calculating the sliding of the Coulomb active-passive wedge mechanism that is formed due to the seismic bearing capacity failure of the foundation. Nevertheless, the particular study considers shallow foundations without any SSI effect. Thus, the purpose of the present section is to estimate the aggravating effects of SSI on settlements and provide analytical relationships that can be used as correction factors for the Richards et al. (1993) analytical predictions.

6.2.2.2 Numerical response

To demonstrate the SSI effects on system response under non-liquefiable conditions, **Figure 6.1** compares numerical results of the reference SFS system and the equivalent FS system, for the same base excitation. It is reminded that the reference case is an SFS system close to resonance, i.e. with period ratio T_{sys}/T_{exc} = 1.37, overburden pressure q = 80kPa and with the SSI parameters being γ = 4.00 and h/r = 1.06. The base excitation is a harmonic acceleration signal with peak acceleration a_{max} = 0.15g and N = 12 number of cycles. In **Figure 6.1** the comparison is made in terms of the time-histories of (a) the footing settlement and (b) rotation, (c) the horizontal displacements of the structural mass and the footing of the SFS system as well as of (d) the FS system footing. The supporting soil response is described by time-histories of (e) the deviatoric stresses and (f) strains under the footing edge at the depth of 0.5m. In addition, **Figure 6.2** shows the (a) moment-rotation (M-θ) and (b) settlement-rotation graphs.

These results highlight the aggravating role of SSI on settlement accumulation and reveal the main mechanism of settlement accumulation. More specifically, the SFS system settles more compared to the equivalent FS system during shaking, with the total settlement of the former being approximately 2-3 times larger than that of the latter, (i.e. 13cm against 5cm). The main difference between the two systems lies on the structural vibration which translates to significant footing rotation for the SFS system (**Figure 6.1e**), as compared to the negligible footing rotations of the FS system, i.e., one order of magnitude smaller. As a result, the soil underneath the footing edges of the SFS system is subjected to significant shear straining, as observed in **Figure 6.1e** and **f**, which results in soil softening as manifested in the

hysteretic response of the footing moment-rotation loops in **Figure 6.2a**. It is interesting to note that for the SFS system, while footing rocking results in oscillations of the deviatoric stresses around the constant value of q ≈ 25 kPa, the immersion of the footing during shaking results in a steady deviatoric strain accumulation, which exhibits characteristic "spikes" that coincide with the maximum footing rotations. **Figure 6.2b** shows that the rate of footing settlement decreases with time as strain accumulation increases (**Figure 6.1f**). Additionally, the positive settlement rate during shaking, observed in the same Figure, indicates that significant uplift of the footing edges does not occur.

Consequently, the vast difference between deviatoric strains under the footing edge in the SFS and the FS systems indicates that settlement accumulation due to rocking-induced soil softening is the governing mechanism in the case of the SFS system. Contours of shear strains and horizontal displacements in **Figure 6.3** shed more light in the aforementioned phenomena. In the case of the FS system, **Figure 6.3c** shows that at the moment of maximum footing rotation, shear strain distribution under the footing is quite uniform, suggesting that rocking-induced strains are negligible in this case. Additionally, **Figure 6.3d** shows the formation of a soil wedge under and to the left of the footing, thus, implying bearing capacity failure**.** On the contrary, the shear strain distribution under the footing, in the case of the SFS system, is uneven, since local concentration is observed under the footing edge at the moment of maximum structural deflection and, consequently, footing rotation (**Figure 6.3a**). Furthermore, maximum shear strains develop in a much shallower zone, compared to the FS system, thus, indicating the important contribution of *rocking-induced soil softening* in settlement accumulation. As a result, the formation of the soil wedge mechanism cannot be clearly seen (**Figure 6.3b**), as it was the case for the FS system. Concluding, it can be asserted that only a smaller portion of the overall settlements can be attributed to wedge sliding due to the soil inertia and bearing capacity degradation.

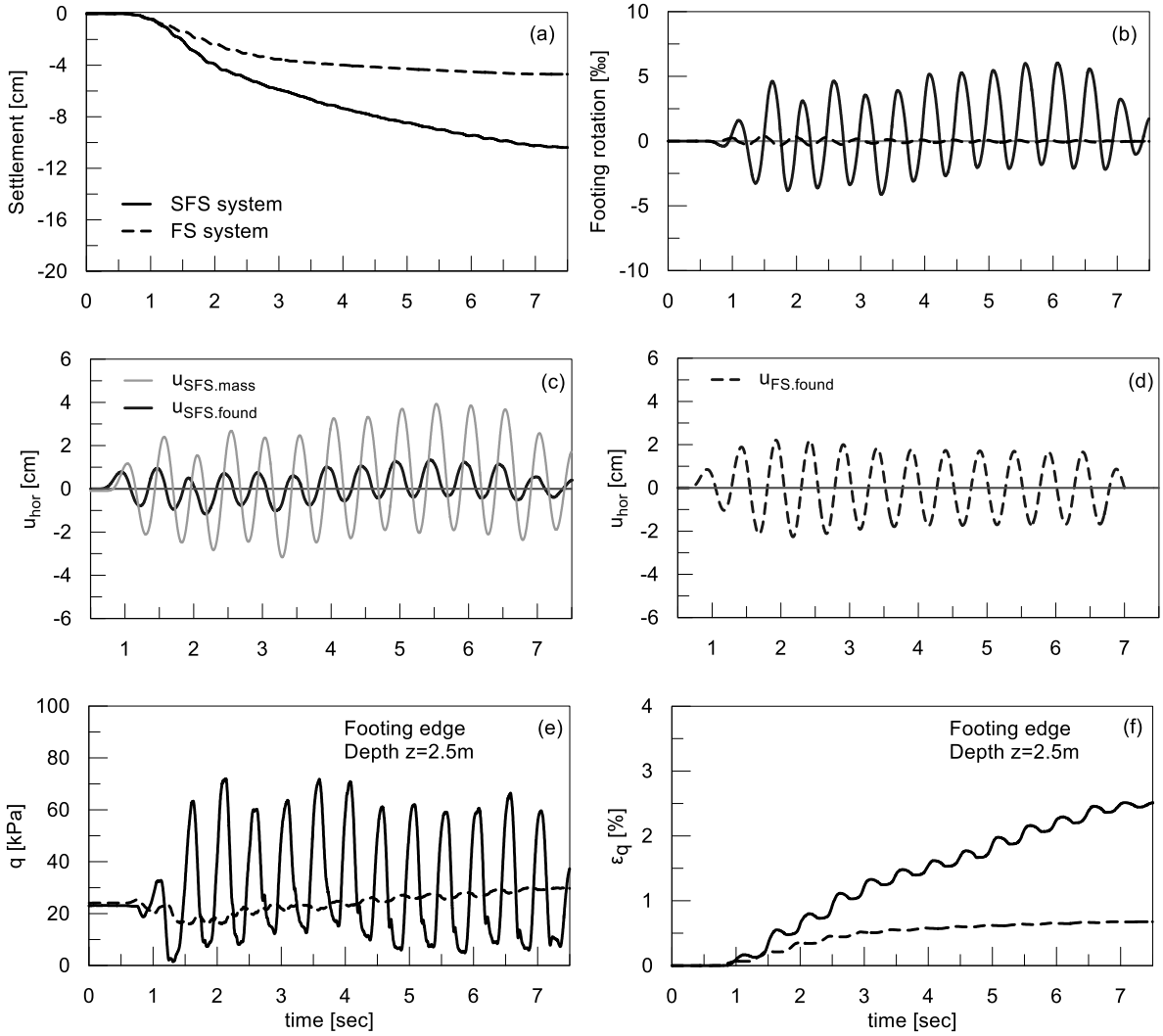

Figure 6.1: Typical time-histories of SFS and FS system response; (a) footing settlement and (b) rotation, (c) SFS and (d) FS system horizontal displacements, (e) deviatoric stresses and (f) strains under the footing edge.

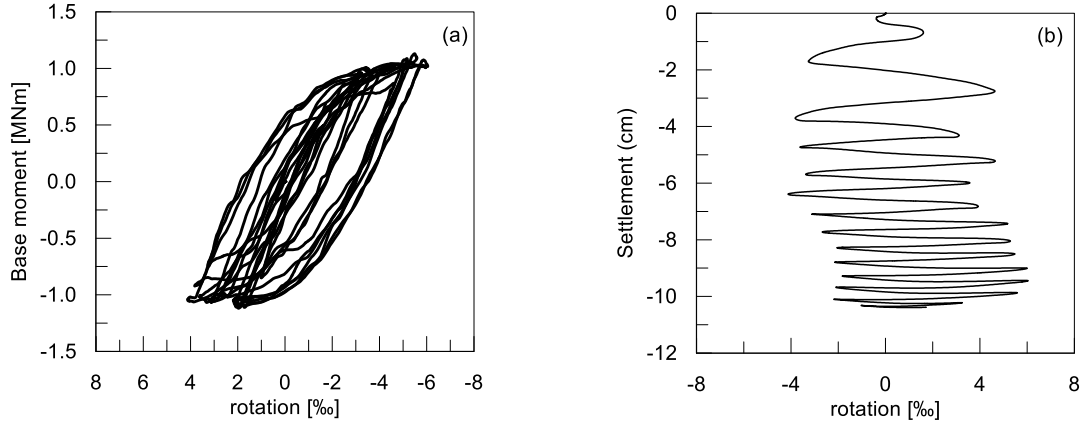

Figure 6.2: Typical time-histories of SFS system response; (a) moment-rotation (M-θ) and (b) settlement-rotation.

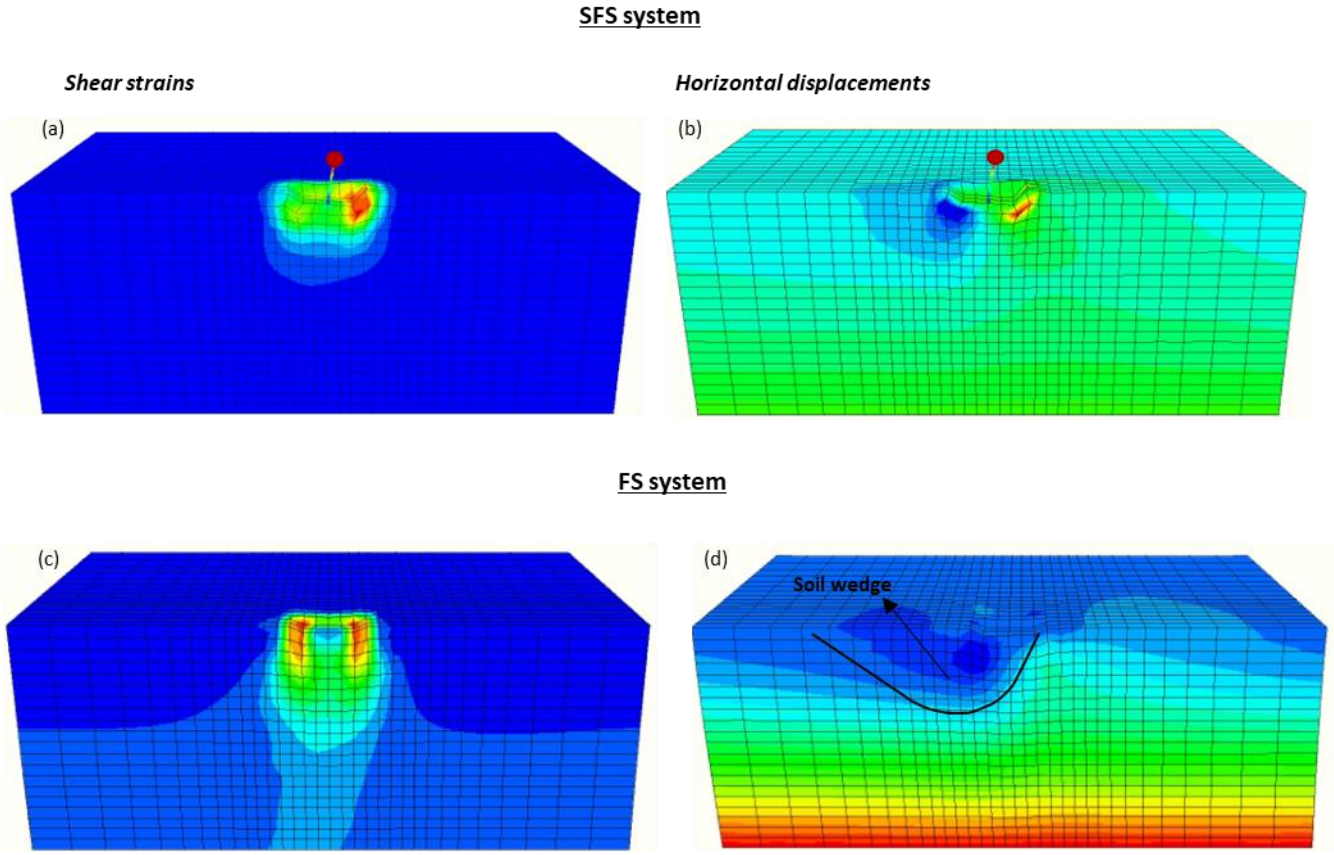

Figure 6.3: Contours of shear strain (a, c) and horizontal displacement (b, d) for the SFS (1st row) and FS system (2nd row) at the moment of maximum footing rotation.

6.3 Parametric investigation

6.3.1 Input data and assumptions

This section focuses on the comparative parametric investigation of the structure-foundation-soil (SFS) and foundation-soil (FS) system response. The procedure implemented herein is similar to the procedure of Chapter 5. Specifically, numerical analyses are performed in order to examine the effects of the crucial SSI and excitation parameters, summarized in **Table 6.1**. The examined structural parameters (highlighted with blue) are also expressed in terms of the SSI framework (highlighted with green). In particular, the examined parameters are:

- The mass M_{str} – concentrated at the top of the structure for the SFS systems and at the foundation level for the equivalent FS system – is M_{str} = 54.4, 74.4, 89.7 and 114.4Mgr. These values of mass correspond to overburden pressures equal to q = 52, 68, 80, 100kPa and relative mass ratios equal to γ = 2.40, 3.30, 4.00, 5.10.
- The structural height is h = 3.0, 3.9, 5.1m, corresponding to slenderness ratios *h/r* = 1.06, 1.38, 1.88, with *r* being the equivalent foundation radius, i.e. r = 2.82m.
- The excitation periods of the input motion are T_{exc} = 0.25, 0.35, 0.45, 0.50, 0.60, 0.70, 0.80, 0.90, 1.10, 1.20, 1.30, 1.40sec, with N=4, 8, 12 number of cycles.
- Peak ground acceleration values are *PGA*= 0.23, 0.30, 0.36.

The basic geotechnical parameters of the model are identical to the previous case of liquefied soil conditions, i.e., the relative density of the natural and the improved soil is D_r = 45 and 60%, respectively, improved zone thickness is H = 2m and thickness of the liquefiable sand layer is z_{liq} = 18m. Furthermore, the SSI parameter structure-to-soil stiffness ratios s was examined in the previous chapter and its effect on system response was found minimal, given that all other parameters are kept constant. As a result, in the present chapter the basic *s* ratio equal to 0.05 is considered, which corresponds to the value of fixed-base natural period of the structure $T_{str.f}$ = 0.35 sec.

Table 6.1: Input data of 3-dimensional parametric analyses (colored cells indicate the examined parameter).

No	System	Structural Parameters			Excitation Parameters			SSI Parameters			
		M_{str} (tn)	$T_{str.f}$ (sec)	h (m)	T_{exc} (sec)	PGA (g)	N	h/r	γ	s	$T_{sys.el}$ / $T_{str.f}$
1	SFS	54.4	0.35	3	0.25	0.30	12	1.06	2.40	0.05	1.20
2	SFS	54.4	0.35	3	0.30	0.30	12	1.06	2.40	0.05	1.20
3	SFS	54.4	0.35	3	0.35	0.30	12	1.06	2.40	0.05	1.20
4	SFS	54.4	0.35	3	0.40	0.30	12	1.06	2.40	0.05	1.20
5	SFS	54.4	0.35	3	0.45	0.30	12	1.06	2.40	0.05	1.20
6	SFS	54.4	0.35	3	0.50	0.30	12	1.06	2.40	0.05	1.20
7	SFS	54.4	0.35	3	0.60	0.30	12	1.06	2.40	0.05	1.20
8	SFS	54.4	0.35	3	0.70	0.30	12	1.06	2.40	0.05	1.20
9	SFS	54.4	0.35	3	0.80	0.30	12	1.06	2.40	0.05	1.20
10	SFS	54.4	0.35	3	0.90	0.30	12	1.06	2.40	0.05	1.20
11	SFS	54.4	0.35	3	1.10	0.30	12	1.06	2.40	0.05	1.20
12	FS	54.4	0.35	3	0.25	0.30	12	-	-	-	-
13	FS	54.4	0.35	3	0.30	0.30	12	-	-	-	-
14	FS	54.4	0.35	3	0.35	0.30	12	-	-	-	-
15	FS	54.4	0.35	3	0.40	0.30	12	-	-	-	-
16	FS	54.4	0.35	3	0.45	0.30	12	-	-	-	-

No	System	Structural Parameters			Excitation Parameters			SSI Parameters			
		M_{str} (tn)	$T_{str.f}$ (sec)	h (m)	T_{exc} (sec)	PGA (g)	N	h/r	γ	s	$T_{sys.el}$ / $T_{str.f}$
17	FS	54.4	0.35	3	0.50	0.30	12	-	-	-	-
17	FS	54.4	0.35	3	0.60	0.30	12	-	-	-	-
18	FS	54.4	0.35	3	0.70	0.30	12	-	-	-	-
19	FS	54.4	0.35	3	0.80	0.30	12	-	-	-	-
20	FS	54.4	0.35	3	0.90	0.30	12	-	-	-	-
21	FS	54.4	0.35	3	1.10	0.30	12				
22	SFS	74.4	0.35	3	0.25	0.30	12	1.06	3.30	0.05	1.27
23	SFS	74.4	0.35	3	0.30	0.30	12	1.06	3.30	0.05	1.27
24	SFS	74.4	0.35	3	0.35	0.30	12	1.06	3.30	0.05	1.27
25	SFS	74.4	0.35	3	0.40	0.30	12	1.06	3.30	0.05	1.27
26	SFS	74.4	0.35	3	0.45	0.30	12	1.06	3.30	0.05	1.27
27	SFS	74.4	0.35	3	0.50	0.30	12	1.06	3.30	0.05	1.27
28	SFS	74.4	0.35	3	0.60	0.30	12	1.06	3.30	0.05	1.27
29	SFS	74.4	0.35	3	0.70	0.30	12	1.06	3.30	0.05	1.27
30	SFS	74.4	0.35	3	0.80	0.30	12	1.06	3.30	0.05	1.27
31	SFS	74.4	0.35	3	0.90	0.30	12	1.06	3.30	0.05	1.27
32	SFS	74.4	0.35	3	1.10	0.30	12	1.06	3.30	0.05	1.27
33	FS	74.4	0.35	3	0.25	-	12	-	-	-	-
34	FS	74.4	0.35	3	0.30	-	12	-	-	-	-
35	FS	74.4	0.35	3	0.35	-	12	-	-	-	-
36	FS	74.4	0.35	3	0.40	-	12	-	-	-	-
37	FS	74.4	0.35	3	0.45	-	12	-	-	-	-
38	FS	74.4	0.35	3	0.50	-	12	-	-	-	-
39	FS	74.4	0.35	3	0.60	-	12	-	-	-	-
40	FS	74.4	0.35	3	0.70	-	12	-	-	-	-
41	FS	74.4	0.35	3	0.80	-	12	-	-	-	-
42	FS	74.4	0.35	3	0.90	-	12	-	-	-	-
43	FS	74.4	0.35	3	1.10	-	12	-	-	-	-
44	SFS	89.7	0.35	3	0.25	0.30	12	1.06	4.00	0.05	1.32
45	SFS	89.7	0.35	3	0.30	0.30	12	1.06	4.00	0.05	1.32
46	SFS	89.7	0.35	3	0.35	0.30	12	1.06	4.00	0.05	1.32
47	SFS	89.7	0.35	3	0.40	0.30	12	1.06	4.00	0.05	1.32
48	SFS	89.7	0.35	3	0.45	0.30	12	1.06	4.00	0.05	1.32
49	SFS	89.7	0.35	3	0.50	0.30	12	1.06	4.00	0.05	1.32
50	SFS	89.7	0.35	3	0.60	0.30	12	1.06	4.00	0.05	1.32
51	SFS	89.7	0.35	3	0.70	0.30	12	1.06	4.00	0.05	1.32
52	SFS	89.7	0.35	3	0.80	0.30	12	1.06	4.00	0.05	1.32
53	SFS	89.7	0.35	3	0.90	0.30	12	1.06	4.00	0.05	1.32
54	SFS	89.7	0.35	3	1.10	0.30	12	1.06	4.00	0.05	1.32
55	FS	89.7	0.35	3	0.25	-	12	-	-	-	-
56	FS	89.7	0.35	3	0.30	-	12	-	-	-	-
57	FS	89.7	0.35	3	0.35	-	12	-	-	-	-
58	FS	89.7	0.35	3	0.40	-	12	-	-	-	-
59	FS	89.7	0.35	3	0.45	-	12	-	-	-	-

No	System	Structural Parameters			Excitation Parameters			SSI Parameters			
		M_{str} (tn)	$T_{str.f}$ (sec)	h (m)	T_{exc} (sec)	PGA (g)	N	h/r	γ	s	$T_{sys.el}$ / $T_{str.f}$
60	FS	89.7	0.35	3	0.50	-	12	-	-	-	-
61	FS	89.7	0.35	3	0.60	-	12	-	-	-	-
62	FS	89.7	0.35	3	0.70	-	12	-	-	-	-
63	FS	89.7	0.35	3	0.80	-	12	-	-	-	-
64	FS	89.7	0.35	3	0.90	-	12	-	-	-	-
65	FS	89.7	0.35	3	1.10	-	12	-	-	-	-
66	SFS	114.4	0.35	3	0.25	0.30	12	1.06	5.10	0.05	1.39
67	SFS	114.4	0.35	3	0.30	0.30	12	1.06	5.10	0.05	1.39
68	SFS	114.4	0.35	3	0.35	0.30	12	1.06	5.10	0.05	1.39
69	SFS	114.4	0.35	3	0.40	0.30	12	1.06	5.10	0.05	1.39
70	SFS	114.4	0.35	3	0.45	0.30	12	1.06	5.10	0.05	1.39
71	SFS	114.4	0.35	3	0.50	0.30	12	1.06	5.10	0.05	1.39
72	SFS	114.4	0.35	3	0.60	0.30	12	1.06	5.10	0.05	1.39
73	SFS	114.4	0.35	3	0.70	0.30	12	1.06	5.10	0.05	1.39
74	SFS	114.4	0.35	3	0.80	0.30	12	1.06	5.10	0.05	1.39
75	SFS	114.4	0.35	3	0.90	0.30	12	1.06	5.10	0.05	1.39
76	SFS	114.4	0.35	3	1.10	0.30	12	1.06	5.10	0.05	1.39
77	FS	114.4	0.35	3	0.25	0.30	12	-	-	-	-
78	FS	114.4	0.35	3	0.30	0.30	12	-	-	-	-
79	FS	114.4	0.35	3	0.35	0.30	12	-	-	-	-
80	FS	114.4	0.35	3	0.40	0.30	12	-	-	-	-
81	FS	114.4	0.35	3	0.45	0.30	12	-	-	-	-
82	FS	114.4	0.35	3	0.50	0.30	12	-	-	-	-
83	FS	114.4	0.35	3	0.60	0.30	12	-	-	-	-
84	FS	114.4	0.35	3	0.70	0.30	12	-	-	-	-
85	FS	114.4	0.35	3	0.80	0.30	12	-	-	-	-
86	FS	114.4	0.35	3	0.90	0.30	12	-	-	-	-
87	FS	114.4	0.35	3	1.10	0.30	12	-	-	-	-
88	SFS	89.7	0.35	3.9	0.25	0.30	12	1.38	4.00	0.06	1.49
89	SFS	89.7	0.35	3.9	0.30	0.30	12	1.38	4.00	0.06	1.49
90	SFS	89.7	0.35	3.9	0.35	0.30	12	1.38	4.00	0.06	1.49
91	SFS	89.7	0.35	3.9	0.40	0.30	12	1.38	4.00	0.06	1.49
92	SFS	89.7	0.35	3.9	0.45	0.30	12	1.38	4.00	0.06	1.49
93	SFS	89.7	0.35	3.9	0.50	0.30	12	1.38	4.00	0.06	1.49
94	SFS	89.7	0.35	3.9	0.60	0.30	12	1.38	4.00	0.06	1.49
95	SFS	89.7	0.35	3.9	0.70	0.30	12	1.38	4.00	0.06	1.49
96	SFS	89.7	0.35	3.9	0.80	0.30	12	1.38	4.00	0.06	1.49
97	SFS	89.7	0.35	3.9	0.90	0.30	12	1.38	4.00	0.06	1.49
98	SFS	89.7	0.35	3.9	1.10	0.30	12	1.38	4.00	0.06	1.49
99	SFS	89.7	0.35	5.1	0.25	0.30	12	1.88	4.00	0.08	1.74
100	SFS	89.7	0.35	5.1	0.30	0.30	12	1.88	4.00	0.08	1.74
101	SFS	89.7	0.35	5.1	0.35	0.30	12	1.88	4.00	0.08	1.74
102	SFS	89.7	0.35	5.1	0.40	0.30	12	1.88	4.00	0.08	1.74
103	SFS	89.7	0.35	5.1	0.45	0.30	12	1.88	4.00	0.08	1.74

No	System	Structural Parameters			Excitation Parameters			SSI Parameters			
		M_{str} (tn)	$T_{str.f}$ (sec)	h (m)	T_{exc} (sec)	PGA (g)	N	h/r	γ	s	$T_{sys.el}$ / $T_{str.f}$
104	SFS	89.7	0.35	5.1	0.50	0.30	12	1.88	4.00	0.08	1.74
105	SFS	89.7	0.35	5.1	0.60	0.30	12	1.88	4.00	0.08	1.74
106	SFS	89.7	0.35	5.1	0.70	0.30	12	1.88	4.00	0.08	1.74
107	SFS	89.7	0.35	5.1	0.80	0.30	12	1.88	4.00	0.08	1.74
108	SFS	89.7	0.35	5.1	0.90	0.30	12	1.88	4.00	0.08	1.74
109	SFS	89.7	0.35	5.1	1.10	0.30	12	1.88	4.00	0.08	1.74
110	SFS	89.7	0.35	5.1	1.20	0.30	12	1.88	4.00	0.08	1.74
111	SFS	89.7	0.35	5.1	1.30	0.30	12	1.88	4.00	0.08	1.74
112	SFS	89.7	0.35	5.1	1.40	0.30	12	1.88	4.00	0.08	1.74
113	SFS	89.7	0.35	3	0.25	0.23	12	1.06	4.00	0.05	1.32
114	SFS	89.7	0.35	3	0.35	0.23	12	1.06	4.00	0.05	1.32
115	SFS	89.7	0.35	3	0.40	0.23	12	1.06	4.00	0.05	1.32
116	SFS	89.7	0.35	3	0.50	0.23	12	1.06	4.00	0.05	1.32
117	SFS	89.7	0.35	3	0.60	0.23	12	1.06	4.00	0.05	1.32
118	SFS	89.7	0.35	3	0.70	0.23	12	1.06	4.00	0.05	1.32
119	SFS	89.7	0.35	3	0.80	0.23	12	1.06	4.00	0.05	1.32
120	SFS	89.7	0.35	3	0.90	0.23	12	1.06	4.00	0.05	1.32
121	SFS	89.7	0.35	3	1.10	0.23	12	1.06	4.00	0.05	1.32
122	FS	89.7	0.35	3	0.25	0.23	12	-	-	-	-
123	FS	89.7	0.35	3	0.35	0.23	12	-	-	-	-
124	FS	89.7	0.35	3	0.40	0.23	12	-	-	-	-
125	FS	89.7	0.35	3	0.50	0.23	12	-	-	-	-
126	FS	89.7	0.35	3	0.60	0.23	12	-	-	-	-
127	FS	89.7	0.35	3	0.70	0.23	12	-	-	-	-
128	FS	89.7	0.35	3	0.80	0.23	12	-	-	-	-
129	FS	89.7	0.35	3	0.90	0.23	12	-	-	-	-
130	FS	89.7	0.35	3	1.10	0.23	12	-	-	-	-
131	SFS	89.7	0.35	3	0.25	0.36	12	1.06	4.00	0.05	1.32
132	SFS	89.7	0.35	3	0.35	0.36	12	1.06	4.00	0.05	1.32
133	SFS	89.7	0.35	3	0.50	0.36	12	1.06	4.00	0.05	1.32
134	SFS	89.7	0.35	3	0.60	0.36	12	1.06	4.00	0.05	1.32
135	SFS	89.7	0.35	3	0.70	0.36	12	1.06	4.00	0.05	1.32
136	SFS	89.7	0.35	3	0.80	0.36	12	1.06	4.00	0.05	1.32
137	SFS	89.7	0.35	3	0.90	0.36	12	1.06	4.00	0.05	1.32
138	SFS	89.7	0.35	3	1.10	0.36	12	1.06	4.00	0.05	1.32
139	FS	89.7	0.35	3	0.25	0.36	12	1.06	4.00	0.05	1.32
140	FS	89.7	0.35	3	0.35	0.36	12	-	-	-	-
141	FS	89.7	0.35	3	0.50	0.36	12	-	-	-	-
142	FS	89.7	0.35	3	0.60	0.36	12	-	-	-	-
143	FS	89.7	0.35	3	0.70	0.36	12	-	-	-	-
144	FS	89.7	0.35	3	0.80	0.36	12	-	-	-	-
145	FS	89.7	0.35	3	0.90	0.36	12	-	-	-	-
146	FS	89.7	0.35	3	1.10	0.36	12	-	-	-	-
147	SFS	89.7	0.35	3	0.25	0.30	8	1.06	4.00	0.05	1.32

No	System	Structural Parameters			Excitation Parameters			SSI Parameters			
		M_{str} (tn)	$T_{str.f}$ (sec)	h (m)	T_{exc} (sec)	PGA (g)	N	h/r	γ	s	$T_{sys.el}$ / $T_{str.f}$
148	SFS	89.7	0.35	3	0.30	0.30	8	1.06	4.00	0.05	1.32
149	SFS	89.7	0.35	3	0.35	0.30	8	1.06	4.00	0.05	1.32
150	SFS	89.7	0.35	3	0.45	0.30	8	1.06	4.00	0.05	1.32
151	SFS	89.7	0.35	3	0.50	0.30	8	1.06	4.00	0.05	1.32
152	SFS	89.7	0.35	3	0.60	0.30	8	1.06	4.00	0.05	1.32
153	SFS	89.7	0.35	3	0.70	0.30	8	1.06	4.00	0.05	1.32
154	SFS	89.7	0.35	3	0.80	0.30	8	1.06	4.00	0.05	1.32
155	SFS	89.7	0.35	3	0.90	0.30	8	1.06	4.00	0.05	1.32
156	SFS	89.7	0.35	3	1.10	0.30	8	1.06	4.00	0.05	1.32
157	FS	89.7	0.35	3	0.25	-	8	-	-	-	-
158	FS	89.7	0.35	3	0.30	-	8	-	-	-	-
159	FS	89.7	0.35	3	0.35	-	8	-	-	-	-
160	FS	89.7	0.35	3	0.45	-	8	-	-	-	-
161	FS	89.7	0.35	3	0.50	-	8	-	-	-	-
162	FS	89.7	0.35	3	0.60	-	8	-	-	-	-
163	FS	89.7	0.35	3	0.70	-	8	-	-	-	-
164	FS	89.7	0.35	3	0.80	-	8	-	-	-	-
165	FS	89.7	0.35	3	0.90	-	8	-	-	-	-
166	FS	89.7	0.35	3	1.10	-	8	-	-	-	-

6.3.2 Effect of T_{sys}/T_{exc}

The present section examines the effect of period ratio T_{sys}/T_{exc} on the settlement ratio between the structure-foundation-soil (SFS) and foundation-soil (FS) system. To that end, **Figure 6.4** presents the response characteristics of the two systems. In more detail, **Figure 6.4a** examines the SFS-to-FS system seismic settlement ratio, while **Figure 6.4b** shows the elastic response spectrum of the normalized absolute acceleration of the structural mass S_a/PGA and **Figure 6.4c** shows the phase difference ϕ between the vibration of the structural mass and the vibration of the foundation.

In contrast to the previously examined liquefied soil conditions, for non-liquefiable soil conditions the numerical predictions show that SSI aggravates the performance of the SFS system. More specifically, the following observations can be remarked:

- *Stiff* SFS systems ($T_{sys}/T_{exc} \rightarrow 0$) settle more than FS systems ($\rho_{SFS}/\rho_{FS} \approx 1.4$). The reason for this is that although spectral accelerations are not amplified ($S_a/PGA \rightarrow 1.0$), they act in-phase with the

foundation movement ($\phi \approx 0^o$) and consequently foundation rocking and associated seismic settlements are aggravated.

- *Flexible* SFS systems ($T_{sys}/T_{exc} \rightarrow \infty$) settle equally with the FS systems ($\rho_{SFS}/\rho_{FS} \approx 1.0$). In this case, spectral accelerations are de-amplified ($S_a/PGA \leq 1.0$) and they also act out-of-phase ($\phi \rightarrow 180^o$) with the foundation movement. Thus, although rocking is still evident, it is out-of-phase with the translation of the footing and sliding of the mobilized soil wedge, thus, counteracting rocking-induced settlements.
- *At resonance* ($T_{sys}/T_{exc} \approx 0.50\text{-}1.50$) SFS systems settle considerably more than FS systems ($\rho_{SFS}/\rho_{FS} \approx 4.0$). This is attributed to the considerable increase of spectral accelerations ($S_a/PGA \approx 2\text{-}2.5$), while the phase difference between mass and foundation displacement is not high enough ($\varphi \approx 50\text{-}110^o$). Thus, the large inertial forces render rocking the governing mechanism of settlement accumulation for the SFS system, with relatively minor counteracting effects due to the asynchronous mass versus foundation vibration.

Concluding, the vast difference between shear strains under the footing edge in the SFS and the FS systems indicates that rocking-induced settlement accumulation is the governing mechanism in the case of the SFS system. Only a small percentage of the excessive settlements can be attributed to wedge sliding due to the degradation of bearing capacity, which is the governing mechanism of seismically-induced settlements in the case of single footings (FS systems).

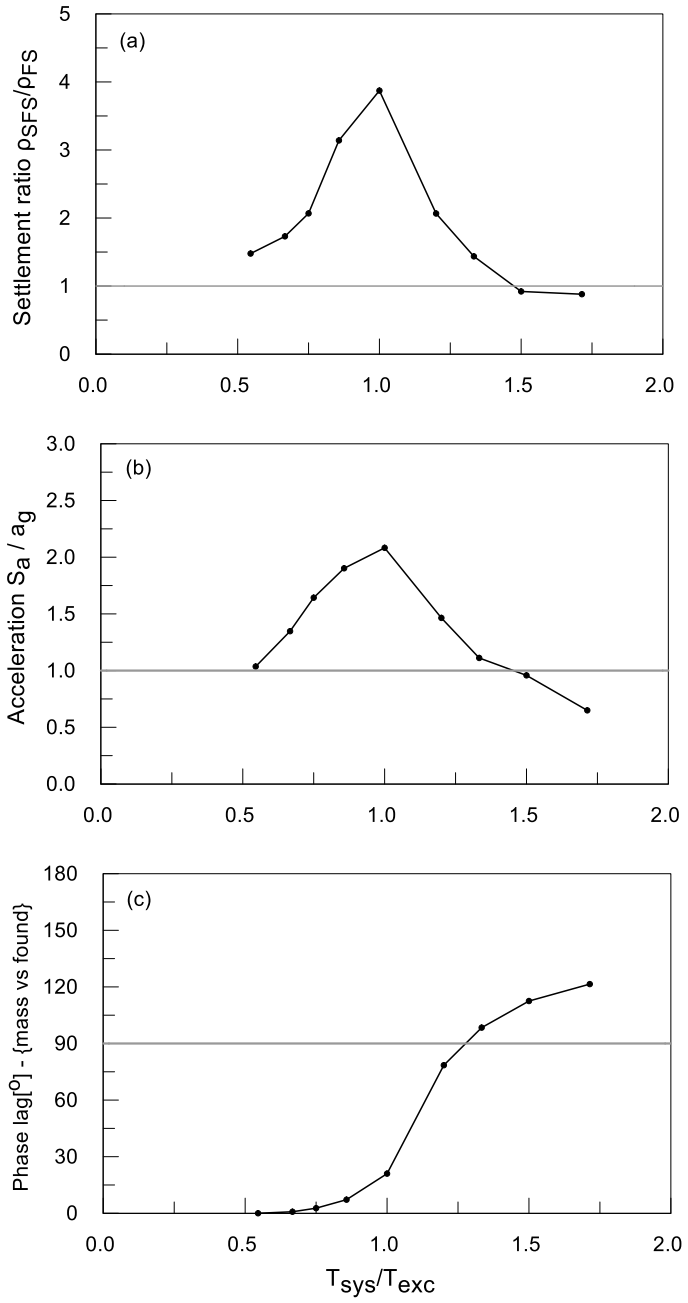

Figure 6.4: (a) Seismic settlement ratio of SFS-to-FS systems and (b)-(c) response spectra of the normalized absolute acceleration of the structural mass Sa/ag and phase angle ϕ between the vibration of structural mass and the vibration of the foundation.

6.3.3 Effect of slenderness ratio

This section examines the effect of slenderness ratio *h/r* on the dynamic response of SFS and FS systems, i.e., in terms of the settlement ratio ρ_{SFS}/ρ_{FS}, as well as the SFS system spectral accelerations and phase difference (**Figure 6.5**). The structural, excitation and SSI properties of the examined systems are

summarized in **Table 6.1** (Analyses No 44-65, 88-112). The variation of slenderness ratio is performed using the same framework as in Chapter 4, i.e., by varying the structural height, while keeping the fixed-base natural period $T_{str.f}$ constant.

The effective system period $T_{sys.eff}$ is a key-role parameter for the characterization of the system response. The developed methodology of Chapter 4 provides estimates of $T_{sys.eff}$ for different values of slenderness ratio, which are calculated in the case of non-liquefiable soil conditions using the smoothed spectral predominant system period $T_{sys.o}$, as defined in Section 4.3.2 and the obtained values are summarized in **Table 6.2** (5th column). The linear part of period elongation $T_{sys.el}/T_{str.f,}$ is calculated with the use of the analytical procedures of Design Codes and the resulting values are summarized in the 3rd column of Table 6.2. The nonlinear part of period elongation $T_{sys.eff}/T_{sys.el}$ is calculated with the use of Transfer Functions with the previously described procedure of chapter 4.3.2. The obtained results are shown in Table 6.2 (4th column). Overall, the effective system period $T_{sys.eff}$ is significantly affected by the slenderness ratio, with computed values ranging from $T_{sys.eff}$ = 0.68sec to 0.76sec. The increase of $T_{sys.eff}$ is primarily attributed to the increase of the elastic part of period elongation $T_{sys.el}/T_{str.f}$. The aforementioned procedure of system period estimation is described herein in order to provide a further insight on the procedure used to compute the system period T_{sys}. Nevertheless, the values of T_{sys} in the following numerical predictions of **Figure 6.5** are calibrated so that peak values of settlement ratios are presented for a period ratio T_{sys}/T_{exc} equal to unity.

Table 6.2: Period elongation data of the numerical analyses for varying slenderness ratio.

h (m)	h/r	Tsys.el/Tstr.f	Tsys.eff/Tsys.el	Tsys.eff (sec)
3.0	*1.06*	*1.32*	*1.48*	*0.68*
3.9	1.38	1.49	1.39	0.71
5.1	1.88	1.74	1.28	0.76

The aforementioned vibrational characteristics of the examined SFS and FS system response are presented in **Figure 6.5a-c.** The following can be noted:

- Rocking-induced soil shearing is the principal mechanism of settlement accumulation for SFS systems irrespective of the slenderness ratio. Specifically, at resonance, i.e. $T_{sys}/T_{exc} \approx 1.0$, peak settlement ratios ρ_{SFS}/ρ_{FS} are increased up to 21% when h/r increases from 1.06 to 1.88. On the other hand, for

stiff systems, i.e. $T_{sys}/T_{exc} \leq 0.5$, settlement ratios are not affected by the slenderness ratio, while for slender systems, i.e. $T_{sys}/T_{exc} \geq 1.5$, only a minimal increase of ρ_{SFS}/ρ_{FS} values is observed for larger values of slenderness ratios.

- Spectral accelerations S_a/PGA are rather not sensitive to the slenderness ratio. Since all the examined systems have the same structural mass, the aforementioned observation implies that the shear force and overturning moment transmitted to the foundation also remain constant. The overturning moment developed on the foundation level is directly proportional to the structural height, hence, it is directly proportional to the slenderness ratio.
- The phase difference φ between the motion of the structural mass and the one of the foundation is related to the magnitude of rocking-induced soil softening. As a result, the greatest levels of phase difference are observed for larger values of the slenderness ratio, i.e. $h/r = 1.88$. It is noted that the discussed phase difference is mainly kinematically affected by the additional plastic deformation of the foundation soil, rather than the typical damping forces that oppose the mass movement as described in the theory of vibrations.

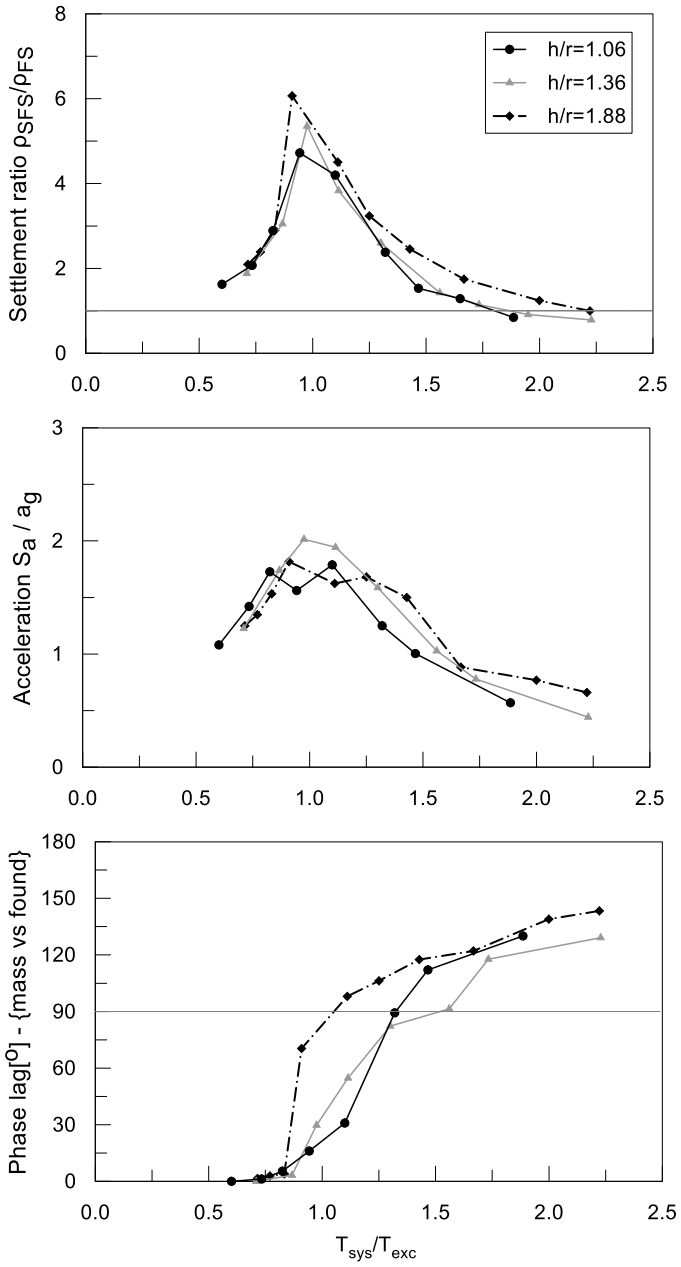

Figure 6.5: Variation of settlement ratio ρ_{SFS}/ρ_{FS}, normalized spectral accelerations S_a/PGA and phase difference ϕ with period ratio T_{sys}/T_{exc} for different data sets of slenderness ratio h/r.

6.3.4 Effect of relative mass ratio

The effect of relative mass ratio γ on the dynamic response of SFS and FS systems is parametrically investigated with the aid of **Table 6.3** and **Figure 6.6**. Structural, excitation and SSI properties of the examined systems are summarized in **Table 6.1** (numerical analyses No 1-87). To ensure equivalent fixed-

base structural period $T_{str.f}$ and, thus, structure-to-soil-stiffness ratio s (=$h/V_sT_{str.f}$), structural stiffness k_{str} was varied along with the variation of structural mass.

As shown in **Table 6.3**, the effect of relative mass ratio on both the elastic part $T_{sys.el}/T_{str.f}$ and the inelastic part $T_{sys.eff}/T_{sys.el}$ of period elongation is moderate. Namely, elastic period elongation $T_{sys.el}/T_{str.f}$ is only marginally increased, i.e. up to 6%, with the relative mass ratio (Table 6.3, 3rd column). The particular increase is related with the greater values of the measured shear wave velocity V_s under the footing due to the increased Shear Modulus G associated with the applied overburden pressure. The procedure followed to obtain the aforementioned elastic system period is described in detail in section 4.3.1. Similarly, the inelastic part of period elongation $T_{sys.eff}/T_{sys.el}$ is only mildly affected by the relative mass ratio (Table 6.3, 4th column). The maximum increase in the examined range of relative mass ratios is up to 9% and is attributed to additional soil softening due to the increased inertial forces of the structure.

Table 6.3: Period elongation data of the numerical analyses for varying relative mass ratio.

Mstr (Mgr)	γ	Tsys.el/Tstr.f	Tsys.eff/Tsys.el	Tsys.eff (sec)
54.4	2.40	1.25	1.40	0.59
74.4	3.30	1.29	1.49	0.66
89.7	4.00	1.32	1.48	0.68
114.4	5.10	1.32	1.53	0.71

Figure 6.6a-c evaluates the effect of relative mass ratio on the vibration characteristics of the SFS and FS systems, using the same format as the previous section. The following remarks can be made:

- Settlement ratios are significantly and systematically affected by relative mass ratio values. Namely, in the central (resonant) spectral region T_{sys}/T_{exc} = 0.75÷1.35 settlement ratios increase up to 70% when relative mass ratio increases from 2.40 to 5.10. Irrespective of the value of the relative mass ratio, settlement ratios tend to the value of 1.5 for stiff SFS systems ($T_{sys}/T_{exc} \leq 0.5$) and to 1.0 for flexible systems, while the corresponding ratios for flexible systems ($T_{sys}/T_{exc} \geq 1.5$) tend to unity.
- Spectral accelerations S_a/PGA at resonance exhibit a slight decrease with increasing values of the relative mass ratio due to increase of the system damping.
- Overall, the significant increase of settlements with relative mass ratio is directly related with the increase of structural inertial forces and the associated rocking-induced soil softening. For example,

a system with γ = 5.10 experiences maximum spectral acceleration $S_a/PGA \approx 1.8$ and, therefore, the corresponding inertial force of the structure – assuming a_g = 1 m/s^2 – is $F_i = m \cdot S_a$ =114.4 Mgr·1.8 m/s^2 = 206kN, whereas a system with γ = 2.40 experiences maximum spectral acceleration $S_a/PGA \approx 2.2$ and the corresponding inertial force of the structure in this case is $Fi = m \cdot Sa$ =54.4 Mgr·2.2 m/s^2 = 120kN.

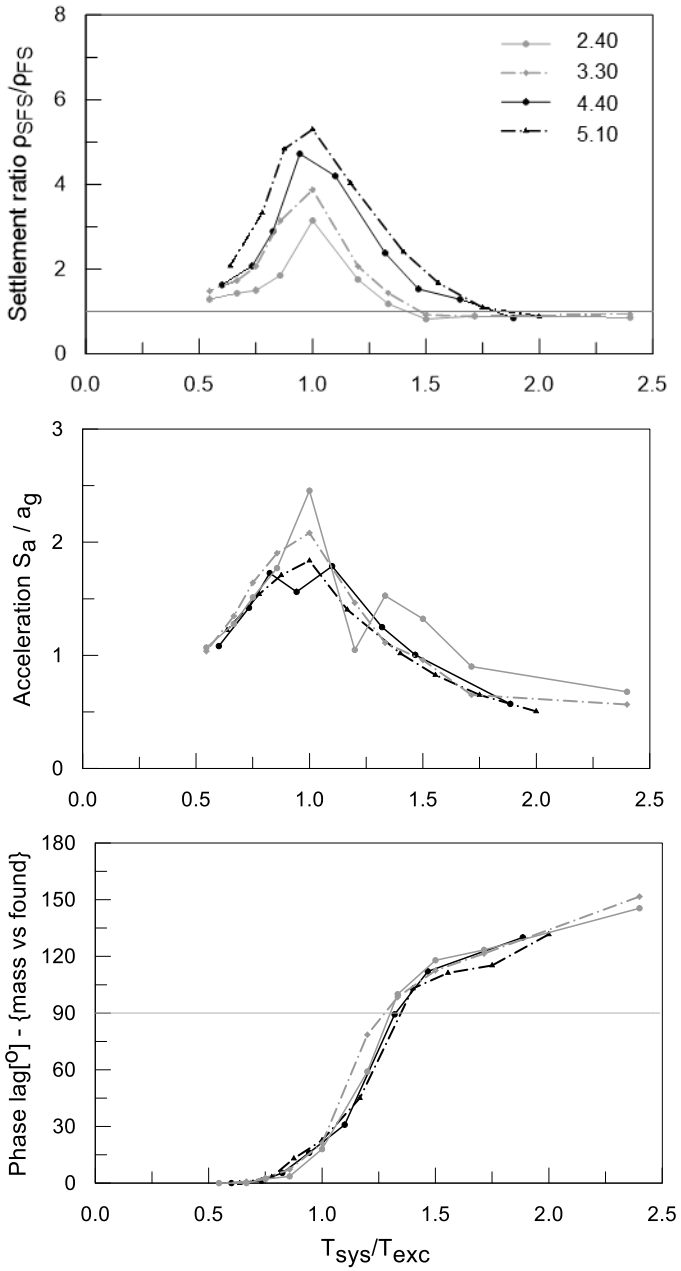

Figure 6.6: Variation of settlement ratio ρ_{SFS}/ρ_{FS}, normalized spectral accelerations *Sa/PGA* and phase lag φ with the period ratio *Tsys/Texc* for different data sets of relative mass ratios γ.

6.3.5 Excitation characteristics effect

The present section examines the effects of the excitation characteristics on the SFS system response. The characteristics of interest are i) the peak ground acceleration *PGA* and ii) the number of cycles N_o of the harmonic input motion. The range of the examined acceleration amplitudes *PGA* is such that it corresponds to the range of engineering interest. As mentioned in section 4.5.2, to relate the actual peak ground acceleration *PGA* with the amplitude of the input base motion a^b_{max} , it is considered that: i) The surface motion is amplified with respect to the bedrock motion, and ii) the constant amplitude of the harmonic motion is equivalent to the effective amplitude of an actual record which is typically assumed to be 2/3 of the peak ground acceleration for earthquake magnitudes of about 6 to 7 [based on the empirical estimate (M-1)/10]. **Figure 6.7a-b** present results of the aforementioned parametric numerical analyses performed for the reference system with SSI parameters s = 0.07, h/r = 1.06 and γ = 4.00. It may be observed that:

- The intensity of seismic acceleration *PGA* is a significant factor that aggravates settlement accumulation of SFS systems. Namely, at resonance, i.e. $T_{sys}/T_{exc} \approx 1.0$, the increase of the input motion magnitude *PGA* from 0.23g to 0.36g results to a corresponding increase of settlement ratios from $\rho_{SFS}/\rho_{FS} = 3.4$ to 6.8, i.e. up to 100%. For both stiff, i.e. $T_{sys}/T_{exc} \rightarrow 0.0$, and flexible systems, i.e. $T_{sys}/T_{exc} \rightarrow 2.5$, the effect of earthquake intensity on settlement ratios is minimized.
- The number of cycles of the harmonic input motion N_o affects the settlement of SFS systems but to a lesser degree compared to *PGA*. Specifically, at resonance settlement ratios are increased by 30% with increasing number of cycles from 4 to 12. On the other hand, settlement ratios of stiff and flexible systems seem to be unaffected by the number of cycles N_o.
- The relatively small effect of the number of cycles N_o on settlement ratio suggests that most of the settlement accumulation of SFS systems takes place in the first part of shaking. Literature studies on cyclic loading of sands have shown that the rate of volumetric strain accumulation gradually decreases with the number of cycles, up to a point where volumetric strains approach a constant value (Silver and Seed 1971; Bouckovalas et al. 1984). As a result, settlement accumulation is not proportional to the number of cycles and further settlement is prohibited.

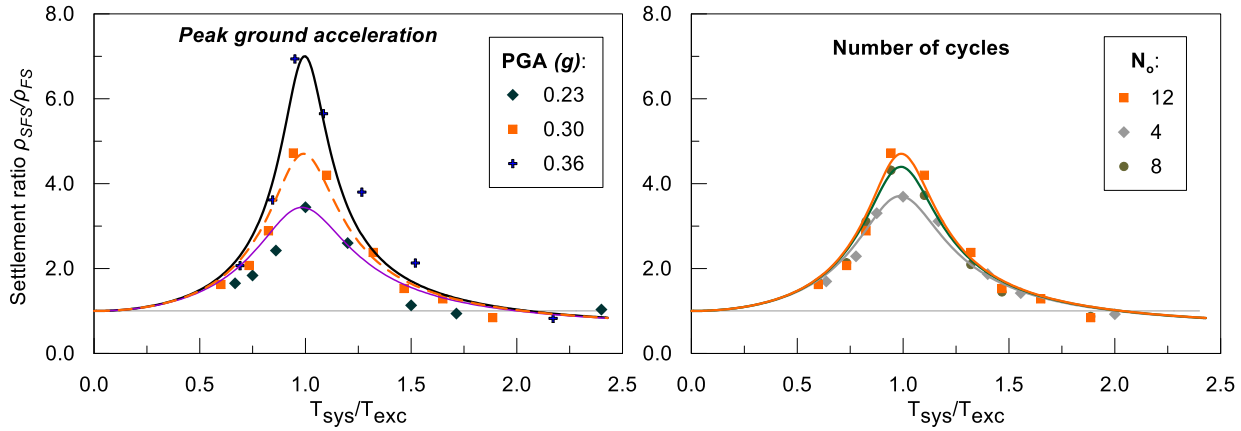

Figure 6.7: Variation of settlement ratio ρ_{SFS}/ρ_{FS} with the period ratio *Tsys/Texc* for different data sets of (a) the peak outcropping bedrock acceleration PGA_x and (b) the number of excitation cycles N_o.

6.4 Analytical relationships for SSI effects

This section aims at the development of analytical expressions for the settlement ratio ρ_{SFS}/ρ_{FS} between SFS and FS systems by exploiting the numerical analysis results. The main parameters that affect the problem have been identified by the parametric investigation of the previous sections and they are explicitly introduced in the analytical relationships that follow. The parameters under consideration are: the period ratio T_{sys}/T_{exc}, the slenderness ratio h/r, the relative mass ratio γ, the peak ground acceleration *PGA* and the number of excitation cycles N_o. Multivariable approximate relationships are developed following a multi-variable statistical analysis of the numerical results.

The developed expressions are not statistically "blind" but consistent with the physical mechanisms that govern the problem. Namely, following the discussions in the previous sections, settlement ratios exhibit a bell-type variation with the governing SSI parameter, i.e. the period ratio T_{sys}/T_{exc}. For this reason, the proposed relation to capture the variation of ρ_{SFS}/ρ_{FS} with T_{sys}/T_{exc} is based on the relationships that are typically used to describe the amplification spectrum of a single-degree-of-freedom system. In its general form, the expression of the settlement ratio ρ_{SFS}/ρ_{FS} is written as a function of the period ratio T_{sys}/T_{exc} through the use of 4 coefficients, i.e.:

$$\frac{\rho_{SFS}}{\rho_{FS}} = \frac{C_1 + C_2 \left(T_{sys}/T_{exc}\right)^2}{\sqrt{\left[C_3{}^2 - \left(T_{sys}/T_{exc}\right)^2\right]^2 + C_4{}^2 \left(T_{sys}/T_{exc}\right)^2}} \qquad 6.1$$

As it was also described in the previous chapter, the determination of the four independent coefficients (C_1, C_2, C_3, C_4) was based on some characteristic conditions: the limit values at the right- and left-end of

the spectrum, the peak value of the curve and the point of zero curvature. The following equations emerge by substituting the aforementioned boundary conditions to Equation 6.1:

$$\frac{\rho_{SFS}}{\rho_{FS}} = \begin{cases} C_1/C_3 & T_{sys}/T_{exc} \to 0 \\ \frac{\sqrt{C_3 \cdot C_4}}{C_3 \cdot C_2 + C_1} & T_{sys}/T_{exc} = 1.0 \\ C_2 & T_{sys}/T_{exc} \to \infty \end{cases}$$

$$\frac{d(\rho_{SFS}/\rho_{FS})}{d(T_{sys}/T_{exc})} = 0 \qquad T_{sys}/T_{exc} = 1.0$$

The above coefficients are functions of the remaining variables, i.e. *h/r*, *γ*, PGA and N_o. Based on the available numerical predictions and in order to simplify the proposed expressions, it can be reasonably assumed that for stiff systems ($T_{sys}/T_{exc} \to 0$) the settlement ratio tends to unity. On the other hand, for flexible systems ($T_{sys}/T_{exc} \to \infty$), it is assumed - that the limiting value of settlement ratios depends only on the variables *γ* and *h/r*, while it tends to a constant value (0.8) for different values of *PGA* and N_o. Based on the aforementioned conditions, the derived coefficients are presented in **Table 6.4**.

Table 6.4: Values of the coefficients (C_1, C_2, C_3, C_4) used in the proposed methodology.

Variables				**Coefficients**			
h/r	***γ***	***PGA***	***N₀***	***C₁***	***C₂***	***C₃***	***C₄***
1.06	4.00	0.30	12	1.00	0.53	1.00	0.11
1.36	4.00	0.30	12		0.58		0.09
1.88	4.00	0.30	12		0.63		0.06
1.06	2.40	0.30	12		0.09		0.15
1.06	3.30	0.30	12		0.34		0.13
1.06	5.10	0.30	12		0.58		0.09
1.06	4.00	0.23	12		0.53		0.20
1.06	4.00	0.36	12		0.53		0.06
1.06	4.00	0.30	4		0.53		0.17
1.06	4.00	0.30	8		0.53		0.12

The coefficients in Equation 5.10 are determined with a multi-variable statistical analysis of the available data in order to capture the working range of the examined variables. According to this, the following relationships are proposed for the coefficients C_2, C_4:

$$C_1 = 1.0 \tag{6.2}$$

$$C_2 = f_1(\gamma) \cdot f_2(h/r) \tag{6.3}$$

with

$$f_1(\gamma) = min\{a_2 + b_2 \cdot e^{c_2 \cdot \gamma}, 0\} \tag{6.4}$$

$$f_2(h/r) = d_2 + e_2 \cdot (h/r) \tag{6.5}$$

$$C_3 = 1.0 \tag{6.6}$$

$$C_4 = g_1(\gamma) \cdot g_2(h/r) \cdot g_3(PGA) \cdot g_4(N_{o)} \tag{6.7}$$

with

$$g_1(\gamma) = a_4 + b_4 \cdot \gamma \tag{6.8}$$

$$g_2(h/r) = c_4 + d_4 \cdot (h/r) \tag{6.9}$$

$$g_3\left(a_{max}^b\right) = e_4 + f_4 \cdot PGA \tag{6.10}$$

$$g_4(N_o) = \min\{g_4 + h_4 \cdot e^{i_4 \cdot N_o}, 0.3\} \tag{6.11}$$

The constants in the above equations obtained from the regression analysis of all available data are: a_1=0.68, b_1=-3.47, c_1=-1.46, d_1=0.82, e_1=0.24, a_2=1.79, b_2=-0.40, c_2=1.52, d_2=-0.53, e_2=3.85, f_2=-9.45, g_2=0.11, h_2=0.31, i_2=-0.40. The relevant plots of the aforementioned coefficients are presented in the subplots of **Figure 6.8**. **Figure 6.9**,Figure **6.10**,Figure **6.11** and **Figure 6.12** present in detail the numerical predictions of settlement ratios ρ_{SFS}/ρ_{FS} as a function of the period ratio T_{sys}/T_{exc} as well as the associated proposed relationships of Equations 5.10 (with the coefficient values shown in Table 6.4) for each of the examined variables, namely, the relative mass ratio (Figure 6.9), the slenderness ratio (Figure 6.10), the peak bedrock acceleration (Figure 6.11) and the number of cycles of the input motion (Figure 6.12).

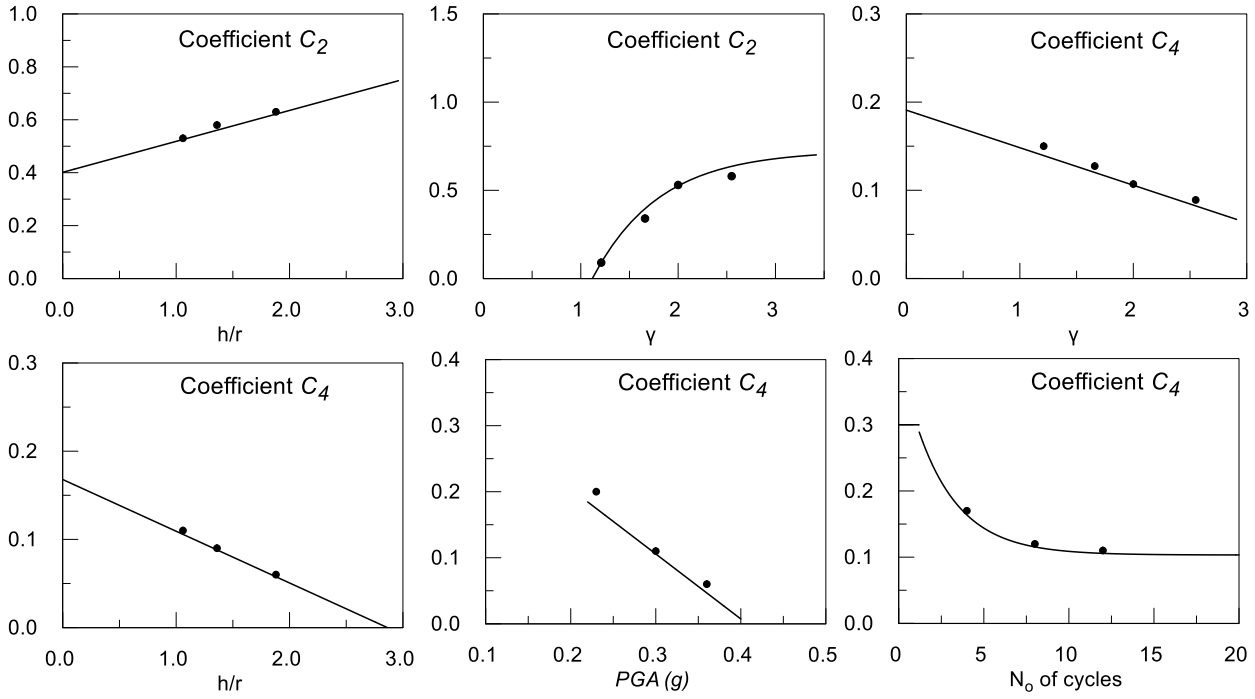

Figure 6.8: Plots of coefficients used in the proposed methodology as a function of the slenderness ratio and relative mass ratio.

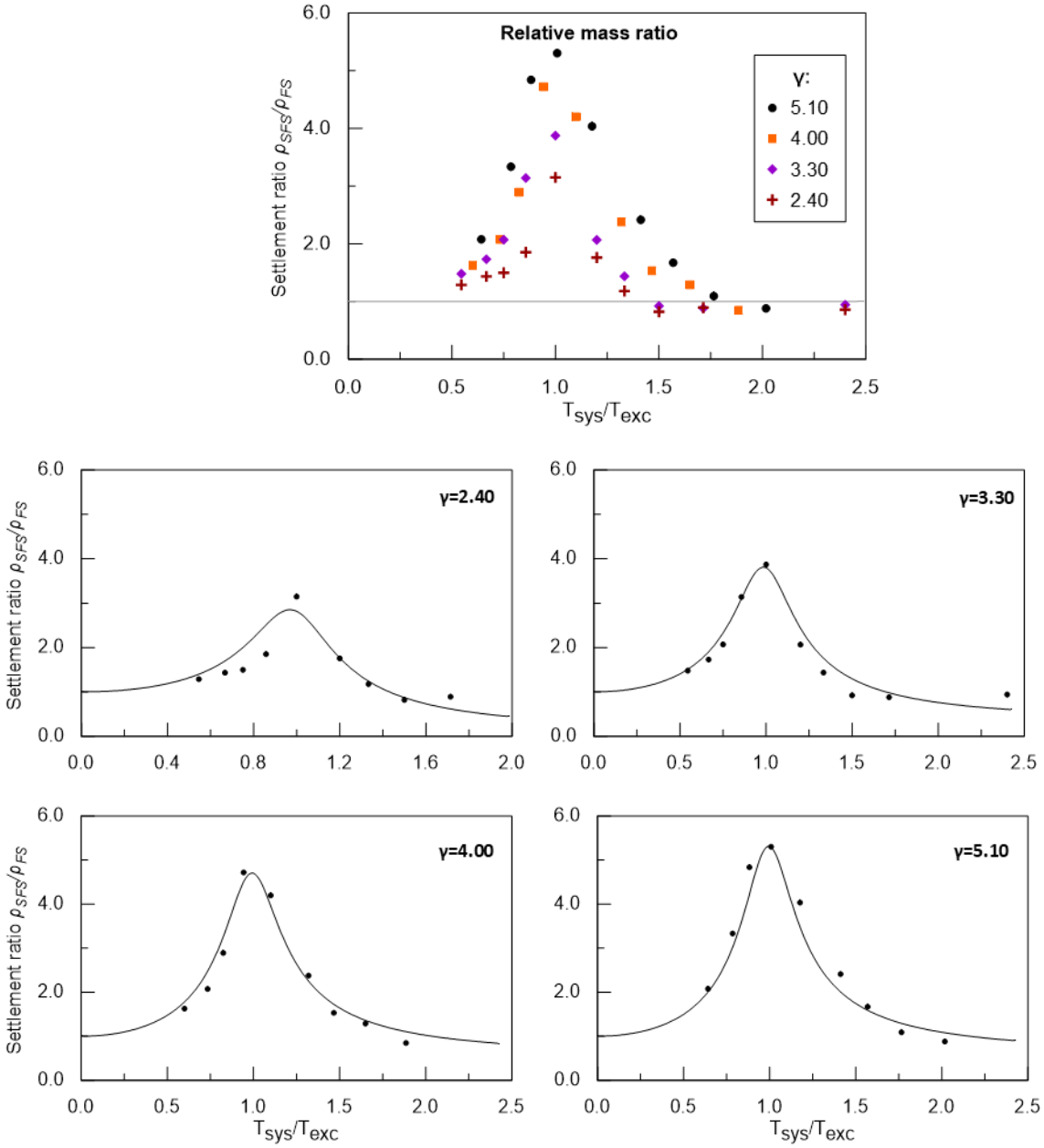

Figure 6.9: (a) Numerical predictions and (b)-(e) analytical expressions for the prediction of settlement ratio ρ_{SFS}/ρ_{FS}: effect of the relative mass ratio.

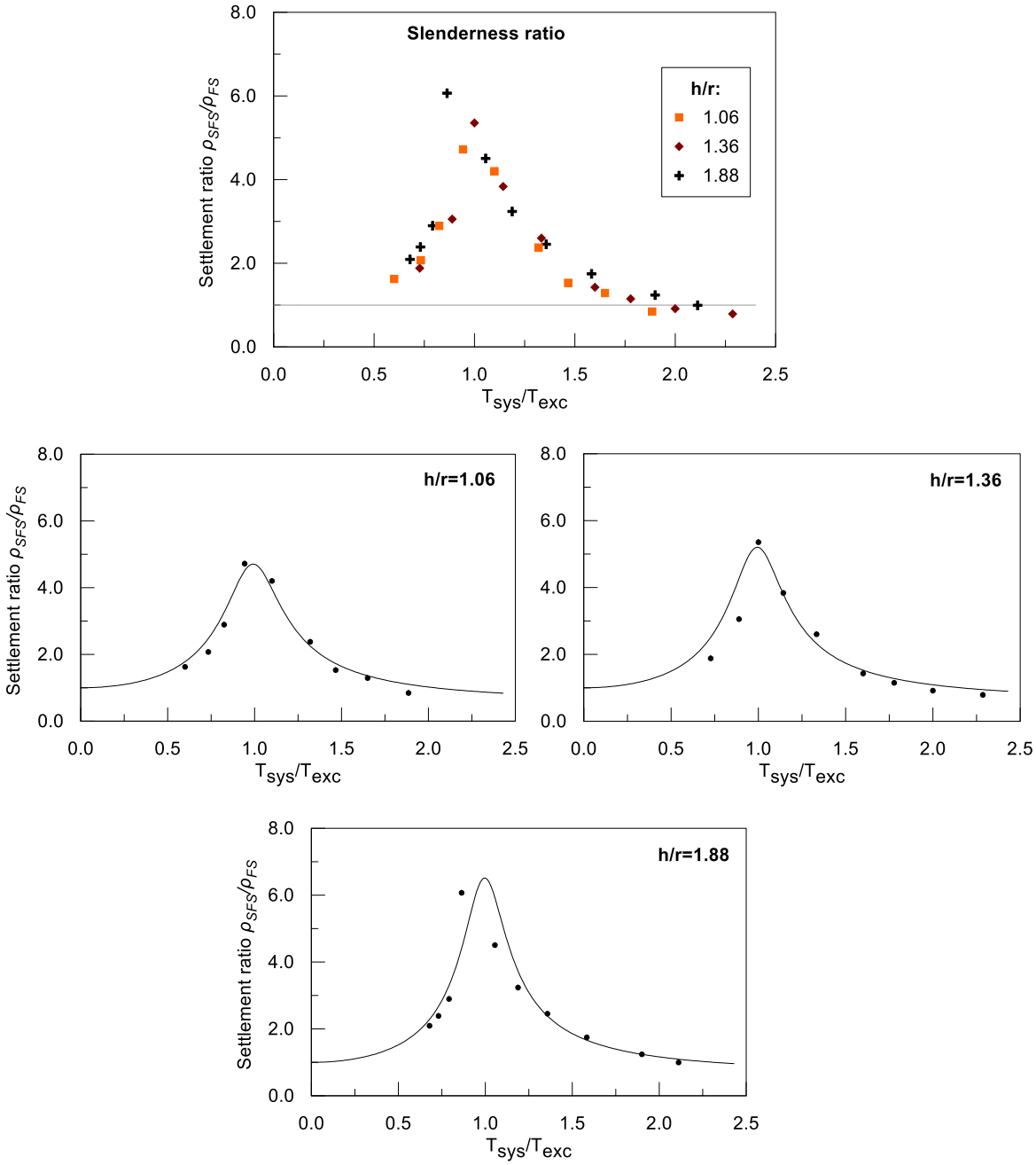

Figure 6.10: (a) Numerical predictions and (b)-(d) analytical expressions for the prediction of settlement ratio ρ_{SFS}/ρ_{FS}: effect of the slenderness ratio.

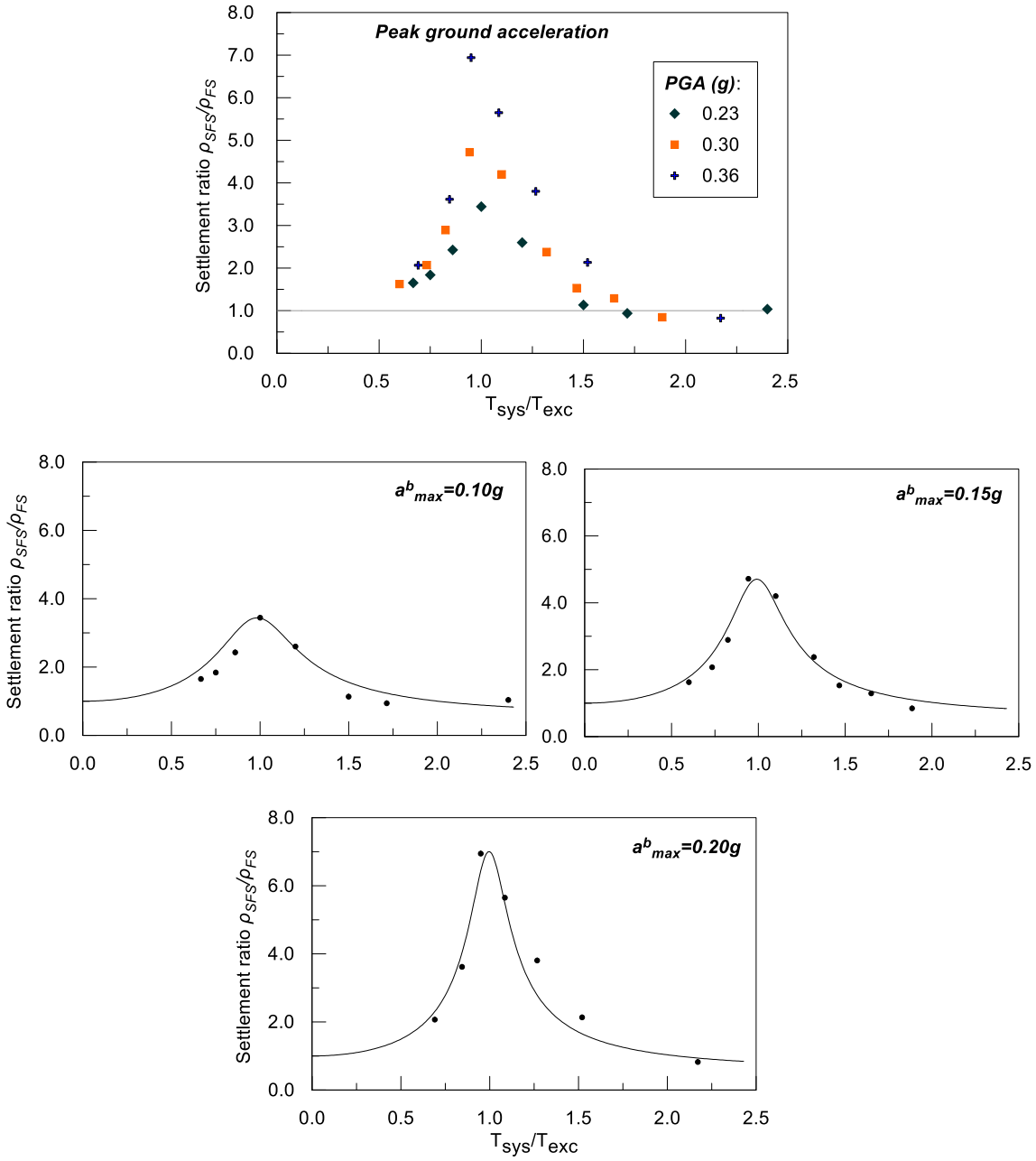

Figure 6.11: (a) Numerical predictions and (b)-(d) analytical expressions for the prediction of settlement ratio ρ_{SFS}/ρ_{FS}: effect of the peak bedrock acceleration.

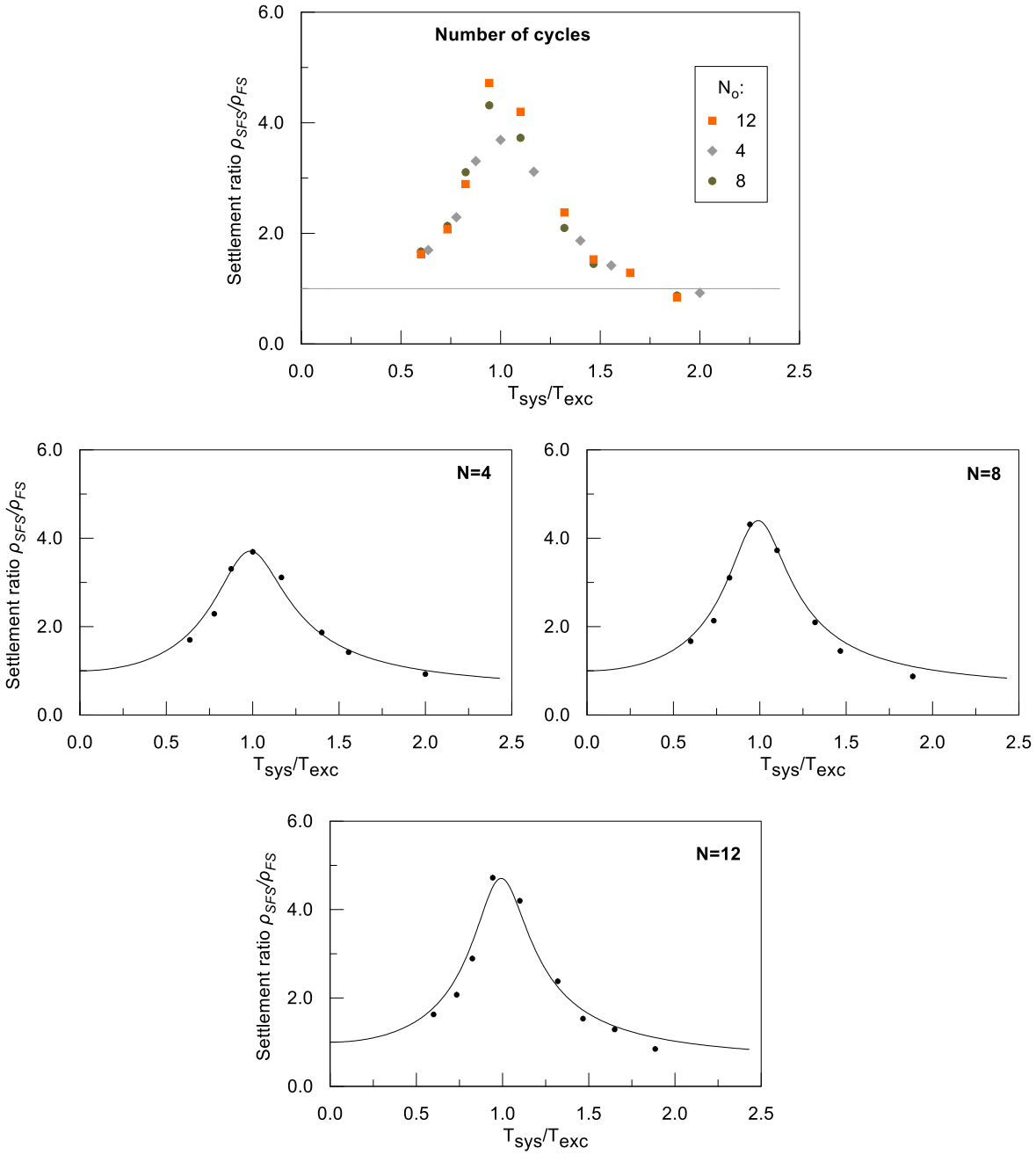

Figure 6.12: (a) Numerical predictions and (b)-(d) analytical expressions for the prediction of settlement ratio ρ_{SFS}/ρ_{FS}: effect of the number of excitation cycles.

The proposed analytical methodology is evaluated in the following by comparing its predictions with the corresponding numerical analyses results. The relative error between the analytical and the numerical predictions is employed to quantify the accuracy of the predictions, defined as:

$$Relative\ error = \frac{Observed - Numerical}{Observed} \quad 6.12$$

The statistical evaluation of relative errors in the prediction of settlement ratios ρ_{SFS}/ρ_{FS} for every – separately examined – independent variable is presented in **Table 6.5** and **Figure 6.13**. Statistical analysis showed that the standard deviation and average value of relative errors for the aggregate of predictions are 0.18 and -0.04, respectively. Overall, results show a relatively small concentration of errors both for the total as well as for the separate examination of the independent variables. Additionally, the distribution of errors is quite uniform for all the examined variables.

Table 6.5: Relative error of the proposed methodology against numerical predictions for separate sets of variable examination.

γ	*h/r*	*PGA*	N_o	**Average Relative Error (%)**	**St.deviation of Relative Errors (%)**
4.00	1.06	0.30	12	-5.8	14.1
4.00	1.36	0.30	12	-9.6	19.1
4.00	1.88	0.30	12	-4.6	17.0
2.40	1.06	0.30	12	-0.4	29.5
3.30	1.06	0.30	12	-7.9	19.8
5.10	1.06	0.30	12	3.0	19.1
4.00	1.06	0.23	12	-13.6	18.8
4.00	1.06	0.36	12	5.0	16.3
4.00	1.06	0.30	4	0.4	12.4
4.00	1.06	0.30	8	-5.7	12.9

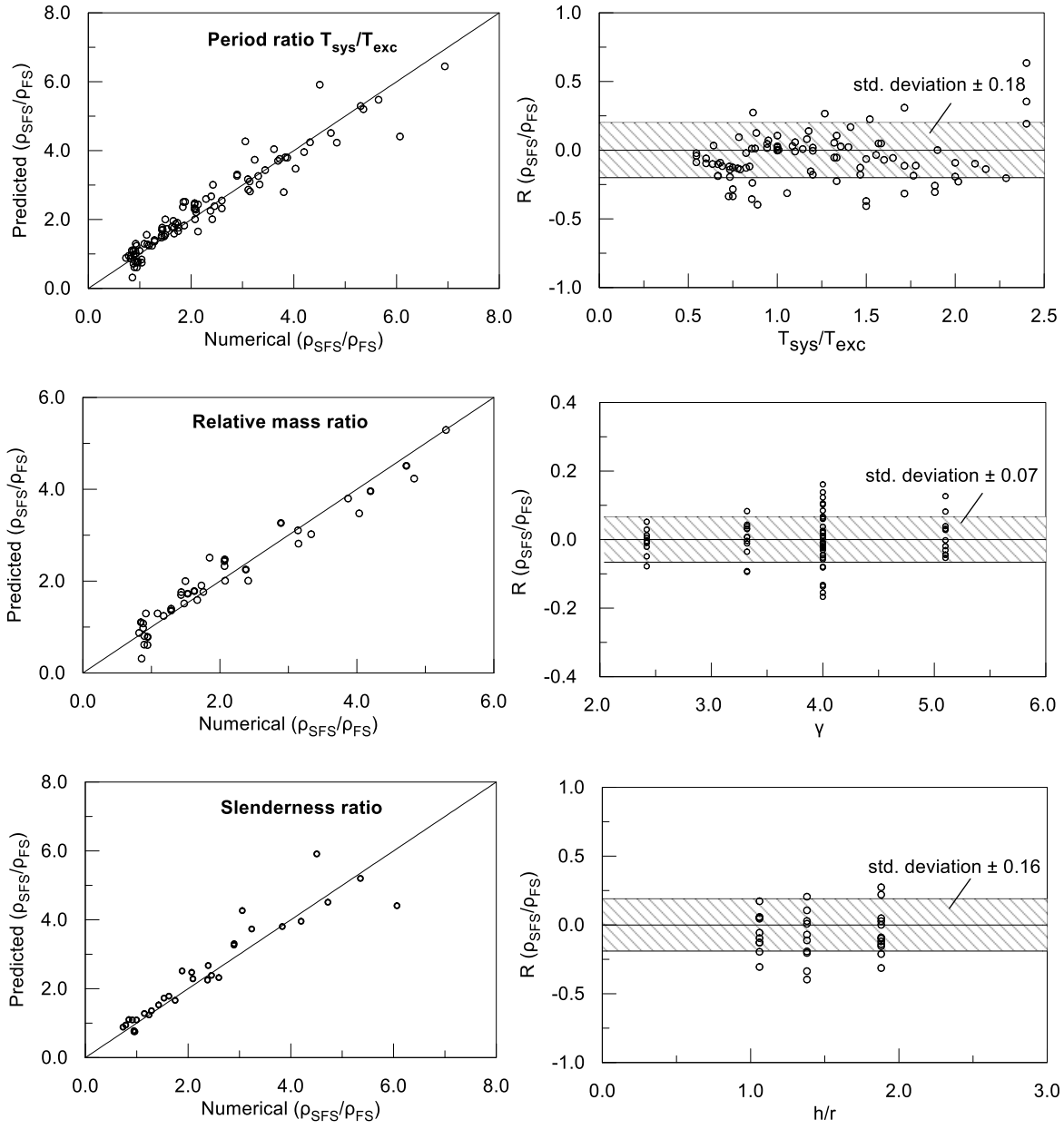

Figure 6.13: Relative error evaluation in the calculation of ρ_{SFS}/ρ_{FS} against numerical predictions by separate examination of the SSI variables: (a) period ratio Tsys/Texc, (b) relative mass ratio γ, (c) slenderness ratio h/r.

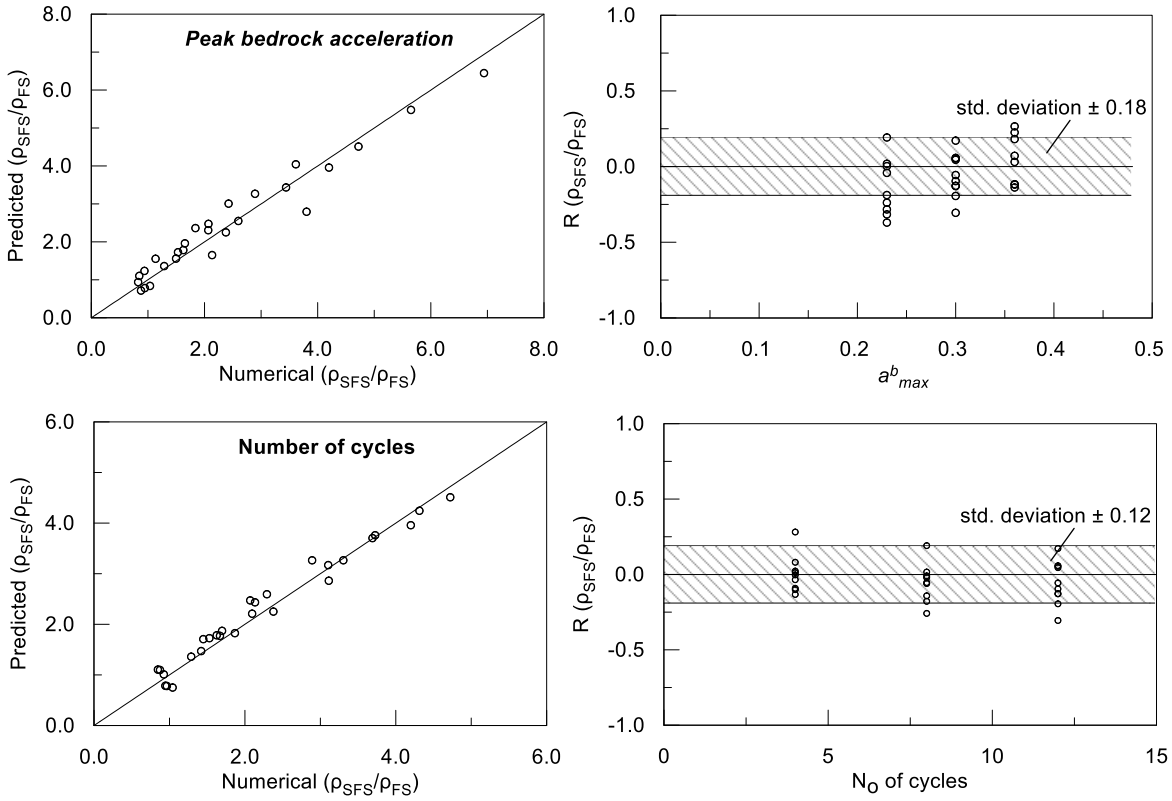

Figure 6.14: Relative error evaluation in the calculation of ρ_{SFS}/ρ_{FS} against numerical predictions by separate examination of the variables concerning the earthquake intensity: (a) peak ground acceleration *PGA* and (b) number of excitation cycles N_o.

6.5 Summary and conclusions

The present chapter examines the effect of SSI on structural settlements under non-liquefiable soil conditions. The critical factors affecting settlements are examined as dimensional parameters within the framework of SSI. In order to quantify the effect of structural inertia on settlements, the dynamic response of structure-foundation-soil (SFS) systems is examined comparatively with the response of equivalent foundation-soil (FS) systems. Finally, analytical relationships are developed for the settlement ratio ρ_{SFS}/ρ_{FS} following a statistical analysis of the numerical results. These relationships may serve as correction factors that can be applied to established procedures for the estimation of seismic settlements of single footings (e.g. Richards et al. 1993) without the effect of SSI. Overall, the following conclusions can be drawn:

- Seismic settlements of SFS systems are profoundly increased due to rocking-induced softening of the foundation soil. As a result, shear strain distribution under the structure appears to be

swallower compared to the typical – and deeper – formation of Coulomb-type wedges and additionally maximum strains are symmetrically concentrated under the footing edges.

- Due to the correlation of settlement accumulation with foundation rocking the most crucial parameter for SSI settlement aggravation is the period ratio T_{sys}/T_{exc} between the system and the excitation. Resonance conditions may lead to amplification of spectral accelerations and settlement ratios ρ_{SFS}/ρ_{FS} up to 2 and 6 times, respectively.
- The relative mass ratio γ and slenderness ratio h/r also affect significantly settlement accumulation of SFS systems. The associated effects are related with the aggravated structural rocking for increasing levels of these ratios. In the case of relative mass ratio, structural rocking is aggravated due to the increase of structural inertial forces, whereas in the case of slenderness ratio due to the increase of overturning moments. Overall, settlement ratios are increased quite uniformly in the period range 0.75÷1.35 sec from 3.0 to 5.2 (i.e. up to 70%) when γ increases from 2.40 το 5.10. On the other hand, the settlement ratio increase with slenderness ratio is foremostly concentrated in the spectral region of resonant systems, with the maximum increase being 21% as h/r increases from 1.06 to 1.88.
- The seismic excitation characteristics affect system response mostly through the peak ground acceleration and – to a lesser degree – through the number of excitation cycles N_o. Regarding the former, settlement ratios appear to increase uniformly with peak ground acceleration, in the whole T_{sys}/T_{exc} spectrum, with the maximum increase being approximately 110% when PGA increases from 0.23g to 0.36g. The number of excitations cycles increases the settlement ratio over a narrower T_{sys}/T_{exc} range, i.e. around 0.80÷1.20 sec. The increase is up to 30% when N_o is raised from 4 to 12.
- Lastly, analytical relationships were developed based on the statistical analysis of the available numerical results. These relationships aim to serve as correction factors for the prediction of seismic settlements of SFS systems based on existing procedures for FS systems (e.g. Richards et al. 1993). The proposed relationships include the key-role SSI parameters (slenderness and relative mass ratio), as well as the excitation parameters (peak ground acceleration, number of excitation cycles). The evaluation of the proposed methodology showed sufficient accuracy with the aggregate standard deviation of the relative errors being equal to 0.18.

Chapter 7

Design Methodology

7.1 General

The previous chapters focused on the effect of SSI on the accumulation of seismic settlements of footings on sand, either under *non-liquefiable* or under *liquefied* conditions. As a result, correction factors are proposed which should be multiplied with settlement estimates for footings without any interaction-induced shear and moment loading in order to give the anticipated settlements for the complete structure and foundation system. It is thus realized that, from a design point of view, the final settlement computation requires analytical estimates of the reference settlement values, i.e., for footings under a uniform vertical pressure representing the dead load of the structure.

In view of the above, the present Chapter will initially present published analytical methodologies for seismic settlement computation, under *non-liquefiable* and *liquefied* soil conditions, without any SSI effects. As it is discussed in the following, these methods have been mainly developed for the simper 2D case of strip footings, and not for the rectangular footings examined herein. For this reason, they will be evaluated and, when necessary, modified in order to fit the results of the reference numerical analyses of this study for rectangular footings without SSI effects.

In the sequel, it will be demonstrated how the proposed correction factors may be applied in design practice. The general case will be examined where the foundation lays on a liquefiable sand deposit with an improved non-liquefiable crust, where liquefaction is triggered some time after the initiation of shaking. In this case, it may be assumed that "*non-liquefied"* soil conditions prevail until the onset of initial liquefaction (i.e until r_u = 0.60-0.70) and *liquefied* soil conditions prevail thereafter, until the end of shaking. The duration of *non-liquefiable* and *liquefied* soil conditions is controlled by the value of the Factor of Safety against liquefaction FS_L, with the

special cases of purely *non-liquefiable* or purely *liquefiable* conditions corresponding approximately to $FS_L > 1.0$ and $FS_L < 0.30$ respectively. A method relating the time of liquefaction onset to FS_L, for actual soil and seismic excitation conditions, will be also presented and evaluated.

7.2 Equivalent harmonic excitation

In engineering practice, the irregularity of seismic ground motions is typically overcome by the identification of the most important ground motion characteristics, namely the: i) amplitude, ii) frequency content and iii) duration of the actual seismic event. Various methods have been proposed in literature for this purpose. Regarding the amplitude of the ground motion, an effective acceleration is proposed which is related to the "… structural response and to the damage potential of an earthquake" (Newmark and Hall 1982). This reduction of the acceleration magnitude accounts for the fact that the actual peak ground acceleration recorded during the event is usually related to high frequency pulses and, as a result, it does not induce response from the structures that typically have much lower eigen-frequencies. (Tokimatsu and Yoshimi 1983) relate the effective acceleration with peak ground acceleration a_{max} and the earthquake magnitude M_w, as follows:

$$a_{eff} = \frac{M_w - 1}{10} a_{max} \tag{7.1}$$

Regarding the frequency content of the ground motion, a variety of parameters has been proposed in literature in order to better characterize the distribution of spectral frequencies. The most commonly used frequency idealization is to adopt the predominant excitation period T_p which corresponds to the peak amplitude of the elastic response spectrum or the Fourier amplitude spectrum of the actual seismic ground motion. More sophisticated spectral parameters use various methods in order to consider the distribution of spectral amplitudes (Rathje et al. 1998b).

The duration of the ground motion constitutes a crucial parameter in earthquake engineering, since it is directly related to some important soil response features, such as stiffness and strength degradation, plastic strain accumulation, as well as pore water pressure increase and liquefaction. Most frequently, the duration of an irregular seismic acceleration history is approximated by the an equivalent number of significant cycles N_{eq} and the corresponding total duration of the seismic event T_d, expressed as:

$$T_d = N_{eq} \cdot T_{exc} \quad 7.2$$

where T_{exc} is the period of the equivalent harmonic excitation. Based on the requirement that the harmonic wave has the same amount of kinetic energy with the actual ground motion, the equivalent number of cycles N_{eq} can be computed by solving the following equation:

$$a_{eff} \cdot N_{eq} \cdot {T_{exc}}^2 = \pi^2 \int_0^{Td} |v(t)| dt \quad 7.3$$

where *v(t)* denotes the time-history of the seismic velocity.

7.3 Time of liquefaction onset

7.3.1 Available methodologies

The proposed methodology for the calculation of building settlements on liquefiable soil is necessarily based on previous studies which enable the separation seismic motions in two parts, i.e. *prior* to ($t \leq t_{L,gr}$) and *after* ($t > t_{L,gr}$) liquefaction (Bouckovalas et al. 2017; Kramer et al. 2016; Özener et al. 2020; Youd and Carter 2005). The key for this separation lies in the fact that soil softening due to liquefaction is severe enough to induce a distinct phase of shaking which is characterized by significantly altered soil properties (V_s, T_{soil}) compared to the initial, *pre*-liquefaction, properties. Moreover, the transition from the initial fundamental site period $T_{soil,0}$ to the liquefied one $T_{soil,L}$ is quite abrupt. Namely, T_{soil} is only slightly affected for pore pressure ratios r_u less than about 0.80, but it increases rapidly as pore pressure ratios approach the value of 1.0 (Kramer et al. 2016). This is shown in **Figure 7.1,** which presents the variation of the fundamental site period elongation $T_{soil}/T_{soil.0}$ with the excess pore pressure ratio r_u.

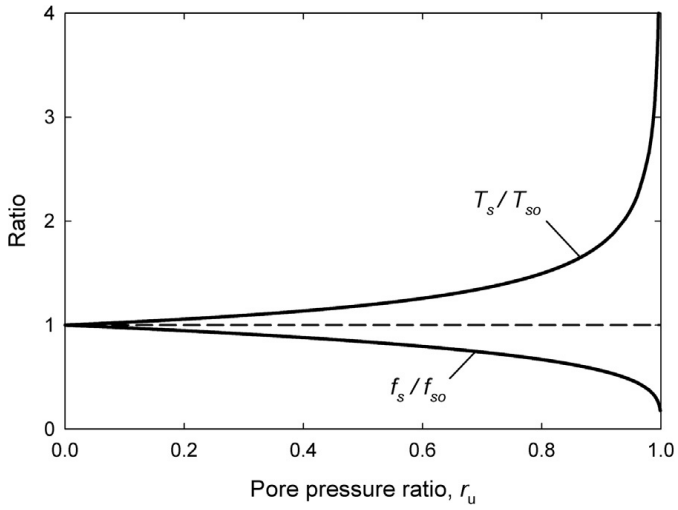

Figure 7.1: Liquefaction-induced site period elongation ratio $T_s/T_{s,o}$ (or frequency shortening ratio $f_s/f_{s,o}$) versus excess pore pressure ratio r_u (Kramer et al. 2016).

Various approaches are proposed in literature for the estimation of the liquefaction onset time t_L. (Kramer et al. 2016) proposed the identification of site period evolution in recorded ground motions in order to relate the onset of liquefaction with the elongation of site period due to soil softening. For this purpose, the authors developed a Stockwell spectrum-based procedure which captures the changing frequency content of ground motion by decomposing a signal into time-windows consisting of wavelets with a particular frequency range. **Figure 7.2** presents the ground acceleration time-history and the normalized (by the peak Stockwell amplitude at each time-window) Stockwell spectrum of the Kawagishi-cho record from Niigita earthquake (1964). Results show that after 8-10 sec of seismic motion the frequency content of the signal shifts from high-frequency to low-frequency components. For the last 30 seconds of motion the Stockwell spectrum maintains a stationary frequency value of approximately 0.2 Hz, thus, indicating liquefaction.

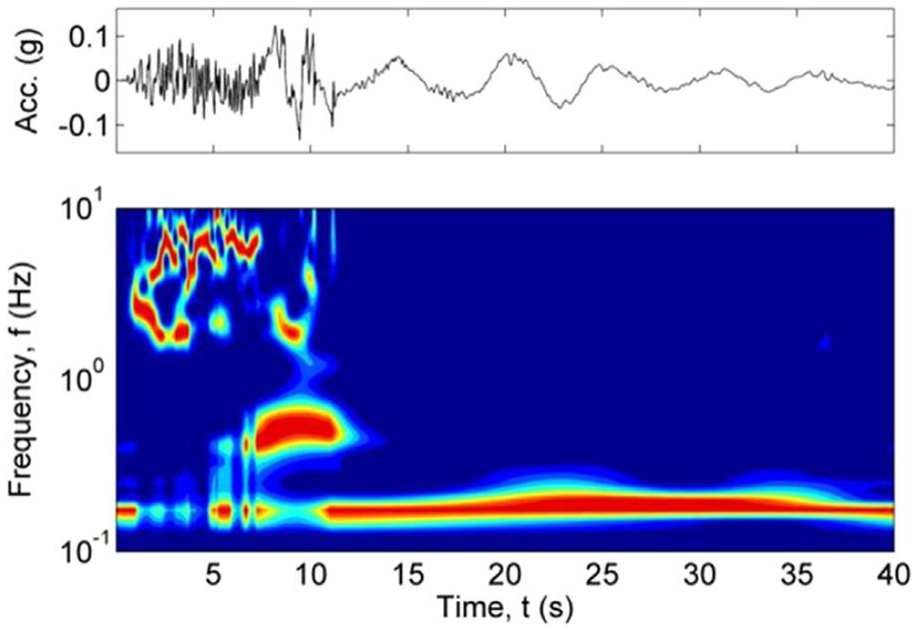

Figure 7.2: (a) Ground acceleration time-history and (b) normalized Stockwell spectrum of the Kawagishi-cho record from the Niigita earthquake (1964) (Kramer et al. 2016).

(Bouckovalas et al. 2017), on the other hand, estimated the liquefaction onset time t_L by visual comparison between acceleration recordings at the ground surface and at different depths in the subsoil. This procedure draws upon the fact that the presence of one or more liquefied layers in the subsoil may act as a natural seismic isolation that prevents the propagation of shear waves to the free ground surface (Bouckovalas et al. 2016b). To demonstrate this, **Figure 7.3** presents the effect of liquefaction onset on the surface motion and the corresponding elastic response spectrum recorded at the Wild Life Array (WLA) site during the Superstition Hills earthquake (1987). It is observed that the liquefaction onset, signified by the elimination of high frequencies in the acceleration recording of **Figure 7.3a**, corresponds to excess pore pressure build up ratios $r_u \approx 0.4$-0.5 in **Figure 7.3b**. In addition, the elastic response spectrum of **Figure 7.3c** shows that liquefaction-induced soil softening results in the amplification of long-period (i.e. $T > 1.2$ sec) amplitudes, and de-amplification of short-period (i.e. $T > 1.2$ sec) amplitudes.

Based on parametric numerical analyses for varying relative density and thickness (H_L) of the liquefiable layer, the onset time of liquefaction at the ground surface $t_{L.gr}$ was correlated with: i) the average onset time of liquefaction over the entire liquefiable soil depth $t_{L,av}$ (**Figure 7.4a**), and ii) the minimum with depth liquefaction time $t_{L,min}$ for all liquefiable soil layers (**Figure 7.4b**). Results show that the correlation between $t_{L.gr}$ and the minimum liquefaction time $t_{L,min}$ has

significantly reduced scatter, in contrast to the large scatter of the correlation with $t_{L,av}$. Hence, the following best-fit relationship was proposed for the estimation of $t_{L,gr}$ (**Figure 7.4b)**:

$$t_{L,gr} = 0.84 \cdot t_{L,min} \qquad 7.4$$

These findings indicate that for the initiation of liquefaction effects on the ground surface, it is sufficient that the most weak layer in the subsoil liquefies. The fact that $t_{L,gr}$ is somewhat less than $t_{L,min}$ implies that liquefaction effects are first evidenced at the ground surface a little before excess pore pressure ratios reach the critical value of r_u = 1.0.

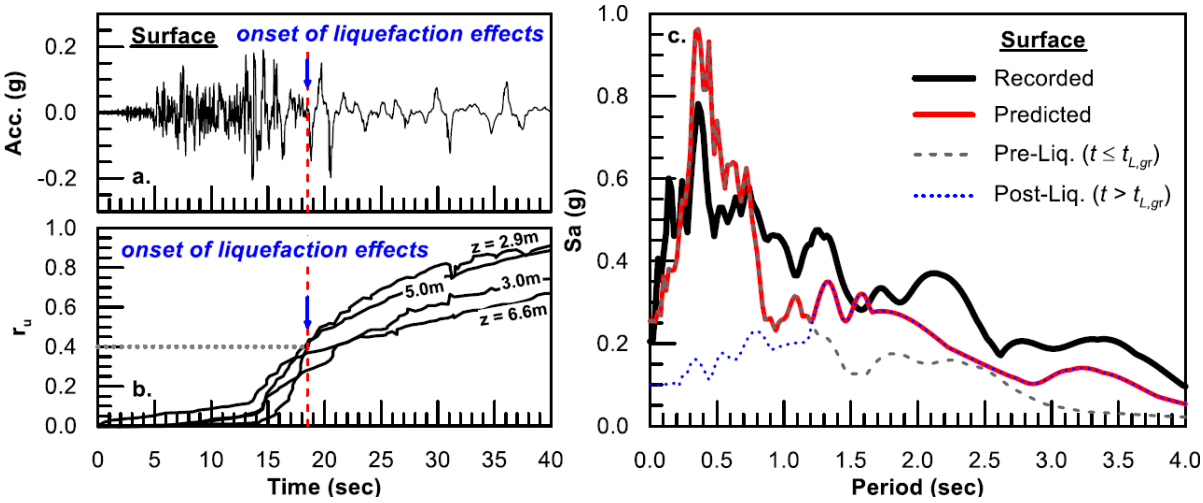

Figure 7.3: (a) Acceleration time-history at the ground surface, (b) excess pore pressure ratios within the liquefiable soil layers and (c) elastic response spectra of the total ground motion as well as of the pre- and post-liquefaction time-windows (Tsiapas 2017b).

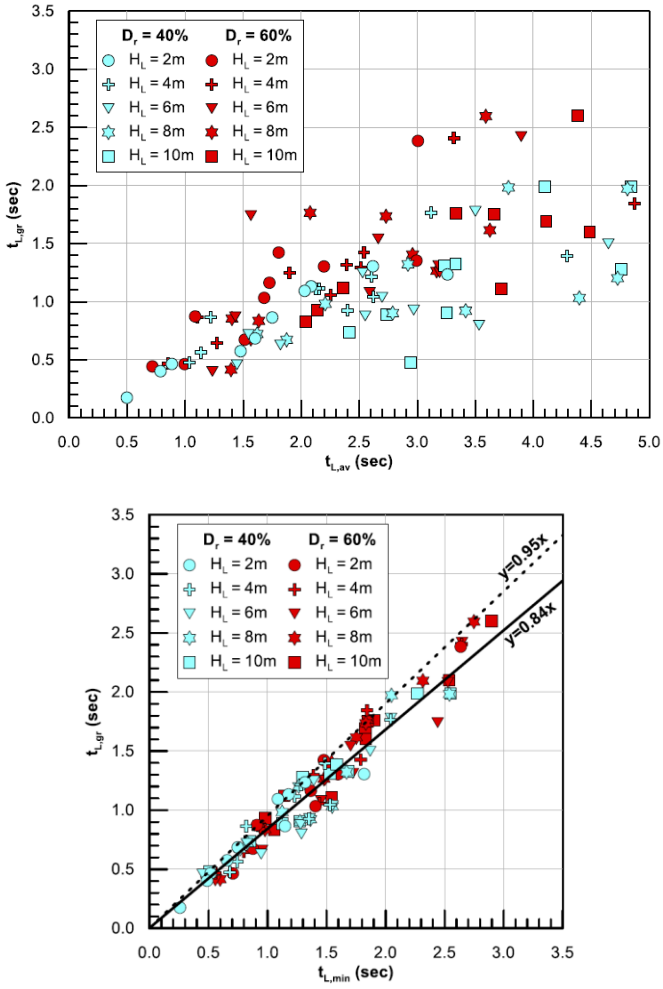

Figure 7.4: One-to-one comparison between onset of surface liquefaction $t_{L,av}$ versus (a) average over depth onset time $t_{L,av}$ and (b) minimum onset time $t_{L,min}$ (Tsiapas 2017b).

7.3.2 Application in practice

The aforementioned procedures estimate the liquefaction onset time t_L based on numerical analyses of the seismic ground response. Therefore, it is possible, in the particular studies, to estimate directly the initiation of liquefaction phenomena on any given soil sublayer by monitoring the excess pore pressure ratio r_u or the fundamental soil period T_{soil}. However, in practical applications, the liquefaction potential of different sites is not evaluated from numerical soil response analyses but from the empirically computed Factor of Safety against liquefaction FS_L. Therefore, Bouckovalas et al. (2017) proposed to correlate the liquefaction onset time t_L with FS_L. To that end, the liquefaction onset time for a uniform soil layer subjected to a harmonic

excitation with period T_{exc} may be computed as the number of loading cycles to liquefaction N_L (i.e. until r_u = 1.0) times the harmonic excitation period (T_{exc}):

$$t_L = N_L \cdot T_{exc} \tag{7.5}$$

Laboratory and model experiments have shown that the resistance of sands to liquefaction, expressed in terms of the Cyclic Stress Ratio (*CSR*)

$$CSR = \frac{\tau_{cyc}}{\sigma'_{vc}} \tag{7.6}$$

is principally dependent on the number of loading cycles *N*, the relative density and the confining stress. For instance, **Figure 7.5** shows results from shaking table tests on liquefiable sand (De Alba et al. 1976) which demonstrate the effect of the number of cycles and relative density for initial overburden stress of 100kPa. In general, such experimentally determined liquefaction resistance curves may be analytically described as:

$$CSR = a \cdot K_\sigma \cdot {N_L}^{-b} \tag{7.7}$$

with coefficients *a* and *b* being functions of the soil type and loading conditions and $K_\sigma = 1 - 0.26ln(\sigma'_{v0}/p_a)$.

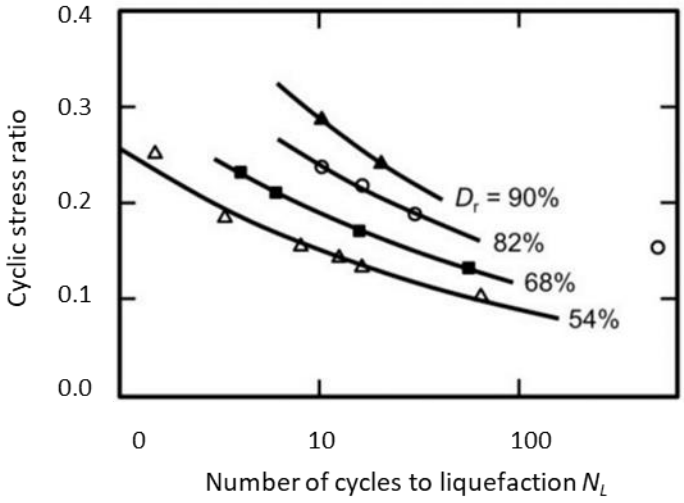

Figure 7.5: Variation of cyclic stress ratio with the number of cycles required for liquefaction triggering, obtained from simple shear tests (De Alba et al. 1976).

In essence, Equation 7.7 can be used inversely to estimate the number of loading cycles N_L required to cause liquefaction under harmonic cyclic loading with a given *CSR*. Alternatively, given the number of loading cycles N_{eq}, Equation 7.7 provides the threshold *CSR* values required for liquefaction, denoted as Cyclic Resistance stress Ratio *CRR*. Hence, Equation 7.7 can be transformed to:

$$CRR = a \cdot {N_{eq}}^{-b} \tag{7.8}$$

Combination of Equations 7.7 – 7.8 results to the following definition of the Factor of Safety against liquefaction:

$$FS_L = \frac{CRR}{CSR} = \left(\frac{N_L}{N_{eq}}\right)^b \tag{7.9}$$

Hence, in practical applications the estimation of the liquefaction onset time t_L is possible by calculating N_L from Equation 7.7, for the given soil profile and seismic excitation properties. For practical applications, FS_L is obtained empirically in terms of the N_{SPT} values. On the other hand, based on Equation 7.3, N_{eq} may be analytically computed as:

$$N_{eq} = \frac{\pi^2 \int_0^{Td} |v(t)| dt}{a_{eff} \cdot {T_{exc}}^2} \tag{7.10}$$

7.4 Analytical computation of seismic settlements for footings in non-liquefiable conditions

7.4.1 Overview

Seismic settlements of footings on granular soils are principally attributed to the shear strength degradation of the foundation soil during shaking, as well as, to the lateral inertial forces that act upon the structure and the foundation soil. The bearing capacity reduction has been widely examined in literature, typically with upper limit analyses that use a Coulomb-type mechanism (Budhu and Al-Karni 1993; Knappett et al. 2006; Paolucci and Pecker 1997; Soubra 1999). More recent studies have additionally introduced the effect of structural inertial forces, by means of moments acting upon the foundation (Knappett et al. 2006). Nevertheless, the estimation of the

associated seismic settlements has not received equal attention. In fact, the only available analytical method is that of Richards et al. (1993), which draws upon the "sliding-block" approach used for the calculation of lateral displacements of retaining walls and slopes. According to that method, the footing is replaced by a uniform overburden pressure *q*, thus, neglecting any effects of the superstructure inertia in terms of shear forces or overturning moments.

In the following, the aforementioned analytical methodology is briefly presented and then used for the calculation of footing settlements for FS systems. The accuracy of the analytical predictions is evaluated against the results of the relevant numerical analyses presented in Chapter 6. It is worth noting that the analytical methodology of Richards et al. (1993) has been developed as an upper bound prediction method for strip foundations. Hence, before comparing with the results of numerical analyses, the simplest possible modifications were introduced in an attempt to account for the rectangular shape of the foundations examined herein.

7.4.2 The methodology of Richards et al (1993)

According to this method, seismic settlements are correlated to the sliding of the Coulomb-type wedge which occurs below a footing in the case of bearing capacity failure. It is assumed that there is a critical acceleration level, referenced as *critical acceleration* α_{cr}, above which the active-passive wedge sliding initiates. Footing settlements follow the lateral sliding of the active wedge with angle ρ_{AE} (see **Figure 7.6**) and the subsequent movement of the passive wedge to the side. The sliding of the wedge continues as long as the relative velocity of the wedge remains greater than zero. Thus, the cumulative wedge sliding can be computed as the integration of the positive relative velocity during every shaking cycle. To this end, various studies provide solutions for the computation of wedge sliding along the failure surface using this "sliding-block" approach. In the case of footings, the sliding wedge displacement that is responsible for the seismic settlement is shown in **Figure 7.6** as the movement from point d to point f. The most common relationships for the computation of the sliding wedge displacement are the following:

$$\Delta = 0.50 \frac{V_{max}^2}{a_{max} \cdot g} \left| \frac{a_{cr}}{a_{max}} \right|^{-2} \quad \text{(Newmark 1965a)} \quad 7.11$$

$$\Delta = 0.087 \frac{V_{max}^2}{a_{max} \cdot g} \left| \frac{a_{cr}}{a_{max}} \right|^{-4} \quad \text{(Richards et al. 1993b)} \quad 7.12$$

where Δ = the sliding wedge displacement, V_{max} and α_{max} are the peak velocity and acceleration coefficients of the seismic motion and α_{cr} is the critical acceleration coefficient.

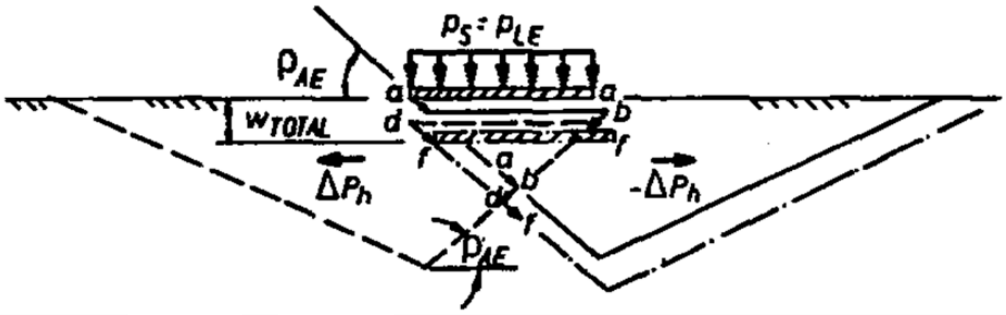

Figure 7.6: Seismic settlement mechanism according to the "sliding-block" approach (Richards et al. 1993a).

In the case of retaining walls and slopes, the critical acceleration α_{cr} is obtained by setting the pseudo-static Factor of Safety against sliding equal to one, as at the initiation of sliding. In the present problem of footing settlements, Richards et al. (1993) correlate the critical acceleration with the Static Factor of Safety FS_s. This correlation is shown in **Figure 7.7**, for different levels of the soil friction angle ϕ and the embedment depth ratio d/B of the footing, where d is the embedment depth and B is the width of the footing.

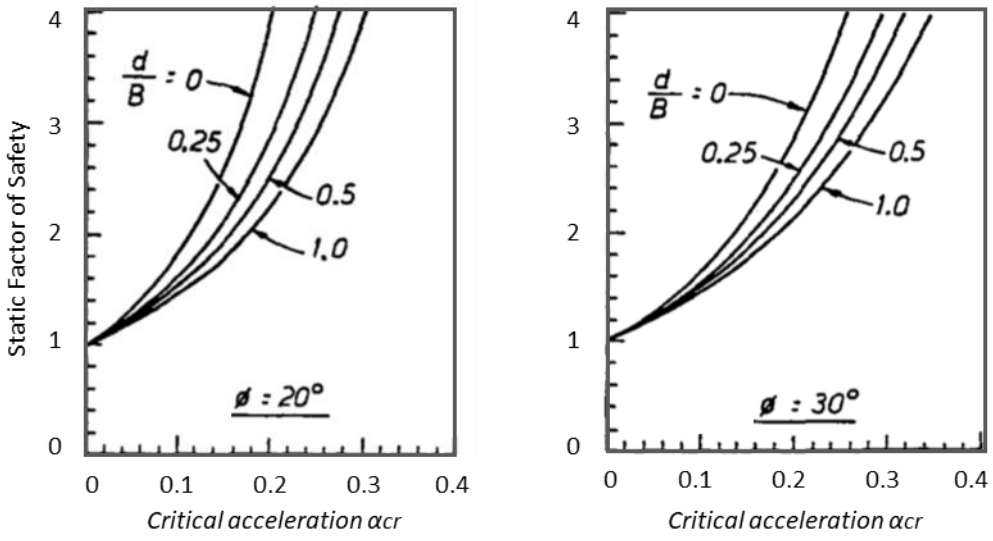

Figure 7.7: Design charts that correlate the critical acceleration α_{cr} with the static Factor of Safety FS_s for different values of the soil friction angle ϕ and the embedment depth ratio d/B (Richards et al. 1993b).

For practical applications regarding surface foundations (i.e. with D/B=0), the correlations of **Figure 7.7** were fitted with the following analytical expressions:

$$a_{cr} = a \cdot (FS_s - 1)^b \quad (7.13a)$$

with

$$a = 0.083 + 0.0016 \cdot \varphi \text{ (deg)} \quad (7.13b)$$

$$b = \begin{cases} 0.75 - 0.0047 \cdot \varphi \text{ (deg)} & for\ \varphi \leq 30° \\ 0.61 & for\ \varphi \geq 30° \end{cases} \quad (7.13c)$$

The actual footing settlement is, then, calculated as a function of the sliding wedge displacement *Δ* and the active wedge angle ρ_{AE}, as follows:

$$\rho_{dyn} = 2\Delta \cdot tan\rho_{AE} \quad (7.14)$$

Figure 7.8 Error! Reference source not found. presents the variation of the active wedge angle ρ_{AE} with the critical acceleration a_{cr} for different levels of soil friction angle ϕ according to (Richards et al. 1993). It is thus shown show that decreasing values of the friction angle ϕ or increasing values of the critical acceleration a_{cr} result in a shallower formation of the wedge mechanism. To simplify computations, the graphs in Figure7.8 were fitted with the following analytical relationships:

$$tan\rho_{AE} = c + d \cdot a_{cr} \quad (7.15a)$$

with

$$c = 3.75 - 0.028 \cdot \varphi \text{ (deg)} \quad (7.15b)$$

$$d = 0.39 + 0.035 \cdot \varphi \text{ (deg)} \quad (7.15c)$$

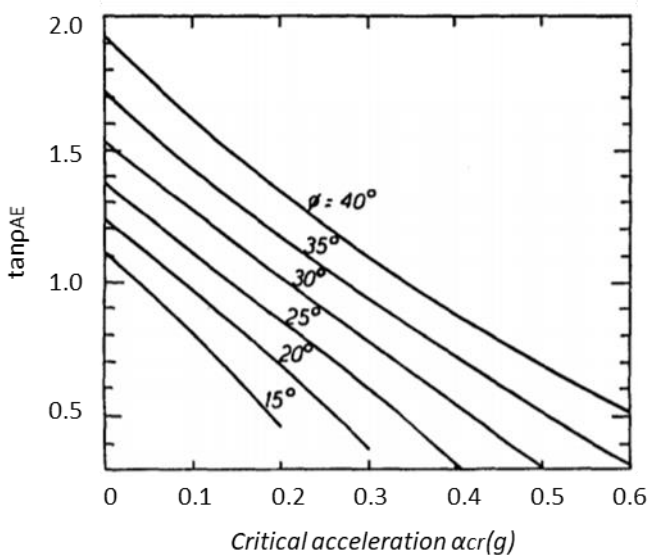

Figure 7.8: Variation of the active wedge angle with the critical acceleration a_{cr} for different values of the soil friction angle ϕ (Richards et al. 1993b).

7.4.3 Comparison with numerical predictions

The accuracy of Richards et al. (1993) analytical methodology, described above, is evaluated through comparison with the numerical predictions of seismic settlements for foundation-soil (FS) systems presented in Chapter 6 (i.e. numerical analyses No 55-65, 77-87 in Table 6.1). The examined numerical analyses have different ground motion characteristics (a_{max}, V_{max}), contact pressures (i.e. q = 80kPa and 100kPa), and corresponding static Factors of Safety (i.e. *FS* = 3.00 and 3.75).

Concerning the analytical computation of seismic settlements, the properties of the numerical configuration (a_{max}, V_{max}, q_o, φ) are used as input data for the calculations. The steps of the analytical procedure can be summarized as follows:

i. The static bearing capacity of the footing q_{ult} is calculated using the typical solutions of Limit Analysis (Terzaghi 1943, Meyerhof 1963, Vesic 1973). Namely, in the examined case of granular soils with zero surcharge, q_{ult} is computed as:

$$q_{ult} = \frac{1}{2}\gamma B N_\gamma s_\gamma \qquad 7.16$$

where

γ is the soil unit weight

B is the footing width

s_γ is the footing shape coefficient (=1-0.2B/L)

N_γ is the dimensionless bearing capacity factor according to Meyerhof:

$$N_\gamma = \left(N_q - 1\right)\tan(1.4\varphi) = [e^{\pi \cdot tan\varphi} tan^2(45 + \varphi/2) - 1]\tan(1.4\varphi) \quad 7.17$$

The corresponding static Factor of Safety is calculated as $FS_s = q_{ult} / q$.

ii. The critical acceleration a_{cr} -required to trigger wedge sliding- is obtained for the given Static Factor of Safety FS_s and the soil friction angle ϕ, using either the design charts of **Figure 7.7** or **Equation 7.15.**

iii. The displacement of the sliding wedge *Δ* is calculated using Newmark (1965) and Richards and Elms (1979) analytical relationships, which provide solutions for the seismic settlement estimation of retaining walls. The particular solutions are described by **Equations 7.11** and **7.12**.

iv. The inclination of the failure surface ρ_{AE} is estimated with the use of **Figure 7.8** or **Equation 7.15**.

v. Finally, **Equation 5.10** is used to calculate the footing settlement *ρ*, given the displacement *Δ* of the sliding wedge and the wedge inclination ρ_{AE}.

Table 7.1 and **Figure 7.9** compare numerical and analytical predictions of footing seismic settlements. The examined systems have embedment ratio d/B equal to zero while the friction angle was set to ϕ ≈ 32°, based on triaxial element test simulations with the NTUA constitutive model, for fine Nevada sand with relative density D_r = 45% (Dimitriadi 2014). The ground motion characteristics (a_{max}, V_{max}) used for the analytical calculations are predicted numerically for the free ground surface. It is noted that the harmonic base motions used in the numerical analyses are characterized by a constant amplitude, i.e. a^b_{max}=0.15g, and a varying excitation period T_{exc}. As a result, the peak ground acceleration, denoted here as a_{max}, is obtained from the numerical analyses, while the peak ground velocity, denoted here as V_{max}, is computed as $V_{max} = a_{max} \cdot T_{exc}/2\pi$. Additionally, it should be noted that, in order to focus on the accuracy of the analytical prediction method per se, the bearing capacity of the footing q_{ult} was that computed numerically and not analytically Equation 7.13.

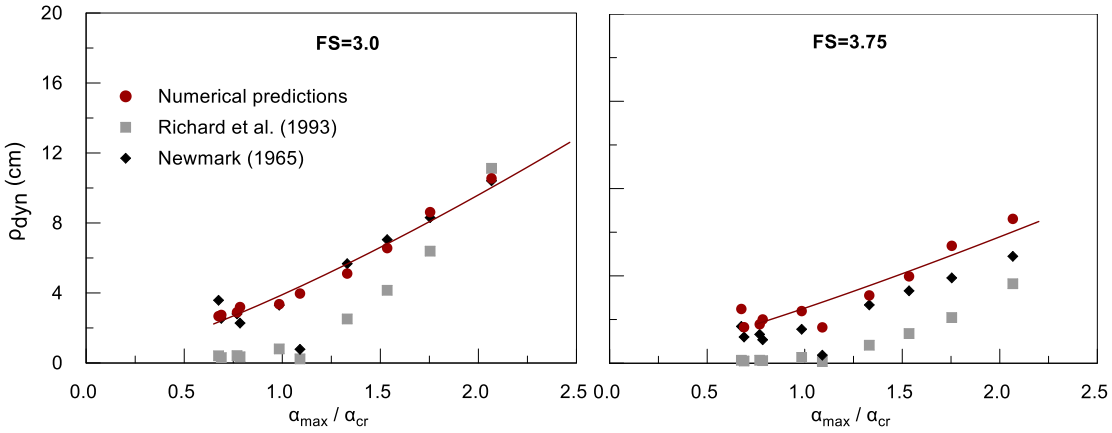

Figure 7.9: Variation of the footing seismic settlements ρ_{dyn} with the peak ground acceleration using analytical [Richards et. al. (1993), Newmark (1965)] and numerical predictions, for Static Factor of Safety FS_s = 3.00 and 3.75.

It is observed that the analytical and the numerical predictions are in good agreement when (Newmark 1965) relation (Eq. 7.1) is used for the computation of the wedge sliding displacement *Δ*. In the case of FS_s = 3.00 (**Figure 7.9a**), the standard deviation of relative error is 0.32 and the corresponding average is -0.03 indicating that the prediction bias is insignificant. In the case of FS_s = 3.75 (**Figure 7.9b**), the standard deviation of relative error is even smaller, i.e. equal to 0.22, but there is a systematic under-prediction (negative bias) as the average value of relative error is 0.26. Regarding the analytical predictions obtained with the (Richards and Elms 1979) methodology (i.e. Eq. 7.2), the comparison shows a systematic and quite significant under-prediction. The only exception occurs for high critical acceleration ratios a_{max}/a_{cr} *>2.0* and FS_s = 3.00*,* where the analytical predictions are much larger than the numerical.

Table 7.1: Input data and seismic settlement predictions of the analytical $\rho_{analytical}$ and numerical $\rho_{numerical}$ procedures. (Analyses No 55-66, 78-88, see Table 5.1)

Input Data				***Analytical calculations***				***Comparison with Numerical results***		
a_{max} [m/s^2]	V_{max} [m/s^2]	q_0	*FS*	a_{cr} *(g)*	$tan\rho_{AE}$	$\rho_{analytical}$ [cm] (Richards et al. 1993b)	$\rho_{analytical}$ [cm] (Newmark 1965a)	$\rho_{num.}$ [cm]	*Relative Error (%)* (Richards et al. 1993)	*Relative Error (%)* (Newmark 1965)
6.0	0.33					22.9	15.8	14.4	-58.8	-9.1
5.1	0.32					13.2	12.6	11.7	-12.5	-7.3
4.5	0.32					8.6	10.7	8.9	3.4	-20.4
3.9	0.31					5.2	8.6	6.8	23.8	-26.2
3.2	0.13	100	3.00	0.21	1.01	0.5	1.2	4.6	89.5	74.1
2.9	0.27					1.7	5.0	4.9	66.0	-3.0
2.3	0.25					0.7	3.4	4.2	82.8	17.8
2.2	0.28					0.9	4.2	3.9	78.0	-8.9
2.0	0.29					0.6	3.9	3.7	83.3	-3.1
								st.dev. :	51.3	32.2
								average:	43.3	-3.1
6.0	0.33					9.2	9.3	12.2	24.3	23.4
5.1	0.32					5.3	7.4	9.8	46.1	24.3
4.5	0.32					3.4	6.3	7.3	52.7	13.2
3.9	0.31					2.1	5.1	5.6	62.7	9.0
3.2	0.13	80	3.75	0.26	0.88	0.2	0.7	3.5	94.6	80.3
2.9	0.27					0.7	3.0	4.0	83.4	25.7
2.3	0.25					0.3	2.0	3.5	91.7	41.8
2.2	0.28					0.3	2.5	3.2	89.4	22.2
2.0	0.29					0.3	2.3	3.1	91.8	25.4
2.0	0.34					0.3	3.2	3.1	89.1	-3.4
								st.dev. :	25.1	22.2
								average:	73.2	26.1

(1) Relative Error=(ρ_{num}-$\rho_{analytical}$)/ρ_{num}

Finally, **Figure 7.10** shows a one-to-one comparison between the numerical and analytical predictions using the Newmark's (1965) and Richards and Elms' (1979) analytical relationships for the computation of *Δ*. No distinction is made for data points with different static Factors of Safety. In this way, it appears that the analytical predictions with Newmarks's analytical relations are within ±25% of the corresponding numerical predictions, while those obtained with the Richards and Elms' analytical relations are significantly lower.

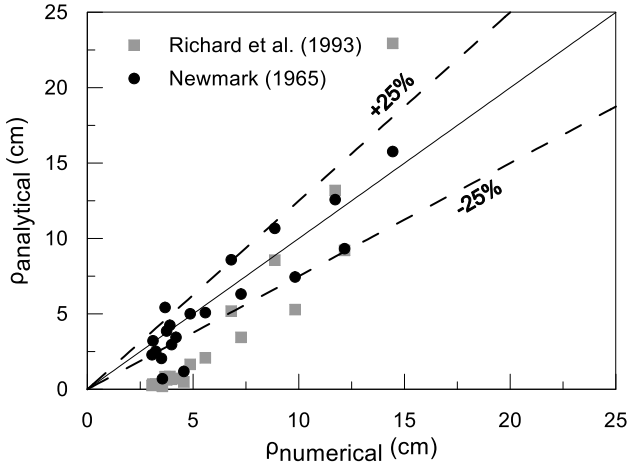

Figure 7.10: Evaluation of the analytical predictions for footing seismic settlements $\rho_{analytical}$ with regard to the numerically obtained value $\rho_{numerical}$ on a one-to-one basis.

Concluding, it appears that the Richards et al. (1993) analytical methodology, modified in order to take into account the effect of foundation shape (square instead of strip) on the static Factor of Safety, matches the numerical predictions of seismic settlement on the condition that sliding wedge displacements Δ are computed with Newmark's (1965) theory. Nevertheless, it should be noted that Newmark's theory is well known to over-predict sliding block displacements Δ for seismic acceleration ratios *a*max*/a*cr less than about 2.5, as is the case with all numerical analyses compared in Figures 7.9 and 7.10. Thus, the good agreement witnessed in Figures 7.9 and 7.10 is rather accidental, as it is the result of two counter-acting approximations: over-prediction of Δ with Newmark's *analytical relationship* and under-prediction of $tan\rho_{AE}$ with the Richards et al. (1993) methodology and the static Factor of Safety for square (instead of strip) foundations. Hence, the analytical methodology presented and evaluated in the previous paragraphs has not general use, but should only be employed for the range of soil and foundation parameters adopted in the examined numerical analyses, most importantly for *a*max*/a*cr = 1.0-2.5.

7.5 Analytical computation of seismic settlements for footings in liquefiable soil

7.5.1 General

The conventional design of structures on soils susceptible to liquefaction involves the construction of piles, in order to transfer loads into deeper non-liquefiable layers, in combination with ground improvement. The contemporary approach of designing structures with only shallow foundations – instead of piles – has been investigated, in the last two decades, with a number of experimental and theoretical studies (Adalier et al. 2003; Dashti et al. 2010; Dimitriadi et al. 2017; Liu and Dobry 1997; Naesgaard et al. 1998; Sitar and Hausler 2012). Settlement accumulation of footings is primarily attributed to shear-induced deformation of the foundation soil, while secondary effects are attributed to post-liquefaction sedimentation and consolidation, as well as volumetric strains due to drainage and the outflow of soil-ejecta to the surface.

The critical parameters controlling footing settlements have been thoroughly investigated, with emphasis on the geotechnical aspects of the problem, such as the liquefied layer thickness and relative density, the footing width, the applied pressure, etc. Most recently, analytical relationships have been also proposed to predict the shear-induced building settlements during shaking (Bray and Macedo 2017; Bullock et al. 2019; Dimitriadi et al. 2017). The proposed relationships are based on regression analysis of the numerical predictions of settlements for a number of different geotechnical, earthquake and building characteristics. Among them, the present section employs the aforementioned methodology of Dimitriadi et al. (2017) which proposes a clearly defined step-by-step computation sequence for shallow foundations on liquefiable ground. The range of the examined design parameters (improved crust, underlying natural soil of Nevada sand etc.), as well as the numerical modelling characteristics (constitutive model, soil damping, boundary conditions etc.) are compatible with the corresponding features of the present study. Following a brief methodology outline, this section evaluates the accuracy of the corresponding analytical predictions against the results of the relevant numerical analyses of this Thesis, presented in detail in Chapter 5.

7.5.2 Methodology outline

Dimitriadi et al. (2017) developed an analytical methodology for the performance-based design of shallow strip foundations on liquefiable ground. The particular design procedure ensures the safety of the foundation by improvement of a superficial soil zone which involves: i) increase of the relative density with vibrocompaction, and ii) enabling the quick dissipation of excess pore water pressures with the

installation of gravel drains. More specifically, the proposed methodology for the performance-based design of foundations on liquefiable soil includes in the following stages:

- The replacement ratio α_s is selected for the non-liquefiable crust, based on i) the initial relative density of the improved soil $D_{r.o}$, ii) the thickness of the improved zone H_{imp} and iii) the maximum excess pore pressure ratio $r_{u,max}$ permitted to develop within this zone, i.e. $r_{u,max} \approx$ 0.3-0.5.
- The determination of the – increased – relative density $D_{r.imp}$ and permeability k_{eq} of the improved zone based on the previously selected replacement ratio α_s. Thus, it is possible for the numerical model to simulate the improved zone using as input parameters the aforementioned $D_{r.imp}$ and k_{eq}.
- Given the specified equivalent properties and thickness of the improved soil crust, the seismic settlements of footings (FS systems) for the described two-layered soil formation are computed analytically. The particular methodology relates seismic settlements ρ_{dyn} and the degraded post-shaking bearing capacity $q_{ult,deg}$ to a number of basic problem parameters, namely:
  i. The excitation characteristics, i.e. the peak bedrock acceleration a_{max} (g), the number of significant cycles N_o and the excitation period T_{exc}.
  ii. The footing characteristics, i.e. the contact pressure q and the footing width B.
  iii. The elastic fundamental natural period of the soil deposit T_{soil}.

In the case of laterally infinite soil improvement, in terms of the horizontal area around the foundation, ρ_{dyn} is computed from the following relations:

$$\rho_{dyn} = c_1 (T_{exc} + aT_{soil})^2 (N_o + 2) \left(\frac{1}{FS_{deg}^{inf}} \right)^{c_2} \left[1 + c_3 \left(\frac{1}{FS_{deg}^{inf}} \right)^{c_4} \right] \quad 7.18$$

with c_1=0.019, c_2=0.45, c_3=0.25, c_4=4.5 and a=0.633. In the case of rectangular foundations, the authors proposed the recalibration of this expression based on the results of 3D numerical analyses of rectangular footings (Bouckovalas et al. 2017b). The proposed coefficients in this case are: $c_1 = 0.011 \cdot (1 + 0.067\, B/L) \leq 0.015, c_2 = 0.5, c_3 = 0.15, c_4 = 5$. The degraded Factor of Safety (i.e. FS_{deg} = $q_{ult.deg}/q$) in Equation 7.18 is an idealized evaluation of the footing's bearing capacity at the end of shaking, based on the Meyerhof and Hanna (1978) composite failure mechanism for footings on a two-layer (strong-over-weak) sand profile. According to this, the original relationships proposed by Meyerhof & Hanna for the computation of the bearing capacity are modified as follows for the degraded bearing capacity $q_{ult.deg}$:

$$q_{ult.deg} = min\left\{\begin{matrix} 1/2\gamma' BN\gamma_1 \\ \gamma' H_1^2 K_s \frac{tan\varphi_{1.deg}}{B} + \gamma'[(1+a)^2 - 1]H_1^2 K_s \frac{tan\varphi_{2.deg}}{B} + \\ + \frac{1}{2\gamma' BN_{\gamma 3}} + \gamma'(1+\alpha)H_1 N_{q3} \end{matrix}\right\} \quad 7.19$$

Coefficients N_q and N_γ are given as:

$$N_{q3} = tan^2(45 + \varphi_{3,deg}/2)e^{\pi tan\varphi_{3,deg}}$$
$$N_{\gamma 3} = 2(N_q + 1)tan\varphi_{3,deg} \quad 7.20$$

Coefficient *a* refers to the thickness of the partially liquefied layer which lies underneath the improved crust. It depends on the improved zone properties (k_{eq}, H_{imp}) as well as the excitation characteristics (T_{exc}, N_o). Following the statistical processing of the numerical predictions the coefficient C_a is set to 3.76 and the expression of coefficient *a* is:

$$a = C_a\left[\frac{k_{eq}T_{exc}N_o}{H_{imp}}\right]^{0.256} \quad 7.21$$

The initial friction angle φ_{ini} depends on both soil properties and loading conditions. As a result, values of the friction angle vary spatially under the footing. The authors propose considering the average value between the one-element tests of Triaxial Compression, Triaxial Extension and Direct Simple Shear obtained numerically for Nevada Sand with the NTUA Sand model (Annex B of (Dimitriadi 2014):

$$\varphi_{i,ini} = \frac{\varphi_{i,TX-C} + \varphi_{i,TX-E} + \varphi_{i,DSS}}{3} \quad 7.22$$

Typical results of the above simulation tests, shown **Figure 7.11**, present the variation of the peak friction angle ϕ_{peak} as well as of the residual friction angle ϕ_{res} with the relative density D_r for three different sets of non-isotropic consolidation vertical stress σ'_{vo} (i.e. 10, 50 and 100kPa).

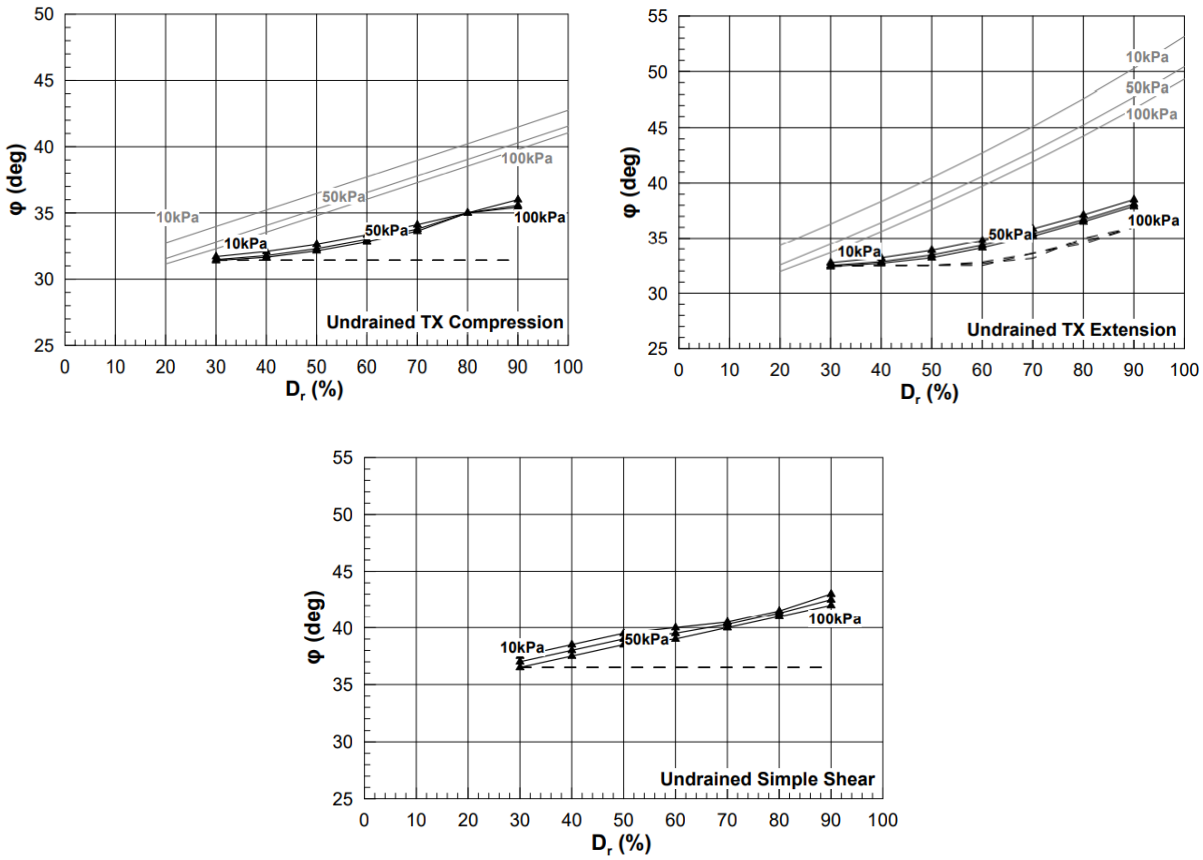

Figure 7.11: Undrained test simulations of the peak (solid lines) and residual (dashed lines) values of the friction angle as a function of the relative density D_r (%) for different sets of non-isotropic consolidation vertical stresses σ'_{vo}. Three types of tests were modeled: (a) triaxial compression, (b) triaxial extension and (c) simple shear.

The parameter U_1 refers to the average excess pore pressure ratios that develop in the improved zone at the end of shaking. It is expressed as a portion of the allowable excess pore pressure ratio U_{design} as follows:

$$U_1 = 0.54U_{design} \tag{7.23}$$

The parameter U_2 refers to the excess pore pressure ratios that develop in the transition zone between the improved zone and the underlying natural soil. It is expressed as the average value of the two, assuming complete liquefaction of the latter.

$$U_2 = \frac{1 + U_1}{2} = \frac{1 + 0.54U_{design}}{2} \tag{7.24}$$

The parameter U_3 refers to the excess pore pressure ratios that develop over a representative area under and around the footing. The estimated values of U_3 are expressed (for C_{U3}=0.86 and p_a=98.1kPa) as follows:

$$U_3 = C_{U_3}\left(\frac{q_{ult.deg}}{p_a}\right)^{-0.18} \leq 1.0 \quad 7.25$$

The degraded friction angle $\varphi_{i,deg}$ refers to the reduced friction angle of the foundation soil due to development of excess pore pressures during shaking. The subscript i denotes the values of friction angle in the improved zone (i=1), in the transition zone (i=2) and in the liquefied natural deposit (i=3).

$$\varphi_{i,deg} = tan^{-1}[(1 - U_i)tan\varphi_{i,ini}] \quad 7.26$$

The coefficient K_s represents the shear strength of the foundation subsoil, i.e. including the improved zone and the underlying natural soil. It is expressed as follows (with C_{Ks}=1.0):

$$K_S = C_{K_s}\left(\frac{q_{ult.deg}}{p_a}\right)^{-0.18} \quad 7.27$$

The correlation of normalized seismic settlements with the inverse of the degraded factor of safety is shown in **Figure 7.12**, for the numerical predictions as well as the described analytical procedure.

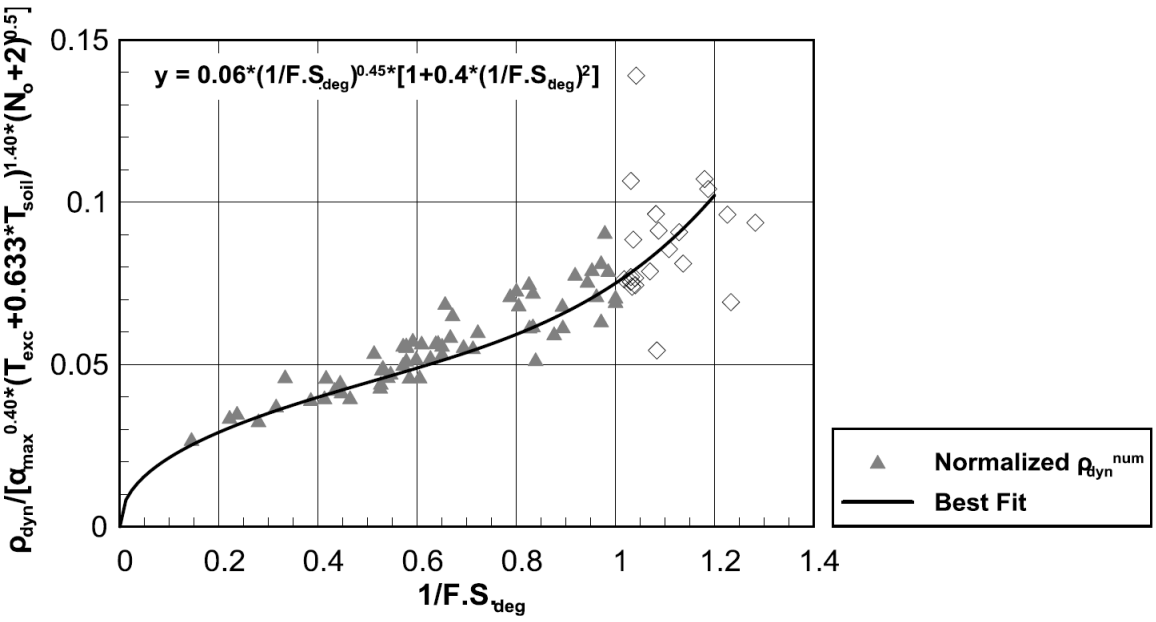

Figure 7.12: Variation of normalized seismic settlements ρ_{dyn} with the inverse of the degraded factor of safety $1/FS_{deg}$ (Dimitriadi et al. 2017b).

7.5.3 Comparison with numerical predictions

The described analytical methodology of Dimitriadi et al. (2017) and Bouckovalas et al. (2017b) is evaluated by comparing the predicted values with the corresponding values from numerical predictions

of this study, described in detail in Chapter 5 (Table 5.1). The accuracy of the analytically calculated seismic settlements ρ_{dyn} predictions is evaluated in **Figure 7.12**, via one-to-one comparison with the corresponding numerical predictions. It is observed that the bulk of the analytical predictions falls in the ±25% range of the numerical ones, while the analytical predictions seem to underpredict (negative bias) settlements in the low value range, i.e. ρ_{dyn} < 15cm. A statistical analysis of these data an aggregate value of standard deviation equal to 8.2%.

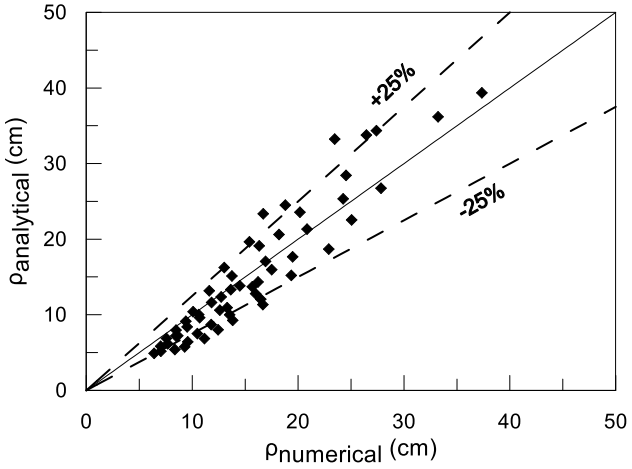

Figure 7.13: Evaluation of the analytical procedure by Dimitriadi et al. (2017) with regard to the numerically obtained seismic settlements ρ_{dyn}.

7.6 Design application

7.6.1 General

The present section demonstrates the design application of the developed methodology for the estimation of seismic settlements of SFS systems. For this purpose, numerical analyses are performed for SFS systems with SSI properties selected within the described framework of the previous chapters. In parallel with the numerical results, the design procedure developed in the present Thesis is implemented and evaluated as a step-by-step application. In more detail, the simulated soil profile is based on the properties of the actual soil profile located within the riverbed of Strymonas river in Nothern Greece consisting of a 23m deep liquefiable silty sand layer. The seismic excitation used as an input base motion is the Matahima Dam (083) recording of the New Zealand earthquake (1987). In order to correlate the liquefaction potential with seismic settlement accumulation, four scenarios of varying earthquake magnitude are considered, in terms of peak bedrock acceleration a^b_{max}. Variation of the earthquake magnitude results in different values of the Factor of Safety against liquefaction FS_L, which in turn leads to varying liquefaction onset time t_L. Having defined t_L, it is possible to distinguish, as a next step,

settlement accumulation into the part *prior* to liquefaction onset ($t < t_L$). which is compatible with "non-liquefiable" conditions, and the part *post*-liquefaction onset ($t > t_L$), which is compatible with liquefied conditions.

7.6.2 Soil profile and liquefaction potential

In this design application, the properties of the actual liquefiable soil profile of Strymonas river were selected for the numerical simulation of SFS systems, instead of the custom profiles used for the parametric numerical analyses of previous chapters. Following the proposed concept of designing structures under liquefiable conditions, a superficial soil crust with thickness H_L=2m is selected to be improved by means of gravel drains. The improved zone is simulated as an *equivalent uniform improved zone* with increased relative density (i.e. D_r = 60%) and permeability ($k = 2 \cdot 10^{-3}$m/s). The design procedure for the crust improvement is described in detail in Section 3.2. The corrected *SPT* blow counts $N_{1,60}$ of the examined soil profile are presented in **Figure 7.14**. The coefficient of permeability was set equal to k = 5.5×10^{-5} m/sec for the whole liquefiable soil profile, which is a typical value for sands with some silt content. In the case of the improved crust, the coefficient of permeability was set equal to 5.5×10^{-4} m/sec, using the procedure of Chapter 3 for the numerical simulation of the gravel performance. **Table 7.2** summarizes the selected soil profile properties.

Table 7.2: Variation of soil properties with depth for the soil profile of Strymonas river.

Depth Interval (m)	Dr (%)	K_o	Permeability (m/sec)
0.0-2.0 (improved crust)	60	0.5	5.5×10^{-4}
0.0-3.0	40	0.5	5.5×10^{-5}
3.0-7.0	50	0.5	5.5×10^{-5}
7.0-11.0	60	0.5	5.5×10^{-5}
11.0-14.0	65	0.5	5.5×10^{-5}
14.0-16.5	50	0.5	5.5×10^{-5}
16.5-19.0	50	0.5	5.5×10^{-5}
19.0-23.0	75	0.5	5.5×10^{-5}

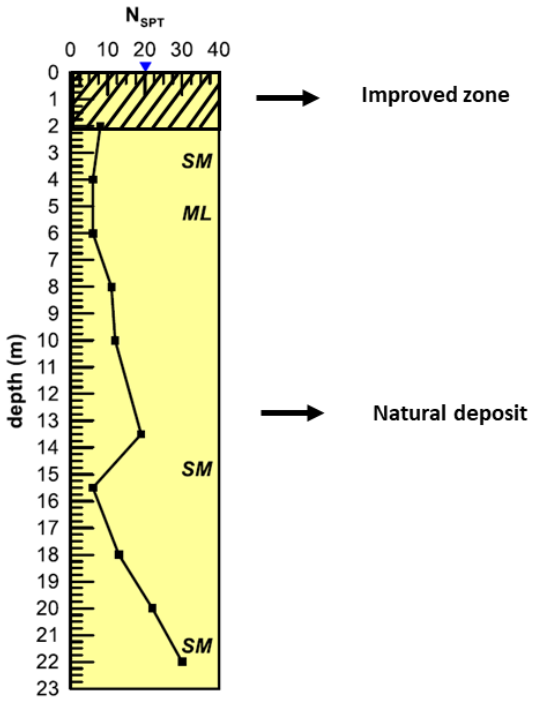

Figure 7.14: Soil profile and SPT results in the riverbed of Strymonas river.

Liquefaction potential of soil deposits is typically evaluated in engineering practice by procedures that correlate the results of SPT and CPT tests with soil's resistance to liquefaction (Boulanger and Idriss 2014; Seed and Idriss 1971; Youd et al. 2001). For the purposes of this study, though, the evaluation of liquefaction potential can be directly estimated with the use of numerical analyses. In this way, both the resistance to liquefaction and the applied stress can be directly and, thus, more accurately assessed compared to the empirical correlations. More specifically, the Factor of Safety against liquefaction FS_L can be directly calculated as the ratio of the soil's resistance to liquefaction – or the minimum cyclic shear stress required to trigger liquefaction *CRR* – to the applied cyclic stress ratio *CSR*, i.e.:

$$FS_L = \frac{CRR}{CSR} \tag{7.28}$$

In the case of a soil layer approaching **complete liquefaction**, i.e. $r_u \approx 1.0$ and $FS_L < 1.0$, FS_L is essentially equal to the ratio of the maximum cyclic shear stress developed during shaking, i.e. the maximum *resistance CRR*, over the cyclic stress that the earthquake motion *would* apply in the absence of liquefaction, i.e. *CSR*. As a consequence, the former is measured as the maximum ratio τ_d/σ'_{v0} that develops during shaking when liquefaction takes place. In order to calculate the maximum applied cyclic stress ratio *CSR,* though*,* conjugate numerical analyses without liquefaction need to be performed. These

analyses are identical in terms of seismic excitation and soil properties, but they are artificially hindered from developing excess pore pressures by assuming water bulk modulus equal to zero. The comparison of the shear stress time-histories between the numerical analyses with and without liquefaction is presented in **Figure 7.15.** The examined time-histories are obtained at an intermediate depth equal to z=8.5m, where the build-up of excess pore pressures is most critical. Four different scenarios of peak bedrock acceleration (i.e. a^b_{max} = 0.04g, 0.10g, 0.26g and 0.40g) were considered, thus, representing four different levels of applied cyclic stress ratio *CSR*. The earthquake motion used is the Matahima Dam (083) record from the New Zealand earthquake (1987), which was appropriately scaled to represent the four different levels of seismic intensity. The estimation of *CSR* and *CRR* values from the shear stress time-histories is presented in **Figure 7.15** for varying a^b_{max} values. **Table 7.3** summarized the obtained *CSR* and *CRR* values as well as the corresponding FS_L values. It is noted that in order to better represent the magnitude of the earthquake-induced *CSR*, a representative value equal to 65% of the peak cyclic shear stress is typically introduced (Seed and Idriss 1971). This approach is followed herein, therefore values of CSR_{eff} = 0.65·*CSR* are presented in the sequence.

In cases where only **partial liquefaction** takes place during shaking, i.e. $r_u < 1.0$ and $FS_L > 1.0$, soil resistance to liquefaction, in terms of *CRR,* has not been reached and as a result FS_L cannot be directly calculated as previously. It is possible, though, to correlate the factor of safety against liquefaction FS_L with the maximum value of excess pore pressure ratio r_u during shaking using empirical relations (Bouckovalas et al. 2011; Kalogeraki and Zontanou 2014; Tokimatsu and Yoshimi 1983). The methodology of Tokimatsu and Yoshimi (1983) is based on the empirical relationship of Seed et. al (1976) for the calculation of r_u:

$$r_u = \frac{2}{\pi} sin^{-1}\left[\left(\frac{N}{N_L}\right)^{1/(2A)}\right] \quad 7.29$$

or

$$\frac{N}{N_L} = \left[\sin\left(\frac{\pi}{2} r_{u,max}\right)\right]^{2A} \quad 7.30$$

where *N* is the number of excitation cycles, N_L is the number of cycles required for liquefaction triggering and A is an empirical coefficient. By modifying Equation 7.30, the Factor of Safety against liquefaction can be calculated as:

$$FS_L = \left[\sin\left(\frac{\pi}{2} r_{u,max}\right)\right]^{-2A\beta} \quad 7.31$$

The values of coefficients A and β are estimated for sand with relative density D_r = 45% equal to 1.60 and 0.15, respectively (Bouckovalas et al. 2011; Kalogeraki and Zontanou 2014).

Table 7.3: Results of FS_L values for different levels of seismic intensity.

Scenario No	a^b_{max} *(g)*	CSR_{eff}	*CRR*	FS_L
1	0.05	-	-	1.05(1)
2	0.10	0.17	0.10	0.59(2)
3	0.30	0.26	0.10	0.38(2)
4	0.45	0.30	0.10	0.33(2)

(1): FS_L for partial liquefaction is calculated using Equation 7.31.

(2): FS_L for complete liquefaction is calculated from the numerical analyses of Figure 7.15.

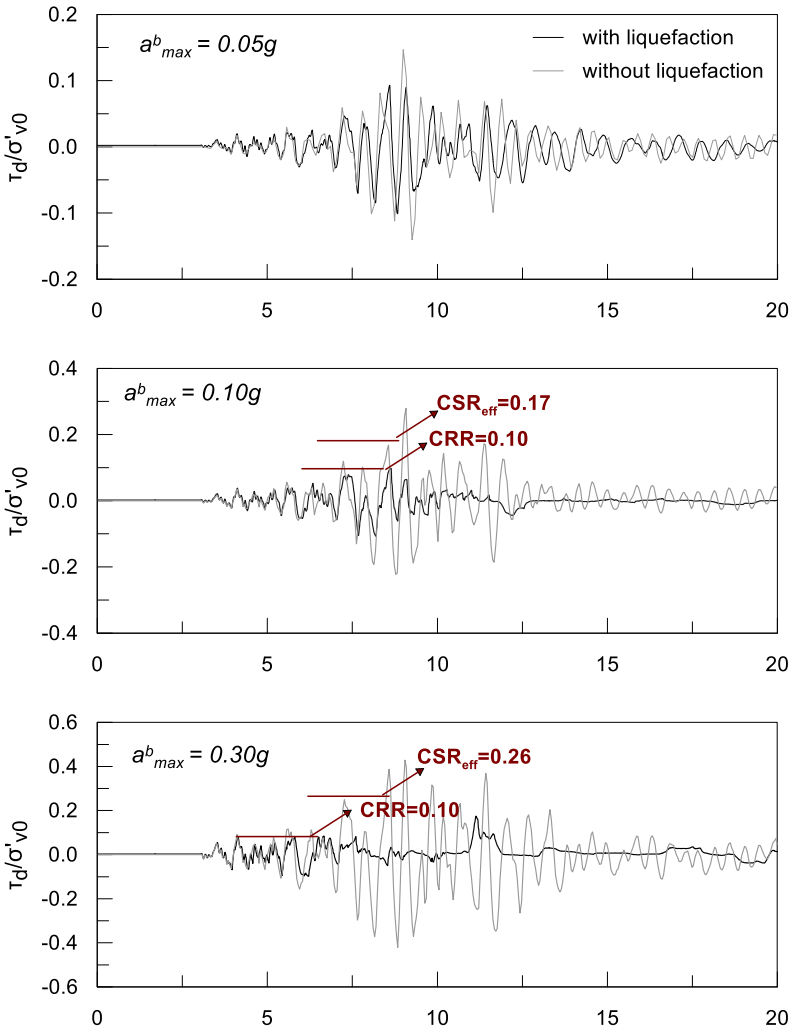

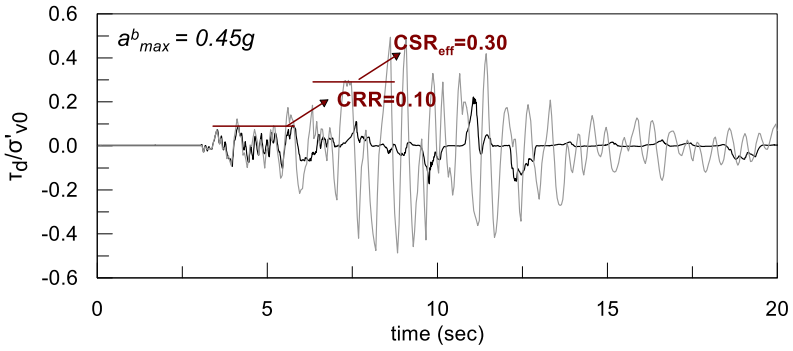

Figure 7.15: Time-histories of the applied shear stress ratio τ_d/σ'_{vo} (at the intermediate depth z=8.5m) with liquefaction (*black* line) and conjugate time-histories of τ_d/σ'_{vo} without permitting liquefaction (*gray* line).

7.6.3 Detailed examination of the SFS system subjected to earthquake excitation

- **Separation of earthquake motion: *non-liquefied* and *liquefied* part**

The present section examines the dynamic response of the reference SFS system subjected to the seismic acceleration recording of Matahima Dam (083) during the New Zealand earthquake (1987). The soil conditions vary with regard to the liquefaction potential, with the Factor of Safety against liquefaction being within the aforementioned range, i.e., FS_L = 0.33-1.05. The selected range of FS_L enables the examination of system responses with varying liquefaction onset time $t_{L.gr}$. As a result, the duration of the *pre*- and *post*-liquefaction parts of shaking also vary along with FS_L.

The determination of liquefaction onset time $t_{L.gr}$ and the distinction of shaking into *pre*- and *post*-liquefaction part is presented in **Figure 7.16**. Namely, the four different scenarios of earthquake intensity, i.e. a^b_{max} = 0.04g, 0.10g, 0.26g and 0.40g, are examined in terms of the following time-histories: i) the excess pore pressure ratio r_u at the intermediate – and most critical – depth z=8.5m and ii) the surface and base accelerations.

Literature findings have shown that liquefaction phenomena on the ground surface emerge as soon as the weakest subsoil layer approaches liquefaction (Bouckovalas et al. 2017a). In fact, the authors suggest that the development of average excess pore pressure ratios r_u in the range 0.6-0.8 along the soil profile suffices for the initiation of liquefaction phenomena on the ground surface. For this reason, the surface liquefaction onset time $t_{L.gr}$ (i.e. when surface motion starts to de-amplify) takes place earlier than the liquefaction onset time $t_{L.min}$ of the weakest subsoil layer (i.e. when $r_u \approx 1.0$ in the particular layer). The above are presented in **Figure 7.16**. The emergence of surface liquefaction is designated in the acceleration time-histories of **Figure 7.16** (2nd column) as the point in time, i.e. $t_{L.gr}$, after which surface motion starts to de-amplify. As expected, $t_{L.gr}$ is reduced with increasing a^b_{max} or -alternatively- with

increasing FS_L. In the case of FS_L = 1.05, excess pore pressure ratios reach up to $r_u \approx 0.80$ only at the end of shaking, thus, liquefaction phenomena do not emerge on the surface. For the cases of complete liquefaction, it is further observed that $t_{L.gr}$ (estimated by the surface motion) coincides with excess pore pressure ratios of the weakest soil layer around $r_u \approx 0.80$, thus, confirming that $t_{L.gr} < t_{L.min}$. Results of $t_{L.gr}$ for different scenarios of FS_L are summarized in **Table 7.4**.

Table 7.4: Values of liquefaction onset time $t_{L.gr}$ for different scenarios of FS_L.

Scenario No	FS_L	$t_{L.gr}$ *(sec)*
1	1.05	-
2	0.59	8.8
3	0.40	6.6
4	0.33	5.8

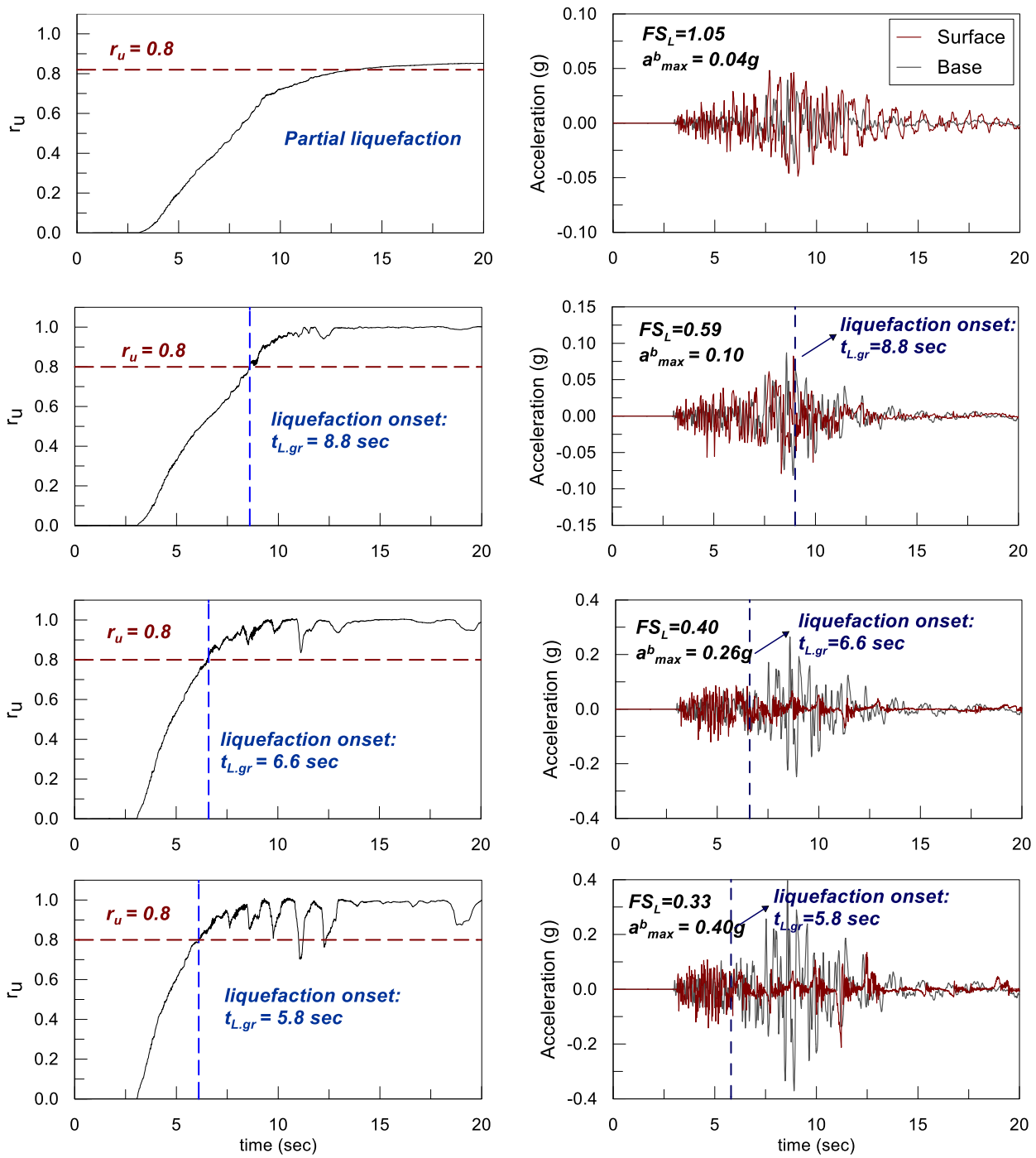

Figure 7.16: (1st column) Time-histories of excess pore pressure ratios r_u of the weakest soil sublayer (depth z=8.5m) and (2nd column) accelerations for varying Factors of Safety against liquefaction FS_L.

- **Calculation of the effective system period $T_{sys.eff}$**

In the described design problem, the dynamic characteristics of the examined systems depend on the structural, geotechnical and seismic excitation properties; thus, they vary for different analyses as well as

for the *pre*- and *post*-liquefaction part of each dynamic analysis. In more detail, the reference SFS system (see Chapter 3) is used in the numerical analyses of the present section, with SSI properties h/r = 1.06, γ = 4.00, s = 0.07 and natural period of the *fixed-base* structure $T_{str.f}$ = 0.35sec. In order to calculate the elastic system period $T_{sys.el}$, the analytical procedure, typically, used in Code Provisions ((Federal Emergency Management Agency (FEMA) 1997) is implemented here, as described in Section 4.2.1. According to this, the elastic period elongation $T_{sys.el}/T_{str.f}$ is calculated with the following expression:

$$\frac{T_{sys.el}}{T_{str.fix}} = \sqrt{1 + \frac{k_{str}}{k_x} + \frac{k_{str} \cdot h^2}{k_{ry}}} \tag{7.32}$$

Next, the nonlinear part of period elongation $T_{sys.eff}/T_{sys.el}$ can be estimated using the proposed methodology of Section 4.3.2. Contrary to the dependency of the elastic system period $T_{sys.el}$ on initial soil properties, effective system period $T_{sys.eff}$ depends on the time-varying soil properties during shaking. Therefore, $T_{sys.eff}$ is considered separately for the non-liquefied and for the liquefied part of shaking. Regarding the first, $T_{sys.eff}$ predictions are obtained using Equation 4.8, which utilizes the smoothed spectral predominant system period $T_{sys,o}$ as an estimate for the characterization of the Transfer Function frequency content. Statistical analysis of the numerical predictions led to the following expression for the non-liquefied (*NL*) part, i.e.:

$$\left(\frac{T_{sys.eff}}{T_{sys.el}}\right)_{NL} = (0.91 + 0.55 \cdot PGA^{0.21}) \frac{1.53 + 0.94\left(T_{soil}/T_{sys.el}\right)^2}{\sqrt{\left[2.04 - \left(T_{soil}/T_{sys.el}\right)^2\right]^2 + 3.65 \cdot \left(T_{soil}/T_{sys.el}\right)^2}} \tag{7.33}$$

In the case of liquefied conditions, Equation 4.18 is employed here, which uses the spectral predominant system period $T_{sys,p}$ for the estimation of $T_{sys.eff}$. The following expression is used:

$$\left(\frac{T_{sys.eff}}{T_{sys.el}}\right)_{L} = 1.00 \qquad for\ PGA \leq 0.075g$$

$$\left(\frac{T_{sys.eff}}{T_{sys.el}}\right)_{L} = 1.69 \cdot PGA^{0.014} \qquad for\ PGA > 0.075g \tag{7.34}$$

Therefore, the calculation of $T_{sys.eff}$ using Equations 7.33 and 7.34 requires as input parameters the elastic system period $T_{sys.el}$, as already discussed, the peak ground acceleration *PGA* and, in the case of non-

liquefiable conditions, the fundamental soil period T_{soil}. Values of *PGA* can be readily obtained using the analytical framework of seismic ground response analysis. In the present section, the more accurate data of numerical predictions are obtained from the surface acceleration time-histories of **Figure 7.15** and they are summarized in **Table 7.5**. Lastly, the fundamental soil period T_{soil} refers to nonlinear soil properties and therefore it depends on the properties of the soil profile as well as of the earthquake excitation. The nonlinear soil period elongation has been correlated to the average elastic shear wave velocity $V_{s,o}$ and the peak acceleration at the outcropping bedrock a_{max}^{b} by Bouckovalas and Papadimitriou (2003), as explained in Chapter 4. The proposed expression is repeated here:

$$\frac{T_{soil}}{T_{soil,o}} = 1 + d_{1,T}\left(\bar{V}_{s,o}\right)^{d_{2,T}} \left(\frac{a_{max}^{b}}{g}\right)^{d_{3,T}} \quad 7.35$$

with the coefficients being $d_{1,T}$ = 5330, $d_{2,T}$ = -1.30 and $d_{3,T}$=1.04.

Table 7.5 summarizes results of the aforementioned procedure for the calculation of $T_{sys.eff}$. Calculations refer to the different scenarios of peak bedrock acceleration a^{b}_{max} (see **Table 7.3**). Results are separately reported for each analysis and for each part of shaking, i.e. *before (NL)* and *after (L)* the onset of liquefaction.

Overall, the described methodology proposes values of $T_{sys.eff}$ that are greater for the *pre*-liquefaction part of shaking (i.e. $T^{NL}_{sys.eff}$ = 0.64-0.68sec) compared to the *post*-liquefaction part (i.e. $T^{L}_{sys.eff}$ = 0.46-0.50sec). As previously discussed, this finding confirms that the combination of i) small r_u values under the footing and ii) de-amplified structural motion due to the presence of liquefied layers, ensures that nonlinear period elongation remains small even for swallow soil improvement. On the other hand, in the absence of liquefied layers, rocking-induced soil softening of the foundation soil leads to greater nonlinear period elongation. Additionally, it can be remarked that the narrow range of the recorded *PGA* values (i.e. *PGA* = 0.048g-0.115g) leads to limited increase of $T_{sys.eff}$, which is up to 6.3% and 8.4% for the *pre*- and *post*-liquefaction parts, respectively.

Table 7.5: Result of the proposed methodology (Chapter 4) for the calculation of the effective system period $T_{sys.eff}$ for the numerical analyses with varying FS_L.

Scenario No	*Part of motion*	*PGA (g)*	T_{soil} / $T_{soil.o}$	$T_{sys.eff}$ / $T_{sys.el}$	$T_{sys.eff}$ *(sec)*
1	*NL*	0.048	1.17	1.40	0.64
	L[(1)]	-	-	-	-
2	*NL*	0.098	1.43	1.45	0.66
	L	0.068	-	1.00	0.46
3	*NL*	0.110	1.35	1.46	0.67
	L	0.070	-	1.00	0.47
4	*NL*	0.115	1.44	1.47	0.68
	L	0.102	-	1.09	0.50

Notes: *NL* refers to the the non-liquefied part of shaking. *L* refers to the liquefied part of shaking.

(1): The particular numerical analysis with FS_L = 1.05 exhibits only partial liquefaction (i.e. r_u < 0.8).

- **Estimation of SFS system dynamic response**

Following the separation of shaking into two parts (i.e. *pre-* and *post-liquefaction*) and the determination of the corresponding effective system period $T_{sys.eff}$ for these parts, it is possible, as a next step, to identify the dynamic response of the SFS system subjected to an earthquake excitation. To that end, it is necessary to identify the frequency content of the seismic excitation (at the ground surface level). **Figure 7.17** compares the elastic response spectra of the surface and base motion with the effective system period of the non-liquefied $T^{NL}_{sys.eff}$ (*blue color*) and liquefied $T^{L}_{sys.eff}$ (*red color*) part of shaking for different scenarios of peak bedrock acceleration a^{b}_{max}. In order to quantify amplification effects between $T_{sys.eff}$ and the excitation period (at the ground surface) T_{exc}, a single-parameter characterization of the ground motion response spectrum (*black color*) is required. The following frequency content estimates of Section 4.3.2 are repeated and utilized here:

- The *predominant period* $T_{p,}$ which is the period corresponding to the maximum value of spectral accelerations
- The *smoothed spectral predominant period* T_o defined as

$$T_o = \frac{\sum_i T_i \cdot \ln\left[S_a(T_i)\right]]}{\sum_i \ln\left[S_a(T_i)\right]} \qquad 7.36$$

Results in **Table 7.6**, designate the *predominant excitation period* as $T_{exc.p}$ and the *mean excitation period* as $T_{exc.o}$. Ratios of $T_{sys.eff}$ over $T_{exc.p}$ and $T_{exc.o}$ are presented comparatively in the last two columns of the

Table in order to quantify any amplification or de-amplification effects between the system and the excitation frequency content. Results are presented for the *pre-* and *post*-liquefaction part of shaking considering the aforementioned scenarios of a^b_{max}. It is noted that the appropriate selection of the peak amplitude, in the case of $T_{exc.p}$, or of the spectral range, in the case of $T_{exc.o}$, is often case-specific and relies on engineering judgement. In the particular investigation, the amplitude peak closer to the effective system period (i.e. $T_{exc.p}$ ≈ 0.50-0.60 sec) is selected as the predominant period $T_{exc.p}$, rather than the absolute spectral maximum (i.e. $T_{exc.p}$ ≈ 0.12 sec), since the latter would lead to misleading results. Additionally, for the calculation of $T_{exc.o}$, the spectral range of the contributing frequencies needs to be limited to T ≈ 1.0-1.5 sec.

Overall, results show that the *predominant period* $T_{exc.p}$ has a constant value equal to 0.60sec for a^b_{max} = 0.04g - 0.26g and it is reduced to $T_{exc.p}$ = 0.55sec for a^b_{max} = 0.40g. These findings suggest the T_p does not adequately capture the frequency content of the response spectra; a phenomenon that is intensified for increasing earthquake intensity, due to the diminishing importance of a single – predominant – period. On the other hand, the *smoothed spectral predominant period* $T_{exc.o}$ shows a better correlation of period elongation with seismic intensity, i.e. $T_{exc.o}$ = 0.52-0.59 sec.

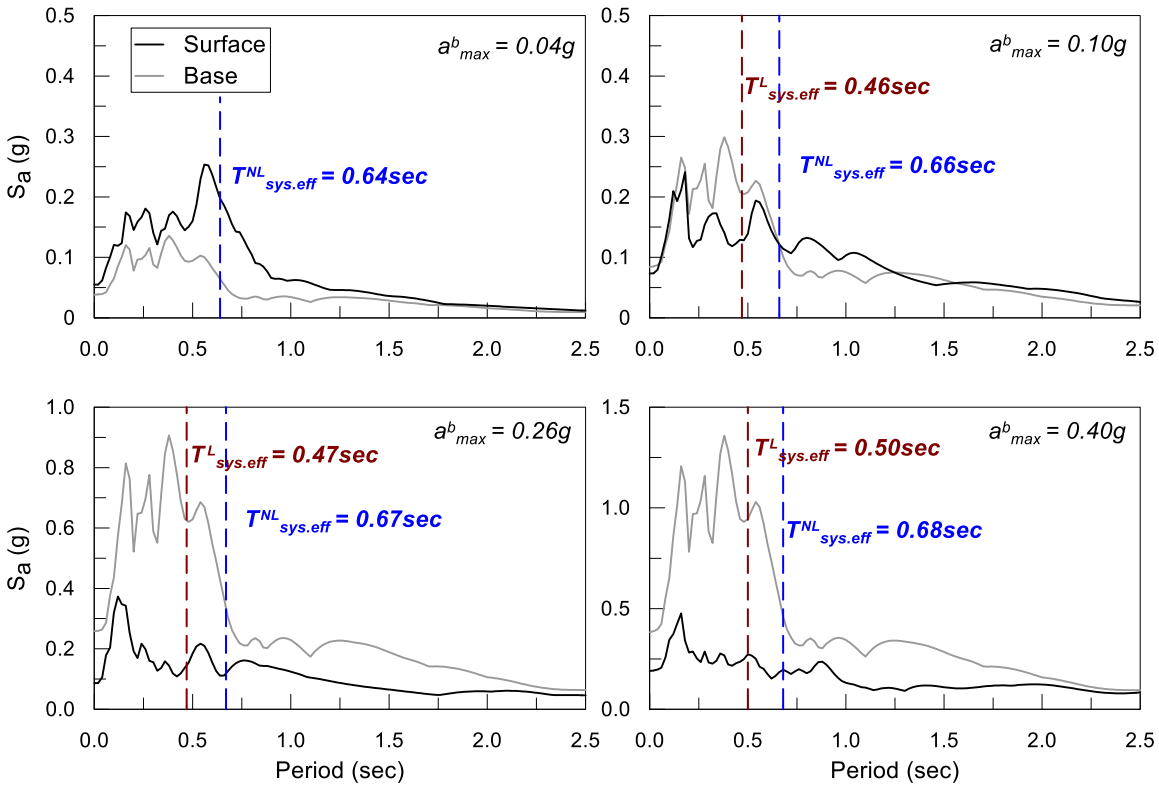

Figure 7.17: Elastic response spectra of the surface and base motion for the Matahima Dam (083) recording of the New Zealand earthquake (1986). Four levels of peak bedrock acceleration a^b_{max} are considered: 0.04g, 0.10g, 0.26g

and 0.40g. The effective system periods of the *non-liquefied* $T^{NL}_{sys.eff}$ (*blue line*) and *liquefied* $T^{L}_{sys.eff}$ (*red line*) part of shaking are plotted comparatively.

Table 7.6: Frequency content estimation of the surface motion and corresponding period ratios between the system and the excitation.

Scenario No	*Part of motion*	*Tsys.eff (sec)*	*Texc.p (sec)*	*Texc.o (sec)*	*Tsys.eff / Texc.p*	*Tsys.eff / Texc.o*
1	*NL*	0.64	0.60	0.52	*1.06*	*1.23*
	L[(1)]	-			-	-
2	*NL*	0.66	0.60	0.55	*1.10*	*1.39*
	L	0.46			*0.76*	*0.83*
3	*NL*	0.67	0.60	0.53	*1.16*	*1.48*
	L	0.47			*0.78*	*0.89*
4	*NL*	0.68	0.55	0.59	*1.23*	*1.49*
	L	0.50			*0.91*	*0.85*

- **Seismic settlement estimation for the SFS system**

Having already determined the dynamic characteristics of the system, in terms of *SSI* and period ratio $T_{sys.eff}/T_{exc}$, settlement accumulation during the actual earthquake motion can be assessed next. **Figure 7.18** compares settlement accumulation time-histories between SFS and FS systems for the discussed scenarios of varying FS_L or, alternatively, a^b_{max}. Settlement accumulation is distinguished into two phases, i.e. *pre*- and *post*-liquefaction, for the numerical analyses with $FS_L < 1.0$. In the case of the first numerical analysis of **Figure 7.18** non-liquefied conditions prevail, since excess pore pressure ratios in the subsoil are equal or smaller than 0.8 (see **Figure 7.16**).

Results in **Figure 7.18** show the profound difference in settlement accumulation before and after liquefaction. Namely, during the non-liquefied part of motion the effect of the superstructure is significant and its role is detrimental for the performance of the system, since the SFS system settles considerably more than the FS one. The duration of this part of shaking is a most influential factor for final values of ρ_{SFS}/ρ_{FS} ratios, within the examined range (i.e. for durations up to 15-20sec). These observations come in agreement with results from the preceding response spectra analysis, where the dynamic response of the system during the *non-liquefied* part of shaking is characterized from resonant up to flexible behavior, with period ratios $T_{sys.eff}/T_{exc}$ being within the range 1.06-1.49 (**Table 7.6**). The parametric investigation of Chapter 6 has identified significant increase of settlement accumulation for the SFS system compared to the equivalent FS system in the particular period range.

On the contrary, during the liquefied part of motion the effect of the superstructure is smaller and its role proves to be beneficial for settlement accumulation, as it is discussed in Chapter 5. Results from the preceding response spectra analyses showed that the dynamic response of the system lies within the rigid-to-resonant spectral region, i.e. $T_{sys.eff}/T_{exc}$ ≈ 0.76-0.81 (**Table 7.6**). The parametric investigation of Chapter 6 has identified reduction of settlement accumulation for the SFS system compared to the equivalent FS system.

The overall conclusion is that final (end-of-shake) values of ρ_{SFS}/ρ_{FS} ratios decrease for decreasing FS_L. This finding is attributed to the correlation of FS_L with the liquefaction onset time $t_{L.gr}$ or, alternatively, with the duration of pre- and post-liquefaction part of shaking. Nevertheless, the total settlement ρ_{SFS} of the SFS system increases with decreasing FS_L.

To demonstrate the application of the proposed design methodology for the calculation of ρ_{SFS}/ρ_{FS} ratios, results from the numerical analyses are compared with analytical predictions developed in previous Chapters 5 and 6. Settlement ratios at the end of the non-liquefied part are evaluated with the use of Equation 6.1 of Chapter 6, that predicts settlement ratios in non-liquefiable conditions, denoted as $(\rho_{SFS}/\rho_{FS})_{NL}$. It is repeated here:

$$\left(\frac{\rho_{SFS}}{\rho_{FS}}\right)_{NL} = \frac{1+C_2\left(T_{sys}/T_{exc}\right)^2}{\sqrt{\left[1-\left(T_{sys}/T_{exc}\right)^2\right]^2+{C_4}^2\left(T_{sys}/T_{exc}\right)^2}} \quad 7.37$$

This expression is a function of the independent variables T_{sys}/T_{exc}, h/r, γ, a^b_{max} and N. The values of these variables for the particular design example are: T_{sys}/T_{exc} = 1.06-1.53, h/r = 1.06, γ = 4.00, a^b_{max} = 0.04g, 0.10g, 0.26g, 0.40g and N = 11, 5.5, 3.9, 1.0. It is noted that for the calculation of the period ratio T_{sys}/T_{exc}, both frequency estimates of the excitation response spectrum (i.e. $T_{exc.p}$ and $T_{exc.o}$) are considered here for comparison reasons. Additionally, to ensure the compatibility between the duration of the non-liquefied part of shaking and the variable N (number of excitation cycles), the equivalent number of cycles N_{eq} is introduced, derived from Equation 7.3:

$$N_{eq} = \frac{\pi^2 \int_0^{Td} |v(t)| dt}{a_{eff} \cdot {T_{exc}}^2} \quad 7.38$$

Results of the described analytical procedure are summarized and compared with the corresponding results of the numerical analyses in **Table 7.7**. Values of $(\rho_{SFS}/\rho_{FS})_{NL}$ refer to the end of the non-liquefied

part, i.e. at the time $t_{L.gr}$. Overall, it is observed that both procedures predict decreasing values of ρ_{SFS}/ρ_{FS} for decreasing FS_L, i.e. $(\rho_{SFS}/\rho_{FS})_{NL}$ ratios are in the range 4.02-1.44 and 5.58-1.78 for numerical and analytical analyses, respectively. Better agreement between analytical and numerical predictions is found when employing the smoothed spectral predominant period $T_{exc.o}$ as the frequency estimate of the excitation response spectra (better agreement is marked with green color in **Table 7.7**).

Next, the numerical and analytical predictions of settlement ratios during the liquefied part of shaking are compared. The particular settlements are calculated by deducing the non-liquefied part of settlement from the total settlement, i.e. at the end of shaking. Thus, the "liquefied" settlement ratio is denoted here as $(\rho_{SFS}/\rho_{FS})_L$ and defined as:

$$\left(\frac{\rho_{SFS}}{\rho_{FS}}\right)_L = \frac{(\rho_{SFS})_{Total} - (\rho_{SFS})_{NL}}{(\rho_{FS})_{Total} - (\rho_{SFS})_{NL}} \tag{7.39}$$

The analytical procedure of Chapter 5 is employed here for the calculation of $(\rho_{SFS}/\rho_{FS})_L$ ratios in liquefied conditions. Equation 5.9 is repeated here:

$$\left(\frac{\rho_{SFS}}{\rho_{FS}}\right)_L = \begin{cases} 1 + C_a \cdot \left(T_{sys}/T_{exc}\right)^2 & T_{sys}/T_{exc} \leq 0.80 \\ \left[\dfrac{C_{1.b} + C_{2.b}\left(T_{sys}/T_{exc}\right)^2}{\sqrt{\left[C_{3.b} - \left(T_{sys}/T_{exc}\right)^2\right]^2 + C_{4.b} \cdot \left(T_{sys}/T_{exc}\right)^2}}\right]^{-1} & T_{sys}/T_{exc} \geq 0.80 \end{cases} \tag{7.40}$$

The values of the independent variables for the particular design example are: T_{sys}/T_{exc} = 0.76-0.91, h/r = 1.06 and γ = 4.00, with T_{exc} being estimated with both frequency estimates of the excitation response spectrum (i.e. $T_{exc.p}$ and $T_{exc.o}$).

Results of the described analytical procedure are summarized and compared with the corresponding results of the numerical analyses in **Table 7.7.** Overall, values of $(\rho_{SFS}/\rho_{FS})_L$ range from 0.70 to 0.88 in the case of numerical predictions and from 0.88 to 1.00 in the case of analytical predictions. As in the non-liquefied case, better agreement of the predictions is found with the use of the smoothed spectral predominant period $T_{exc.o}$ for two out of three cases. In contrast to the non-liquefied case, though, the variation of $(\rho_{SFS}/\rho_{FS})_L$ ratios with FS_L is minimal; a finding that is related to the, also, minimal effect of the duration of shaking to settlement ratios.

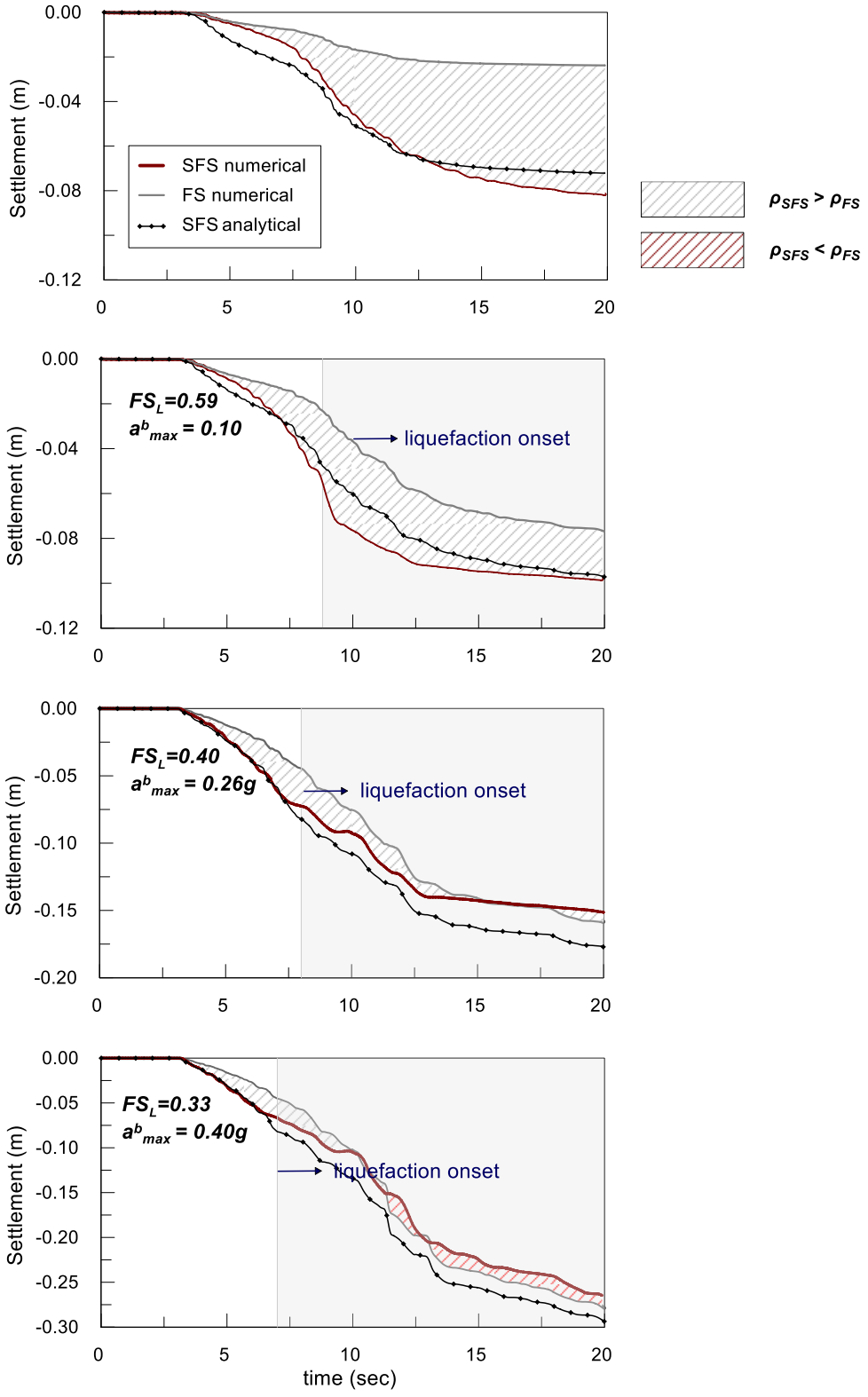

Figure 7.18: Time-histories of settlement accumulation for SFS and FS systems subjected to the Matahima Dam recording (083) of New Zealand earthquake (1986), for different scenarios of Factors of Safety against liquefaction

FS_L. Numerical (dark red line) and analytical (dashed line) predictions of the SFS system settlement accumulation are compared.

Table 7.7: Analytical and numerical predictions of settlement ratios $\rho_{SFS}/\rho_{FS.}$

Scenario No	***Part of motion***	***Analytical*** ρ_{SFS}/ρ_{FS}		***Numerical*** ρ_{SFS}/ρ_{FS}
		Texc.p	***Texc.o***	
1	Pre-liquefaction	5.58	3.03	4.02
	Post-liquefaction(1)	-	-	-
2	Pre-liquefaction	5.05	2.01	2.03
	Post-liquefaction	1.00	0.92	0.70
3	Pre-liquefaction	3.65	1.81	1.56
	Post-liquefaction	0.95	0.89	0.74
4	Pre-liquefaction	3.51	1.78	1.44
	Post-liquefaction	0.88	0.91	0.88

Note: green color marks the best agreement between analytical and numerical predictions.

7.6.4 Summary of the design procedure

The analytical methodology described in the present Chapter is summarized in this section. The purpose is to provide a detailed description of the necessary stages for the performance-based design of structures in liquefiable conditions. The following stages are proposed:

- **Calculation of the footing's seismic settlements $\rho_{FS.NL}$ for *non-liquefiable* conditions**. The modified procedure of Richards et al. (1993), described in Section 7.4 (Equations 7.11-7.15) is employed. The proposed expression of Newmark (1965) was found to provide more accurate predictions of seismic settlements, especially for values of *PGA* close to the critical acceleration a_{cr}.
- **Calculation of the footing's seismic settlements $\rho_{FS.L}$ for *liquefied* conditions.** The procedure of Dimitriadi et al. (2017) can be used for this purpose, as described in Section 7.5.
- **Calculation of the effective system period $T_{sys.eff}$.**
  - Firstly, the analytical procedures of Design Codes (NIST 2012b) are employed for the calculation of the elastic part of period elongation $T_{sys.el}/T_{str.f}$. At this stage, soil properties -usually in terms of shear modulus *G*- are introduced with the initial -measured- values (Section 4.3.1).
  - Next, the nonlinear part of period elongation $T_{sys.eff}/T_{sys.el}$ can be computed for the non-liquefied part of shaking using Equation 4.12 and for the liquefied part using Equation 4.18.

- **Calculation of liquefaction onset time $t_{L.gr}$.** Based on results of in-situ tests -in terms of FS_L- and the properties of the excitation motion, $t_{L.gr}$ can be estimated using the procedure described in Section 7.3.2. Thus, shaking is distinguished into the pre- and post-liquefaction parts.
- **Estimation of the excitation motion frequency content.** Various estimates are proposed in literature and can be used for this purpose. In this study, the predominant period T_p and the smoothed predominant period T_o are opted for (Section 7.6.3).
- **Calculation of $(\rho_{SFS}/\rho_{FS})_{NL}$ ratios for the *non-liquefied* part of shaking.** The effect of superstructure on seismic settlements is introduced as the correction factor $(\rho_{SFS}/\rho_{FS})_{NL}$ to the analytically calculated $\rho_{FS.NL}$. The proposed methodology is described in Chapter 6 (Equations 6.1-6.11).
- **Calculation of $(\rho_{SFS}/\rho_{FS})_{L}$ ratios for the *liquefied* part of shaking.** The effect of superstructure on seismic settlements is introduced as the correction factor $(\rho_{SFS}/\rho_{FS})_{L}$ to the analytically calculated $\rho_{FS.L}$. The proposed methodology is described in Chapter 5 (Equations 5.9-5.14).

Chapter 8

Summary, Conclusions and Recommendations for Future Research

8.1 Summary and conclusions

The aim of this Thesis is to expand the novel design concept, which has been developed in recent studies, of designing structures founded on liquefiable soils with only shallow foundations. As a first step, the Thesis aims to investigate the mechanisms that govern the seismic response of structures with shallow foundations, especially with respect to the accumulation of seismic settlements. A primary goal of this Thesis is to develop a robust as well as simplified procedure for the estimation of seismic settlements of structures, which is realistically applicable from an engineering point of view.

The core assumptions of the study can be summarized in the following:

i) The design concept involves the construction of only a shallow foundation along with the improvement of a surficial zone. The improved zone has increased density and is non-liquefiable due to vibrocompaction and the installation of vertical drains. The benefit of this design concept is the exploitation of the “natural isolation” of the liquefied sublayer while, at the same time, the integrity of the foundation soil is ensured.

ii) The developed methodology for the simplified calculation of seismic settlements in liquefiable conditions includes the effects of the superstructure in the form of correction factors. Thus, it assumes that the engineer will employ established procedures for i) the estimation of settlements of simple foundations (i.e., FS systems) and ii) the estimation of the liquefaction onset time in order to distinguish shaking into prior to and after liquefaction.

iii) Within the employed framework of performance-based design, emphasis is given to the estimation of seismic settlements, since other design parameters are either correlated with settlements or require different modeling of the physical problem. For example, the estimation of structural parameters (such as interstory drifts or bending moments of the column) would require a more detailed modeling of the superstructure including the realistic incorporation of material nonlinearity (i.e., of the concrete pier as well as the reinforcement bars). Concerning other geotechnical parameters of design (such as rotations, horizontal displacements and uplifting), it is selected not to be further discussed in this study, since they are correlated to the magnitude of settlements and, additionally, they are usually restrained in engineering practice, where a number of construction details (connecting beams, foundation embankment etc.) aims to prevent excessive foundation rotation, horizontal displacements and uplifting.

iv) The effects of various geotechnical aspects are examined in previous studies with a similar modeling setup. Thus, emphasis in this study is given to the properties of the SFS system within the typical SSI framework. Thus, the underlying assumption in the present study is that the structural effects on the accumulation of seismic settlements act in an uncoupled manner with the corresponding effects of other geotechnical parameters.

v) The calculation of seismic settlement of structures incorporates the effect of the rocking-induced shear strains as well as the volumetric strains due to the partial drainage during shaking. Yet, the post-shaking volumetric strains due to excess pore pressure drainage is ignored in this study since, on one hand, structural settlements due to these strains are found to be negligible and, on the other hand, such settlement between the structure and the free field are comparable in magnitude, thus, the relative settlement between the foundation and the free field is minimal.

Following the completion of the Thesis tasks, the main findings and conclusions are summarized:

i) A **numerical methodology** has been developed for the performance-based design of the foundation system of structures in liquefiable conditions. The Finite Difference Code *FLAC3D* (Itasca 2012) was employed for the numerical analyses, while the cyclic behavior of sand was modeled with the user-defined critical state constitutive model NTUA-Sand (Andrianopoulos et al. 2010; Karamitros 2010). A series of dynamic analyses of structure-foundation-soil systems was performed in order to shed more light into the mechanisms

that govern the dynamic response of structures in liquefiable conditions. Emphasis is given to the key elements of the system response, i.e., the natural period of the SFS system and the seismic settlements during shaking. The abrupt change of soil properties after the onset of liquefaction is taken into consideration by distinguishing shaking into two phases, i.e., prior to and post liquefaction. Based on the results of the parametric investigation multi-variable relations are developed for the prediction of the natural period of the SFS systems during shaking as well as the effect of SSI in settlement accumulation. The proposed methodology is demonstrated with a design example where a SFS system is subjected to a set of ground motion recordings along with a step-by-step application of the procedure for the calculation of seismic settlements.

ii) The dynamic response of SFS systems during a particular seismic event is greatly correlated with the **liquefaction onset time** of the subsoil. Previous studies have shown that soil softening due to liquefaction is severe enough to induce a distinct phase of shaking which is characterized by significantly altered soil properties (V_s, T_{soil}) compared to the initial, *pre*-liquefaction, properties. This transition to the liquefied state of soil is rather abrupt and typically occurs for pore pressure ratios less than about 0.8. The onset time of liquefaction effects on the ground surface is shown to be slightly less (about 15%) than the time required for complete liquefaction (i.e., r_u=1.0) of the weakest sublayer.

iii) Based on these findings, the dynamic response of structures is distinguished into two phases, i.e., ***prior to*** and ***post*** liquefaction. The duration of *non-liquefiable* and *liquefied* soil conditions is controlled by the value of the Factor of Safety against liquefaction FS_L, with the special cases of purely *non-liquefiable* or purely *liquefiable* conditions corresponding approximately to $FS_L > 1.0$ and $FS_L < 0.30$ respectively.

iv) In the typical SSI framework, **the natural period of the flexible-base** structure-foundation-soil system incorporates soil nonlinearity indirectly, in terms of shear modulus reduction and damping ratio increase, neglecting dominant patterns of cyclic soil behavior such as densification, loss of strength due to pore water pressure build up etc. This over-simplification can either be on the safe or on the unsafe side depending on whether period elongation – related to soil softening – may lead to an increase or decrease of seismic spectral demand. During strong seismic events or – especially – in the case of liquefaction, the time-varying degradation of soil stiffness renders the direct

calculation of the natural period dependent on the appropriate selection of an equivalent shear modulus for the supporting soil.

v) To overcome this difficulty, the nonlinear system period is identified indirectly, through the Transfer Function between the input (*free field*) and output (*structural*) acceleration signals in the frequency domain. Within this framework the factors of system nonlinearity can be related to an actual – or *effective* – natural period of the SFS system. In this study, the **effective period** is estimated for systems excited at the soil base with white-noise signals, for both liquefied and non-liquefiable soil conditions, employing the widely used frequency content estimates of the *predominant period* T_p and *smoothed spectral predominant period* T_o.

vi) The contribution of soil nonlinearity in period elongation is significant in the case of **non-liquefiable** conditions and this is manifested by TFs of structure-to-surface motion that exhibit amplifications in a wide range of periods. The estimated effective periods are mostly influenced by *earthquake intensity* and *soil-structure resonance* phenomena. Greater values of *PGA* lead to an increase of the effective system period up to 80% compared to the "elastic" system period. It is noteworthy that, even for moderate to low earthquakes intensities (e.g. *PGA* ≈ 0.20g), consideration of the "elastic" system period would result in underestimation of the effective period to the magnitude of 40%. Due to the gradual degradation of soil stiffness, effective system periods are better estimated by smoothed spectral predominant system periods $T_{sys.o}$ that capture the time-varying nature of periods.

vii) In the case of **liquefied conditions**, structural response is governed by soil properties at the liquefied state. This is manifested by TFs of structure-to-surface motion that exhibit a singular peak corresponding to the system period at the liquefied state. As a result, effective system periods are better estimated by the predominant system period $T_{sys.p}$. The effect of *earthquake intensity* has an upper limit of about 20% in nonlinear period elongation compared to "elastic" values, due to the fact that liquefied sublayers act as "natural seismic isolation" and attenuate surface motion. The depth of the improved zone H_{imp} has a minor effect on period elongation compared to its role in the overall foundation performance.

viii) **Seismic settlements of SFS systems** are compared with the respective settlements of equivalent foundation-soil systems (FS) in order to isolate the effects of structural inertia on the dynamic response of systems. Multi-variable relations are developed for the prediction of settlement ratios between the aforementioned SFS-to-FS systems, in order

to take advantage of existing literature studies for estimating seismic settlement accumulation of FS systems with shallow foundations. These relations are expressed in terms of correction factors that add up to the established procedures of settlement calculation for FS systems. The effect of structural inertia on settlement accumulation is investigated through parametric consideration of the critical soil-structure interaction (SSI) parameters, i.e., system-to-excitation period ratio T_{sys}/T_{exc}, slenderness ratio h/r, relative mass ratio γ and structure-to-soil stiffness ratio s. These relations are expressed in terms of correction factors that add up to the established procedures of settlement calculation for FS systems.

ix) Seismic settlements of SFS systems on **liquefied ground** are controlled by a **Coulomb-type wedge sliding**, which takes place due to the severe degradation of the bearing capacity of the foundation soil. The effect of the superstructure is mainly introduced as an inertial force that acts in-phase or out-of-phase with the wedge sliding, thus amplifying or de-amplifying the overall seismic settlement. The most crucial parameter in the SFS system response is the period ratio between the fundamental period of the system and the predominant period of the excitation. In the case of resonance, the – quarter cycle – lag of the structural vibration with respect to the foundation results in the greatest reduction of the wedge sliding and, hence, the greatest reduction of settlement accumulation, which can be up to 40%. Rigid systems tend to settle equally with the equivalent FS systems, whereas flexible systems experience out-of-phase motion which, also, results in settlement reduction, but less intense than that at resonance. Relative mass ratio γ and slenderness ratio h/r affect the SFS system response, although to a lesser degree compared to the period ratio T_{sys}/T_{exc}. It is noteworthy that in the case of semi-rigid structures (T_{sys}/T_{exc} = 0.55-0.80) with high slenderness ratios (h/r > 1.36), the settlements are increased by up to 20% with respect to the FS systems due to the additional rocking-induced soil softening.

x) On the other hand, seismic settlements of SFS systems in **non-liquefiable** conditions are profoundly increased due to **rocking-induced softening** of the foundation soil. As a result, shear strain distribution under the structure appears to be swallower compared to the typical – and deeper – formation of Coulomb-type wedges and additionally maximum strains are symmetrically concentrated under the footing edges. Due to the correlation of settlement accumulation with foundation rocking the most crucial parameter for SSI settlement aggravation is the period ratio T_{sys}/T_{exc} between the system and the excitation. Resonance conditions may lead to amplification of spectral accelerations and settlement

ratios ρ_{SFS}/ρ_{FS} up to 2 and 6 times, respectively. The relative mass ratio *γ* and slenderness ratio *h/r* also affect significantly settlement accumulation of SFS systems. The associated effects are related with the aggravated structural rocking for increasing levels of these ratios. In the case of relative mass ratio, structural rocking is aggravated due to the increase of structural inertial forces, whereas in the case of slenderness ratio due to the increase of overturning moments. The seismic excitation characteristics affect system response mostly through the peak seismic acceleration and, to a lesser degree, through the number of excitation cycles N_o.

8.2 Recommendations for future research

This Thesis aims to further develop the novel concept of designing structures in liquefiable conditions with shallow foundations, which can decidedly change the current engineering practice in liquefiable soils to the benefit of cost and construction duration of the project. Pertinent research has extensively investigated the effect of various geotechnical, excitation and structural parameters on the response of foundations in such conditions. Nevertheless, the state of current understanding is not mature enough to enable a generalized application in practice. This is due to a number of simplifying assumptions that might be typical in research stages, yet they are often violated in engineering practice. In order to overcame such limitations, the following areas of further research are proposed:

i) The constitutive model NTUA-Sand employed in the numerical analyses of the present Thesis models the monotonic and cyclic response of Nevada sand. This type of soil is a uniformly graded, fine sand and its properties have been experimentally investigated in many tests. In order to enable a generalized application in practice of the developed procedure, it would be important to include the effect of a wider range of liquefiable soils into the numerical methodology, such as sands with different gradation and particle shape, nonplastic cohesionless silts as well as other representative soil composition derived from field experience. This procedure is, undoubtably, time-consuming since it requires the repetition of model parameters calibration. Although the qualitative findings of the present Thesis are not expected to change for different soil types, such a procedure is necessary for the quantitative precision of the methodology.

ii) Pertinent studies on the subject, including the present, have focused on various aspects of the foundation design, e.g., soil profile layering, soil properties, foundation type and

embedment depth, structural properties, improved zone dimensions. Thus, the current level of investigation on the subject covers an adequately detailed range of parameters. Nevertheless, the application of this methodology in engineering practice would require in many cases to separately include the effects of the aforementioned parameters, thus, assume a coupled relation between them. In order to increase the accuracy of the methodology a validation of this simplified assumption would be necessary.

iii) The vast majority of the experimental and numerical studies assumes soil profiles with uniform distribution of sand properties, i.e., in terms of relative density and gradation, within the liquefiable soil layers. Under these conditions, liquefaction initiates from the top layers due to the combination of increased applied shear stress and reduced resistance to liquefaction and propagates to the bottom of the soil profile. Nevertheless, in actual field conditions it is often the case that a "weak" layer (e.g., of low relative density) is interlaid within the soil profile. This "weak" layer will liquefy first and thereafter it will possibly act as a natural isolation preventing the upper layers from liquefying. Thus, a more elaborate consideration of the soil formation may ensure the feasibility of the upper – surficial – soil layers and eliminate the need of ground improvement.

iv) The main focus of this Thesis as well as the bulk of literature studies in evaluation the foundation performance are the liquefaction-induced building settlements. On the other hand, footing rotations, which are equally important for the integrity of the foundation, are grossly overlooked. This has happened for a number of reasons. Most importantly, the simulation of settlements requires a deterministic approach regarding soil properties whereas the simulation of rotations demands a probabilistic approach that includes accidental imperfections of various soil conditions (e.g., layer distribution, surface inclination, angle of the incoming wave). Except for the simulation difficulties, footing rotations are overlooked since they are often considered i) to be restricted due to construction details and ii) to be correlated with the magnitude of settlements.

References

"FEMA 440 Improvement of Nonlinear Static Seismic Analysis Procedures." (2005). Washington.

Acacio, A. A., Kobayashi, Y., Towhata, I., Bautista, R. T., and Ishihara, K. (2001). "Subsidence of Building Foundation Resting Upon Liquefied Subsoil: Case Studies and Assessment." *Soils and Foundations*, 41(6), 111–128.

Adachi, T., Iwai, S., Yasui, M., and Sato, Y. (1992). "Settlement and inclination of reinforced concrete buildings in Dagupan City due to liquefaction during the 1990 Philippine earthquake." *Proc., 10th World Conf. on Earthquake Engineering, International Association for Earthquake Engineering (IAEE)*, Madrid, Spain, 147–152.

Adalier, K., Elgamal, A., Meneses, J., and Baez, J. . (2003). "Stone columns as liquefaction countermeasure in non-plastic silty soils." *Soil Dynamics and Earthquake Engineering*, 23(7), 571–584.

Andrianopoulos, K. I., Papadimitriou, A. G., and Bouckovalas, G. D. (2010). "Bounding surface plasticity model for the seismic liquefaction analysis of geostructures." *Soil Dynamics and Earthquake Engineering*, 30(10), 895–911.

Apostolou, M. (2011). "Soil–structure interaction under strong seismic moment: Material and geometric nonlinearity." *PhD, NTUA, Athens*.

Arulmoli, K., Muraleetharan, K. K., Hossain, M. M., and Fruth, L. S. (1992). "VELACS: verification of liquefaction analyses by centrifuge studies; Laboratory Testing Program – Soil Data Report." *Research Report, The Earth. Technology Corporation*.

Blagov, D., Georgiev, T., Kisliakov, D., Pavlov, P., Petrov, B., and Traykova, M. (2020). "Rapid structural assessment of buildings – experience after the 26 th November 2019 Earthquake in Albania." *IOP Conference Series: Materials Science and Engineering*, 951, 012019.

Bouckovalas, G., Whitman, R., and Marr, W. (1984). "Permanent Displacement of Sand With Cyclic Loading." *Journal of Geotechnical Engineering*, American Society of Civil Engineers, 110(11), 1606–1623.

Bouckovalas, G. D., and Papadimitriou, A. G. (2003). "Multi-variable relations for soil effects on seismic ground motion." *Earthquake Engineering & Structural Dynamics*, 32(12), 1867–1896.

Bouckovalas, G. D., Papadimitriou, A. G., Niarchos, D. G., and Tsiapas, Y. Z. (2011). "Sand fabric evolution effects on drain design for liquefaction mitigation." *Soil Dynamics and Earthquake Engineering*, 31(10), 1426–1439.

Bouckovalas, G. D., Tsiapas, Y. Z., Theocharis, A. I., and Chaloulos, Y. K. (2016). "Ground response at liquefied sites: seismic isolation or amplification?" *Soil Dynamics and Earthquake Engineering*, 91, 329–339.

Bouckovalas, G. D., Tsiapas, Y. Z., Zontanou, V. A., and Kalogeraki, C. G. (2017). "Equivalent Linear Computation of Response Spectra for Liquefiable Sites: The Spectral Envelope Method." *Journal of Geotechnical and Geoenvironmental Engineering*, 143(4), 04016115.

Bouckovalas, G. D., Theocharis, A., Tsiapas, Y. Z., and Chaloulos, Y. K. (2013). "Numerical analysis of liquefied ground response." *International Conference on Earthquake Geotechnical Engineering, from Case History to Practice, in Honor of Professor Kenji Ishihara (ICEGE2013), Istanbul, Turkey, June 17-19*.

Boulanger, R. W., and Idriss, I. M. (2014). *CPT and SPT based liquefaction triggering procedures. Report No. UCD/CGM-14/01, Center for Geotechnical Modeling, University of California, Davis*.

Boulanger, R. W., and Ziotopoulou, K. (2013). "Formulation of a sand plasticity plane-strain model for earthquake engineering applications." *Soil Dynamics and Earthquake Engineering*, 53, 254–267.

Bray, J. D., and Macedo, J. (2017). "6th Ishihara lecture: Simplified procedure for estimating liquefaction-induced building settlement." *Soil Dynamics and Earthquake Engineering*, 102, 215–231.

Bray, J., Cubrinovski, M., Zupan, J., and Taylor, M. (2014). "Liquefaction Effects on Buildings in the Central Business District of Christchurch." *Earthquake Spectra*, 30(1), 85–109.

Bullock, Z., Karimi, Z., Dashti, S., Porter, K., Liel, A. B., and Franke, K. W. (2019). "A physics-informed semi-empirical probabilistic model for the settlement of shallow-founded structures on liquefiable ground." *Géotechnique*, 69(5), 406–419.

Byrne, P. M., Park, S.-S., Beaty, M., Sharp, M., Gonzalez, L., and Abdoun, T. (2004). "Numerical modeling of liquefaction and comparison with centrifuge tests." *Canadian Geotechnical Journal*, 41(2), 193–211.

Carnevalle, R., and Elgamal, A. (1994). "Experimental results of RPI centrifuge model No. 12." *Proceedings of the international conference on verification of numerical procedures for the analysis of soil liquefaction problems, Davis*, CA, 17-20, 1019–1026.

Chen, Z., Trombetta, N. W., Hutchinson, T. C., Mason, H. B., Bray, J. D., and Kutter, B. L. (2013). "Seismic System Identification Using Centrifuge-based Soil-Structure Interaction Test Data." *Journal of Earthquake Engineering*, 17(4), 469–496.

Cheng, Z., and Detournay, C. (2021). "Formulation, validation and application of a practice-oriented two-surface plasticity sand model." *Computers and Geotechnics*, 132, 103984.

Coelho, P. A. L. F., Haigh, S. K., and Madabhushi, S. P. G. (2004). "Centrifuge modelling of the effects of earthquake-induced liquefaction on bridge foundations." *Proc. 11th International Conferene on Soil Dynamics and Earthquake Engineering*, Berkeley, California.

Cubrinovski, M., Bray, J. D., Taylor, M., Giorgini, S., Bradley, B., Wotherspoon, L., and Zupan, J. (2011). "Soil Liquefaction Effects in the Central Business District during the February 2011 Christchurch Earthquake." *Seismological Research Letters*, 82(6), 893–904.

Cubrinovski, M., Bradley, B., Wotherspoon, L., Green, R., Bray, J., Wood, C., Pender, M., Allen, J., Bradshaw, A., Rix, G., Taylor, M., Robinson, K., Henderson, D., Giorgini, S., Ma, K., Winkley, A., Zupan, J., O'Rourke, T., DePascale, G., and Wells, D. (2011). "Geotechnical aspects of the 22 February 2011 Christchurch earthquake." *Bulletin of the New Zealand Society for Earthquake Engineering*, 44(4), 205–226.

Cubrinovski, M., and Ishihara, K. (1998). "State Concept and Modified Elastoplasticity for Sand Modelling." *Soils and Foundations*, 38(4), 213–225.

Daja, S., Agp, B., and Muci, R. (2016). "Liquefaction potential in the adriatic coastal areas in Albania." *Proceedings of the 14th International Congress*, Thessaloniki.

Dashti, S., and Bray, J. D. (2013). "Numerical Simulation of Building Response on Liquefiable Sand." *Journal of Geotechnical and Geoenvironmental Engineering*, 139(8), 1235–1249.

Dashti, S., Bray, J. D., Pestana, J. M., Riemer, M., and Wilson, D. (2010). "Mechanisms of Seismically Induced Settlement of Buildings with Shallow Foundations on Liquefiable Soil." *Journal of Geotechnical and Geoenvironmental Engineering*, American Society of Civil Engineers, 136(1), 151–164.

De Alba, P., Chan, C. K., and Seed, R. B. (1976). "Sand Liquefaction in Large-Scale Simple Shear Tests." *Journal of the Geotechnical Engineering Division*, 102(9), 909–927.

de Barros, F., and Luco, J. (1995). “Identification of foundation impedance functions and soil properties from vibration tests of the Hualien containment model.” *Soil Dynamics and Earthquake Engineering*, 14(4), 229–248.

Deng, L., and Kutter, B. L. (2012). “Characterization of rocking shallow foundations using centrifuge model tests.” *Earthquake Engineering & Structural Dynamics*, 41(5), 1043–1060.

Dimitriadi, V. (2014). “Performance Based Design and Soil Improvement Methods of Shallow Foundations on Liquefiable Soils.” PhD Thesis, Dept of Civil Engineering, NTUA, Athens.

Dimitriadi, V. E., Bouckovalas, G. D., and Papadimitriou, A. G. (2017). “Seismic performance of strip foundations on liquefiable soils with a permeable crust.” *Soil Dynamics and Earthquake Engineering*, Elsevier Ltd, 100, 396–409.

Dimitriadi, V. E., Bouckovalas, G. D., Chaloulos, Y. K., and Aggelis, A. S. (2018). “Seismic liquefaction performance of strip foundations: Effect of ground improvement dimensions.” *Soil Dynamics and Earthquake Engineering*, Elsevier, 106, 298–307.

Dobry, R., and Gazetas, G. (1986). “Dynamic Response of Arbitrarily Shaped Foundations.” *Journal of Geotechnical Engineering*, 112(2), 109–135.

Drosos, V., Georgarakos, T., Loli, M., Anastasopoulos, I., Zarzouras, O., and Gazetas, G. (2012). “Soil-Foundation-Structure Interaction with Mobilization of Bearing Capacity: Experimental Study on Sand.” *Journal of Geotechnical and Geoenvironmental Engineering*, 138(11), 1369–1386.

Duni, L., and Theodoulidis, N. (2020). “Short Note on the November 26, 2019, Durrës (Albania) M6.4 Earthquake: Strong Ground Motion with Emphasis in Durrës City.” *EMSC on Line Report*.

Elgamal, A., Lu, J., and Yang, Z. (2005). “Liquefaction-induced settlement of shallow foundations and remediation: 3D numerical simulation.” *Journal of Earthquake Engineering*, Department of Structural Engineering, University of California, San Diego, San Diego, CA 92093, United States, 9(SPEC. ISS.), 17–45.

Elgamal, A., Yang, Z., and Parra, E. (2002). “Computational modeling of cyclic mobility and post-liquefaction site response.” *Soil Dynamics and Earthquake Engineering*, 22(4), 259–271.

Farrel, T., and Kutter, B. L. (1994). “Experimental results of Model No. 12.” *Proceedings of the international conference on verification of numerical procedures for the analysis of soil liquefaction problems, Davis*, CA, 17-20, 1019–1026.

Federal Emergency Management Agency (FEMA). (1997). *NEHRP guidelines for the seismic rehabilitation of buildings*. (FEMA Publication No 273, ed.), Washington, D.C.

Gajan, S., and Kutter, B. L. (2008). "Capacity, settlement, and energy dissipation of shallow footings subjected to rocking." *Journal of Geotechnical and Geoenvironmental Engineering*, 134(8), 1129–1141.

Gajan, S., Kutter, B. L., Phalen, J. D., Hutchinson, T. C., and Martin, G. R. (2005). "Centrifuge modeling of load-deformation behavior of rocking shallow foundations." *Soil Dynamics and Earthquake Engineering*, 25(7–10), 773–783.

Garini, E., Anastasopoulos, I., and Gazetas, G. (2019). "Soil, basin and soil–building–soil interaction effects on motions of Mexico City during seven earthquakes." *Géotechnique*, 1–27.

Gazetas, G. (1991). "Foundation Vibrations." *Foundation Engineering Handbook*, Springer US, Boston, MA, 553–593.

Ghosh, B., and Madabhushi, S. P. G. (2007). "Centrifuge modelling of seismic soil structure interaction effects." *Nuclear Engineering and Design*, 237(8), 887–896.

Ghosh, B., and Madabhushi, S. P. G. (2003). "A numerical investigation into effects of single and multiple frequency earthquake motions." *Soil Dynamics and Earthquake Engineering*, Geotechnical Research Group, Department of Engineering, University of Cambridge, Cambridge, United Kingdom, 23(8), 691–704.

Hellenic Society of Earthquake Eng. (2020). *Albania earthquake of November 26, 2019 - HAEE Report on Structural and Geotechnical Damage*.

Hughes, F. E., and Madabhushi, S. P. G. (2019). "Liquefaction induced displacement and rotation of structures with wide basements." *Soil Dynamics and Earthquake Engineering*, 120, 75–84.

Ishihara, K., Acacio, A. A., and Towhata, I. (1993). "Liquefaction-Induced Ground Damage in Dagupan in the July 16, 1990 Luzon Earthquake." *Soils and Foundations*, 33(1), 133–154.

Ishihara, K., and Yoshimine, M. (1992). "Evaluation of Settlements in Sand Deposits Following Liquefaction During Earthquakes." *Soils and Foundations*, 32(1).

Itasca. (2012). "FLAC3D version 5.0." *Itasca Consulting Group Inc.*

Kalogeraki, C., and Zontanou, V. (2014). "Re-evalution of factor of safety against seismic liquefaction." Diploma Thesis, NTUA, Athens.

Kammerer, A. ., Wu, J., Riemer, M., Pestana, J. M., and Seed, R. B. (2001). "Use of Cyclic Simple Shear Testing in Evaluation of the Deformation Potential of Liquefiable Soils." *4th International Conference on Recent Advances in Geotechnical Earthquake Engineering and Soil Dynamics*.

Karamitros, D. K. (2010). "Development of a Numerical Algorithm for The Dynamic Elastoplastic Analysis of Geotechnical Structures in Two and Three Dimensions." PhD Thesis, Dept of Civil Engineering, NTUA, Athens.

Karamitros, D. K., Bouckovalas, G. D., and Chaloulos, Y. K. (2013). "Insight into the Seismic Liquefaction Performance of Shallow Foundations." *Journal of Geotechnical and Geoenvironmental Engineering*, American Society of Civil Engineers, 139(4), 599–607.

Karamitros, D. K., Bouckovalas, G. D., and Chaloulos, Y. K. (2013). "Seismic settlements of shallow foundations on liquefiable soil with a clay crust." *Soil Dynamics and Earthquake Engineering*, 46(0), 64–76.

Karamitros, D. K., Bouckovalas, G. D., Chaloulos, Y. K., and Andrianopoulos, K. I. (2013). "Numerical analysis of liquefaction-induced bearing capacity degradation of shallow foundations on a two-layered soil profile." *Soil Dynamics and Earthquake Engineering*, 44(0), 90–101.

Karimi, Z., and Dashti, S. (2016). "Seismic Performance of Shallow Founded Structures on Liquefiable Ground: Validation of Numerical Simulations Using Centrifuge Experiments." *Journal of Geotechnical and Geoenvironmental Engineering*, 142(6), 04016011.

Karimi, Z., and Dashti, S. (2015). "Numerical Simulation of Earthquake Induced Soil Liquefaction: Validation against Centrifuge Experimental Results." *IFCEE 2015*, American Society of Civil Engineers, Reston, VA, 11–20.

Karimi, Z., and Dashti, S. (2016). "Numerical and Centrifuge Modeling of Seismic Soil–Foundation–Structure Interaction on Liquefiable Ground." *Journal of Geotechnical and Geoenvironmental Engineering*, 142(1), 04015061.

Kawasaki, K., Sakai, T., Yasuda, S., and Satoh, M. (1998). "Earthquake-induced settlement of an isolated footing for power transmission power." *Centrifuge 98*, 271–276.

Kishida, H. (1966). "Damage to Reinforced Concrete Buildings in Niigata City with Special Reference to Foundation Engineering." *Soils and Foundations*, 6(1), 71–88.

Knappett, J. A., Haigh, S. K., Madabhushi, S. P. G., Paolucci, R., Shirato, M., and Yilmaz, M. T. (2008). "Seismic behaviour of shallow foundations: Shaking table

experimentsvs numerical modelling." *Earthquake Engineering & Structural Dynamics*, 37(4), 577–595.

Kociu, S. (2004). "Induced Seismic Impacts Observed in Coastal Area of Albania: Case Studies." *5th Conference of the International Conference on Case Histories in Geotechnical Engineering*, New York, NY.

Kokkali, P., Abdoun, T., and Anastasopoulos, I. (2015). "Centrifuge Modeling of Rocking Foundations on Improved Soil." *Journal of Geotechnical and Geoenvironmental Engineering*, 141(10), 04015041.

Kourkoulis, R., Anastasopoulos, I., Gelagoti, F., and Kokkali, P. (2012). "Dimensional Analysis of SDOF Systems Rocking on Inelastic Soil." *Journal of Earthquake Engineering*, 16(7), 995–1022.

Kramer, S. L., Sideras, S. S., and Greenfield, M. W. (2016). "The timing of liquefaction and its utility in liquefaction hazard evaluation." *Soil Dynamics and Earthquake Engineering*, 91, 133–146.

Krstelj, I., and Prevost, J. (1994). "Experimental results of Model No. 12." *Proceedings of the international conference on verification of numerical procedures for the analysis of soil liquefaction problems, Davis*, CA, 17-20, 1007–1017.

Kutter, B. L., Chen, Y., and Shen, C. K. (1994). "Triaxial and torsional shear test results for sand." *Report CR94.003-SHR*, Naval Facilities Engineering Services Center, Port Hueneme, CA.

Liu, L., and Dobry, R. (1997). "Seismic response of shallow foundation on liquefiable sand." *Journal of Geotechnical and Geoenvironmental Engineering*, ASCE, 123(6), 557–566.

Manzari, M. T., and Dafalias, Y. F. (1997). "A critical state two-surface plasticity model for sands." *Géotechnique*, 47(2), 255–272.

Maravas, A., Mylonakis, G., and Karabalis, D. L. (2014). "Simplified discrete systems for dynamic analysis of structures on footings and piles." *Soil Dynamics and Earthquake Engineering*, 61.

Meyerhof, G. G., and Hanna, A. M. (1978). "Ultimate bearing capacity of foundations on layered soils under inclined load." *Canadian Geotechnical Journal*, NRC Research Press, 15(4), 565–572.

Mylonakis, G., and Karatzia, X. (2019). "Η Παράμετρος Κύματος (1/σ) στην Ανάλυση της Αλληλεπίδρασης Εδάφους – Κατασκευής." *4ο Πανελλήνιο συνέδριο Αντισεισμικής Μηχανικής και Τεχνικής Σεισμολογίας*.

Mylonakis, G., Nikolaou, S., and Gazetas, G. (2006). “Footings under seismic loading: Analysis and design issues with emphasis on bridge foundations.” *Soil Dynamics and Earthquake Engineering*, 26(9), 824–853.

Naesgaard, E., Byrne, P. M., and Ven Huizen, G. (1998). “Behaviour of light structures founded on soil ‘crust’ over liquefied ground.” *Geotechnical Special Publication*, 75, 422–433.

Newmark, N. M. (1965). “Effects of Earthquakes on Dams and Embankments.” *Géotechnique*, Thomas Telford Ltd , 15(2), 139–160.

Newmark, N. M., and Hall, W. (1982). “Earthquake spectra and design.” *Earthquake Engineering Research Institute*.

NIST, G. (2012). *Soil-Structure Interaction for Building Structures*.

Olarte, J., Dashti, S., and Liel, A. B. (2018). “Can ground densification improve seismic performance of the soil-foundation-structure system on liquefiable soils?” *Earthquake Engineering & Structural Dynamics*, 47(5), 1193–1211.

Oshaki, Y. (1966). “Niigata Earthquake, 1964-Building damage and soil condition.” *Soils and Foundations*, 6, 112–128.

Özener, P. T., Greenfield, M. W., Sideras, S. S., and Kramer, S. L. (2020). “Identification of time of liquefaction triggering.” *Soil Dynamics and Earthquake Engineering*, 128, 105895.

P.Wolf, J. (1985). *Dynamic Soil-Structure Interaction*.

Pais, A., and Kausel, E. (1988). “Approximate formulas for dynamic stiffnesses of rigid foundations.” *Soil Dynamics and Earthquake Engineering*, 7(4), 213–227.

Paolucci, R., Figini, R., and Petrini, L. (2013). “Introducing Dynamic Nonlinear Soil-Foundation-Structure Interaction Effects in Displacement-Based Seismic Design.” *Earthquake Spectra*, 29(2), 475–496.

Papadimitriou, A. G., and Bouckovalas, G. D. (2002). “Plasticity model for sand under small and large cyclic strains: a multiaxial formulation.” *Soil Dynamics and Earthquake Engineering*, 22(3), 191–204.

Papadimitriou, A. G., Bouckovalas, G. D., and Dafalias, Y. F. (2001). “Plasticity Model for Sand under Small and Large Cyclic Strains.” *Journal of Geotechnical and Geoenvironmental Engineering*, 127(11), 973–983.

Pecker, A., Paolucci, R., Chatzigogos, C., Correia, A. A., and Figini, R. (2014). "The role of non-linear dynamic soil-foundation interaction on the seismic response of structures." *Bulletin of Earthquake Engineering*, 12(3), 1157–1176.

Prevost, J., Krstelj, I., and Popescu, R. (1994). "Overview of experimental results for centrifuge model No. 12." *Proceedings of the international conference on verification of numerical procedures for the analysis of soil liquefaction problems, Davis*, CA, 17-20, 1619–1634.

Quigley, M. C., Bastin, S., and Bradley, B. A. (2013). "Recurrent liquefaction in Christchurch, New Zealand, during the Canterbury earthquake sequence." *Geology*, 41(4), 419–422.

Ramberg, W., and Osgood, W. R. (1943). *Description of stress-strain curve by three parameters*. Washington,D.C.

Rathje, E. M., Abrahamson, N. A., and Bray, J. D. (1998). "Simplified Frequency Content Estimates of Earthquake Ground Motions." *Journal of Geotechnical and Geoenvironmental Engineering*, 124(2), 150–159.

Richards, R., Elms, D. G., and Budhu, M. (1993). "Seismic Bearing Capacity and Settlements of Foundations." *Journal of Geotechnical Engineering*, American Society of Civil Engineers, 119(4), 662–674.

Richards, R., Elms, D. G., and Budhu, M. (1990). "Dynamic Fluidization of Soils." *Journal of Geotechnical Engineering*, 116(5), 740–759.

Ross, G. A., Seed, H. B., and Migliaccio, R. R. (1969). "Bridge Foundation Behavior In Alaska Earthquake." *Journal of the Soil Mechanics and Foundations Division*, 95(4), 1007–1036.

Sancio, R. ., Bray, J. ., Stewart, J. ., Youd, T. ., Durgunoğlu, H. ., Önalp, A., Seed, R. ., Christensen, C., Baturay, M. ., and Karadayılar, T. (2002). "Correlation between ground failure and soil conditions in Adapazari, Turkey." *Soil Dynamics and Earthquake Engineering*, 22(9–12), 1093–1102.

Schofield, A. N. (1980). "Cambridge Geotechnical Centrifuge Operations." *Géotechnique*, 30(3), 227–268.

Schofield, A. N. (1981). "Dynamic and earthquake geotechnical centrifuge modelling." *Proc. Int. Conf. Recent Advances in Soil Dynamics and Earthquake Engrg.*, Missouri.

Seed, H. B., and Idriss, I. M. (1971). "Simplified Procedure for Evaluating Soil Liquefaction Potential." *Journal of the Soil Mechanics and Foundations Division*, 97(9), 1249–1273.

Seed, H. (1982). “Ground motions and soil liquefaction during earthquakes.” *Earthquake engineering research insititue*.

Seed, H., and Idrisss, I. (1967). “Analysis of soil liquefaction: Niigata Earthquake.” *J. SMFD, ASCE*, 93, 83–108.

Silver, M., and Seed, H. B. (1971). “Volume Changes in Sands During Cyclic Loading.” *Journal of the Soil Mechanics and Foundations Division*, 97(9), 1171–1182.

Sitar, N., and Hausler, E. A. (2012). “Influence of Ground Improvement on Liquefaction Induced Settlements: Observations from Case Histories and Centrifuge Experiments.” *Invited Lecture presented to the Korean Geotechnical Society*, Seoul, Korea, March 22.

Stewart, J. P., Fenves, G. L., and Seed, R. B. (1999). “Seismic soil-structure interaction in buildings. I: Analytical methods.” *Journal of Geotechnical and Geoenvironmental Engineering*.

Stewart, J. P., Seed, R. B., and Fenves, G. L. (1999). “Seismic Soil-Structure Interaction in Buildings. II: Empirical Findings.” *Journal of Geotechnical and Geoenvironmental Engineering*, 125(1), 38–48.

Stewart, J., and Fenves, G. (1998). “System identification for evaluating soil–structure interaction effects in buildings from strong motion recordings.” *Earthquake Engineering & Structural Dynamics*.

Tasiopoulou, P., and Gerolymos, N. (2016). “Constitutive modeling of sand: Formulation of a new plasticity approach.” *Soil Dynamics and Earthquake Engineering*, 82, 205–221.

Tileylioglu, S., Stewart, J. P., and Nigbor, R. L. (2011). “Dynamic stiffness and damping of a shallow foundation from forced vibration of a field test structure.” *Journal of Geotechnical and Geoenvironmental Engineering*, 137(4), 344–353.

Todorovska, M. I. (2002). “Full-scale experimental studies of soil-structure interaction.” *ISET Journal of Earthquake Technology*, 39(422), 139–165.

Tokimatsu, K., and Seed, H. B. (1987). “Evaluation of Settlement in Sands due to Earthquake Shaking.” *Journal of geotechnical engineering*, Tokyo Inst of Technology, Tokyo, Jpn, Tokyo Inst of Technology, Tokyo, Jpn, 113(8), 861–878.

Tokimatsu, K., Hino, K., Suzuki, H., Ohno, K., Tamura, S., and Suzuki, Y. (2019). “Liquefaction-induced settlement and tilting of buildings with shallow foundations based on field and laboratory observation.” *Soil Dynamics and Earthquake Engineering*, 124, 268–279.

Tokimatsu, K., Kojima, H., Kuwayama, S., Abe, A., and Midorikawa, S. (1994). "Liquefaction-Induced Damage to Buildings in 1990 Luzon Earthquake." *Journal of Geotechnical Engineering*, 120(2), 290–307.

Tokimatsu, K., and Yoshimi, Y. (1983). "Empirical correlation of soil liquefaction based on SPT N-value and fines content." *Soils and Foundations*, 23(4), 56–74.

Trifunac, M. D., Ivanović, S. S., and Todorovska, M. I. (2001). "Apparent Periods of a Building. I: Fourier Analysis." *Journal of Structural Engineering*, 127(5), 517–526.

Trombetta, N. W., Mason, H. B., Chen, Z., Hutchinson, T. C., Bray, J. D., and Kutter, B. L. (2013). "Nonlinear dynamic foundation and frame structure response observed in geotechnical centrifuge experiments." *Soil Dynamics and Earthquake Engineering*, 50, 117–133.

Tsiapas, Y. Z. (2017). "Seismic Response Analysis of Liquefiable Ground with Computational Methods." PhD Thesis, Dept of Civil Engineering, NTUA, Athens.

Tsiapas, Y. Z., and Bouckovalas, G. D. (2018). "Selective Filtering of Numerical Noise in Liquefiable Site Response Analyses." *Geotechnical Earthquake Engineering and Soil Dynamics V*, American Society of Civil Engineers, Austin, TX, June 10-13, 248–257.

Vlachakis, G., Vlachaki, E., and Lourenço, P. B. (2020). "Learning from failure: Damage and failure of masonry structures, after the 2017 Lesvos earthquake (Greece)." *Engineering Failure Analysis*, 117, 104803.

Vucetic, M., and Dobry, R. (1991). "Effect of soil plasticity on cyclic response." *Journal of geotechnical engineering*, 117(1), 89–107.

Wong, H. L., and Luco, J. E. (1985). "Tables of impedance functions for square foundations on layered media." *International Journal of Soil Dynamics and Earthquake Engineering*, 4(2), 64–81.

Yamamuro, J. A., and Lade, P. V. (1998). "Steady-State Concepts and Static Liquefaction of Silty Sands." *Journal of Geotechnical and Geoenvironmental Engineering*, 124(9), 868–877.

Yang, M., Taiebat, M., and Dafalias, Y. F. (2020). "SANISAND-MSf: a sand plasticity model with memory surface and semifluidised state." *Géotechnique*, 1–20.

Yang, Z., Elgamal, A., and Parra, E. (2003). "Computational Model for Cyclic Mobility and Associated Shear Deformation." *Journal of Geotechnical and Geoenvironmental Engineering*, 129(12), 1119–1127.

Yoshida, N., Tokimatsu, K., Yasuda, S., Kokusho, T., and Okimura, T. (2001). "Geotechnical Aspects of Damage in Adapazari City During 1999 Kocaeli, Turkey Earthquake." *Soils and Foundations*, 41(4), 25–45.

Yoshimi, Y., and Tokimatsu, K. (1977). "Settlement of Buildings on Saturated Sand During Earthquakes." *Soils and Foundations*, 17(1), 23–38.

Youd, T. L., and Carter, B. L. (2005). "Influence of Soil Softening and Liquefaction on Spectral Acceleration." *Journal of Geotechnical and Geoenvironmental Engineering*, 131(7), 811–825.

Youd, T., Idriss, I., Andrus, R., Arango, I., Castro, G., Christian, J., Dobry, R., Finn, W., Harder, L., Hynes, M., Ishihara, K., Koester, J., Liao, S., Marcuson, W., Martin, G., Mitchell, J., Moriwaki, Y., Power, M., Robertson, P., Seed, R., and Stokoe, K. (2001). "Liquefaction Resistance of Soils: Summary Report from the 1996 NCEER and 1998 NCEER/NSF Workshops on Evaluation of Liquefaction Resistance of Soils." *Journal of Geotechnical and Geoenvironmental Engineering*, American Society of Civil Engineers, 127(10), 817–833.

Zamani, N., and El Shamy, U. (2012). "Analysis of the seismic response of soil–foundation–structure systems using a microscale framework." *Soil Dynamics and Earthquake Engineering*, 43, 398–412.